THERMO-HYDRO-MECHANICAL ANALYSIS OF FRACTURES AND WELLBORES IN PETROLEUM/GEOTHERMAL RESERVOIRS

A Dissertation

by

MOHAMMADREZA SAFARIFOROSHANI

Submitted to the Office of Graduate Studies of
Texas A&M University
in partial fulfillment of the requirements for the degree of

DOCTOR OF PHILOSOPHY

Chair of Committee,	Ahmad Ghassemi
Committee Members,	Stephen A. Holditch
	Peter P. Valko
	Eduardo Gildin
	Amine Benzerga
Head of Department,	A. Daniel Hill

August 2013

Major Subject: Petroleum Engineering

ABSTRACT

The thesis considers three-dimensional analyses of fractures and wellbores in low-permeability petroleum/geothermal reservoirs, with a special emphasis on the role of coupled thermo-hydro-mechanical processes. Thermoporoelastic displacement discontinuity and stress discontinuity methods are elaborated for infinite media. Furthermore, injection/production-induced mass and heat transport inside fractures are studied by coupling the displacement discontinuity method with the finite element method. The resulting method is then used to simulate problems of interest in wellbores and fractures for related to drilling and stimulation.

In the examination of fracture deformation, the nonlinear behavior of discontinuities and the change in status from joint (hydraulically open, mechanically closed) to hydraulic fracture (hydraulically open, mechanically open) are taken into account. Examples are presented to highlight the versatility of the method and the role of thermal and hydraulic effects, three-dimensionality, hydraulic/natural fracture deformation, and induced micro earthquakes. Specifically, injection/extraction operations in enhanced geothermal reservoirs and hydraulic/thermal stimulation of fractured reservoirs are studied and analyzed with reference to induced seismicity. In addition, the fictitious stress method is used to study three-dimensional wellbore stresses in the presence of a weakness plane. It is shown that the coupling of hydro-thermo-mechanical processes plays a very important role in low-permeability reservoirs and should be considered when predicting the behavior of fractures and wellbores.

DEDICATION

This dissertation is gratefully dedicated to my wife, Samaneh, and my parents, Mohammad and Fatemeh. Without their never ending support and love, my work would never have been completed.

ACKNOWLEDGEMENTS

I would like to express my deepest gratitude to my adviser Professor Ahmad Ghassemi for his consistent support and guidance throughout my PhD studies. His deep knowledge on displacement discontinuity and coupled physics analysis had a tremendous effect on this research. It would have been impossible to complete this work without his helpful supervision. The lessons learned from him will be an invaluable asset in my career.

I would also like to thank professors in my committee for their timely advice and directions in completing the project. Furthermore, I would like to spread my appreciation to Dr. A. Nourzad and Professor S. Mohammadi in University of Tehran, civil engineering department, who familiarize me with advanced numerical methods.

Moreover, I extend my sincere appreciation to fellow graduate students in the petroleum engineering department, who have accompanied me in this exciting journey.

Finally, I want to thank my parents and my wonderful wife, Samaneh for their endless support and patience over years of my study.

TABLE OF CONTENTS

LIST OF FIGURES

LIST OF TABLES

1. INTRODUCTION

1.1. Overview

The simulation of hydraulic/natural fractures and stress analysis of wellbores in low-permeability petroleum/geothermal reservoirs often requires a three-dimensional (3D) multiphysics approach that considers fluid and heat flow in relation to the mechanics of the surrounding rocks. Although three-dimensionality and the effects of pore pressure and temperature are frequently omitted for mathematical and physical convenience, their effects in reservoir geomechanics problems are substantial, especially in distributions of failure potentials around an injection-induced fracture in naturally fractured rock (reservoir stimulated volume), analyses of enhanced geothermal reservoir performance, and wellbore stress analysis [1-3].

Fluid flow and heat transfer in the porous rock matrix and fracture network and modifications in the fracture aperture due to pressure and temperature must also be considered in the hydraulic/thermal stimulation of fractured enhanced geothermal and petroleum reservoirs. Moreover, in stimulation processes, the shear slip of pre-existing natural fracture is the dominated failure mode [4, 5]. Shear slip increases the permeability of the fracture through dilation [5, 6]. It is therefore necessary to model the occurrence of shear slip to predict stimulated reservoir volume, permeability dynamics, and the occurrence of failure (microseismicity) during the development of enhanced geothermal reservoirs or during hydraulic fracturing in fractured reservoirs.

Moreover, temperature and pressure gradients, the presence of weakening planes or natural fractures, and an arbitrarily oriented stress field are important parameters to

consider in stress analyses of wellbores in unconventional reservoirs [1, 7, 8]. Therefore, proper analyses of wellbores need to consider 3D coupled thermoporomechanical physics in fractured reservoirs.

The numerical technique developed in the current study includes 3D coupled thermoporomechanical behavior of fractured rock in the analysis of wellbores, enhanced geothermal systems, and hydraulic/thermal stimulation of naturally fractured reservoirs.

1.2. Objectives and significance

The overarching objective of the present study is to develop a numerical model to study the effect of thermoporomechanical processes on fractures and wellbores in low-permeability reservoirs. To achieve this objective, mixed source/discontinuity technique (fluid source, heat source, and displacement or stress discontinuity), is coupled with the finite element method. The significance of the study is revealed through analyses of three major reservoir geomechanics problems: (a) a 3D study of failure or microseismic events possible during hydraulic or thermal stimulation of fractured reservoirs, (b) a response analysis of enhanced geothermal reservoirs, that considers the role of thermoporomechanics and fracture deformation, and (c) a 3D wellbore stress analysis in which plane strain or axisymmetric conditions are not fulfilled.

1.3. Motivations

Given the complexity of rock formations and the existence of natural fractures, pure elastic and continuum models by themselves are insufficient to provide accurate stress analysis in many problems of reservoir geomechanics. One of the reasons for this

has to do with the porous medium behavior of rock. Rock pores are usually saturated with fluid and represent a specific distribution of pressure and temperature throughout the reservoir. Drilling or injection/production into the saturated fractured rock disturbs the initial pore pressure and temperature. Stress analyses of these processes must take into account the influences of changes in pore pressure and temperature induced by fluid flow and those induced by stresses.

The method developed here incorporate thermoporomechanical processes into the injection/extraction of fluid into or from a manmade or natural fracture system with variable rate, opening and shearing displacement discontinuity (DD), and the possibility of fracture propagation in different modes. Moreover, the interaction of preexisting natural discontinuities and the hydraulic fracture is also considered. Analyses of geomechanical problems that use the proposed method can shed light on hydraulic/thermal stimulation mechanisms of fractured reservoirs.

Like stimulation problems in geothermal and petroleum reservoirs, wellbore stress analysis in fractured reservoirs necessitates 3D thermoporomechanical analysis, especially when a wellbore passes through a weakening plane, or stress distribution around wellbore is interested at the end section (leak-off test). The model considers mechanical, hydraulic, and thermal interactions during the drilling process. Time-dependent characteristics of the problem are also taken into account. In wellbore stress analyses, rock is treated as a continuous material that was formed in an environment of complex stress, including discontinuities.

1.4. Literature review

Biot [9, 10] and Biot and Willis[11] were the pioneers who stablishe fully coupling of fluid pressure and solid structure stress fields. Time-dependent fluid flow is incorporated into the poroelastic theory by combining the mass conservation of fluid with Darcy's law. Following Biot's study, the theory of poroelasticity was developed by many researchers, including Verruijt [12] in a specialized version for soil mechanics and Rice and Cleary[13], who linked poroelastic parameters to rock and soil mechanics. In particular, Rice and Cleary emphasized the two asymptotic behaviors of a saturated rock: drained and undrained. Rice and Cleary's formulation significantly makes the explanation of poroelastic phenomena simpler.

In fluid-saturated porous rock, thermal gradients as well as pressure gradient, can significantly modify the stresses and pore pressure fields. This induces volumetric deformation due to thermal expansion and contraction of both the pore fluid and the rock solid. If the rock is heated and its structure prevented from moving, expansion of the fluid can lead to a substantial increase in pore pressure, and vice versa in the case of cooling. Therefore, the time-dependent poromechanical processes should be fully coupled to the transient temperature field. Thermally induced stresses have attracted the attention of many researchers. Carslaw and Jaeger[14] presented analytical solutions for many thermal conduction problems; however, they did not consider the coupling effect of mechanical or hydraulic processes. Yet drilling and injection/extraction phenomena affect the initial stresses, pore pressure, and temperature field, and they should be considered simultaneously.

The theory of thermoporomechanics analysis was initially developed by Schiffman [15] based on Biot's linear poroelasticity. After Schiffman's study, Palciauskas and Domenico [16] established thermoporoelasticity, assuming isothermal linear poroelasticity in combination with some nonisothermal parameters describing fluids, solid, and pore volume expansivities. McTigue[17] recast Palciauskas and Domenico's work to obtain a diffusion equation for a combination of mean total stress, fluid pressure, and temperature. Kurashige [18] extended the theory to incorporate the transportation of heat by pore fluid flow in addition to the effect of difference in expansibility between pore fluid and skeletal solid. The thermoporoelasticity theory used in the current study is in most respects identical to that outlined by McTigue.

In thermoporoelasticity theory, although the equations of hydromechanics are fully coupled in the sense that pore pressure influences deformation and deformation influences pore pressure, the coupling of temperature and mechanical work is unidirectional. Unidirectional coupling means that temperature has a large influence on stresses and strains, but strains do not lead to significant change in temperature. This is also the case for the relationship between pore pressure and temperature.

Briefly, the coupling among mechanical, hydrological, and thermal processes in this study is related directly and the stress and pore pressure fields cannot be calculated independent of temperature. Interactions of these three main components of thermoporoelasticity theory are indicated in Figure 1.

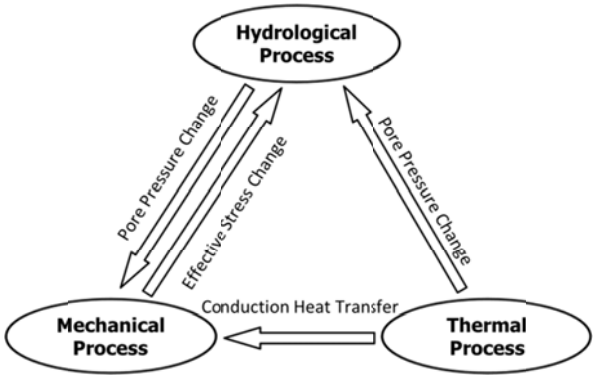

Figure 1. Coupling between thermal, hydrological and mechanical processes.

As is clear from Figure 1, convective heat transport is ignored. Convective heat transport is frequently ignored in low-permeability rocks [19] such as shale and granite. This is because in such rocks fluid flow velocity is extremely low and heat conduction controls the heat transfer process and heat convection is insignificant.

Although substantial improvements have been made in numerical modeling of the coupled thermoporoelastic response of fully saturated rock in reservoir geomechanics problems, some important technical issues specific to thermal and hydraulic stimulation of fractured reservoir and wellbore stress analysis still remain unresolved. In the following sections, the advantages and disadvantages of various analysis methods are reviewed briefly with reference to improvements in the current study.

1.4.1. Prior work on hydraulic/thermal stimulation analysis

In low-permeability reservoirs, fractures are the main pathway for fluid flow and heat exchange. Therefore, the analysis of the spatial/temporal of fractures has been the focus of many studies.

Many studies have shown that coupled thermo-hydro-mechanical processes have a large influence on the evolution of fracture permeability. Moreover, reservoir stimulation involves a combination of manmade fracture and natural fractures. Two approaches can be used to model a constructed fracture system response to injection/extraction: (a) a statistical fracture network approach in which the reservoir is simulated using a system of fractured rock blocks and (b) a deterministic fracture modeling approach in which major fractures are directly modeled. These fractures are often distinguished by direct imaging of the wellbore and geological/geophysical studies. In the past decades, various analytical models have been developed and used in each category. The current section briefly reviews some of the existing stochastic and deterministic models of a fracture system response to injection/extraction.

Elastic two-dimensional (2D) analytical models was used to formulized early models of reservoir hydraulic stimulation [20, 21] and ignored the effects of poroelasticity and thermoelasticity. Gringarten et al. [22, 23] modeled heat transfer in multiple fractures inside of impermeable hot dry rock by assuming that fractures were the same distance from each other and had a constant aperture. They assumed that the injection rate was constant, that only gravitational force resulted in fluid transport, and that mechanical processes were negligible. Nemat-Naser and Ohtsubo [24] presented governing equations for coupled fluid flow and heat transfer inside a fracture in an impermeable geothermal reservoir. They discretized derived steady state governing equations with the finite element model. They also implicitly considered the effects of secondary thermal fractures with increasing fracture conductivity. Bazant and Ohtsubo

[25] considered the same problem, retaining the effects of buoyancy, velocity head (kinetic energy), and head loss due to viscous friction in the flow equation. They also discretized governing equations with finite element methods.

Applications of linear elastic indirect boundary element methods in mining and reservoir rock mechanics were introduced by Crouch and Starfield [26]. They developed a flexible computational tool to analyze and calculate stresses around underground excavation and fractures in 2D configurations. They did not consider the effect of hydraulic or thermal phenomena, which are crucial in petroleum/geothermal reservoir geomechanics problems.

A thermoelastic analysis of enhanced geothermal reservoir was performed by Abe et al. [27] and Perkins and Gonzalez [28]. They took into account the possibility of secondary cracks creation during reservoir development. However, they ignore the effects of poroelasticity.

To better understand the effects of injection/extraction rate on reservoir response, Asgain [29] simulated fluid flow in a fracture system in an elastic 2D reservoir with elastic DD. Effects of leak-off from the fracture surface into the reservoir and the thermoporoelastic behavior of rock were not considered.

Detournay and Cheng [30] presented fundamental solutions for poroelastic DD in plane strain media. These fundamental solutions have been used by many researchers to analyze injection/extraction into a fracture system in poroelastic media. Vendamme et al. [31, 32], Carvalho [33], and Detournay and Cheng [34] introduced a 2D poroelastic analysis of a stationary crack in a reservoir. They showed the time-dependent property of

the fracture aperture during its surface pressurization. They did not consider fluid flow inside the fracture, the effect of thermoelasticity, or the coupling of poroelasticity and thermoelasticity. Swenson and Beikmann [35] coupled the fluid flow in rock joints with rock mass displacement in 2D configurations. They did not consider nonlinear behavior of joints in the normal direction. Moreover, they did not include fluid leak-off from the joint surface into the rock mass.

Kohl et al. [36] and Kohl and Hopkirk [37] presented a comprehensive thermo-hydro-mechanical analysis of the coupling of fluid flow in a rock joint with the finite element method while considering nonlinear behavior of the joint in the normal direction and buoyancy effects. Swenson and Hardemann[38] examined the same concept in 2D configurations and studied the effect of multiple fractures and their interactions. Neither Kohl et al., Kohl and Hopkirk, nor Swenson and Hardemann included the shear ride effect on permeability enhancement. They also did not consider the possibility of change in the rock joint behavior from mechanically closed to mechanically open.

Ghassemi [39] used a 3D poroelastic higher order DD method to investigate the behavior of a fracture with fluid flow. Fluid flow in the fracture was considered as a 2D steady state flow in a parallel plate and was treated using the finite element method. Although Ghassemi considered the three-dimensionality of problem and coupled the fluid flow inside the fracture with its mechanical response, he did not study the effects of multiple cracks or increased permeability due to shear ride.

Bruel [40] introduced a stochastic simplified thermoporoelastic method for simulating a circulation test in the Soultz-sous-Forets geothermal project in Rhine

Garben, France, without explicit consideration of flow through the rock. He used a discrete fracture network concept to study thermal and hydraulic effects on reservoir status. Rahman et al. [41] simulated natural fractures using a stochastic approach with a simplifying assumption regarding pressure distribution within fractures. They did not consider thermal effects. They included shear slippage of natural fractures and their effects on increased permeability in their analysis. Wang and Ghassemi [42] used a similar approach but with flow and poroelasticity as well as heat transport.

Warpinski et al. [5] presented an analysis and predictions of failure due to reservoir response to hydraulic stimulation. They included only an analytical approximation of hydrological stresses in their model and did not consider thermal effects. They also ignored the presence of natural fractures and their effects. Settari et al. [43] presented a different numerical model to relate reservoir failure to fracture geometry. They considered thermal effects and the heterogeneity properties of the reservoir. They calibrated a continuum model with a discrete jointed rock model. However, they did not consider the effects of multiple fractures and fluid flow inside of fractures.

Ghassemi et al. [44] applied the heat source element and integral equation method to investigate effects of 3D heat transfer over the life of an enhanced geothermal reservoir. Building on their earlier work, Ghassemi et al. [45, 46] developed a 3D heat extraction/thermal stress solution that was tied to an elastic stress/displacement analysis. They studied fracture aperture and ride variation in response to the injection of cold fluid into a single fracture in an assumed stress field. They did not study the effects of

multiple fractures or nonlinear behavior of the fracture in the normal direction. Ghassemi and Zhang [47] later made a fully coupled thermoporoelastic analysis of a crack. They used a 2D DD technique without flow modeling inside of fractures or the ability to model mechanically closed rock joints.

Murdoch and Germanovich [48] presented a poroelastic analysis of fluid flow in a single fracture and considered the transient behavior of rock joints from mechanically closed to mechanically open. However, they ignored thermal and shear ride effects on the increasing permeability of the fracture.

Ge and Ghassemi [49] developed an analytical technique to measure failure potential near enhanced geothermal reservoirs or hydraulic fractures due to fluid injection. They considered poroelastic and thermoelastic stresses but did not study the interactions of multiple fractures or fracture behavior in different states (mechanically open, mechanically closed). Rutqvist and Oldenberg [4] also studied induced failure due to injection/production in the Geysers Geothermal Field. They included coupled thermo-hydro-mechanical processes in 2D configurations. However, they did not study the effects of discontinuity and their interactions.

Ghassemi et al. [50] modified previous studies and coupled flow inside of fracture using simultaneous coupling of thermoelasticity and poroelasticity (pore pressure indirectly affected by temperature: Thermo-poroelasticity). They assumed a constant leak-off rate and plane fracture. They did not consider nonlinear behavior of rock joints. Tao and Ghassemi [51, 52] and Lee and Ghassemi [53] used a 2D coupled thermoporoelastic DD and finite difference method to study the problem. They

considered an increase in permeability due to shear ride and nonlinear behavior of a single joint in the normal direction.

Koh et al.[54] studied injection/production into a discrete fracture network. They considered shear ride on the fracture surface, its effect on increased permeability, and nonlinear behavior of the rock joint in the normal direction. They did not consider the possibility of change in the rock joint from mechanically closed to mechanically open.

Zhou et al.[55] used poroelastic 3D DD to study hydromechanical behavior of fluid flow inside of a fracture. They improved their model by simulating shear DD on the fracture surface [56]. Building on their previous work, they coupled fluid flow and convective heat transport inside the fracture to the fracture response in the normal and shear direction [57].

The current study is an improvement on the Ghassemi and Zhou [57] model. Improvements were made by considering thermal conduction inside of the fracture, nonlinear behavior of elastic rock joints in the normal direction [58-60], shear ride and its effect on increased permeability of the fracture, transient behavior of rock joints from mechanically closed to mechanically open (hydraulic fracture), and the interaction of multiple (natural) fractures on one another.

1.4.2. Previous work on wellbore stress analysis

Wellbore stress analysis is a procedure used to define concentrations of stress around a wellbore to investigate failure of the wellbore in a realistic state. When drilling occurs, the original stress state of the rock is disturbed and stress concentration forms. Early wellbore stress analysis models [61] relied on elastic 2D analytical models. These

elastic models considered only far-field stresses and traction boundaries at the wellbore surface (mud pressure) and ignored the effects of poroelasticity and thermoelasticity. A poroelastic stress analysis of a wellbore was presented by Detournay and Cheng [62]. They considered complete interactions between hydraulics and mechanics, but did not study wellbore inclination.

Rajapakse [63] introduced an analytical technique for determining the axisymmetric response of a cylindrical wellbore in a poroelastic medium. The medium was assumed to be fully saturated and governed by Biot's classic theory. He did not study the effect of thermal processes or the existence of discontinuities, which are inherent properties of fractured, low-permeability reservoirs.

A couple analytical solution for transient fluid flow and conductive heat diffusion from an injection well into a 2D, plane strain poroelastic medium under non hydrostatic principal direction loading was presented by Wang and Papamichos [64]. The same problem was solved analytically by Li and Roegiers [8, 65] under conditions of general loading. Both studies considered the medium to be continuous rock with a plane strain condition. However, it is clear that in fractured reservoirs the continuity of reservoir and plane strain conditions are not satisfied. Abousleiman and Cui [66] presented an analytical solution for an inclined wellbore in anisotropic media. They did not take into account thermal effects or the presence of discontinuity.

Freij-Ayoub et al.[67] introduced 2D coupled numerical analysis of wellbores in shale. They considered hydraulic, thermal, and mechanical processes. Wang and Dusseault [68], and Chen and Ewy [1] presented a fully thermoporoelastic coupled

solution for wellbores that considered convection in addition to conduction heat transfer. However, none of these authors studied the effect of discontinuity near the wellbore wall or the distribution of stress near the end section of wellbore. Zhang and Ghassemi [69] presented a fully coupled wellbore stability problem in a plane strain condition. They considered effect of discontinuity near the wellbore.

Kang et al. [70] critically reviewed methods for analyzing wellbore stability and presented a numerical method based on discrete element techniques to study the distribution of stress around wellbores in 2D configurations. They considered only mechanical processes and ignored the effect of discontinuity near the wellbore. Lee and Ghassemi [7, 71] presented a real coupled 3D wellbore analysis using the mixed finite element method and damage mechanics. Before this, Tao and Ghassemi [72], and Wu et al. [73] solved the same problem in 2D configurations. These authors did not consider the presence of discontinuity or a weakening plane at the beginning of problem, but because they used damage mechanics, the model was able to capture alterations in the elastic modulus due to the initiation and propagation of cracks.

Some investigators who have considered the presence of discontinuity [69, 74, 75] have assumed a plane strain condition that is not realistic in fractured media or near the end of a wellbore.

In the current study, a 2D model presented by Zhou and Ghassemi [69] was improved for use with 3D thermoporoelastic media. Moreover, the presence of an end section of a wellbore and/or a weakening plane was considered.

1.5. Research plan

To acchieve the goals and objectives of the study, the following tasks were completed:

1. A review of field equations for coupled thermoporoelasticity
2. The development of 3D fully coupled thermoporoelastic DD and fictitious stress (FS) techniques based on previous works by Ghassemi and Zhou[57] and Zhang and Ghassemi [69]
3. The coupling of heat and mass transport inside of fracture and rock joints to study injection/extraction in a fracture system
4. The application of numerical methods in petroleum/geothermal reservoir geomechanics problems, enhanced geothermal reservoirs, failure potential in reservoirs due to injection/extraction, and wellbore stress analysis in the presence of discontinuity.

1.5.1. Field equations for thermoporoelasticity

This part of study primarily presents the volumetric response of linear, homogeneous, and isotropic thermoporoelastic material. Total stress (tensile positive), variation in pore pressure, and variation in temperature are chosen as basic variables, and the corresponding conjugate kinematic quantities are solid strain, fluid content change for unit matrix volume, and heat flux.

After governing equations are presentation for thermoporoelastic media, the study focuses on the main problems and describes the method chosen to solve the problems (the indirect boundary element method).

1.5.2. Thermoporoelastic indirect boundary element method

To study the response of fractures and wellbores within the frame of an indirect boundary element method, a 3D numerical model based on source/discontinuity elements was developed. It was used to simulate and analyze multiple arbitrary shape fractures and a combination of wellbores and weakening planes.

To distinguish between conditions in which pre-existing crack geometry propagates during hydraulic/thermal stimulation, Mode I and II stress intensity factors (SIFs) are calculated based on the fracture opening and shear rides at the fracture tip. If the value of calculated SIFs is more than the fracture toughness for each specific mode, the perturbation to the system will be reduced to keep the fracture from propagating.

1.5.3. Heat transport and fluid flow inside of fractures

By considering the fact that fluid diffusion and heat advection-diffusion processes are coupled with the fracture aperture, a governing partial differential equation for fluid/heat transport based on mass and energy conservation is derived. The derived partial differential equations are discretized using the Galerkin finite element or streamline upwind Petrove-Galerkin finite element method, and consequent relations are simultaneously solved with a source/discontinuity algebraic equation.

1.5.4. Constitutive model for reservoir discontinuities

In addition to coupling of heat transfer and fluid flow equations inside of fractures to the source/discontinuity method, it is necessary to be able to model the progressive shear failure of pre-existing natural joints and the change in their behavior

from mechanically closed to mechanically open. In the current study, the slip-weakening model is chosen to describe the progressive shear failure of pre-existing natural discontinuities under compression loading. Slip weakening was developed initially to simulate post-shear failure of faults [76-78]. This model was used by Palmer and Rice [79] to study fracture in overconsolidated clay specimens under simple shear. The same approach as Palmer and Rice used was used in present study to model progressive shear failure.

1.5.5. Applications of method in reservoir geomechanics

The proposed method is applied to following problems:

1. An investigation of failure potential near a hydraulic fracture or multiple hydraulic fractures
2. A study of enhanced geothermal reservoir performance during injection/extraction, and the behavior of natural fractures during hydraulic/thermal stimulation
3. A study of 3D wellbore stress analysis when the wellbore passes through a weakening plane, or a natural fracture

After the results of each problem are presented, a discussion and physical interpretation will be discussed.

2. LINEAR THEORY OF THERMOPOROELASTICITY

The current section provides an overview of thermoporoelasticity theory and the indirect boundary element method. Thermoporoelasticity theory is presented, and then field equations are derived based on some simplifications. Then the indirect boundary element method, which used singular solutions of thermoporoelasticity field equations, is presented and discussed.

2.1. Overview

The theory of thermoporoelasticity was developed by Palciauskas and Domenico [16] and later established by McTigue and Kurashige [17, 18]. McTigue and Kurashige formulated thermoporoelastic constitutive equations by extending Biot's self-consistent theory for fluid-saturated porous media [9, 13] to non-isothermal case. The theory couples the transient heat transfer process with poroelastic behavior.

A mathematical system that describes stress, pore pressure, heat and fluid flux, and displacement in a thermoporoelastic medium must include, constitutive laws, mass, momentum, and energy conservation principles. The stated relations constitute the governing equations of thermoporoelastic media. The relations are reduced through substitution and elimination of variables to produce a system of partial differential equations amenable for mathematical treatment, which is discussed here as a system of field equations.

2.2. Assumptions

The theory of thermoporoelasticity as applied in the current study incorporates the following major assumptions:

1. Negligible effects of pore pressure and mechanical work on temperature field (Figure 1). A number of geomechanical problems require temperature analysis inside of poroelasticity. In the past few decades thermoelastic problems have been solved by considering semi-coupling between temperature and mechanical work [80]. In semi-coupled thermoelasticity it is assumed that strains from boundary load and body force induce a negligible amount of temperature change. Carter and Booker [81] showed that semi-coupled thermoelasticity produces sufficient accuracy for solving almost all geomechanical problems.
2. Infinitesimal deformations of the matrix. The Eulerian strain tensor applies and Darcy's law can be defined in terms of absolute fluid velocity instead of relative velocity.
3. A single liquid phase. More effort is required to simulate multiphase flow in a matrix because of the need to drive a new fundamental solution; therefore it is ignored in the current study. However, multiphase flow inside of a fracture can be accounted for easily by changing the equations governing flow in fractures.

4. Negligible chemical effects. It is assumed that the chemical potential of injected fluid is same as that of pore fluid. In other words, produced water is used for the reinjection procedure.
5. Insignificant creep behavior. Usually creep is a major concern in mudstone, salt deposits, and reach-clay shale [82]. In the current study, it is assumed that low-permeability reservoirs are not rich in total organic content and that creep effects or viscoelasticity can be ignored.
6. Identical temperature for the matrix and pore fluid at the same location. This assumption is based on the fact that local heat exchanges between solid and pore fluid occur as rapidly as global heat and fluid diffusions.
7. Negligible dynamic effects. Generally the rate of applied load to reservoir owing to injection or rock removal (drilling) is very low and can be considered static. As a consequence, deformations are considered as a quasi-static field.
8. Transient linear heat conduction (no advection) in porous media. In low-permeability reservoirs, because of extremely low speed of fluid movement in the matrix, conduction governs heat transfer phenomena and advection can be ignored.
9. Homogeneous, isotropic, infinite porous media. Comparisons of fracture scale or wellbore scale to reservoir scale reveal that the boundary of the reservoir does not contribute to the fracture or wellbore response. Therefore, fractures and wellbores can be considered in an infinite region.

However, because of inherent limitations of the boundary element method the infinite region cannot be inhomogeneous and anisotropic.

10. Constant material parameters for different temperatures. Although in enhanced geothermal reservoirs rock temperature can change considerably, for the sake of simplicity relation between rock constants and temperature is ignored.
11. Fluid flow in a low-permeability reservoir governed by Darcy's law.
12. Thermal expansion of pores, with pore shapes remaining similar. In other words, the volumetric thermal expansion coefficient of the pore space is equal to the volumetric thermal expansion of matrix times to porosity.

2.3. Governing equations

Governing equations for thermoporoelasticity, within the context defined previously, are reviewed next. These equations consist of constitutive equations, transport laws, and conservation laws.

2.3.1. Constitutive equations

The constitutive equations (tension positive) for porous matrix and the pore space can be achieved based on principles of thermodynamics for fluid-saturated thermoelastic porous rock [18, 83]. The constitutive equations for the relations between induced strain, pore pressure change, and temperature change are as follows [8] (considering the in-situ state as a basis):

$$\sigma_{ij} = 2G\varepsilon_{ij} + \frac{2G\nu}{1-2\nu}\delta_{ij}\varepsilon_{kk} - \alpha\delta_{ij}p - \frac{2G(1+\nu)}{3(1-2\nu)}\beta_m\ \delta_{ij}T$$
$$\zeta = \frac{\alpha(1-2\nu)}{2G(1+\nu)}\sigma_{kk} + \frac{\alpha^2(1-2\nu)^2(1+\nu_u)}{2G(1+\nu)(\nu_u-\nu)}p + (\beta_p - \varphi\ \beta_f)T \tag{2.1}$$

where σ_{ij} is total stress tensor components, ε_{ij} is an average strain tensor components, p is induced pore pressure, T is induced temperature, ζ is fluid content change per unit reference volume, G is shear modulus, ν is drained Poisson's ratio, ν_u is undrained Poisson's ratio, δ_{ij} is Kronecker delta, α is Biot's constant, β_m is volumetric thermal expansion of porous matrix, β_p is volumetric thermal expansion coefficient of pore space, β_f is volumetric thermal expansion coefficient of pore fluid and φ is porosity.

2.3.2. Transport laws

By ignoring the cross-effect between mass and heat diffusion (thermo-osmosis and Dufour's effects) in isotropic porous material, the following mass and heat diffusion equation (Darcy's law and Fourier's law) can be obtained [18, 83]:

$$q_i = -\kappa\ p_{,i}$$
$$h_i = -k_m^T\ T_{,i} \tag{2.2}$$

where q_i is fluid flux in "i" direction (unit fluid volume per unit area), $\kappa = k/\mu$ is mobility (k is intrinsic permeability having dimension of length squared, and μ is fluid dynamic viscosity), h_i is heat flux in "i" direction (unit heat per unit area), k_m^T is thermal conductivity of porous matrix and pressure (p) and temperature (T) with subscript ",i" means its derivative with respect to that coordinate component.

Equation (2.2) shows that the transport laws for fluid flow and heat flow are similar to each other.

2.3.3. Conservation laws

In a quasi-static nonisothermal framework, three conservation laws exist [8]:

1. Momentum linear balance or equilibrium equation:

$$\sigma_{ij,j} = -F_i \tag{2.3}$$

where F_i is total or bulk body force in i direction.

2. Local fluid mass conservation:

$$\frac{\partial \zeta}{\partial t} + q_{i,i} = \gamma_f \tag{2.4}$$

where γ_f is fluid source or sink (fluid source is positive).

3. Energy conservation. By ignoring terms representing the interconvertibility of thermal and mechanical energy, and ignoring convective heat transfer through pore fluid flow, energy balance for the representative volume element yields the following equation:

$$\frac{\partial \left(\rho_m C_m T\right)}{\partial t} + h_{i,i} = \gamma_h \tag{2.5}$$

where ρ_m and C_m are mass density and specific heat for porous matrix, and γ_h is heat source or sink (heat source is positive). The first term of equation (2.5) represents conductive heat transfer through the matrix.

Equation (2.5) is based on effective heat transfer. In other words, the mean temperatures of the matrix solid and fluid phases are identical for a representative volume element. Energy balance for fluid-saturated porous media can also expressed by distinguishing the mean temperature between the matrix and the pore fluid. In this case, energy balance equations are established for each phase (fluid and solid), and the heat flux transferred from one phase to another is expressed using a heat transfer coefficient. Compared to the model used in the current study, this model is more difficult to use. This is because more parameters are involved, and some of them, such as the heat transfer coefficient between the two phases, are difficult to define accurately. However, it is the more appropriate model to use when fluid velocity is high and significant differences in temperature between the solid and fluid phases are possible.

2.4. Field equations for thermoporoelasticity

A set of nine material constants, G, α, ν, ν_u, κ, β_m, $\beta_{m,u}$, C_m, k_m^T, is needed to fully characterize a linear homogeneous isotropic thermoporoelastic system. Of parameters $\beta_{m,u}$ is the undrained volumetric thermal expansion of porous media. From the presented constitutive equations, conservation laws, and transport laws and the geometric relationship for small deformations, the following field equations (a modified Navier equation and pressure and temperature diffusion equations) can be derived:

Modified Navier equation:

$$G u_{i,jj} + \frac{G}{1-2\nu} u_{j,ji} - \alpha p_{,i} - \frac{2G\beta_m(1+\nu)}{3(1-2\nu)} T_{,i} = -F_i \tag{2.6}$$

where u_i are displacement components. Pressure diffusion equation:

$$\frac{\partial p}{\partial t} = M\left[\kappa p_{,jj} - \gamma_f - \alpha\frac{\partial \varepsilon_{kk}}{\partial t} + \frac{1}{3}\left(\alpha\,\beta_m + \beta_f\,\varphi - \beta_p\right)\frac{\partial T}{\partial t}\right]$$
$$M = \frac{2G\left(\nu_u - \nu\right)}{\alpha^2\left(1-2\nu\right)\left(1-2\nu_u\right)},\quad \beta_p = \varphi\,\beta_m \tag{2.7}$$

where M is Biot's modulus. Temperature diffusion equation:

$$\frac{\partial T}{\partial t} = c^T T_{,ii} + \frac{\gamma_h}{\rho_m\, C_m}$$
$$c^T = \frac{k_m^T}{\rho_m\, C_m} \tag{2.8}$$

where c^T is the thermal diffusivity coefficient for matrix.

Heat transfer is calculated separately because it is assumed that temperature field does not change by stress and pressure changes (semi-coupled thermoelasticity). Also, note that convective heat transport is ignored.

As can be seen from equations (2.6), (2.7), and (2.8), displacement, pore pressure, and temperature field equations derived for a fluid-saturated, isotropic, thermoporoelastic body are completely coupled with one another.

2.5. Field equations for thermoelasticity and poroelasticity

Thermo-poroelasticity is another term for the intrinsic coupling of thermoelasticity and poroelasticity. Poroelasticity and thermoelasticity can be considered two special cases of thermoporoelasticity.

A set of five material constants, G, α, ν, ν_u, κ, is needed to characterize a linear isotropic homogeneous poroelastic system. Likewise, a set of five material constants,

G, ν, β_m, c^T, k_m^T, is needed to characterize isotropic homogeneous thermoelastic material. Field equations for poroelasticity and thermoelasticity can be derived from thermoporoelastic equations by ignoring temperature or pore pressure effects in equations (2.6) and (2.7).

Ignoring temperature in equations (2.6) and (2.7) results in the following modified 3D Navier and diffusion equation for poroelasticity [84]:

$$\begin{aligned} G u_{i,jj} + \frac{G}{1-2\nu} u_{j,ji} - \alpha p_{,i} &= -F_i \\ \frac{\partial p}{\partial t} &= M\left[\kappa p_{,jj} - \gamma_f - \alpha \frac{\partial \varepsilon_{kk}}{\partial t}\right] \end{aligned} \tag{2.9}$$

Correspondingly, ignoring pore pressure in the thermoporoelasticity field equations results in field equations for thermoelasticity [14]:

$$\begin{aligned} G u_{i,jj} + \frac{G}{1-2\nu} u_{j,ji} - \frac{2G\beta_m(1+\nu)}{3(1-2\nu)} T_{,i} &= -F_i \\ \frac{\partial T}{\partial t} &= c^T T_{,ii} + \frac{\gamma_h}{\rho_m C_m} \end{aligned} \tag{2.10}$$

Equations (2.9) and (2.10) constitute governing field equations for poroelasticity and thermoelasticity, respectively, in fully saturated porous rock matrix. Moreover, a set of boundary and initial conditions is essential to solve a problem in thermoporoelastic media.

2.6. Problem statements

The problems that are the focus of the current study are referenced in Figure 2. The figure shows an infinite 3D thermoporoelastic medium with two types of boundaries; a fracture surface and a wellbore surface.

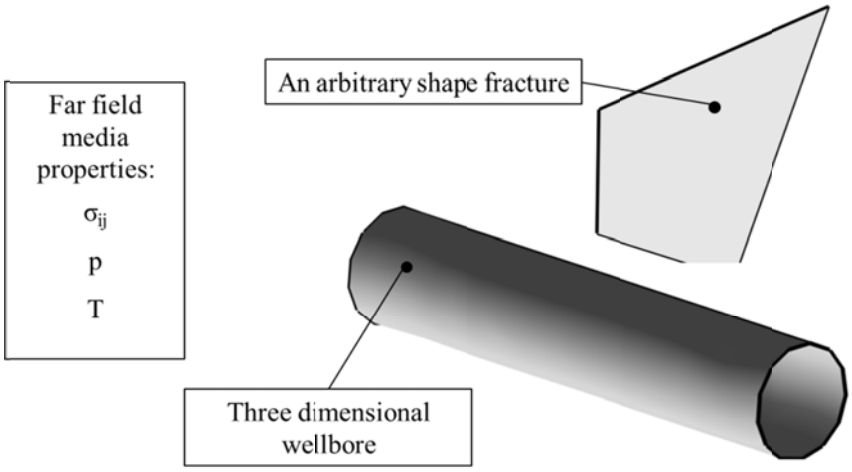

Figure 2. Two types of boundary in the current study.

Each point on the fracture surface in the infinite thermoporoelastic medium is a source of DD in three local directions (one normal DD and two shear DDs) and heat and fluid source/sink. In contrast, each point on the wellbore wall is a cause of traction (or force) discontinuity in three local directions (one normal traction and two shear tractions) and heat and fluid source/sink.

The response of linear thermoporoelastic media (equations (2.6), (2.7), and (2.8)) to a point disturbance (DD, traction discontinuity, heat source/sink, or fluid source/sink) at a specific time and point in an infinite region is known as the singular solution. An analysis of infinite media in the presence of fractures and wellbores can be done by integrating the strengths of all singular solutions over time and the discontinuity surfaces (fracture and wellbore surfaces). Note that integrating singular solutions in time and space results in an accurate response of media if the governing equations (equations (2.6), (2.7), and (2.8)) are linear.

2.7. Singular solution characteristics

As pointed out in the previous section, all discontinuity surfaces can be modeled mathematically as a distribution of impulse point DD, point traction discontinuities (FS), fluid source/sink, and heat source/sink over time and space. Several researchers have discussed methods for deriving solutions to thermoporoelastic or poroelastic/thermoelastic field equations for various impulse point disturbances [13, 83, 85-89]. The approach to solve the problem is generally established on a particular decomposition of the displacement field, as initially suggested by Biot [10]. The systematic solution method was first proposed by Cheng and Liggett [86] to derive a singular solution for poroelastic field equations. The proposed method is more organized than other methods that have been described in the literature [83, 87, 88]. Singular solutions of field equations to various continuous point disturbances are presented in Appendix A. Characteristics of these singular solutions for specific properties of thermoporoelastic media properties are discussed in Appendix B.

3. INDIRECT BOUNDARY ELEMENT METHOD

3.1. Introduction

Coupled thermoelasticity, poroelasticity, and thermoporoelasticity formalisms have been used to accurately solve reservoir problems. However, majority of geomechanical problems cannot be solved analytically and need to be treated numerically. The boundary element method (BEM) is a great numerical tool for solving systems ruled by linear partial differential equations in an infinite region [90, 91]. The BEM has many of its roots in potential theory [92], where field behavior is simulated by the superposition of proper analytical solutions. Corresponding analytical solutions result from the response of infinite media to an impulse at a point. The impulse can represent point fluid source/sink, point heat source/sink, DD in different directions, or tractions discontinuity in different directions. The analytical solutions of field equations to such an impulse are called singular solutions because, mathematically speaking, they behave normally everywhere in the region except at the point of the impulse, where there is a mathematical singularity.

Boundary element method formulation has been used for elastic [26, 93], poroelastic[31, 56, 84], thermoelastic[44-46] and thermo-poroelastic[47, 50, 52, 53, 57, 69] analyses of petroleum geomechanics problems. The value of the method is that it decreases problem dimensionality by one.

In the BEM literature, the direct method and the indirect method are two different types of integral equations. Green's second identity or reciprocity of work principle [84, 90] is the basis of integral equation in drect boundary element method. In

this method, integral expressions include physical quantities, such as potential, flux, displacement, or stress. In contrast, the integral expressions in the indirect method contain fictitious parameters [26]. Connections between the two stated boundary integral equations for elasticity problems are well known and have been discussed in literature [85]. In the indirect method, fictitious parameter densities are accompanying with jumps between solutions of the corresponding exterior and interior domain problems under an identical set of boundary conditions. Physical quantities like stresses and pore pressure restore after defining fictitious densities by applying second application of integral equations.

The numerical method discussed in this Section can be formally classified as an indirect boundary element method. It is a boundary element method because only the boundaries of the considered problem (the discontinuity/source surfaces within the region) need to be discretized, not the whole region as in finite difference and finite element methods. It is an indirect boundary element method because before the stress or displacement fields can be computed, intermediate variables (tractions or DDs and fluid/heat sources) have to be calculated.

The indirect BEM has two categories: DD method and the stress discontinuity or fictitious stress (FS) method [26]. The former uses a fundamental solution based on a constant DD with three components in an infinite solid. Intrinsic jumps in displacement field from one side of a crack to other side are not fictional quantities and can be considered as a physical dislocation in the media. This makes the DD method the

preferred choice for modeling cracks. The advantage of the DD method is that it can model two surfaces of a crack as one entity.

The other indirect boundary element method, the FS method, is based on a fundamental solution of a point force (or a traction applied on a surface) in an infinite solid. It is a very useful technique for simulating underground openings with a random configuration. The FS method is not suitable for use with crack problems, because the effects of elements placed along one crack surface are indistinguishable from the effects of elements placed along the other surface [26].

A more descriptive term for the two indirect methods would be the superposition of a fundamental solution. Based on the superposition concept, the methods can be built up using the following steps:

I. An analytical solution (in this case an analytical solution due to point DD, traction discontinuity, fluid and heat source in thermoporoelastic media) is integrated over a surface segment with a known distribution of discontinuities and sources along the surface segment. The surface segment is called the “element”.

II. All discontinuity surfaces in media are traced using DD (for cracks) and FS (for wellbores) elements (see Figure 3), and the distribution of physical properties such as stress, pressure, and temperature in thermoporoelastic media is approximated by summing the effects of all elements.

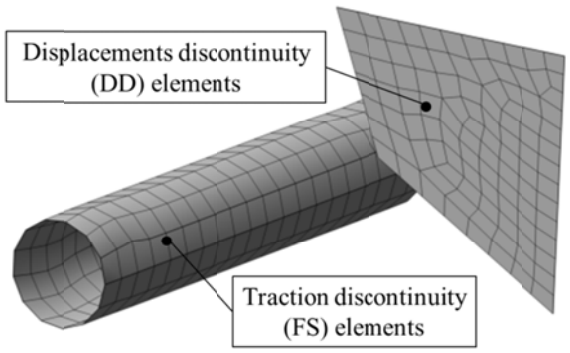

Figure 3. Fractures and wellbores tessellation with two types of elements.

III. Boundary conditions (imposed on all discontinuity surfaces) are satisfied at discrete points along the discontinuity surfaces (this is usually called a "collocation procedure"). Sufficient collocation points for all boundary conditions are chosen to determine the parameters that control discontinuities or source distributions. Stresses, temperature, and pressure fields throughout the region are determined using the calculated parameters.

In both types of indirect boundary element method, when elements are of equal size and the curvature of discontinuity element is low, the system of algebraic equations that is formed using these steps is well conditioned and strongly diagonally dominant [26]. It should be clear from these characteristics of the indirect boundary element method that this method is appropriate for capturing effects in thermoporoelastic media.

3.2. Thermoporoelastic fictitious stress

In the FS method, fictitious traction applied on the surface of an element results in a stress jump across the element [94]. The 3D elastic FS method applies Kelvin's

solution [95], which is an analytical solution of a point force in an infinite solid, to an area of an element. As a result, displacement and stress components can be evaluated over the problem domain.

The elastic FS method can be extended to a thermoporoelastic method. In the thermoporoelastic FS method, temperature, pore pressure, stress, and displacement fields on all discontinuity surfaces (wellbore perimeter) can be estimated using the following process (remember that heat diffusion is one-way coupled to pressure diffusion and mechanical work):

I. Wellbore perimeter should be discretized with four node quadrilateral elements (Figure 4). Elements are thermoporoelastic; therefore, traction discontinuity and fluid/ heat source exist across them (Figure 5).

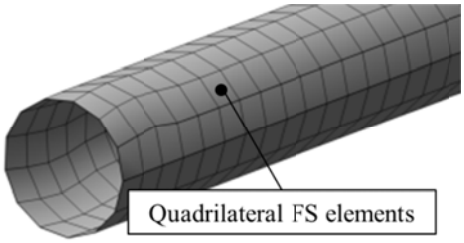

Figure 4. Discretization of wellbores with FS quadrilateral elements.

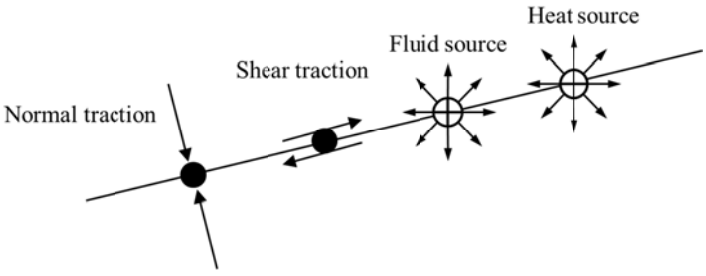

Figure 5. Point source/traction discontinuity across FS surface.

II. The temperature at each element vertex at time t is the sum of effects of all heat sources at time $0 \le \tau \le t$. The strengths of heat sources, which are a function of time and space, are calculated in such a way that they satisfy the temperature field at every time at all element vertices.

III. The pore pressure at each element node at time t is the sum of effects of traction discontinuities at all element centers and fluid and heat sources at all element nodes at time $0 \le \tau \le t$. The strengths of fluid sources and traction discontinuity, which are functions of time and space, are calculated in such a way that they satisfy pressure and stress fields at all collocation points.

IV. The stress fields at each element center at time t are the sum of effects of three traction discontinuities at the element center and fluid and heat sources at all nodes at time $0 \le \tau \le t$. The strength of the heat source is known from step (II).

V. By satisfying pressure and stress boundary conditions on the wellbore perimeter, the strengths of three traction discontinuities and fluid sources can be determined because contributions from heat sources are known. At the end of the current step all unknowns for FS elements (see Figure 6) — the strength of the three traction discontinuities at all element centers, the strength of the fluid source at four nodes of all quadrilateral elements, and the strength of heat source at four nodes of all elements— will be defined.

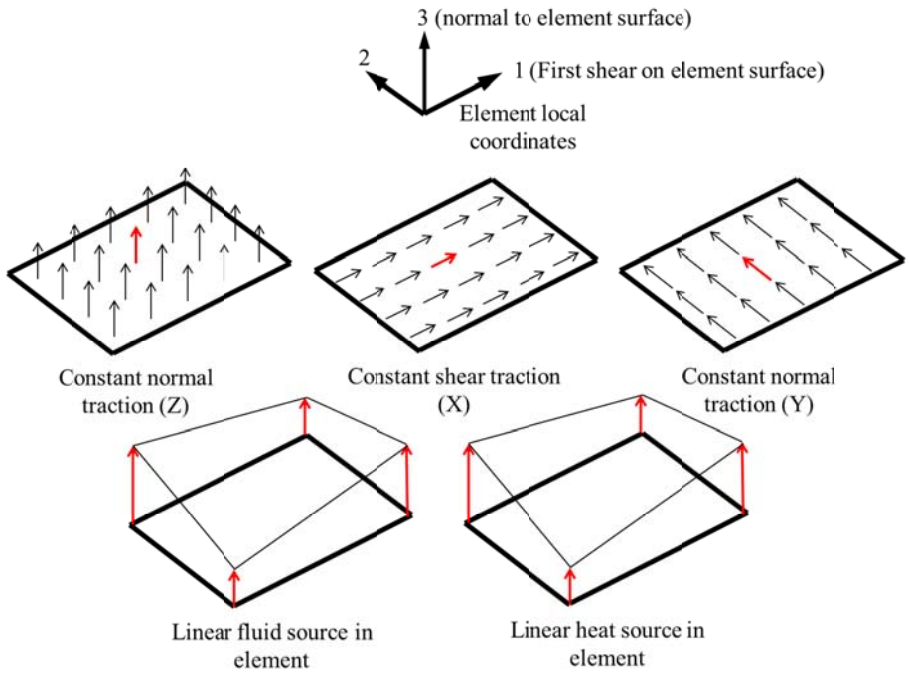

Figure 6. Unknowns in thermoporoelastic FS element, number of red components show number of unknowns in the FS element

3.2.1. Boundary integral equations

The solution to the general stress discontinuity problem shown in Figure 7 can be obtained in an indirect way. Consider an infinite thermoporoelastic medium that contains an arbitrary shape stress discontinuity boundary (Γ). Across the boundary, there exists normal traction discontinuity $F_n(\chi,t)$, first shear traction discontinuity $F_{s1}(\chi,t)$, second shear traction discontinuity $F_{s2}(\chi,t)$, fluid source $f(\chi,t)$, and heat source $h(\chi,t)$ (χ denotes the spatial coordinates of a node on the boundary and t represents the time considered).

The strengths of the heat source, the fluid source, and the traction discontinuities can be found from the known history of temperature, pore pressure, and stress or displacement along the boundary. Determining the five unknowns requires solving a set of five boundary integral equations.

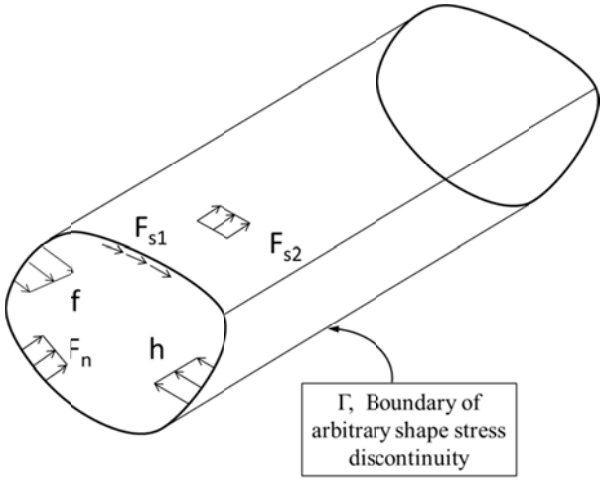

Figure 7. Arbitrary shape stress discontinuity boundary in an infinite thermoporoelastic media with different unknowns' distribution in space at a specific time.

Integral equations can be obtained by using an approach based on a reciprocal theorem [85] or by applying the superposition concept (adopted in the current study). Accordingly, based on the superposition concept thermoporoelastic FS boundary integral equations are given by:

$$\sigma_{ij}\left(\mathbf{x},t\right)=\int_{0}^{t}\int_{\Gamma}\left\{\begin{array}{l}\sigma_{ijk}^{Fi}\left(\mathbf{x},t;\boldsymbol{\chi},\tau\right)\times F_{k}\left(\boldsymbol{\chi},\tau\right)+\\ \sigma_{ij}^{si}\left(\mathbf{x},t;\boldsymbol{\chi},\tau\right)\times f\left(\boldsymbol{\chi},\tau\right)\ +\\ \sigma_{ij}^{hi}\left(\mathbf{x},t;\boldsymbol{\chi},\tau\right)\times h\left(\boldsymbol{\chi},\tau\right)\end{array}\right\}d\Gamma\left(\boldsymbol{\chi}\right)\,d\tau+\sigma_{ij}\left(\mathbf{x},0\right)\qquad(3.1)$$

$$u_i(\mathbf{x},t)=\int_0^t\int_\Gamma\begin{Bmatrix}u_{ik}^{Fi}(\mathbf{x},t;\boldsymbol{\chi},\tau)\times F_k(\boldsymbol{\chi},\tau)+\\ u_i^{si}(\mathbf{x},t;\boldsymbol{\chi},\tau)\times f(\boldsymbol{\chi},\tau)\ +\\ u_i^{hi}(\mathbf{x},t;\boldsymbol{\chi},\tau)\times h(\boldsymbol{\chi},\tau)\end{Bmatrix} d\Gamma(\boldsymbol{\chi})\,d\tau+u_i(\mathbf{x},0) \tag{3.2}$$

$$p(\mathbf{x},t)=\int_0^t\int_\Gamma\begin{Bmatrix}p_k^{Fi}(\mathbf{x},t;\boldsymbol{\chi},\tau)\times F_k(\boldsymbol{\chi},\tau)+\\ p^{si}(\mathbf{x},t;\boldsymbol{\chi},\tau)\times f(\boldsymbol{\chi},\tau)\end{Bmatrix} d\Gamma(\boldsymbol{\chi})\,d\tau+p(\mathbf{x},0) \tag{3.3}$$

$$T(\mathbf{x},t)=\int_0^t\int_\Gamma\left\{T^{hi}(\mathbf{x},t;\boldsymbol{\chi},\tau)\times h(\boldsymbol{\chi},\tau)\right\} d\Gamma(\boldsymbol{\chi})\,d\tau+T(\mathbf{x},0) \tag{3.4}$$

where Γ is stress discontinuity boundary, $\mathbf{x}$ is spatial coordinates of influenced point (which is located inside of media), $\boldsymbol{\chi}$ is spatial coordinates of influencing point (which is located on Γ), t is influenced time, τ is influencing time, σ_{ijk}^{Fi} is induced ij stress component due to instantaneous unit point traction in k direction, σ_{ij}^{si} is induced ij stress component due to instantaneous unit point fluid source, σ_{ij}^{hi} is induced ij stress component due to instantaneous unit point heat source, u_{ik}^{Fi} is induced i component of displacement field due to instantaneous unit point traction in k direction, u_i^{si} is induced i component of displacement field due to instantaneous unit point fluid source, u_i^{hi} is induced i component of displacement field due to instantaneous unit point heat source, p_k^{Fi} is induced pore pressure due to instantaneous unit point force in k direction, p^{si} is induced pore pressure due to instantaneous unit point fluid source, T^{hi} is induced temperature due to instantaneous unit heat source, and $F_k(\boldsymbol{\chi},\tau)$, $f(\boldsymbol{\chi},\tau)$, $h(\boldsymbol{\chi},\tau)$ are strength of instantaneous point force in k direction, point fluid source and point heat

source respectively. Subscript i, j, k can take number 1,2 or 3, which denotes three local directions (see Figure 6) and summation is enforced by repeated subscript.

Note that equation (3.1) is written with the stress components on the left-hand side and presents six relations. However, from the point of view of traction (one normal and two shear tractions on a surface), the equations represent only three independent relations. Also, equations (3.1) and (3.2) are used interchangeably base on the type of stress discontinuity boundary. Equation (3.1) used for boundaries with known tractions. A wellbore surface is an example of a condition with defined tractions. In contrast, equation (3.2) is used for boundaries with known displacements. The sliding of a box on a free surface with a displacement control tool is one example of this. This problem is studied in section 5 using a combination of DD and FS elements to show the post-shear failure behavior of joint elements.

There exist five unknowns at any time in integral equations: $F_1(\boldsymbol{\chi},\tau)$, $F_2(\boldsymbol{\chi},\tau)$, $F_3(\boldsymbol{\chi},\tau)$, $f(\boldsymbol{\chi},\tau)$, $h(\boldsymbol{\chi},\tau)$ (1, 2, and 3 are three components of traction discontinuity on the element surface). To define the unknowns, one must determine the left-hand sides of the equations. The positions for which the distributions of tractions (or displacements), pressure, and temperature are known at the time of solution are the boundaries of the model (wellbore or fracture surfaces). Therefore, $\mathbf{x}$ (the field point) must move toward the boundary to make known the left-hand side of the equation. When $\mathbf{x}$ moves toward the boundary, some of the boundary integrals only exist in the sense of a limiting value. This existence issue occurs only in the case of self-influence integral evaluation. One example of self-influence integral involves integration

over an FS element to evaluate the stress distribution of the same element. Existence issues also occur on a DD element when the displacement-defined boundary is treated or when the displacement field on both sides of the DD element is estimated.

The simplest way to evaluate problematic integrals when $\mathbf{x}$ moves toward the boundary is to consider that a field point is located on the boundary but that the domain itself is augmented by a hemisphere of radius ε, as shown in Figure 8, and the value of ε in the limiting sense approaches zero. Note that the normal in the figure can be toward the outside or the inside of medium and each normal represents different surfaces. Here the surface with the outward normal is considered when evaluating the problematic integral. A special procedure for evaluating the integral is represented in the following [90, 91]:

$$\int_{\Gamma} \Phi^c \left(\mathbf{x} - \boldsymbol{\chi}, t - \tau \right) d\left(\boldsymbol{\chi} \right) = \int_{\Gamma} \Phi^c \left(\mathbf{x} - \boldsymbol{\chi}, t - \tau \right) d\Gamma + \left(\textit{free term} \right) \tag{3.5}$$

where the function $\Phi^c \left(\mathbf{x} - \boldsymbol{\chi}, t - \tau \right)$ represents continuous stress fundamental solution, $\mathbf{x}$ is field point that is positioned on original boundary and $\boldsymbol{\chi}$ is boundary point that is placed in the imaginary hemisphere boundary) and improper integral is calculated as sum of Cauchy principal-value integral and free term. Cauchy principal-value integral evaluation is described in Appendix C.

The free term can be estimated by performing the following integration over the small hemispherical region:

$$\textit{free term} = \lim_{\varepsilon \to 0} \int_{\Gamma_\varepsilon} \Phi^c \left(\mathbf{x} - \boldsymbol{\chi}, t - \tau \right) d\Gamma_\varepsilon \tag{3.6}$$

where Γ_ε is hemisphere boundary with radius of ε.

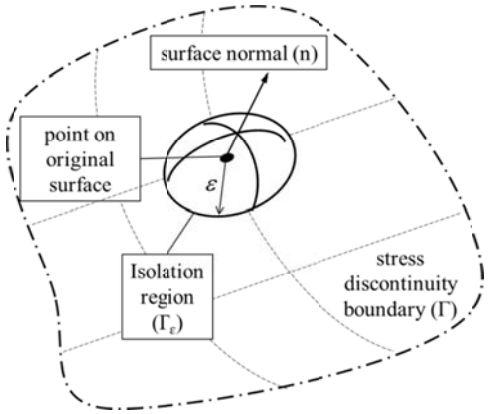

Figure 8. Isolation hemisphere around an influenced point which is located on stress discontinuity boundary.

To evaluate the free term for stress components due to an FS element, consider Figure 9 and the stress fundamental solution. The stress fundamental solution can be represented in indicial notation as follows:

$$\sigma_{ijk}\left(\mathbf{x}-\boldsymbol{\chi},t-\tau\right)=\frac{1}{8\pi\left(1-\nu\right)}\frac{1}{R^2}\left\{\begin{array}{l}\left(1-2\nu\right)\left(\delta_{ij}r_{,k}-\delta_{ik}r_{,j}-\delta_{jk}r_{,i}\right)-3\,r_{,i}\,r_{,j}\,r_{,k}-\\ \dfrac{\nu_u-\nu}{1-\nu_u}\left[\delta_{ij}r_{,k}D-\left(\delta_{ik}r_{,j}+\delta_{jk}r_{,i}\right)E+3\,r_{,i}\,r_{,j}\,r_{,k}F\right]\end{array}\right\} \tag{3.7}$$

$$=\frac{1}{8\pi\left(1-\nu\right)}\frac{1}{R^2}\;\Lambda_{ijk}$$

where D, E, and F are function of time and will be zeros whenever r goes to zero, therefore they do not change order of singularity. Note that i and j are indices for stress components and can take 1, 2, or 3. k is the traction discontinuity direction and can also take 1, 2 or 3. As can be seen from equation (3.7), the term $1/R^2$ is the major cause of singularity. By considering Figure 9 and the spherical coordinates system, a small part of surface can be presented as follows:

$$dS=\varepsilon^2\sin\varphi\,d\varphi\,d\theta \tag{3.8}$$

This relation is used instead of $d\Gamma_\varepsilon$ in equation (3.6). By substituting equations (3.8) and (3.7) into equation (3.6), one can represent the free term as follows (note that R and ε are the same):

$$\lim_{\varepsilon\to 0}\int_{\Gamma_\varepsilon}\Phi^c\left(\mathbf{x}-\boldsymbol{\chi},t-\tau\right)d\Gamma_\varepsilon=\frac{1}{8\pi\left(1-\nu\right)}\lim_{\varepsilon\to 0}\int_0^{2\pi}\left(\int_0^{\pi/2}\Lambda_{ijk}\,\sin\varphi\;d\varphi\right)d\theta \qquad (3.9)$$

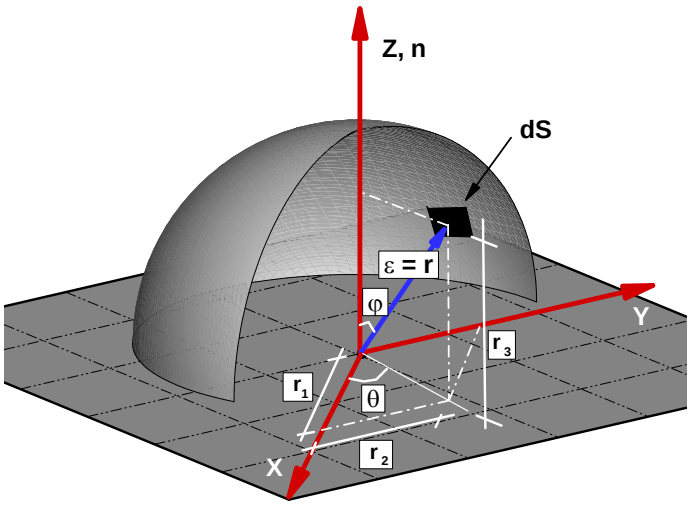

Figure 9. Augmented hemisphere geometry with radius ε, 1, 2, and 3 are X, Y and Z respectively, Z axis is also normal vector which is directed outside of media.

The free term can be evaluated for every stress component due to every stress discontinuity on the hemisphere region by evaluating equation (3.9). Note that, in the equation, initially induced stresses should be calculated in spherical coordinates and then transferred to Cartesian coordinates (Appendix D). For example, the free term for a normal stress component due to stress discontinuity in normal or direction 3, is calculated as follows:

$$FT_{333}=\frac{1}{8\pi\left(1-\nu\right)}\lim_{\varepsilon\to 0}\int_0^{2\pi}\left(\int_0^{\pi/2}\left\{-2\left(1-2\nu\right)\left(\cos\varphi\right)-4\left(\cos\varphi\right)^3\right\}\sin\varphi\;d\varphi\right)d\theta=\frac{1}{2}$$

If normal direction in Figure 9 is changed and point toward –Z, the free term changes to:

$$FT_{333} = \frac{1}{8\pi(1-\nu)} \lim_{\varepsilon \to 0} \int_0^{2\pi} \left(\int_{\pi/2}^{-\pi/2} \left\{ -2(1-2\nu)(\cos\varphi) - 4(\cos\varphi)^3 \right\} \sin\varphi \, d\varphi \right) d\theta = -\frac{1}{2}$$

The free term will be either +0.5 or -0.5 based on the normal vector direction. Therefore the value of the free term depends on the way the boundary is traversed (by its normal vector). To make the issue more clear, consider an imaginary 3D boundary in Figure 10 and define two sides of the boundary, Γ^+ (n toward the interior region, blue vector) and Γ^- (n toward the exterior region, red vector). Make a convention that curves Γ^+ with the normal vector toward the interior region represent the exterior problem and curve Γ^- with the normal vector toward the exterior region represent the interior problem. Therefore, if Γ^+ with the blue vector as a normal is used to represent exterior problems (like wellbores), a field point in the medium is always approaching the boundary of the wellbore problem from n^- and the value of the free term would be +0.5. However, hand if Γ^- with the red vector as a normal is used to represent interior problems (like cores), a field point in the interior problem is always approaching the boundary from n^-, and value of free term is again +0.5. Hence by using the stated convention for boundary representation (the normal of the element should point toward the interior region for modeling exterior problems, and the normal of the element should point toward the exterior region for modeling interior problems), one avoids using different values for the free term.

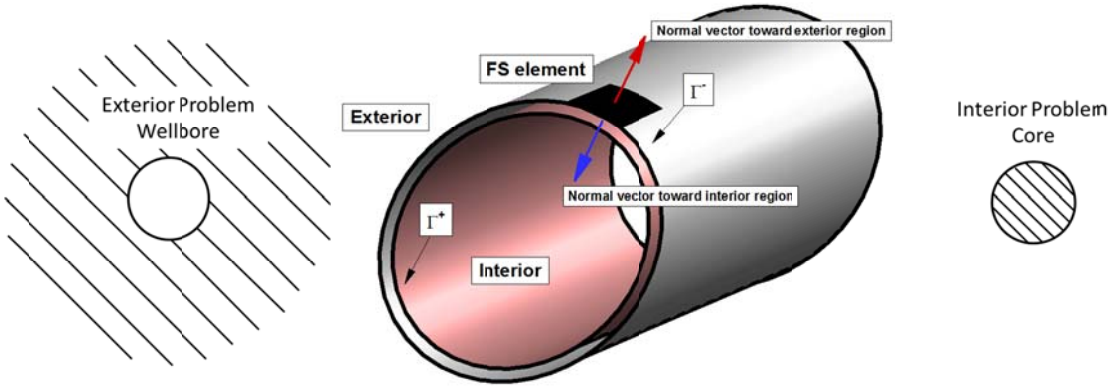

Figure 10. Interior and exterior region of curve Γ .

3.2.2. Temporal integration

In the thermoporoelastic boundary integral equations presented in equations (3.1), (3.2), (3.3), and (3.4), fundamental solutions correspond to instantaneous singular impulses (in space and time). Therefore, both spatial and temporal integrals are needed. To change temporal integrals into summation, continuous fundamental solutions can be used. Continuous fundamental solutions can be obtained by integrating corresponding solutions for instantaneous impulses with respect to time [33, 39]. To derive a continuous fundamental solution, consider the following convolution integral:

$$\Re = \int_0^t \Phi^i \left(\mathbf{x} - \boldsymbol{\chi}, t - \tau\right) \mathrm{X}\left(\boldsymbol{\chi}, \tau\right) \, d\tau \tag{3.10}$$

where Φ^i can be any instantaneous singular solutions and X can be strength of any boundary discontinuities or source densities. Assuming an arbitrary variation for X (see Figure 11), it can be represented as

$$\mathrm{X}\left(\boldsymbol{\chi}, \tau\right) = \sum_{\ell=0}^{s} H\left(t - \tau_\ell\right) \, \Delta \mathrm{X}_\ell \left(\boldsymbol{\chi}\right) \tag{3.11}$$

where, $H\left(t-\tau_\ell\right)$ is Heaviside function and s is number of time increments.

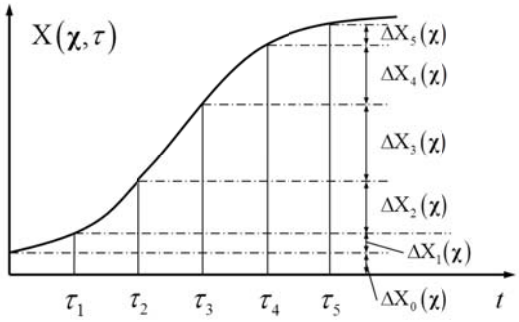

Figure 11. Continuous source approximation.

By substituting equation (3.11) into equation (3.10), $\Re$ can be represented as

$$\Re = \int_0^t \Phi^i\left(\mathbf{x}-\boldsymbol{\chi},t-\tau\right)\sum_{\ell=0}^{s} H\left(t-\tau_\ell\right)\,\Delta \mathrm{X}_\ell\left(\boldsymbol{\chi}\right)\,d\tau \tag{3.12}$$

By expanding summation, $\Re$ can be rewritten as

$$\Re = \sum_{\ell=0}^{s}\int_{\tau_\ell}^{t} \Phi^i\left(\mathbf{x}-\boldsymbol{\chi},t-\tau\right)\Delta \mathrm{X}_\ell\left(\boldsymbol{\chi}\right)d\tau \tag{3.13}$$

$\Delta \mathrm{X}_\ell\left(\boldsymbol{\chi}\right)$ is constant from τ_ℓ to t and $\int_{\tau_\ell}^{t} \Phi^i\left(\underline{x}-\underline{\chi},t-\tau\right)d\tau$ is by definition singular solution due to continuous source applied at time τ_ℓ and expressed as $\Phi^c\left(\mathbf{x}-\boldsymbol{\chi},t-\tau\right)$. All continuous singular solutions are presented in Appendix A.

By using the stated approximation in time, equations (3.1), (3.2), (3.3), and (3.4) can be rewritten in following form:

$$\sigma_{ij}\left(\mathbf{x},t\right) = \sum_{\ell=0}^{s}\int_{\Gamma}\left\{\begin{array}{l}\sigma_{ijk}^{Fc}\left(\mathbf{x}-\boldsymbol{\chi},t-\tau_\ell\right)\times\Delta F_k\left(\boldsymbol{\chi},\tau_\ell\right)+\\ \sigma_{ij}^{sc}\left(\mathbf{x}-\boldsymbol{\chi},t-\tau_\ell\right)\times\Delta f\left(\boldsymbol{\chi},\tau_\ell\right)\ +\\ \sigma_{ij}^{hc}\left(\mathbf{x}-\boldsymbol{\chi},t-\tau_\ell\right)\times\Delta h\left(\boldsymbol{\chi},\tau_\ell\right)\end{array}\right\} d\boldsymbol{\Gamma}\left(\boldsymbol{\chi}\right)+\sigma_{ij}\left(\mathbf{x},0\right) \tag{3.14}$$

$$u_i(\mathbf{x},t)=\sum_{\ell=0}^{s}\int_{\Gamma}\begin{Bmatrix}u_{ijk}^{Fc}(\mathbf{x}-\boldsymbol{\chi},t-\tau_\ell)\times\Delta F_k(\boldsymbol{\chi},\tau_\ell)+\\ u_{ij}^{sc}(\mathbf{x}-\boldsymbol{\chi},t-\tau_\ell)\times\Delta f(\boldsymbol{\chi},\tau_\ell)\ +\\ u_{ij}^{hc}(\mathbf{x}-\boldsymbol{\chi},t-\tau_\ell)\times\Delta h(\boldsymbol{\chi},\tau_\ell)\end{Bmatrix} d\Gamma(\boldsymbol{\chi})+u_i(\mathbf{x},0) \tag{3.15}$$

$$p(\mathbf{x},t)=\sum_{\ell=0}^{s}\int_{\Gamma}\begin{Bmatrix}p_k^{Fc}(\mathbf{x}-\boldsymbol{\chi},t-\tau_\ell)\times\Delta F_k(\boldsymbol{\chi},\tau_\ell)+\\ p^{sc}(\mathbf{x}-\boldsymbol{\chi},t-\tau_\ell)\times\Delta f(\boldsymbol{\chi},\tau_\ell)\end{Bmatrix} d\Gamma(\boldsymbol{\chi})+p(\mathbf{x},0) \tag{3.16}$$

$$T(\mathbf{x},t)=\sum_{\ell=0}^{s}\int_{\Gamma}\left\{T^{hc}(\mathbf{x}-\boldsymbol{\chi},t-\tau_\ell)\times\Delta h(\boldsymbol{\chi},\tau_\ell)\right\} d\Gamma(\boldsymbol{\chi})+T(\mathbf{x},0) \tag{3.17}$$

Note that in equation (3.14), spatial integration includes the free term and Cauchy principal-value integral evaluation, and these terms are calculated once during the solving procedure.

3.2.3. Numerical implementation

Usually in wellbore problems, the prescribed boundary conditions are tractions, temperature, and pressure. The initial step in the numerical implementation of the technique is establishing a set of integral equations for stated quantities that were derived previously in equations (3.14), (3.16), and (3.17). Note that the boundary integral equations presented here are in the form of no body forces.

The unknowns in equations (3.14), (3.16), and (3.17) are normal and shear traction discontinuities and heat and fluid sources. The equations generally cannot be solved analytically. Therefore, the use of a numerical procedure is required. The following numerical process is used:

1. The wellbore perimeter is divided into a number of quadrilateral FS elements (see Figure 4).

2. The distribution of traction discontinuities and fluid and heat sources are approximated over each element (see Figure 6). It is assumed that traction discontinuities have constant strength throughout an element and that the fluid and heat source distributions can be approximated using piecewise polynomial linear shape functions in space. Note that the strength of the unknowns during a time step is constant (because of continuous approach, the strength is constant during each time step).
3. A sufficient number of collocation points are chosen along FS elements for traction discontinuities (an element's center; one collocation point is enough for traction discontinuities due to the constant strength inside the element) and temperature and pressure (an element's four vertices; owing to linear variation in the fluid and heat source throughout the element). Then with the help of numerical integration over each element, equations (3.14), (3.16), and (3.17) can be represented by a system of algebraic equations.
4. The strengths of the unknowns at the collocation points are found by solving the system of algebraic equations.

Accordingly, induced stresses, pore pressure, and temperature on a collocation point in element m due to constant distribution of continuous tractions and the linear spatial distribution of continuous heat and fluid sources on element r at current time t are given by:

$$\sigma_{ij}\left(\mathbf{x}^m,t\right)=\tilde{S}_{ijk}^{Fc}\left(\mathbf{x}^m-\boldsymbol{\chi}^r,t\right)\times\Delta F_k^t\left(\boldsymbol{\chi}^r\right)+\sum_{q=1}^{4}\left\{\tilde{S}_{ij}^{sc}\left(\mathbf{x}^m-\boldsymbol{\chi}_q^r,t\right)\times\Delta f^t\left(\boldsymbol{\chi}_q^r\right)\right\}$$
$$+\sum_{q=1}^{4}\left\{\tilde{S}_{ij}^{hc}\left(\mathbf{x}^m-\boldsymbol{\chi}_q^r,t\right)\times\Delta h^t\left(\boldsymbol{\chi}_q^r\right)\right\} \tag{3.18}$$

$$p\left(\mathbf{x}_w^m,t\right)=\tilde{P}_k^{Fc}\left(\mathbf{x}_w^m-\boldsymbol{\chi}^r,t\right)\times\Delta F_k^t\left(\boldsymbol{\chi}^r\right)+\sum_{q=1}^{4}\left\{\tilde{P}^{sc}\left(\mathbf{x}_w^m-\boldsymbol{\chi}_q^r,t\right)\times\Delta f^t\left(\boldsymbol{\chi}_q^r\right)\right\} \tag{3.19}$$

$$T\left(\mathbf{x}_w^m,t\right)=\sum_{q=1}^{4}\left\{\tilde{T}^{hc}\left(\mathbf{x}_w^m-\boldsymbol{\chi}_q^r,t\right)\times\Delta h^t\left(\boldsymbol{\chi}_q^r\right)\right\} \tag{3.20}$$

where $\Delta F_k^t\left(\boldsymbol{\chi}^r\right)$ is increment of traction discontinuities in k direction at the center of element r at time t, $\Delta f^t\left(\boldsymbol{\chi}_q^r\right)$ is increment of fluid source at node q of element r at time t which has $\boldsymbol{\chi}_q^r$ coordinate, and $\Delta h^t\left(\boldsymbol{\chi}_q^r\right)$ is increment of heat source at node q of element r at time t. In the preceding equations, $\mathbf{x}^m$ is coordinates of influenced element center, $\boldsymbol{\chi}^r$ is coordinates of influencing element center, $\mathbf{x}_w^m$ and $\boldsymbol{\chi}_q^r$,$\boldsymbol{\chi}_w^r$ (w,q=1,2,3,4) is one of four vertices coordinates of an influenced or influencing element. Note that influenced and influencing elements are referred by superscripts m and r. All quantities have to be in the local coordinate system of an influenced element.

Relations that present effects of traction discontinuities and fluid and heat sources in influencing elements on the stress, pressure, and temperature distribution of influenced elements are given by:

$$\begin{aligned}
\tilde{S}_{ijk}^{Fc}\left(\mathbf{x}^m-\boldsymbol{\chi}^r,t\right)&=a_{il}\,a_{jm}\int_{S_r}\sigma_{lmk}^{Fc}\left(\mathbf{x}^m-\boldsymbol{\chi}^r,t\right)\,dS_r\\
\tilde{S}_{ij}^{sc}\left(\mathbf{x}^m-\boldsymbol{\chi}_q^r,t\right)&=a_{il}\,a_{jm}\int_{S_r}\sigma_{lm}^{sc}\left(\mathbf{x}^m-\boldsymbol{\chi}_q^r,t\right)\times N_q\;dS_r\\
\tilde{S}_{ij}^{hc}\left(\mathbf{x}^m-\boldsymbol{\chi}_q^r,t\right)&=a_{il}\,a_{jm}\int_{S_r}\sigma_{lm}^{hc}\left(\mathbf{x}^m-\boldsymbol{\chi}_q^r,t\right)\times N_q\;dS_r
\end{aligned} \tag{3.21}$$

$$\tilde{P}_k^{Fc}\left(\mathbf{x}_w^m-\boldsymbol{\chi}^r,t\right)=\int_{S_r} p_k^{Fc}\left(\mathbf{x}_w^m-\boldsymbol{\chi}^r,t\right)\,dS_r$$
$$\tilde{P}^{sc}\left(\mathbf{x}_w^m-\boldsymbol{\chi}_q^r,t\right)=\int_{S_r} p^{sc}\left(\mathbf{x}_w^m-\boldsymbol{\chi}_q^r,t\right)\times N_q\;dS_r \tag{3.22}$$

$$\tilde{T}^{hc}\left(\mathbf{x}_w^m-\boldsymbol{\chi}_q^r,t\right)=\int_{S_r} T^{sc}\left(\mathbf{x}_w^m-\boldsymbol{\chi}_q^r,t\right)\times N_q\;dS_r \tag{3.23}$$

where a_{il} are components of transformation matrix. The matrix transforms local coordinates of influencing element into local coordinates of influenced element. The transformation matrix is presented in Appendix D. In the preceding equations, N_q are linear shape functions (Figure 6). Note that as described in the steps of the numerical procedure, applied quadrilateral elements are not isoparametric. The following relations present linear shape functions in local coordinates of mapped quadrilateral elements:

$$N_1=0.25(1-\xi_1)(1-\xi_2) \qquad N_2=0.25(1+\xi_1)(1-\xi_2)$$
$$N_3=0.25(1-\xi_1)(1+\xi_2) \qquad N_4=0.25(1+\xi_1)(1+\xi_2) \tag{3.24}$$

where ξ_1 and ξ_2 are two local coordinates of mapped element (see Figure 12).

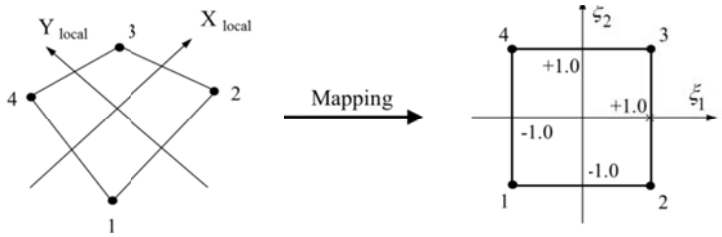

Figure 12. Local coordinates of mapped quadrilateral element.

Integrations of fundamental solutions on all quadrilateral elements are performed numerically. Through the numerical evaluation of integrations, in the case of the same influenced and influencing element, different mathematical singularity occurrs. Singular integrals require a special evaluation procedure that is presented in Appendix C.

For regular integrals, 20 × 20 Gauss numerical integration is performed. In this case 20 × 20 points are chosen to be sure that the variation in the fundamental solution is captured in an element. For singular integral evaluation, a special numerical algorithm is proposed [96, 97] (see Appendix C). In the method, any singular integral is equivalent to the sum of double and 2D regular integrals. A Gaussian quadrature with 40 × 40 integral points is used, which ensures the accuracy for the singular integrals. Note that stresses are presented at influenced element local coordinates and that normal and two shear stress components are essential constituents. Spatial and temporal discretized forms of equations (3.15), (3.17), and (3.18) representing the boundary of the wellbore by M FS elements and time by s equal time steps are given by

$$\begin{bmatrix} \sigma_{i3}\left(\mathbf{x}^m, t\right) \\ -\sigma_{i3}\left(\mathbf{x}^m, 0\right) \end{bmatrix}_{i=1,2,\,or\,3} = \sum_{r=1}^{M} \begin{bmatrix} S_{i3k}^{Fc}\left(\mathbf{x}^m - \boldsymbol{\chi}^r, \Delta t\right)\Delta F_k^{r,t} + \\ \sum_{q=1}^{4}\left\{S_{i3}^{sc}\left(\mathbf{x}^m - \boldsymbol{\chi}_q^r, \Delta t\right)\Delta f_q^{r,t}\right\} \\ \sum_{q=1}^{4}\left\{S_{i3}^{hc}\left(\mathbf{x}^m - \boldsymbol{\chi}_q^r, \Delta t\right)\Delta h_q^{r,t}\right\} \end{bmatrix} + \sum_{\ell=0}^{s-1}\sum_{r=1}^{M} \begin{bmatrix} S_{i3k}^{Fc}\left(\mathbf{x}^m - \boldsymbol{\chi}^r, \ell\Delta t\right)\Delta F_k^{r,(p-\ell)\Delta t} + \\ \sum_{q=1}^{4}\left\{S_{i3}^{sc}\left(\mathbf{x}^m - \boldsymbol{\chi}_q^r, \ell\Delta t\right)\Delta f_q^{r,(p-\ell)\Delta t}\right\} \\ \sum_{q=1}^{4}\left\{S_{i3}^{hc}\left(\mathbf{x}^m - \boldsymbol{\chi}_q^r, \ell\Delta t\right)\Delta h_q^{r,(p-\ell)\Delta t}\right\} \end{bmatrix} \tag{3.25}$$

$$\begin{bmatrix} p\left(\mathbf{x}_p^m, t\right) \\ -p\left(\mathbf{x}_p^m, 0\right) \end{bmatrix} = \sum_{r=1}^{M} \begin{bmatrix} P_k^{Fc}\left(\mathbf{x}_p^m - \boldsymbol{\chi}^r, \Delta t\right)\Delta F_k^{r,t} + \\ \sum_{q=1}^{4}\left\{P^{sc}\left(\mathbf{x}_p^m - \boldsymbol{\chi}_q^r, \Delta t\right)\Delta f_q^{r,t}\right\} \end{bmatrix} + \sum_{\ell=0}^{s-1}\sum_{r=1}^{M} \begin{bmatrix} P_k^{Fc}\left(\mathbf{x}_p^m - \boldsymbol{\chi}^r, \ell\Delta t\right)\Delta F_k^{r,(p-\ell)\Delta t} + \\ \sum_{q=1}^{4}\left\{P^{sc}\left(\mathbf{x}_p^m - \boldsymbol{\chi}_q^r, \ell\Delta t\right)\Delta f_q^{r,(p-\ell)\Delta t}\right\} \end{bmatrix} \tag{3.26}$$

$$\begin{bmatrix} T\left(\mathbf{x}_p^m, t\right) \\ -T\left(\mathbf{x}_p^m, 0\right) \end{bmatrix} = \sum_{r=1}^{M} \begin{bmatrix} \sum_{q=1}^{4}\left\{\tilde{T}^{hc}\left(\mathbf{x}_p^m - \boldsymbol{\chi}_q^r, \Delta t\right)\Delta h_q^{r,t}\right\} \end{bmatrix} + \sum_{\ell=0}^{s-1}\sum_{r=1}^{M} \begin{bmatrix} \sum_{q=1}^{4}\left\{\tilde{T}^{hc}\left(\mathbf{x}_p^m - \boldsymbol{\chi}_q^r, \ell\Delta t\right)\Delta h_q^{r,(p-\ell)\Delta t}\right\} \end{bmatrix} \tag{3.27}$$

where $\Delta F_k^{r,t}$, $\Delta f_q^{r,t}$ and $\Delta h_q^{r,t}$, are the increment of traction discontinuities at the center of element r, the increment of the fluid source at vertex q of element r, and the increment of the heat source at vertex q of element r at time t, respectively.

Equations (3.25), (3.26), and (3.27) establish a set of linear algebraic equations that should be solved to define stress discontinuities and fluid and heat sources.

Note that the procedures described here are only used to solve boundary conditions specified by stresses or displacements, pore pressure, and temperature. For boundary conditions defined by fluid flux and heat flux, consistent fundamental solutions are needed. Nevertheless, the process of numerical implementation is similar.

3.3. Thermoporoelastic displacement discontinuity

DD and FS share similar principles in terms of formulation. The main difference is in the singular solutions that control the formation of influence coefficients.

An elastic DD method for elastic nonporous media was developed by Crouch and Starfield [26] and was used to model rock joint opening and slip due to mining operations. A coupled poroelastic DD method was presented by Cleary[83, 84] and Detournay and Cheng[30] for fluid-saturated porous media. They also provided singular solutions for pore pressure, displacement, and stress induced by constant DDs or continuous fluid source along a plane of crack in an infinite saturated media. Using the linear theory of thermoporoelasticity[17], Ghassemi et al. [47] established a 2D thermoporoelastic DD method that was recently used by Ghassemi and Zhou [57] to develop a 3D coupled thermoelasticity and poroelasticity DD method. Ghassemi and

Zhou's studied a single planar crack behavior and did not consider the interaction of multiple cracks. These researchers also did not consider the direct effect of temperature on pore pressure. In other words, the model that was proposed by Ghassemi and Zhou is not fully coupled thermoporoelastic. However, it is used in the current study to reach beyond some of its limitations.

Each crack in a saturated thermoporoelastic infinite medium is considered as a boundary. All unknowns (DDs, heat source, and fluid source) can be found out if the distribution of temperature, stress, and pressure in cracks are known. In other words, the DDs, heat and fluid sources can be determined by solving a set of linear equations. The fully coupled DD method could be used to study the variation in crack opening and the leak-off and heat source between cracks and the matrix.

The thermoporoelastic DD method is constructed on the superposition of singular solution for constant normal and shear discontinuities in a displacement field. The discontinuity occurs over a finite surface in an infinite medium, as shown in Figure 13.

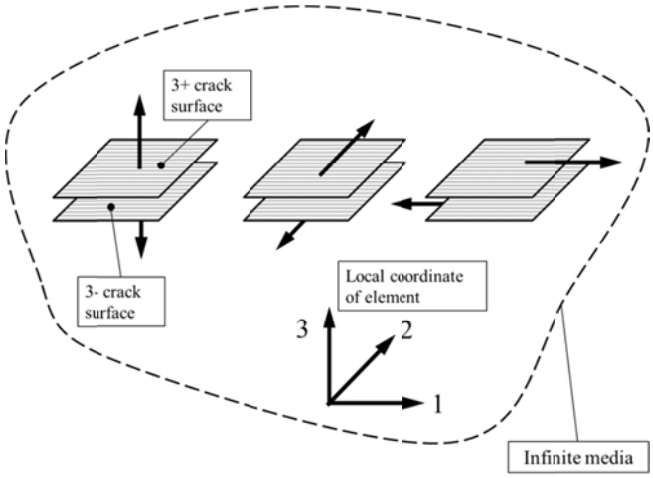

Figure 13. Normal and two shears displacement discontinuities, and local coordinates of DD element.

Physically speaking, a DD element can be considered a planar crack. The crack has a normal vector in the local 3 direction. A crack's two surfaces can be distinguish by saying that one is on the positive side (in Figure 13, 3^{+}) and the other is on the negative side (in Figure 13, 3^{-}). By moving from one side of crack to the other, displacements (u_1, u_2, u_3) experience certain changes in value. By defining DD as the difference in displacement between the two sides of the segment, one can represent these changes as follows:

$$\begin{aligned} D_{13} &= u_1^{+} - u_1^{-} \\ D_{23} &= u_2^{+} - u_2^{-} \\ D_{33} &= u_3^{+} - u_3^{-} \end{aligned} \tag{3.28}$$

where the first subscript shows the direction of the discontinuities (1, 2, and 3) and the second subscript shows the direction of the normal to the surface.

Poroelastic solutions to unit DDs were given by Cleary [83, 84] and Cheng et al.[85, 86]. As mentioned previously, non-isothermal poroelasticity can be decoupled to thermoelasticity and poroelasticity (compare to fully coupled thermoporoelasticity). Hence, for DD and fluid source, the presented solution in Cheng at al. [85] can be used, and because of similarity between thermoelasticity and poroelasticity fundamental solutions, the temperature and stresses induced by the heat source in thermoelastic media can be found easily. For fully coupled thermoporoelasticity, Berchenko [89] derived singular solutions that are presented in Appendix A.

Using corresponding fundamental solutions, one can define stress components, temperature, and pore pressure all over thermoporoelastic media as a function of DDs,

fluid sources, and heat sources. Similar to the FS method, the distributions of fluid and heat sources are assumed to be linear across DD elements (see Figure 6), and the distribution of DDs are assumed to be constant throughout an element. Therefore, across each element, three DD components, fluid source, and heat source are the unknowns.

3.3.1. Boundary integral equations

Similar to the FS method, the DD method can be used to obtain stresses, pore pressure, and temperature at any point inside of a medium using the known history of heat sources, fluid sources, and DD components along the boundary. In the thermoporoelastic method, problems are modeled by distributing DD and fluid and heat sources on the crack surface and requiring that the superposition of their effects satisfy the prescribed traction, pressure, and temperature on all cracks. Determining the discontinuities and sources requires solving a set of three integral equations. The boundary integral equations for stresses, pore pressure, and temperature can be written as follows [57]:

$$\sigma_{ij}\left(\mathbf{x},t\right)=\int_0^t\int_\Gamma\left\{\begin{array}{l}\sigma_{ijkn}^{di}\left(\mathbf{x},t;\boldsymbol{\chi},\tau\right)\times DD_{kn}\left(\boldsymbol{\chi},\tau\right)+\\ \sigma_{ij}^{si}\left(\mathbf{x},t;\boldsymbol{\chi},\tau\right)\times f\left(\boldsymbol{\chi},\tau\right)\ +\\ \sigma_{ij}^{hi}\left(\mathbf{x},t;\boldsymbol{\chi},\tau\right)\times h\left(\boldsymbol{\chi},\tau\right)\end{array}\right\}d\Gamma\left(\boldsymbol{\chi}\right)\,d\tau+\sigma_{ij}\left(\mathbf{x},0\right) \tag{3.29}$$

$$p\left(\mathbf{x},t\right)=\int_0^t\int_\Gamma\left\{\begin{array}{l}p_{kn}^{di}\left(\mathbf{x},t;\boldsymbol{\chi},\tau\right)\times DD_{kn}\left(\boldsymbol{\chi},\tau\right)+\\ p^{si}\left(\mathbf{x},t;\boldsymbol{\chi},\tau\right)\times f\left(\boldsymbol{\chi},\tau\right)\end{array}\right\}d\Gamma\left(\boldsymbol{\chi}\right)\,d\tau+p\left(\mathbf{x},0\right) \tag{3.30}$$

$$T\left(\mathbf{x},t\right)=\int_0^t\int_\Gamma\left\{T^{hi}\left(\mathbf{x},t;\boldsymbol{\chi},\tau\right)\times h\left(\boldsymbol{\chi},\tau\right)\right\}\,d\Gamma\left(\boldsymbol{\chi}\right)\,d\tau+T\left(\mathbf{x},0\right) \tag{3.31}$$

where DD_{kn} is component "kn" of displacement discontinuities, σ_{ijkn}^{di} is induced stress of component "ij" due to instantaneous point DD of component "kn", and p_{kn}^{di} is induced pore pressure due to instantaneous point DD of component "kn". In these integral equations for thermoporoelastic DD, equation (3.31) is the same as equation (3.4), which is induced temperature due to a heat source in the thermoporoelastic FS method. This is because the temperature-governing equation is decoupled from the hydraulic and mechanical part, and same field equation for heat diffusion governs the behavior of media in both the DD and FS methods.

Note that because displacement on the fracture surface is not predefined, there is no need to define the free term for DD formulation. However, if a non-crack surface will be modeled with a DD element and displacement is predefined on that, it is essential to calculate the free term. However, such a case is not investigated in the current study.

3.3.2. Temporal integration

In the primary formulation of thermoporoelastic DD and FS methods, corresponding fundamental solutions are instantaneous impulses. As described in section 3.2.2, fundamental solutions for continuous DD impulses can be obtained by integrating the consistent solutions for instantaneous impulses with respect to time. Continuous fundamental solutions for the DD method are presented in Appendix A.

There are different approaches to the temporal integration of corresponding fundamental solutions. One approach is to solve equations at the end of one time step and then use the results as the initial conditions for the next time step, and so on. The

shortcoming of this method is that it requires discretizing the spatial domain of the problem, which is almost impossible in the case of semi-infinite or infinite problems. Another approach is the time-marching technique. In this method, the solution is sought at the end of each time step and saved. Then the effect of the previous time step, based on the time difference, is used to find the solution for next time step [90, 91]. This method allows for change in singular impulses over time. It involves incrementing the strengths of singular impulses at each time step and including the influence of all previous increments (see section 3.2.2). This technique eliminates the need for discretization of the spatial domain, but a disadvantage of the method is that the influencing coefficient must be known to be used as required. Implementation of the time-marching scheme is much easier by considering the fact that the effective parameter is the time interval between the influencing and influenced effects rather than absolute time. This is because of the translation property of fundamental solutions, which is also applicable to the space axis. For example, stresses at point $\mathbf{x}$ and time t due to a heat source at point $\boldsymbol{\chi}$ and time τ are equal to the stress at the relative location of $\mathbf{x}-\boldsymbol{\chi}$ and time $t-\tau$ due to a heat source at the origin of time and space. The translation properties can be shown as follows:

$$\sigma_{ij}^{hc}\left(\mathbf{x},t;\boldsymbol{\chi},\tau\right)=\sigma_{ij}^{hc}\left(0,0;\mathbf{x}-\boldsymbol{\chi},t-\tau\right) \tag{3.32}$$

Because of the translation property of fundamental solutions, the influenced and influencing time and location can be shifted along the time and space axis without affecting the values of the fundamental solutions. Consequently, the influence coefficient can be calculated only once during the calculation history.

3.3.3. Numerical implementation

As in the FS method, the numerical implementation of boundary integral equations of thermoporoelastic DD requires spatial and temporal discretization. Spatial discretization is achieved by dividing the boundary of the problem into a number of DD elements and replacing the integrals over the boundary with a sum of integrals over DD elements. Temporal discretization is realized by dividing the time domain into a number of time increments, as described in section 3.2.2. Because of the similarity in structure of the DD and FS methods, details of the numerical procedures for the DD method are omitted here. Suppose that s is the number of time increments. Then boundary integral equations for stresses, pore pressure, and temperature in the medium can be rewritten as follows:

$$\sigma_{ij}\left(\mathbf{x},t\right)=\sum_{\ell=0}^{s}\int_{\Gamma}\left\{\begin{array}{l}\sigma_{ijkn}^{dc}\left(\mathbf{x}-\boldsymbol{\chi},t-\tau_{\ell}\right)\times\Delta DD_{kn}\left(\boldsymbol{\chi},\tau_{\ell}\right)+\\ \sigma_{ij}^{sc}\left(\mathbf{x}-\boldsymbol{\chi},t-\tau_{\ell}\right)\times\Delta f\left(\boldsymbol{\chi},\tau_{\ell}\right)\ +\\ \sigma_{ij}^{hc}\left(\mathbf{x}-\boldsymbol{\chi},t-\tau_{\ell}\right)\times\Delta h\left(\boldsymbol{\chi},\tau_{\ell}\right)\end{array}\right\}d\Gamma\left(\boldsymbol{\chi}\right)+\sigma_{ij}\left(\mathbf{x},0\right)\qquad(3.33)$$

$$p\left(\mathbf{x},t\right)=\sum_{\ell=0}^{s}\int_{\Gamma}\left\{\begin{array}{l}p_{kn}^{dc}\left(\mathbf{x}-\boldsymbol{\chi},t-\tau_{\ell}\right)\times\Delta DD_{kn}\left(\boldsymbol{\chi},\tau_{\ell}\right)+\\ p^{sc}\left(\mathbf{x}-\boldsymbol{\chi},t-\tau_{\ell}\right)\times\Delta f\left(\boldsymbol{\chi},\tau_{\ell}\right)\end{array}\right\}d\Gamma\left(\boldsymbol{\chi}\right)+p\left(\mathbf{x},0\right)\qquad(3.34)$$

$$T\left(\mathbf{x},t\right)=\sum_{\ell=0}^{s}\int_{\Gamma}\left\{T^{hc}\left(\mathbf{x}-\boldsymbol{\chi},t-\tau_{\ell}\right)\times\Delta h\left(\boldsymbol{\chi},\tau_{\ell}\right)\right\}d\Gamma\left(\boldsymbol{\chi}\right)+T\left(\mathbf{x},0\right)\qquad(3.35)$$

where $DD_{kn}\left(\boldsymbol{\chi},\tau_{\ell}\right)$, $f\left(\boldsymbol{\chi},\tau_{\ell}\right)$ and $h\left(\boldsymbol{\chi},\tau_{\ell}\right)$ are strengths of continuous point DD, fluid source and heat source in time increment ℓ. Assume that N is the number of elements used to discretize the boundary. The spatial integrals over the boundary are replaced with the sum of the integrals over the elements.

Induced total stresses, pore pressure, and temperature on element m due to constant spatial distribution of continuous DDs and linear spatial distribution of fluid and heat sources on element r are given by

$$\begin{aligned}\sigma_{ij}\left(\mathbf{x}^m,t\right)=\tilde{S}_{ijkn}^{dc}\left(\mathbf{x}^m-\boldsymbol{\chi}^r,t\right)\times\Delta DD_{kn}^{t}\left(\boldsymbol{\chi}^r\right)+\sum_{q=1}^{4}\left\{\tilde{S}_{ij}^{sc}\left(\mathbf{x}^m-\boldsymbol{\chi}_q^r,t\right)\times\Delta f^{t}\left(\boldsymbol{\chi}_q^r\right)\right\}\\+\sum_{q=1}^{4}\left\{\tilde{S}_{ij}^{hc}\left(\mathbf{x}^m-\boldsymbol{\chi}_q^r,t\right)\times\Delta h^{t}\left(\boldsymbol{\chi}_q^r\right)\right\}\end{aligned}\tag{3.36}$$

$$p\left(\mathbf{x}_p^m,t\right)=\tilde{P}_{kn}^{dc}\left(\mathbf{x}_p^m-\boldsymbol{\chi}^r,t\right)\times\Delta DD_{kn}^{t}\left(\boldsymbol{\chi}^r\right)+\sum_{q=1}^{4}\left\{\tilde{P}^{sc}\left(\mathbf{x}_p^m-\boldsymbol{\chi}_q^r,t\right)\times\Delta f^{t}\left(\boldsymbol{\chi}_q^r\right)\right\}\tag{3.37}$$

$$T\left(\mathbf{x}_p^m,t\right)=\sum_{q=1}^{4}\left\{\tilde{T}^{hc}\left(\mathbf{x}_p^m-\boldsymbol{\chi}_q^r,t\right)\times\Delta h^{t}\left(\boldsymbol{\chi}_q^r\right)\right\}\tag{3.38}$$

Influence coefficients denote the influences of element r which are obtained by integrating fundamental solutions for continuous point impulses over the influencing element. The spatial integration over the plane quadrilateral elements is given by

$$\begin{aligned}\tilde{S}_{ijkn}^{dc}\left(\mathbf{x}^m-\boldsymbol{\chi}^r,t\right)&=a_{il}\,a_{jm}\int_{S_r}\sigma_{lmkn}^{dc}\left(\mathbf{x}^m-\boldsymbol{\chi}^r,t\right)\,dS_r\\\tilde{S}_{ij}^{sc}\left(\mathbf{x}^m-\boldsymbol{\chi}_q^r,t\right)&=a_{il}\,a_{jm}\int_{S_r}\sigma_{lm}^{sc}\left(\mathbf{x}^m-\boldsymbol{\chi}_q^r,t\right)\times N_q\;dS_r\\\tilde{S}_{ij}^{hc}\left(\mathbf{x}^m-\boldsymbol{\chi}_q^r,t\right)&=a_{il}\,a_{jm}\int_{S_r}\sigma_{lm}^{hc}\left(\mathbf{x}^m-\boldsymbol{\chi}_q^r,t\right)\times N_q\;dS_r\end{aligned}\tag{3.39}$$

$$\begin{aligned}\tilde{P}_{kn}^{dc}\left(\mathbf{x}_p^m-\boldsymbol{\chi}^r,t\right)&=\int_{S_r}p_{kn}^{dc}\left(\mathbf{x}_p^m-\boldsymbol{\chi}^r,t\right)\,dS_r\\\tilde{P}^{sc}\left(\mathbf{x}_p^m-\boldsymbol{\chi}_q^r,t\right)&=\int_{S_r}p^{sc}\left(\mathbf{x}_p^m-\boldsymbol{\chi}_q^r,t\right)\times N_q\;dS_r\end{aligned}\tag{3.40}$$

Singularities are handled the same as in the FS method. The singularity in the DD method is known as hyper-singularity and is 1 degree worse than in the FS method. However, the general method described in Appendix D can be used to model strong and

hyper-singularities. By representing the boundary of fractures by N elements, DD boundary integral equations are given by

$$\begin{bmatrix} \sigma_{i3}\left(\mathbf{x}^m,t\right)- \\ \sigma_{i3}\left(\mathbf{x}^m,0\right) \end{bmatrix}_{i=1,2,\ and\ 3} = \sum_{r=1}^{N}\begin{bmatrix} S_{i3k3}^{dc}\left(\mathbf{x}^m-\boldsymbol{\chi}^r,\Delta t\right)\Delta DD_{k3}^{r,t}+ \\ \sum_{q=1}^{4}\left\{S_{i3}^{sc}\left(\mathbf{x}^m-\boldsymbol{\chi}_q^r,\Delta t\right)\Delta f_q^{r,t}\right\} \\ \sum_{q=1}^{4}\left\{S_{i3}^{hc}\left(\mathbf{x}^m-\boldsymbol{\chi}_q^r,\Delta t\right)\Delta h_q^{r,t}\right\} \end{bmatrix} + \sum_{\ell=0}^{s-1}\sum_{r=1}^{N}\begin{bmatrix} S_{i3k}^{dc}\left(\mathbf{x}^m-\boldsymbol{\chi}^r,\ell\Delta t\right)\Delta DD_{k3}^{r,(s-\ell)\Delta t}+ \\ \sum_{q=1}^{4}\left\{S_{i3}^{sc}\left(\mathbf{x}^m-\boldsymbol{\chi}_q^r,\ell\Delta t\right)\Delta f_q^{r,(s-\ell)\Delta t}\right\} \\ \sum_{q=1}^{4}\left\{S_{i3}^{hc}\left(\mathbf{x}^m-\boldsymbol{\chi}_q^r,\ell\Delta t\right)\Delta h_q^{r,(s-\ell)\Delta t}\right\} \end{bmatrix} \tag{3.41}$$

$$\begin{bmatrix} p\left(\mathbf{x}_p^m,t\right)- \\ p\left(\mathbf{x}_p^m,0\right) \end{bmatrix} = \sum_{r=1}^{M}\begin{bmatrix} P_{k3}^{dc}\left(\mathbf{x}_p^m-\boldsymbol{\chi}^r,\Delta t\right)\Delta DD_{k3}^{r,t}+ \\ \sum_{q=1}^{4}\left\{P^{sc}\left(\mathbf{x}_p^m-\boldsymbol{\chi}_q^r,\Delta t\right)\Delta f_q^{r,t}\right\} \end{bmatrix} + \sum_{\ell=0}^{s-1}\sum_{r=1}^{M}\begin{bmatrix} P_{k3}^{Fc}\left(\mathbf{x}_p^m-\boldsymbol{\chi}^r,\ell\Delta t\right)\Delta DD_{k3}^{r,(s-\ell)\Delta t}+ \\ \sum_{q=1}^{4}\left\{P^{sc}\left(\mathbf{x}_p^m-\boldsymbol{\chi}_q^r,\ell\Delta t\right)\Delta f_q^{r,(s-\ell)\Delta t}\right\} \end{bmatrix} \tag{3.42}$$

$$T\left(\mathbf{x}_p^m,t\right) = \sum_{r=1}^{M}\left[\sum_{q=1}^{4}\left\{\tilde{T}^{hc}\left(\mathbf{x}_p^m-\boldsymbol{\chi}_q^r,\Delta t\right)\Delta h_q^{r,t}\right\}\right] + \sum_{\ell=0}^{s-1}\sum_{r=1}^{M}\left[\sum_{q=1}^{4}\left\{\tilde{T}^{hc}\left(\mathbf{x}_p^m-\boldsymbol{\chi}_q^r,\ell\Delta t\right)\Delta h_q^{r,(s-\ell)\Delta t}\right\}\right] \tag{3.43}$$

Equations (3.41), (3.42), and (3.43) establish a set of linear algebraic equations whose unknowns are increments of continuous discontinuities and sources. They can be solved by applying the boundary conditions on all crack surfaces.

3.3.4. Crack initiation

During pressurization or injection/production into cracks, the surrounding rock is subjected to a system of external loads (stress, temperature, and pore pressure). The application of the load might cause the formation of a new crack within the rock mass. From a mathematical viewpoint, two types of issues can be distinguished during the

formation of a new crack: crack propagation and crack initiation. The current study does not consider crack propagation; however, it is useful to review the conditions for crack initiation and to consider it in the disturbance of a fracture system. Understanding crack initiation is essential for understanding the behavior of stationary existing cracks in geothermal fields and reservoir development.

To determine the conditions for crack initiation, one needs to evaluate the critical level of applied loads that correspond to the inception of a new crack in a reservoir environment. Having an appropriate crack initiation criterion is necessary to enhance the analysis of deformation and stresses. Several criteria exist for modeling rock failure in various applications [98]. Maximum tensile stress theory is often used to predict the tensile failure of crack and fracture initiation in petroleum or geothermal reservoirs. However, there are indications that shear might be a mode of failure in the initiation of cracks [5, 6, 41, 99]. Some investigators [100] have argued that hydraulic fracture is induced by shear rather by than tensile failure and have thus used the Mohr–Coulomb shear failure criterion. Neither the tensile nor the shear failure criterion is capable of predicting high breakdown pressures observed in the laboratory. The fracture mechanics model that is based on the concept of unstable fracture propagation using the fracture toughness criterion seems more promising [101]. In the current study, crack initiation is investigated within the framework of linear elastic fracture mechanics, a framework with its roots in the work of Griffith [102].

Irwin [103] showed that Griffith's criterion for crack growth is essentially identical to that of crack growth when the SIF, K, reaches a critical value K_c. This

parameter is known as fracture toughness. Fracture toughness is a material property that can be determined experimentally [104].

Hydraulically driven cracks are usually considered to propagate in Mode I, or the opening mode. In addition to a crack loaded in uniaxial tension, Irwin [103] considered other configurations of loading and classified them into three independent modes (see Figure 14). Mode I is the opening of crack, Mode II refers to a crack loaded tangentially to the crack surface in the direction of propagation, and Mode III is defined by a crack loaded tangentially to the crack surface perpendicular to the direction of propagation. The relations for the SIFs for each mode in 3D geometry, based on Figure 14, are given below [105, 106]. In the following relations it is assumed that the stress around the crack tip is plane strain with the crack tip as a normal to the plane.

$$SIF_I = DD_{33}\frac{E}{4\left(1-\nu^2\right)}\sqrt{\frac{\pi}{2d}}$$
$$SIF_{II} = DD_{13}\frac{E}{4\left(1-\nu^2\right)}\sqrt{\frac{\pi}{2d}} \qquad (3.44)$$

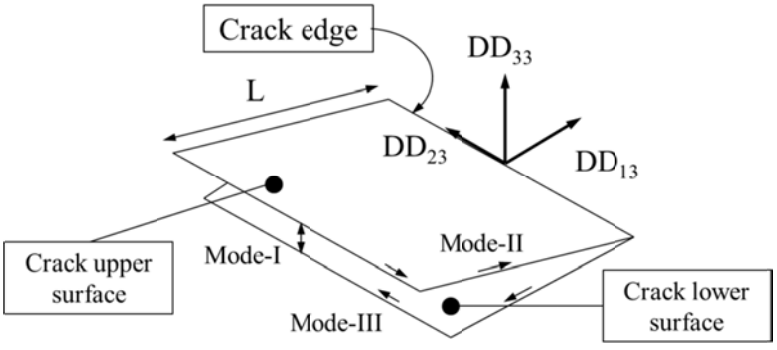

Figure 14. Four node quadrilateral element at crack edge.

In the current study, the point d=0.8L is used to calculate SIFs [69].

As mentioned previously, crack initiation criteria are met when the calculated SIF for each mode is equal to the critical SIF for the corresponding mode.

$$\begin{aligned} SIF_I &= K_{Ic} \\ SIF_{II} &= K_{IIc} \end{aligned} \tag{3.45}$$

3.4. Combining fictitious stress and displacement discontinuity

To model problems that involve both wellbores and cracks (see Figure 3), one can combine the FS and DD methods into a single model. This is relatively easy to do because of the similarity between the two methods. In a thermoporoelastic system, the difference between the FS and DD methods lies in the thermoporoelastic fundamental solutions.

There are two possible types of discontinuities in reservoir geomechanics problems: boundaries of wellbores and crack-type boundaries. Crack discontinuity is discretized into N plane quadrilateral DD elements with constant DD and linear fluid and heat sources across it. The wellbore boundary is divided by M quadrilateral FS elements with constant traction discontinuity and linear fluid and heat sources. From the principle of superposition, induced stresses, pore pressure, and temperature are sum of the effects of all M fictitious stresses; N DDs, M + N fluid sources, and M + N heat sources.

.

4. INDIRECT BOUNDARY ELEMENT MODEL TESTING

Based on the thermoporoelastic DD and FS formulation presented in the previous section, a FORTRAN computer code was developed to study the response of wellbores and fractures in real reservoir environments.

Numerical methods, like indirect boundary element techniques, have the benefit of being able to solve real problems with complex boundary conditions. However, it is very helpful to verify the computer code developed before applying it to a realistic problem. It is almost impossible to find an analytical solution for most real reservoir problems. Hence, the verification process aims to create a set of conditions that most closely resemble analytical conditions.

To verify the 3D thermoporoelastic FS and DD models, variety of examples are considered in simplified conditions. The results are compared to closed–form solutions or previously published results.

4.1. Sudden removal of sphere from reservoir (isothermal)

In this section, the behavior of a saturated sphere of rock that is suddenly removed from a formation and subjected to an abrupt elimination of hydrostatic load or internal pore pressure ($p = p_0$) throughout sphere surface is considered. The sudden removal of the sphere from this environment is characterized by the following two boundary conditions: (a) $\sigma_{rr}\left(R, t = 0+\right) = 0.0$ and (b) $p\left(R, t = 0+\right) = 0.0$, where R is the sphere radius. To simulate the problem, consider a saturated sphere of rock with radius 1.0 m. From time t = 0, the sphere is subjected to an elimination of uniform hydrostatic

load that is equal to 1.0 MPa. Moreover, the surface temperature is kept at the reservoir state during simulation; therefore, thermal loading does not contribute to the response of the sphere. Note that it is permitted that at the surface of the sphere pore fluid escapes freely.

Cryer [107] developed a closed-form solution for the sphere response. He showed that pore fluid pressure inside the sphere increased by a certain amount when the surface normal traction was removed and then continued to increase for some time before decreasing. This phenomenon, a rise in pore pressure that is followed by dissipation during consolidation of the saturated sphere, is called the Mandel–Cryer effect. The physical explanation for the Mandel–Cryer effect is that the sphere contracts near the drained surface boundary because of a dissipation of the induced pore pressure. Strain compatibility requires contraction, and hence additional pore pressure builds up in the interior [108]. Therefore, the Mandel–Cryer effect can be viewed as a transfer of toward the interior. The Mandel–Cryer effect can only be simulated by considering the fully coupled poroelastic equations presented in section 2.

Discretization of the sphere is illustrated in Figure 15. The surface of sphere is discretized with 5605 quadrilateral FS elements and 5607 nodes. Then 4 h is chosen as the time step. Pressure on the sphere surface was removed at the start of the analysis. The poroelastic properties of rock are presented in Table 1.

Dissipation of excess pore fluid pressure at the center of the sphere in different time steps is selected for the verification parameter. Figure 16 is the normalized pore fluid pressure at the center of the sphere versus the square root of Cryer's dimensionless

time throughout sequential time stages. In this figure p is 1.0 MPa, the initial pore pressure of sphere, and T is Cryer's dimensionless time. As shown in the figure, the numerical results agree well with the analytical solution. However, as time passes, the numerical results diverge a little bit from the analytical results. This is due to numerical error that accumulates at different times. The results show that the FS numerical technique accurately simulates fully coupled poroelasticity behavior.

Table 1. Poroelastic properties to model saturated sphere.

Shear modulus	(GPa)	8.30 (1204 Ksi)
Drained Poisson's ratio	(-)	0.33
Undrained Poisson's ratio	(-)	0.40
Biot coefficient	(-)	0.89
Base permeability	(m^2)	1.00×10^{-17} (10 Micro Darcy)
Fluid density	(kg/m^3)	1000.00 (0.433 psi/ft.)
Fluid viscosity	($N.s/m^2$)	1.00×10^{-3} (1.0 cp)
Fluid Diffusivity	(m^2/s)	1.417×10^{-4} (1.52×10^{-3} ft^2/s)

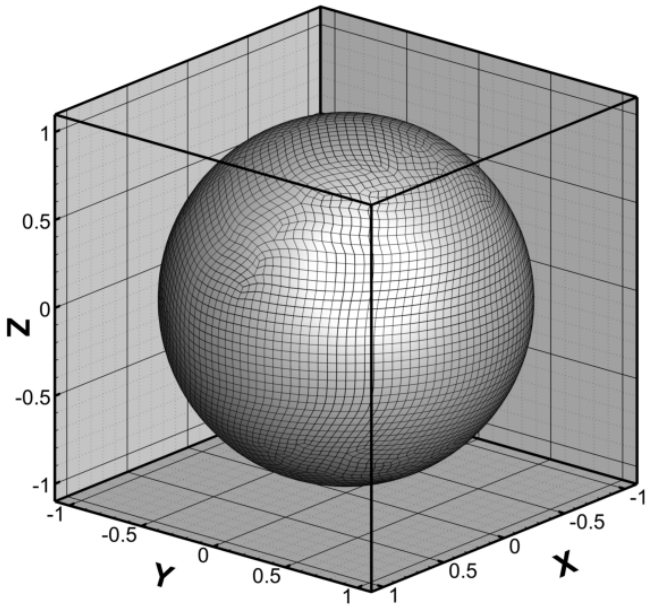

Figure 15. Discretized unit radius sphere with quadrilateral FS elements.

Cryer [107] did not investigate the time evolution of stress and strain components during the consolidation of the sphere, but with the proposed FS technique, all stress components and displacements can be presented.

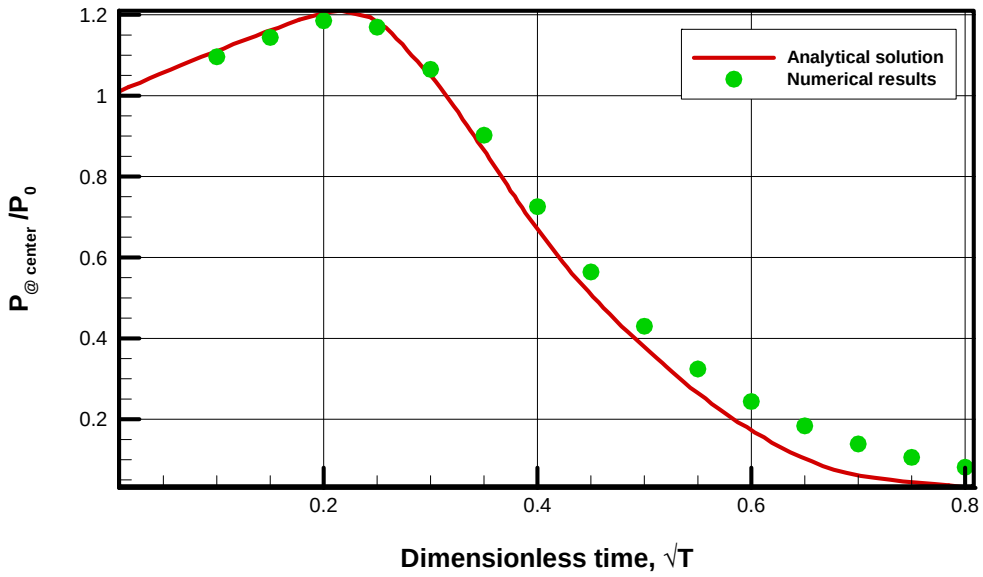

Figure 16. Comparison between analytical solution and FS numerical result.

In Figure 17 and Figure 18 pore pressure and principal stress evolution inside the sphere are represented by a 1/8 sphere. Figure 17 shows the evolution of pore pressure in the sphere over 80 h. The blue outer surface is the region with the higher degree of consolidation. In this zone, the excess pore pressure approaches zero. The red zone, which is in the central region of the sphere, has a pore pressure larger than the initial pore pressure of 1 MPa. The consolidated zone (blue zone) gradually progress inward until the pore fluid pressure is completely dissipated.

Figure 18 shows the evolution of tangential stress over 80 h. As expected, initially tangential stress on the sphere perimeter is maximum tensile (0.35 MPa) in the

red zone. As time passes and the sphere becomes more consolidated, tensile stress on the perimeter of the sphere decreases until it completely disappears. Note that in the spherical coordinates, tangential stresses are equal and minimum principal stress is radial stress.

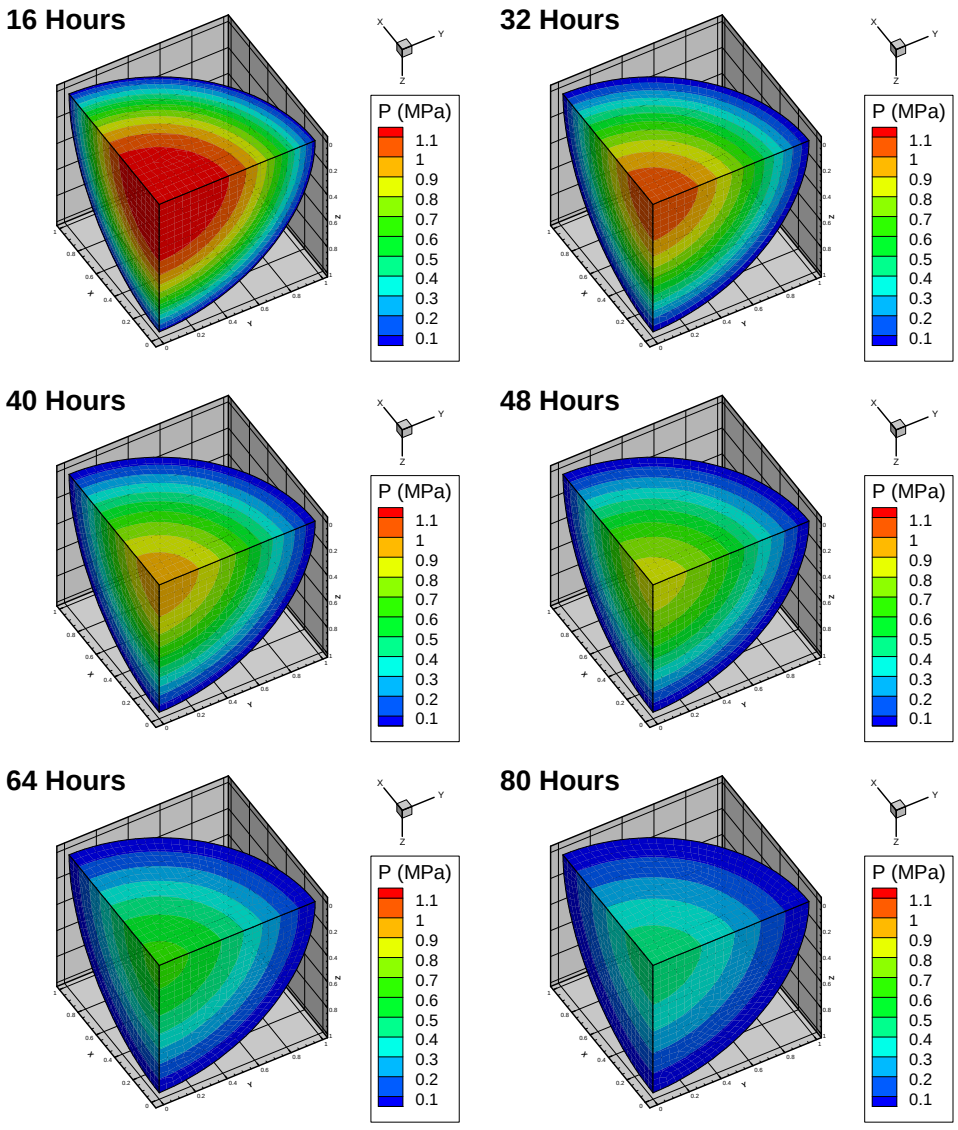

Figure 17. Pore pressure evolution during 80 hours of sphere consolidation.

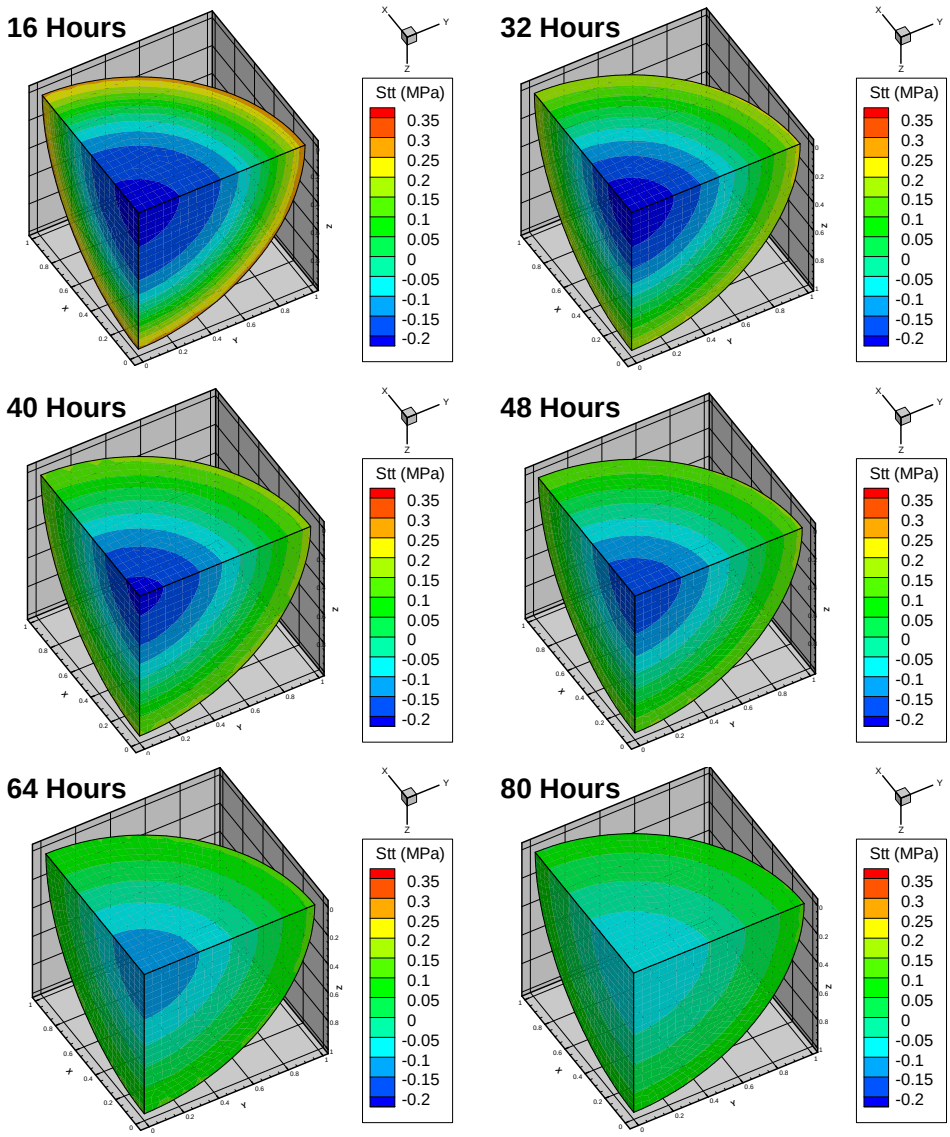

Figure 18. Tangential stress evolution during 80 hours of sphere consolidation.

4.2. Poroelastic stress analysis of wellbore

Induced pore pressure and stresses around a borehole are a key concern in drilling and hydraulic fracturing. Prior to drilling, a porous rock exists in a state of in–situ stress, pore pressure, and temperature. Drilling results in the elimination of

supporting stress at the wellbore wall and thus a redistribution of stresses. Hydraulic and thermal gradients developed between drilling mud and the formation also modify the stress state near the borehole. In this section, the isothermal drilling of a horizontal wellbore under a general loading condition is considered to examine more completely the FS computer code.

Using the FS method, one can predict stresses, pore pressure, and temperature fields around a wellbore by solving equations (3.25), (3.26), and (3.27). The numerical results of the problem are compared with a plane strain analytical solution presented by Detournay and Cheng [30].

Following Carter and Booker [109] and Detournay and Cheng [62], a general solution can be perceived by dividing the load into three loading modes and superimposing the results from the three loading modes onto the original condition. Assume that a wellbore is aligned along in–situ principal stress directions. An in–situ stress condition can generally be decomposed into three major modes. Among these discrete loading modes, Mode 1 and 2 are axisymmetric and Mode 3 is asymmetric.

A case of general loading that can create a plane strain condition in a 3D model (as shown in Figure 19) is considered and described as follows:

$$\sigma_{zz} = -\left(P_0 + S_0\right), \quad \sigma_{xx} = -\left(P_0 - S_0\right), \quad p = p_0 \tag{4.1}$$

where mean stress or hydrostatic stress is P_0, S_0 is the deviatoric stress, and p_0 is background pore pressure.

Consider 3.0 m of an end section of a horizontal circular well with a 0.1 m radius in a saturated rock. Assume that the wellbore is subjected to uniform in–situ anisotropic

stress and background pore pressure without any internal pressure and temperature difference. The essential input parameters to simulate the wellbore are listed in Table 2.

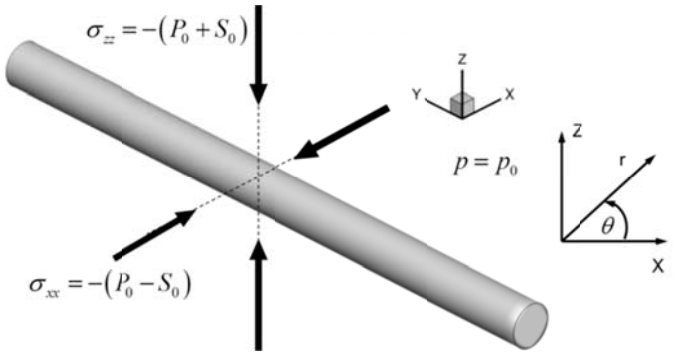

Figure 19. End section of circular wellbore under non-hydrostatic stress loading.

Table 2. Properties of rock to model poroelastic loading of wellbore.

Shear modulus	(GPa)	8.30 (1204 Ksi)
Drained Poisson's ratio	(-)	0.20
Undrained Poisson's ratio	(-)	0.40
Biot coefficient	(-)	0.89
Base permeability	(m^2)	1.00×10^{-17} (10 Micro Darcy)
Fluid density	(kg/m^3)	1000.00 (0.433 psi/ft.)
Fluid viscosity at reservoir condition	($N.s/m^2$)	3.00×10^{-4} (0.3 cp)

The three loading modes in cylindrical coordinates can be represented as follows:

- Mode 1, far-field isotropic stress:

$$\sigma_{rr} = -P_0 \quad , \sigma_{r\theta} = 0.0 \quad , p = 0.0 \tag{4.2}$$

- Mode 2, background pore pressure:

$$\sigma_{rr} = 0.0 \quad , \sigma_{r\theta} = 0.0 \quad , p = p_0 \tag{4.3}$$

- Mode 3, far-field stress deviator:

$$\sigma_{rr} = -S_0 \cos(2\theta) \quad , \sigma_{r\theta} = S_0 \sin(2\theta) \quad , p = 0.0 \tag{4.4}$$

where r and θ are polar coordinates defined in Figure 19. These loading modes are applied at infinity, and all stress components and pore pressure at the wellbore boundary are kept at zero.

In the current section, 3D numerical results for stresses and pressure around a wellbore are verified with plane strain analytical results. Notice that there is an intrinsic difference between plane strain and 3D model: After a long time (depending on the dimensions of the wellbore and the diffusivity coefficient), end effects will be sensed by the whole wellbore, and as a consequence all stresses and pore pressure will be affected. Therefore, in the comparison of numerical results and analytical results, effects of the inherent difference should be considered.

For each loading mode, induced stress and pore pressure fields are examined and analyzed using the FS model. About 3 m of the end section of the wellbore is considered, and its surface is discretized with 2100 FS elements and 2121 nodes, as shown in Figure 20. It is clear from the figure that the end wall of the wellbore is also discretized. Each element is about 10° on the wellbore perimeter. In the presented results, analysis time is normalized by $t^* = t\ c/R^2$, where c is fluid diffusivity and R is the radius of the wellbore.

The wellbore is analyzed by one time step for each time period. Results of analyses with a single time step and with increasing time steps were compared, and very small differences were found. Therefore, to save computational time, one time step was chosen for the analysis of each period. To compare the numerical results with the plane strain ones, and to realize the end effects on the results, two cross sections with the same

field points in the middle of the wellbore and at the end of it are considered as shown in Figure 21. Sec. 1 is the end section and Sec. 2 is the middle section.

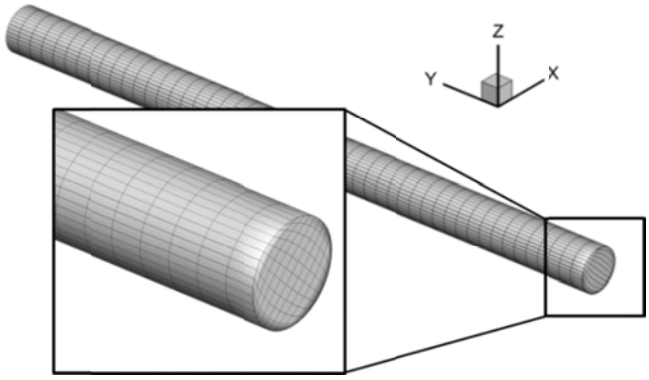

Figure 20. Discretization of wellbore with FS elements.

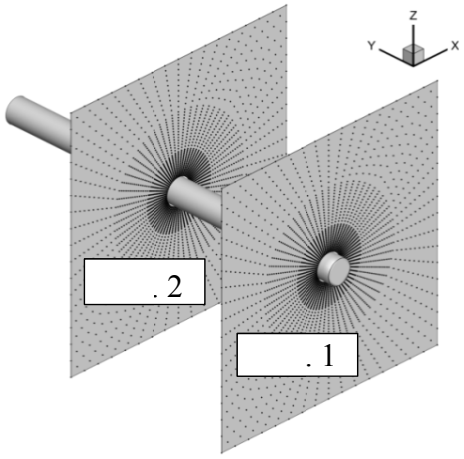

Figure 21. Sections inside of media for numerical results compared with analytical ones.

4.2.1. Mode 1: Hydrostatic stress loading

Mode 1 is hydrostatic stress loading. The far-field stress is considered to be -10 MPa (tension positive) everywhere. That is, the magnitude of hydrostatic stress P_0 = 10 MPa. There is no initial pore pressure in the current loading mode, and the background formation temperature is considered to be zero. All three traction components, pressure,

and temperature at the wellbore boundary are considered to be zero (poroelastic model). The classical analytical solution for Mode 1 in the plane stress condition is

$$\sigma_{rr}/P_0 = -1 + (r/R)^2, \qquad \sigma_{\theta\theta}/P_0 = -1 - (r/R)^2$$

Tangential, radial stresses, and pore pressure near the wellbore are plotted for Sec. 1 and Sec. 2 at normalized time t* = 0.01 and t* = 10 in Figure 22 and Figure 23. In these figures and those that follow, the solid lines show the analytical solutions and symbols show numerical results. There is excellent agreement between 3D FS code results for Sec. 2 (Figure 23) and the plane strain analytical solution. However, there are insignificant differences between the analytical and numerical results in Sec. 1 in Figure 22. This is because of wellbore end effects, which cause deviation of the numerical result from the analytical solution.

4.2.2. Mode 2: Pore pressure loading

To study the response of the wellbore under Mode 2 loading, the background pore pressure is kept at 1.0 MPa and the pressure inside of wellbore is suddenly changed to zero. Far-field stresses and temperature are considered to be zero. Figure 24 and Figure 25 show the pore pressure history inside of media at various locations. As is clear from the figures, after t*=10 for Sec. 1 (the end section) and t*=1000 for Sec. 2 (the middle section), the numerical results deviate from the plane strain analytical solutions. This is because the end of the wellbore is sensed by the medium after some time. Note that p_0 is the background pore pressure.

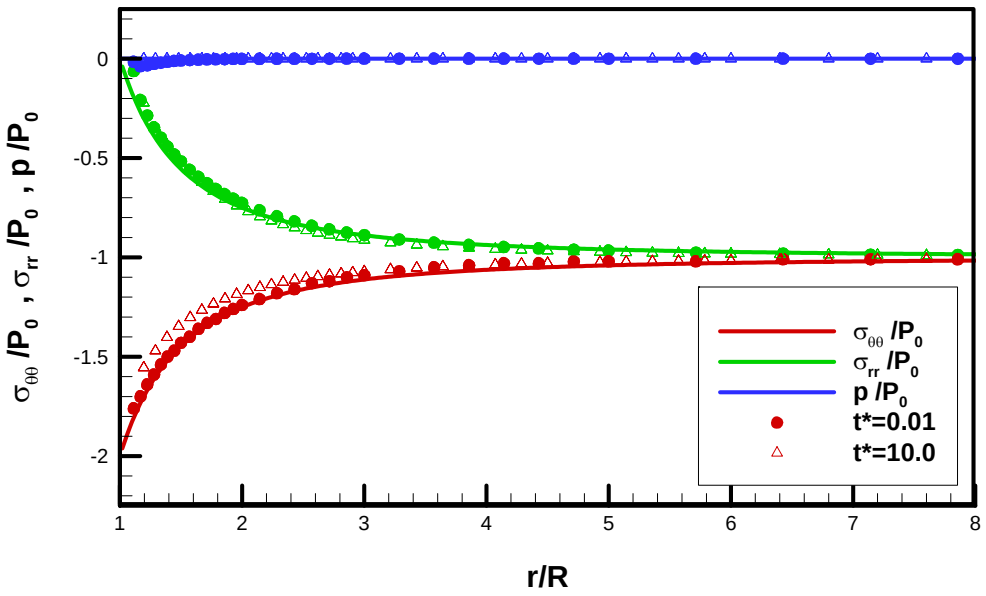

Figure 22. Radial, tangential stress and pore pressure distribution in field point in Sec. 1 of wellbore in two different time scale.

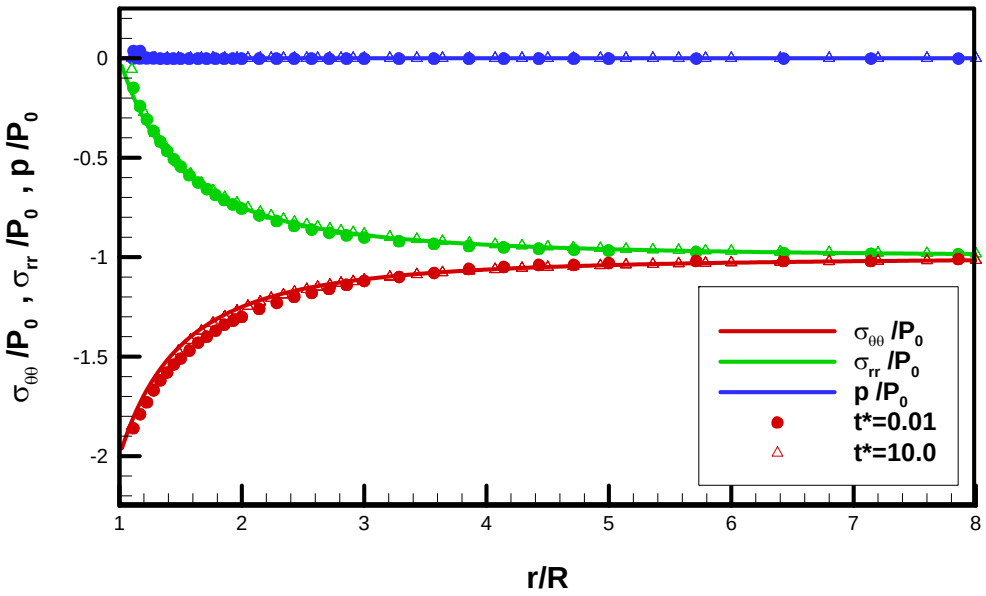

Figure 23. Radial stress, tangential stress, and pore pressure distribution in field point in Sec. 2 or middle section of wellbore.

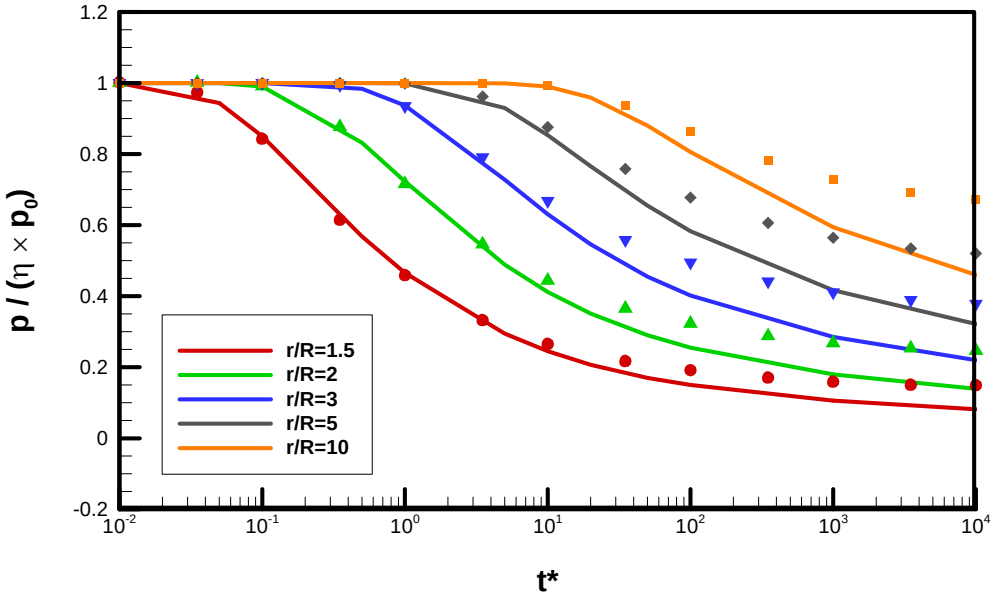

Figure 24. Pore pressure history inside of media for Sec.1 at various r/R for Mode 2.

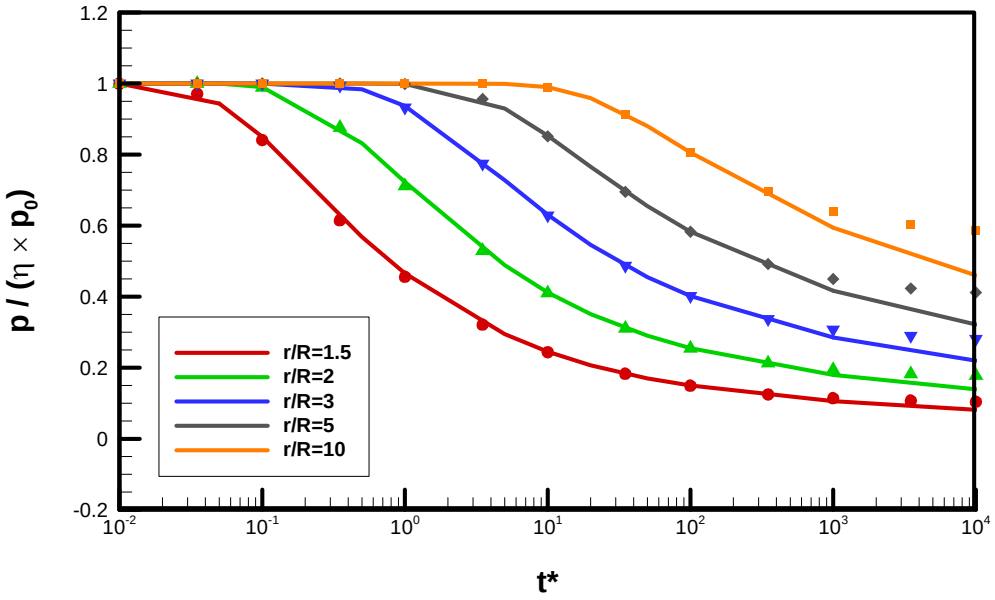

Figure 25. Pore pressure history inside of media for Sec. 2 at various r/R for Mode 2.

Figure 26 and Figure 27 show the tangential stress for Sec. 1 and Sec. 2, respectively. Stresses are normalized by $(\eta \times p_0)$, where η is the poroelastic coefficient given by

$$\eta = \alpha(1-2\nu)/2(1-\nu)$$

Both plots agree well with the plane strain analytical solutions. However, a slight deviation from the analytical solution is clear after a time (t*=1000) for Sec. 1 and Sec. 2. The observed deviation is a manifestation of wellbore end effects. As mentioned previously, because of the 3D characteristics of the numerical solution, after some time passes, points in the medium sense the end of the wellbore and the numerical results deviate from analytical solution. Note that wellbore end effects are different on Sec. 1 and Sec. 2.

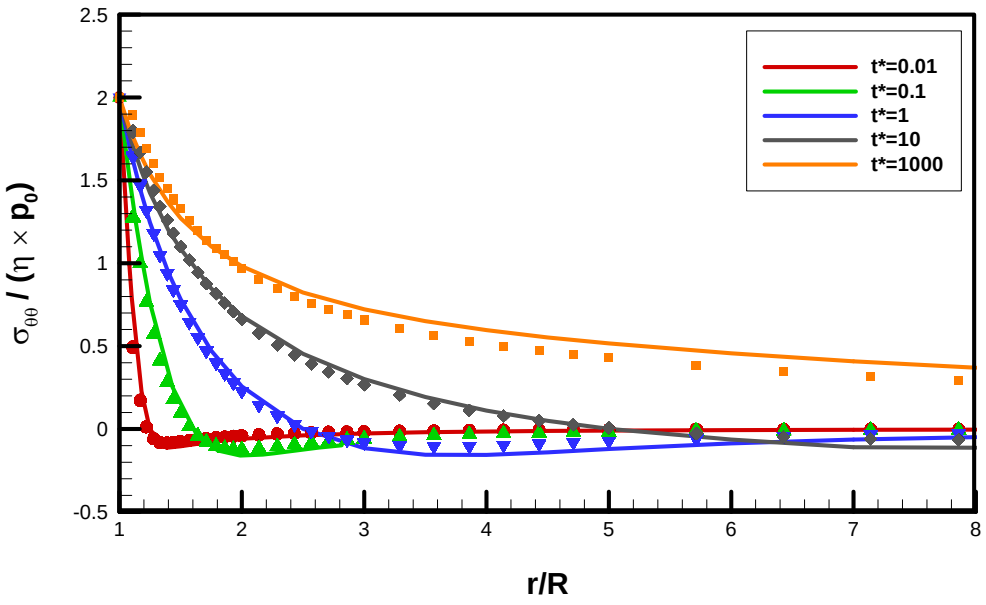

Figure 26. Tangential stress distribution inside of media for Sec. 1 at various times.

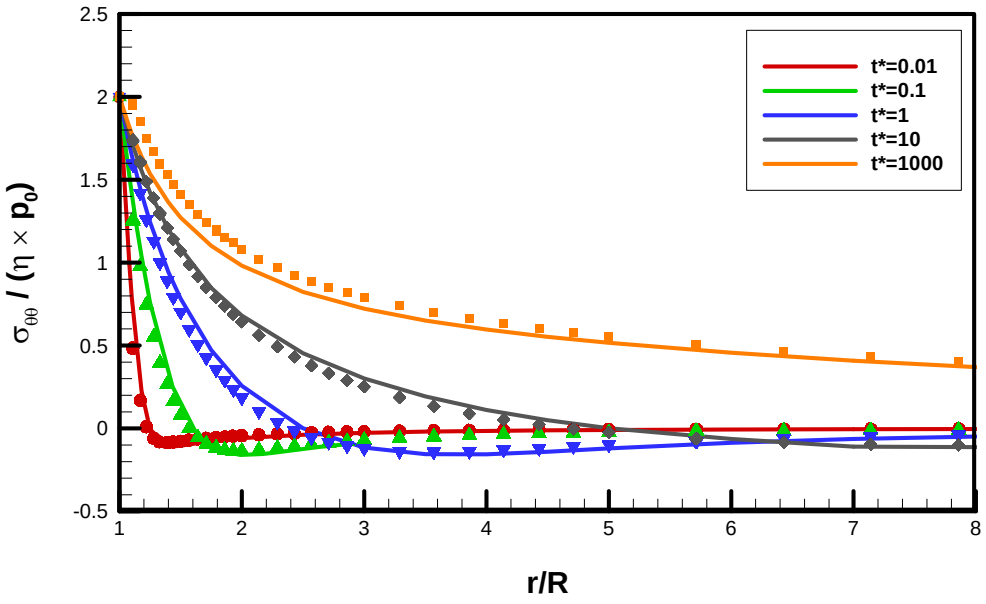

Figure 27. Tangential stress distribution inside of media for Sec. 2 at various times.

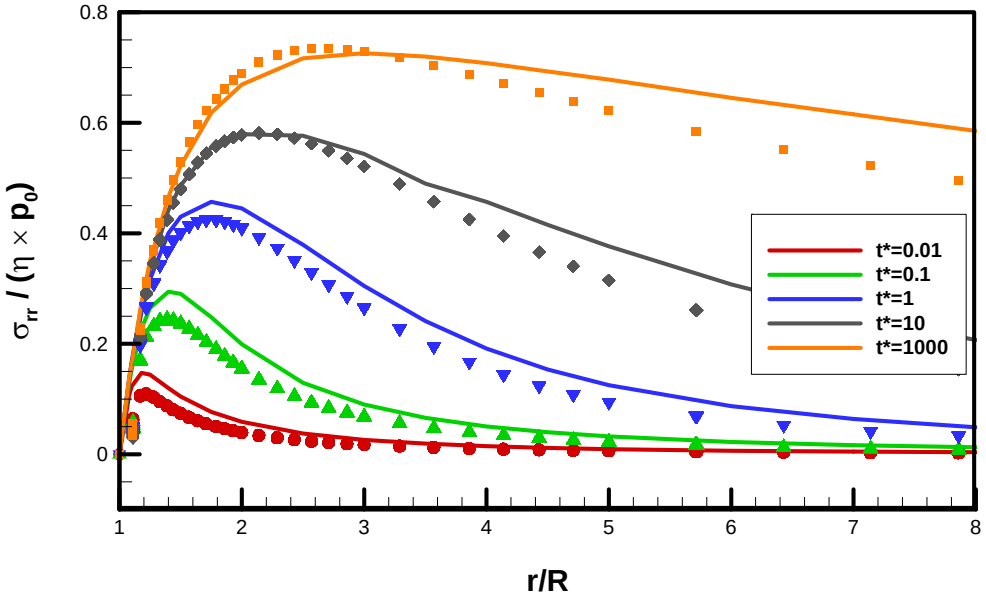

Figure 28. Radial stress distribution inside of media for Sec. 1 at various times.

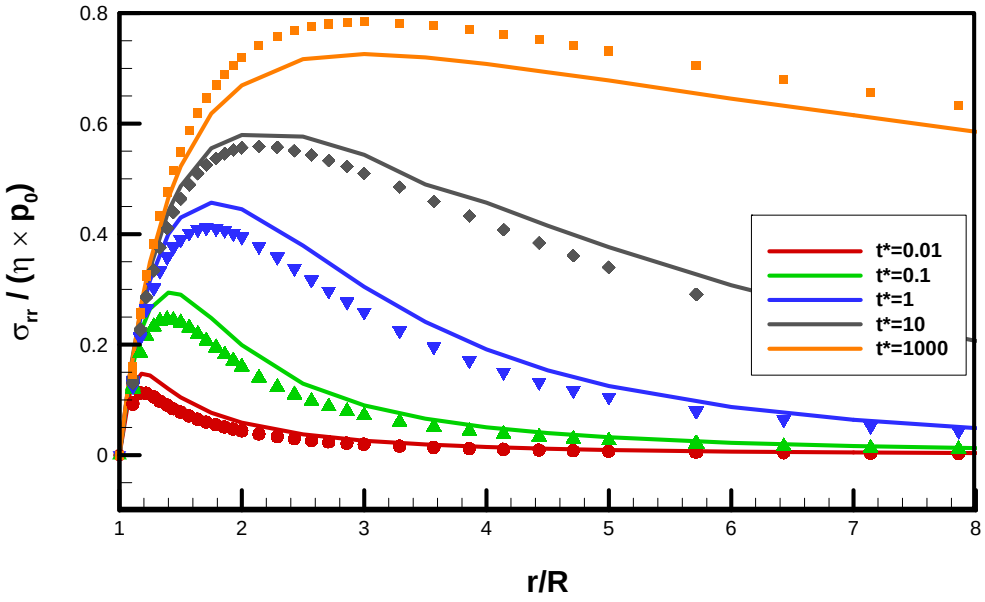

Figure 29. Radial stress distribution inside of media for Sec. 2 at various times.

Figure 28 and Figure 29 show the distribution of radial stress for Sec. 1 and Sec. 2, respectively. As with the distribution of tangential stress, the strength of the radial stress is normalized by $(\eta \times p_0)$. It is clear from the figures that the analytical and numerical results do not agree perfectly for a long time and for nodes far from the wellbore wall. This is another manifestation of the inherent difference between the plane strain condition and the 3D model. In addition, when the element degree decreases from 10 to 5 and less, the results getting closer to analytical results (not remarkably). However, increasing number of elements is very expensive in term of computation cost. By comparing the distribution of radial and tangential stress around the wellbore, it becomes clear that radial stress senses the effects of the wellbore end wall more so than tangential stress.

The value of tangential stress at the wellbore wall is tensile in terms of total stress ($\sigma_{\theta\theta} = 2\eta p_0$) but compressive in terms of Terzaghi effective stress ($\sigma_{\theta\theta} + p = (2\eta - 1) p_0, \ \ 0.0 \le \eta \le 0.5$) [62].

4.2.3. Mode 3: Deviatoric stress loading

Mode 3 is deviatoric stress loading without background pore pressure and temperature. It is assumed that in–situ stress is 10.0 MPa at X direction and -10.0 MPa at Z direction, that is, the magnitude of stress deviator S_0 = 10.0 MPa.

Total pore pressure, tangential stress, and radial stress fields for θ=0 are plotted in Figure 30 to Figure 35 for both the middle and end sections.

It can be seen from Figure 30 and Figure 31 that a sharp gradient in pore pressure exists early on. This sharp gradient is caused by the rapid drainage of fluid at the wellbore wall. The pore pressure peak decreases with time and moves away from the wellbore wall. The numerical results agree well with the plane strain analytical results, but again some differences result from the contribution of third dimension.

Figure 32 and Figure 33 show the distribution of tangential stress for θ=0 at the end and middle sections respectively, at various time. As is clear, the numerical results agree well with the analytical results for tangential stress, which decreases monotonically with increasing distance from the wellbore wall. Note that tangential stress at the wellbore wall at t*=1 is fairly close to the long-term elastic value at θ = 0 which is $-4S_0$ [62].

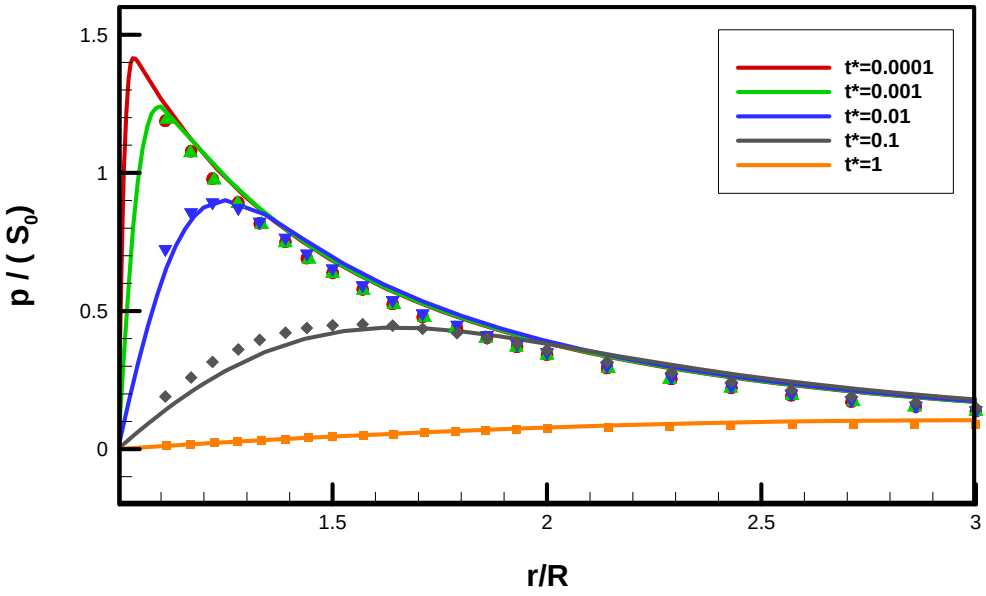

Figure 30. Pore pressure distribution at θ=0 for Mode 3 in Sec. 1.

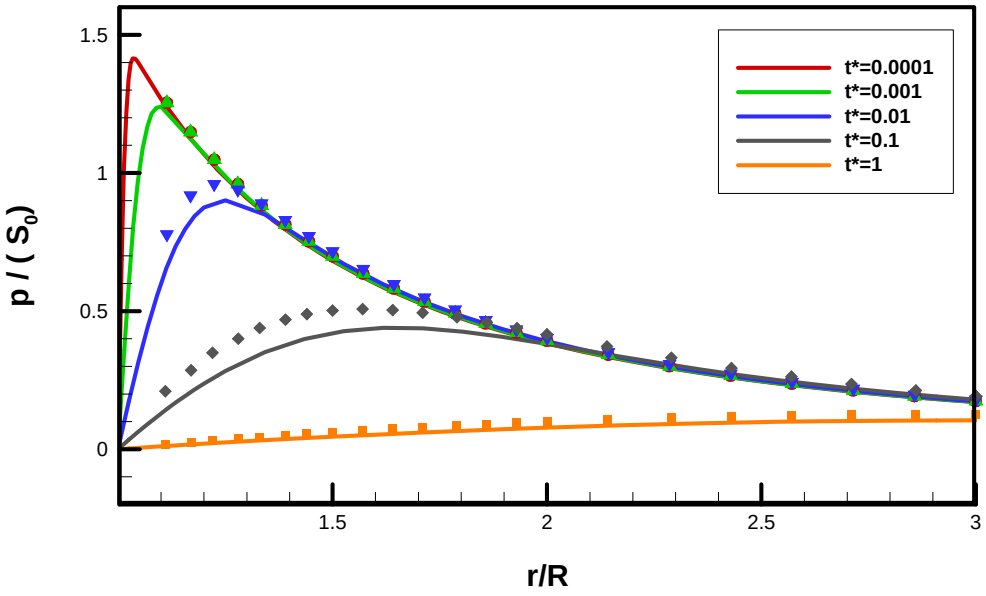

Figure 31. Pore pressure distribution at θ=0 for Mode 3 in Sec. 2.

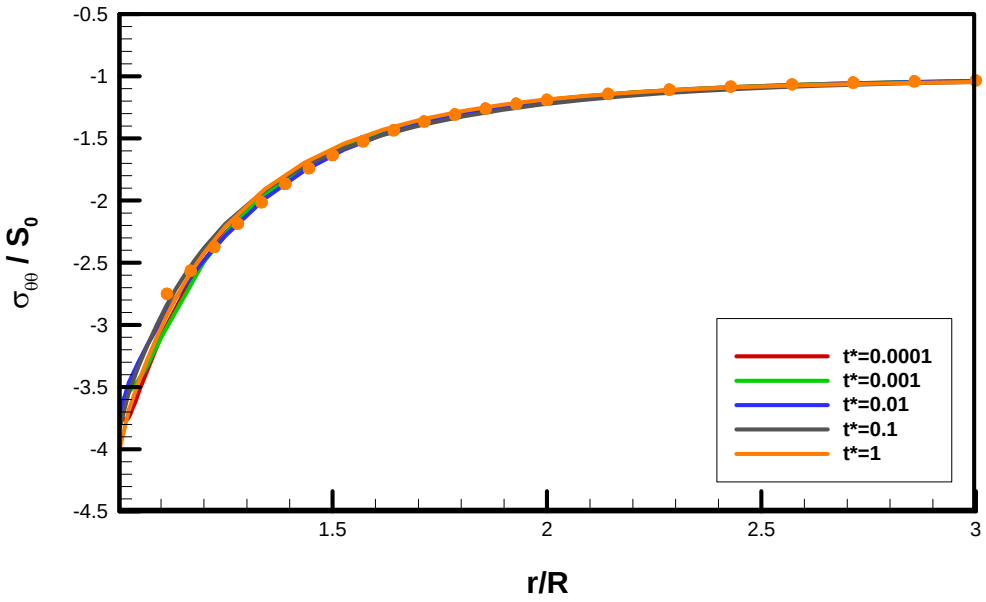

Figure 32. Tangential stress variation at θ=0, π for Mode 3 in Sec. 1.

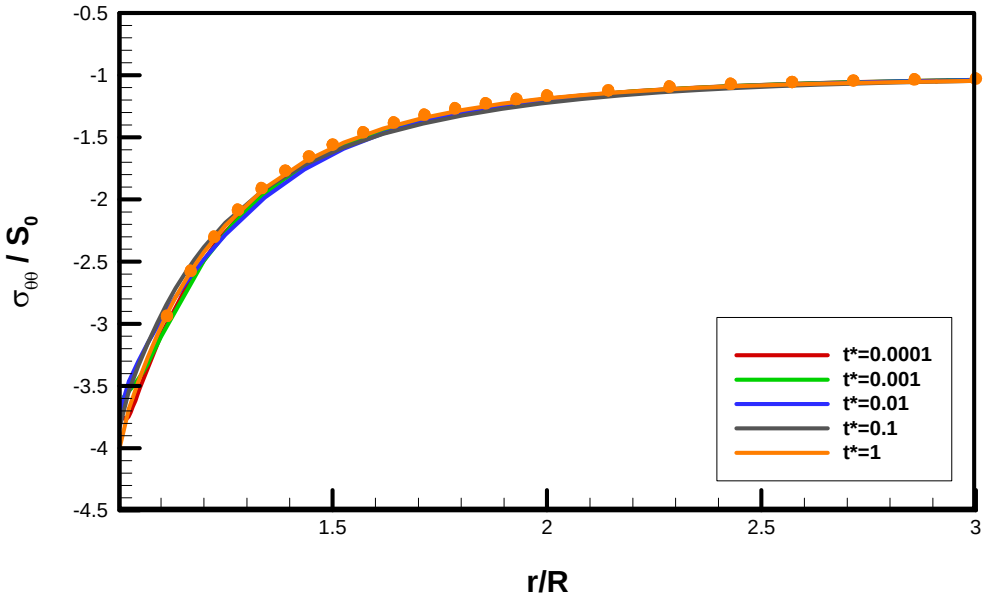

Figure 33. Tangential stress variation at θ=0, π for Mode 3 in Sec. 2.

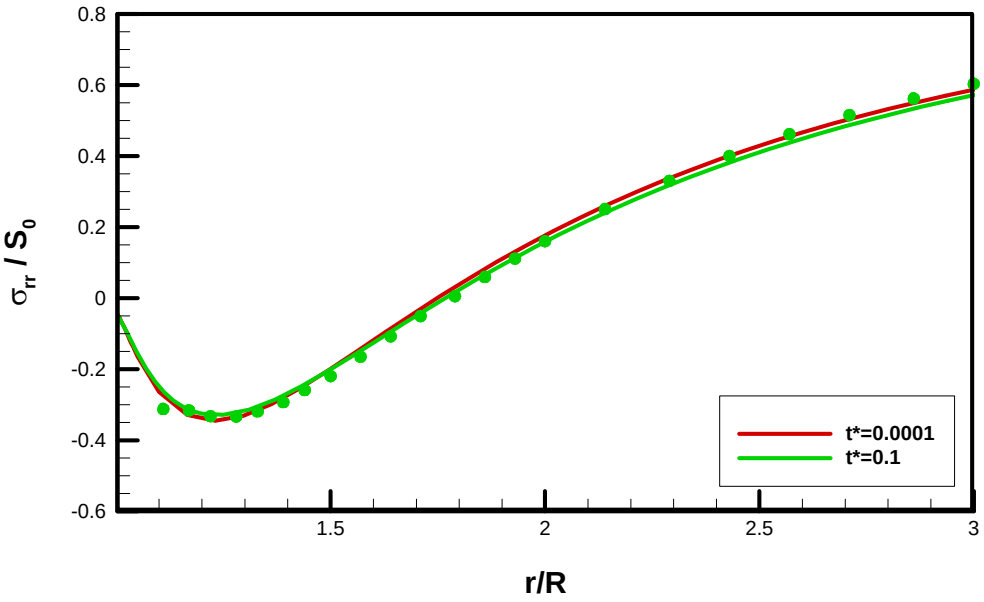

Figure 34. Radial stress distribution at θ=0, π for Mode 3 in Sec. 1.

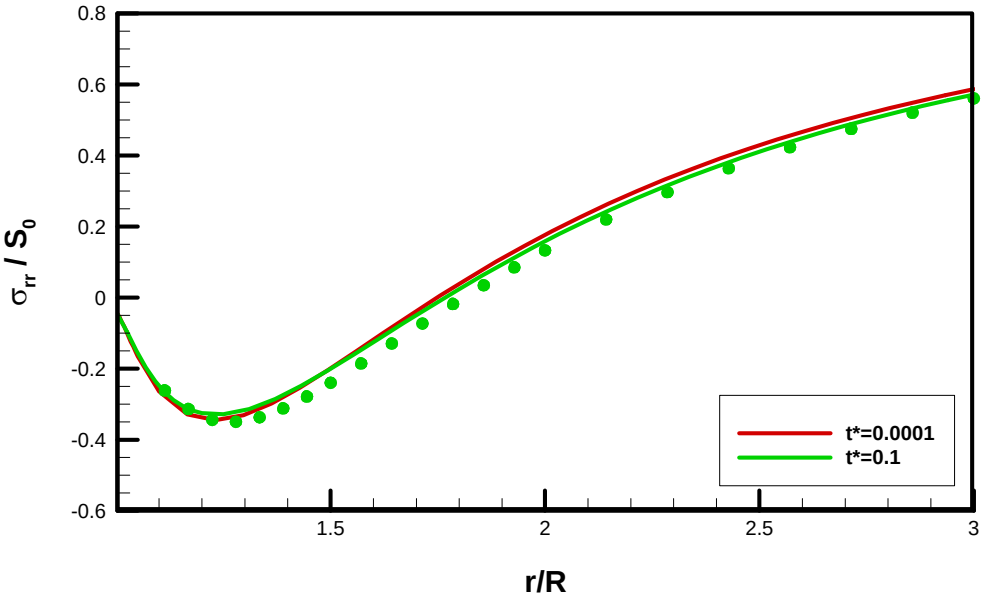

Figure 35. Radial stress distribution at θ=0, π for Mode 3 in Sec. 2.

Figure 34 and Figure 35 shows the distribution of radial stress in Sec. 1 and Sec. 2 respectively. Like tangential stress, radial stress around the wellbore experiences insignificant variation with time. It is clear that very small differences exist between the figures, differences that once again are due to the effects of third dimension.

4.3. Thermal loading of wellbore

Pore pressure and stresses that are induced by temperature variations between mud and the formation are used to examine the coupling function of thermoporoelasticity in the FS code. The wellbore response under thermal loading was analytically solved using plane strain theory; the solution can be found in Li [8].

Consider a wellbore with radius R = 0.1 m, as shown in Figure 19, in a reservoir with a background temperature of 200°C and with properties shown in Table 3.

Table 3. Reservoir properties for thermal loading of wellbore.

Shear modulus	(GPa)	15.0 (1450.38 Ksi)
Drained Poisson's ratio	(-)	0.25
Undrained Poisson's ratio	(-)	0.33
Biot coefficient	(-)	0.815
Base permeability	(m^2)	4.00×10^{-19} (0.4 Micro Darcy)
Porosity	(-)	0.01
Rock density	(kg/m^3)	2650.00(1.15 psi/ft.)
Fluid density	(kg/m^3)	1000.00(0.433 psi/ft.)
Fluid viscosity	($N.s/m^2$)	2.54×10^{-3}(2.54 cp)
Rock thermal conductivity	(W/m/K)	10.70
Specific heat capacity of rock	(J/kg/K)	790.00
Specific heat capacity of fluid	(J/kg/K)	4200.00
Linear thermal expansion of rock	(1/K)	8.00×10^{-6}
Linear thermal expansion of fluid	(1/K)	1.00×10^{-4}

The temperature of wellbore wall is assumed to change from formation temperature and rapidly cooled by mud and kept at 80°C. To simplify investigation of the role of temperature, pressure inside of the well does not differ from formation pore pressure and no in-situ stress is considered. In other words, the far-field pore pressure and stresses are considered to be zero. The wellbore geometry is the same as in section 4.2, and the same discretization is used here (see Figure 20).

Figure 36 and Figure 37 compare temperature variations along the wellbore radius at different times and at different distances from the wellbore wall at the end (Sec. 1) and middle (Sec. 2) sections, respectively. The numerical solution gives a very good approximation at Sec. 2, at times less than 10^4 s. For Sec. 1 after 10^2 s the numerical results deviate from the analytical solution. Furthermore, after about 1.5 days, the response predicted by the numerical solution in both sections is totally different from the analytical solution. This is because of the influence of different outer boundary conditions in the numerical and analytical models. In the numerical model, the wellbore length is predetermined as a finite length (3 m), whereas in the plane strain analytical model, the wellbore length is assumed to be infinite. In this problem, after 10^4 s the developing temperature from the end section of the wellbore hits the field points in Sec. 2 in the middle of the wellbore, and the temperature at this location differs from that of analytical solution. Therefore, the two results cannot be compared after the temperature from the end section hits the field points. As can be seen by comparing Figure 36 and Figure 37, the interference time of the end wall of the wellbore differs depending on the location of the field point.

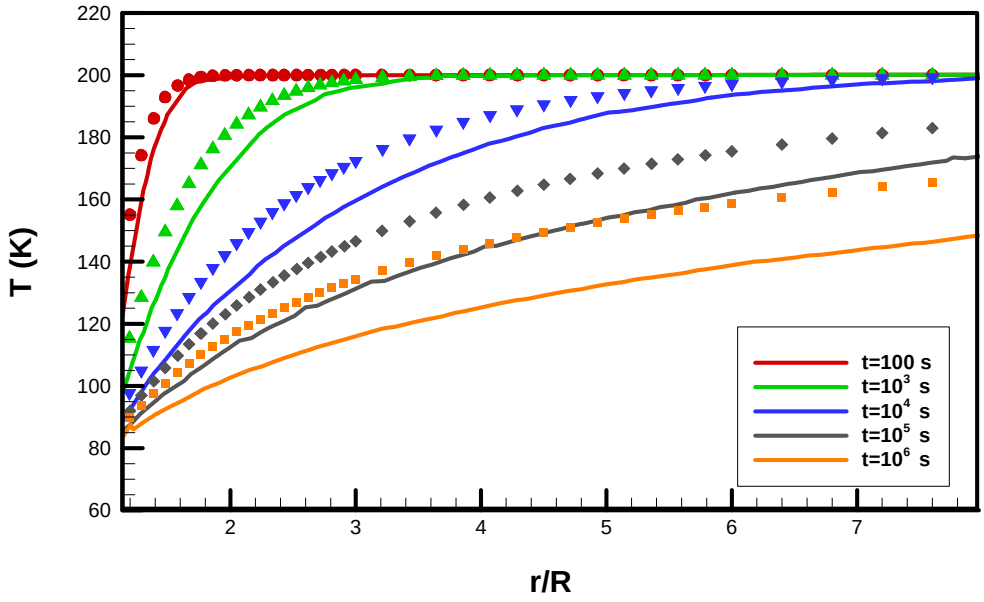

Figure 36. Temperature distribution along wellbore radius in various times at Sec.1.

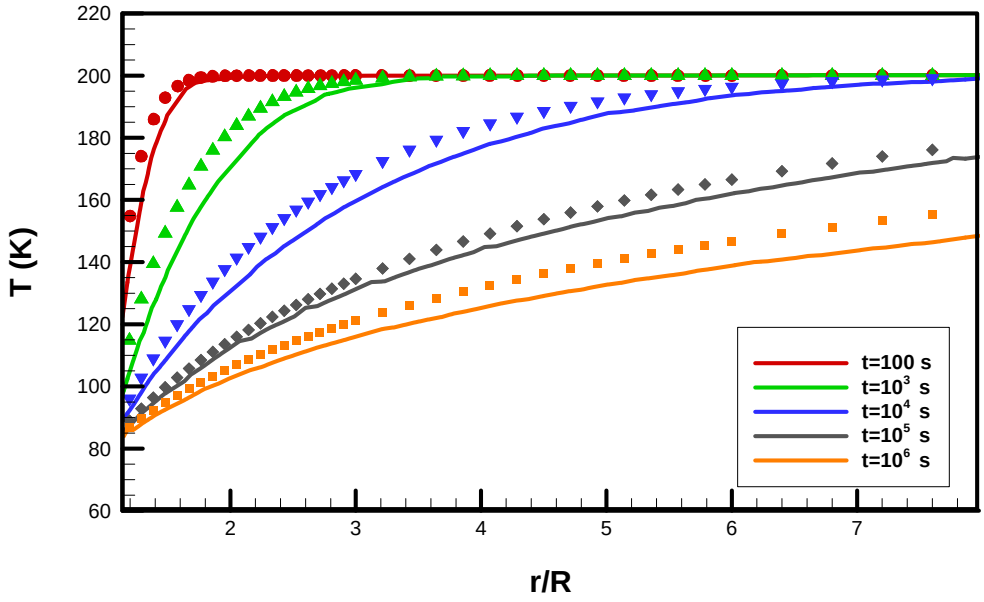

Figure 37. Temperature distribution along wellbore radius in various times at Sec.2.

Figure 38 and Figure 39 show the distribution of pore pressure induced by thermal diffusion. Similar to the temperature profiles, good agreement between the analytical and numerical solutions is obtained at times less than 10^4 s for Sec.2 and 10^2 s for Sec.1. A drop in pressure profile is generated near the wellbore wall early on. As time passes, the pore pressure gradually recovers toward its original state.

Figure 40 to Figure 43 compare of the total radial and tangential stresses along the wellbore radius at different cross sections. It is clear that radial stresses at the two cross sections start to deviate from the analytical results at same time as the temperature and pore pressure profiles. A significant peak in radial tensile stress is formed inside the formation. Note that when time passes, radial tensile stress moves far from wellbore toward formation and the peak value increase.

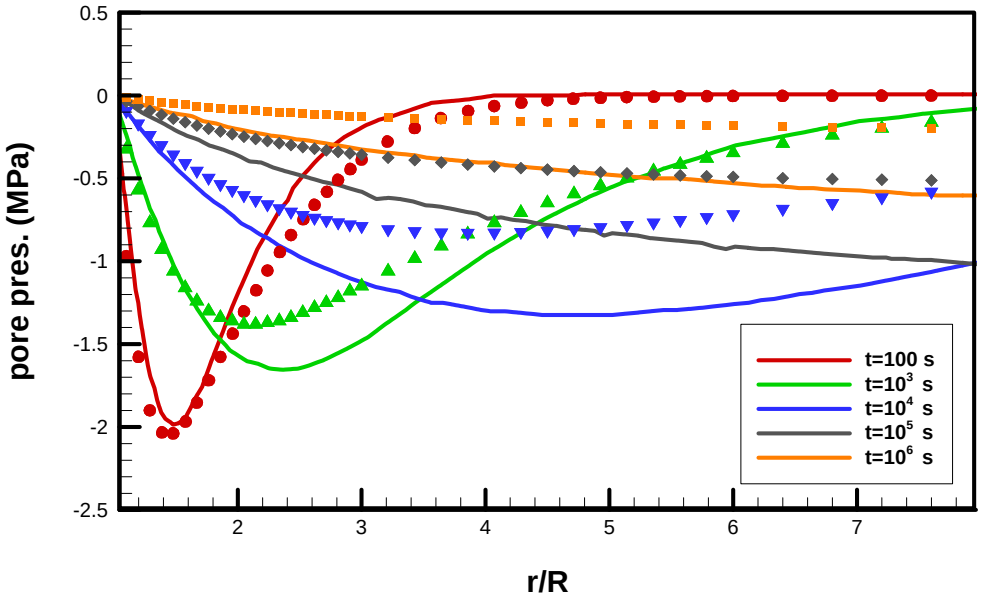

Figure 38. Pore pressure distribution which induced by thermal diffusion at Sec.1.

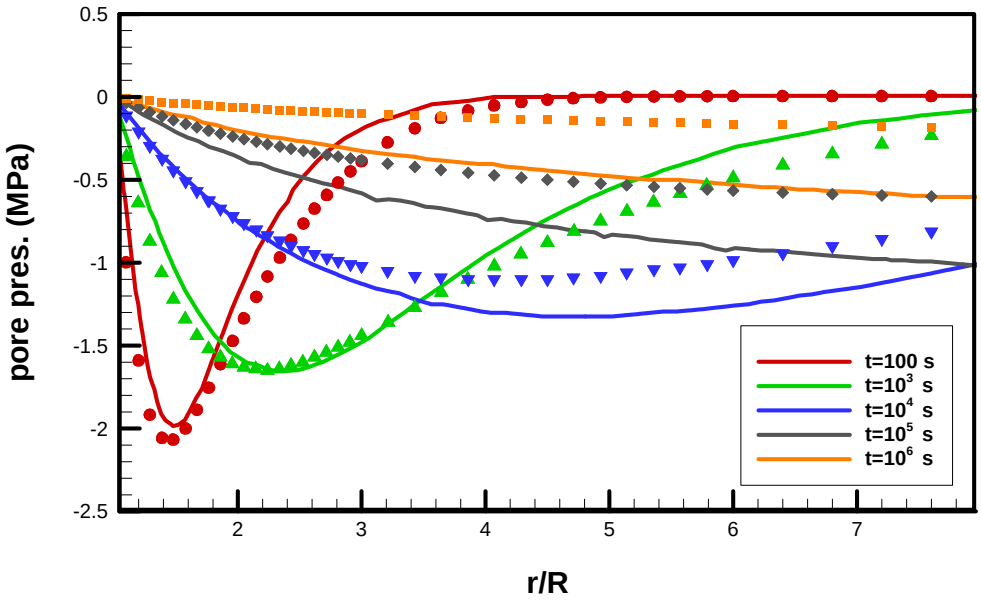

Figure 39. Pore pressure distribution which induced by thermal diffusion at Sec.2.

Tangential stress does not differ much from the analytical solution at different times (Figure 42 and Figure 43). This is because during temperature loading the end wellbore wall does not contribute to tangential stress as much as radial stress. As is clear from the tangential stress profile, with cooling, significant tensile stress is induced around the wellbore. This is caused by rock shrinking near the perimeter of the wellbore. Far from the wellbore wall, induced tensile stress magnitude decreases and at some radial distances inside the formation its sign changes and the stress turns into a compressive one. This is again because contraction of the material at the inner face of the wellbore geometry. The compressive zone disappears with increasing distance from the wellbore wall and gradually moves away.

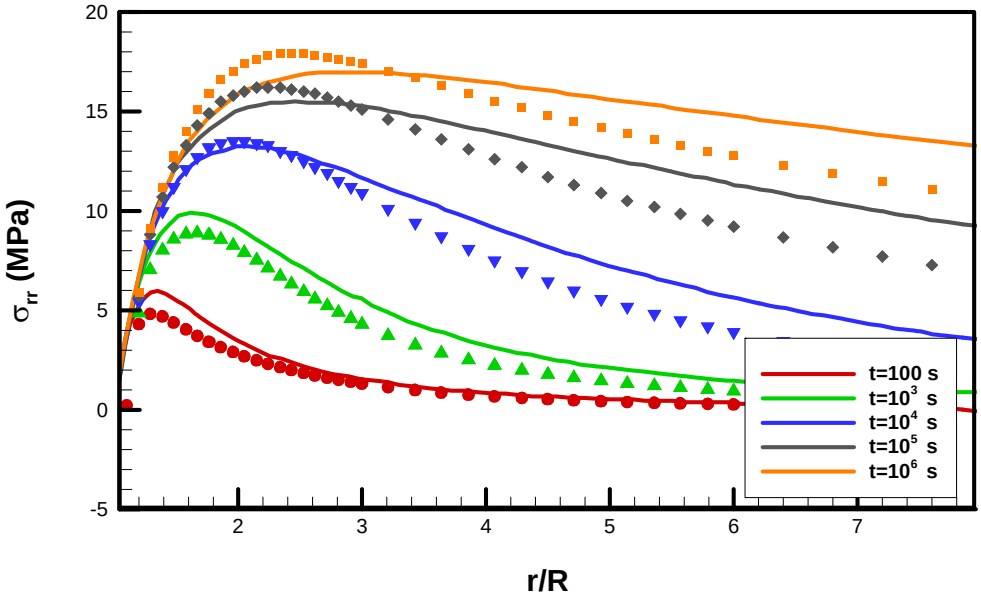

Figure 40. Radial stress distribution which induced by thermal diffusion at Sec.1.

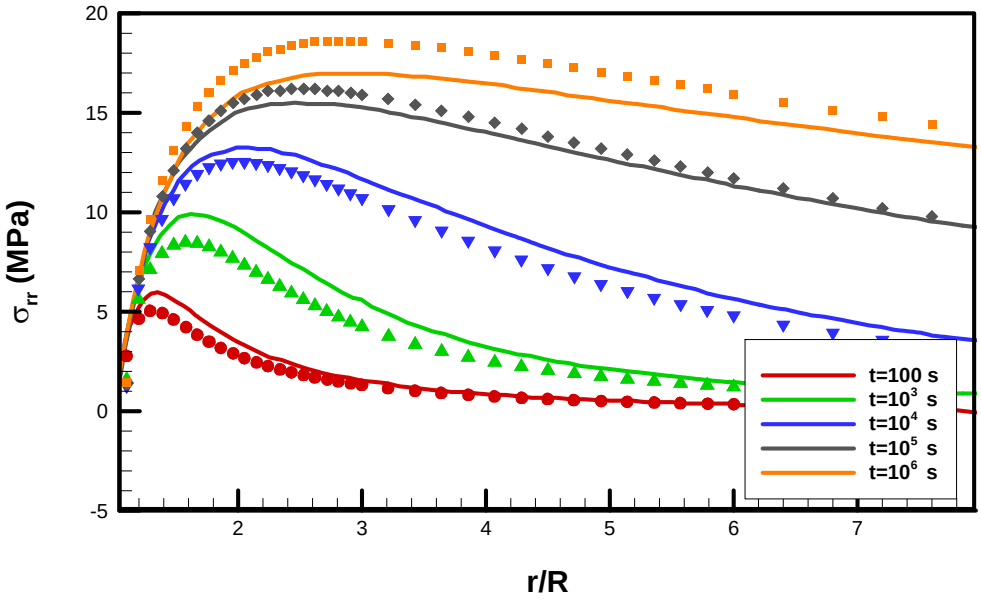

Figure 41. Radial stress distribution which induced by thermal diffusion at Sec.2.

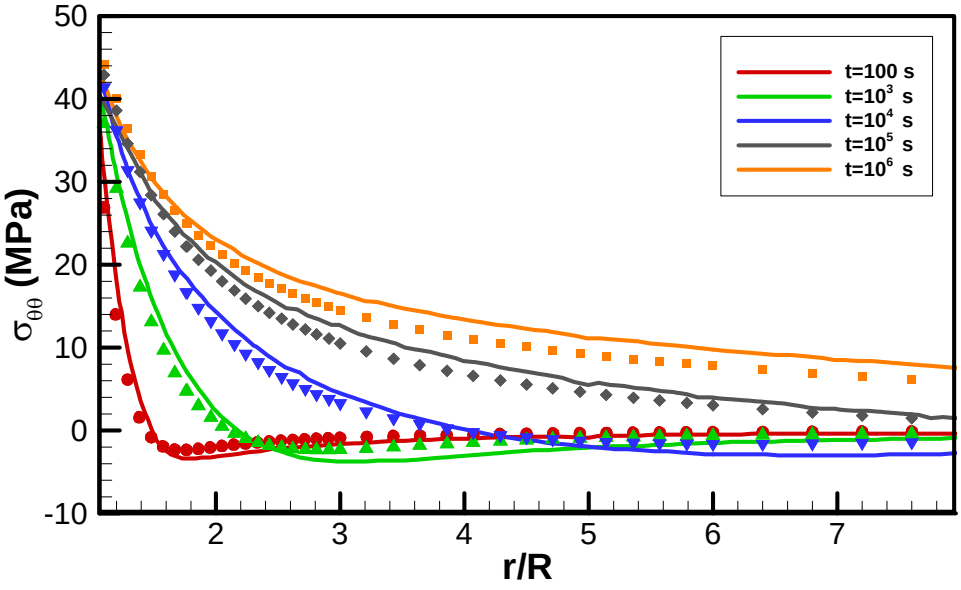

Figure 42. Tangential stress distribution which induced by thermal diffusion at Sec.1.

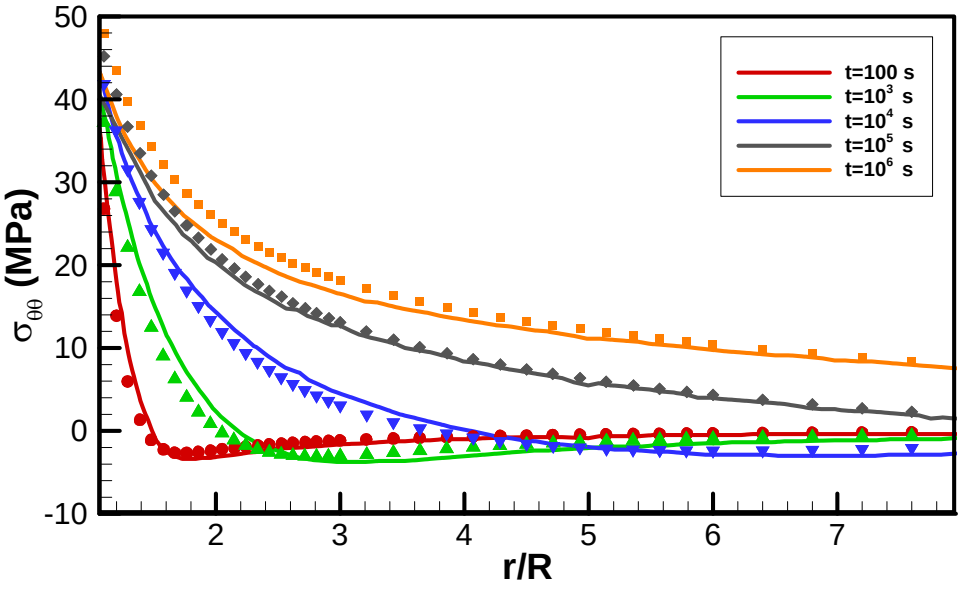

Figure 43. Tangential stress distribution which induced by thermal diffusion at Sec.2.

It is obvious from these observations that the cooling process during mud circulation increases the potential for fracturing because of tensile tangential stress induced by material shrinkage. A tensile stress zone will develop around the wellbore with time, which can inspire time-delayed fracture development.

By comparing previous examples to the corresponding plane strain solution, one can see that the effect of the end section of the wellbore is very important in stress analysis, and thus a 2D plane strain analytical solution cannot be used for the end section.

4.3.1. Thermoporoelastic vs. thermo-poroelastic loading

To investigate the functionality of direct (thermoporoelastic) and indirect (thermo-poroelastic) coupling in the response of a wellbore, a well geometry as presented in Figure 20 and media properties as presented in Table 3 are considered. As in the previous section, the formation is initially set to a temperature of 200°C, the mud (or wellbore walls) is set to 80°C, and there are no in situ stresses or pore pressure. Note that the thermal diffusion equation in both models is equal and that the difference is in the pore pressure diffusion relation and displacement field equations.

Figure 44 to Figure 46 compare induced pore pressure, tangential stresses, and radial stresses at Sec. 2 at different times along the wellbore radius for fully coupled (thermoporoelastic) and partially coupled (thermo-poroelastic) models. The solid data points are for thermoporoelastic coupling, and the open data points are for thermo-poroelastic coupling.

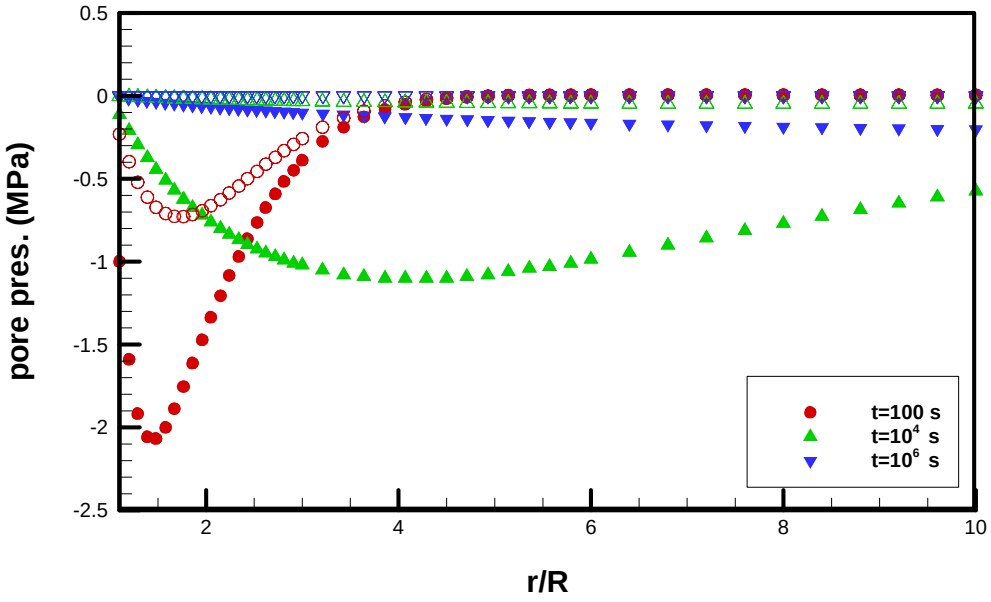

Figure 44. Pressure comparison for thermoporoelastic and thermoelastic model in Sec.2.

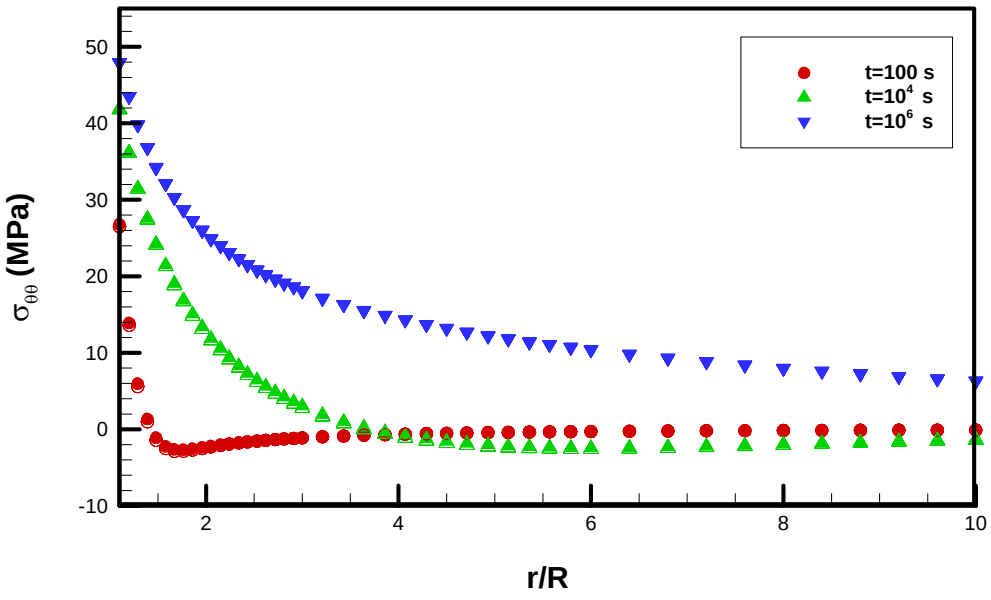

Figure 45. Total tangential stress comparison for thermoporoelastic and therm-poroelastic model in Sec.2.

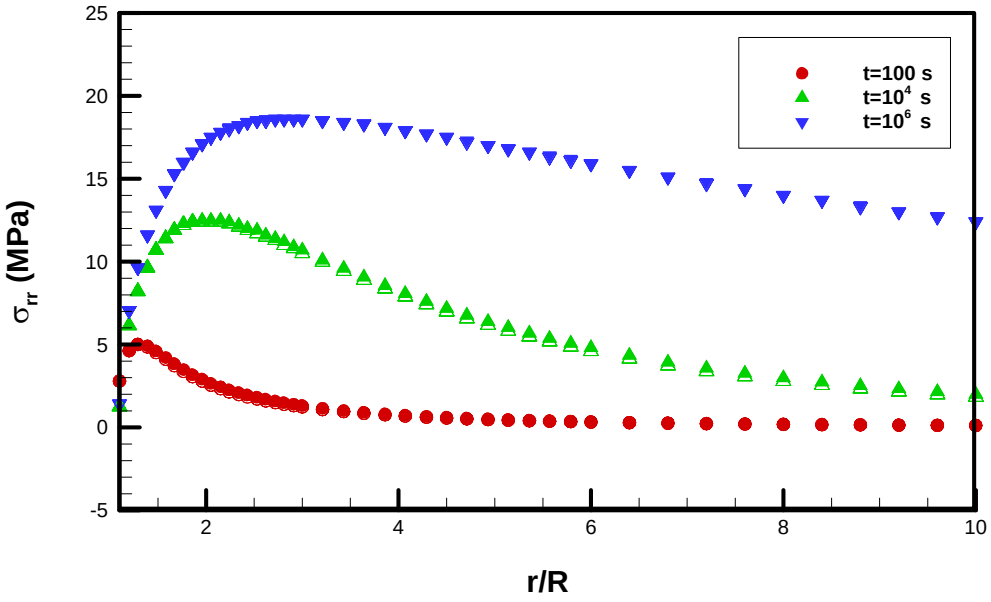

Figure 46 Total radial stress distribution comparison for thermoporoelastic and thermoelastic model in Sec.2.

It can be seen from Figure 44 that induced negative pore pressure in the thermo-poroelastic model is about 30% of that in the thermoporoelastic model. This difference might have a large influence on the evaluation of failure potential near the wellbore. Because of a cooling or heating effect, induced pore pressure can cause instability near the wellbore wall.

Total tangential and radial stresses are shown in Figure 45 and Figure 46. There is an insignificant difference in radial and tangential stresses between the two models. The differences between thermo-poroelasticity and thermoporoelasticity may be entirely dependent on properties of the formation, and their difference might be more or less significant than mentioned previously (see Tao and Ghassemi [72]).

4.4. Pressurized penny-shape crack

The current section examines isothermal thermoporoelastic DD code in the normal direction to the crack surface. The objective is to study the response of a penny-shape crack with radius a = 10.0 m (shown in Figure 47) under sudden pressure P = 1.0 MPa in a reservoir with properties as presented in Table 4. The initial reservoir conditions are as follows: zero in situ stresses, pore pressure, and temperature. Following Detournay and Cheng [34], crack pressurization in poroelastic media can be categorized into two fundamental modes of loading, namely a normal stress loading and a pore pressure loading, as shown here:

Mode 1, stress loading: $\sigma_n(r,t) = -P, \quad p(r,t) = 0.0$

Mode 2, pressure loading: $\sigma_n(r,t) = 0.0, \quad p(r,t) = P$

Table 4. Properties of rock to model poroelastic loading of crack.

Shear modulus	(GPa)	8.30 (1204 Ksi)
Drained Poisson's ratio	(-)	0.25
Undrained Poisson's ratio	(-)	0.46
Biot coefficient	(-)	0.89
Base permeability	(m^2)	1.00×10^{-17} (10 Micro Darcy)
Fluid density	(kg/m^3)	1000.00 (0.433 psi/ft.)
Fluid viscosity at reservoir condition	($N.s/m^2$)	3.00×10^{-4} (0.3 cp)

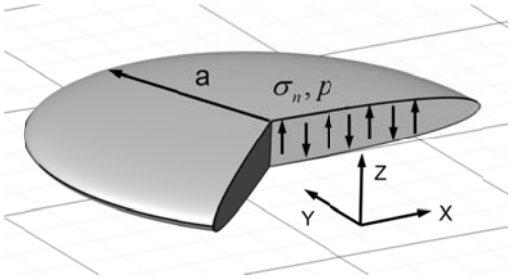

Figure 47. Uniformly pressurization of penny shape crack in infinite media.

4.4.1. Mode 1: Stress loading

Mode 1 loading controls the crack opening. The normal relative displacement of two crack surfaces (opening) for the current mode was solved analytically by Sneddon [110] for elastic media. The analytical solution can be represented as follows [110]:

$$w_f = \frac{4Pa(1-\nu)}{\pi G}\sqrt{1-\left(\frac{r}{a}\right)^2}$$

It is clear that because of the diffusion process, the response of the crack opening 0is a function of time. At time t = 0+, the fracture opens according to the analytical solution with undrained material properties. As time passes, the crack opens and reaches the steady-state solution with drained material properties. The crack considered in the current section is simulated at these two limiting conditions with a developed DD code. The penny-shape crack is discretized with 2809 nodes and 2704 elements. Discretization is shown in Figure 48 .

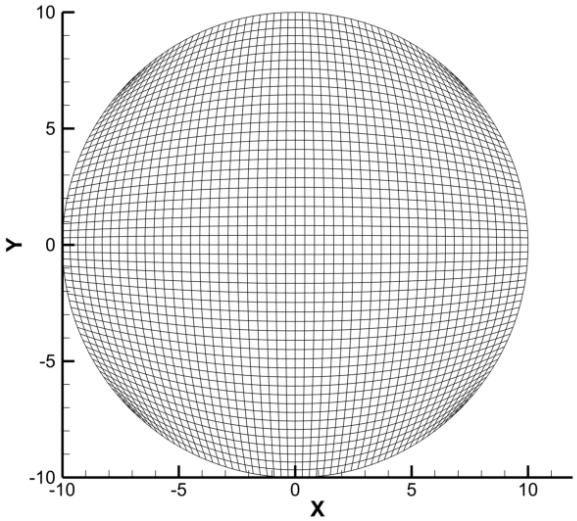

Figure 48. Penny shape fracture discretization.

Short-term (t = 1.0 s, undrained behavior) and long-term (t = 10^6 s, drained behavior) analytical and numerical results are shown in Figure 49. The results of the DD code agree very well with the analytical solution at both limiting conditions. Note that the DD code results are less accurate near the crack tip. The discrepancy can be attributed to the use of constant DD elements—that is, constant displacement approximation on each element. The results will be more accurate if the number of elements is increased. By comparing two crack apertures at different time scales, it becomes clear that the crack opens more over a long time. This is because of softer material behavior in the drained condition or a long time scale. Discrepancies in the numerical results are due to elements of different shapes and sizes on the crack surface (in the same radius, from zero angle to 45, element shape change from square to diamond as can be seen in Figure 48).

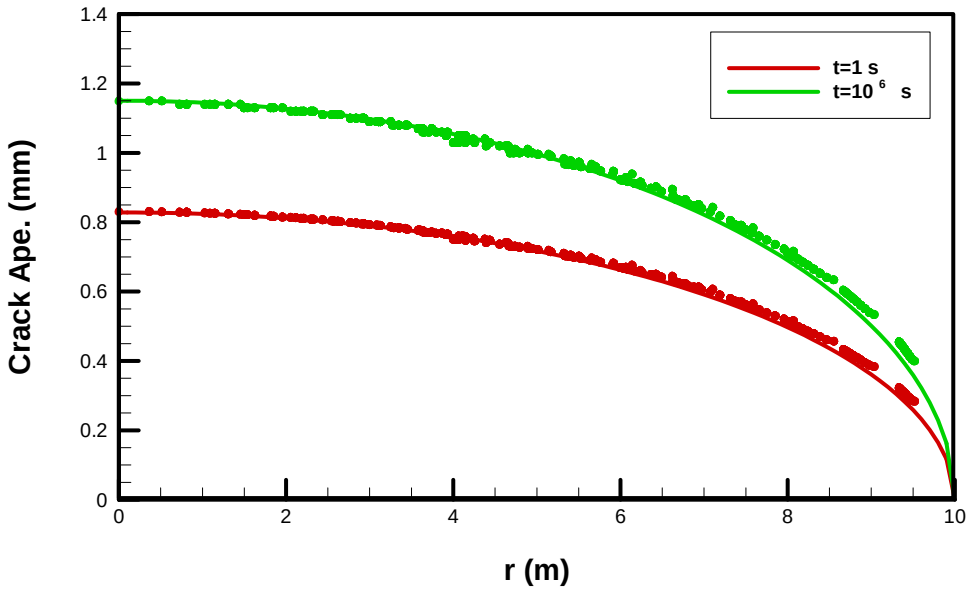

Figure 49. Short-term (1 s) and long-term (10^6 s) crack opening under uniformly stress loading, Mode I.

During the evolution of a crack response from an undrained condition to a drained one, the maximum opening along the crack occurs at its center. The maximum opening can be defined in the two limiting conditions as follows:

$$w_{\max}^{Drained} = \frac{4Pa(1-\nu)}{\pi G}, \qquad w_{\max}^{Un-drained} = \frac{4Pa(1-\nu_u)}{\pi G}$$

The maximum opening should evolve over time from an undrained value to a drained one. Figure 50 plots the maximum opening as a function of time. It is clear that the maximum opening predicted by the DD code agrees very well with closed form results for the two limiting conditions. The little bump in the numerical solution with very small and large time is due to a change in the way the error function (an essential function to calculating a time-dependent fundamental solution) is calculated. The Taylor series and asymptotic expansion is used to approximate the function.

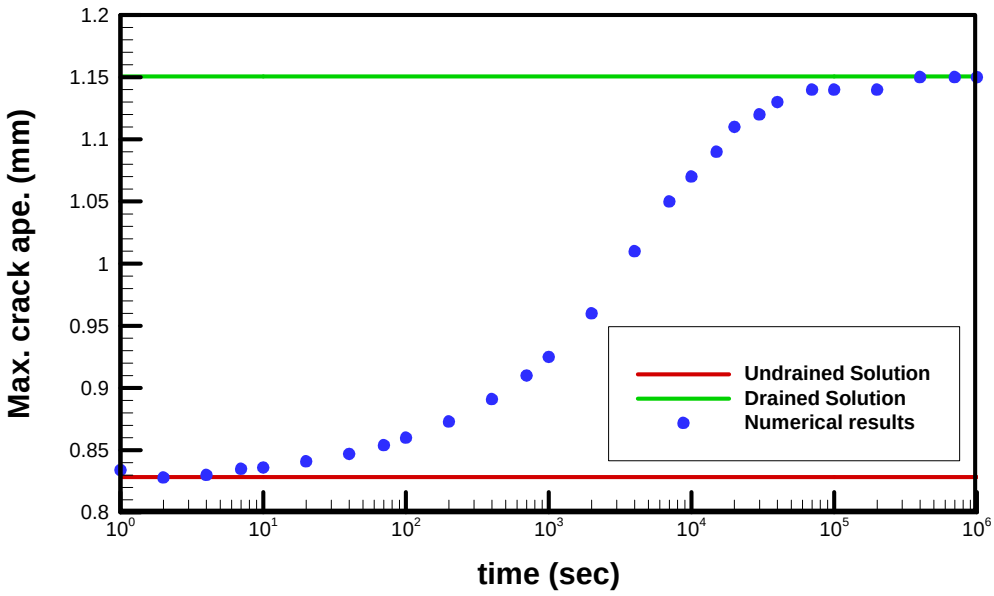

Figure 50. Maximum crack opening history under stress loading (Mode I).

As mentioned in section 3, SIFs are used to define the magnitude of the singular stress and displacement fields around the crack edge. This concept originated from studies of elastic materials. However, it can be used with other type of materials as well (e.g., poroelastic, thermoelastic, and thermoporoelastic materials). The form of stress singularity around the crack tip does not change with temperature or pressure field. Therefore, one can use the typical method for calculating elastic SIFs in thermoporoelastic problems. The classical elastic relationship between the normal stress loading of a penny-shape crack and Mode I SIF has been given by many researchers and can be found in Kundu [111]. Mode I SIF in an elastic pressurized penny shape crack can be represented as follow: $K_I = 2P\sqrt{a/\pi}$, where P is the strength of normal stress on the crack surface and a is the radius of the penny-shape crack. The analytical value can be compared with the SIF calculated from this model for a long time period. The Mode I SIF over time is plotted in Figure 51. This shows that the DD code can predict SIF values with acceptable accuracy.

4.4.2. Mode 2: Pressure loading

Mode 2 loading decreases the opening of the crack. As pressure inside the crack diffuses into formation, pore pressure increases and fracture starts to close. The increase of pore pressure in the formation causes an enlargement of pores in the rock around the crack and creates some back stress. The crack aperture response under Mode 2 loading is illustrated in Figure 52, which indicates that the crack closes progressively. The crack closure starts at zero and approaches the drained condition closure (steady state). The

analytical solution for the drained condition is obtained by using the analytical solution given by Gordeyev [112]. It can be seen from the plot that the numerical results agree well with the analytical solution for a long time period ($t = 10^9$ s).

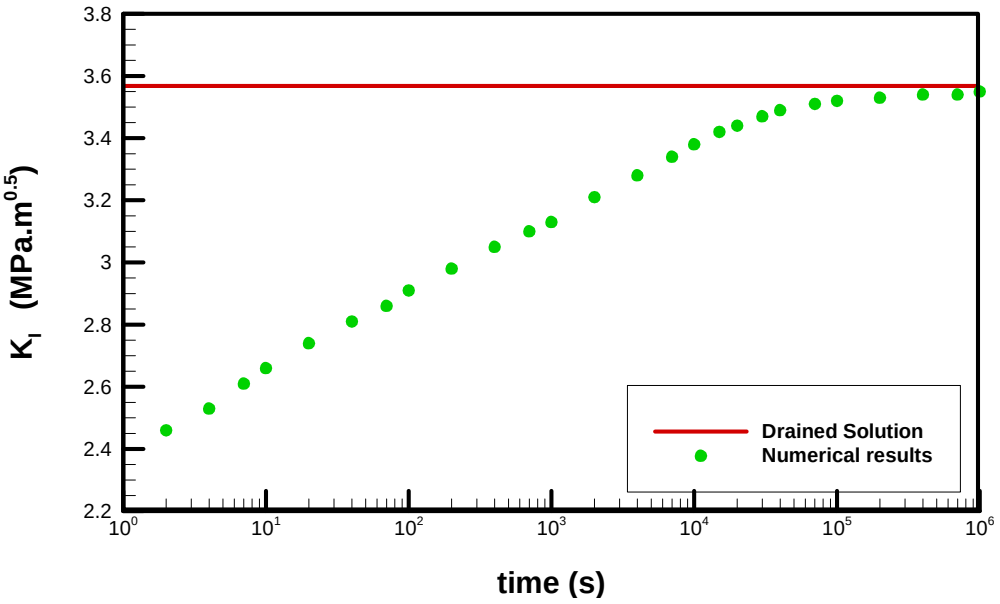

Figure 51. Mode I SIF of penny shape crack under stress loading.

The maximum crack closure that evolves over time is shown in Figure 53. As can be seen, the crack closes more with time. However, two crack surfaces will not overlap in the real world, and closure is possible only if the crack remains open under a combination of Mode 1 and Mode 2 loading.

4.5. Penny-shape crack under pure shear

In the current section, a penny-shape crack with radius a =10.0 m (shown in Figure 54) is considered under pure shear in X direction. The strength of the pure shear is S = 1.0 MPa and the properties of the reservoir are presented in Table 4.

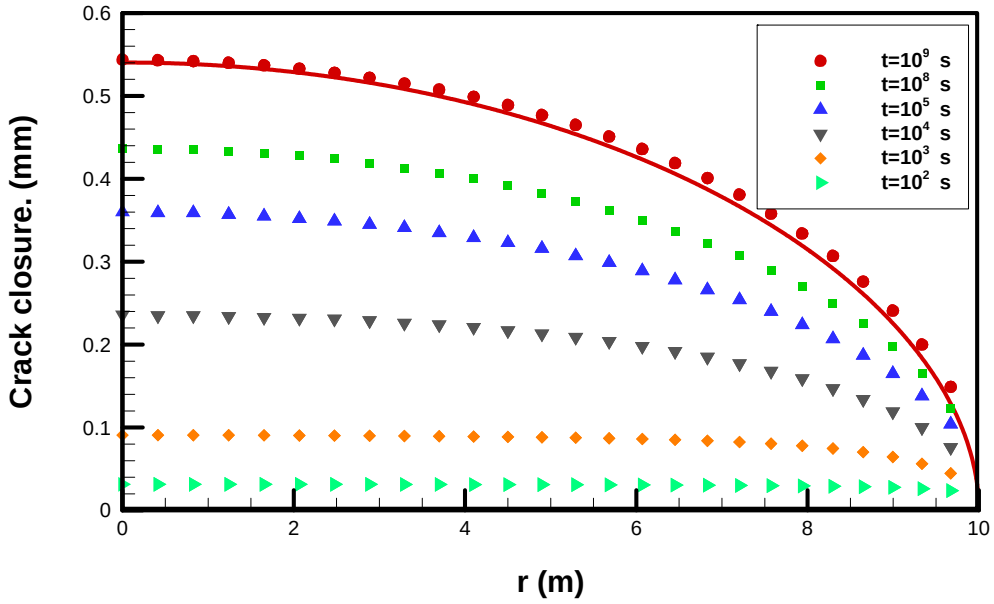

Figure 52. Penny shape crack closure at different time, mode 2 loading, red line is analytical solution.

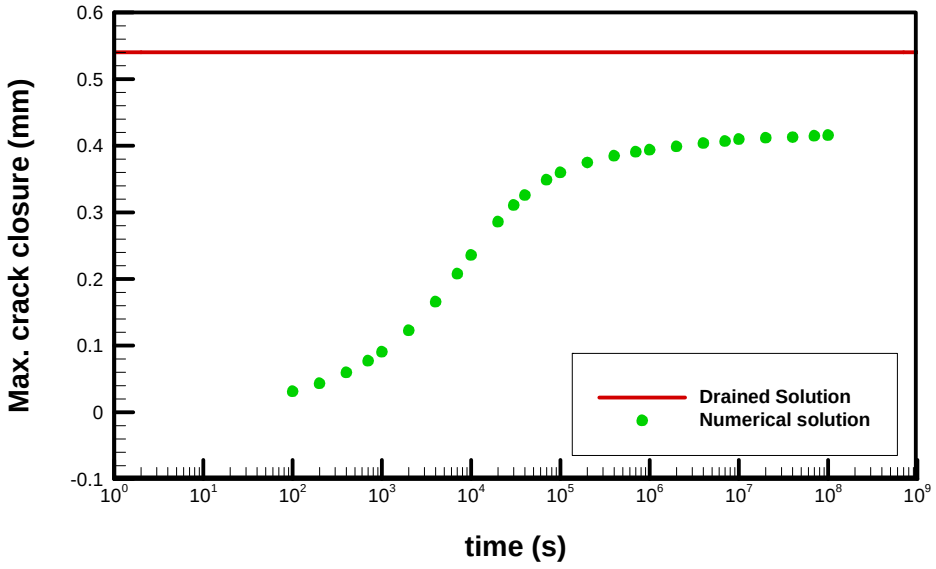

Figure 53. Penny shape crack maximum closure evolution by time, mode 2 loading.

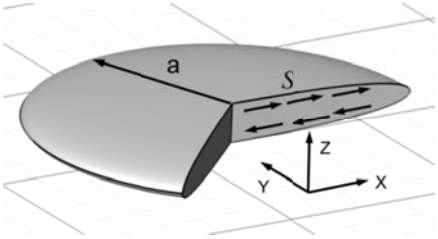

Figure 54. Penny shape crack under pure shear S, in infinite media.

The same discretization as shown in Figure 48 is used here. Segedin [113] solved the problem of a penny-shape crack subjected to pure shear. The analytical solution for crack shear ride can be represented as follows:

$$u_f = \pm \frac{4(1-\nu)Sa}{\pi G(2-\nu)} \sqrt{1-\left(\frac{r}{a}\right)^2}$$

As with the crack opening during Mode 1 loading, the crack ride (shear DD) response is a function of time. At time t = 0+, the crack experiences shear displacement with undrained material properties. As time passes, the crack experiences more shear ride under drained material properties. The response of the crack over a short time (t = 1.0 s, undrained condition) and a long time (t = 10^6 s, drained condition) is presented in Figure 55. The numerical results agree well with the analytical solution for the two limiting conditions.

As in section 4.4, the maximum crack shear ride in the drained and undrained conditions can be defined as follows:

$$u_{\max}^{Drained} = \frac{4Sa(1-\nu)}{\pi G(2-\nu)}, \qquad u_{\max}^{Un-drained} = \frac{4Sa(1-\nu_u)}{\pi G(2-\nu_u)}$$

The maximum shear ride should progress over time from undrained formation

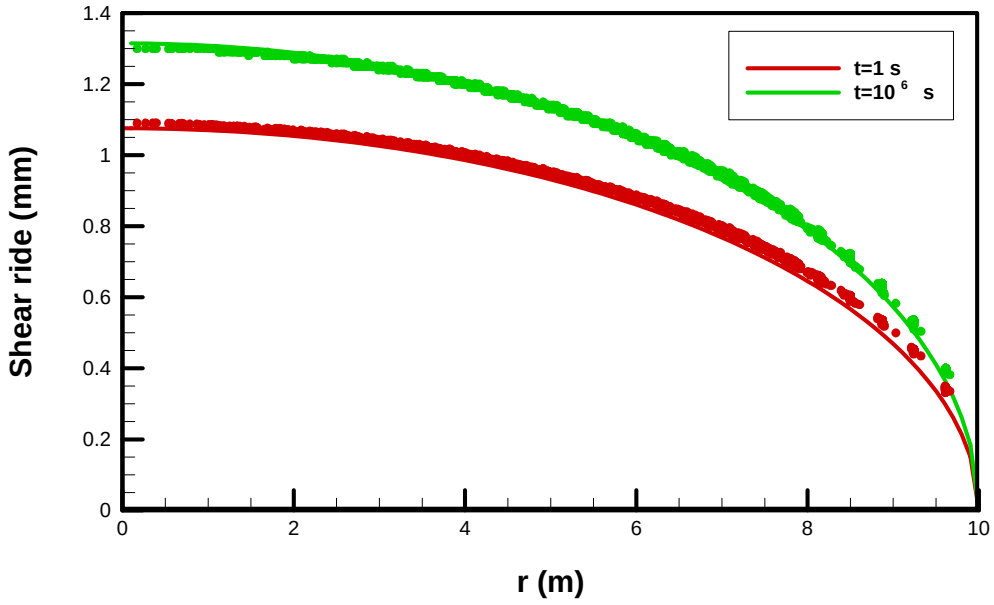

Figure 55. Penny shape crack shear ride at short-term (1 s) and long-term (10^6 s).

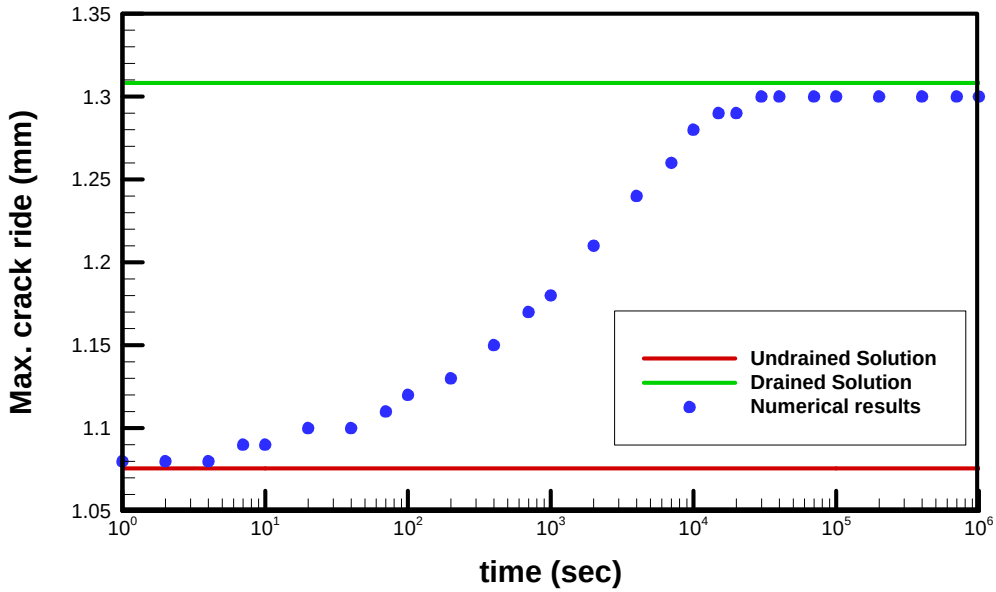

Figure 56. Maximum crack ride under pure shear loading during time.

behavior to drained behavior. Figure 56 plots the maximum shear ride over time. The maximum shear ride predicted by the DD code agrees very well with the closed-form results of the drained and undrained solutions.

The classical elastic relationship between the pure shear loading of a penny-shape crack and Mode II SIF is given by Kundu [111]. The Mode II SIF of a penny-shape crack in elastic media under pure shear can be represented as follows:

$$K_{II} = \frac{4S\sqrt{\pi a}}{\pi(2-\nu)}$$

The analytical value is compared with the M mode II SIF calculated from the developed program. The comparison is shown in Figure 57. The figure shows that the DD code can accurately predict Mode II SIF.

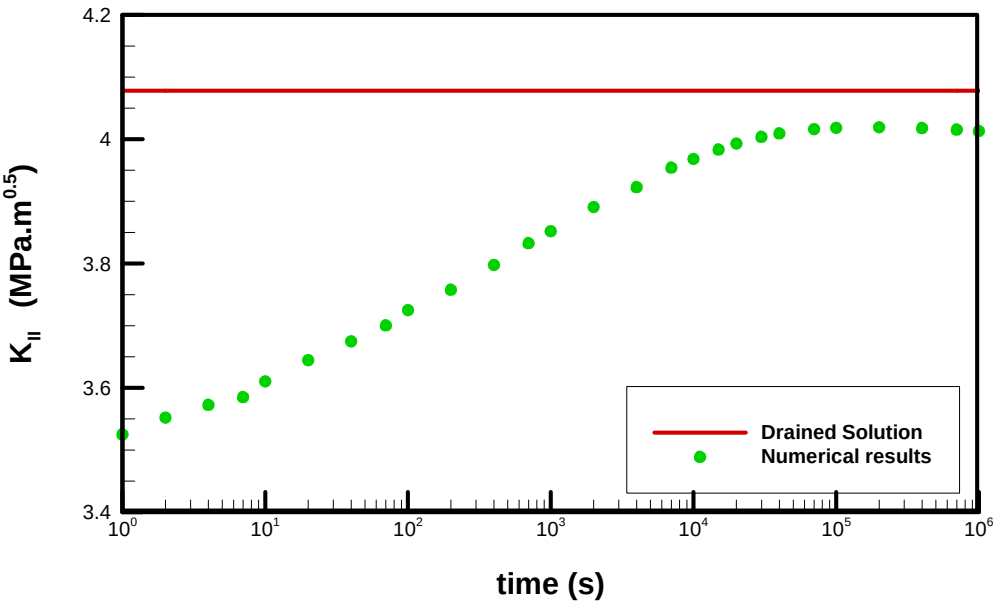

Figure 57. Mode II SIF of penny shape crack under pure shear loading.

4.6. Thermal loading of penny-shape crack

In the current section, the thermoporoelasticity behavior of a crack is investigated. A formation with the properties presented in Table 3 is considered. The formation has an initial temperature of 200°C, but is gradually cooled down by keeping the temperature of the crack surfaces constant at 0°C. The far-field stresses and pore pressure in the formation are assumed to be zero. The same geometry and discretization as the penny-shape crack in section 4.4 (shown in Figure 48) is used here.

This problem in thermoelastic media with a steady state condition (drained condition in thermoporoelastic media) is solved analytically and presented by Olesiak and Sneddon [114] and by Sneddon and Lowengrub [115]. The closed form solution for long term behavior (steady state condition) can be represented as follows [114, 115]:

$$w_f = 16\, a\, \beta_m\, \Delta T / 9\pi \times (1+\nu)\sqrt{1-(r/a)^2}$$

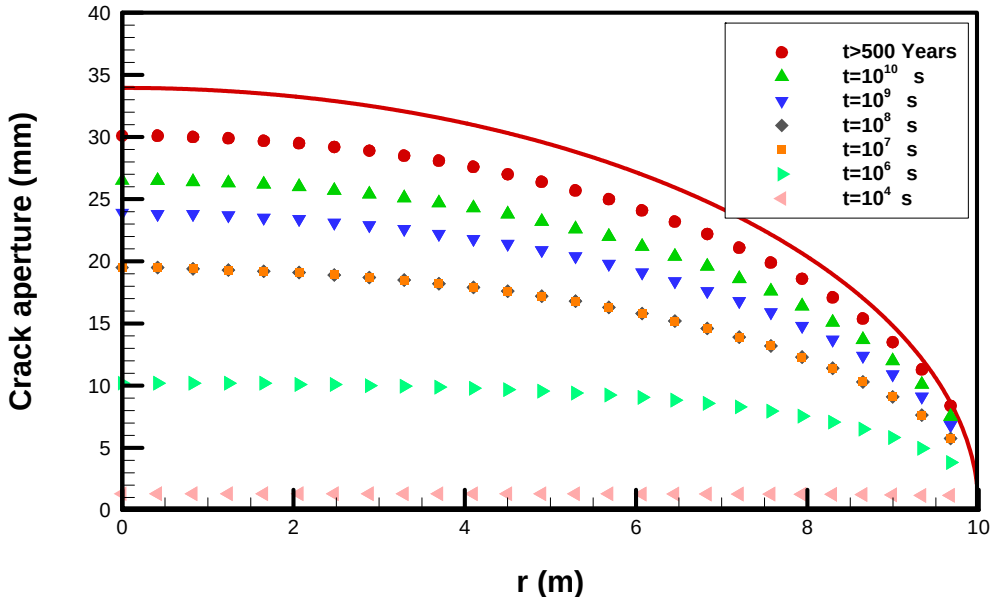

Figure 58. Crack aperture evolution during time, thermal loading, red line is analytical solution.

Figure 58 shows the evolution of the crack aperture over time. After about 500 years the numerical result approaches an acceptable approximation of the steady state solution. This is because of the inherent behavior of thermoporoelastic media. Cooling on the crack surface creates negative pore pressure inside the formation. This negative pore pressure acts as back stress and closes the crack until all induced negative pressure diffuses. After a very long time (more than 500 years), temperature-induced pore pressure will be diffused.

The maximum opening of the crack is plotted as a function of time in Figure 59. The crack gradually opens as time increases and finally reaches an asymptotic value for the steady state as given by the analytical solution. This crack response can be explained by the contraction of the formation due to the cooling process, which pulls the crack surface back and gradually opens it up.

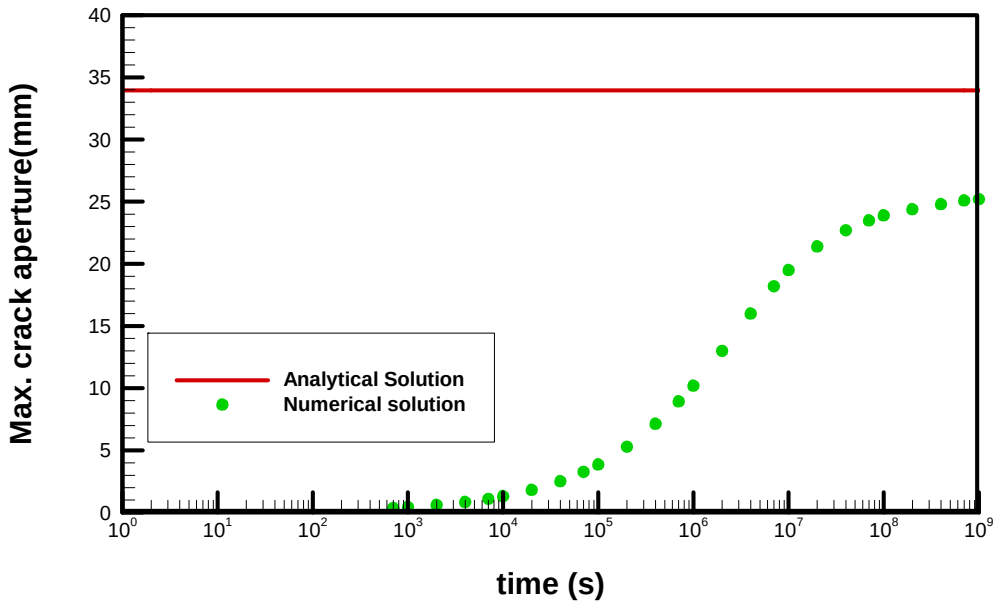

Figure 59. Maximum crack opening due to cooling effect, thermoporoelastic model.

The SIF for the thermal loading of a penny-shape crack in a steady state condition of thermoelastic media can be easily found by similarity between poroelasticity and thermoelasticity. Thus, the Mode I SIF for the steady state condition of the thermal loading of a penny-shape crack can be represented as follows:

$$K_I = 8G\beta_m \Delta T (1+\nu)/9\pi(1-\nu)\times\sqrt{\pi a}$$

The SIF induced by cooling is plotted in Figure 60 by time. The figure indicates that cooling increases the SIF, which results in a higher potential for fracture propagation. After much time passes, the SIF begins to approach a steady state value.

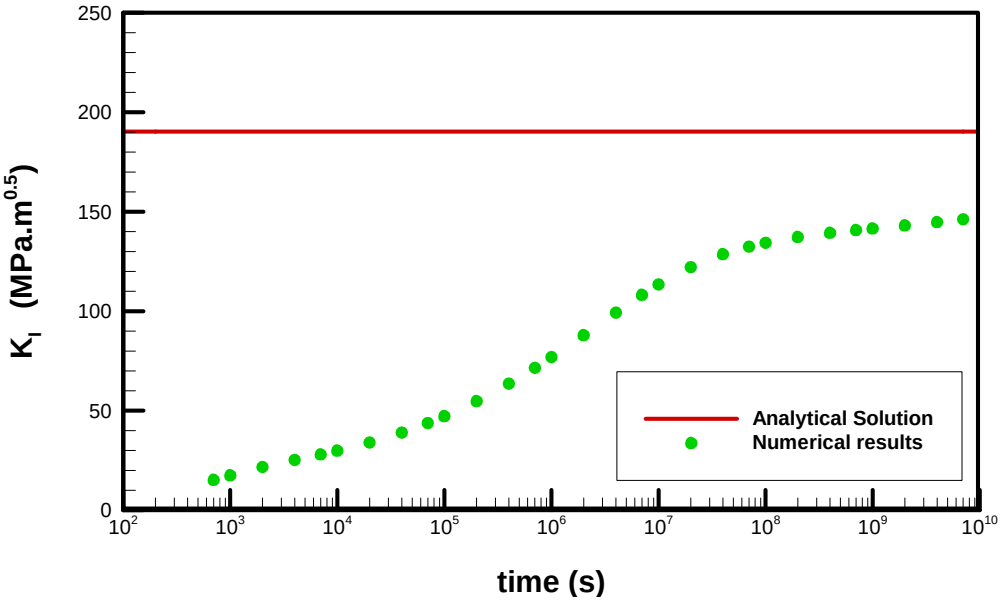

Figure 60. Mode I stress intensity factor under cooling effect, thermoporoelastic model.

4.6.1. Thermoporoelastic vs. thermo-poroelastic loading

In the current section, the difference between full and partial coupling of thermal, hydraulic, and mechanical procedures is investigated. The effects are studied on induced pore pressure inside of media.

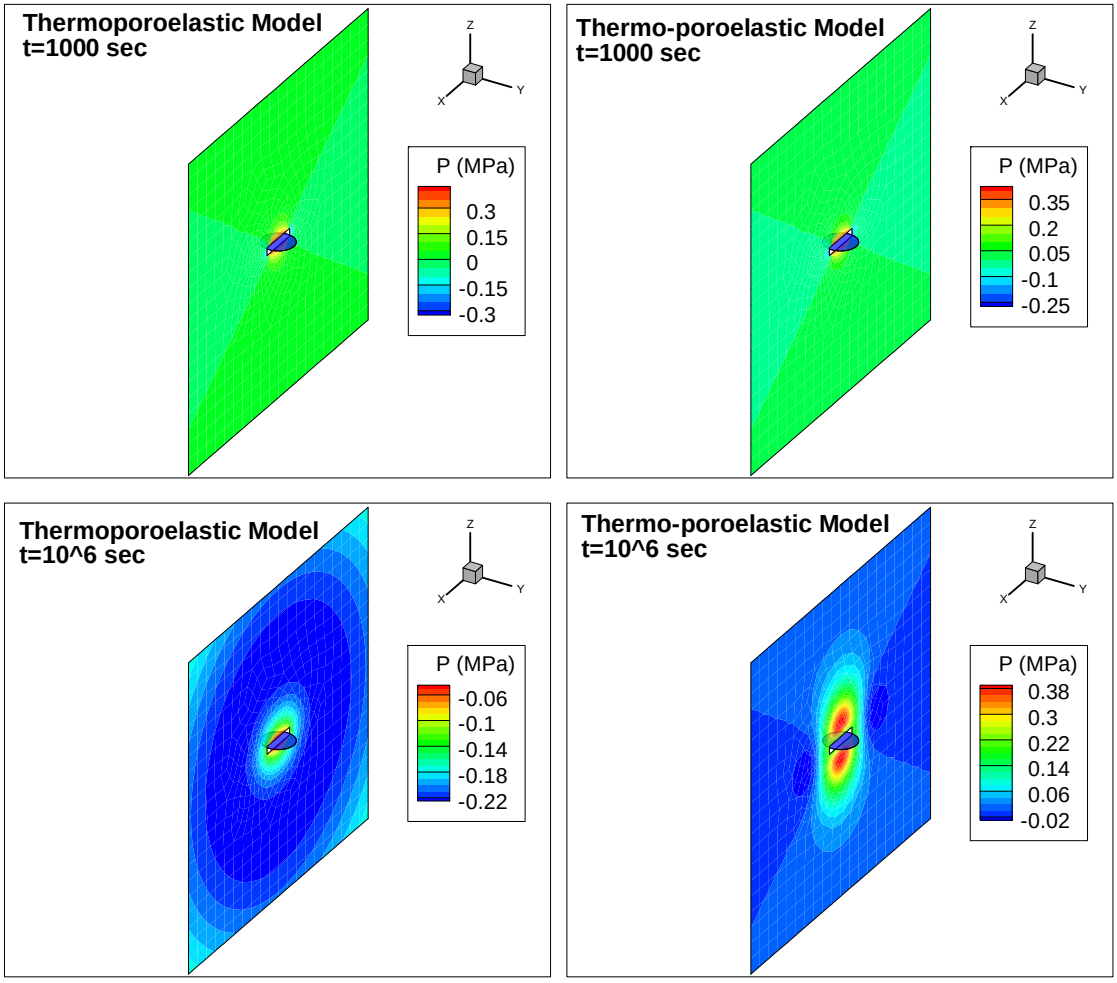

Figure 61. Pressure distribution inside of media for thermoporoelastic and thermo-poroelastic media at two different times.

Figure 61 illustrates the distribution of pore pressure inside of media for two types of coupling—fully coupling (thermoporoelasticity) and partial coupling (thermo-poroelasticity)—at two different times. The pore pressure inside the formation can be induced by temperature (directly or indirectly) and by the crack opening. It is clear from the figure that initially both models predict equivalent distribution of pore pressure, but as time passes, the difference increases. In the thermoporoelastic model there is a

symmetric negative pore pressure, and in the thermo-poroelastic model there is a positive pore pressure field. The negative pressure in the thermoporoelastic model is due to the fact that the cooling effects of pore fluid pressure overcome the opening effect of the crack, and thus the total induced pore pressure is negative. However, in the thermo-poroelastic model there is no direct induced pore pressure. Therefore, the induced pore pressure is solely because of the crack opening, which can increase the pore pressure on the area near the two surfaces of crack.

5. INJECTION/EXTRACTION INTO FRACTURE SYSTEM

In many petroleum/geothermal formations with low matrix permeability, fluid flow takes place mainly through fractures. In some cases the majority of flow takes place through a single fracture, whereas in others the flow occurs through network of fractures. Fracture-dominated flow is important in many situations, such as hydraulic fracturing and enhanced geothermal field development.

Hydraulic fracturing and heat extraction from enhanced geothermal reservoirs is based on enforced nonisothermal fluid flow through a created fracture network. Many parameters affect the performance of a fracture during injection and production, such as in situ stress and fracture geometry. Moreover, variation in pore pressure and temperature inside both the fracture and the rock matrix is a crucial factor that must be taken into account. Therefore, in the current section, the derivation and discretization of governing equations for flow and transport are presented to consider temporal and spatial variation in temperature and pressure.

In the developed model, flow of incompressible fluid and conductive and convective heat transfer inside the fracture are considered and governing PDEs are discretized with the help of the finite element method. Note that the 3D incompressible fluid diffusion and heat transfer in the reservoir rock are treated using the thermoporoelastic DD method presented in section 3. The effect of fracture opening variation on fluid flow and heat transfer inside the fracture is also included in the model.

In reality, fracture surfaces can be separated, stick together (elastic shear deformation), or slip on each other (mechanical closure in the latter two states). The state

of fracture surface in any DD element could be changed from one time step to another. Hence, the state of each fracture element must be determined anew at every time step because the required constitutive relations in the solution process vary by element state (see section 5.2).

5.1. Governing equations and discretization

Fluid injection into a fracture in a low-permeability thermoporoelastic medium include flow of injected fluid and conductive and advective heat transfer within the fracture, flow of injected fluid and conductive heat transfer in the matrix, and fracture propagation. In the proposed technique, the initiation of new fracture, fluid flow, and conductive heat transport in the matrix is handled with the thermoporoelastic DD method presented in section 3.3. In the current section, governing equations for fluid flow and heat transport inside of fractures are derived and discretized in time and space using the finite element method and the forward/backward Euler time-stepping scheme, respectively. In the derivation process it is assumed that the laminar flow occurs inside the fracture and that the fracture is of a finite size and is surrounded in an infinite size rock matrix.

Note that in the following sections, lowercase variables in bold are vectors and uppercase variables in bold are matrices.

5.1.1. Fluid flow in fracture

The simplest model of flow through a rock fracture is the cubic law, in which the fracture is assumed to be bounded by two smooth, parallel plates separated by an

aperture, as shown in Figure 62. The cubic law can also be used to estimate the fracture aperture for closed rough fractures (instead of smooth fractures) with a correction coefficient [116].

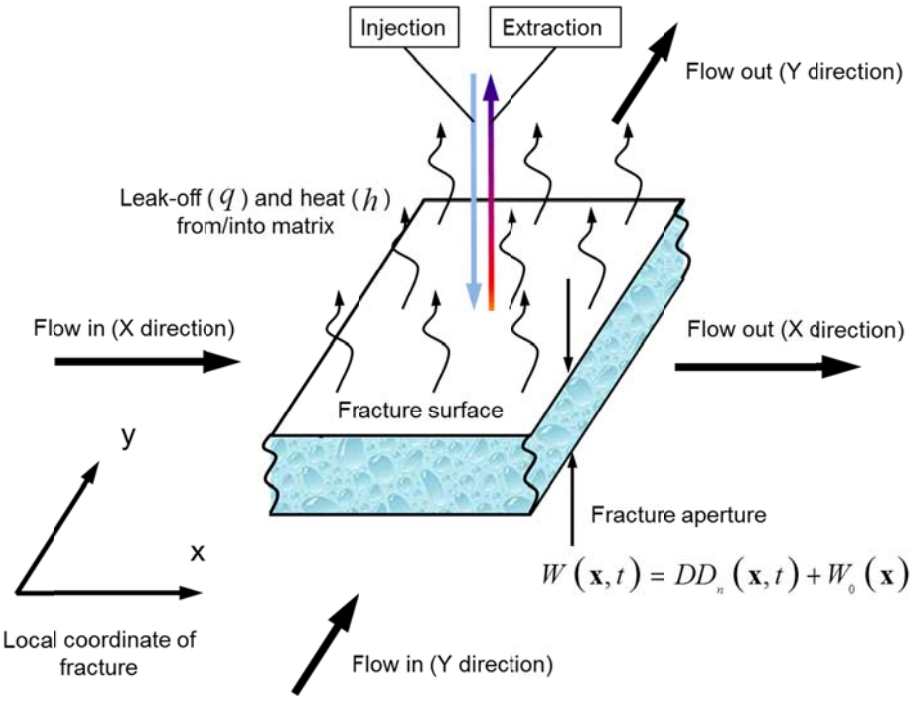

Figure 62. Representative fluid and fracture volume element in rock matrix.

The current model of fluid flow in fractures, assumes that the fracture aperture (on each element) varies smoothly such that the injected incompressible fluid flow in the fracture is laminar [117]. The model can be presented as follows [117]:

$$\nabla p_f(\mathbf{x},t) = -\left(12\mu / W^2(\mathbf{x},t)\right)\mathbf{u}(\mathbf{x},t) \tag{5.1}$$

where ∇ is gradient operator in fracture plane, $p_f(\mathbf{x},t)$ is pressure inside of fracture at $\mathbf{x}(x,y)$ local location and time t, μ is fluid viscosity, $W(\mathbf{x},t)$ is fracture aperture which

is equal to normal DD plus initial fracture aperture as shown in Figure 62, and $\mathbf{u}(\mathbf{x},t)$ is flow velocity field inside of fracture.

In addition to the cubic law, fluid continuity for incompressible fluid governs the flow inside the fracture. This can be written using the following equation [57]:

$$-\nabla.(\mathbf{u}\,W)=\frac{\partial W}{\partial t}-Q_{inj}(t)\,\delta(\mathbf{x}_{inj})+Q_{ext}(t)\,\delta(\mathbf{x}_{ext})+2\upsilon \tag{5.2}$$

where $Q_{inj}(\mathbf{x}_{inj})$ and $Q_{ext}(\mathbf{x}_{ext})$ are fluid injection and extraction rate at injection ($\mathbf{x}_{inj}$) and extraction ($\mathbf{x}_{ext}$) well locations respectively, $\partial W/\partial t$ is the rate of volume increase, υ is the fluid leak-off from one side of the fracture wall into reservoir matrix, and δ is delta Dirac function. Note that all terms in equation (5.2) are in m/sec unit. Equation (5.2) is expressed using a fluid velocity vector and fracture aperture term. However, one can substitute equation (5.1) into equation (5.2) and eliminate the fluid velocity vector.

By substituting equation (5.1) into equation (5.2), one derives the following governing equation for incompressible liquid flow in a fracture:

$$\nabla_2\left(\frac{W^3(\mathbf{x},t)}{12\mu}\nabla_2 p_f(\mathbf{x},t)\right)=\left\{\begin{matrix}\dfrac{\partial W(\mathbf{x},t)}{\partial t}-Q_{inj}(t)\,\delta(\mathbf{x}_{inj})+\\ Q_{ext}(t)\,\delta(\mathbf{x}_{ext})+2\upsilon(\mathbf{x},t)\end{matrix}\right\} \tag{5.3}$$

Before considering the weak form of the PDE equation and discretization process, let's investigate the right-hand side of equation (5.3) in more detail. The first term on the right-hand side of equation is $\partial W/\partial t$. Ghassemi and Zhou [57] assumed that $\partial W/\partial t$ is constant in every time step. They calculated the parameter numerically at each time step and updated the value after any iteration. However, to solve the transient

boundary value problem presented by PDE equation (5.3) in more systematic way and to eliminate the assumption of having constant $\partial W/\partial t$, the following chain rule is considered and the derivation parameter changed from W to p:

$$\frac{\partial W}{\partial t} = \frac{\partial W}{\partial p_f}\frac{\partial p_f}{\partial t}$$
$$\frac{\partial W}{\partial p_f} = \frac{\partial DD_n}{\partial p_f} \tag{5.4}$$

In equation (5.4), it is assumed that W does not change directly with temperature and that the change in W due to temperature variation is already embedded in the change in W due to pressure. By substituting equation (5.4) into equation (5.3), one can present the governing equation (5.3) as follows:

$$\nabla_2\left(\frac{W^3(\mathbf{x},t)}{12\mu}\nabla_2 p_f(\mathbf{x},t)\right) = \left\{\begin{array}{l}\dfrac{\partial W(\mathbf{x},t)}{\partial p_f}\dfrac{\partial p_f}{\partial t} - Q_{inj}(t)\,\delta(\mathbf{x}_{inj}) + \\ Q_{ext}(t)\,\delta(\mathbf{x}_{ext}) + 2\upsilon(\mathbf{x},t)\end{array}\right\} \tag{5.5}$$

In equation (5.5), the parameter $\partial W(\mathbf{x},t)/\partial p_f$ should be known. To define the parameter, rewrite equations (3.33) and (3.34) without the thermal effect. The thermal effect is not considered because temperature does not change with a change in pressure. However, in reality changes in temperature and pressure are indirectly related: Pressure changes the fracture aperture, and the fracture aperture changes the fluid velocity inside fracture, which in turn changes temperature. Nonetheless, in the current study it is assumed that the indirect effect does not play an important role. Equations (3.33) and (3.34) show the relation between stress components (σ_{ij}) and pressure (p_f) at location

$\mathbf{x}$ and time t, on the fracture surface, to the distribution of DDs (DD_{kn}) and fluid source (f) all over the fracture surface:

$$\begin{aligned}\sigma_{ij}(\mathbf{x},t) &= \sum_{\ell=0}^{s}\int_{\Gamma}\left\{\begin{matrix}\sigma_{ijkn}^{dc}(\mathbf{x}-\boldsymbol{\chi},t-\tau_\ell)\times\Delta DD_{kn}(\boldsymbol{\chi},\tau_\ell)+\\ \sigma_{ij}^{sc}(\mathbf{x}-\boldsymbol{\chi},t-\tau_\ell)\times\Delta f(\boldsymbol{\chi},\tau_\ell)\end{matrix}\right\}d\Gamma(\boldsymbol{\chi})+\sigma_{ij}(\mathbf{x},0)\\ p_f(\mathbf{x},t) &= \sum_{\ell=0}^{s}\int_{\Gamma}\left\{\begin{matrix}p_{kn}^{dc}(\mathbf{x}-\boldsymbol{\chi},t-\tau_\ell)\times\Delta DD_{kn}(\boldsymbol{\chi},\tau_\ell)+\\ p^{sc}(\mathbf{x}-\boldsymbol{\chi},t-\tau_\ell)\times\Delta f(\boldsymbol{\chi},\tau_\ell)\end{matrix}\right\}d\Gamma(\boldsymbol{\chi})+p_f(\mathbf{x},0)\end{aligned} \tag{5.6}$$

Note that in preceding relations $f(\boldsymbol{\chi},\tau_\ell)$ is fluid source (with m/sec unit), which leaks from fracture surface into media and it is equal to $2\upsilon(\boldsymbol{\chi},t)$. Moreover $\sigma_{ij}(\mathbf{x},0)$, $p_f(\mathbf{x},0)$ are in situ stresses and background pressure distribution on fracture surface. If it is assumed that DDs and fluid leak off are the only function of pressure, the derivative of equation (5.6) with respect to p_f can be presented as follows:

$$\begin{aligned}\frac{\partial\sigma_{ij}(\mathbf{x},t)}{\partial p_f} &= \sum_{\ell=0}^{s}\int_{\Gamma}\left\{\sigma_{ijkn}^{dc}(\mathbf{x}-\boldsymbol{\chi},t-\tau_\ell)\times\Delta\frac{\partial DD_{kn}}{\partial p_f}+\sigma_{ij}^{sc}(\mathbf{x}-\boldsymbol{\chi},t-\tau_\ell)\times\Delta\frac{\partial f}{\partial p_f}\right\}d\Gamma(\boldsymbol{\chi})\\ 1.0 &= \sum_{\ell=0}^{s}\int_{\Gamma}\left\{p_{kn}^{dc}(\mathbf{x}-\boldsymbol{\chi},t-\tau_\ell)\times\Delta\frac{\partial DD_{kn}}{\partial p_f}+p^{sc}(\mathbf{x}-\boldsymbol{\chi},t-\tau_\ell)\times\Delta\frac{\partial f}{\partial p_f}\right\}d\Gamma(\boldsymbol{\chi})\end{aligned} \tag{5.7}$$

The strength of $\partial\sigma_{ij}(\mathbf{x},t)/\partial p_f$ is defined in section 5.2, where the constitutive models of joints and hydraulic fracture are defined. By considering the solution of algebraic equation (5.7) and the fact that all left-hand sides of the equations are known, one can define the numerical value of $\partial DD_n/\partial p_f$. Note that according to relation (5.4), parameter $\partial DD_n/\partial p_f$ is equal to $\partial W/\partial p_f$, whose numerical value is essential for solving the governing equation (5.5).

To solve the ordinary PDE equation that will result from the finite element discretization of equation (5.5), one needs to determine whether if the multiplier of $\partial p_f / \partial t$ ($\partial W / \partial p_f$) is a function of p_f [118]. Therefore, the derivative of equations (5.7) due to p_f is taken as follows:

$$\begin{aligned} 0.0 &= \sum_{\ell=0}^{s} \int_{\Gamma} \left\{ \sigma_{ijkn}^{dc}\left(\mathbf{x}-\boldsymbol{\chi}, t-\tau_{\ell}\right) \times \Delta \frac{\partial^2 DD_{kn}}{\partial\left(p_f\right)^2} + \sigma_{ij}^{sc}\left(\mathbf{x}-\boldsymbol{\chi}, t-\tau_{\ell}\right) \times \Delta \frac{\partial^2 f}{\partial\left(p_f\right)^2} \right\} d\Gamma\left(\boldsymbol{\chi}\right) \\ 0.0 &= \sum_{\ell=0}^{s} \int_{\Gamma} \left\{ p_{kn}^{dc}\left(\mathbf{x}-\boldsymbol{\chi}, t-\tau_{\ell}\right) \times \Delta \frac{\partial^2 DD_{kn}}{\partial\left(p_f\right)^2} + p^{sc}\left(\mathbf{x}-\boldsymbol{\chi}, t-\tau_{\ell}\right) \times \Delta \frac{\partial^2 f}{\partial\left(p_f\right)^2} \right\} d\Gamma\left(\boldsymbol{\chi}\right) \end{aligned} \tag{5.8}$$

It is obvious from relations (5.8) that $\partial^2 DD_n / \partial\left(p_f\right)^2$ must be zero, because the only possible solution for the algebraic system in equation (5.8) is a trivial solution. Therefore, $\partial W\left(\mathbf{x}, t\right) / \partial p_f$ is independent of p_f and can be considered a constant (A) in each time step. This means that the fracture aperture changes monotonically with variations in pressure inside the fracture. Hence, the nonlinear PDE equation in equation (5.5) can be rewritten as follows:

$$\begin{aligned} &\nabla_2 \left(\frac{W^3\left(\mathbf{x}, t\right)}{12\mu} \nabla_2 p_f\left(\mathbf{x}, t\right) \right) = A \frac{\partial p_f}{\partial t} - F\left(\mathbf{x}, t\right) \\ &A = \frac{\partial W\left(\mathbf{x}, t\right)}{\partial p_f}, \quad F\left(\mathbf{x}, t\right) = Q_{inj}\left(t\right)\, \delta\left(\mathbf{x}_{inj}\right) - Q_{ext}\left(t\right)\, \delta\left(\mathbf{x}_{ext}\right) - 2\upsilon\left(\mathbf{x}, t\right) \end{aligned} \tag{5.9}$$

Note that the numerical value of A is known at every time step by solving algebraic equation (5.7). Equation (5.9) is a nonlinear transient second-order elliptic PDE. The ellipticity is due to the positivity of $W^3\left(\mathbf{x}, t\right) / 12\mu$. The nonlinearity is due to

the fact that $W(\mathbf{x},t)$ is totally dependent on $p_f(\mathbf{x},t)$. The transient characteristic of the equation manifests on the right-hand side of the equation in parameter $\partial p_f / \partial t$. To solve the equation, it is essential to meet two boundary conditions and one initial condition. The first boundary condition, which is the Neumann type, is shown in Figure 63. This stated boundary condition means that there is no leak-off from the crack edge (Γ_f), which is not unrealistic because the fracture tip, ideally is a line and has no area from which fluid can leak off to media. To have a unique solution, initial boundary value equation (5.9) must meet another boundary condition that defines pressure on at least one point of the fracture surface. However, the relation that defines fracture pressure is already established through the use of the thermoporoelastic DD (equation (3.42)). The essential initial condition needed to solve the PDE equation is initial pressure distribution (background pore pressure) on the fracture surface ($p_0(\mathbf{x})$), which is considered a known function through the fracture domain.

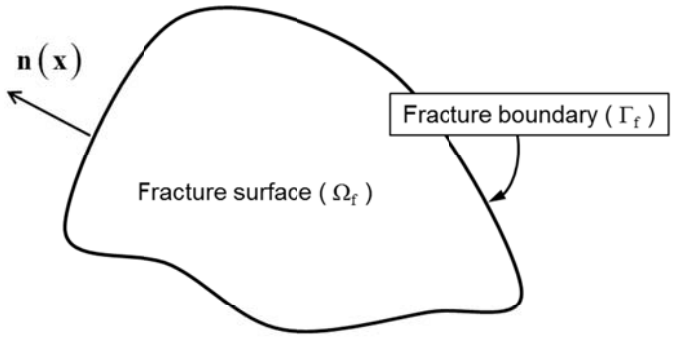

Figure 63. Fracture domain and initial and boundary condition.

5.1.2. Weak form of fluid flow PDE

In the current section, the Galerkin finite element method (Galerkin FEM) is considered as a discretization tool for numerically solving the PDE in equation (5.9), with the initial and boundary conditions as stated in the previous section. The main advantage of using the finite element method is its ability to solve problems that are defined on complex geometries [119].

Before using the Galerkin FEM to solve PDE equation (5.9), it is essential to convert the equation into a more suitable form for solving. Generally speaking, a weak formulation of an elliptic PDE has exactly the same solution as the differential equation. Initially the weak formulation was used to investigate the performance of a PDE solution and to prove the existence and uniqueness of the solution. Later the method is used to produce an approximat solution of a PDE in a constructive way [120]. The weak formulation of equation (5.9) can be derived by multiplying equation (5.9) by a so-called test function w and integrating it over the domain.

The weak formulation of the fluid flow PDE equation (equation for flow diffusion inside the fracture) can be derived by multiplying equation (5.9) by a so-called weighting function w and integrating over it fracture domain (Ω_f). Thus, the weak formulation can be written as follows:

$$\int_{\Omega_f} w\, A\frac{\partial p}{\partial t} d\Omega - \int_{\Omega_f} w\, \nabla_2 \left[\frac{W^3}{12\mu}\nabla_2 p_f\right] d\Omega - \int_{\Omega_f} w\, F d\Omega = 0.0 \qquad (5.10)$$

By using Green's identity and divergence theory to eliminate the second derivative term and noting that $\nabla_2 p_f(\mathbf{x},t).\,\mathbf{n}(\mathbf{x}) = 0.0 \quad in \quad \Gamma_f$, one can write equation (5.10) in the following form:

$$\int_{\Omega_f} w\, A\frac{\partial p}{\partial t} d\Omega - \int_{\Omega_f} \nabla_2 w\,.\,\frac{W^3}{12\mu}\nabla_2 p_f\, d\Omega - \int_{\Omega_f} w\, F d\Omega = 0.0 \tag{5.11}$$

Once the weak formulation of the governing PDE equation (equation (5.9)) is established, the approximate solution based on the Galerkin FEM is determined. To construct the Galerkin FEM approximation, look at the fracture domain as discretized into "nels" four-node quadrilateral elements—the same as essential discretization in DD equations, (3.41), (3.42), and (3.43). Then the solution for equation (5.11) can be approximated using a linear combination of shape functions and pressure at element nodes as follows:

$$p_f(\mathbf{x},t) = \sum_i N_i(\mathbf{x})\,\hat{p}_f(\mathbf{x},t) \tag{5.12}$$

where $N_i(\mathbf{x})$ is the ith shape function at location $\mathbf{x}$ and $\hat{p}_f(\mathbf{x},t)$ is the nodal value of pressure. It is common practice in the Galerkin FEM to confine a solution to a lower degree shape function (linear) [120]. Moreover, in the Galerkin FEM, the weighting function is defined the same as the shape functions:

$$w(\mathbf{x}) = N(\mathbf{x}) \tag{5.13}$$

By using the linear Galerkin FEM approximation (shape functions as presented in equation (3.24)) for geometry and other continuous parameters in equation (5.11), one can establish algebraic equations for finite element approximation of the original PDE

equation. During the construction of algebraic equations the following necessary relation will be generated:

$$\frac{\partial p_f(\mathbf{x},t)}{\partial t} = \mathbf{N}\left(\boldsymbol{\xi}(\mathbf{x})\right)\hat{\mathbf{p}}_f(t) \qquad \mathbf{DN} = \partial N_i / \partial \xi_i,$$

$$\mathbf{x} = \hat{\mathbf{X}}^T\ \mathbf{N}^T \qquad \mathbf{J} = \hat{\mathbf{X}}^T\ \mathbf{DN},$$

$$\mathbf{B} = \mathbf{DN}\ \ \mathbf{J}^{-1} \qquad \mathbf{N} = \begin{bmatrix} N_1 & N_2 & N_3 & N_4 \end{bmatrix} \qquad (5.14)$$

$$\mathbf{DN}^T = \begin{bmatrix} \frac{\partial N_1}{\partial \xi_1} & \frac{\partial N_2}{\partial \xi_1} & \frac{\partial N_3}{\partial \xi_1} & \frac{\partial N_4}{\partial \xi_1} \\ \frac{\partial N_1}{\partial \xi_2} & \frac{\partial N_2}{\partial \xi_2} & \frac{\partial N_3}{\partial \xi_2} & \frac{\partial N_4}{\partial \xi_2} \end{bmatrix} \qquad \hat{\mathbf{X}}^T = \begin{bmatrix} x_1 & x_2 & x_3 & x_4 \\ y_1 & y_2 & y_3 & y_4 \end{bmatrix}$$

$$\hat{\mathbf{p}}_f{}^T = \begin{bmatrix} p_1 & p_2 & p_3 & p_4 \end{bmatrix}$$

In equation (5.14), $(x_i, y_i), i = 1,2,3,4$ are local coordinates of four points of a quadrilateral element, $N_i, i = 1,2,3,4$ are four linear shape functions (equation 3.25), and $\xi_i = (\xi_1, \xi_2)$ are local coordinates of unit square elements (see Figure 12). With the help of relations in equation (5.14), global coefficient matrices based on the assembly of element-level matrices are constructed as follows:

$$\mathbf{M}_{m\times m} = \underset{e=1}{\overset{nele}{\mathcal{A}ssemble}}\left(\mathbf{M}_e\right), \quad \mathbf{M}_e = \int_{-1.0}^{+1.0}\int_{-1.0}^{+1.0} \mathbf{N}^T A\ \mathbf{N}\ \mathbf{J}\ d\xi_1 d\xi_2 \qquad (5.15)$$

$$\mathbf{K}_{m\times m} = \underset{e=1}{\overset{nele}{\mathcal{A}ssemble}}\left(\mathbf{K}_e\right), \quad \mathbf{K}_e = \int_{-1.0}^{+1.0}\int_{-1.0}^{+1.0} \mathbf{B}\ \frac{W^3}{12\mu}\ \mathbf{B}^T\ \mathbf{J}\ d\xi_1 d\xi_2 \qquad (5.16)$$

$$\mathbf{F}_{m\times 1} = \underset{e=1}{\overset{nele}{\mathcal{A}ssemble}}\left(\mathbf{F}_e\right) + \mathbf{Q}, \quad \mathbf{F}_e = \int_{-1.0}^{+1.0}\int_{-1.0}^{+1.0} \mathbf{N}^T\left(-2\upsilon\right)\mathbf{J}\ d\xi_1 d\xi_2$$
$$\mathbf{Q}_{m\times 1} = \begin{bmatrix} 0.0 & \ldots\ldots & Q_{inj}(t) & \ldots\ldots & -Q_{ext}(t) & \ldots 0.0 \end{bmatrix} \qquad (5.17)$$

In the preceding relations, *nele* is the number of elements; m is number of nodes; $\mathcal{A}_{e=1}^{nele}$ is a symbol that shows the assembly process; and $\mathbf{Q}$ is the zero vectors with m × 1 dimensions, which has the value of an injection or extraction rate at the nodes at which injection or extraction happens. Using equations (5.15), (5.16), and (5.17) and the fundamental relation in (5.14), one can write the discretized form of the weak formulation (equation (5.11)) in the following matrix form:

$$\mathbf{M}\,\dot{\mathbf{p}} + \mathbf{K}(\mathbf{p})\,\mathbf{p} = \mathbf{F}(\mathbf{p}) \tag{5.18}$$

There are three unknowns in ordinary differential equation (5.18): the pressure inside the fracture; the amount of leak-off from the fracture to the matrix, which reveal itself in vector $\mathbf{F}$; and the fracture aperture W (DD). Because the fracture aperture depends on the fracture pressure (equation (3.42)), equation (5.18) should be solved in an iterative manner with isothermal DD equations (3.41) and (3.42), with zero thermal effect at the initial iteration (see section 5.3 for a complete workflow). First equation (5.18) is solved assuming zero leak-off and initial fracture aperture, and then the calculated pressure is substituted in thermoporoelastic DD equations (3.41) to (3.42) considering $\Delta h_q^{r,t}$ as constant. Then the amount of leak-off is updated and the new fracture aperture is calculated based on the normal and shear DD distribution. This procedure is performed iteratively until the pressure inside the fracture converges within a certain prescribed error.

Equation (5.18) is a discrete-space, continuous-time approximation of original partial differential equations. A direct time-integration procedure substitutes the continuous-time derivative with an approximation for the history of pressure inside the

fracture. The result is an incremental procedure that progresses the solution by discrete steps in time. In this work, a first-order implicit integration method is used to employ the forward Euler scheme as a predictor with the backward Euler method functioning as the corrector step. Ignoring the details of the derivation, the application of the explicit forward Euler formula to equation (5.18) produces the following:

$$\mathbf{M}\ \mathbf{p}_{predictor}^{n+1} = \mathbf{M}\ \mathbf{p}^{n} + \Delta t\left[\mathbf{F}\left(\mathbf{p}^{n}\right) - \mathbf{K}\left(\mathbf{p}^{n}\right)\mathbf{p}^{n}\right] \tag{5.19}$$

In equation (5.19), the superscript indicates the time step, and Δt is the duration of each time step. The backward Euler (or fully implicit) method is provided as a corrector step of the first-order scheme. Applying equation (5.19) to equation (5.18) yields the following implicit method:

$$\left[\frac{1}{\Delta t}\mathbf{M} + \mathbf{K}\left(\mathbf{p}^{n+1}\right)\right]\mathbf{p}^{n+1} = \frac{1}{\Delta t}\mathbf{M}\ \mathbf{p}^{n} + \mathbf{F}\left(\mathbf{p}^{n+1}\right) \tag{5.20}$$

The implicit nature of the method is obvious from the form of equation (5.20), as it is in result a nonlinear, algebraic system for the variable $\mathbf{p}$ at time step $n+1$.

The solution to equation (5.20) at time step $n+1$ can be achieved using an iteration procedure such as Picard's method[118]. Picard's iterative process consists of constructing a sequence of $\mathbf{p}$ that will get closer and closer to the desired solution. The rate of convergence of Picard's method is significantly amplified if the initial solution approximation is close to the true solution. The solution anticipated from equation (5.19) provides the initial cost-effective guess for the iterative procedure.

5.1.3. Heat transport in fracture

For heat transport inside of a fracture, it is assumed that the heat storage is negligible compared to heat advection and conduction due to fluid flow [121, 122].

To derive the governing equation for heat transport inside of a fracture, one must consider energy conservation. The current study assumes that only thermal energy exists and that other types of energy (e.g., potential and dynamic energy) do not modify the system. Hence, the law of energy conservation results in the heat conservation relation. Figure 62 is considered a representative fluid volume element for heat transfer inside of a fracture. Combining the mass continuity equation with the heat conservation equation results in the following heat advection-diffusion equation [123]:

$$\left(C_f\ \rho_f\ W\left(\mathbf{x},t\right)\right)\mathbf{u}\left(\mathbf{x},t\right).\nabla_2\ T_f\left(\mathbf{x},t\right)-\left(k_f\ W\left(\mathbf{x},t\right)\right)\nabla_2^2\ T_f\left(\mathbf{x},t\right)+h\left(\mathbf{x},t\right)=0.0 \qquad (5.21)$$

In the preceding equation, each of the three terms is in J/s/m^2; C_f is the injected fluid specific heat; ρ_f is the injected fluid density; $T_f\left(\mathbf{x},t\right)$ is the temperature of the fluid inside the fracture which is assumed to be the same as the temperature of the fracture surface; $h\left(\mathbf{x},t\right)$ is the rate of heat transfer from the fracture surface into the medium; and k_f is the injected fluid thermal conductivity. Note that equation (5.21) is a mixed parabolic-hyperbolic second-order partial differential equation. If the first term (advection term) and last term are in the equation, it is classified as parabolic; if the second term (diffusion term) and last term are in the equation, it is classified as a hyperbolic second-order PDE.

In the derivation of equation (5.21), it is assumed that injected fluid density is independent of temperature. This assumption is valid if the injected fluid is water less than 100°C [124]. The partial differential equation is a mixed parabolic-hyperbolic PDE and requires a special numerical technique (the Galerkin FEM cannot be used) to discretize and solve.

Application of Galerkin FEM to mixed parabolic-hyperbolic PDEs has not achieved the same degree of success that has been attained for symmetric operators, such as the elliptic partial differential equation for fluid flow inside fracture [125-127]. This deficiency may be characterized as a lack of best approximation property, which manifests in the form of occasional spurious “wiggles” or oscillations in the temperature field. A number of research efforts have been undertaken to improve the finite element methods appropriate for use with these kinds of nonsymmetric operators. One of the most successful and well-known methods is the streamline upwind Petrov–Galerkin method, in which, unlike in the Galerkin method, the weighting functions are discontinuous [125-127].

5.1.4. Weak form of heat transport PDE and its solution

The mathematics and fundamentals of the weak formulation of the advection-diffusion PDE with the streamline upwind Petrove–Galerkin method is very complex and can be found at Brooks and Hughes [126]. However, the general procedure is same as the Galerkin method as described in Section 5.1.2.

Streamline upwind method is usually implemented by modifying the diffusion term in the Galerkin finite element formulation. Modified diffusion can be interpreted as

artificial diffusion [126]. Streamline upwind method can be implemented in other way by modifying weighting function for the convective term in the partial differential equation. However, the up-winded weight of the convection term between other terms is not consistent. This results in excessively diffuse solutions when transient characteristic of equation is considered or source/sink exit as a boundary condition. Therefore, it is essential to have an up-winded weighting of all terms in the equation. A consistent up-winded Petrov–Galerkin formulation is achieved by modifying weighting function of all terms in the equation. Note that in the usual Galerkin weighted residual method, the continuous weighting functions are considered throughout and across element boundaries. In contrast, in consistent streamline upwind Petrov–Galerkin formulation, a discontinuous weighting function of the following form is needed:

$$\tilde{N} = N + N'$$

where N is the continuous shape function and N' is the discontinuous streamline upwind contribution. Note that the continuous and discontinuous weighting functions are smooth throughout element interior. In the streamline upwind Petrov–Galerkin method, N' has the following form:

$$N_i' = \frac{\bar{k}\ u_j\ N_{i,j}}{\|u\|}$$

where $\bar{k}$ is the upwind parameter (a complete definition can be found at Brooks and Hughes [126]), u_j is a component j of fluid velocity, and $\|u\|$ is the strength of velocity. Following the stated modification of the weighting function, and after applying

the Petrov–Galerkin weak formulation, equation (5.21), can be written in the following form:

$$\mathbf{K}_T\left(\hat{\mathbf{T}}\right)\hat{\mathbf{T}}+\mathbf{H}\left(\hat{\mathbf{T}}\right)\mathbf{h}=0.0$$

$$\mathbf{K}_T\left(\hat{\mathbf{T}}\right)=\underset{e=1}{\overset{Nele}{\mathcal{A}\text{ssemble}}}\left[\begin{array}{l} C_f\rho_f\ W\int_{-1.0}^{+1.0}\int_{-1.0}^{+1.0}\left(N+N'\right)^T\mathbf{u}\ \mathbf{B}^T\ \mathbf{J}\ d\xi d\eta+ \\ \left(k_f\ W\right)\int_{-1.0}^{+1.0}\int_{-1.0}^{+1.0}\mathbf{B}\ \mathbf{B}^T\ \mathbf{J}\ d\xi d\eta \end{array}\right] \tag{5.22}$$

$$\mathbf{H}\left(\hat{\mathbf{T}}\right)=\underset{e=1}{\overset{Nele}{\mathcal{A}\text{ssemble}}}\left[\int_{-1.0}^{+1.0}\int_{-1.0}^{+1.0}\left(N+N'\right)^T\ N\ \mathbf{J}\ d\xi d\eta\right]$$

This algebraic equation is considered with equation (3.43) in the DD method. The two equations form a set of equations with two unknowns: temperature and heat flux. The solution of the equation set is sought after an iterative method for pressure presented in the previous section. Initially temperature is assumed to have a background amount and heat flux with zero value. Then thermoporoelastic DD equations are solved and the velocity field inside the fracture is found. At that time, after the distribution of fluid velocity inside the fracture is defined, the temperature field is found using equations (3.43) and (5.22). The temperature and heat flux are updated, and this procedure is performed iteratively until the temperature field converges (see section 5.3 for the full workflow).

5.2. Natural fracture (joint) behavior

The response of natural fractures is a key factor in hydraulic and thermal stimulation of unconventional resources. Slip on natural fractures increases permeability and results in microseismicity during the injection/production process. Numerical

modeling of these phenomena is needed to predict stimulated volume, permeability dynamics, and the occurrence of microseismicity in geothermal and gas shale reservoirs.

The importance of natural fracture behavior has been recognized in the geothermal and petroleum literatures [6, 128-130], and different approaches used to analyze it [49, 52, 53]. However, the problem has mostly been treated two dimensionally, using the assumption of linear behavior of joints with a perfectly plastic post-peak response. Rahman et al. [41] modeled natural fractures using a stochastic approach with simplified assumptions regarding pressure distribution within fractures. Wang and Ghassemi [42] used a similar approach but considered flow and poroelasticity as well as heat transport. The approach used by Zhou and Ghassemi [131] is used here to couple flow, stress, and fracture deformation and to estimate micro earthquakes. Furthermore, increases in fracture permeability due to shear deformation and dilation due to shear slip are considered.

In the current study, the fundamentals of the DD equations and finite element formulation are the same as in Zhou and Ghassemi[131]. However, the DD equations are modified to simulate the effects of multiple fractures (parallel or intersecting) on each other and of heat transfer. Moreover, a conduction term for heat transfer inside the fracture is added to the energy conservation model inside the fracture. In summary, the model used in the current study combines DD equations with fluid flow and heat transport inside the fracture and mechanical properties of joint/hydraulic fracture. Eventually the combined governing relations result in a set of equations that have following the outcome: spatial and temporal variation of pressure, temperature, fracture

aperture, shear ride, leak-off into the matrix, normal and shear stresses on fracture surface. The Mohr-Coulomb criterion is used to define the slippage threshold, which continues according to a slip-weakening model.

5.2.1. Hydraulic fracture constitutive relations

Variation of stress and fracture deformation in natural fracture network follows specific constitutive relations for that discontinuity. Three complementary equations are suggested by the intrinsic behavior of discontinuities (fractures) in rock. If the effective stress on a fracture surface becomes zero, the fracture element behaves as a hydraulic fracture, which is hydraulically and mechanically open. This means that the two surfaces of the fracture separate from each other, and the total stress on the fracture surface equals the pore pressure. Moreover, the fracture cannot experience any shear stresses. Thus, for a discontinuity that behaves as a hydraulic fracture, the three complementary equations to DD equations can be represented as follows:

$$\sigma_{33}\left(\mathbf{x},t\right) = -p_f\left(\mathbf{x},t\right),\ \sigma_{13}\left(\mathbf{x},t\right) = 0.0,\ \sigma_{23}\left(\mathbf{x},t\right) = 0.0 \tag{5.23}$$

where $\sigma_{33}\left(\mathbf{x},t\right), \sigma_{13}\left(\mathbf{x},t\right)$ and $\sigma_{23}\left(\mathbf{x},t\right)$ are normal, and two shear stress on hydraulic fracture surfaces respectively, and $p_f\left(\mathbf{x},t\right)$ is pressure inside of fracture.

5.2.2. Joint constitutive relations

Many reports contains description of the mechanical properties of rock [58, 132]. If a DD element has not opened completely, it can carry normal and shear stresses. It is assumed that shear tractions are a function of shear DD in the corresponding direction only. However, shear DD affects the net aperture through dilation. For joints, the

following constitutive models can be used (three complementary equations to DD equations):

$$\begin{aligned}
\sigma_{33}\left(\mathbf{x},t\right) &= F_n\left(D_{33}\left(\mathbf{x},t\right)\right) + F_s\left(D_{13}\left(\mathbf{x},t\right), D_{23}\left(\mathbf{x},t\right)\right) \\
\sigma_{13}\left(\mathbf{x},t\right) &= F_1\left(D_{13}\left(\mathbf{x},t\right)\right) \\
\sigma_{23}\left(\mathbf{x},t\right) &= F_2\left(D_{23}\left(\mathbf{x},t\right)\right)
\end{aligned} \tag{5.24}$$

where $F_n\left(D_{33}\left(\mathbf{x},t\right)\right)$ describes closing/opening behavior of joins, $F_s\left(D_{13}\left(\mathbf{x},t\right), D_{23}\left(\mathbf{x},t\right)\right)$ explains dilation effect, and $F_1\left(D_{13}\left(\mathbf{x},t\right)\right)$, $F_2\left(D_{23}\left(\mathbf{x},t\right)\right)$ define shear traction versus shear deformation relations.

The normal behavior of joints is entirely related to the amount of effective stress on the fracture surface (see Figure 64). According to the fundamentals of rock joint behavior [58], the normal direction constitutive model of joints can be represented as follows:

$$\begin{aligned}
&\boldsymbol{\sigma}'^{\,n+1}_{\text{On joint surface}} = \boldsymbol{\sigma}'^{\,n}_{\text{On joint surface}} + \left(\Delta\boldsymbol{\sigma}'^{n+1}_{\text{Mechanical}} + \boldsymbol{\sigma}'^{n+1}_{\text{Dilation}}\right) \\
&\Delta\boldsymbol{\sigma}'^{n+1}_{\text{Mechanical}} + \boldsymbol{\sigma}'^{n+1}_{\text{Dilation}} = \mathbf{K}^{n+1}_{\text{normal}} \times \Delta DD^{n+1}_{\text{normal}} - \mathbf{K}^{n+1}_{\text{normal}} \times DD^{n+1}_{\text{dil}} \\
&\Delta DD^{n+1}_{\text{normal}} = DD^{n+1}_{\text{normal}} - DD^{n}_{\text{normal}} \\
&DD^{n+1}_{\text{dil}} = \left(\Delta DD^{n+1}_{\text{shear}}\right) \times \tan\phi_{\text{dil}}, \qquad DD^{n+1}_{\text{shear}} = \sqrt{\left(DD^{n+1}_{13}\right)^2 + \left(DD^{n+1}_{23}\right)^2} \\
&\boldsymbol{\sigma}'^{\,n+1}_{\text{On joint surface}} = \boldsymbol{\sigma}'^{\,n}_{\text{On joint surface}} + \mathbf{K}^{n+1}_{\text{normal}} \times DD^{n+1}_{\text{normal}} - \mathbf{K}^{n+1}_{\text{normal}}\left(DD^{n}_{\text{normal}} + DD^{n+1}_{\text{dil}}\right)
\end{aligned} \tag{5.25}$$

where, $\boldsymbol{\sigma}'^{\,n}_{\text{On joint surface}}$ is effective stress on joint surface at time $n\Delta t$, $\boldsymbol{\sigma}'^{\,n}_{\text{Mechanical}}$ is mechanical share of effective stress, $\boldsymbol{\sigma}'^{\,n}_{\text{Dilation}}$ is dilation share of effective stress, $\mathbf{K}^{n}_{\text{normal}}$ is normal stiffness of joint at time $n\Delta t$, and ϕ_{dil} is dilation angle. As shown in Figure 64, when effective stress is large enough (e.g., larger than 2 MPa), behavior is completely

linearly elastic and $\mathbf{K}^{n}_{\text{normal}}$ can be assumed to be constant [132]. However, when effective stress is near zero, behavior is fully nonlinearly elastic and $\mathbf{K}^{n}_{\text{normal}}$ can be defined by the following general nonlinear relation[60]:

$$\frac{\boldsymbol{\sigma}'^{n+1}_{\text{Mechanical}} - \boldsymbol{\sigma}'^{0}_{\text{Mechanical}}}{\boldsymbol{\sigma}'^{0}_{\text{Mechanical}}} = \hat{A}\left(\frac{\Delta DD^{n+1}_{\text{normal}}}{DD^{0}_{\text{normal}} - \Delta DD^{n+1}_{\text{normal}}}\right)^{\hat{t}} \tag{5.26}$$

where, $\hat{A}$ and $\hat{t}$ are fitted parameters, $\boldsymbol{\sigma}'^{0}_{\text{Mechanical}}$ is initial effective stress on joint surface, and DD^{0}_{normal} is initial fracture aperture. It can be assumed that $\hat{A}$ and $\hat{t}$ are equal to 1.0 [60]; therefore, the behavior can be simplified to

$$\boldsymbol{\sigma}'^{n+1}_{\text{Mechanical}} \times DD^{n+1}_{\text{normal}} = \boldsymbol{\sigma}'^{0}_{\text{Mechanical}} \times DD^{0}_{\text{normal}} \tag{5.27}$$

The shear behavior of rock joints modeled using elastic-plastic behavior (softening or hardening due to a decrease or increase in effective stress) is shown in Figure 65. The Mohr-Coulomb failure criterion is used to distinguish the start of the plastic part. Because the maximum tolerable shear depends on the amount of effective stress, the choice of softening or hardening behavior is completely dependent on the rate of change in effective stress in the element. If effective stress decreases, the element behaves like a softening branch in the post-elastic part. In contrast, if effective increases, but permanent slip on the joint surface is still a factor, the element follows the hardening branch. For the elastic part, a simple linear model is used to describe the shear direction joint behavior:

$$\begin{aligned} F_1\left(D_{13}(\mathbf{x},t)\right) &\Rightarrow \Delta\sigma_{13}(\mathbf{x},t) = \mathbf{K}_s \times \left(\Delta D_{13}(\mathbf{x},t)\right) \\ F_2\left(D_{23}(\mathbf{x},t)\right) &\Rightarrow \Delta\sigma_{23}(\mathbf{x},t) = \mathbf{K}_s \times \left(\Delta D_{23}(\mathbf{x},t)\right) \end{aligned} \tag{5.28}$$

where $\mathbf{K}_s$ is linear shear stiffness as shown in Figure 65. In the shear model, shear stiffness is equal in both directions. In the post-elastic region of shear behavior, in addition to change in effective stress, the intrinsic friction angle and cohesion of the fracture elements are going to gradually change when the element experiences permanent slip [76-79, 133]. The change in friction angle and cohesion on the element under permanent slip is described by the slip-weakening model.

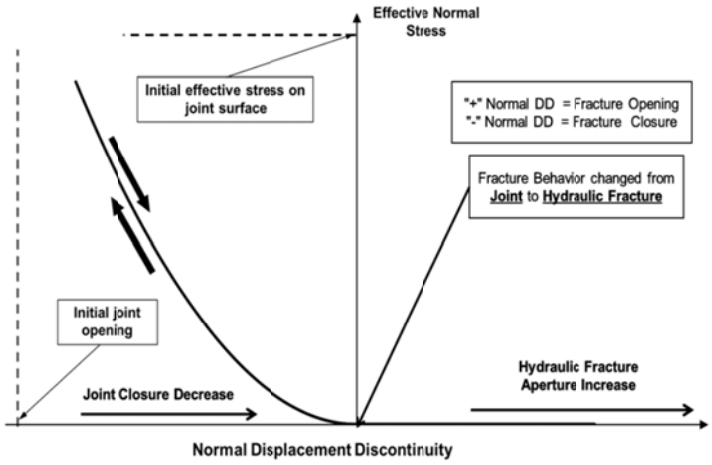

Figure 64. Fracture opening/closure vs. effective stress.

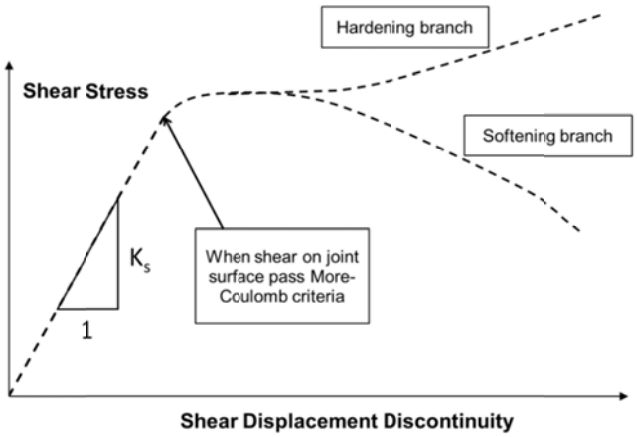

Figure 65. Shear behavior of an element.

5.2.3. Slip-weakening model

The slip-weakening model, which describes the progressive shear failure of preexisting natural discontinuities under compression, was developed to simulate the post-failure of faults [76-78]. This model has been used by Palmer and Rice [79] to study fracture in over-consolidated clay specimens under simple shear. A schematic result of their test is shown in Figure 66.

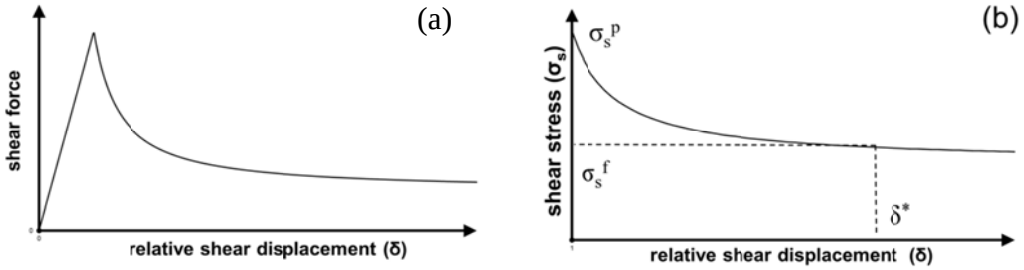

Figure 66. After Palmer and Rice[79], (a) relation between shear force and displacements; (b) relation between shear stress and relative displacements.

In Figure 66, it is obvious that a peak force is reached at small shear displacement, after which the force required to produce further relative movements decreases continuously and approaches a residual value. The residual shear strength σ_s^f occurs when the relative shear slip along the crack overcomes a critical value (δ^*).

To apply the slip-weakening model to natural fractures, a linear law is used to model variation in the resistance parameters [133], as shown in Figure 67. In this case, the friction angle decays from the peak value to the residual value and the cohesion from peak to zero for a certain value of relative shear slip along the crack. As a result, shear strength decreases from the peak value to the residual value as a function of D_s on all

discontinuity elements. The sustained shear stresses on the slipped elements are always less than or equal to the shear strength. In addition, only the plastic value of shear displacement (D_{sp}) is taken into account when determining the resistance parameters. In each step, the value can be calculated as shown in Figure 68, and can be represented as follows:

$$D_{sp}^{ele\ i} = D_{s}^{ele\ i} - \sigma_{s}^{ele\ i} / K_{s}$$

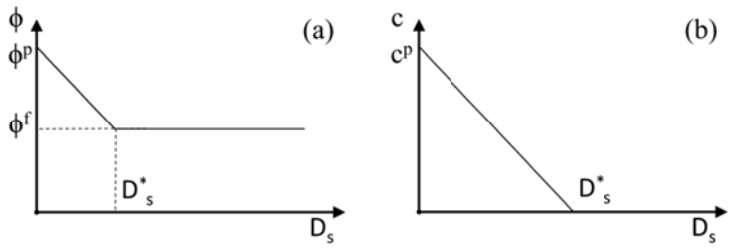

Figure 67. Linear slip-weakening law chosen for friction angle φ (a) cohesion c (b).

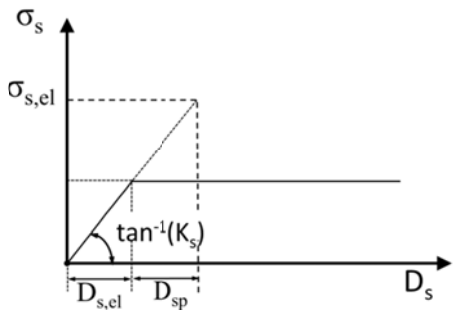

Figure 68. Elastic and plastic tangential displacement discontinuity on a discontinuity element in residual condition.

If D_{sp} is greater than the critical value, then cohesion is zero and friction angle is equal to its residual value. If D_{sp} is less than the critical value, the shear strength can be calculated using the linear law[133]. These statements can be represented as follows:

$$c^{ele\ i} = c^{p}\left(1-\frac{D_{sp}^{ele\ i}}{D_{s}^{*}}\right), \qquad \varphi^{ele\ i} = \varphi^{p}\left(1-\frac{D_{sp}^{ele\ i}}{D_{s}^{*}}\right)+\varphi^{f}\ \frac{D_{sp}^{ele\ i}}{D_{s}^{*}} \tag{5.29}$$

Therefore, the slip-weakening modifications are applied on all elements that have experienced permanent slip, and their properties are gradually changed by increasing the plastic shear DD.

5.3. Simulation of the injection/extraction process

Based on the DD equation in section 3, the finite element form of fluid flow and heat transfer relations inside a fracture, and complementary constitutive relations for natural and hydraulic fractures, the following numerical implementation is proposed:

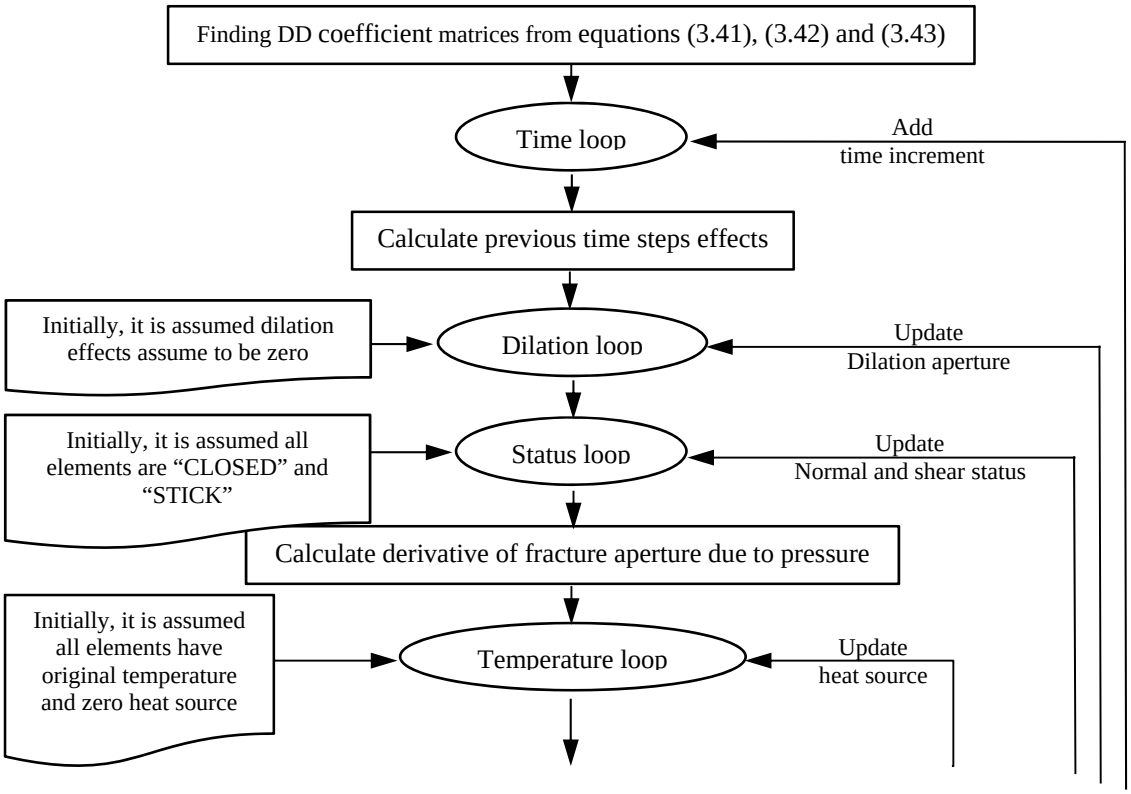

Figure 69. Flow chart of injection/extraction process simulation.

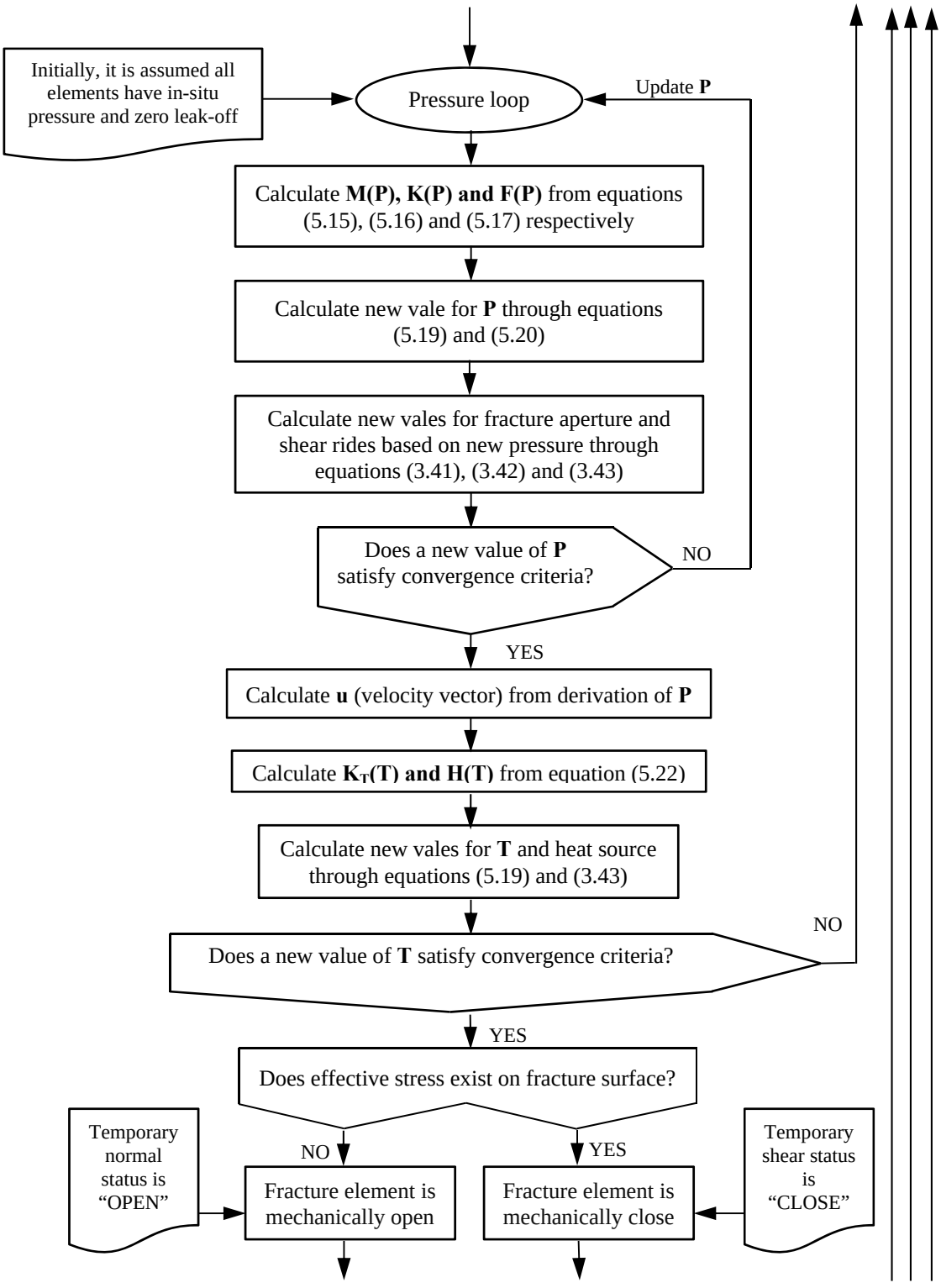

Figure 69. Continued.

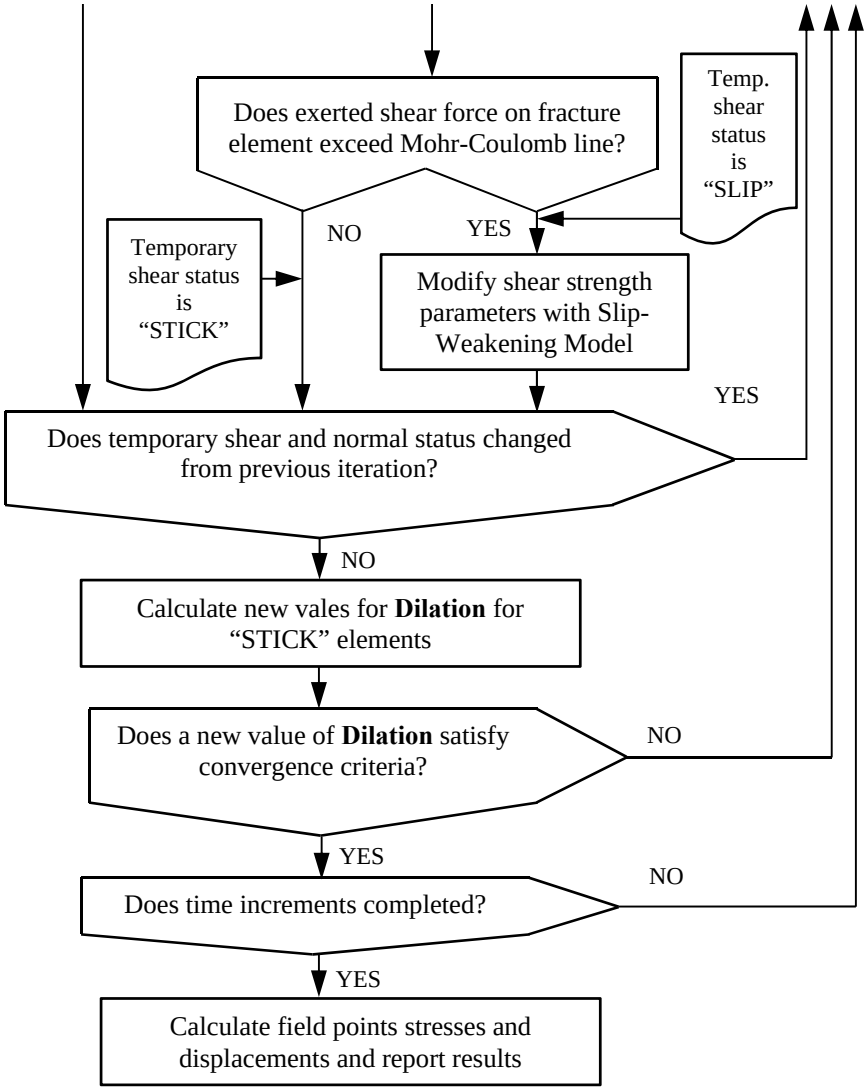

Figure 69. Continued.

The flow chart in Figure 69 is simulates injection/extraction into stationary fractures. In the case of non-stationary fractures (which tend to propagate as a result of injection/extraction), the injection rate will decrease to keep the fractures stationary. The procedure is applied by additional loop after time loop in Figure 69.

6. MODEL APPLICATION TO FRACTURE/WELLBORE ANALYSIS

In the current section, the theoretical developments described in Section 3 (indirect boundary element, DD, and FS techniques) and Section 5 (finite element method and joint/hydraulic fracture constitutive behavior) are applied to several problems of interest in reservoir geomechanics. The versatility of the developed model is shown by an investigation of pore pressure and stress fields around hydraulic fractures, rock joints, and wellbores under coupled thermo-hydro-mechanical loading.

The following analyses are described here:

1. An analysis of pore pressure, stresses, and failure distribution around single and double hydraulic fractures
2. A thermo-hydro-mechanical analysis of a huff-and-Puff test conductd during the GeneSys project in the North German basin
3. A study of post-failure behavior of a box sliding on a frictional surface
4. An analysis of injection into a single inclined rectangular joint under normal faulting stress with a slip-weakening approach
5. An analysis of injection into a single vertical joint with a high injection rate and a study of the joint's transient behavior from mechanically closed to mechanically open
6. A hydraulic stimulation of the same vertical rectangular joint as in example 5 in the presence of natural fractures
7. An analysis of the behavior of intersecting/parallel circular joints during low injection/production processes considering variation in in-situ stress

8. A study of the thermo-hydro-mechanical behavior of an irregularly shaped joint during injection when it intersects with natural fractures
9. A study of the propagation of a natural fracture intersecting a horizontal inclined wellbore during well pressurization

6.1. Hydraulic fracture analysis

Few hydraulic fracture simulation models consider the existence of natural fractures and/or the interaction between different stages of hydraulic fracturing. To do this, the analysis must consider the hydro-mechanical behavior of intact rock and any existing discontinuities inside the reservoir, as described in Sections 3 and 5.

6.1.1. Single hydraulic fracture

It is well known that hydraulic fractures alter the stress around themselves, and if one tries to place a fracture near existing one, the stress shadow becomes a factor. Stress shadow effects include a smaller fracture aperture, a higher net pressure, and often change in the hydraulic fracture direction [134]. Moreover, trends in and the amount of micro-seismicity might change from one stage of stimulation to the next. In the current section the constructed numerical model is used to investigate the effects of single hydraulic fracturing on the neighborhood area.

Figure 70 shows the fracture geometry and mesh used. The fracture is discretized with 1166 nodes and 1098 quadrilateral elements. The fracture plane is in the ZY plane, and the minimum horizontal stress is applied in the X direction. Table 5 presents the hydromechanical constants of intact rock and hydraulic fracture. The hydraulic fracture

is subjected to 0.8 MPa net pressure. To illustrate the hydraulic fracture effects in the surrounding medium, two cross sections are considered (see Figure 71). The planes are for the presentation of field stress and variations in pore pressure, and the failed zone around the fracture. The planes are not explicitly modeled with hydraulic fracture.

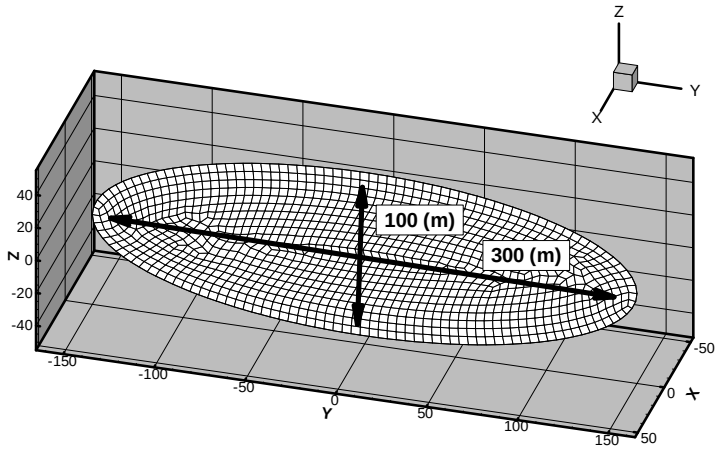

Figure 70. Single hydraulic fracture, geometry and mesh.

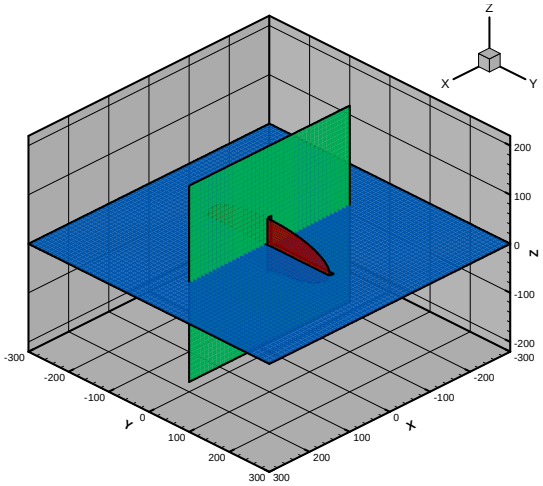

Figure 71. Cross sections and hydraulic fracture, hydraulic fracture is red, "XY" cross section is blue, and "XZ" cross section is green.

Table 5. Input parameters for rock and fracture.

Shear modulus	(GPa)	18.75 (2719 Ksi)
Drained Poisson's ratio	(-)	0.20
Undrained Poisson's ratio	(-)	0.33
Skempton's coefficient	(-)	0.77
Base permeability	(m^2)	1.00×10^{-18}(1 Micro Darcy)
Initial in situ stresses (X direction)	(MPa)	33.29(4828 psi)
Initial in situ stresses (Y direction)	(MPa)	33.78(4900 psi)
Initial in situ stresses (Z direction)	(MPa)	50.26(7290 psi)
Initial pore pressure	(MPa)	26.89(3900 psi)
Fluid density	(kg/m^3)	1000.00(0.433 psi/ft.)
Fluid viscosity	($N.s/m^2$)	1.00×10^{-3}(1.0 cp)
Rock density	(kg/m^3)	2650.00(1.15 psi/ft.)
Rock cohesion	(MPa)	1.0 (145 psi)
Rock friction angle	(-)	31
Mode I critical fracture toughness	($MPa.m^{0.5}$)	6.00(5460 $psi.in^{0.5}$)
Mode II critical fracture toughness	($MPa.m^{0.5}$)	10.00(9100 $psi.in^{0.5}$)

Figure 72 shows the fracture aperture due to 0.80 MPa net pressure after 1 h and 24 h. As is expected, the fracture aperture has its maximum value in the middle of the fracture and decreases as time increases. The fracture aperture decreases with time because the pore pressure in the rock is increases and forces the fracture to close. Therefore, hereafter, because the fracture aperture peaks after 1 h, only results of simulations after 1 h are presented.

Figure 73, shows the Mode I fracture toughness after 1 h of pressurization. With 0.80 MPa net pressure, the fracture is on the verge of propagation, and if the pressure increases further, the fracture will start to propagate in the tensile mode. Figure 74 shows the minimum stress, whose direction is initially perpendicular to the surface of the hydraulic fracture (X direction in the model). In the figure, the hydraulic fracture is shown in gray.

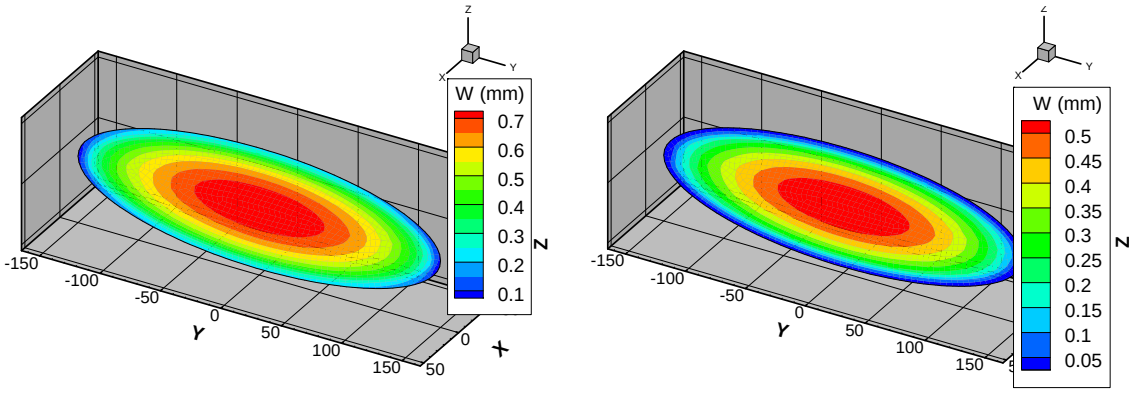

Figure 72. Fracture aperture due to 1.0 MPa net pressure after 1 and 24 hours.

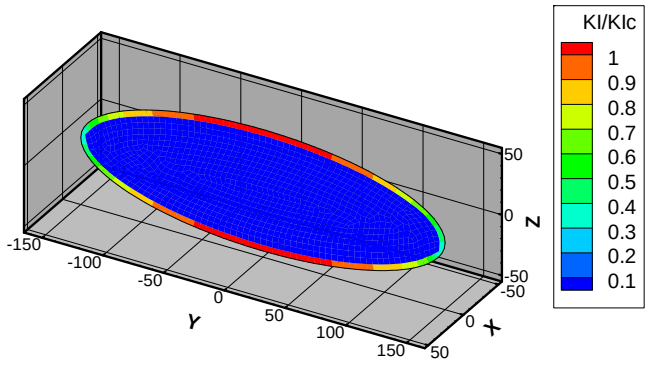

Figure 73. Mode I SIF after one hour of pressurization.

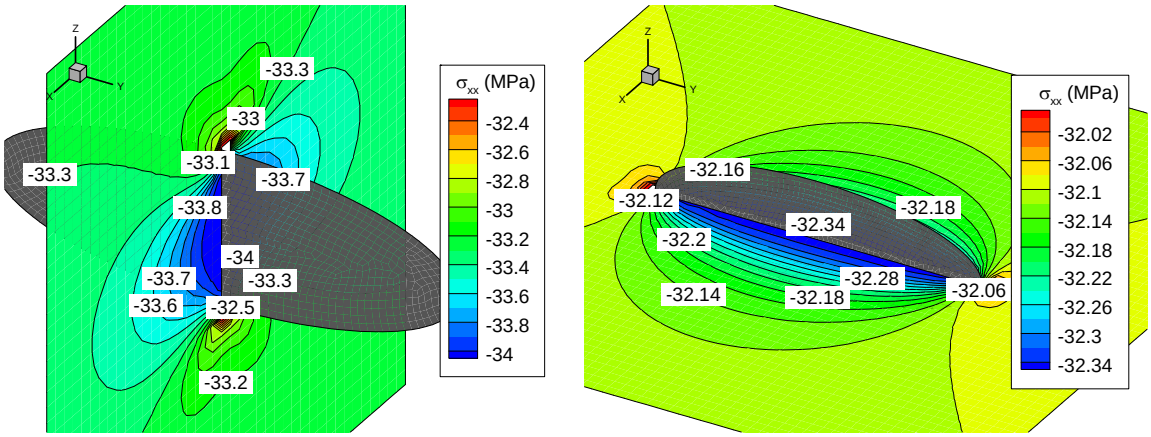

Figure 74. Induced XX stress (minimum horizontal stress) due to 0.8 MPa net pressure after 1 hour, in-situ minimum stress is 33.29 MPa.

The perpendicular surfaces to the fracture, shown in Figure 74 (XY and XZ), are cross sections. In Figure 74 and subsequent figures, the negative sign represents compression stress and the positive sign represents tension stress.

It can be seen from Figure 74, that after 1 h of fracture pressurization, the minimum principal stress around the region in front of the fracture surface has increased by almost the same amount of net pressure (0.8 MPa), and far from the fracture surface the stress has increased by a negligible amount. This effect is due to pressurization and opening of the hydraulic fracture and would not be as great if the fracture were less open. More interesting is that the tensile stress, which happens near the fracture tip. This is also due to the fracture opening. Induced tensile stress near the fracture tip increases the possibility of failure and may result in more microseismic events in that region.

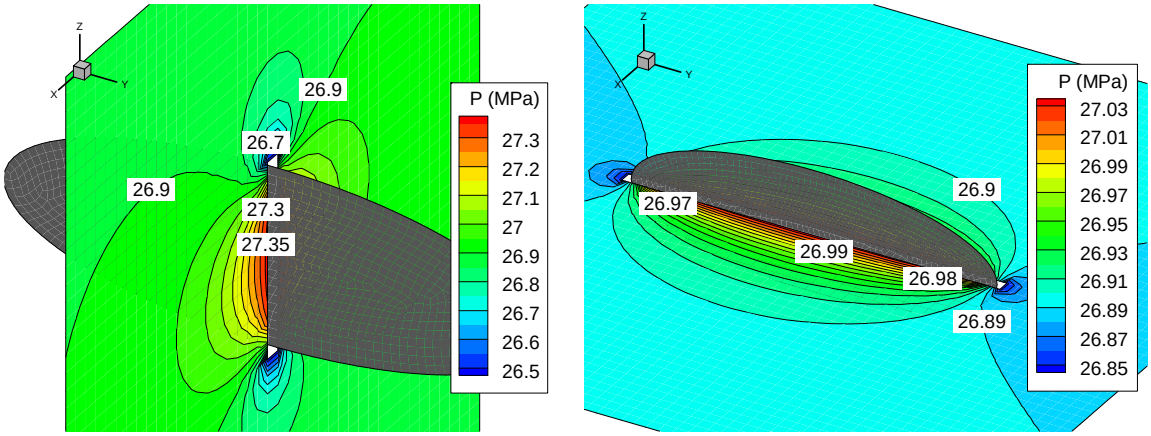

Figure 75. Pore pressure change after 1 hour due to 1.0 MPa net pressure, background pore pressure is 26.89 MPa.

Figure 75 shows the variation in pore pressure after 1 h of fracture pressurization. Very near the fracture face, the pore pressure has increased, and the induced pore pressure has decreased and spread out from the fracture surface. Note that in both cross

sections the existing pore pressure near the fracture tip is less than the in situ pore pressure. The negative induced pore pressure is due to the fracture opening, which creates flow from the reservoir into the fracture.

Note that the increase in minimum in situ stress might affect the stability of natural fractures; however, induced shear stress is a better indicator of instability. Figure 76 shows the shear stress induced by 0.80 MPa net pressure. Note that the shear stress component in the XZ plane is Sxz and that in the XY plane is Sxy.

It is clear from Figure 76 that the maximum shear stress occurs just behind the tip of the fracture. The amount of induced shear stress is a linear function of net pressure; when the net pressure doubles, the induced shear stress doubles as well.

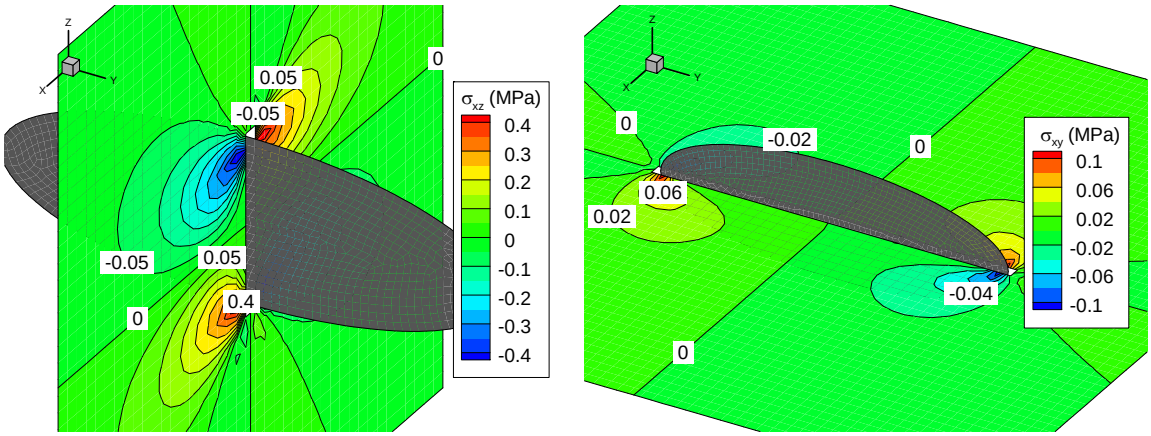

Figure 76. Induced shear stress due to 1.0 MPa net pressure after 1 hour.

Another effect of induced shear stress is to change the direction of the maximum stress near the fracture tip. This is shown in Figure 77. As can be seen from Figure 77, the direction of the maximum principal stress (local) around the hydraulic fracture tip turns toward the tip of the fracture. This is the primary reason why when if one tries to

do hydraulic fracturing near an existing fracture, the new fracture turns. More interesting is the change in the direction of the maximum stress in front of the hydraulic fracture. In that region, the direction of the maximum stress changes 90° to perpendicular to the hydraulic fracture.

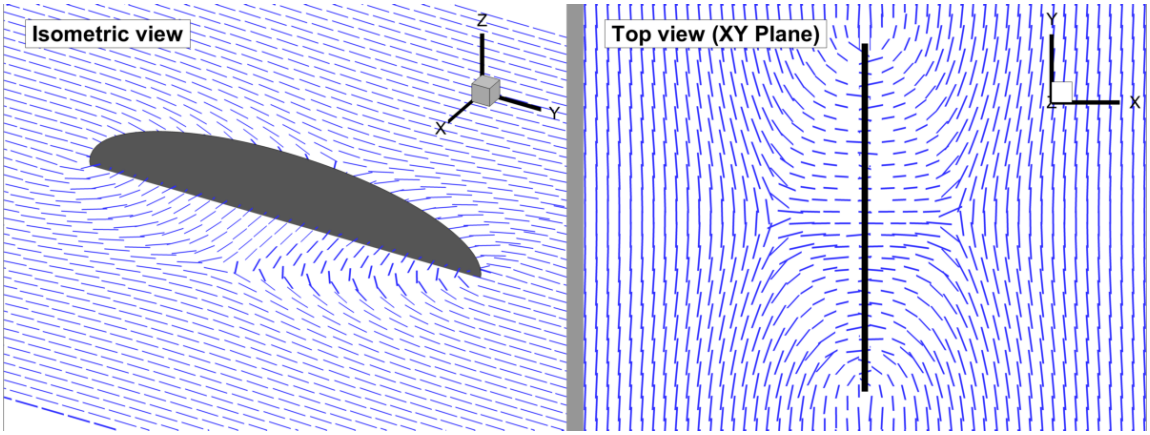

Figure 77. Change of direction of maximum principal stress due to fracture pressurization.

Figure 78 shows the failed region around the hydraulic fracture. Each spheroid in the figure represents a potential microseismic event. As is clear from the figure, microseismicity covers more area than the hydraulic fracture itself. Moreover, it is clear from comparing Figure 76 and Figure 78 that the failed zone is located in the region with the maximum induced shear stress. This can help in calculation of stimulated reservoir volume.

6.1.2. Double hydraulic fracture

Multiple hydraulic fracturing is the most popular method of fracturing in horizontal wells in shale reservoirs. The current section considers hydraulic fracture

interactions, stress shadowing, pore pressure distribution, and failure of the rock around double hydraulic fractures due to simultaneous pressurizing. Note that the behavior is studied after 1 h of uniform pressurization.

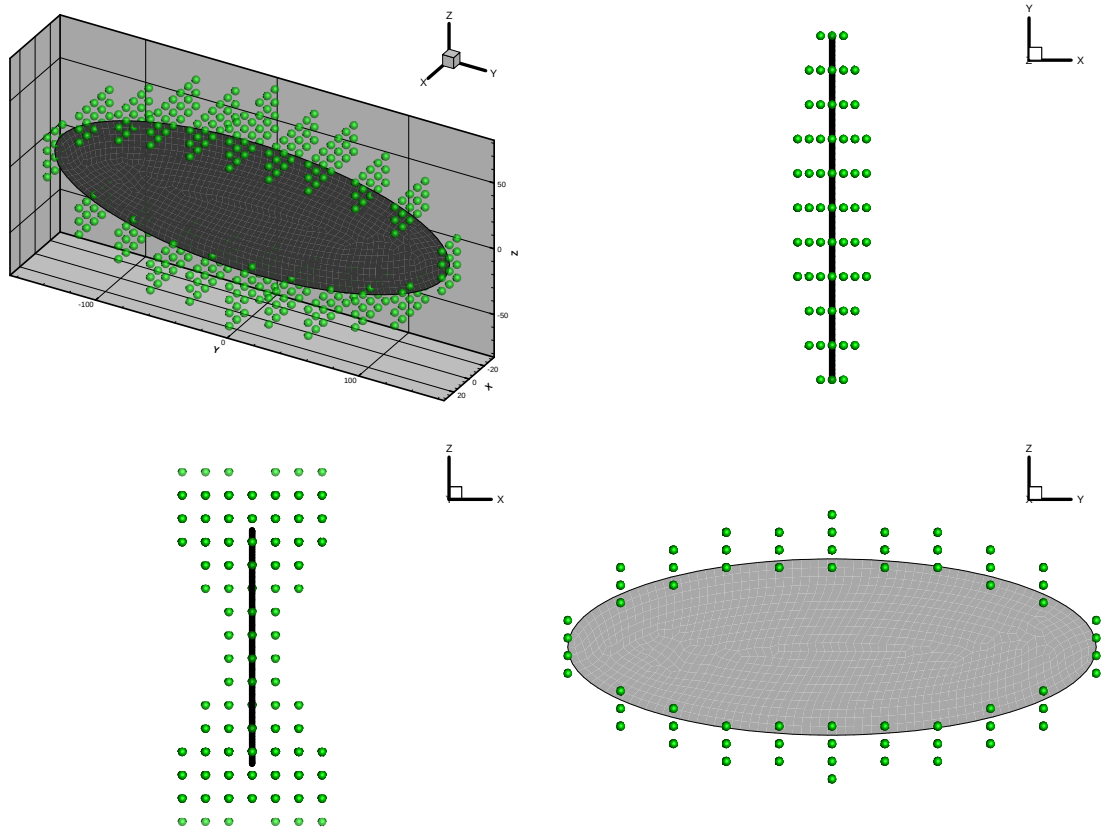

Figure 78. Failed region (potential micro-seismic event location) around hydraulic fracture.

Figure 79 shows the geometry and meshes that were used to discretize two elliptical parallel hydraulic fractures. Each fracture is discretized with 1180 nodes and 1112 quadrilateral elements. Like the single fracture in the previous section, the two fractures are under 0.8 MPa net pressure. The hydromechanical constants of the intact rock and hydraulic fracture are presented in Table 5. To study the effect of the distance

of the hydraulic fractures from each other, three models of 25 m, 50 m, and 100 m are considered.

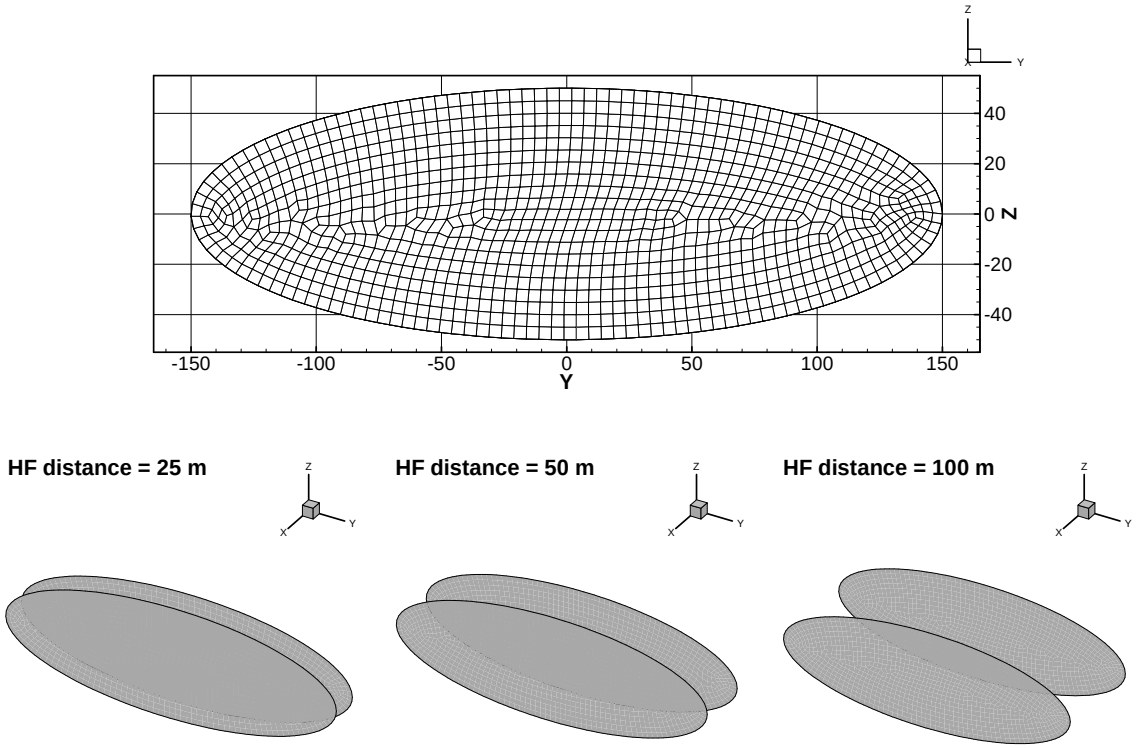

Figure 79. Two parallel hydraulic fracture, geometry and mesh.

Figure 80 shows the fracture aperture and two shear rides for both hydraulic fractures after 1 h. Not surprisingly, the fracture aperture is less than that of the single fracture and increases as the distance between the two fractures increases. A decreasing fracture aperture in comparison with a single hydraulic fracture is the one of the primary effects of the interaction of multiple hydraulic fractures. Note the induced shear rides on the fractures due to their mutual opening. The shear rides decrease as the distance between the two fractures increases. Opening and shearing of hydraulic fractures induce Mode I and II SIFs.

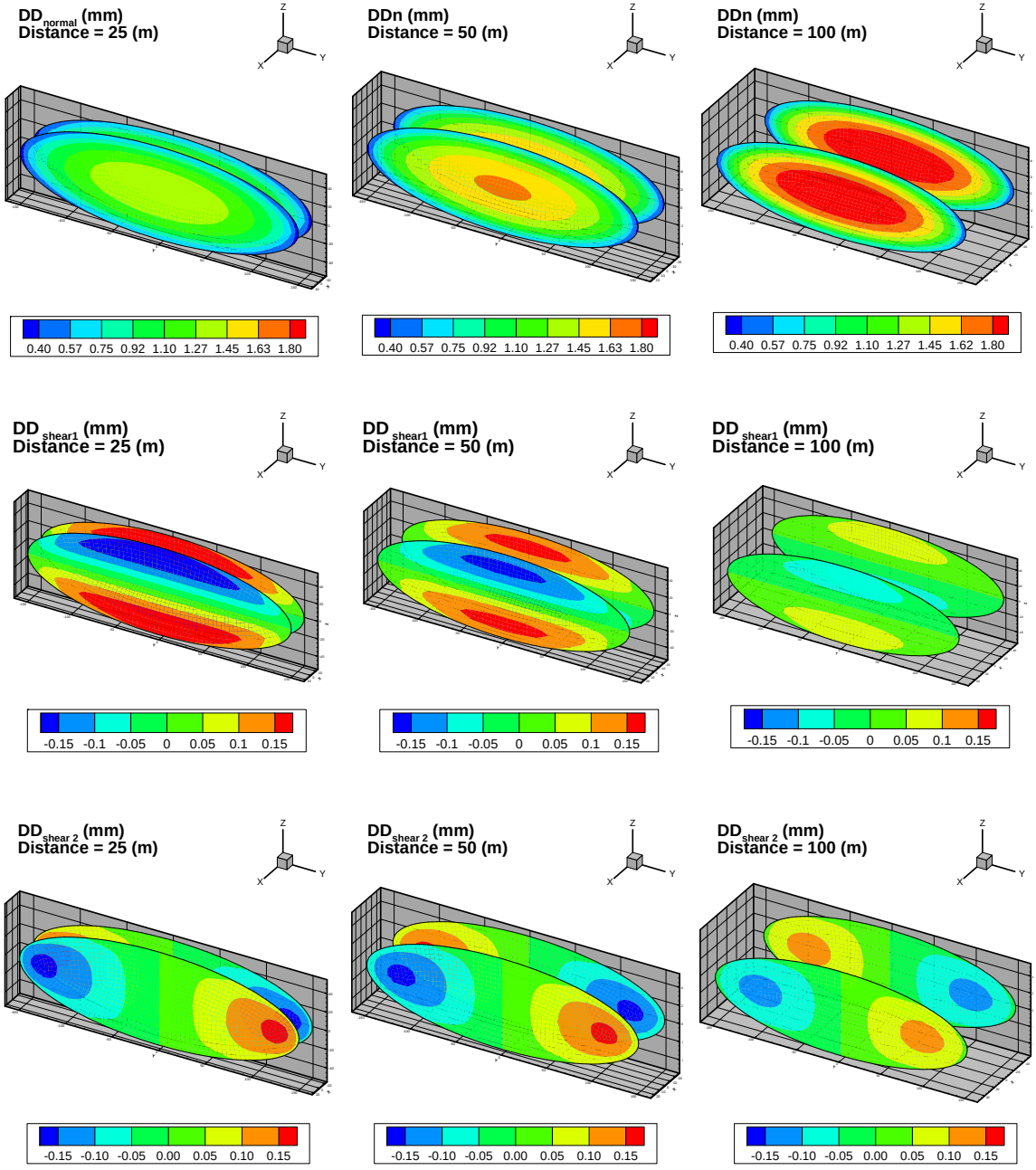

Figure 80. Aperture and shear rides due to simultaneous 0.8 MPa net pressure.

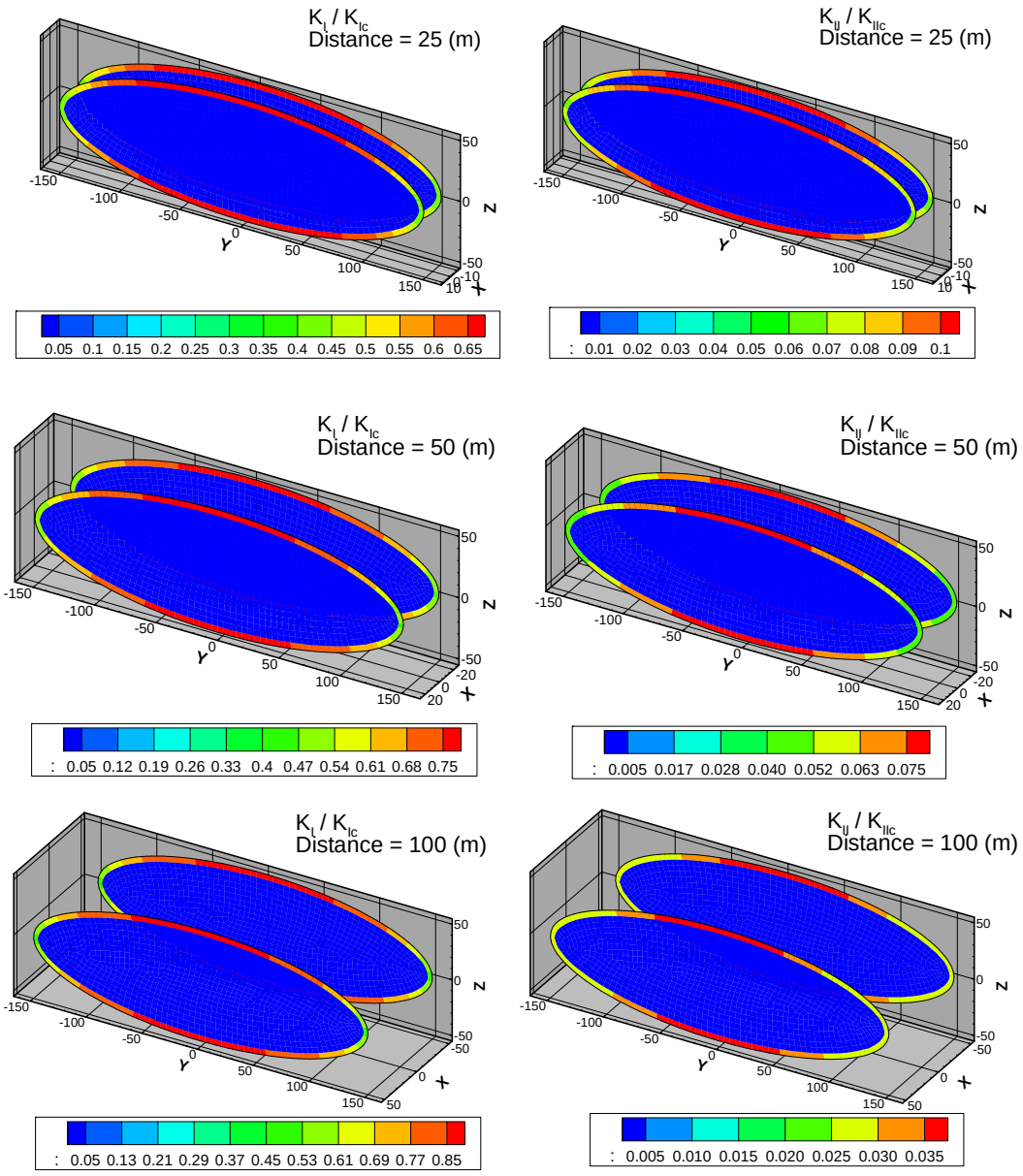

Figure 81. Mode I and Mode II fracture toughness due to simultaneous 0.8 MPa net pressure.

It can be seen from Figure 81 that when the distance increases, Mode I toughness increases and Mode II decreases, the same as with the opening and shearing of fractures.

Consequently, multiple fractures will propagate in shear mode when they are near to each other and will propagate in tensile mode when they are further away.

Figure 82 presents the change in minimum horizontal stress (X direction). In the region between two hydraulic fractures, the induced horizontal stress is increased by almost the same amount of net pressure. The distribution of induced horizontal stress is a function of fracture spacing. Of interest is that when the distance between fractures increases, local induced tensile stress near the fracture edge increases, affecting the failed region around the fracture tips.

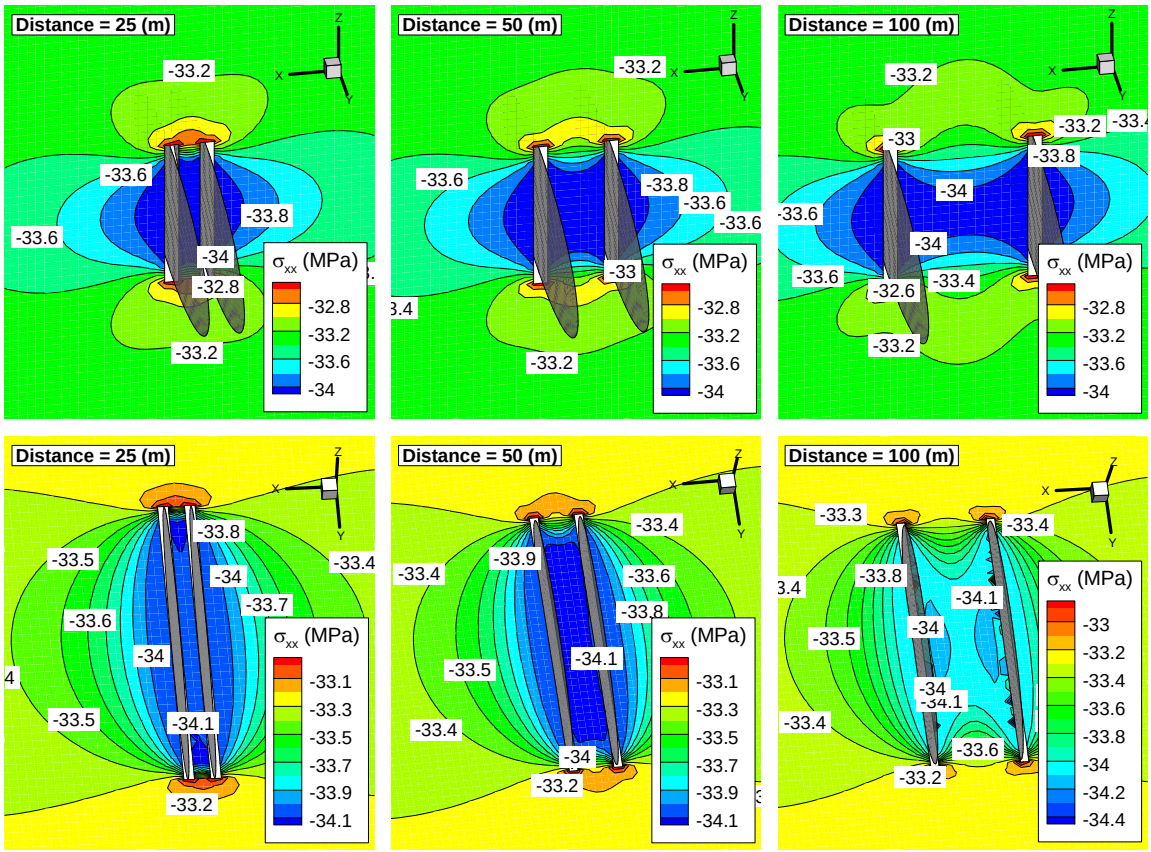

Figure 82. Change in minimum stress due to 1.0 MPa net pressure after 1 hour.

Figure 83 shows the induced pore pressure after 1 h. Pore pressure increases in the region between the two hydraulic fractures and very near the fracture surface. When the distance between two hydraulic fractures is small, induced negative pore pressure is extended to the region near the fracture tip between the fractures.

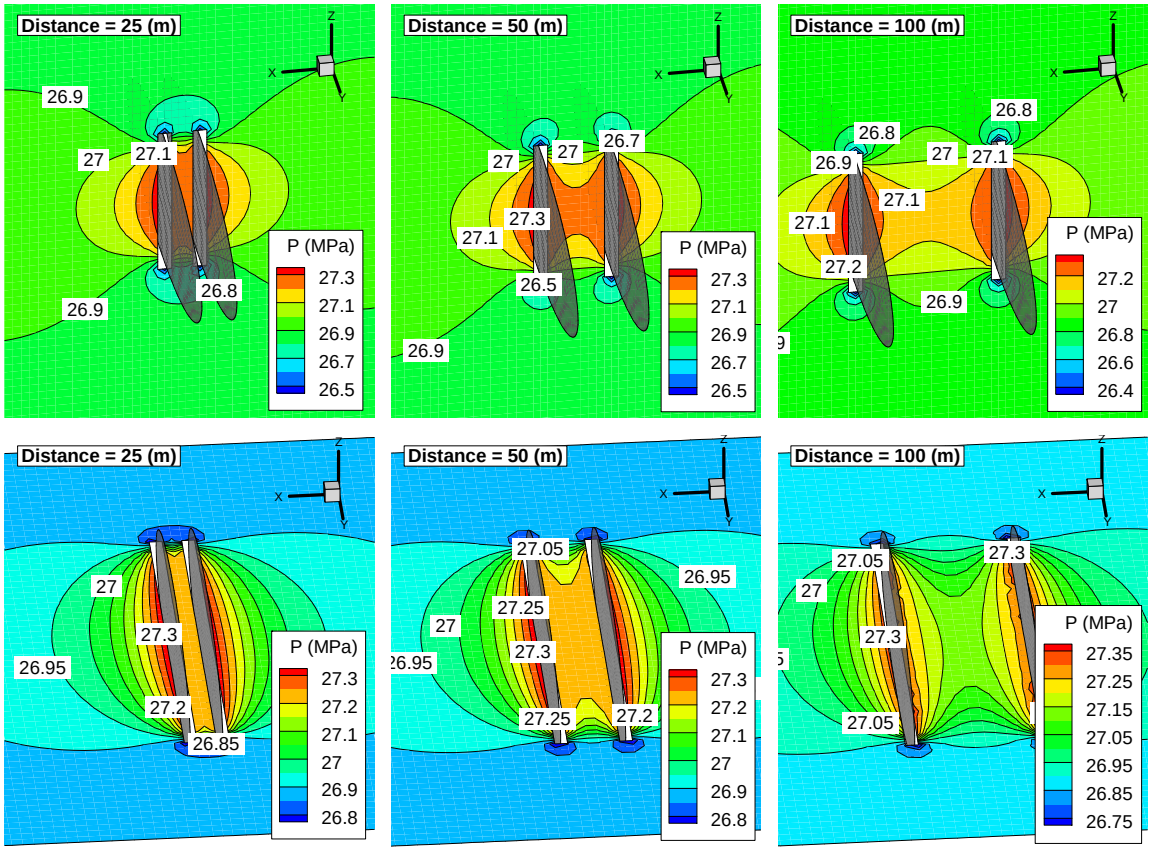

Figure 83. Pore pressure change due to 1.0 MPa net pressure after 1 hour.

Figure 84 shows the induced shear stress. Between two fractures, the induced shear is less than outside the inner fracture space. This is because induced shear due to each fracture opening cancels induced shear in the inner region. In addition, when the distance between hydraulic fractures decreases, due to decreasing fracture opening,

induced shear is decreases. Note that the combination of induced pore pressure and shear stress might destabilize preexisting natural fractures.

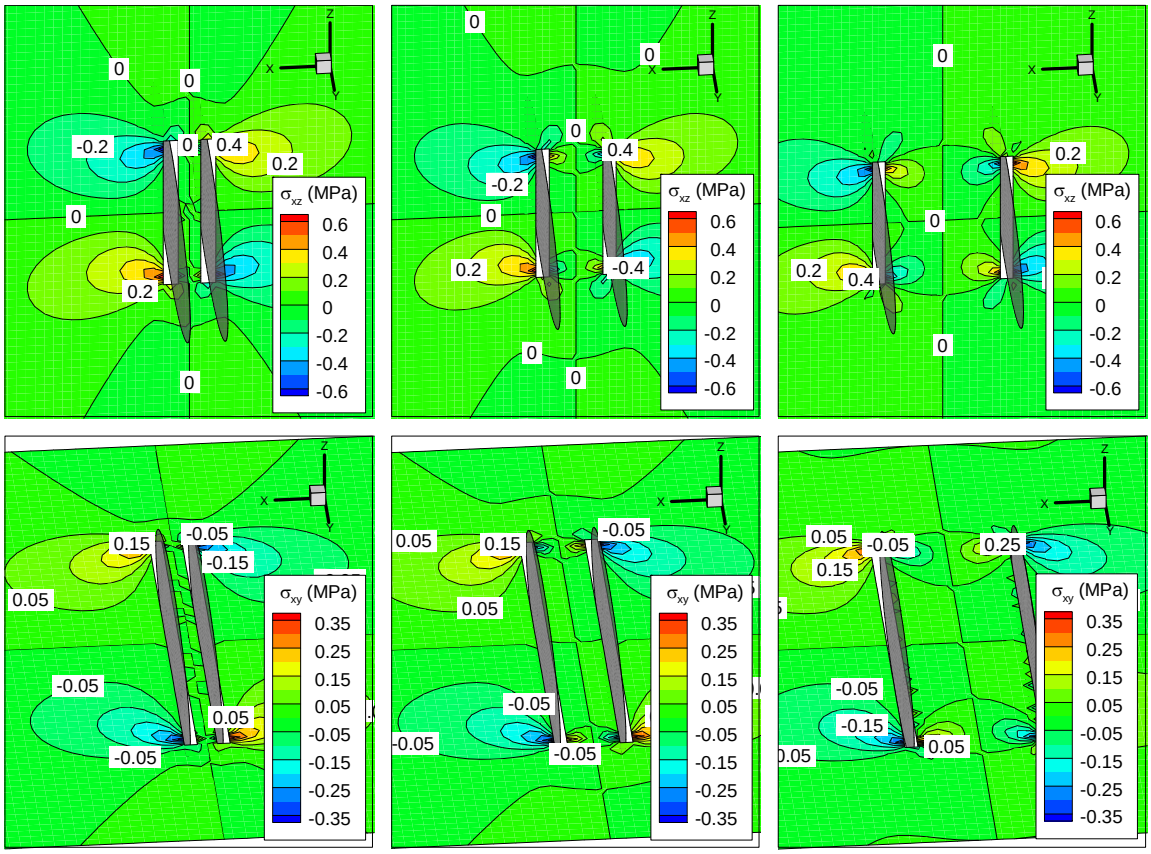

Figure 84. Induced shear stress due to 0.8 MPa net pressure, after 1 hour.

Failure regions (shear failure by Mohr-Coulomb criteria) around the double hydraulic fractures are shown in Figure 85, Figure 86, and Figure 87. A comparison of the figures shows that the failure region is completely a function of hydraulic fracture distance. When the fracture distance increases, the failure between the two fractures decreases, and for a 100 m distance failure region is completely separate. A comparison of the plot with the altered minimum stress plot reveals that failed zone is located in the minimum stress region between the two tips of the fractures.

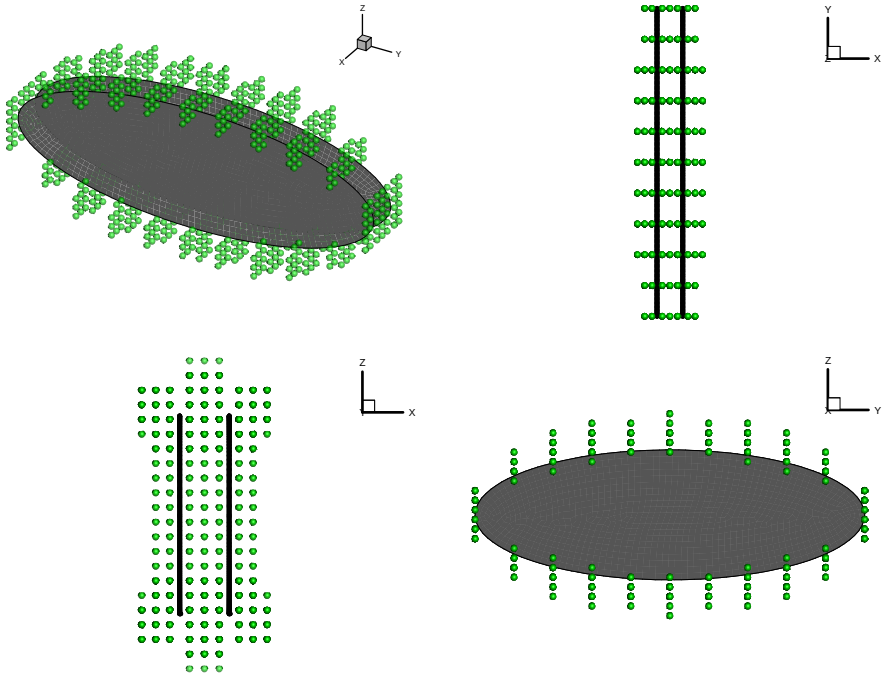

Figure 85. Failure region around two hydraulic fractures, Distance 25 m.

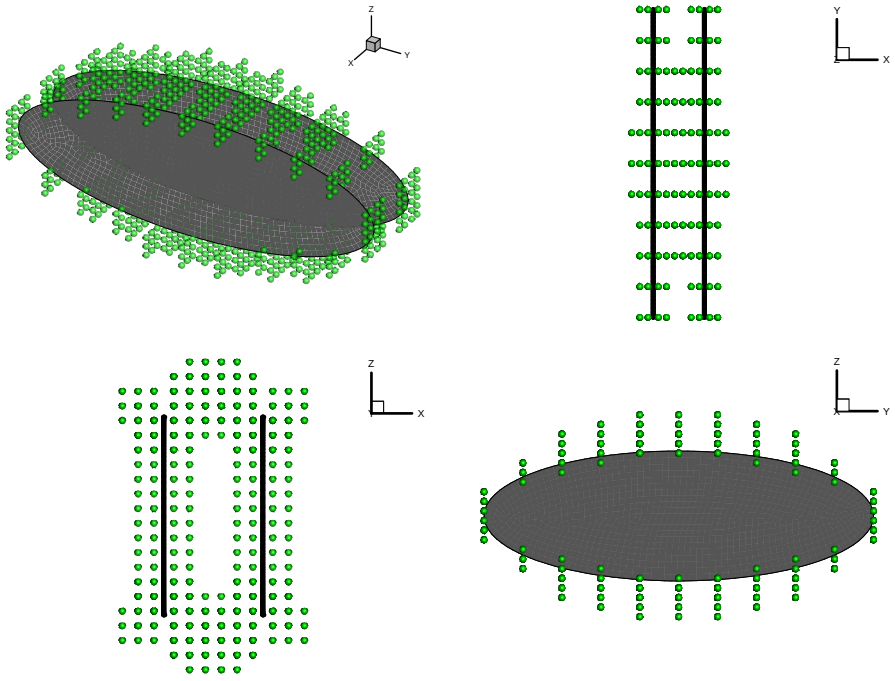

Figure 86. Failure region around two hydraulic fractures, Distance 50 m.

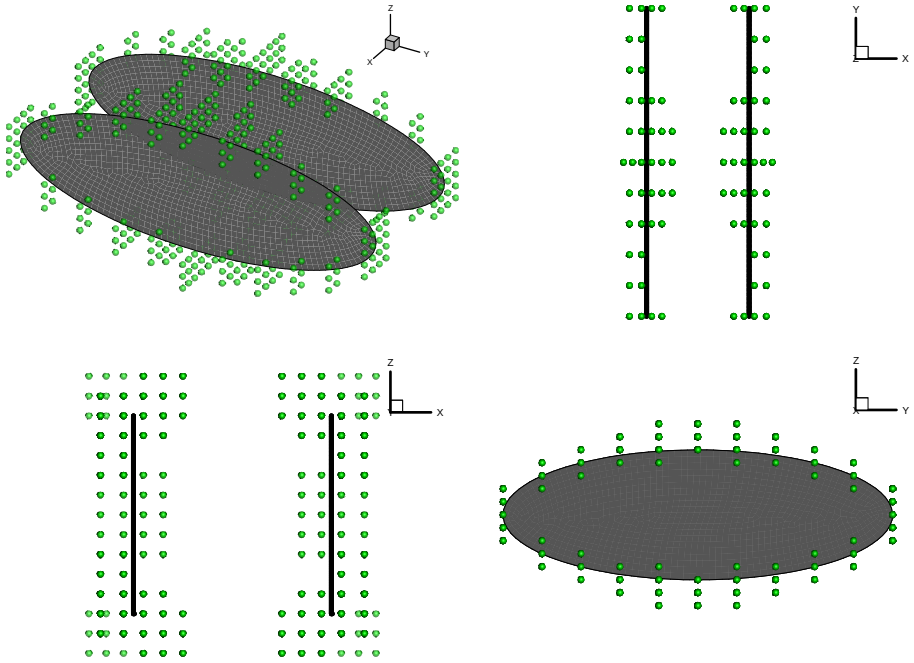

Figure 87. Failure region around two hydraulic fractures, Distance 100 m.

6.2. Simulation of the huff-and-puff test in geothermal reservoirs

Extraction of heat from deep, dry, and hot rocks for energy production is based on water circulation through manmade or natural fractures. Variation in pore pressure and temperature in enhanced geothermal reservoirs is of interest here. When modeling these phenomena, one must consider both fluid flow in fractures and modification in the fracture aperture due to applied pressure and temperature [135, 136]. Consequently, the use of a numerical model that considers the thermo-hydro-mechanical response of preexisting fractured rock is necessary to achieve realistic results. In recent years, field scale enhanced geothermal reservoir tests have been done to study the possibility of heat

extraction from hot, dry, and tight sedimentary formations [137, 138]. Often the source of the heat exchange is prescribed as a single rock joint [139, 140].

In this section, a poroelastic and thermoporoelastic analysis of a geothermal huff-and-puff (cyclic fluid injection/extraction) field test is presented. The test was conducted in an abandoned gas well in the North German Basin about 80 km northeast of Hanover, Germany [139, 140]. The analysis involves the thermo-hydro-mechanical response of a penny-shape fracture. In thermo-hydro-mechanical fracture behavior, a change in fracture fluid pressure or temperature affects effective stress and causes a change in the fracture aperture.

The huff-and-puff test was performed at adepth of 3800 m. A previous analysis [139, 140] showed that only the coupled physics of fracture behavior could explain the down-hole pressure profile (buildups and decays) that was recorded during the test.

Here the possibility of a rock joint status change from joints to hydraulic fracture and the possibility of fracture propagation are investigated. It is assumed that a single penny-shape fracture exists in the reservoir at the beginning of the test and is subjected at its center to injection/extraction as depicted in Figure 88. The injection phase involves the injection of 2592 m^3 of cold water (30°C) over 36 h (20 L/s). The possibility of fracture propagation is considered during the injection process and the Mode I SIF is calculated. The injected cold water then heats up during the subsequent shut-in phase, which lasts over 30 h. After the initial shut-in phase, five daily cycles of 15 h of hot water production with an average of 9.0 L/s and 9 h rest are carried out.

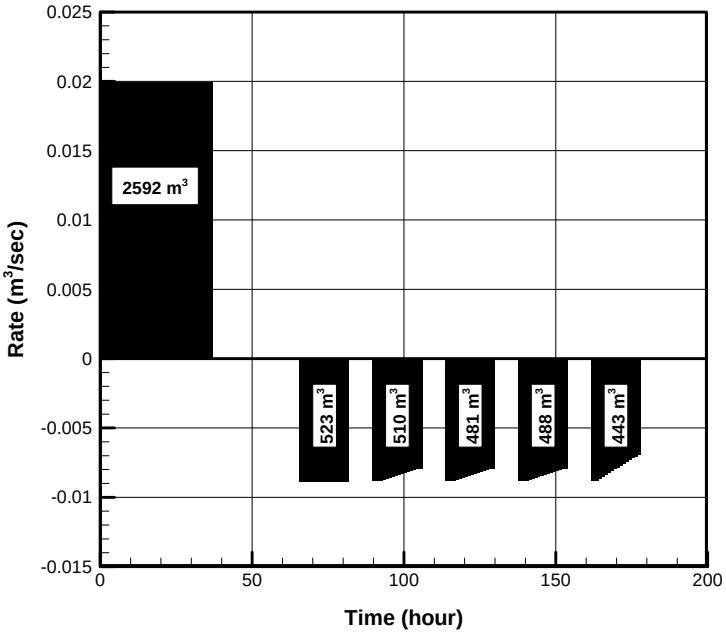

Figure 88. Injection extraction rate from huff and puff test.

From the test results (injection point pressure and temperature profile), one can determine the thermal, hydraulic, and mechanical properties of the reservoir. Sulzbacher and Jung [141] simulated the problem and estimated the permeability of the reservoir by matching the injection pressure profile. They did not consider the hydromechanical behavior of the fracture. The injection point pressure profile calculated by Sulzbacher and Jung [141] differed noticeably from the pressure measured during the injection and first shut-in phases. Mathias et al. [139] also modeled the problem without any coupling of hydrological and mechanical properties. They assumed a constant total stress and fracture aperture throughout the fracture during the injection/extraction cycles. Wessling et al. [140] simulated the huff-and-puff test with hydromechanical coupling using 2D-ROCMAS finite element software. They came up with an acceptable result for the

down-hole pressure profile. They simulated the whole medium as a 2D configuration with a one-dimensional fracture. Moreover, they did not consider thermal processes in their analysis.

Here the proposed numerical thermo-hydro-mechanical algorithm is used to model the problem. Isothermal and nonisothermal analyses of the test are presented in the following subsections. Table 6 presents the necessary parameters for modeling the problem. In the following analysis, linear and nonlinear normal joint behavior is considered, and the sensitivity of the method to joint behavior is investigated. Nonlinear normal joint behavior due to equation (5.27) and joint parameters in Table 6 is shown in Figure 89.

6.2.1. Isothermal analysis

In the isothermal simulation, it is assumed that the injected fluid and reservoir rock have the same temperature and that the joint behaves hydro-mechanically. The single joint hydro-mechanical behavior is reflected in the down-hole pressure history recorded during the huff-and-puff process. The presented model is used to analyze the variation in pore pressure and stresses in the joint when water is injected/extracted into the circular joint. Figure 90 shows the four types of mesh used for the analysis. The number of elements and nodes increased to investigate mesh dependency and convergence of the method.

Table 6. Input parameters to model Huff and Puff test.

Shear modulus	(GPa)	10.30 (1494 Ksi)
Drained Poisson's ratio	(-)	0.25
Undrained Poisson's ratio	(-)	0.42
Biot coefficient	(-)	1.00
Base permeability	(m^2)	4.00×10^{-17} (40 Micro Darcy)
Initial joint aperture	(m)	4.00×10^{-4} (0.004 inch)
Minimum joint aperture	(m)	1.00×10^{-5} (0.002 inch)
Initial in situ stress	(MPa)	68.50 (9935 psi)
Initial pore pressure	(MPa)	60.00 (8702 psi)
Porosity	(-)	0.05
Fluid density	(kg/m^3)	1000.00 (0.433 psi/ft.)
Fluid viscosity	($N.s/m^2$)	1.00×10^{-3} (1.0 cp)
Rock density	(kg/m^3)	2650.00 (1.15 psi/ft.)
Rock thermal conductivity	(W/m/K)	5.00
Fluid thermal conductivity	(W/m/K)	0.60
Specific heat capacity of rock	(J/kg/K)	700.00
Specific heat capacity of fluid	(J/kg/K)	4200.00
Linear thermal expansion of rock	(1/K)	8.00×10^{-6}
Linear thermal expansion of fluid	(1/K)	1.00×10^{-4}
Initial background temperature	(K)	403.15
Injected fluid temperature	(K)	306.15

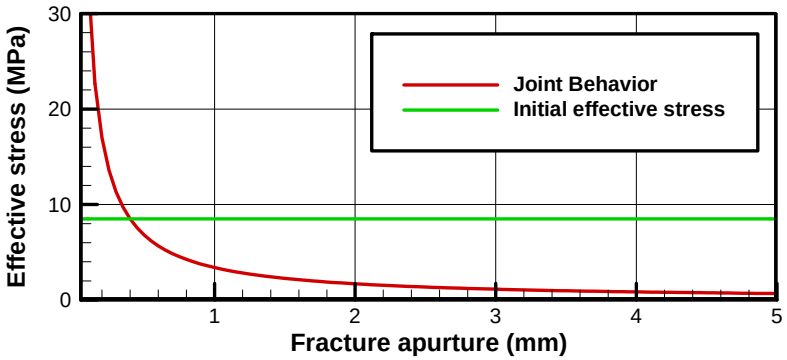

Figure 89. Nonlinear joint behavior.

The pressure and aperture profiles at shut-in time (36 h) for all meshes in Figure 90 are depicted in Figure 91 and Figure 92, respectively. It is clear that when the number

of elements increases, the pressure and fracture aperture converge to the real response. It is also clear that the method is very reliable for use with both structured and unstructured meshes, and unstructured mesh can be used for any combination of fractures.

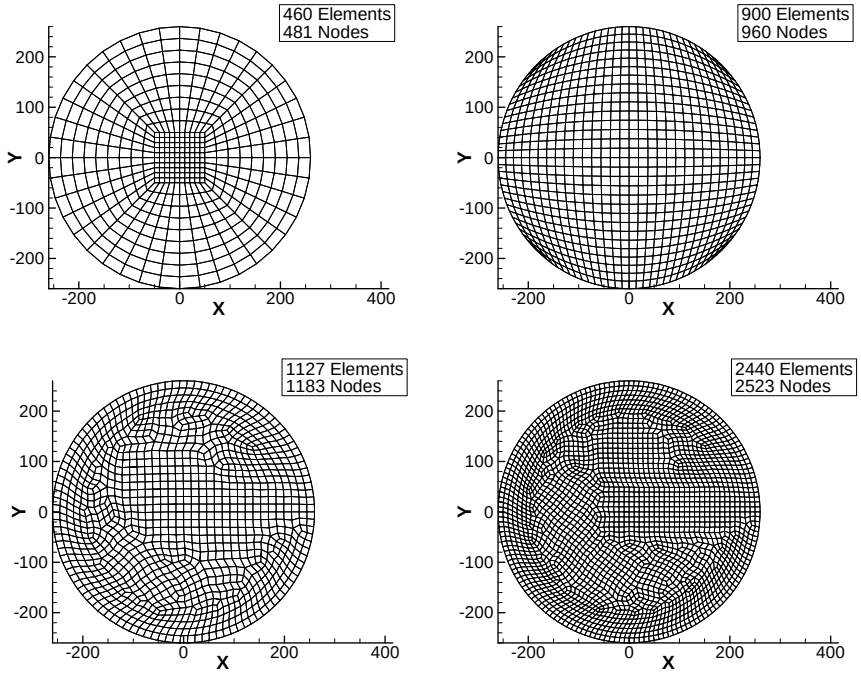

Figure 90. Four different meshes used for circular joint.

The pressure distribution in the joint at the end of the injection process is shown in Figure 93. As can be seen, the distribution is almost uniform. The same scenario can be seen in Figure 91. Once again, the assumption of constant pressure in each time steps is considered by Mathias et al. to solve the problem [139].

The pressure history for the midpoint of the joint is shown in Figure 94. The profile of the down-hole pressure agrees well with the recorded data. Note that the physical properties of the medium and fractures are almost the same as those used by Wessling et al.[140], who used optimization to match the down-hole pressure profile.

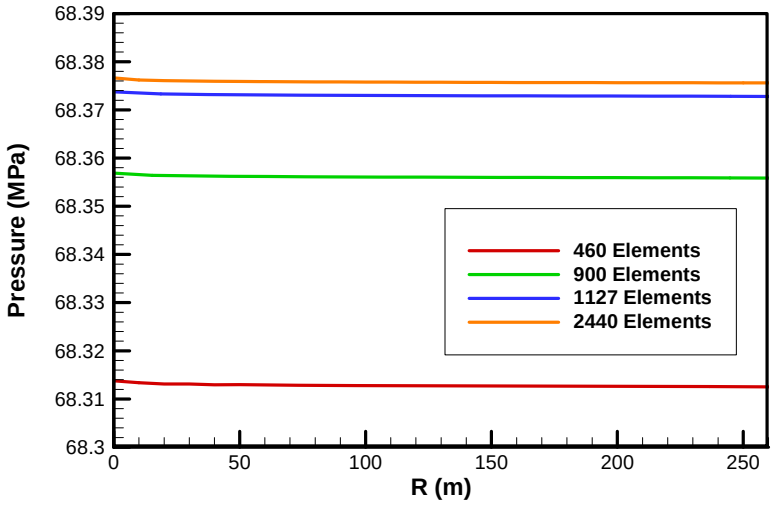

Figure 91. Injection point pressure profile for different meshes at the end of injection phase (36 hours).

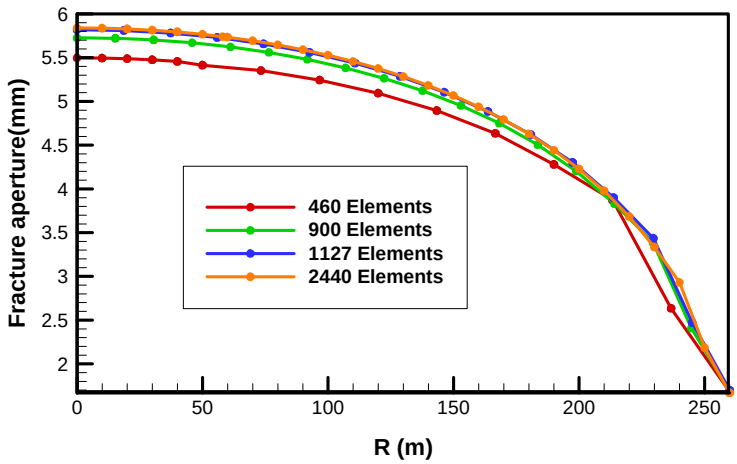

Figure 92. Fracture aperture profile for different meshes at the end of injection phase (36 hours).

The differences between the field test and the numerical results in Figure 94, which increase by production/rest sequence, might be attributed to the fact that the current model does not consider joint hysteresis in loading and unloading sequences. In addition, the differences might be due to the homogeneous and isotropic modeling of rock. Alternatively, the difference between the numerical results and field test could be

caused by temperature diffusion during the test, which is considered in the next subsection.

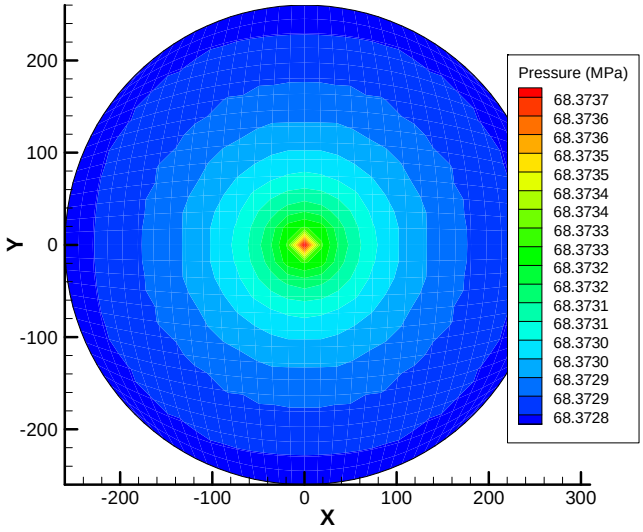

Figure 93. Pressure distribution in fracture for nonlinear joint behavior at the end of injection phase. Note that the pressure in nearly uniform.

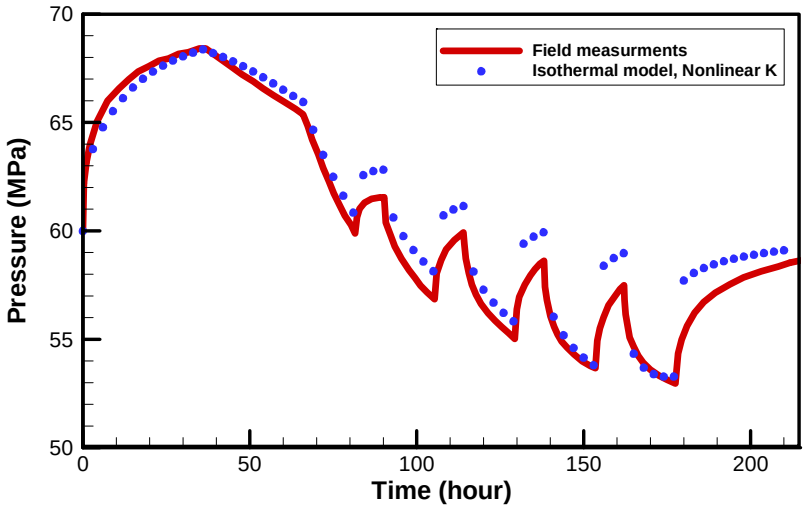

Figure 94. Injection point pressure profile, Isothermal case with non-linear joint behavior.

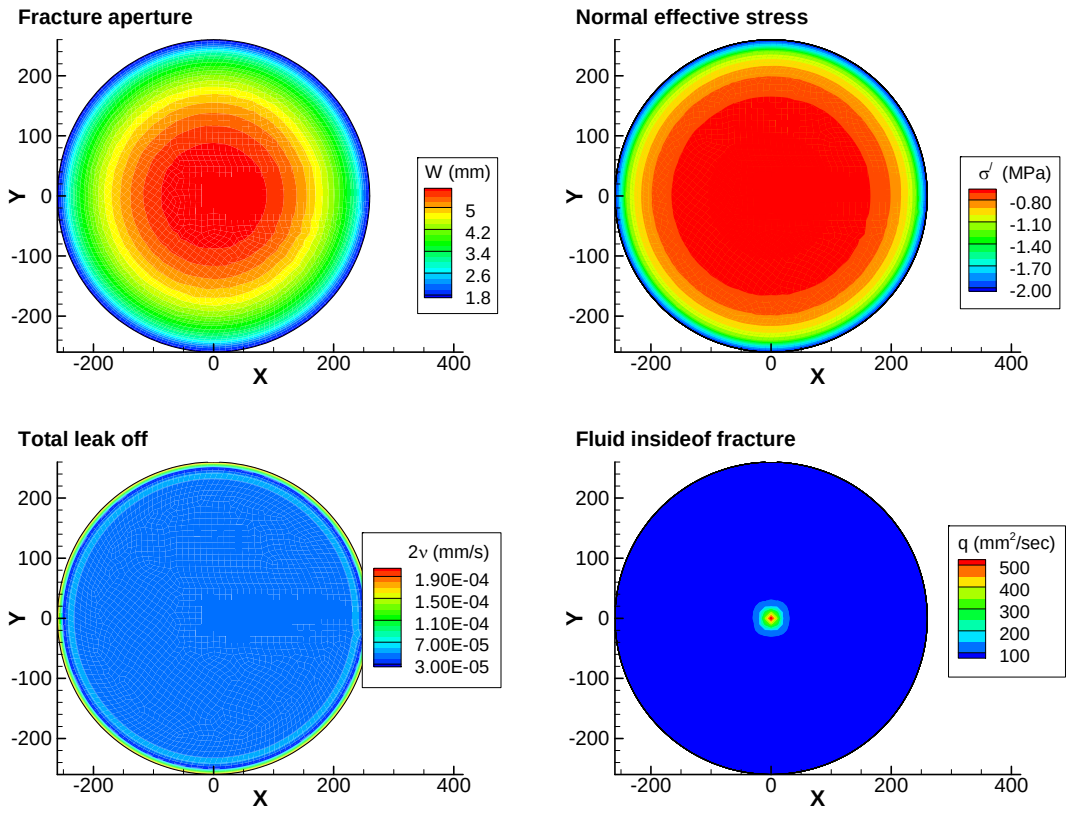

Figure 95. Fracture aperture, effective normal stress, leak off and amount of fluid in fracture at the end of injection phase.

The fracture aperture, effective normal stress, leak-off, and the amount of fluid inside the fracture at the end of the injection phase are presented in Figure 95. The fracture aperture and effective stress change considerably from the center to the boundary of the joint, and thus it is incorrect to assume that the fracture aperture or effective stress is constant at every time step. Yet Mathias et al [139] assumed constant aperture, pressure, and effective stress in their solution. As is clear from Figure 95, the maximum fluid flow inside the fracture takes place in the center of the fracture. This is

mainly due to the maximum aperture in the middle of the joint. Note that the amount of leak-off is almost constant because of the constant pressure inside the fracture.

The sensitivity of the method to the mechanical behavior of joints is shown by comparing the pressure profile of the injection point for an isothermal analysis with linear and non-linear normal joint behavior. The pressure is greater for linear behavior than non-linear behavior. This is because a linear joint is stiffer than a nonlinear one and opens less when cold water is injected into it.

It is clear that method is highly sensitive to the mechanical behavior of rock joints as shown in Figure 96. The difference between the results for linear stiffness and a nonlinear Goodman joint is substantial and reflects strong coupling between the mechanical and hydraulic behavior of the joint. In the model for linear behavior, as is expected, when the pressure inside the joint is greater than 68.5 MPa (minimum total stress), some part of the joint is mechanically opened and the behavior changes from joint to hydraulic fracture. Figure 97 shows the opening process for the joint during the injection procedure. After 18 h, 400 m^2 of joint will be open and will change its behavior from joint to hydraulic fracture. Elements continue to open until the end of the injection phase, at which point 25600 m^2 of the joint are open.

The conservation of total mass can be checked using a simple calculation (Table 7). In the injection phase, 2592 m^3 water is injected into the joint. It can be seen from Figure 95 that the fracture aperture after 36 h is about 4.4 mm; therefore volume of the injected fluid stores in the joint is 946.57 m^3. The total volume of the leak-off after 36 h is 1710 m^3. Table 7 shows the leak-off rate for each time step up to 36 h. The total

volume of leak-off fluid and fluid stored inside the fracture differs by 70 m^3 from the amount of fluid injected into the fracture.

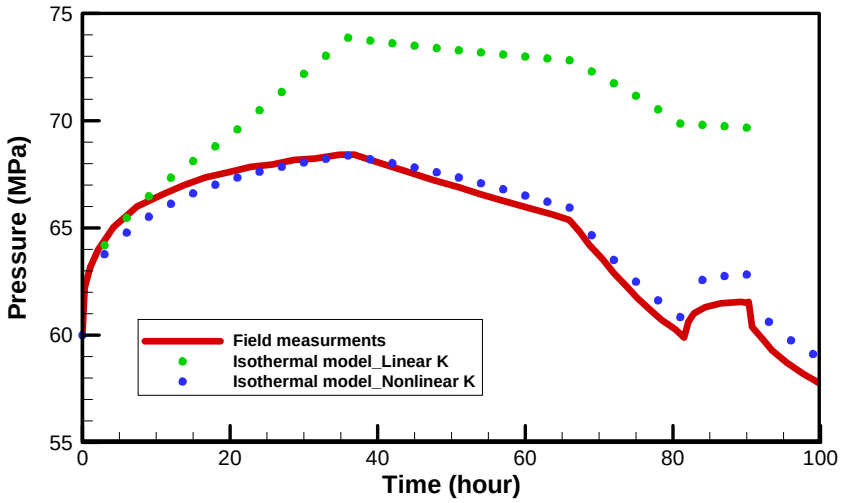

Figure 96. Comparing linear and non-linear behavior of joint.

Table 7. Leak off volume at each time steps during injection period.

Time (hour)	Average leak off (m/s)	Volume of leak off (m^3)
3	8.34E-08	1.91E+02
6	8.05E-08	1.85E+02
9	7.50E-08	1.72E+02
12	7.08E-08	1.62E+02
15	6.66E-08	1.53E+02
18	6.26E-08	1.44E+02
21	5.78E-08	1.33E+02
24	5.54E-08	1.27E+02
27	5.22E-08	1.20E+02
30	4.94E-08	1.13E+02
33	4.70E-08	1.08E+02
36	4.48E-08	1.03E+02
Total Volume of Leak off (m^3) =		1710.09
Total Volume of Fracture (m^3) =		946.57
Total Volume of Fluid (m^3) =		2656.66

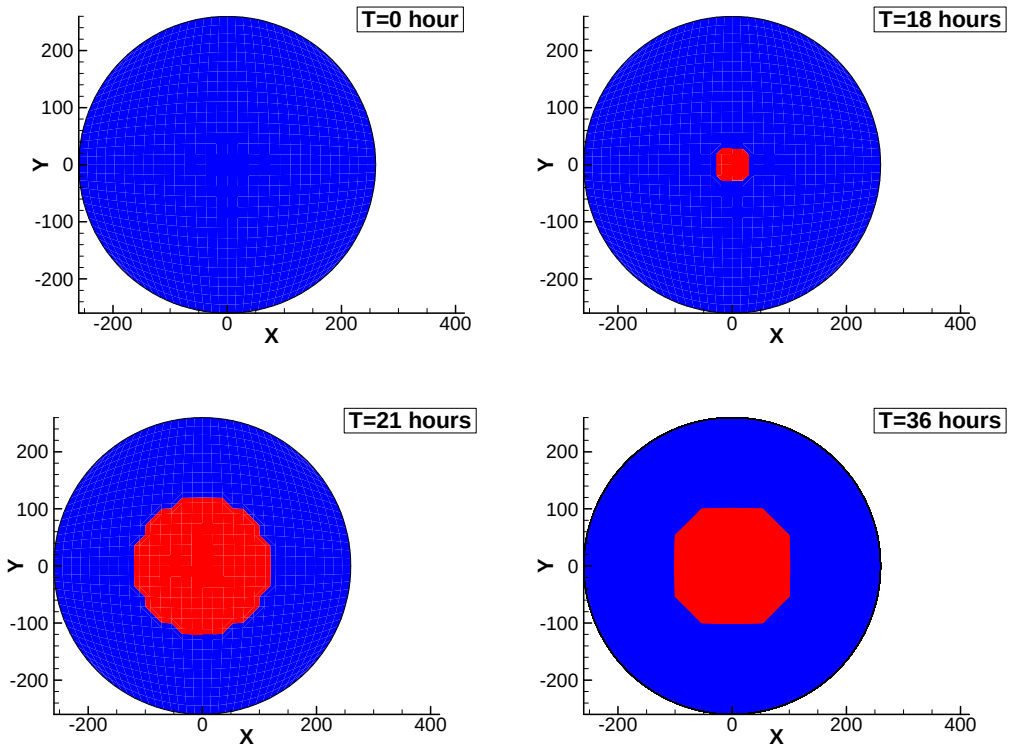

Figure 97. Mechanically open elements for linear isothermal model during injection phase.

6.2.2. Nonisothermal analysis

Nonisothermal analysis can be used to find the thermo-poroelastic properties of media. More important, non-isothermal analysis is used to determine whether thermal diffusion is responsible for the difference between the numerical results and the field measurements for the injection point pressure profile. Table 6 presents the general properties of media for which the best match found between field measurements and numerical results for pressure and temperature.

Figure 99 compares the pressure profiles as measured in the field and as calculated using the numerical method. Initially during the shut-in phase the

nonisothermal and isothermal results do not differ. This is because of the small amount time during the injection phase. In this period, the temperature diffusion is very small and does not have a considerable effect. Over five consecutive periods of rest and production, the nonisothermal results start to differ from the isothermal ones. By this time the temperature of the injected fluid has already increased to match the temperature of the field.

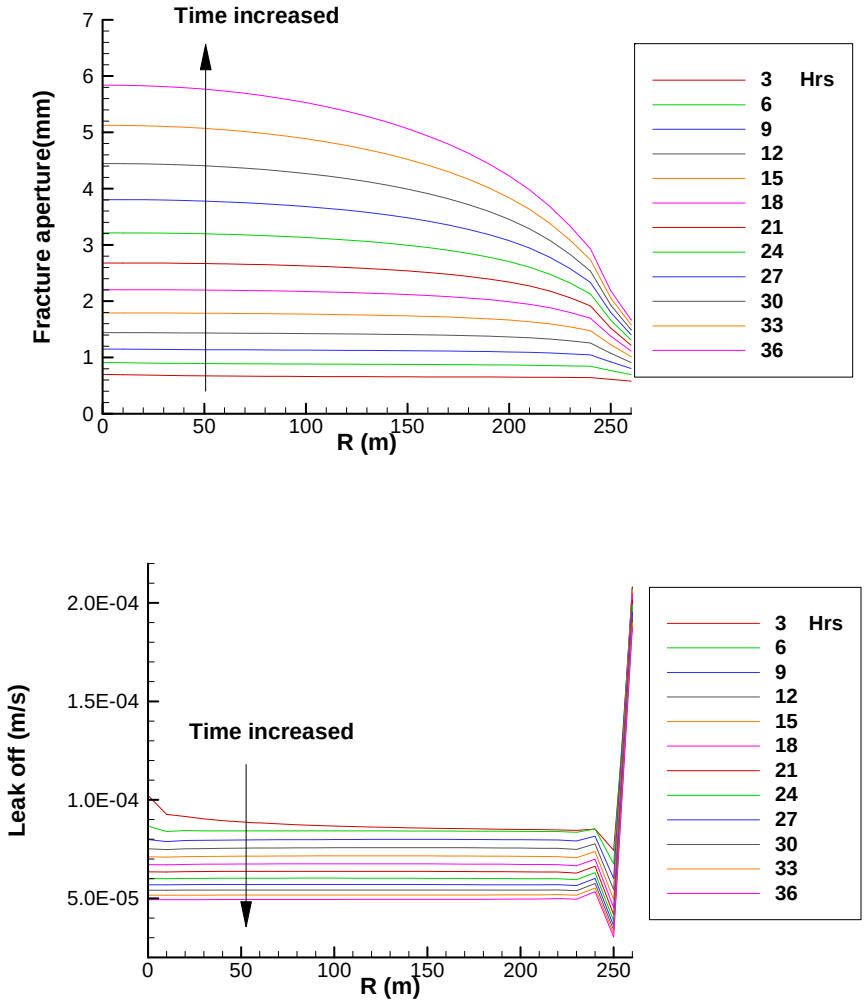

Figure 98. Fracture aperture and leak off during initial injection period

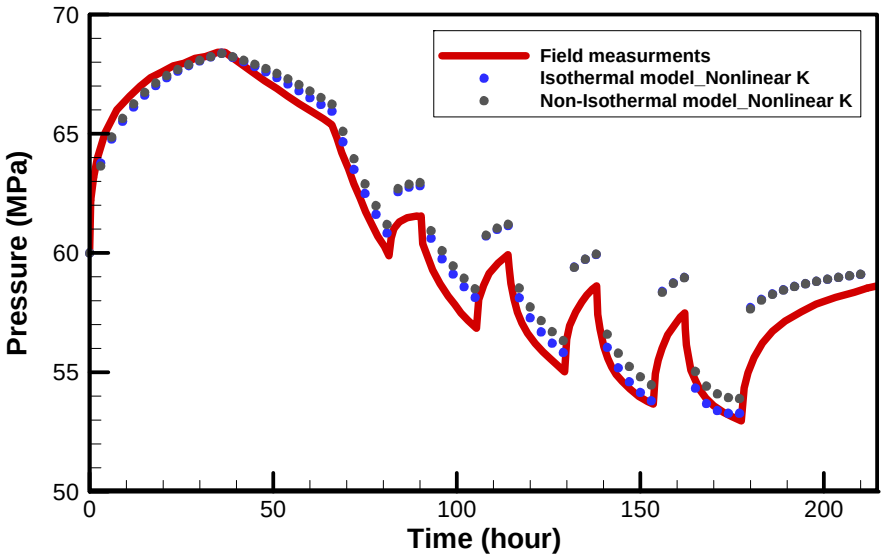

Figure 99. Comparison between isothermal and non-isothermal case.

From Figure 99, it is clear that the difference between the numerical results and the field data is not due to thermal diffusion.

Figure 100 compares the temperature as measured in the field and as calculated using the numerical model. At the beginning of the injection phase the temperature as measured in the field matches the far-field temperature, but then suddenly decreased. However, the numerical results show that from the beginning the temperature at the injection point is the same as that of the water being injected. This is a manifestation of the assumption that the temperatures of the rock and fluid are assumed constant. Yet this assumption is not correct at the beginning of injection or during transition behavior.

After the shut-in phase, there is large difference between the measured temperature and the temperature as found using the numerical model. It is believed that the reported temperature at this stage is not correct because after shut-in phase the

temperature keep continues to decrease without any apparent source of cooling. After the initial rest phase, the temperature for five periods of production and rest agrees well with the field and numerical results.

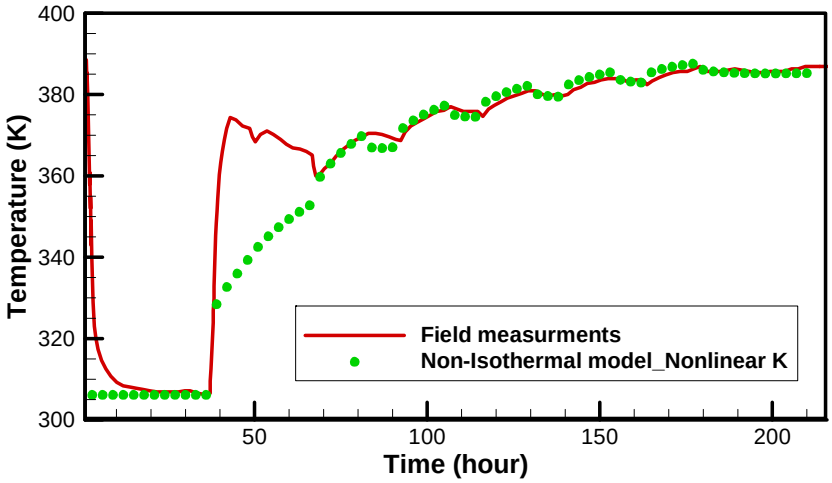

Figure 100. Temperature profile of injection point, comparison between field measurement and model result.

Figure 101 shows the temperature distribution inside the joint during the test. At the end of the injection phase, a circle with a radius of 18 m is cooled down to the temperature of the injection fluid, and then during the shut-in/production phases it returns to its original temperature.

6.3. Post failure behavior of a box sliding on free space

In this section, post-failure behavior of a box sliding on a surface is used to verify the slip-weakening model.

Initially, the situation depicted in Figure 102 looks like an elementary problem in mechanics: a square block of negligible weight sits on the surface of a half space and is

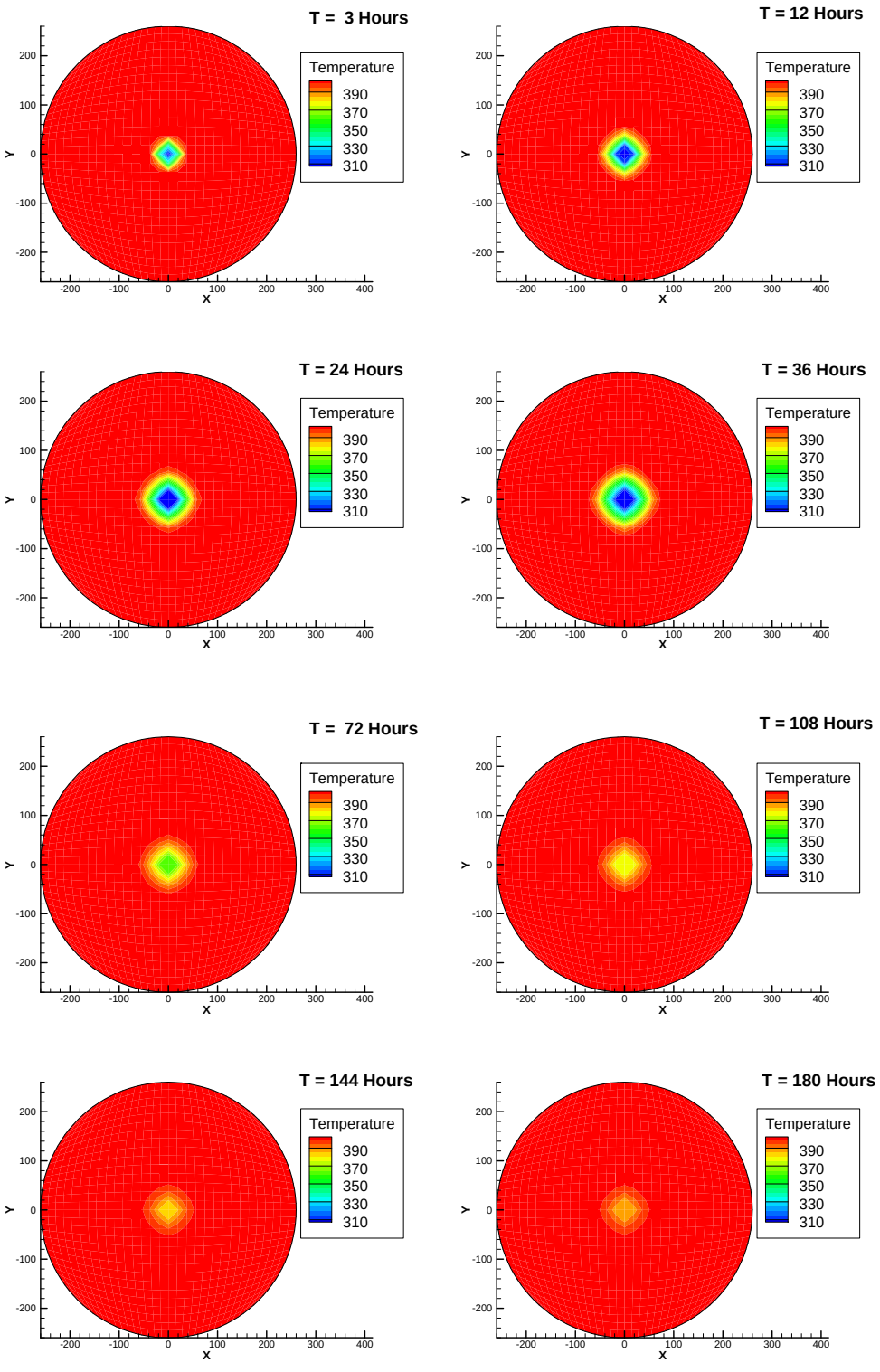

Figure 101. Temperature distribution in joint in different time.

forced to slide by an applied shear displacement in X direction. A vertical load is applied to the top of the block to activate the frictional strength of the block to resist the shear slide.

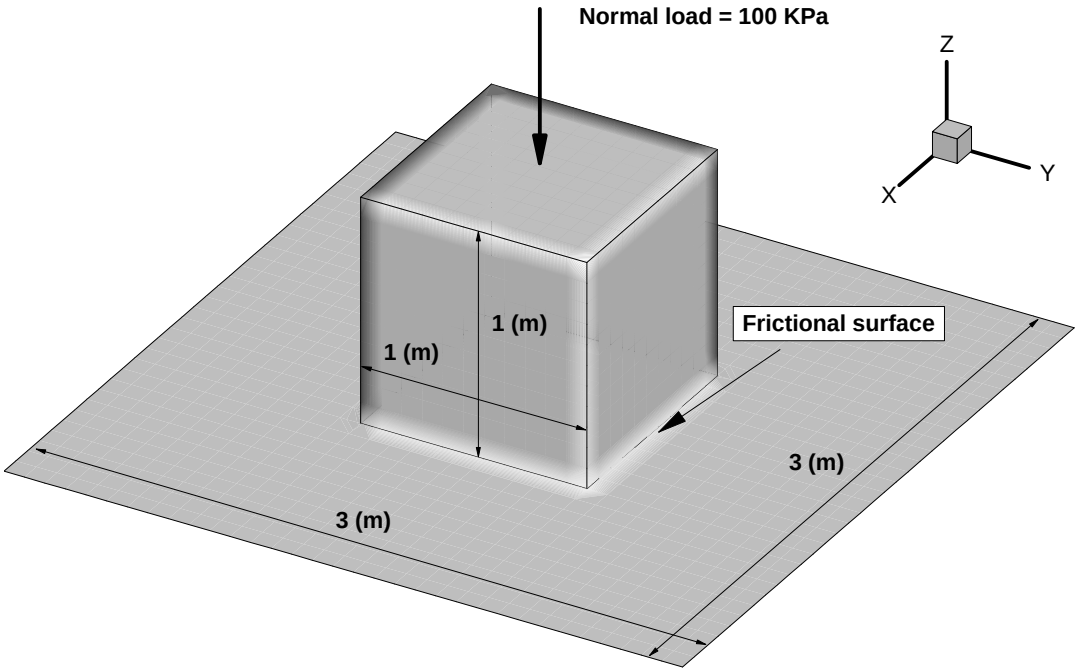

Figure 102. Sliding box on a surface of half-space.

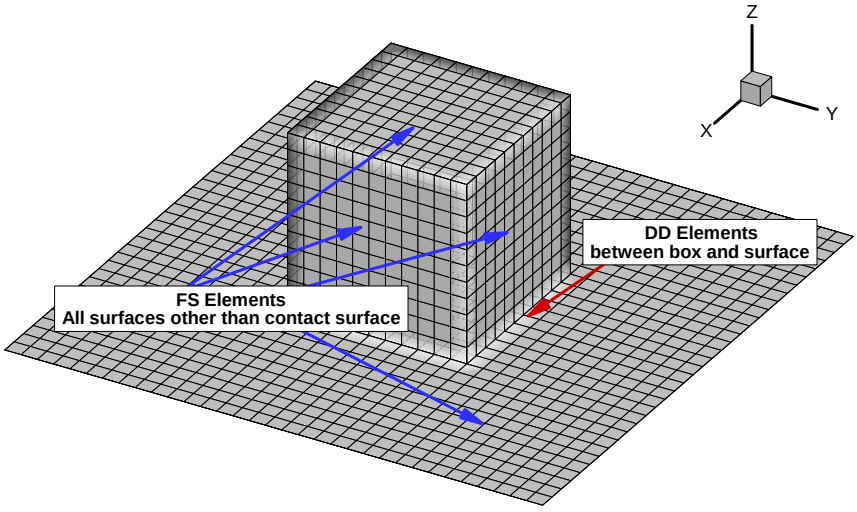

Figure 103. Discretization of box and surface with FS and DD elements.

Figure 103 shows the discretization of the box and free surface with quadrilateral elements. The free surface and the box surfaces (on the area that is not in contact) are discretized with 1573 FS elements. In addition, the contact surface between the box and the free surface is discretized with 121 DD elements whose behavior is enhanced by the slip-weakening model.

By considering 1.0 as a frictional coefficient and applying 100 KPa to the top of the box, one can compute the essential horizontal load necessary to move the box by x shear displacement. Here it is assumed that the box and half space deform elastically; their properties are defined in Table 8.

Table 8. Essential parameters to model box sliding on half space surface.

Shear modulus	(MPa)	4.16 (603 psi)
Drained Poisson's ratio	(-)	0.20
Undrained Poisson's ratio	(-)	0.205
Biot coefficient	(-)	1.0
Base permeability	(m^2)	1.00×10^{-13} (0.1 Darcy)

The problem is modeled by discretizing the box surfaces (excluding the surface that is in contact with the half space surface) with fictitious elements and the frictional surface with DD elements. The DD element behavior is controlled by the Mohr-Coulomb criterion and the slip-weakening laws described in section 5.2.3. Table 9 presents essential parameters for slip-weakening model.

Note that the initial stresses in the block (and half space) are due to the vertical load, and the box is forced to move in X direction. The results of the simulation summarized in relation between shear force and shear displacement in X direction which are presented in Figure 104. As can be seen from Figure 104, decreasing the residual friction angle

decreases the residual force on the frictional surface. More interesting is the complete softening of the joint, which is very clear for a curve with a residual friction angle equal to 25°. Note that the maximum residual friction force in the case of no slip-weakening (NO SW) is about 96 KPa, which is 4 KPa less than the expected value (for a frictional angle equal to 45° the residual force is expected to be the same as the applied normal force). This is due to the numerical accuracy of the code, which can be improved by increasing the number of elements.

Table 9. Essential parameters for slip weakening law.

Peak Friction Angle		45°
Residual Friction Angle		20°- 40°
Peak Cohesion	(MPa)	0.00 (0.00 psi)
Residual Cohesion	(MPa)	0.00 (0.00 psi)
Dilation Angle		0.00°
Maximum Aperture due to Dilation	(m)	5.00×10^{-4}(0.02 inch)
Critical value for Shear DD, D*	(m)	5.00×10^{-3}(0.2 inch)
Linear normal stiffness	(MPa/m)	1.00×10^{3}(468 Ksi/ft)
Linear shear stiffness	(MPa/m)	1.00×10^{3}(468 Ksi/ft)

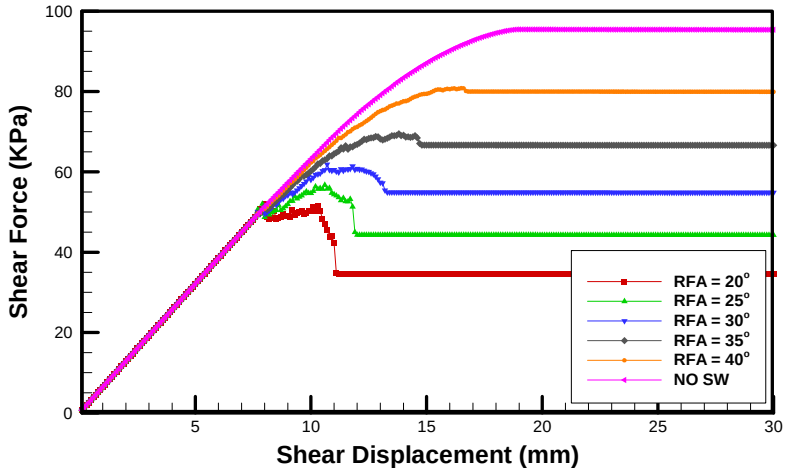

Figure 104. Horizontal shear load in "X" direction for different horizontal displacement, "RFA" stands for "Residual Friction Angle" and "NO SW" stands for simulation results without slip weakening model.

Figure 105 shows the total and X direction displacement of box and half space surface after 20-mm shear displacement which is forced to whole box. Note that the total displacement figure is shown in a deformed shape.

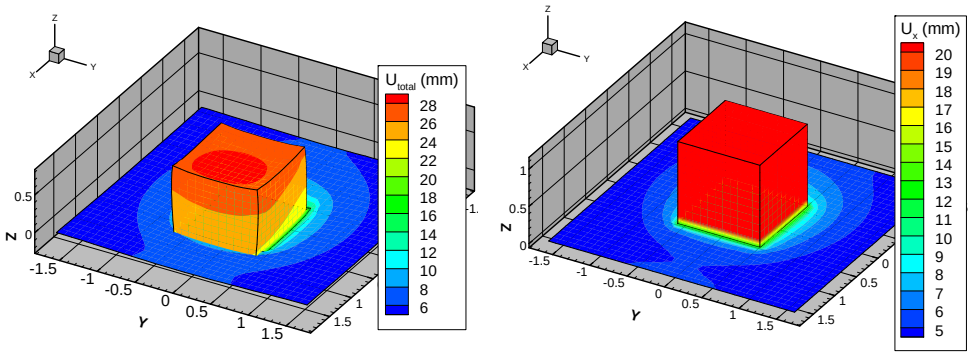

Figure 105. Absolute and "X" direction displacement of box and free surface.

6.4. Hydraulic stimulation of natural fractures under shear force

The response of natural fractures is a key factor during hydraulic stimulation of unconventional resources. Slip on natural fractures is believed to increase permeability and to cause microseismicity in response to injection. Numerical modeling of the behavior of natural fractures under shear stress is needed to help predict stimulated volume, permeability dynamics, and the occurrence of microseismicity in geothermal and gas shale reservoirs. Combining numerical models with experimental observations can help researchers understand how fracture permeability changes during the injection and production phases, therefore, contributing to the optimization of stimulation designs.

In this simulation effort, the natural fracture is discretized with four-noded quadrilateral elements. During pressurization of the fracture, each element can be in a state of either open, close, stick, or slip as described in section 5.2. Note that the status of

any element could vary from current time step to next one. Therefore, the element status must be determined at every time step because the constitutive relations are dissimilar for different element states (as presented in equations (5.23) and (5.24)).

This problem considers the effect of low-rate injection stimulation (an injection rate less than what is needed to propagate the fracture in Mode I or Mode II) and the interactions between natural joint geometry and the in situ stress field and their impact on the evolution of permeability. The problem geometry and wellbore placement are shown in Figure 106. The general parameters and in situ stress values are presented in Table 10. The stress state is one of a normal faulting regime, and the variation in in situ stresses with space is not considered in this problem. The fracture is discretized with 500 quadrilateral elements (10 m × 10 m) and 561 nodes. Fluid injection with the low rate is prescribed on the middle node, as shown in Figure 106, with a constant rate of 7.5 bbl /min (20 L/s) where the well is placed in the mesh.

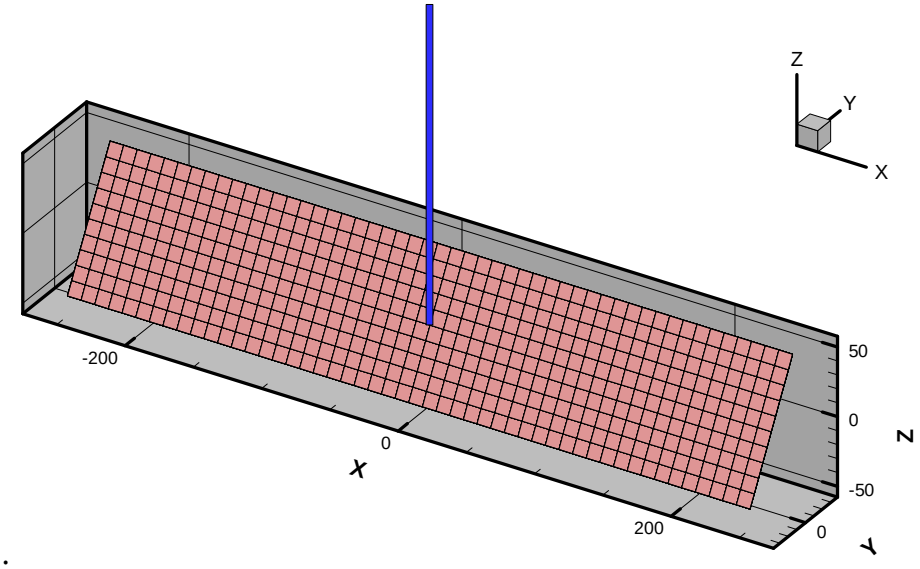

Figure 106. Hydraulic stimulation of natural fracture under shear force.

Initially details of the hydromechanical behavior and coupled processes during the first 3 min of constant-rate injection are investigated, and then the injection rate (as described in section 5.3) is fine-tuned to prevent the existing fracture from propagating and its behavior is studied under a variable injection rate.

Figure 107 shows the shear status of all elements after 2 and 3 min of constant injection (using 1 min as a time step) when the element behavior is enhanced by the slip-weakening model. Regions where the fracture has experienced permanent slip are shown in red. It can be seen from the plot that after 2 min, the fracture starts to experience permanent slip, and after 3 min the whole fracture has slipped. This is because after 2 min elements in the middle of the fracture start to lose their strength (because of slip weakening and the decrease in effective stress) and attempt to pass excessive shear stress on to their neighbor elements. However, the neighbor elements cannot tolerate the induced shear stress, and they also experience permanent slip. Then the shear failure continues to the edge of the fracture and completely changes the hydromechanical behavior. It should be noted that due to dilation effect, the permeability of the fracture is enhanced as can be seen in Figure 108. Accordingly, the pressure inside the fracture decreases after permanent slip. However, because the slipped elements have already become weak and effective stress has decreased, they do not return to the stick condition (no-slip). To determine the validity of the claim that if there is no slip weakening, no sudden slip will be observed, the problem is run without the slip-weakening model. The shear status of an element without any weakening is shown in Figure 109. Without any slip weakening, there is no sudden status change in any area of the fracture after 3 min,

and any change that does occur is gradual, which is not realistic. Note that when there is no slip weakening the stress level is the threshold level, whereas when there is slip weakening the stress level drops and the threshold level also decreases.

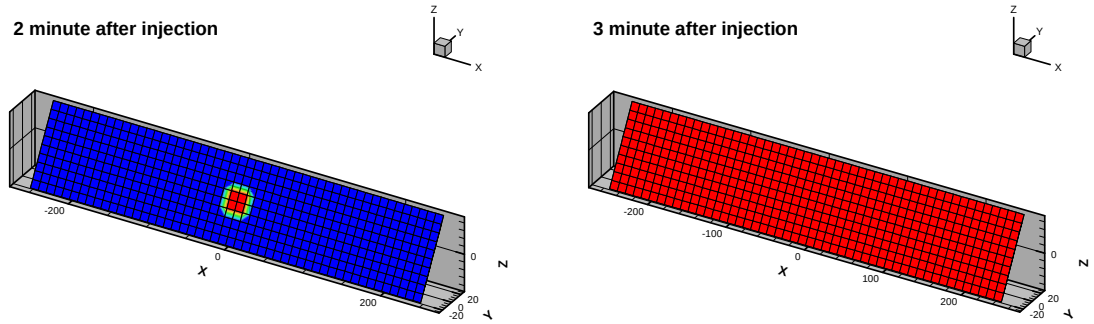

Figure 107. Slip status of elements after 2 and 3 minutes of injection with applying slip-weakening model, red color means slip area and blue means stick.

Figure 110 shows the amount of plastic shear DD on the fracture surface for the slip-weakening model. These are the values used in calculating the moment magnitude of induced micro earthquakes. In Figure 110, plastic shear DD increases as the fluid pressure makes the state of the fracture more critical by lowering the effective normal stress and reducing the fracture shear strength. Thus, the shear slip area increases with time, potentially increasing the magnitude of micro earthquakes.

According to McGarr et al. [142] the seismic moment due to slip u over the slip area can be described as follows:

$$M_0 = \int_{A_{Slip}} Gu \; da \tag{6.1}$$

where G is the shear modulus of the rock. The magnitude of an earthquake generated by the seismic moment can be estimated as follows [143]:

$$M = (2/3)\log_{10} M_0 - 10.7 \quad (6.2)$$

Table 10. Parameters used to model the fracture under shear.

Shear modulus	(GPa)	8.30 (1203 Ksi)
Drained Poisson's ratio	(-)	0.25
Undrained Poisson's ratio	(-)	0.46
Biot coefficient	(-)	0.96
Base permeability	(m^2)	1.00×10^{-17} (10 Micro Darcy)
Initial joint aperture	(m)	1.00×10^{-4} (0.004 inch)
Minimum joint aperture	(m)	1.00×10^{-5}(0.0004 inch)
Stress in "X" direction	(MPa)	43.00 (6236 psi)
Stress in "Y" direction	(MPa)	39.00 (5656 psi)
Stress in "Z" direction	(MPa)	56.50 (8194 psi)
Reservoir pore pressure	(MPa)	28.30 (4104 psi)
Rock density	(kg/m^3)	2650.00(1.15 psi/ft)
Fluid density	(kg/m^3)	1000.00(0.433 psi/ft)
Fluid viscosity	($N.s/m^2$)	3.00×10^{-4}(0.3 cp)
Initial pumping rate	(lit/sec)	20.00 (7.5 bbl/min)
Peak Friction Angle		30°
Residual Friction Angle		20°
Peak Cohesion	(MPa)	0.70 (101 psi)
Residual Cohesion	(MPa)	0.00 (0.00 psi)
Dilation Angle		3°
Maximum Aperture due to Dilation	(m)	5.00×10^{-4}(0.02 inch)
Critical value for Shear DD, D*	(m)	5.00×10^{-3}(0.2 inch)
Linear normal stiffness	(MPa/m)	2.00×10^{4}(9350 Ksi/ft)
Linear shear stiffness	(MPa/m)	2.00×10^{4}(9350 Ksi/ft)
Mode I critical fracture toughness	($MPa.m^{0.5}$)	1.50 (1365 $psi.in^{0.5}$)
Mode II critical fracture toughness	($MPa.m^{0.5}$)	2.00 (1820 $psi.in^{0.5}$)

With the help of equations (6.1) and (6.2), the magnitude of the micro earthquake generated after 3 min with the slip-weakening model has 3.05 magnitude.

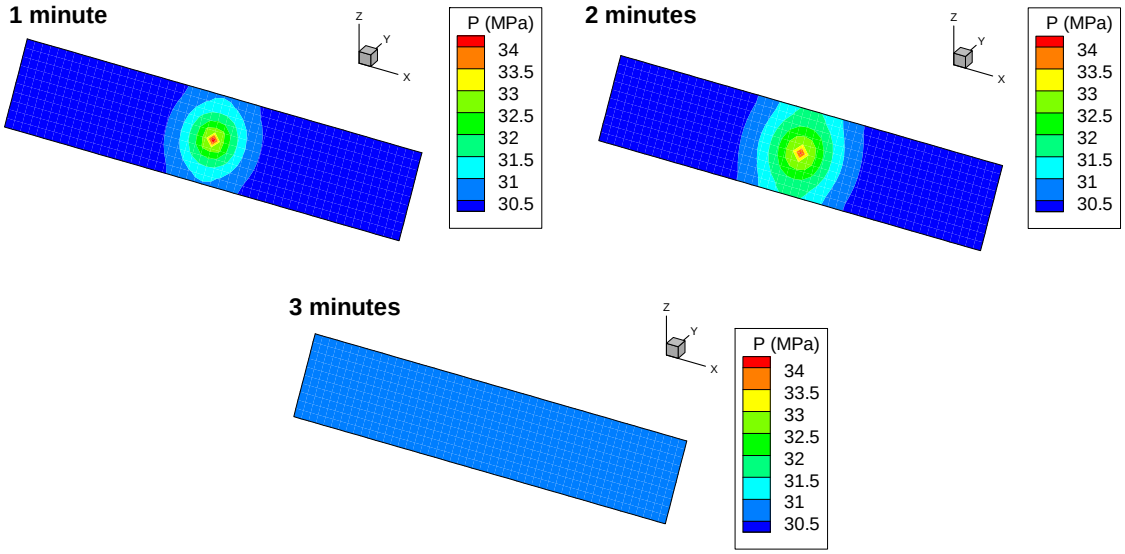

Figure 108. Pressure profile at different time in fracture with constant injection rate with slip weakening model.

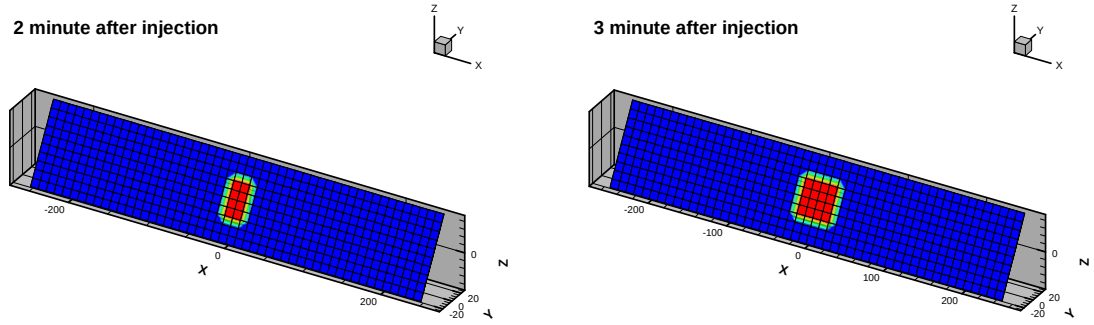

Figure 109. Shear status of elements for simulation without slip weakening, red: slipped elements, blue: stick elements.

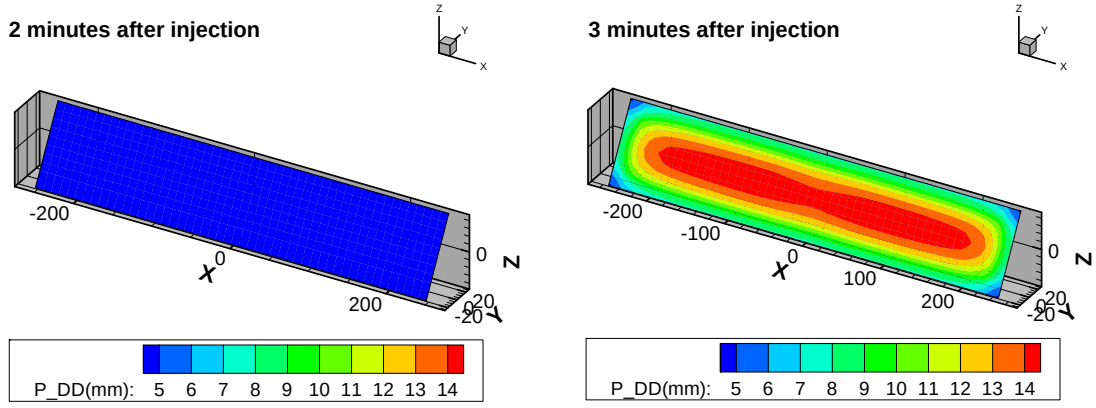

Figure 110. Plastic shear displacement discontinuity distribution with weakening.

As can be seen from Figure 107, after 3 min all elements experience permanent slip, and it is possible that the fracture is no longer stable and starts to propagate. The stability of the fracture in Mode I and Mode II is checked by comparing the critical fracture toughness with calculated SIF as described in Section 5. Figure 111 shows that after 3 min, the fracture is still stable under Mode I. However, the fracture is no longer stable under Mode II, as the ratio of KII to KII_c is about 8.0 at the top and bottom edge, which means that the fracture is going to propagate in Mode II at these locations.

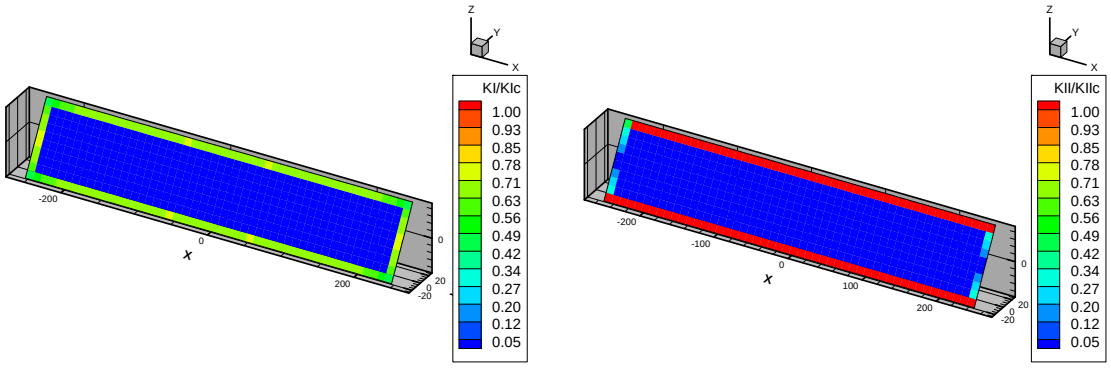

Figure 111. Propagation status of elements in mode I and mode II after 3 minutes.

Therefore, to keep the fracture stable it is essential to modify the injection rate. The injection rate should be modified to keep the fracture in a state of incipient propagation (equilibrium crack), in both opening and shearing modes. Figure 112 shows the change required in the injection rate during the first hour of the stimulation process to keep the fracture in stable condition. Figure 113 shows the Mode I and Mode II status of propagation. It shows that adjusting the injection rate prevents the fracture from becoming to be unstable and propagating in any mode. Only some of the elements experience permanent slip when the injection rate is modified.

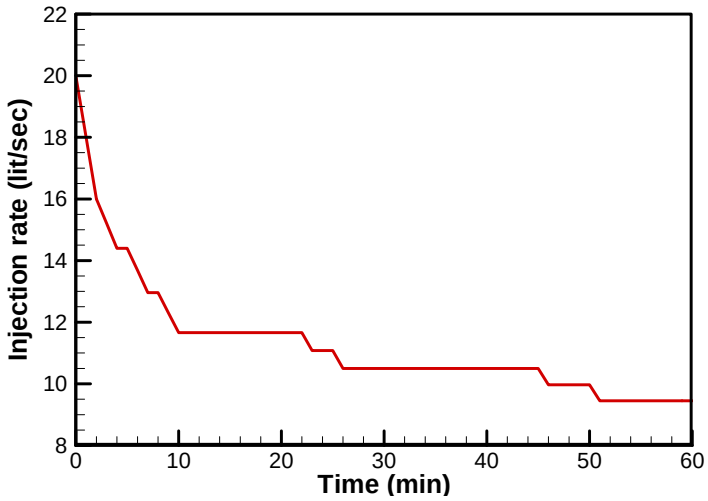

Figure 112. Variable injection rate to keep the fracture on the verge of propagation, considering both mode I and mode II.

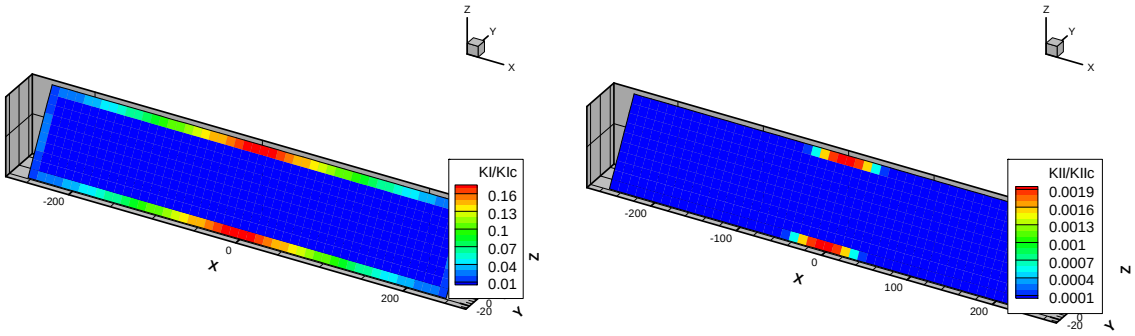

Figure 113. Propagation status of all elements in mode I and mode II after 60 minutes with changing injection rate.

Figure 114 shows the change in the shear status of elements during the stimulation process with the variable injection rate. By comparing Figure 107 and Figure 114, one can see that when the injection rate is adjusted to ensure the stability of the fracture, elements experience permanent slip more gradually.

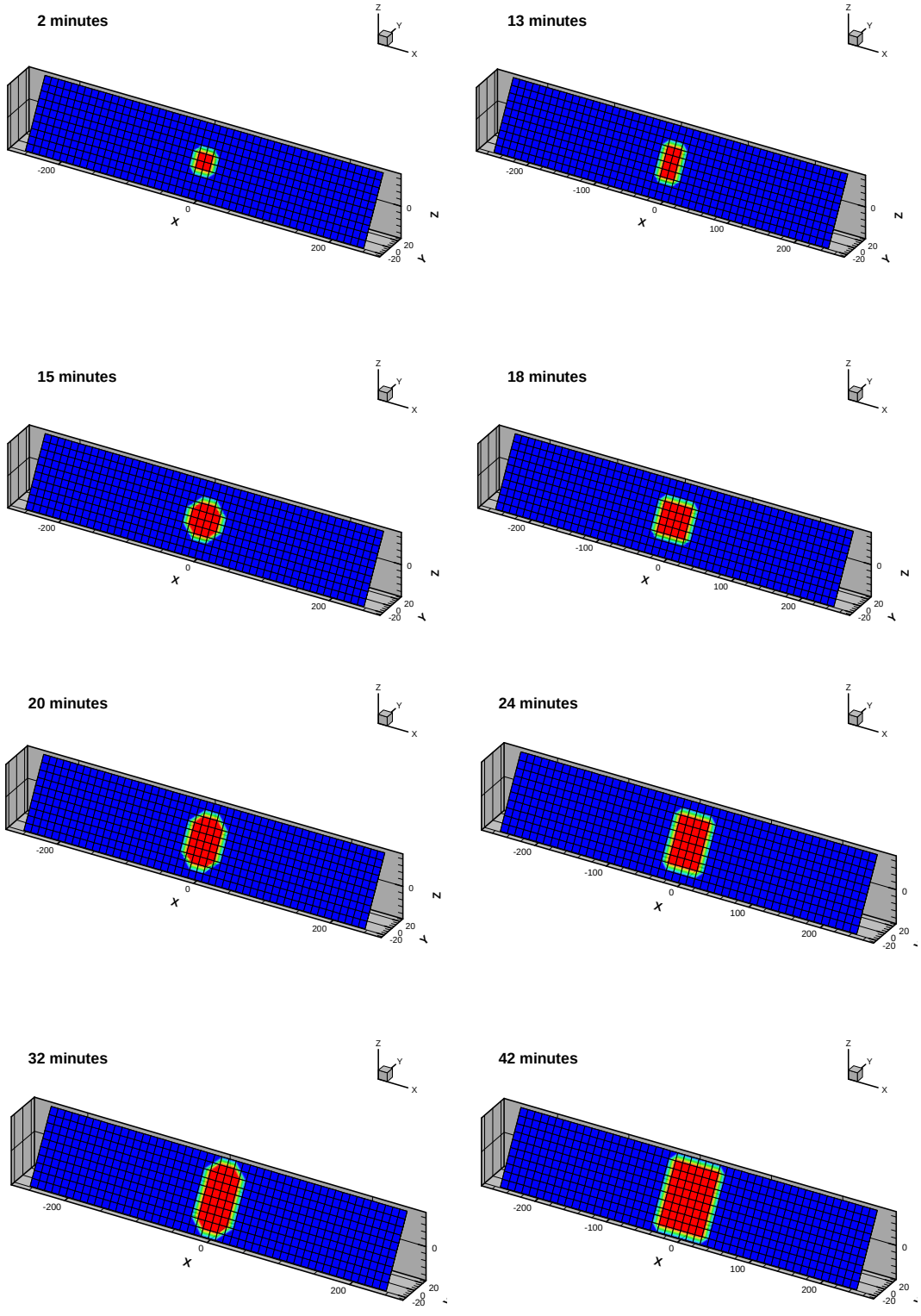

Figure 114. Evolution of shear status of elements during injection rate change.

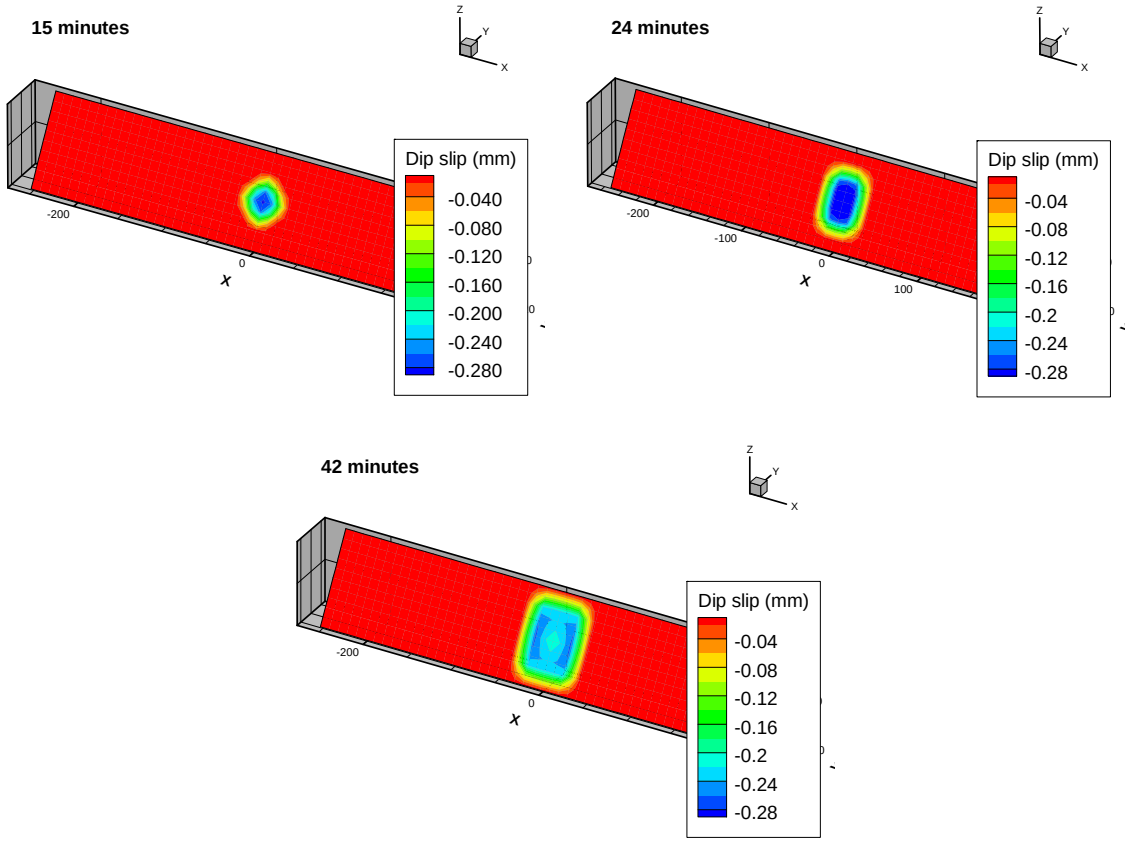

Figure 115. Dip slip or shear displacement discontinuity in dip direction on different time for variable injection rate.

Figure 115 shows the shear DD along the fracture dip after 15, 24, and 42 min of injection. As time passes, the total amount of slipped area increases, resulting in larger fracture apertures because of the dilation effect. This occurs on the fracture surface because of asperities, but after some shear ride asperities break down and dilation is no longer possible. In this example, the value of the maximum fracture aperture due to dilation is 0.5 mm (Table 10). This value is checked every dilation iteration, and if it exceeds the allowable limit, it is reset to 0.5 mm.

The fracture aperture distribution is shown in Figure 116 for four specified times. This distribution is very much affected by the element shear status. The aperture increases over the slipped area and reaches its maximum value at the slipped area during slip propagation inside the fracture. This enhances permeability, which may be reversible to some extent when fluid injection is stopped.

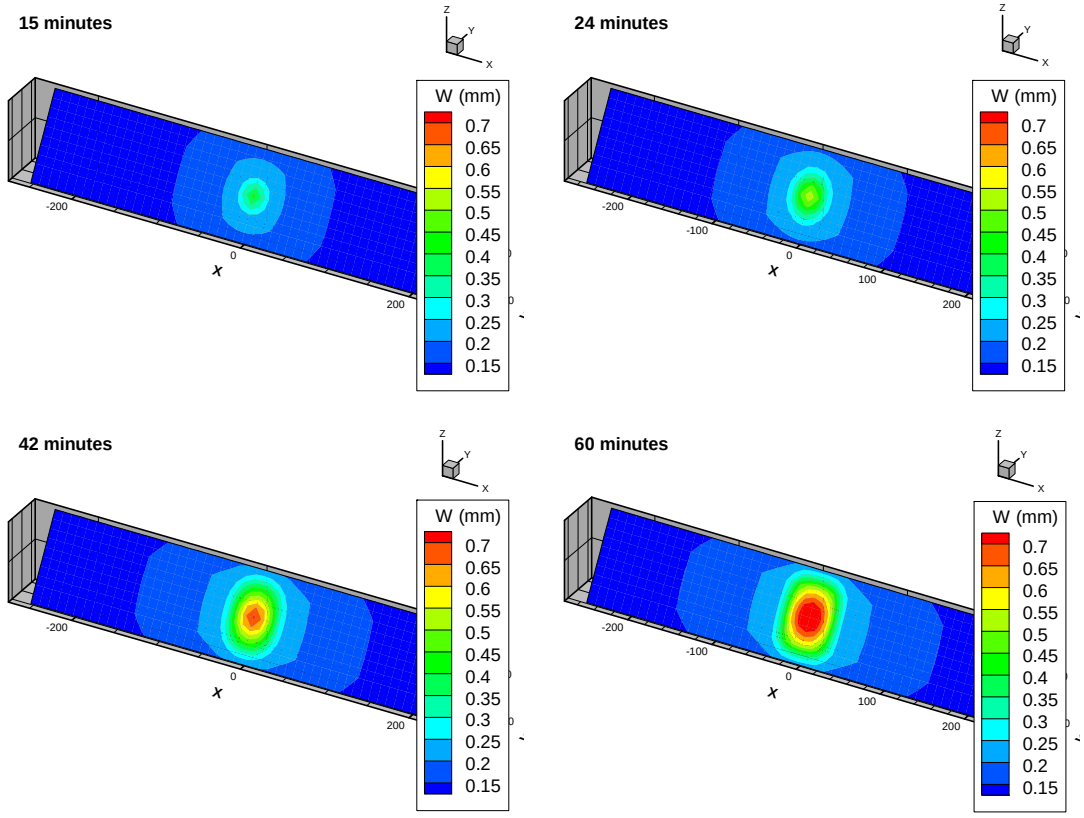

Figure 116. Fracture aperture at three different stages during injection.

Figure 117 shows the distribution of normal effective stress over time. Normal effective stress changes during pressurization, but it never reaches zero. Therefor, none of the elements change their behavior from joint to hydraulic fracture (zero effective

stress on the fracture surface). The high value of effective stress justifies the use of linear joint normal behavior with a stiffness value of 20 GPa/m.

Slip on the fracture begins after 2.0 min and the slip area propagates outward over time, eventually spreading over approximately 4800 m^2 (48 elements) of the fracture after 60.0 min. Figure 113 shows that the fracture will not yet propagate when the slip zone reaches its edges.

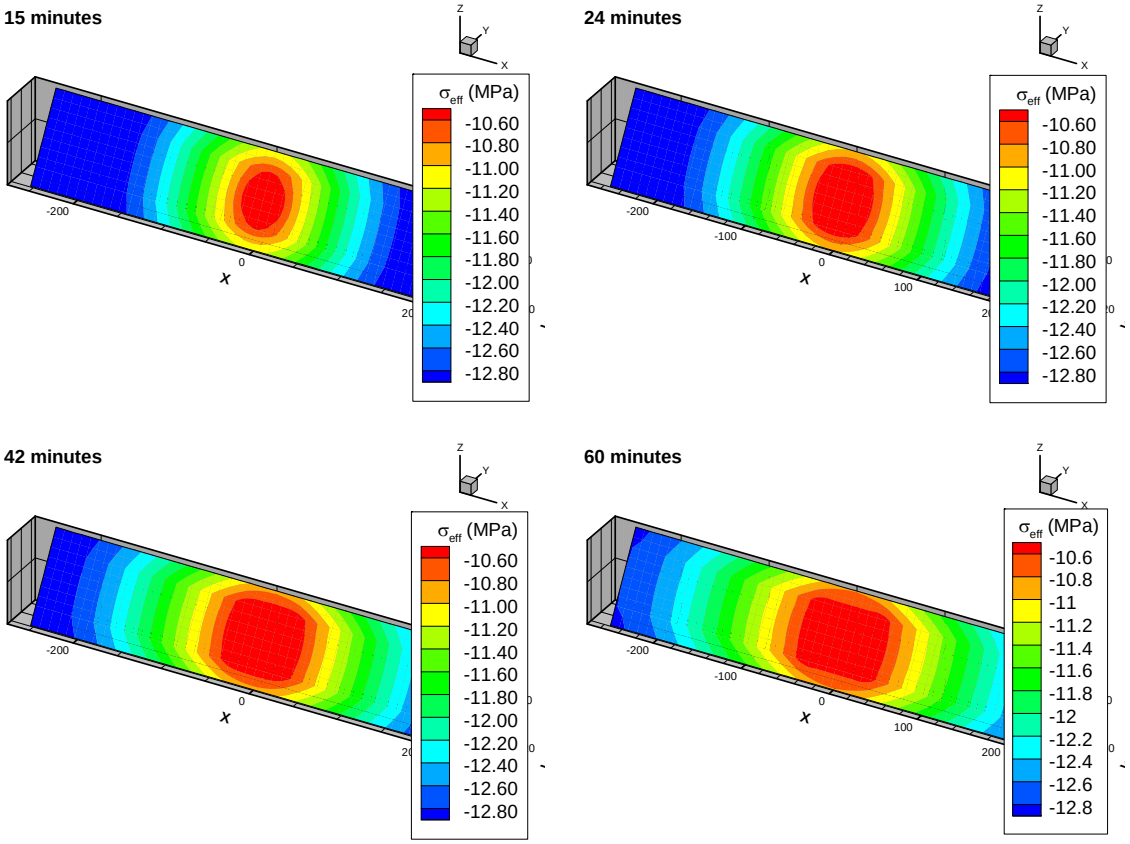

Figure 117. Normal effective stress on fracture.

Figure 118 shows the pressure profile at the injection point for the first hour. It is expected that injecting inside the inclined fracture increases the pressure. However, it

seems from Figure 118 that during the first 26 min, the pressure decreases very rapidly. This rapid decrease in pressure is due to fracture dilation, which causes fracture opening and subsequent permeability enhancement. From 26 min to 32 min, the pressure remains constant. This is because injection compensates for permeability enhancement and prevents the pressure from decreasing further. This behavior is repeated one more time from 38 min to 46 min. These repetitive behaviors are due to competition between increasing shear DDs and the injection rate. Sometimes the injection rate determines behavior, and sometimes dilation effect or permeability enhancement does. Consistent with the slip-weakening model, the buildup of pressure progressively decreases, leading to progressively lower critical shear stress level or dilatancy suppression due to a high level of slip. The corresponding fracture aperture profile for the injection point is shown in Figure 119. It also shows an increasing trend from the start of injection at three nearly constant rates. In the fracture aperture the effects of both injection rate and dilation result in an increase in the fracture aperture.

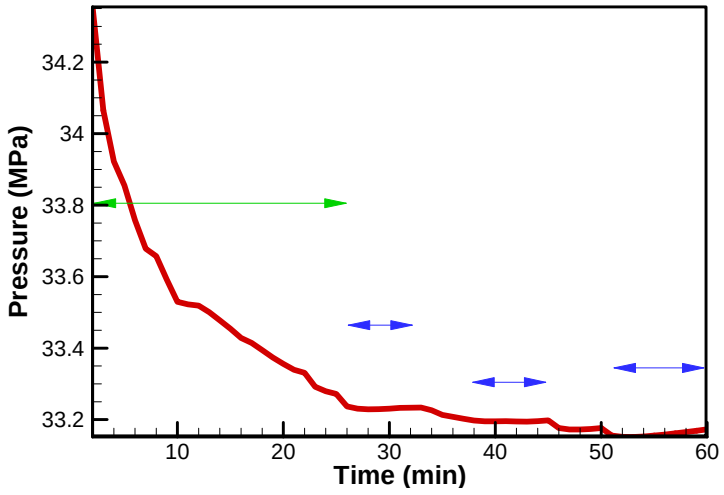

Figure 118. Pressure profile of injection point, Green arrow: effect of permeability enhancement, Blue arrow: intervals of pressure build up due to injection.

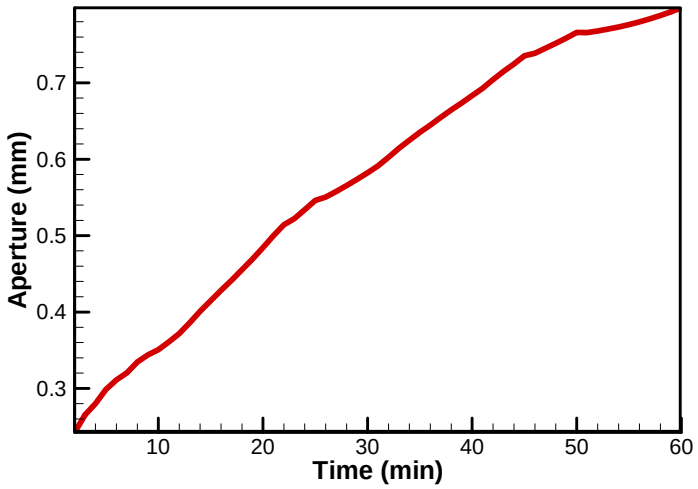

Figure 119. Fracture aperture profile of the injection point.

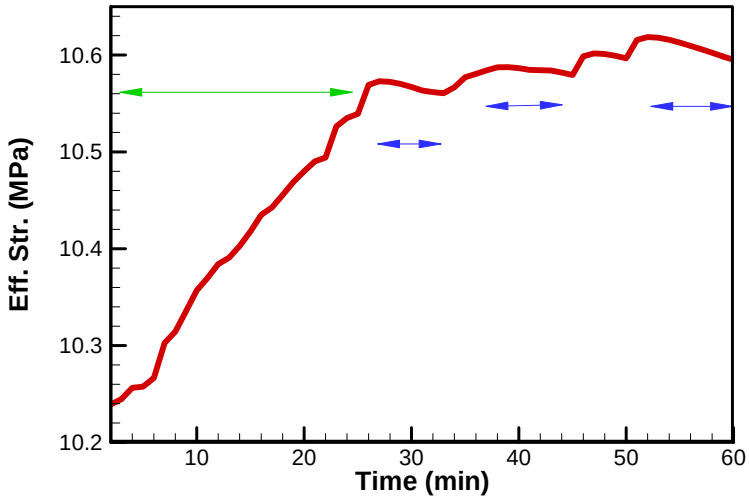

Figure 120. Effective stress profile of injection point.

The normal effective stress profile (see Figure 120) of the injection point shows the same effects as the pressure profile (when pressure decreases, effective stress increases). Effective stress at the injection point initially increases with time (green

arrow). This is because of the dilation effect. Dilation increases effective stress (see equation (5.25)) on the fracture surface, and injection decreases it. In this period, dilation overtakes the fracture, and effective stress increases. After this initial stage, as in the pressure profile, three decreases in effective stress occur. This is because injection overtakes the fracture, forces the fracture surface outward, and decreases effective stress. Like with the change in pressure, the slope of the change in effective stress depends on the injection rate and the normal and shear strength of the joint. A higher injection rate and softer joint result in a steeper slope.

6.5. High injection rate into hydraulic fracture

This example illustrates some fundamentals of the opening mode of closed fractures and their shear failure and induced seismicity in response to injection into a hydraulic fracture and the fracture's interactions with neighboring natural fractures. Figure 121 shows the problem, and Table 10 presents its essential properties. The initial injection rate is increased from 20 L/s in Table 10 (7.5 bbl/min) to 135 L/s (51 bbl/min) to trigger the transition of the vertical fracture from a joint to a hydraulic fracture. The injection rate is adjusted automatically to keep the fracture on the verge of propagation. To better describe the effect of a natural fracture on smaller fractures, first a large fracture without any natural fractures is simulated (Figure 122), and then results for the problem considering natural fractures are presented.

The vertical fracture is discretized with 300 quadrilateral elements (10 m × 10 m) and 341 nodes (Figure 121). The natural fractures are also discretized with 5 m × 5 m quadrilateral elements. The fluid injection rate is prescribed in the middle of the

hydraulic fracture, where the well is placed in the mesh. A small time step duration of 1.0 min is chosen because of nonlinearity and the necessity of capturing the transition from joint to hydraulic fracture.

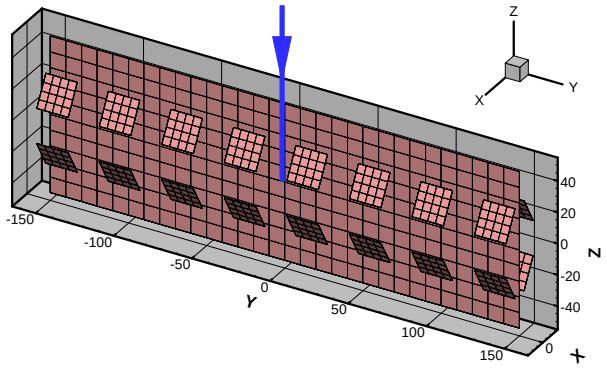

Figure 121. Geometry of a hydraulic fracture and natural fracture network, there are 2 sets of natural fractures with a center to center distance of 40 m in y- and z-directions and minimum 5 m, maximum 15 m in x- direction.

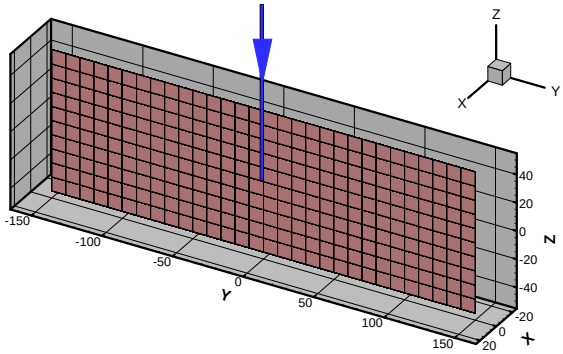

Figure 122. Hydraulic fracture without natural fracture network.

Initially the system is in equilibrium until injection into the vertical fracture begins. The injection profile that keeps the existing fracture stable and prevents it from propagating during the first hour is shown in Figure 123. The injection rate is constant for 26 min (135 L/s) and then suddenly decreases from 26 min to 30 min. The sudden

decrease occurs because after 24 min, elements on the edge of the fracture start to open, causing their aperture to increase and the fracture to move toward propagation. Thus, the injection rate is decreased to prevent it from propagating. The transition of elements from joints to hydraulic fractures at different time steps is shown in Figure 124. The figure shows the transition of elements from hydraulically open but mechanically close to hydraulically and mechanically open. The vertical fracture starts to reopen after 4.0 min and is completely open after 11 min (except for a narrow band at the fracture tip). Then after 24 min, elements on the edge start to open. At this time, the injection rate decreases to prevent the fracture from propagating in Mode I.

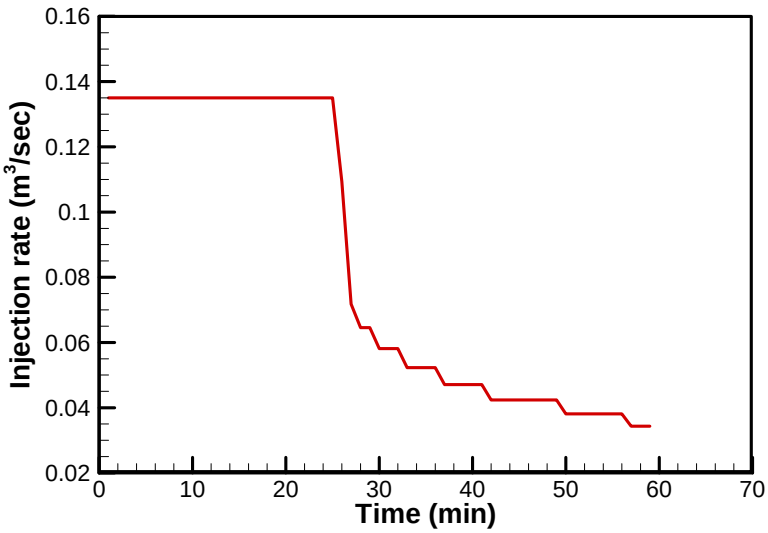

Figure 123. Injection profile during first hour of stimulation.

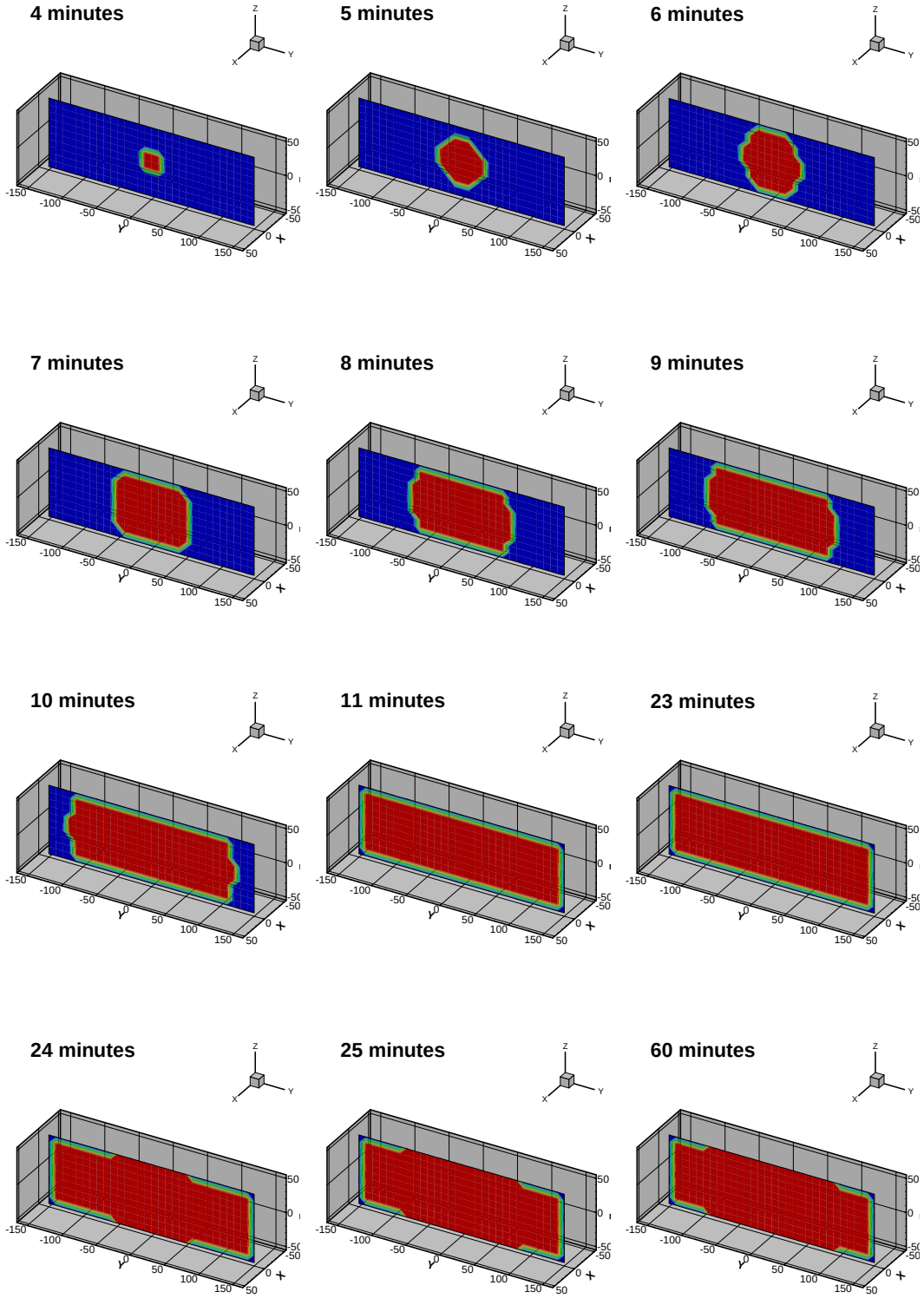

Figure 124. Opening of hydraulic fracture during injection process.

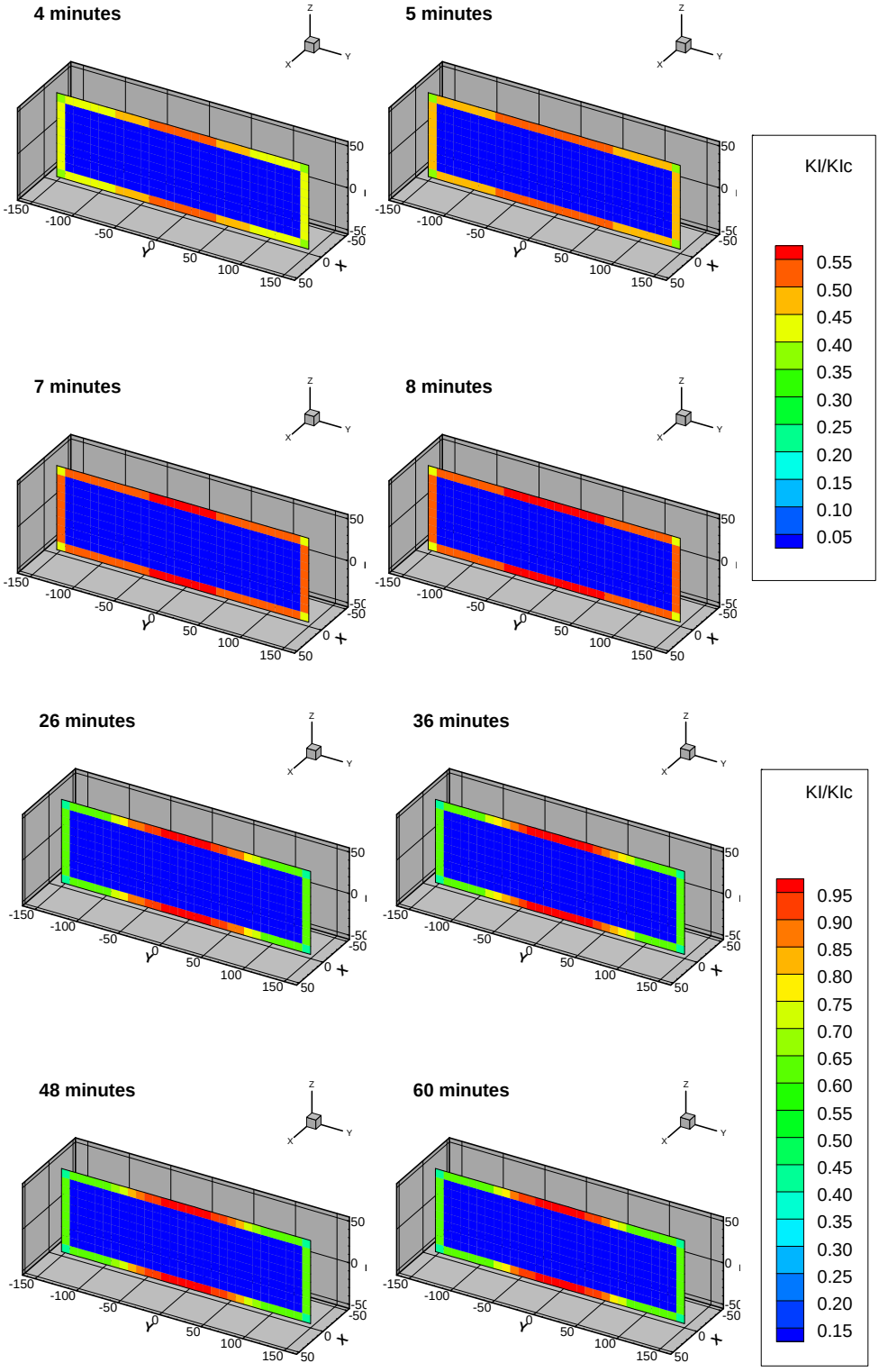

Figure 125. Propagation status of edge element in mode I propagation.

Figure 125 shows the propagation status of the edge elements in Mode I at different time steps during the injection process. Before 26 min measured fracture toughness of critical elements is about 0.56. However, after 26 min of injection at a constant rate of 135 L/s, the fracture approaches propagation, and the injection rate is decreased, and the fracture remains on the verge of propagation ($0.95 < K_I/K_{Ic} < 1.0$).

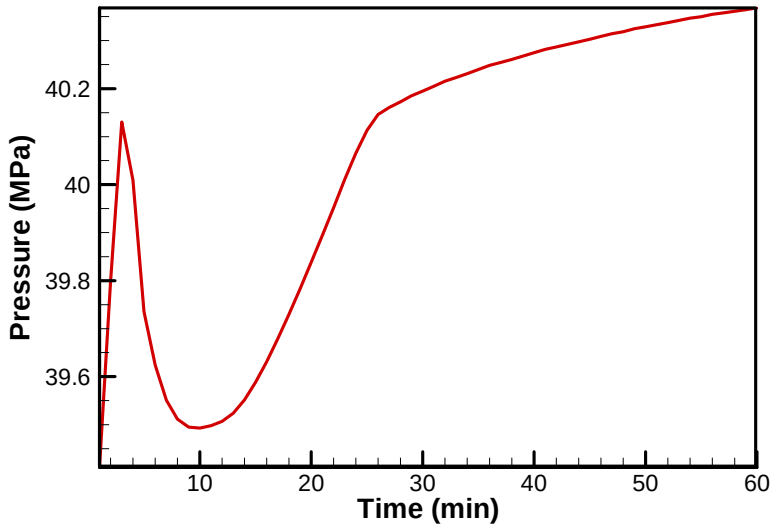

Figure 126. Pressure profile at injection point.

The hydromechanical behavior of vertical fractures during injection and fracture reopening can be summarized in the pressure profile of the injection point (see Figure 126). Figure 126 shows that for times less than 2 min, the pressure increases with a very high slope until the fracture elements start to reopen. Immediately after these elements start to open, the pressure changes completely and rapidly decreases. This is an indication of the reopening of elements and the increasing permeability of the fracture. The pressure continues to decrease until 11 min, when almost all of the elements on the

fracture surface (except for those on the edge) are open. From that time, the pressure builds until the edge elements closest to the injection well start to open (balloon) and the fracture reaches the propagation stage. At this point, as can be seen from Figure 123, the injection rate decreases, and the pressure at the injection point continues to build with a relatively low slope to keep the fracture just below equilibrium. To observe the effect of injection on the stability of natural fractures near a vertical fracture (Figure 121), the same (vertical) fracture is modeled with two sets of natural fractures. Each natural fracture is a 20 m × 20 m square and is discretized by 16 quadrilateral elements (5 m × 5 m). Each natural fracture is located 10 m from vertical fracture in the X and Z directions (minimum distance = 5 m, maximum distance = 15 m). The minimum and maximum distances of the natural fractures from the main fracture are 5 m and 15 m respectively.

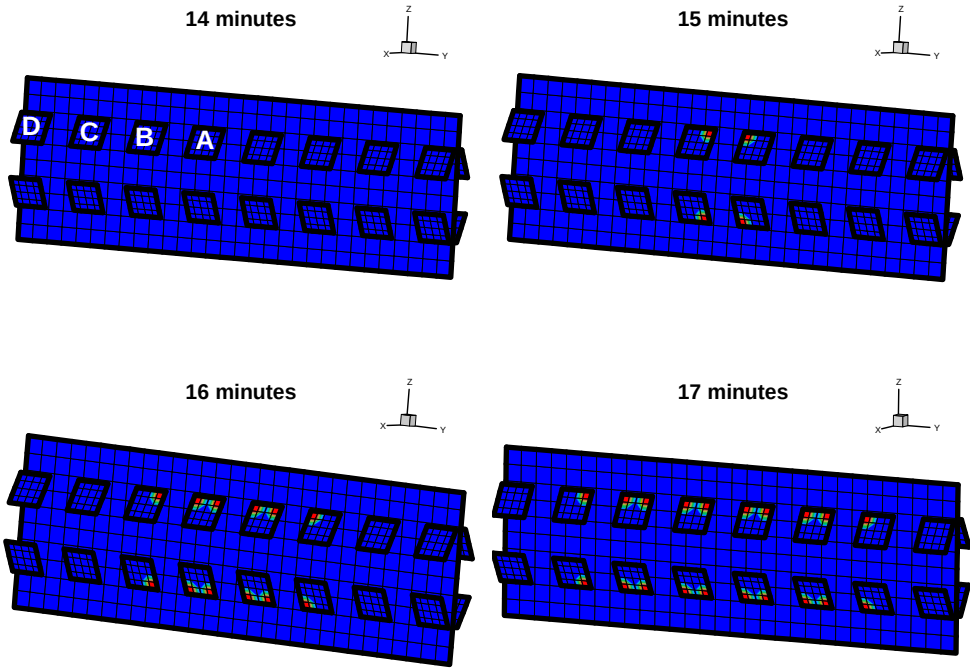

Figure 127. Shear status of natural fractures during different time steps.

The shear status of the fracture system is shown in Figure 127. Fractures A, B, C, and D do not experience permanent slip after 14 min. However, after 15 min of injection into the vertical fracture, fracture A starts to slip from its edges, and the slip continues on the edge of the other natural fractures until it reaches fracture C. After 17 min, Mode II fracture toughness of fracture A exceeds the critical fracture toughness. As a consequence, after 17 min the analysis is stopped automatically.

Shear slip on natural fractures results from the diffusion of pore pressure and the mechanical interaction between natural and vertical fractures. Slip is observed on the edge of each natural fracture. This is because the edge of the natural fracture is very near to the edge of the vertical fracture, where exerted shear due to the vertical fracture opening reaches its maximum value and forces the natural fracture to slip.

The opening of the main fracture is shown in Figure 128. A comparison of this plot with Figure 124 shows that in the presence of natural fractures, the main fracture opens more easily, needing less effort to open completely (the same region opens in less time). This is because of the weakening effect of the natural fractures.

Table 11. Effects of each mechanism on behavior of natural fracture (NF) with particular orientation considered.

Mechanisms	Impact of NF aperture	Impact on effective normal stress of NF	Impact on pressure inside of NF	Impact on shear DD of NF
Stress shadow	Decrease	Increase	Decrease	Increase
Diffusion	Increase	Decrease	Increase	Increase
Fracture dilation	Increase	Increase	Decrease	Increase

The pressure, aperture, normal effective stress, and profile at the midpoint of natural fractures A, B, C, and D are shown in Figure 129 to Figure 132, respectively.

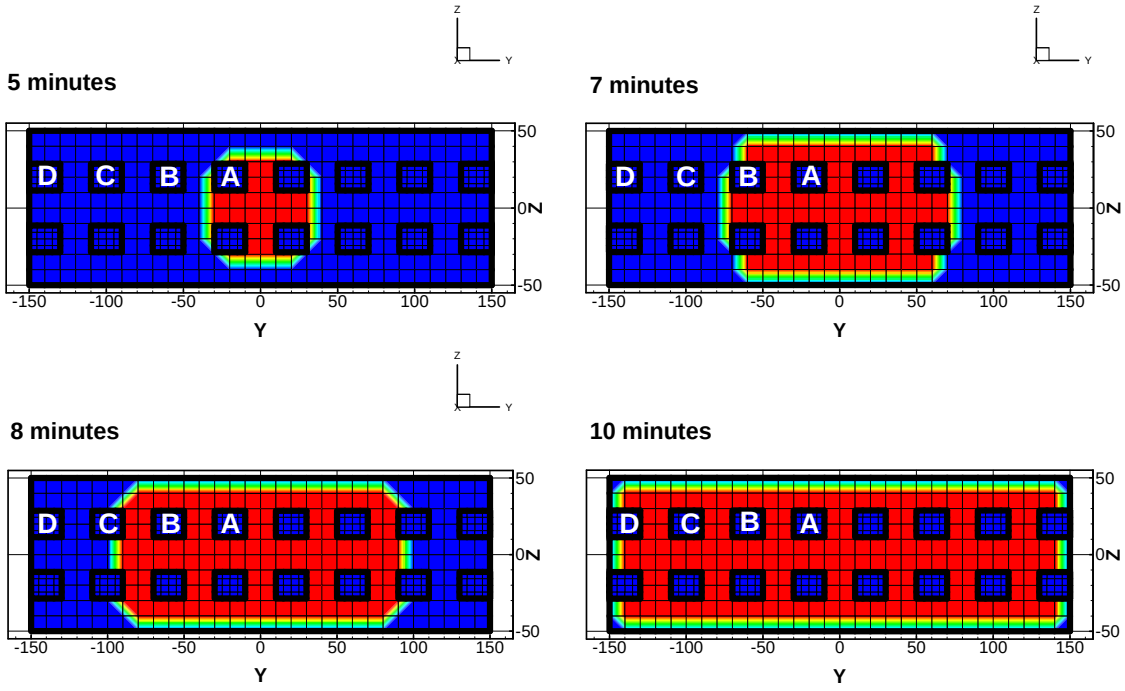

Figure 128. Opening of fracture system with natural fractures in presence.

Three major mechanisms operate simultaneously on the behavior of these natural fractures: (a) the stress shadow due to the opening of the main vertical fracture, (b) pore pressure diffusion due to injection into the main fracture, and (c) dilation of the natural fractures due to far-field stress (shear force exerted on the fracture surface) and induced by the main fracture. The effects of each of these mechanisms on the natural fracture aperture, effective normal stress, pressure, and shear DD are presented in Table 11. For example, because stress shadow, fracture aperture decreases, effective stress, pressure, and shear DD increases. As can be seen from Figure 129 to Figure 132, there are three regions of behavior of natural fractures. In region 1, the behavior of the natural fractures

is initially dominated by the stress shadow of the main fracture. All natural fractures (fracture A, B, C, and D) initially experience a decrease in aperture and an increase in effective stress (the opening of the main fracture closes the natural fractures). Subsequently, the fracture aperture starts to increase as effective stress starts to decrease. This behavior is due to combination of diffusion and dilation effects. In region 1, pressure and total shear DD increase continuously. In region 2, the behavior of natural fractures is dominated by a change in the elements of the main vertical fracture from mechanically closed to mechanically open. Comparing the time for region 2 in natural fracture A with the time when the vertical fracture continues to open (Figure 128), it is clear that after 5 min the region inside of the vertical fracture, in front of fracture A, has changed its status and at the same time there is a sudden change or bump in the behavior of fracture A. Same comparison can be made with the other natural fractures: when the elements of the vertical fracture mechanically open, a sudden change occurs in the behavior of the natural fracture. Thus, region 2 is observed on all natural fractures because of the stress shadow effect. This effect is more intense on fractures A and B than fractures C and D. Region 3 in the behavior of the natural fracture appears when the pore fluid diffusion process takes over the behavior and the fracture aperture, pressure, and shear DD increase while effective stress decreases. In this region, the main fracture has opened completely because of the zero effective stress. As a consequence, the pressure around the natural fractures increases at a higher rate, the fracture aperture and shear DD continue to increase, and effective stress decreases.

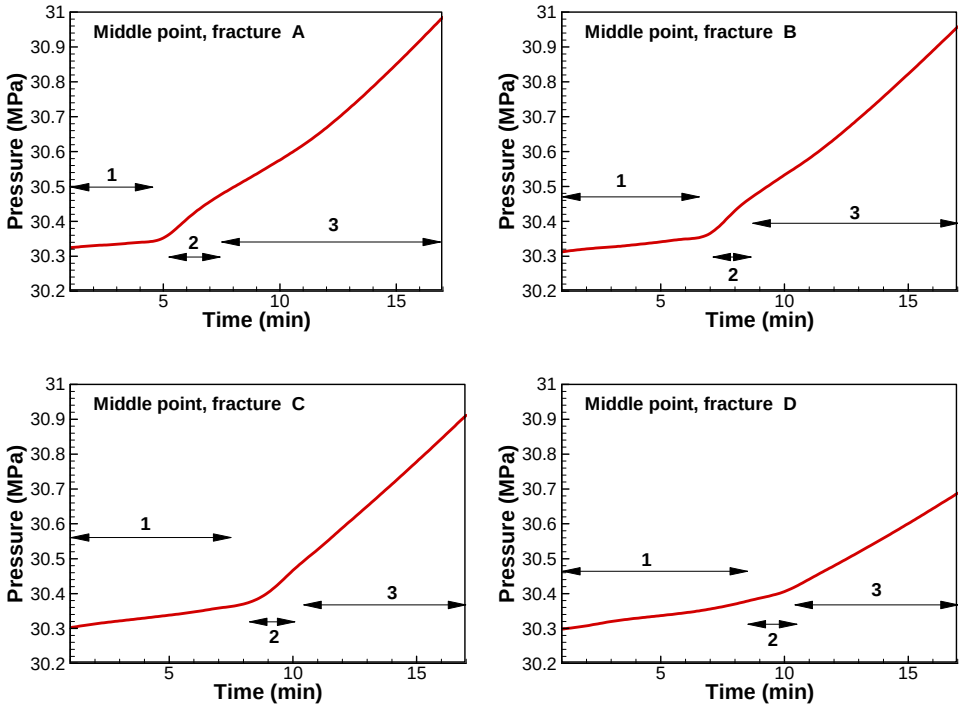

Figure 129. Middle point pressure profile of fracture A, B, C, and D.

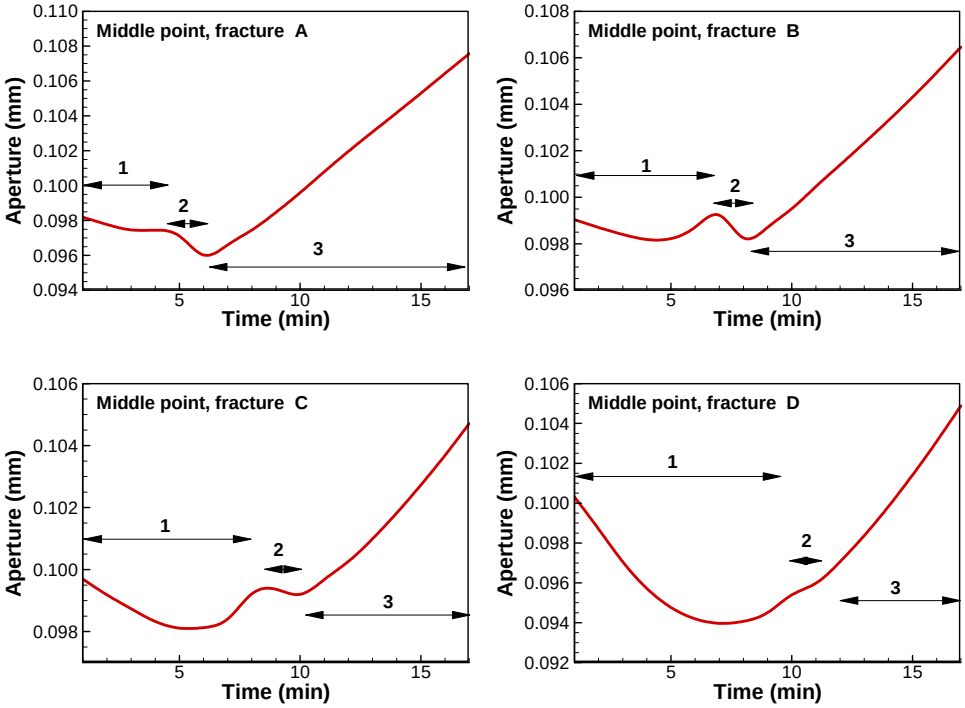

Figure 130. Middle point aperture profile of fracture A, B, C, and D.

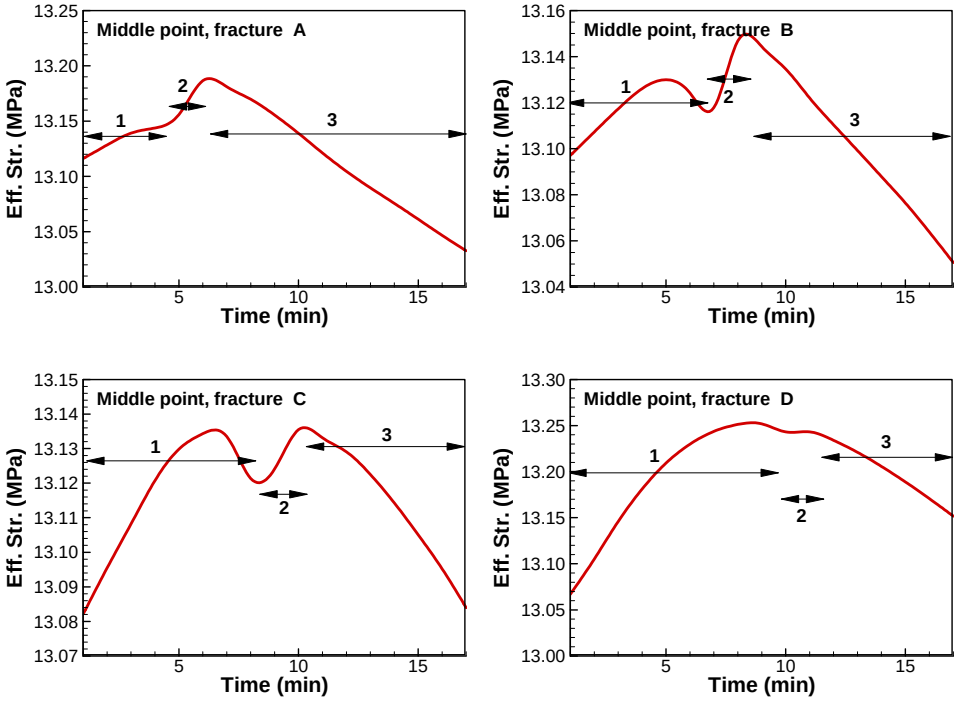

Figure 131. Middle point effective stress profile of fracture A, B, C, and D.

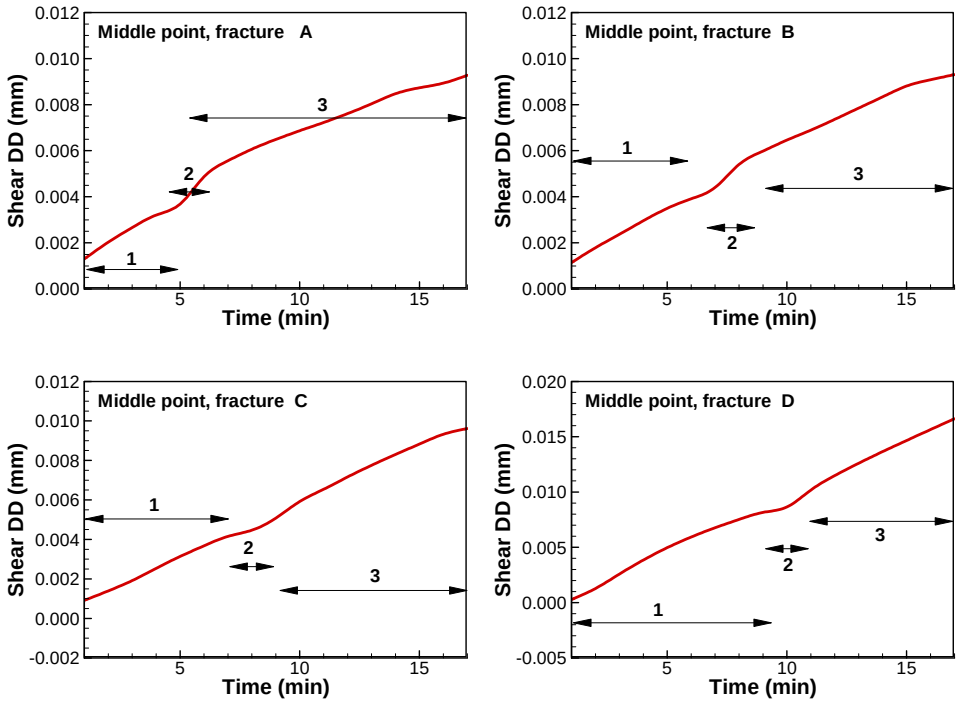

Figure 132. Middle point shear DD profile of fracture A, B, C, and D.

6.6. Hydraulic stimulation of natural fracture network

In this application, the model is used to study the role of fracture deformation, slip, and in situ stress variation on flow path and induced seismicity in a geothermal reservoir consisting of intersecting natural fractures. The simulation models the injection experiment in the Soultz-sous-Forets European Hot Fractured Rock Geothermal Project of Rhine Garben, France, as reported by Bruel [40]. This problem involves a number of circular fractures that were detected in the field and is a good example of the importance of the interactions between natural fracture geometry and the in situ stress field and their impact on the evolution of permeability with injection. The simulations are carried out for a relatively short time so that thermal effects do not fully develop.

Figure 134 shows the problem geometry and the location of the injection and extraction wells. General parameters and in situ stress values are presented in Table 12. The stress state is one of a normal faulting regime. Note that some of the fractures shown in Bruel [40] are not considered here to save computational time (see Figure 133). This problem considers the effect of change in vertical stress on the behavior of the fracture network. Variation in in situ stresses with space is considered as follows:

$$\sigma_z^{in-situ}\left(Pa\right) = -26.5\times10^3 \times z + 80.0\times10^6$$
$$\sigma_x^{in-situ}\left(Pa\right) = 60.0\times10^6$$
$$\sigma_y^{in-situ}\left(Pa\right) = 70.0\times10^6$$

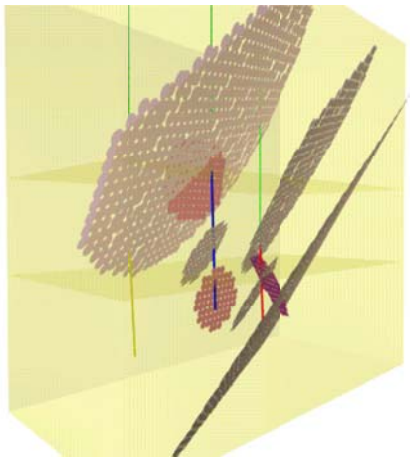

Figure 133. Major faults and main fractures at the wells [40].

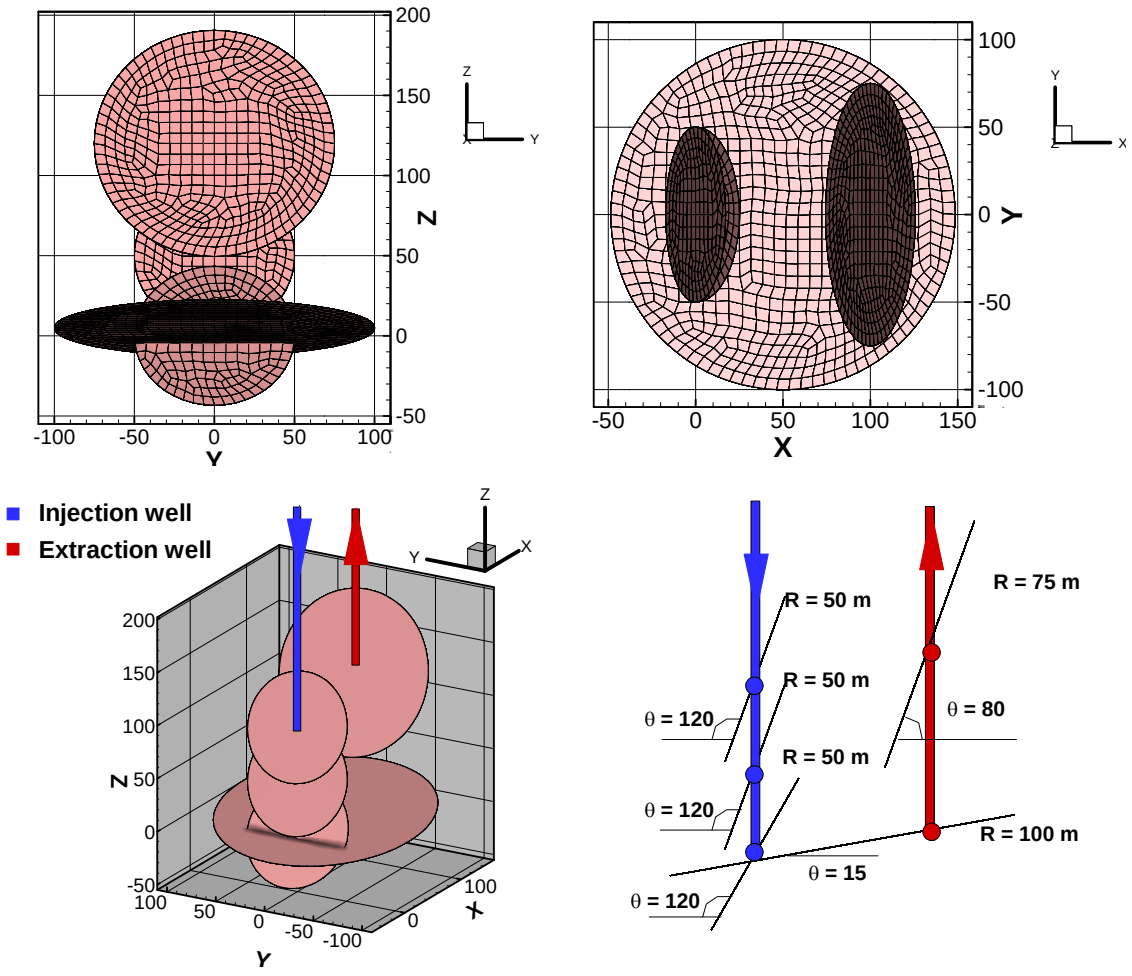

Figure 134. Fracture network geometry and from different view direction.

The circular fractures are discretized using 1814 quadrilateral elements whose behavior is enhanced by the slip-weakening model. The fluid injection and extraction rates are prescribed on the nodes where the well is placed in the mesh. Figure 135 shows the initial distribution of effective and shear stresses on all fractures. Directions 1 and 2 and the fracture number are shown in the figure. Fracture 3 experiences the minimum shear stress along its dip, with a value of approximately 8.5 MPa. This is insufficient to cause slippage on this joint, which has 22 MPa effective normal stress.

Table 12. Multiple fracture modeling parameters.

Shear modulus	(GPa)	10.0 (1450.38 Ksi)
Drained Poisson's ratio	(-)	0.25
Undrained Poisson's ratio	(-)	0.422
Biot coefficient	(-)	1.00
Base permeability	(m^2)	4.00×10^{-17} (40 Micro Darcy)
Initial joint aperture	(m)	4.00×10^{-4} (0.016 inch)
Minimum joint aperture	(m)	1.00×10^{-5}(0.0004 inch)
Stress in "X" direction	(MPa)	60.00(8702 psi)
Stress in "Y" direction	(MPa)	70.00(10153 psi)
Stress in "Z" direction	(MPa)	80.00(11603 psi)
Reservoir pore pressure	(MPa)	45.00(6527 psi)
Rock density	(kg/m^3)	2650.00(1.15 psi/ft)
Fluid density	(kg/m^3)	1000.00(0.433 psi/ft)
Fluid viscosity	($N.s/m^2$)	1.00×10^{-3}(1.0 cp)
Injection rate (Constant)	(lit/sec)	1.80(0.675 bbl/min)
Extraction rate (Constant)	(lit/sec)	1.50(0.57 bbl/min)
Peak Friction Angle		35°
Residual Friction Angle		25°
Peak Cohesion	(MPa)	0.00 (0.00 psi)
Residual Cohesion	(MPa)	0.00 (0.00 psi)
Dilation Angle		5°
Maximum Aperture due to Dilation	(m)	5.00×10^{-4}(0.02 inch)
Critical value for Shear DD, D*	(m)	1.00×10^{-3}(0.04 inch)
Linear normal stiffness	(MPa/m)	2.00×10^{4}(9350 Ksi/ft)
Linear shear stiffness	(MPa/m)	2.00×10^{4}(9350 Ksi/ft)
Mode I critical fracture toughness	($MPa.m^{0.5}$)	1.50(1365 $psi.in^{0.5}$)
Mode II critical fracture toughness	($MPa.m^{0.5}$)	2.00(1820 $psi.in^{0.5}$)

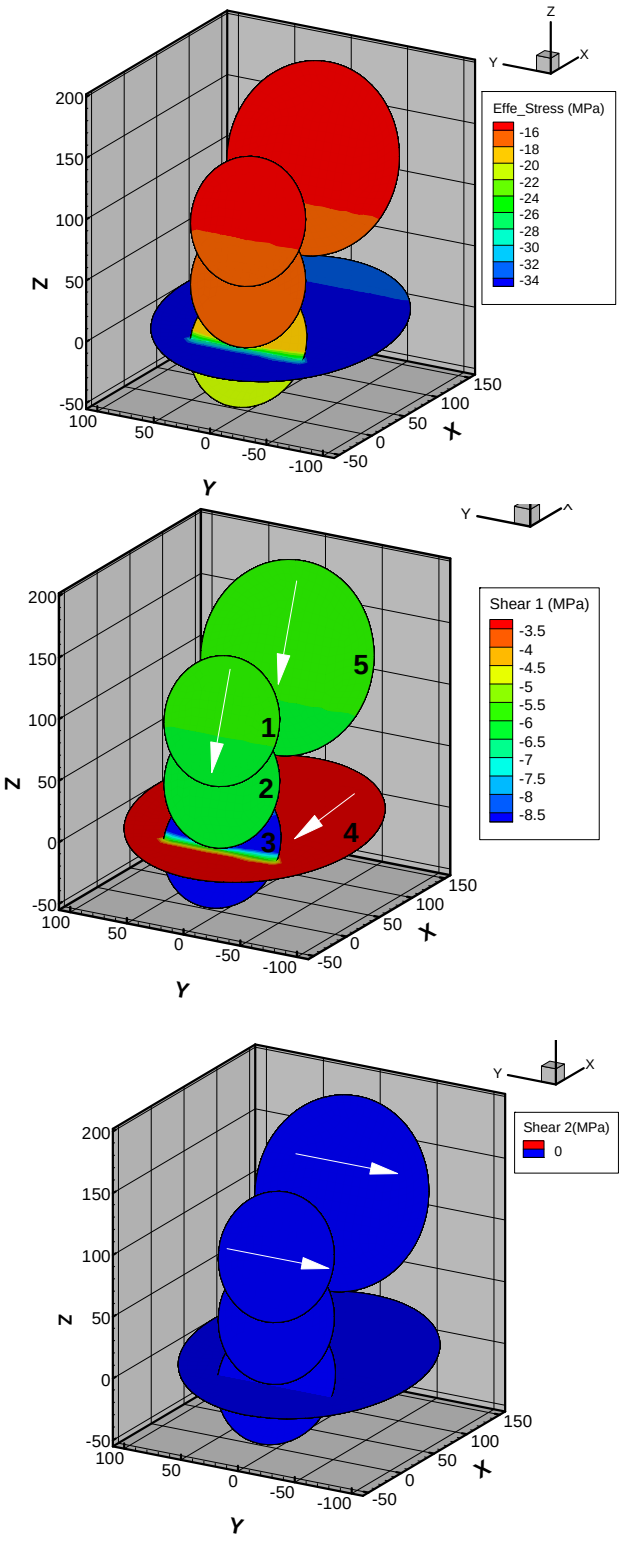

Figure 135. Initial shear and effective stresses on fractures surface.

To better understand the hydromechanical behavior and coupled processes that develop during a short stimulation in such a system, and to assess the possibility of permanent slip, consider 11 h of injection into fractures 1, 2, and 3 at a constant rate and extraction from fractures 4 and 5 (see Figure 134). Water is injected at a rate of 1.8 L/s and extracted at a constant rate of 1.5 L/s. Half an hour is chosen for time step for the analysis. Figure 136 shows the shear status of all elements during 11 h of the injection/extraction process.

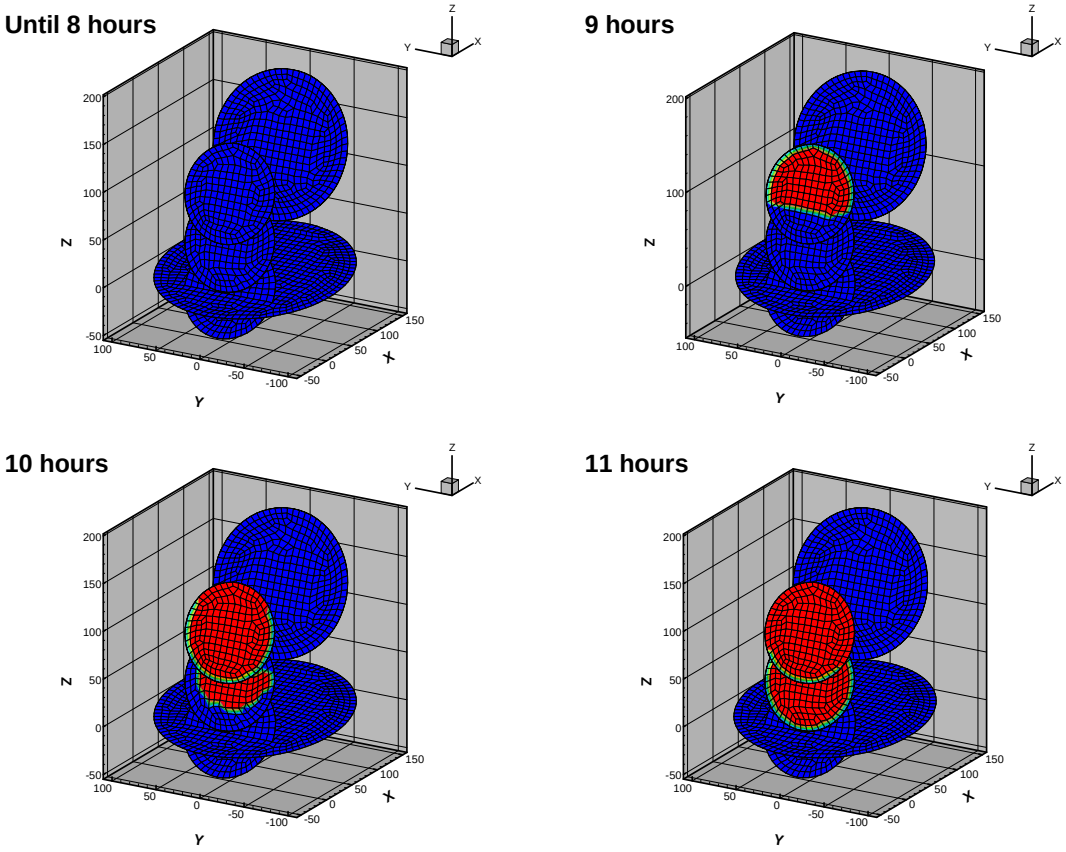

Figure 136. Shear status of elements during injection/extraction with slip weakening consideration.

From Figure 136 it can be seen that after 9 h, more than half of fracture 1 (with an area of 4710 m^2) experiences permanent slip of approximately 0.51 mm. Therefore, based on McGarr et al. [142] and Hanks and Kanamori [143], the magnitude of the seismic moment of the slip area is about 2.4×10^{18} dyne-cm, and the magnitude of earthquakes generated would be about 1.55. After 10 h, an area of 10995 m^2 would experience an average slip of 4 mm. This creates a seismic moment of about 4.38×10^{19} dyne-cm, and the earthquake generated would have a magnitude of nearly 2.4. In Figure 137 shear DD is shown after 9 and 10 h.

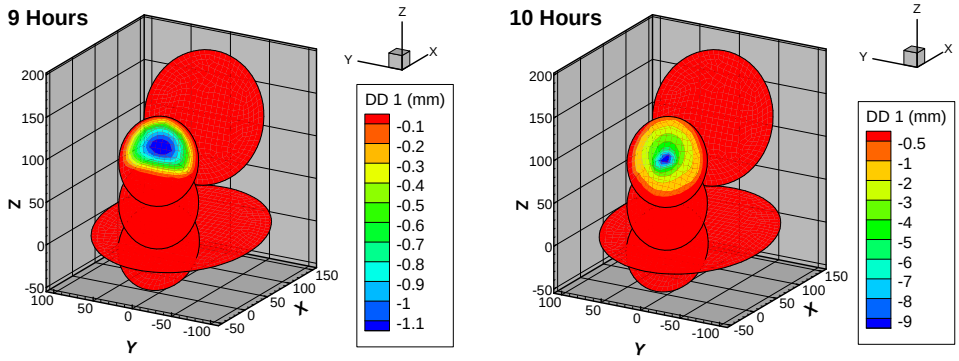

Figure 137. Shear displacement after 9 and 10 hours of injection/extraction.

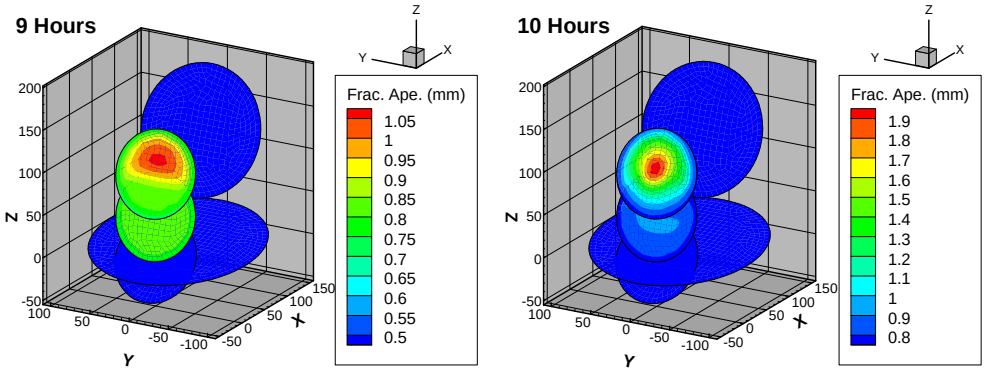

Figure 138. Fracture aperture after 9 and 10 hours of injection/extraction.

It can be seen from Figure 137 that the maximum shear DD occurs in the middle of slipped area in fracture 1. In addition, fracture 2 experiences permanent slip, but because of the minimum effective stress on fracture 1, it experiences more slip.

The fracture aperture is shown in Figure 138. It is clear from this figure that slip has a large effect on the distribution of fracture aperture. The apertures of fractures 1 and 2 are both in the range of 0.7–1.05 mm after 9 h and 0.9–1.9 mm after 10 h. In addition, the distribution of the fracture aperture is nearly symmetric about the injection point. This is because the two fractures partly overlap, and the opening of one fracture induces some closure on the other. The upper part of fracture 1 is less confined than the lower part, and the reverse is true for fracture 2. This confinement determines the performance of the fractures until the entire fracture experiences permanent slip. After all of fracture 1 experiences permanent slip, its aperture will be larger in the middle of the fracture. The aperture of fractures 4 and 5 is in the range of 0.2–0.4 mm, indicating that less flow occurs in these two fractures compared to fractures 1 and 2. Because of contact between fractures 3 and 4, the aperture is smaller near the intersection than in other parts. Moreover, fractures 4 and 5 have a smaller aperture because of fluid is being extracted from them.

The propagation status of the fractures is shown in Figure 139. After 9 h fracture 1 is near propagation in Mode I (without being near the critical state for Mode II propagation). However, after 10 h, because of the increased slipped area in fracture 1, the fracture is likely to propagate in mixed opening and shearing mode.

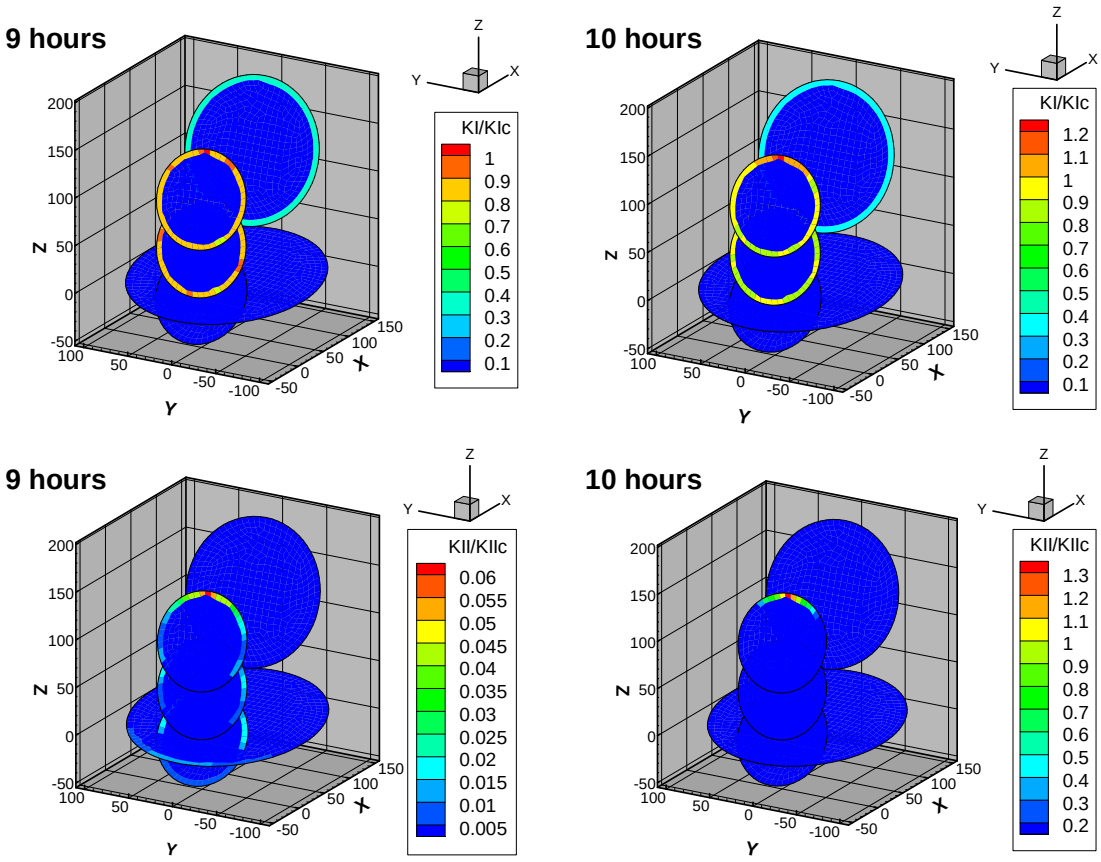

Figure 139. Propagation status of fractures in mode I and mode II after 9 and 10 hours of injection/extraction.

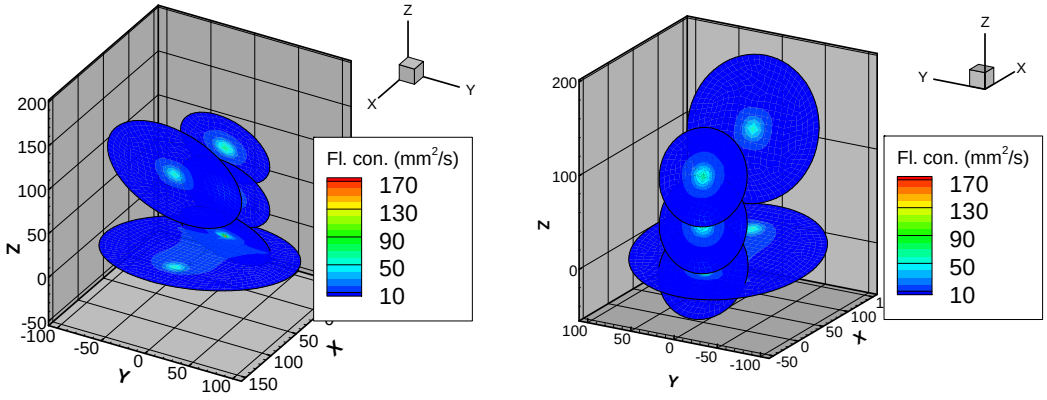

Figure 140. Fluid content inside of fractures after 10 hours.

Figure 140 shows the fluid content of all fractures after 10 h. Multiplying the fluid content by the fracture aperture reveals the total amount of fluid inside the fracture. Fracture 3 and 4 show a connected path, as is expected, and fractures 1, 2, and 5 show similar amounts of fluid.

6.7. Response of irregular fracture in enhanced geothermal reservoir

The numerical procedures developed here (with slip weakening) can be used to analyze fluid injection/extraction into an irregularly shaped fracture when it intersects with natural fractures. Figure 141 shows such a system. All fractures are discretized with 1483 nodes and 1366 elements. All fractures are planar. The essential properties of the media and fractures are presented in Table 13.

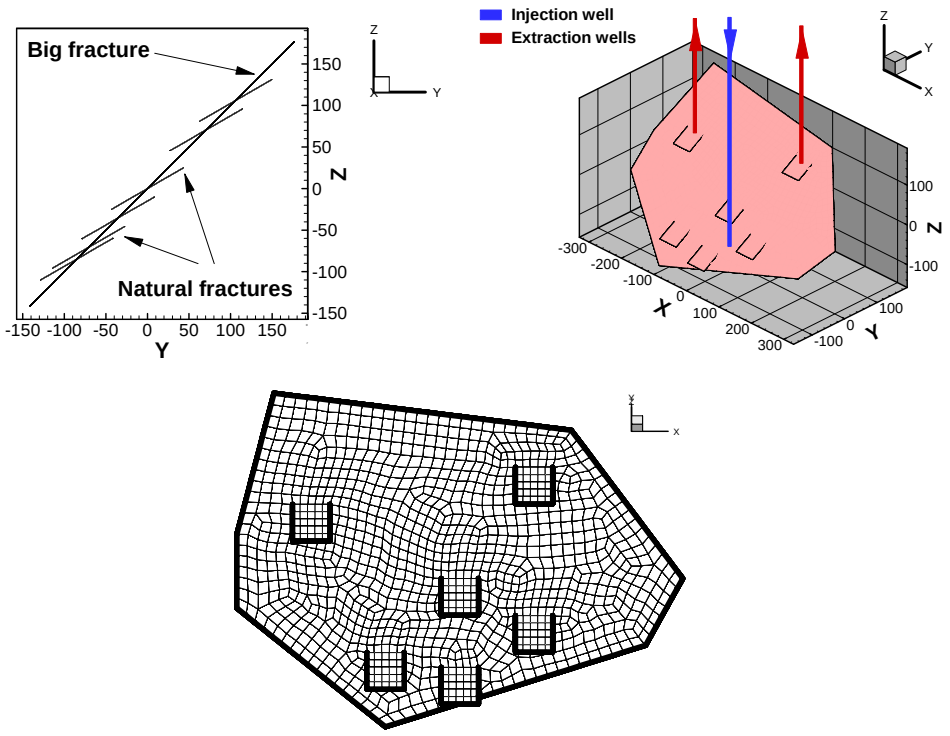

Figure 141. Discretized irregular fracture, position of injection and extraction wells, natural fractures are 50 m x 100 m and oriented 30° from Y direction.

Table 13. Hydro-thermo-mechanical properties of rock and fracture.

Shear modulus	(GPa)	15.0 (1450.38 Ksi)
Drained Poisson's ratio	(-)	0.25
Undrained Poisson's ratio	(-)	0.27
Biot coefficient	(-)	0.47
Base permeability	(m^2)	1.00×10^{-18} (1 Micro Darcy)
Porosity	(-)	0.05
Initial joint aperture	(m)	1.00×10^{-4} (0.004 inch)
Minimum joint aperture	(m)	5.00×10^{-5}(0.002 inch)
Stress in "X" direction	(MPa)	55.88(8105 psi)
Stress in "Y" direction	(MPa)	45.81(6644 psi)
Stress in "Z" direction	(MPa)	65.13(9446 psi)
Reservoir pore pressure	(MPa)	17.40(2523 psi)
Rock density	(kg/m^3)	2650.00(1.15 psi/ft.)
Fluid density	(kg/m^3)	1000.00(0.433 psi/ft.)
Fluid viscosity	($N.s/m^2$)	1.00×10^{-3}(1.0 cp)
Injection rate (Constant)	(lit/sec)	40.0(15.1 bbl./min)
Extraction rate (Constant)	(lit/sec)	-(- bbl./min)
Peak Friction Angle		30°
Residual Friction Angle		26°
Peak Cohesion	(MPa)	0.70 (101.00 psi)
Residual Cohesion	(MPa)	0.00 (0.00 psi)
Dilation Angle		3°
Maximum Aperture due to Dilation	(m)	5.00×10^{-4}(0.02 inch)
Critical value for Shear DD, D*	(m)	1.00×10^{-3}(0.04 inch)
Linear normal stiffness	(MPa/m)	1.00×10^{4}(4675 Ksi/ft)
Linear shear stiffness	(MPa/m)	1.00×10^{4}(4675 Ksi/ft)
Mode I critical fracture toughness	($MPa.m^{0.5}$)	1.50(1365 $psi.in^{0.5}$)
Mode II critical fracture toughness	($MPa.m^{0.5}$)	2.00(1820 $psi.in^{0.5}$)
Rock thermal conductivity	(W/m/K)	2.90
Fluid thermal conductivity	(W/m/K)	0.60
Specific heat capacity of rock	(J/kg/K)	800.00
Specific heat capacity of fluid	(J/kg/K)	4200.00
Linear thermal expansion of rock	(1/K)	8.00×10^{-6}
Linear thermal expansion of fluid	(1/K)	1.00×10^{-4}
Initial background temperature	(K)	420.0
Injected fluid temperature	(K)	300.0

Heat extraction involves an injection well with a constant flow rate of 40 L/s (15 bbl/min) and two extraction wells with a constant down-hole pressure at the initial

reservoir pressure of 17.4 MPa (2523 psi). This example considers the behavior of the fracture system during the first 2 months of the thermoporoelastic injection/extraction process.

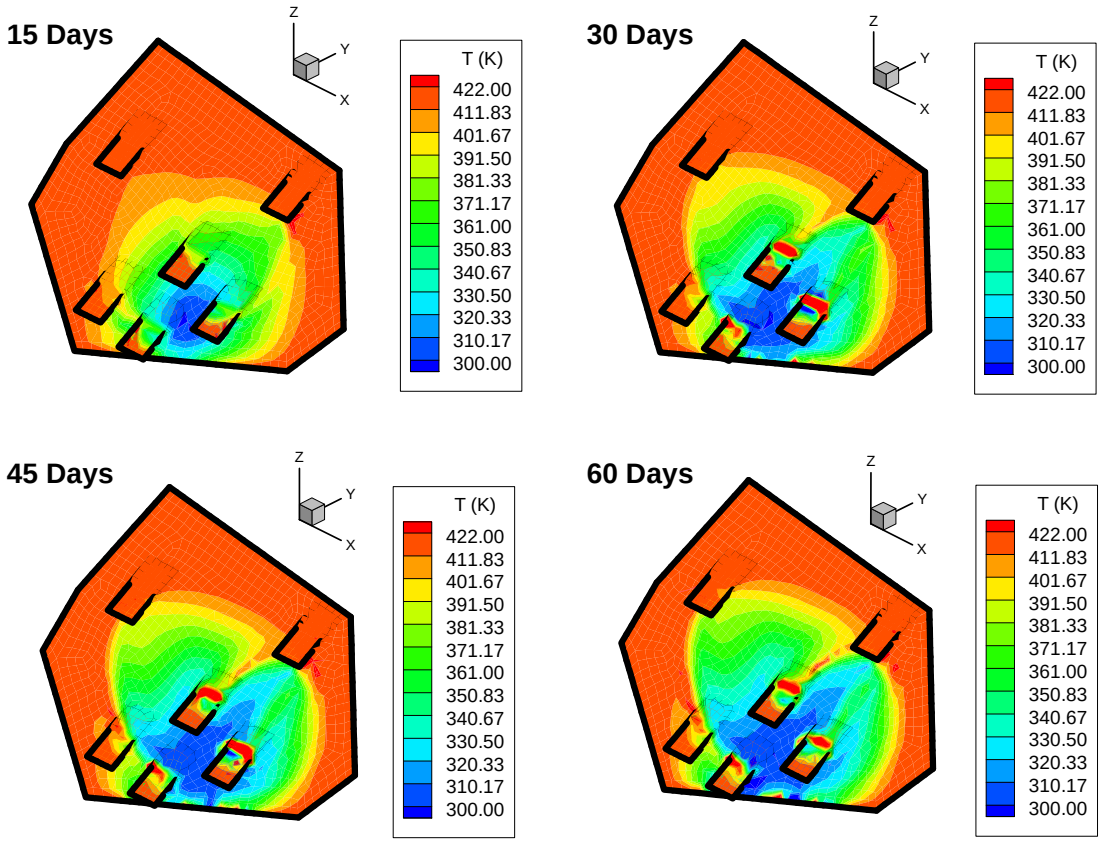

Figure 142. Temperature distribution in the fracture during two months of operation.

The temperature distribution of the system during these first 2 months is shown in Figure 142. As is clear from the figure, as time passes, the cold region extends toward the closer extraction well by passing through the natural fractures. Moreover, over the 2 months of operation, almost all regions between the natural fractures around the injection well contribute to heat depletion.

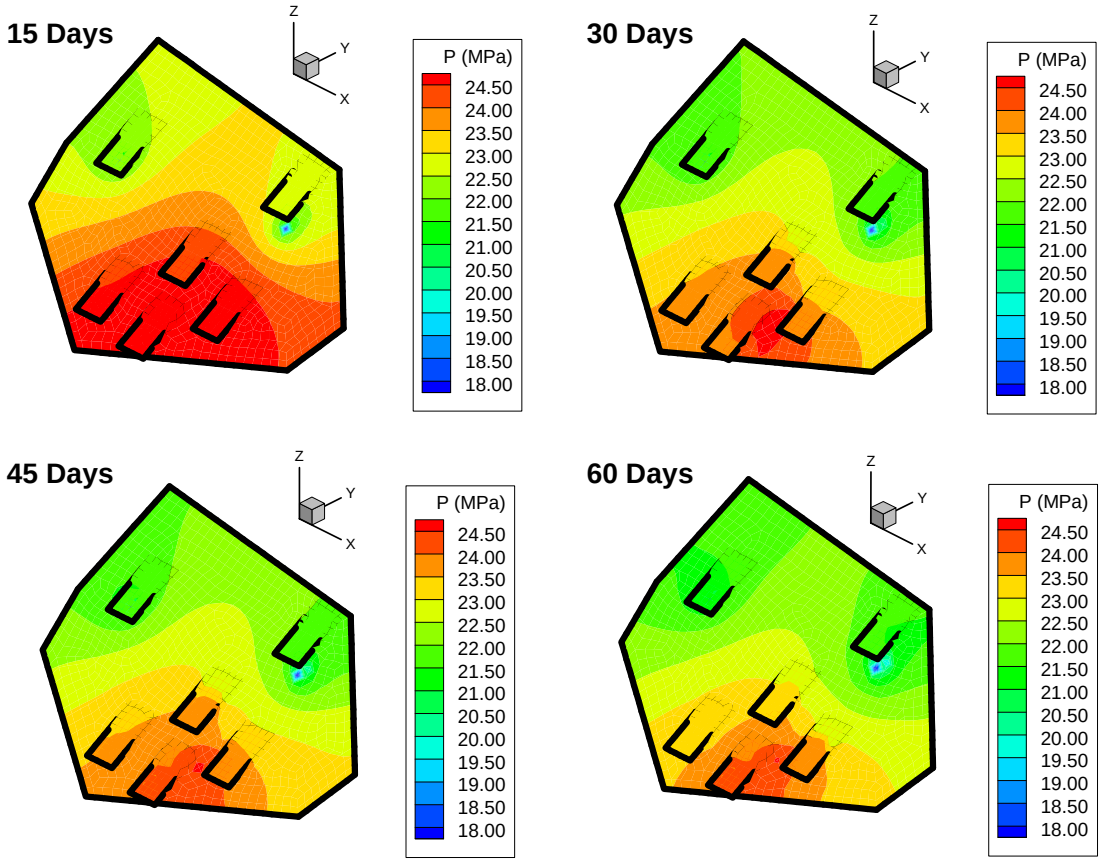

Figure 143. Pressure distribution in the system during first two months.

Pressure and effective normal stress on the system are shown in Figure 143 and Figure 144, respectively. It should not be surprising that the pressure inside the fracture decreases over time. This is mainly because of the cooling process and dilation effect. When regions around the injection well begins to cool, the fracture aperture increases and pressure decreases. Moreover, as time passes shear DD on the fracture surface increases and as a consequence the fracture aperture increases. Also effective stress increases. This effect is due to dilation.

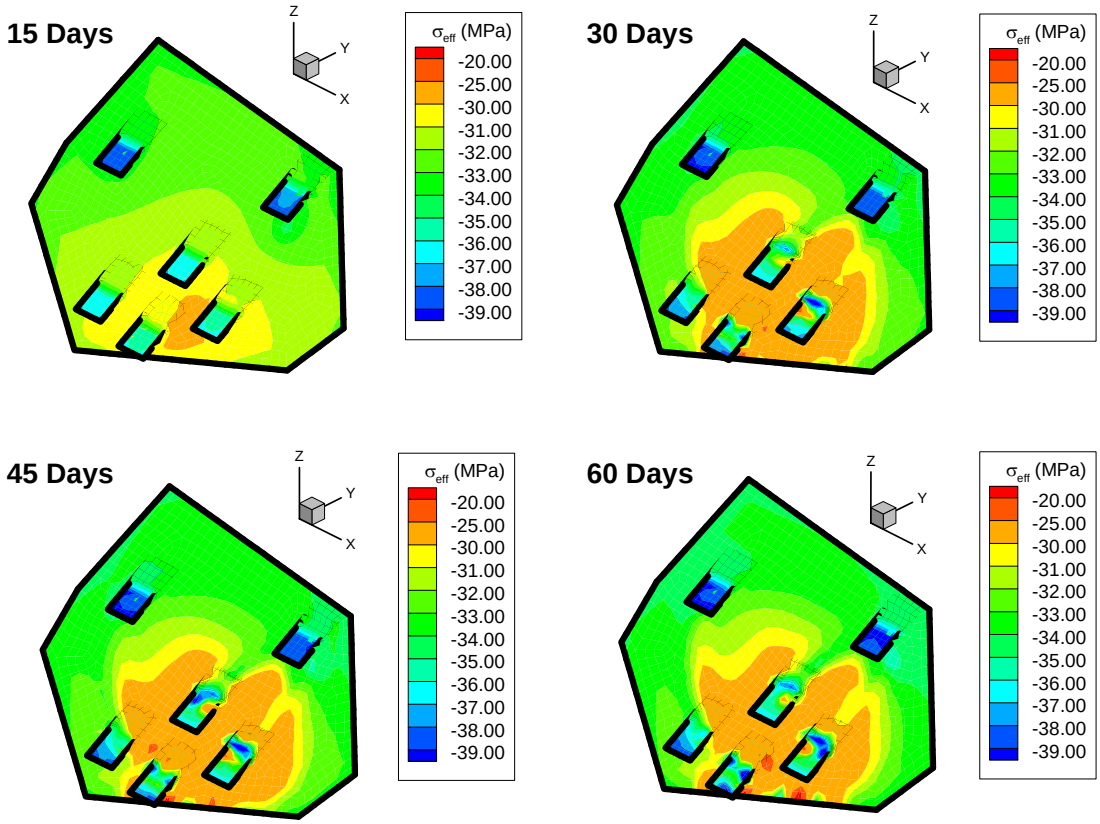

Figure 144. Effective normal stress in the system.

Shear DD and the shear status of all elements are shown in Figure 145 and Figure 146, respectively. After 15 days shear displacement suddenly increases 100 times. This indicates that there should be some permanent shear slip at this time. Figure 146 and Figure 145 show the slipped elements at different times. After 30 days elements around fractures 1 and 2 (top right plot in Figure 146) experience permanent slip. As time passes, the number of slipped elements increases because of cooling and decreasing effective stress on the fracture surface.

The distribution of the fracture aperture is shown in Figure 147. As time passes, the fracture aperture increases. This is again due to dilation and cooling effects. The fracture opening is more around the injection well and less in regions behind the extraction wells because of the influence of thermal stresses.

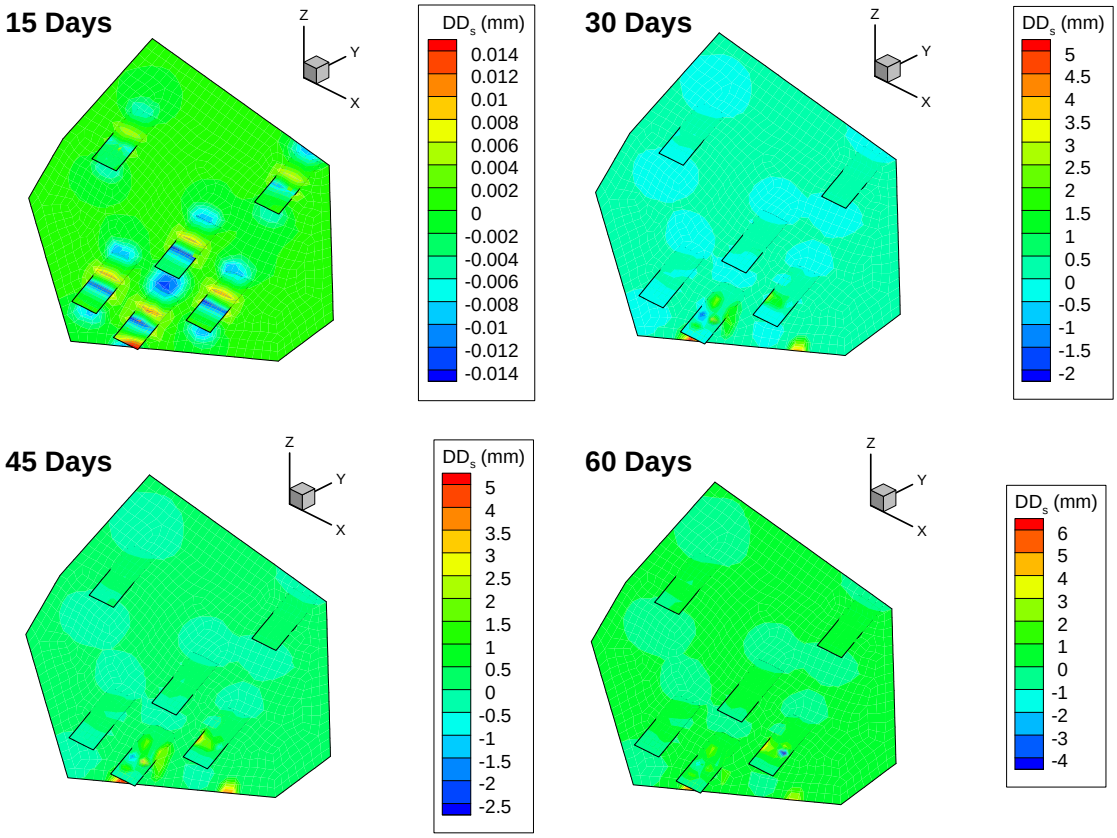

Figure 145. Shear displacement discontinuity.

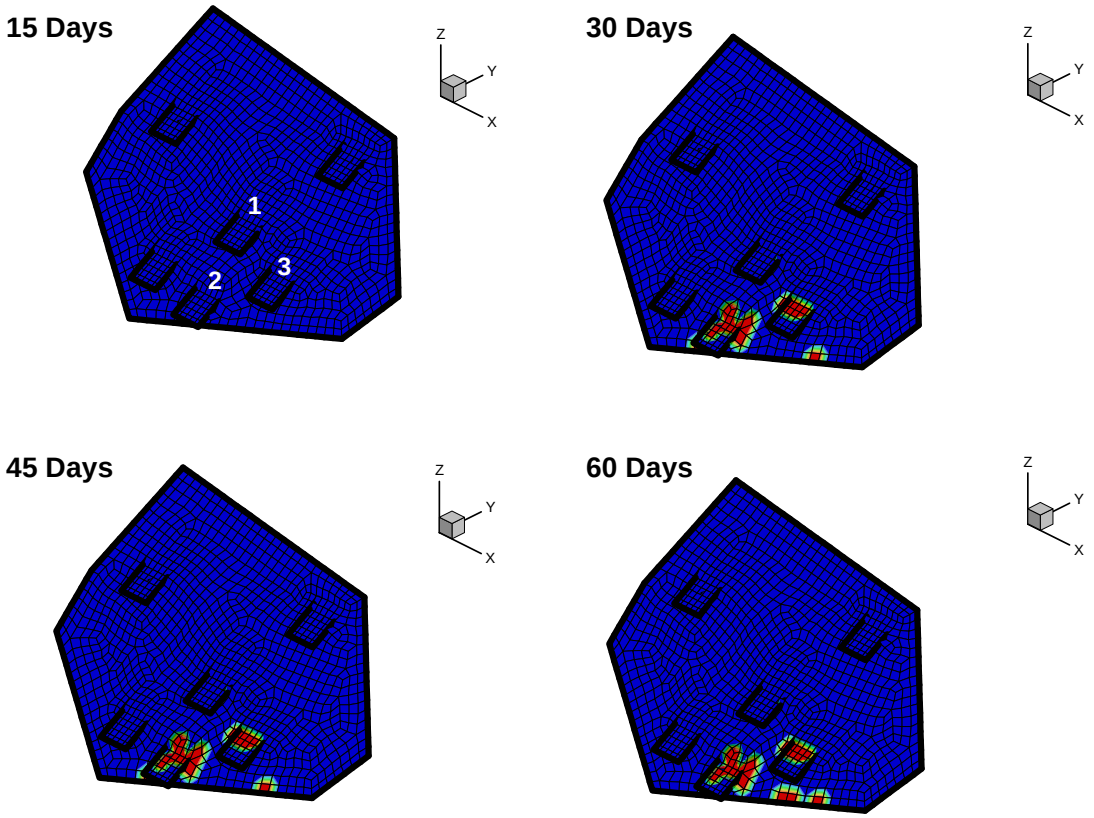

Figure 146. Shear status of elements. Red elements have undergone permanent slip.

6.8. Fracturing pressure in horizontal wellbore with weakening plane

This example shows the ability of method to predict wellbore pressure that causes propagation of a fracture that intersects a wellbore. This is of interest in circulation loss analysis. The simulation deals with the distribution of isothermal stress around the system of a slanted horizontal wellbore and fracture. Isothermal analysis is used because two short time scales of drilling procedure are considered: 10 min and 4 h.

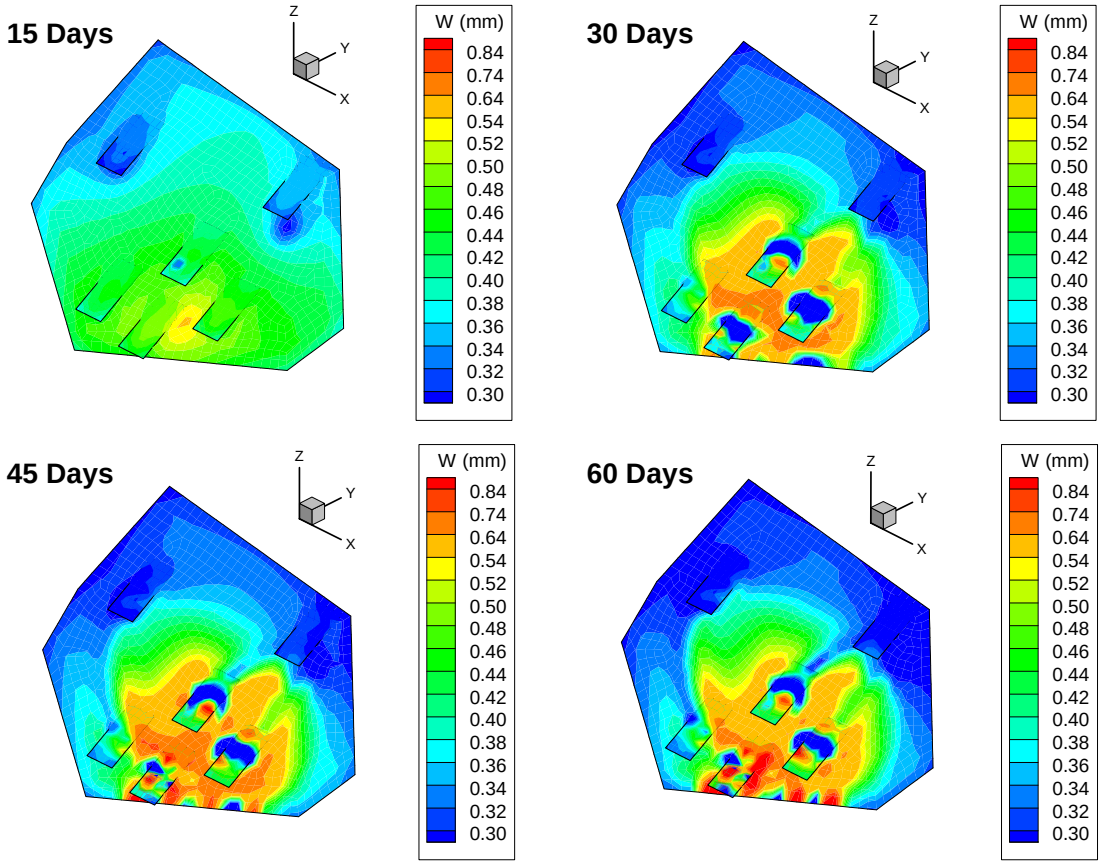

Figure 147. Fracture aperture distribution in the fracture system.

The wellbore and fracture geometry is shown in Figure 148. The wellbore is inclined from a horizontal line (X axis) at a 7° deviation. The wellbore diameter is 5 in (0.127 m) and about 2 m of its length is modeled. The fracture is a square shape of 0.5 m length, and the wellbore passes through the middle of it. The fracture deviates 60° from the horizontal line. In the model, the fracture is located in the middle of the wellbore. The wellbore and fracture system is discretized with 2784 nodes and 2736 quadrilateral elements. Note that DD element is used for the fracture and fictitious element is used for the wellbore. Rock properties and the stress state are presented at Table 14. The modeled

fracture is mechanically open and hydraulically open and experiences the same pressure as exists inside the wellbore (this is the worst case scenario compared to mechanically closed, hydraulically open).

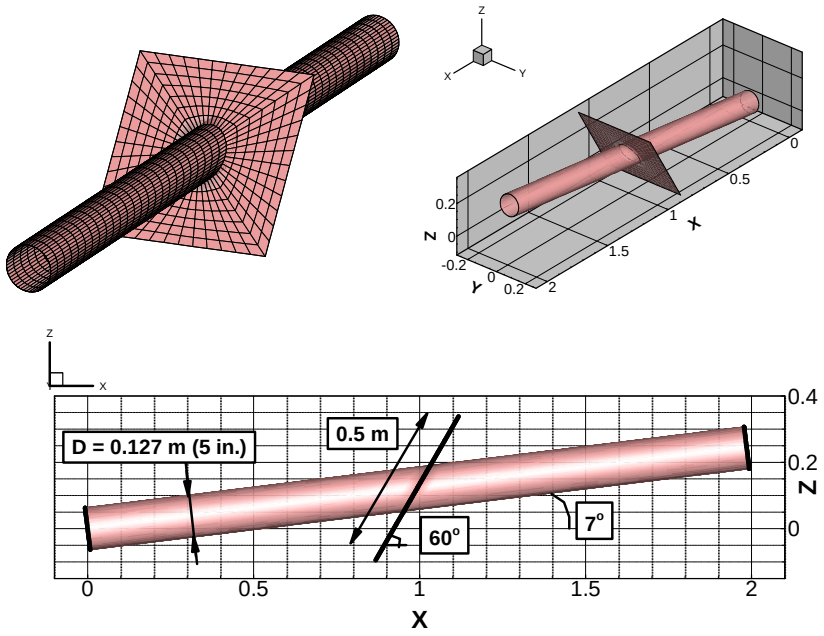

Figure 148. Wellbore and fracture geometry and mesh.

The behavior is studied over a very short time. At a low pressure inside the fracture (25 MPa, less than sh_{min}), the increased pore pressure around the system induces a back stress that tends to close the fracture around the wellbore; therefore, the system shows less criticality with respect to Mode I propagation of the fracture. For Mode II behavior, the pore pressure could change the shear status of the fracture. In fact, the short time analysis shows the shear mode propagation potential on the fracture.

Table 14. Necessary parameters for wellbore/fracture modeling.

Shear modulus	(GPa)	15.0 (2175 Ksi)
Drained Poisson's ratio	(-)	0.25
Undrained Poisson's ratio	(-)	0.27
Biot coefficient	(-)	0.47
Base permeability	(m^2)	1.00×10^{-18} (1 Micro Darcy)
Initial joint aperture	(m)	4.00×10^{-4} (0.004 inch)
Minimum joint aperture	(m)	1.00×10^{-5} (0.002 inch)
Stress in "x" direction	(MPa)	45.81 (6645 psi)
Stress in "y" direction	(MPa)	55.88 (8105 psi)
Stress in "z" direction	(MPa)	65.13 (9446 psi)
Initial pore pressure	(MPa)	17.40 (2523 psi)
Pressure inside of well	(MPa)	25.00 (3625 psi)
Porosity	(-)	0.05
Fluid density	(kg/m^3)	1000.00 (0.433 psi/ft.)
Fluid viscosity	($N.s/m^2$)	1.00×10^{-3} (1.0 cp)
Rock density	(kg/m^3)	2650.00 (1.15 psi/ft.)
Mode I critical fracture toughness	($MPa.m^{0.5}$)	1.50 (1365 $psi.in^{0.5}$)
Mode II critical fracture toughness	($MPa.m^{0.5}$)	2.00 (1820 $psi.in^{0.5}$)

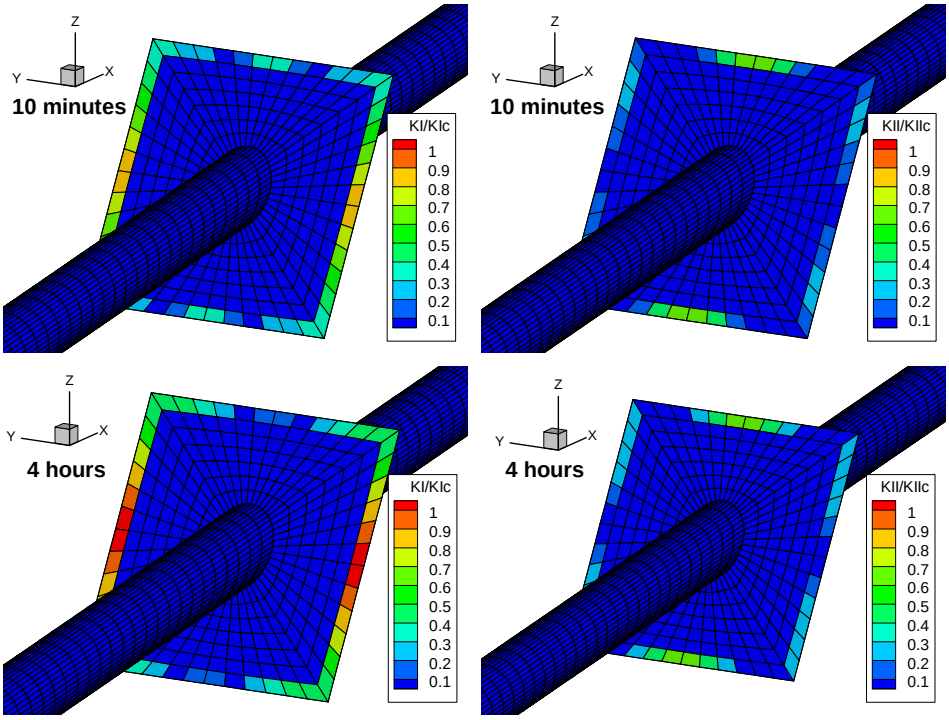

Figure 149. Stress intensity factor of natural fracture, Mode I and II.

Figure 149 shows the propagation status of the intersected fracture after 10 min and 4 h. The fracture tends to propagate in Mode I; the Mode II SIF is less critical than Mode I. As time passes, the Mode I SIF increases, and at 4 h the fracture propagates in the horizontal Y direction because of the redistribution of stress around the wellbore. This redistribution of stress has a significant effect on the behavior of the fracture, especially for fractures that are near wellbore. The distribution of stress on and around the fracture surface is shown in Figure 150.

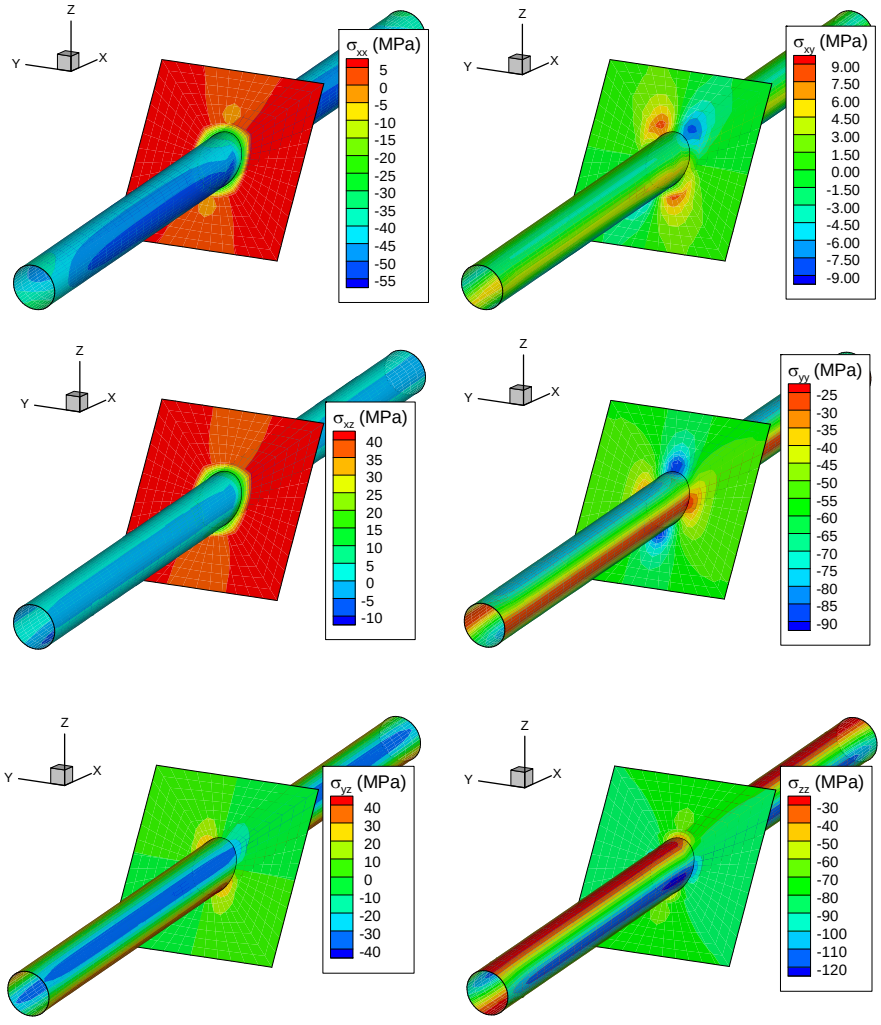

Figure 150. Stress distribution around well.

7. SUMMARY

7.1. Summary and conclusions

A 3D transient indirect boundary element model was developed in the current study to study the coupled thermoporoelastic behavior of fractures and wellbores in hydrocarbon/geothermal reservoirs. The technique was based on linear thermoporoelastic theory and combines the boundary element and finite element methods. The model was tested and verified using a variety of examples for which analytical solutions were presented previously (Section 4). A number of applications related to hydraulic fracturing, interactions between natural and hydraulic fractures, and wellbore analysis were described.

The boundary element modeling effort combined the DD and FS methods to enable the modeling of intersecting wellbores and fractures under thermo-hydro-mechanical loading.

The poroelastic FS approach was verified using the Cryer problem of a sphere of rock removed from a reservoir conditions. The numerical results agreed very well with the analytical solution and showed the fully coupled poroelastic behavior. Moreover, a wellbore under nonhydrostatic stress loading was studied. The numerical results and the analytical results showed good agreement over a short time interval. However, the two solutions diverged after a longer time because of the intrinsic difference between 3D problems and a plane strain solution (the existence of the third dimension).

The impact of thermal effects on wellbore stress analysis was also considered. As expected, the FS method showed that cooling reduces pore pressure around a borehole.

In addition, cooling increases the potential for fracturing due to tangential tensile stress. The numerical results for the thermoporoelastic wellbore agreed very well with the analytical solutions for a short time period but diverged from a long time period.

The DD approach was tested for the behavior of a penny-shape crack under conditions of poroelastic and thermoporoelastic loading. Crack openings and SIFs were calculated and compared with the analytical model. The analytical and numerical solutions were also compared, and it was found that the numerical results represented the behavior of the crack with sufficient accuracy.

The DD method was combined with the finite element method for fluid flow and used to investigate nonisothermal injection into a fracture. The model captured the modification/redirection of stress around a single pressurized hydraulic fracture. Moreover, it showed that modified stress causes failure around the fracture tip which generally covers a bigger area than the fracture itself and results in an overestimation of the stimulated reservoir volume.

The pressurization of two parallel fractures was also studied using the method developed here. As expected, it was found that the distance between hydraulic fractures is the most important factor in modifying the stress state and consequently impacting the extent of the failure region around the fracture. It was also observed that the opening of a fracture induces shear stresses on the other fracture. The SIF for pressurized cracks was calculated for Mode I and Mode II, and it was shown that when the distance between hydraulic fractures increases, the Mode I SIF also increases. However, the Mode SIF decreases.

The fluid flow/fracture deformation model was then used to analyze a huff-and-puff test in geothermal reservoirs. Both down-hole pressure and temperature were calculated and compared with field data. The model results were very sensitive to the joint model. When stress state on a fracture or discontinuity is near the critical state, the constitutive behavior is very important and nonlinear behavior should be considered.

The post shear-failure behavior of joints was studied by examining the slip of a box on a free surface. Also, the permeability enhancement of a single fracture under in situ shear stress due to post-shear failure behavior was studied. It was shown that injection into an inclined fracture can increase so rapidly that the injection rate no longer sufficient to sustain the pressure, and the pressure decreases.

Interactions of natural fractures and a hydraulic fracture were also studied. It was shown that injection into a natural fracture resulted in a gradual change in status from mechanically closed to mechanically open. This change in status governs the hydromechanical behavior of fractures. This was shown that the most important mechanisms that define the behavior of natural fractures are fracture dilation, diffusion of fracture/pore fluid, and also stress shadow of fractures on one another.

Finally, the model was used to study the role of fracture deformation, slip, and variation in in situ stress on flow path and induced seismicity in a geothermal reservoir with parallel and intersecting circular fractures. The magnitudes of micro earthquakes that could potentially occur as a result of the injection/production processes were estimated.

7.2. Contributions

This thesis makes the following contributions to applied research on fractures and wellbores:

1. Variable injection/extraction rates were modeled. In previous versions of the model, it was assumed that the injection/extraction rate was constant. In the current model this assumption was not made.
2. Thermo-hydro-mechanical interactions of parallel/intersecting fractures were simulated. In previous models, only one planar fracture was simulated. The current model was generalized and expanded to enable the modeling of non-planar parallel/intersecting fractures of any shape.
3. Fully coupled thermoporoelastic formulation was considered. Previous version of the model considered partially coupling formulations, in which pressure did not change with temperature. However, in the current study the frame was generalized to include the change in pressure due to the change in temperature.
4. Three-dimensional FS technique was coupled with DD. This combination of indirect boundary element methods enabled the modeling of interactions of fractures and wellbores during wellbore pressurization.
5. Convection heat transfer inside of fractures was considered along with diffusion heat transfer. In previous models only advection heat transfer was considered. However, in the current study complete advection-diffusion heat transfer was considered and discretized using a

discontinuous finite element method (the streamline upwind Petrov–Galerkin method).

6. The computer code was parallelized with shared memory structure programming (OpenMP); because of the very long run time, the FORTRAN computer code was parallelized with almost 90% efficiency.

7.3. Future research

In the current study, nonisothermal, single-phase, incompressible fluid injection/extraction and fully coupled hydro-thermo-mechanical physics was used to study the behavior of fractures and wellbores. A number of improvements can be recommended for future studies. First, fracture propagation could be implemented. Second, researchers should model compressible fluid and/or multi-phase flow in the reservoir due to hydro-thermal stimulation of hydrocarbon/geothermal reservoirs and/or take into account buoyancy effects due to the existing different fluid temperature inside the fracture. Finally, using fast multipole boundary element techniques and distributed memory parallel programming would enhance efficiency and enable the modeling of problems on a larger scale.

REFERENCES

[1] Chen G, Ewy RT. Thermoporoelastic Effect on Wellbore Stability. SPE Journal. 2005;10:pp. 121-9.

[2] Ghassemi A. A Review of Some Rock Mechanics Issues in Geothermal Reservoir Development. Geotechnical and Geological Engineering. 2012;30:647-64.

[3] Jing L, Hudson JA. Numerical Methods in Rock Mechanics. International Journal of Rock Mechanics and Mining Sciences. 2002;39:409-27.

[4] Rutqvist J, Oldenburg CM. Analysis of Injection-Induced Micro-Earthquakes in a Geothermal Steam Reservoir, The Geysers Geothermal Field, California. American Rock Mechanics Association; 2008.

[5] Warpinski NR, Wolhart SL, Wright CA. Analysis and Prediction of Microseismicity Induced by Hydraulic Fracturing. SPE Annual Technical Conference and Exhibition. New Orleans, Louisiana, Society of Petroleum Engineers Inc.; 2001.

[6] Palmer ID, Moschovidis ZA, Cameron J. Modeling Shear Failure and Stimulation of the Barnett Shale After Hydraulic Fracturing. SPE Hydraulic Fracturing Technology Conference. College Station, Texas, U.S.A.: Society of Petroleum Engineers; 2007.

[7] Lee SH, Ghassemi A. A Three-Dimensional Thermo-Poro-Mechanical Finite Element Analysis of a Wellbore On Damage Evolution. American Rock Mechanics Association; 2010.

[8] Li X. Thermoporomechanical Modelling of Inclined Boreholes: University of Oklahoma; 1998.

[9] Biot MA. General Theory of Three-Dimensional Consolidation. Journal of Applied Physics. 1941;12:155-64.

[10] Biot MA. General Solutions of the Equations of Elasticity and Consolidation for a Porous Material. Journal of Applied Mechanics, Trans ASME. 1956;78:91-6.

[11] Biot MA, Willis DG. The Elastic Coefficients of the Theory of Consolidation. Journal of Applied Mechanics. 1957;24:594-601.

[12] Verruijt A. Elastic storage of aquifers. In: Deweist RJM, editor. Flow Through Porous Media. New York: Academic Press; 1969.

[13] Rice JR, Cleary MP. Some Basic Stress Diffusion Solutions for Fluid-Saturated Elastic Porous Media with Compressible Constituents. Reviews Of Geophysics and Space Physics. 1976;14:227-41.

[14] Carslaw HS, Jaeger JC. Conduction of Heat in Solids. Oxford: Clarendon Press; 1959.

[15] Schiffman RL. A Thermoelastic Theory of Consolidation. In: C. CJ, Kreith F, Clark JA, editors. Environmental and Geophysical Heat Transfer. New York: American Society of Mechanical Engineers, Heat Transfer Division; 1971. p. 78-84.

[16] Palciauskas VV, Domenico PA. Characterization of Drained and Undrained Response of Thermally Loaded Repository Rocks. Water Resources Research. 1982;18:281-90.

[17] McTigue DF. Thermoelastic Response of Fluid-Saturated Porous Rock. Journal of Geophysical Research. 1986;91:9533-9542.

[18] Kurashige M. A Thermoelastic Theory of Fluid-Filled Porous Materials. International Journal of Solids and Structures. 1989;25:1039-52.

[19] Delaney PT. Rapid Intrusion of Magma Into Wet Rock: Groundwater Flow due to Pore Pressure Increases. Journal of Geophysical Research. 1982;87:7739-56.

[20] Perkins TK, Kern LR. Widths of Hydraulic Fractures. Journal of Petroleum Technology. 1961;13:937-949.

[21] Geertsma J, Klerk Fd. A Rapid Method of Predicting Width and Extent of Hydraulically Induced Fractures. Journal of Petroleum Technology. 1969;21: 1571-1581.

[22] Gringarten AC, Witherspoon PA. Extraction of Heat from Multiple-Fractured Dry Hot Rock. Geothermics. 1973;2:119-22.

[23] Gringarten AC, Witherspoon PA, Ohnishi Y. Theory of Heat Extraction From Fractured Hot Dry Rock. Journal of Geophysical Research. 1975;80:1120-1124.

[24] Nemat-Nasser S, Ohtsubo H. Fluid Flow and Heat Transfer Through Hydraulically Induced Fractures in Hot, Dry Rock Masses. Journal of Pressure Vessel Technology. 1978;100:277-84.

[25] Bažant ZP, Ohtsubo H. Geothermal Heat Extraction by Water Circulation Through a Large Crack in Dry Hot Rock Mass. International Journal for Numerical and Analytical Methods in Geomechanics. 1978;2:317-27.

[26] Crouch SL, Starfield AM. Boundary Element Methods in Solid Mechanics : with Applications in Rock Mechanics and Geological Engineering. London; Boston: Allen & Unwin; 1982.

[27] Abe H, Sekine H, Shibuya Y. Thermoelastic Analysis of a Cracklike Reservoir in a Hot Dry Rock During Extraction of Geothermal Energy. Journal of Energy Resources Technology. 1983;105:503-8.

[28] Perkins TK, Gonzalez JA. The Effect of Thermoelastic Stresses on Injection Well Fracturing. Society of Petroleum Engineers Journal. 1985;25:78-88.

[29] Asgian MI. A Numerical Study of Fluid Flow in a Deformable, Naturally Fractured Reservoir: The Influence of Pumping Rate on Reservoir Response. A. A. Balkema, Rotterdam. Permission to Distribute - American Rock Mechanics Association; 1988.

[30] Detournay E, Cheng AHD. Poroelastic Solution of a Plane Strain Point Displacement Discontinuity. Journal of Applied Mechanics. 1987;54:783-7.

[31] Vandamme L, Detournay E, Cheng AHD. A Two-Dimensional Poroelastic Displacement Discontinuity Method for Hydraulic Fracture Simulation. International Journal for Numerical and Analytical Methods in Geomechanics. 1989;13:215-24.

[32] Vandamme LM, Roegiers JC. Poroelasticity in Hydraulic Fracturing Simulators. SPE Journal of Petroleum Technology. 1990;42:1199-203.

[33] Carvalho JL. Poroelastic Effects and Influence of Material Interfaces on Hydraulic Fracture Behaviour. Canada: University of Toronto (Canada); 1990.

[34] Detournay E, Cheng AHD. Plane Strain Analysis of a Stationary Hydraulic Fracture in a Poroelastic Medium. International Journal of Solids and Structures. 1991;27:1645-62.

[35] Swenson D, Beikmann M. An Implicitly Coupled Model of Fluid Flow in Jointed Rock. A. A. Balkema, Rotterdam. Permission to Distribute - American Rock Mechanics Association; 1992.

[36] Kohl T, Evansi KF, Hopkirk RJ, Rybach L. Coupled Hydraulic, Thermal and Mechanical Considerations for the Simulation of Hot Dry Rock Reservoirs. Geothermics. 1995;24:345-59.

[37] Kohl T, Hopkirk RJ. “FRACture” — A Simulation Code for Forced Fluid Flow and Transport in Fractured, Porous Rock. Geothermics. 1995;24:333-43.

[38] Swenson D, Hardeman B. The Effects of Thermal Deformation on Flow in a Jointed Geothermal Reservoir. International Journal of Rock Mechanics and Mining Sciences. 1997;34:308-320.

[39] Ghassemi A. Three-Dimensional Poroelastic Hydraulic Fracture Simulation Using the Displacement Discontinuity Method. United States: The University of Oklahoma; 1996.

[40] Bruel D. Impact of Induced Thermal Stresses During Circulation Tests in an Engineered Fractured Geothermal Reservoir. Example of Soultz-sous-Forêts, European Hot Fractured Rock Geothermal Project, Rhine Graben, France. Oil & Gas Science and Technology - Rev IFP. 2002;57:459-70.

[41] Rahman MK, Hossain MM, Rahman SS. A Shear-Dilation-Based Model for Evaluation of Hydraulically Stimulated Naturally Fractured Reservoirs. International Journal for Numerical and Analytical Methods in Geomechanics. 2002;26:469-97.

[42] Wang X, Ghassemi A. A 3d Thermal-Poroelastic Model for Geothermal Reservoir Stimulation. 36th Workshop on Geothermal Reservoir Engineering , Stanford University. CA, USA2012.

[43] Settari A, Sullivan RB, Walters DA, Wawrzynek PA. 3-D Analysis and Prediction of Microseismicity in Fracturing by Coupled Geomechanical Modeling. SPE Gas Technology Symposium. Calgary, Alberta, Canada: 2002,. Society of Petroleum Engineers Inc.; 2002.

[44] Ghassemi A, Tarasovs S, Cheng AHD. An Integral Equation Solution for Three-Dimensional Heat Extraction from Planar Fracture in Hot Dry Rock. International Journal for Numerical and Analytical Methods in Geomechanics. 2003;27:989-1004.

[45] Ghassemi A, Tarasovs S, Cheng AHD. Integral Equation Solution of Heat Extraction-Induced Thermal Stress in Enhanced Geothermal Reservoirs. International Journal for Numerical and Analytical Methods in Geomechanics. 2005;29:829-44.

[46] Ghassemi A, Tarasovs S, Cheng AHD. A 3-D Study of the Effects of Thermomechanical Loads on Fracture Slip in Enhanced Geothermal Reservoirs. International Journal of Rock Mechanics and Mining Sciences. 2007;44:1132-48.

[47] Ghassemi A, Zhang Q. Porothermoelastic Analysis of the Response of a Stationary Crack Using the Displacement Discontinuity Method. Journal of Engineering Mechanics. 2006;132:26-33.

[48] Murdoch LC, Germanovich LN. Analysis of a Deformable Fracture in Permeable Material. International Journal for Numerical and Analytical Methods in Geomechanics. 2006;30:529-61.

[49] Ge J, Ghassemi A. Analysis of Failure Potential around a Hydraulic Fracture in Jointed Rock. American Rock Mechanics Association; 2008.

[50] Ghassemi A, Nygren A, Cheng AHD. Effects of Heat Extraction on Fracture Aperture: A Poro–Thermoelastic Analysis. Geothermics. 2008;37:525-39.

[51] Tao Q. Numerical Modeling of Fracture Permeability Change in Naturally Fractured Reservoirs Using a Fully Coupled Displacement Discontinuity Method. United States: Texas A&M University; 2010.

[52] Tao Q, Ghassemi A. Simulation of Fluid Flow In a Naturally Fractured Poro-Thermoelastic Reservoir. 44th US Rock Mechanics Symposium and 5th US-Canada Rock Mechanics Symposium. Salt Lake City, Utah: American Rock Mechanics Association; 2010.

[53] Lee BT, Ghassemi A. Shear Slip And Permeability Change Caused By Injection/Extraction In a Fractured Reservoir. 45th American Rock Mechanics Association Symposium; 2011.

[54] Koh J, Roshan H, Rahman SS. A Numerical Study on the Long Term Thermo-Poroelastic Effects of Cold Water Injection Into Naturally Fractured Geothermal Reservoirs. Computers and Geotechnics. 2011;38:669-82.

[55] Zhou XX, Ghassemi A, Cheng AHD. A Three-Dimensional Poroelastic Model for Water Injection into a Geothermal Reservoir. 42th American Rock Mechanics Association Symposium; 2008.

[56] Zhou XX, Ghassemi A. Three-Dimensional Poroelastic Displacement Discontinuity Simulation of Natural Fractures. 43th American Rock Mechanics Association Sympoium; 2009.

[57] Ghassemi A, Zhou X. A Three-Dimensional Thermo-Poroelastic Model for Fracture Response to Injection/Extraction in Enhanced Geothermal Systems. Geothermics. 2011;40:39-49.

[58] Amadei B, Saeb S. Constitutive Models of Rock Joints. International Symposium on Rock Joints. Leon, Norway1990.

[59] Bandis SC, Lumsden AC, Barton NR. Fundamentals of Rock Joint Deformation. International Journal of Rock Mechanics and Mining Sciences; Geomechanics Abstracts. 1983;20:249-68.

[60] Goodman RE. The Mechanical Properties of Joints. In: National Academy of Sciences W.DC, USA, editor. 3rd International Congress of International Society of Rock Mechanics. Denver, CO, USA1974. p. 127-40.

[61] Kirsch. Die Theorie Der Elastizität und die Bedürfnisse der Festigkeitslehre. Zeitschrift des Vereines deutscher Ingenieure. 1898;42:797-807.

[62] Detournay E, Cheng AHD. Poroelastic Response of a Borehole in a Non-Hydrostatic Stress Field. International Journal of Rock Mechanics and Mining Sciences; Geomechanics Abstracts. 1988;25:171-82.

[63] Rajapakse RKND. Stress Analysis of Borehole in Poroelastic Medium. Journal of Engineering Mechanics. 1993;119:1205-27.

[64] Wang Y, Papamichos E. Conductive Heat Flow and Thermally Induced Fluid Flow Around a Wellbore in a Poroelastic Medium. Water Resources Research. 1994;30:3375-84.

[65] Li X, Cui L, Roegiers JC. Thermoporoelastic Analyses of Inclined Boreholes. SPE/ISRM Rock Mechanics in Petroleum Engineering. Trondheim, Norway: 1998 Copyright 1998, Society of Petroleum Engineers Inc.; 1998.

[66] Abousleiman Y, Cui L. Poroelastic Solutions in Transversely Isotropic Media for Wellbore and Cylinder. International Journal of Solids and Structures. 1998;35:4905-29.

[67] Freij-Ayoub R, Tan CP, Choi SK. Simulation of Time-Dependent Wellbore Stability in Shales Using A Coupled Mechanical-Thermal-Physico-Chemical Model. SPE/IADC Middle East Drilling Technology Conference and Exhibition. Abu Dhabi, United Arab Emirates: SPE/IADC Middle East Drilling Technology Conference & Exhibition; 2003.

[68] Wang Y, Dusseault MB. A Coupled Conductive–Convective Thermo-Poroelastic Solution and Implications for Wellbore Stability. Journal of Petroleum Science and Engineering. 2003;38:187-98.

[69] Zhang Q, Ghassemi A. A Thermo-Poroelastic Mixed Boundary Element Model For Borehole Stability And Fracture Problems. American Rock Mechanics Association Symposium; 2004.

[70] Kang Y, Yu M, Miska SZ, Takach N. Wellbore Stability: A Critical Review and Introduction to DEM. SPE Annual Technical Conference and Exhibition. New Orleans, Louisiana: Society of Petroleum Engineers; 2009.

[71] Lee SH. Thermo-Poroelastic Modeling of Reservoir Stimulation and Microseismicity Using Finite Element Method with Damage Mechanics. United States: Texas A&M University; 2011.

[72] Tao Q, Ghassemi A. Poro-Thermoelastic Borehole Stress Analysis for Determination of the In Situ Stress and Rock Strength. Geothermics. 2010;39:250-9.

[73] Wu B, Zhang X, Jeffrey RG. A Thermo-Poro-Elastic Analysis of Stress Fields Around a Borehole. 44th American Rock Mechanics Association Symposium; 2010.

[74] Roshan H, Rahman SS. Analysis of Stress and Pore Pressure in Naturally Fractured Shale Formations: A Finite Element Based Chemo-Thermo-Poroplastic Model. SPE Eastern Regional Meeting. Morgantown, West Virginia, USA: Society of Petroleum Engineers; 2010.

[75] Gelet R, Loret B, Khalili N. Borehole Stability Analysis in a Thermoporoelastic Dual-Porosity Medium. International Journal of Rock Mechanics and Mining Sciences. 2012;50:65-76.

[76] Day SM. Three-Dimensional Simulation of Spontaneous Rupture: The Effect of Nonuniform Prestress. Bulletin of the Seismological Society of America. 1982;72:1881-902.

[77] Ida Y. Cohesive Force Across the Tip of a Longitudinal-Shear Crack and Griffith's Specific Surface Energy. Journal of Geophysical Research. 1972;77:3796-805.

[78] Wawersik WR, Brace WF. Post-Failure Behavior of a Granite and Diabase. Rock Mechanics and Rock Engineering. 1971;3:61-85.

[79] Palmer AC, Rice JR. The Growth of Slip Surfaces in the Progressive Failure of Over-Consolidated Clay. Proceedings of the Royal Society of London A Mathematical and Physical Sciences. 1973;332:527-48.

[80] Nowacki W. Thermoelasticity. Oxford: Pergamon Press; 1986.

[81] Carter JP, Booker JR. Finite Element Analysis of Coupled Thermoelasticity. Computers & Structures. 1989;31:73-80.

[82] Sone H. Mechanical Properties of Shale Gas Reservoir Rocks and Its Relation to the In-Situ Stress Variation Observed in Shale Gas Reservoirs: Stanford University; 2012.

[83] Cleary MP. Fundamental Solutions for a Fluid-Saturated Porous Solid. International Journal of Solids and Structures. 1977;13:785-806.

[84] Cleary MP. Fundamental Solutions for Fluid-Saturated Porous Media and Application to Localised Rupture Phenomena. United States: Brown University; 1976.

[85] Cheng AHD, Detournay E. On Singular Integral Equations and Fundamental Solutions of Poroelasticity. International Journal of Solids and Structures. 1998;35:4521-55.

[86] Cheng AHD, Liggett JA. Boundary Integral Equation Method for Linear Porous-Elasticity with Applications to Soil Consolidation. International Journal for Numerical Methods in Engineering. 1984;20:255-78.

[87] Rudnicki JW. On “Fundamental Solutions for a Fluid-Saturated Porous Solid” by M. P. Cleary. International Journal of Solids and Structures. 1981;17:855-7.

[88] Rudnicki JW. Fluid Mass Sources and Point Forces in Linear Elastic Diffusive Solids. Mechanics of Materials. 1986;5:383-93.

[89] Berchenko IE. Thermal Loading of Saturated Rock Mass: Field Experiment and Modeling Using Thermoporoelastic Singular Solutions: University of Minnesota; 1998.

[90] Brebbia CA, Telles JCF, Wrobel LC. Boundary Element Techniques: Theory and Applications in Engineering: Springer; 1984.

[91] Banerjee PK, Butterfield R. Boundary Element Methods in Engineering Science. London; New York: McGraw-Hill Book Co. (UK); 1981.

[92] Kellogg OD. Foundations of Potential Theory. Berlin Verlag Von Julius Springer; 1929.

[93] Vandamme L, Curran JH. A Three-Dimensional Hydraulic Fracturing Simulator. International Journal for Numerical Methods in Engineering. 1989;28:909-27.

[94] Chaudonneret M. On the Discontinuity of the Stress vector in the Boundary Integral Equation Method for Elastic Analysis. In: Brebbia CA, editor. Recent Advances in Boundary Element Methods. London: Pentech Press; 1978. p. 185-94.

[95] Sokolnikoff IS. Mathematical Theory of Elasticity. New York: McGraw-Hill; 1956.

[96] Guiggiani M, Gigante A. A General Algorithm for Multidimensional Cauchy Principal Value Integrals in the Boundary Element Method. Journal of Applied Mechanics. 1990;57:906-15.

[97] Guiggiani M, Krishnasamy G, Rudolphi TJ, Rizzo FJ. A General Algorithm for the Numerical Solution of Hypersingular Boundary Integral Equations. Journal of Applied Mechanics. 1992;59:604-14.

[98] Jaeger JC, Cook NGW. Fundamentals of Rock Mechanics. London; New York: Chapman and Hall ; Wiley; 1976.

[99] Rutqvist J, Birkholzer JT, Tsang CF. Coupled Reservoir–Geomechanical Analysis of the Potential for Tensile and Shear Failure Associated with CO2 Injection in Multilayered Reservoir–Caprock Systems. International Journal of Rock Mechanics and Mining Sciences. 2008;45:132-43.

[100] Callanan MJ. Hydraulic Fracture Initiation by Shear Failure in Formations at Great Depths. In: Hydraulic Fracturing Stress Measurements: National Academy Press, 1983; 181.

[101] Rummel F, Hansen J. Interpretation of Hydrofrac Pressure Recordings Using a Simple Fracture Mechanics Simulation Model. International Journal of Rock Mechanics and Mining Sciences & Geomechanics Abstracts. 1989;26:483-8.

[102] Griffith AA. The Phenomena of Rupture and Flow in Solids. Philosophical Transactions of the Royal Society of London Series A, Containing Papers of a Mathematical or Physical Character. 1921;221:163-198.

[103] Irwin GR. Analysis of Stresses and Strains Near the End of a Crack Traversing a Plate. Journal of Applied Mechanics. 1957;24:361-364.

[104] Roegiers JC, Zhao XL. Rock Fracture Tests In Simulated Downhole Conditions. 32nd U.S. Symposium on Rock Mechanics (USRMS), July 10 - 12, 1991 , Norman, Oklahoma.

[105] Martha LF, Wawrzynek PA, Ingraffea AR. Arbitrary Crack Representation Using Solid Modeling. Engineering with Computers. 1993;9:63-82.

[106] Aliabadi MH. Boundary Element Formulations in Fracture Mechanics. Applied Mechanics Reviews. 1997;50:83-96.

[107] Cryer CW. A Comparison of the Three-Dimensional Consolidation Theories of Biot and Terzaghi. The Quarterly Journal of Mechanics and Applied Mathematics. 1963;16:401-12.

[108] Wang HF. Theory of Linear Poroelasticity with Applications to Geomechanics and Hydrogeology: Princeton University Press; 2000.

[109] Carter JP, Booker JR. Elastic Consolidation Around a Deep Circular Tunnel. International Journal of Solids and Structures. 1982;18:1059-74.

[110] Sneddon IN. The Distribution of Stress in the Neighbourhood of a Crack in an Elastic Solid. Proceedings of the Royal Society of London Series A, Mathematical and Physical Sciences. 1946;187:229-60.

[111] Kundu T. Fundamentals of Fracture Mechanics. Boca Raton, FL: CRC Press; 2008.

[112] Gordeyev YN. Growth of a Cack Produced by Hydraulic Fracture in a Poroelastic Medium. International Journal of Rock Mechanics and Mining Sciences; Geomechanics Abstracts. 1993;30:233-8.

[113] Segedin CM. Note on a Penny-Shaped Crack Under Shear. Mathematical Proceedings of the Cambridge Philosophical Society. 1951;47:396-400.

[114] Olesiak Z, Sneddon I. The Distribution of Thermal Stress in an Infinite Elastic Solid Containing a Penny-Shaped Crack. Archive for Rational Mechanics and Analysis. 1959;4:238-54.

[115] Sneddon IN, Lowengrub M. Crack Problems in the Classical Theory of Elasticity. New York: Wiley; 1969.

[116] Witherspoon PA, Wang JSY, Iwai K, Gale JE. Validity of Cubic Law for fluid flow in a deformable rock fracture. Water Resources Research. 1980;16:1016-24.

[117] Zimmerman RW, Bodvarsson GS. Hydraulic Conductivity of Rock Fractures. Transport in Porous Media. 1996;23:1-30.

[118] Birkhoff G, Rota GC. Ordinary Differential Equations. New York: Wiley; 1989.

[119] Donéa J, Huerta A. Finite Element Methods for Flow Problems. Chichester: Wiley; 2003.

[120] Cuvelier C, Segal A, Steenhoven AA. Finite Element Methods and Navier-Stokes Equations. Dordrecht; Boston; Hingham, MA: D. Reidel ; Distributed in the U.S.A. and Canada by Kluwer Academic; 1986.

[121] Cheng AHD, Ghassemi A, Detournay E. Integral Equation Solution of Heat Extraction From a Fracture in Hot Dry Rock. International Journal for Numerical and Analytical Methods in Geomechanics. 2001;25:1327-38.

[122] Lowell RP. Comments on 'Theory of Heat Extraction From Fractured Hot Dry Rock' by A. C. Gringarten, P. A. Witherspoon, and Yuzo Ohnishi. Journal of Geophysical Research. 1976;81:359-360.

[123] Lee BT. Numerical Investigation of a Fractured Reservoir Response to Injection/Extraction Using a Fully Coupled Displacement Discontinuity Method: Texas A&M University; 2011.

[124] Vedamuthu M, Singh S, Robinson GW. Properties of Liquid Water: Origin of the Density Anomalies. The Journal of Physical Chemistry. 1994;98:2222-30.

[125] Brooks A. A Petrov-Galerkin Finite Element Formulation For Convection Dominated Flows. United States: California Institute of Technology; 1981.

[126] Brooks A, Hughes T. Streamline Upwind/Petrov-Galerkin Formulations for Convection Dominated Flows with Particular Emphasis on the Incompressible Navier-

Stokes Equations. Computer Methods in Applied Mechanics and Engineering. 1982:199-259.

[127] Heinrich JC, Huyakorn PS, Zienkiewicz OC, Mitchell AR. An 'Upwind' Finite Element Scheme for Two-Dimensional Convective Transport Equation. International Journal for Numerical Methods in Engineering. 1977;11:131-43.

[128] Foulger GR, Julian BR, Hill DP, Pitt AM, Malin PE, Shalev E. Non-Double-Couple Microearthquakes at Long Valley Caldera, California, Provide Evidence for Hydraulic Fracturing. Journal of Volcanology and Geothermal Research. 2004;132:45-71.

[129] Rutledge JT, Phillips WS. A Comparison of Microseismicity Induced By Gel-Proppant- and Water-Injected Hydraulic Fractures, Carthage Cotton Valley Gas Field, East Texas Society of Exploration Geophysicist, International Exposition and 72nd Annual Meeting, Salt Lake City, October 6 - 11, 2002.

[130] Shapiro SA, Huenges E, Borm G. Estimating the Crust Permeability from Fluid-Injection-Induced Seismic Emission at the KTB site. Geophysical Journal International. 1997;131:F15-F8.

[131] Zhou XX, Ghassemi A. Three-Dimensional Poroelastic Analysis of a Pressurized Natural Fracture. International Journal of Rock Mechanics and Mining Sciences. 2011;48:527-34.

[132] Bandis SC. Mechanical Properties of Rock Joints. International Symposium on Rock Joints. Leon, Norway1990.

[133] Allodi A, Castelli M, Scavia C. Implementation of the Slip-Weakening Model in a Displacement Discontinuity Method Based Numerical Technique. In: BREBBIA CA, editor. Boundary Elements XXIV. UK.2002.

[134] Sesetty V, Ghassemi A. Modeling and Analysis of Stimulation for Fracture Network Generation. Thirty-Seventh Workshop on Geothermal Reservoir Engineering. Stanford University, Stanford, California2012.

[135] Rutqvist J, Stephansson O. The Role of Hydromechanical Coupling in Fractured Rock Engineering. Hydrogeology Journal. 2003;11:7-40.

[136] Rutqvist J, Börgesson L, Chijimatsu M, Kobayashi A, Jing L, Nguyen TS, et al. Thermohydromechanics of Partially Saturated Geological Media: Governing Equations and Formulation of Four Finite Element Models. International Journal of Rock Mechanics and Mining Sciences. 2001;38:105-27.

[137] Orzol J, Jatho R, Jung R, Kehrer P, Tischner T. The GeneSys Project - Development of Concepts for the Extraction of Heat from Tight Sedimentary Rocks. Zeitschrift fur Angewandte Geologie. 2004;50:17-23.

[138] Orzol J, Jung R, Jatho R, Tischner T, Kehrer P. The GeneSys-Project: Extraction of Geothermal Heat from Tight Sediments. World Geothermal Congress. Antalya, Turkey 2005.

[139] Mathias S, Tsang CF, Reeuwijk MV. Investigation of Hydromechanical Processes during Cyclic Extraction Recovery Testing of a Deformable Rock Fracture. International Journal of Rock Mechanics and Mining Sciences. 2010;47:517-22.

[140] Wessling S, Junker R, Rutqvist J, Silin D, Sulzbacher H, Tischner T, et al. Pressure Analysis of the Hydromechanical Fracture Behaviour in Stimulated Tight Sedimentary Geothermal Reservoirs. Geothermics. 2009;38:211-26.

[141] Sulzbacher H, Jung R, Orzol J. Modellprognosen zum Wärmetauscher Horstberg Z1. Hannover, Germany: Leibniz Institute for Applied Geosciences; 2004.

[142] McGarr A, Spottiswoode SM, Gay NC, Ortlepp WD. Observations Relevant to Seismic Driving Stress, Stress Drop, and Efficiency. Journal of Geophysical Research. 1979;84:2251-61.

[143] Hanks TC, Kanamori H. A Moment Magnitude Scale. Journal of Geophysical Research. 1979;84:2348-50.

APPENDIX A

SINGULAR SOLUTIONS

A.1. Essential parameters

Singular solutions of poroelastic, thermoelastic, and thermo-poroelastic solutions were developed and reported [13, 81, 85]. In the following section the singular solutions are represented based on following parameters:

Influenced point: $\mathbf{x}=(x,y,z)$, Influencing point: $\boldsymbol{\chi}=(X,Y,Z)$

Influenced time = t , Influencing time = τ

$t'=t-\tau$

$R^2=(x-X)^2+(y-Y)^2+(z-Z)^2$, $r_{,1}=\dfrac{X-x}{R}$, $r_{,2}=\dfrac{Y-y}{R}$, $r_{,3}=\dfrac{Z-z}{R}$

$c=\dfrac{2\kappa G(\nu_u-\nu)(1-\nu)}{\alpha^2(1-\nu_u)(1-2\nu)^2}$, $c^T=\dfrac{k_m^T}{\rho_m\ C_m}$, $\omega^2=\dfrac{c}{c^T}$

$\beta_p=\alpha\ \beta_m+\varphi(\beta_f-\beta_m)$, $\beta_o=\beta_p-\dfrac{\alpha\ \beta_m(1+\nu)}{3(1-\nu)}$

$S=\dfrac{\alpha^2(1-\nu_u)(1-2\nu)^2}{2G(\nu_u-\nu)(1-\nu)}$, $\gamma=\dfrac{\beta_o}{S}$

$\lambda_1=\dfrac{2G\beta_m(1+\nu)}{\alpha\ \gamma}$, $\lambda=1+(1-\omega^2)\lambda_1$

$\xi_p=\dfrac{R}{2\sqrt{ct'}}$, $\xi_T=\dfrac{R}{2\sqrt{c^Tt'}}$

A.2. Continuous point isothermal fluid source

In Figure A. 1 sign convention of fluid source is defined. The solution of thermoporoelastic partial differential equations in isothermal condition at each point ($\boldsymbol{\chi}$) at time t due to unit continuous fluid source at location $\mathbf{x}$ and time τ is as follows:

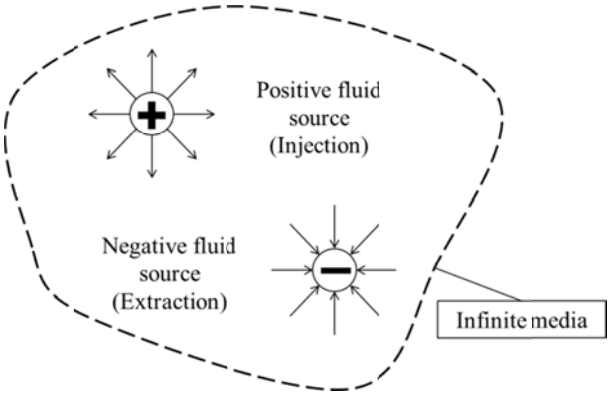

Figure A. 1. Positive and negative fluid source in infinite media

$$\{p\}^{sc} = \frac{1}{4\pi\ \kappa\ R} erfc\left(\xi_p\right)$$

$$\begin{Bmatrix} u_1 \\ u_2 \\ u_3 \end{Bmatrix}^{sc} = \frac{\alpha\left(1-2\nu\right)\times A_p}{16\pi G\ \kappa\left(1-\nu\right)} \begin{Bmatrix} r_{,1} \\ r_{,2} \\ r_{,3} \end{Bmatrix}$$

$$\begin{bmatrix} \sigma_{11} & \sigma_{12} & \sigma_{13} \\ Sym & \sigma_{22} & \sigma_{23} \\ Sym & Sym & \sigma_{33} \end{bmatrix}^{sc} = \frac{\alpha\left(1-2\nu\right)}{8\pi\ \kappa\left(1-\nu\right)} \frac{1}{R} \begin{bmatrix} B_p - \left(r_{,1}\right)^2 \times C_p & -r_{,1} \times r_{,2} \times C_p & -r_{,1} \times r_{,3} \times C_p \\ Sym & B_p - \left(r_{,2}\right)^2 \times C_p & -r_{,2} \times r_{,3} \times C_p \\ Sym & Sym & B_p - \left(r_{,3}\right)^2 \times C_p \end{bmatrix}$$

$$A_p = 1 - \frac{1}{\xi_p \sqrt{\pi}} e^{-\xi_p{}^2} + \left(\frac{1}{2\xi_p{}^2} - 1\right) erf\left(\xi_p\right)$$

$$B_p = \left(\frac{1}{2\xi_p{}^2} + 1\right) erf\left(\xi_p\right) - 1 - \frac{1}{\xi_p \sqrt{\pi}} e^{-\xi_p{}^2}$$

$$C_p = 1 - \frac{3}{\xi_p \sqrt{\pi}} e^{-\xi_p{}^2} + \left(\frac{3}{2\xi_p{}^2} - 1\right) erf\left(\xi_p\right)$$

In the relations, super script "sc" means continuous fluid source, *erf* and *erfc* are error function and complementary error function, respectively, and κ is fluid mobility (absolute permeability over viscosity**)** in thermoporoelastic media. Other parameters were defined in Section 2.

A.3. Continuous point heat source, thermoelasticity

Sign convention for point heat source is same as fluid source in thermoporoelasticity media which is shown in Figure A. 1 (Heat source is positive and heat sink is negative). Following equations are response of thermoelastic partial differential equation (see Section 2) to unit continuous heat source.

$$\{p\}^{hc} = \frac{1}{4\pi\ \kappa\ R} erfc\left(\xi_T\right)$$

$$\begin{Bmatrix} u_1 \\ u_2 \\ u_3 \end{Bmatrix}^{hc} = \frac{\alpha\left(1-2\nu\right)\times A_T}{16\pi G\ \kappa\left(1-\nu\right)} \begin{Bmatrix} r_{,1} \\ r_{,2} \\ r_{,3} \end{Bmatrix}$$

$$\begin{bmatrix} \sigma_{11} & \sigma_{12} & \sigma_{13} \\ Sym & \sigma_{22} & \sigma_{23} \\ Sym & Sym & \sigma_{33} \end{bmatrix}^{hc} = \frac{\alpha\left(1-2\nu\right)}{8\pi\ \kappa\left(1-\nu\right)} \frac{1}{R} \begin{bmatrix} B_T - \left(r_{,1}\right)^2 \times C_T & -r_{,1}\times r_{,2}\times C_T & -r_{,1}\times r_{,3}\times C_T \\ Sym & B_T - \left(r_{,2}\right)^2 \times C_T & -r_{,2}\times r_{,3}\times C_T \\ Sym & Sym & B_T - \left(r_{,3}\right)^2 \times C_T \end{bmatrix}$$

$$A_T = 1 - \frac{1}{\xi_T\sqrt{\pi}} e^{-{\xi_T}^2} + \left(\frac{1}{2{\xi_T}^2} - 1\right) erf\left(\xi_T\right)$$

$$B_T = \left(\frac{1}{2{\xi_T}^2} + 1\right) erf\left(\xi_T\right) - 1 - \frac{1}{\xi_T\sqrt{\pi}} e^{-{\xi_T}^2}$$

$$C_T = 1 - \frac{3}{\xi_T\sqrt{\pi}} e^{-{\xi_T}^2} + \left(\frac{3}{2{\xi_T}^2} - 1\right) erf\left(\xi_T\right)$$

A.4. Continuous point heat source, thermoporoelasticity

In this section, solution of thermoporoelastic partial differential equation to a unit continuous heat source is presented. The difference between this section and previous one is in the field equations and the way that pressure coupled to temperature.

$$\{T\}^{hc} = \frac{1}{4\pi k_m^T R} erfc\left(\xi_T\right)$$

$$\{P\}^{hc} = \frac{1}{4\pi k_m^T R} \times \frac{\gamma\ A_T}{1-\omega^2}$$

$$\begin{Bmatrix} u_1 \\ u_2 \\ u_3 \end{Bmatrix}^{hc} = \frac{\alpha(1-2\nu)}{16\pi k_m^T (1-\nu)} \frac{\gamma\left(\lambda\ B_T - C_T\right)}{G\left(1-\omega^2\right)} \begin{Bmatrix} r_{,1} \\ r_{,2} \\ r_{,3} \end{Bmatrix}$$

$$\begin{bmatrix} \sigma_{11} & \sigma_{12} & \sigma_{13} \\ Sym & \sigma_{22} & \sigma_{23} \\ Sym & Sym & \sigma_{33} \end{bmatrix}^{hc} = \frac{\alpha(1-2\nu)}{8\pi k_m^T (1-\nu)\left(1-\omega^2\right)} \frac{\gamma}{R} \frac{1}{R} \begin{bmatrix} S_{11} & S_{12} & S_{13} \\ Sym & S_{22} & S_{23} \\ Sym & Sym & S_{33} \end{bmatrix}$$

$$S_{11} = \lambda\left(D_T - \left(r_{,1}\right)^2 \times E_T\right) - F_T + \left(r_{,1}\right)^2 \times G_T, \qquad S_{12} = -\lambda \times r_{,1} \times r_{,2} \times E_T + r_{,1} \times r_{,2} \times G_T$$

$$S_{13} = -\lambda \times r_{,1} \times r_{,3} \times E_T + r_{,1} \times r_{,3} \times G_T, \qquad S_{22} = \lambda\left(D_T - \left(r_{,2}\right)^2 \times E_T\right) - F_T + \left(r_{,2}\right)^2 \times G_T$$

$$S_{23} = -\lambda \times r_{,2} \times r_{,3} \times E_T + r_{,2} \times r_{,3} \times G_T, \qquad S_{33} = \lambda\left(D_T - \left(r_{,3}\right)^2 \times E_T\right) - F_T + \left(r_{,3}\right)^2 \times G_T$$

$$A_T = erfc\left(\xi_T\right) - erfc\left(\frac{\xi_T}{\omega}\right)$$

$$B_T = 1 - \frac{1}{\xi_T \sqrt{\pi}} e^{-\xi_T^2} + \left(\frac{1}{2\xi_T^2} - 1\right) erf\left(\xi_T\right), \qquad C_T = 1 - \frac{\omega}{\xi_T \sqrt{\pi}} e^{-\left(\frac{\xi_T}{\omega}\right)^2} + \left(\frac{\omega^2}{2\xi_T^2} - 1\right) erf\left(\frac{\xi_T}{\omega}\right)$$

$$D_T = \left(\frac{1}{2\xi_T^2} + 1\right) erf\left(\xi_T\right) - 1 - \frac{1}{\xi_T \sqrt{\pi}} e^{-\xi_T^2}, \qquad E_T = 1 - \frac{3}{\xi_T \sqrt{\pi}} e^{-\xi_T^2} + \left(\frac{3}{2\xi_T^2} - 1\right) erf\left(\xi_T\right)$$

$$F_T = \left(\frac{\omega^2}{2\xi_T^2} + 1\right) erf\left(\frac{\xi_T}{\omega}\right) - 1 - \frac{\omega}{\xi_T \sqrt{\pi}} e^{-\left(\frac{\xi_T}{\omega}\right)^2}, \qquad G_T = 1 - \frac{3\omega}{\xi_T \sqrt{\pi}} e^{-\left(\frac{\xi_T}{\omega}\right)^2} + \left(\frac{3\omega^2}{2\xi_T^2} - 1\right) erf\left(\frac{\xi_T}{\omega}\right)$$

For $\omega^2 \neq 1.0$, and

$$\{T\}^{hc} = \frac{1}{4\pi k_m^T R} erfc\left(\xi_T\right)$$

$$\{P\}^{hc} = \frac{1}{4\pi k_m^T R} \frac{\xi_T\, e^{-\xi_T^2}}{\sqrt{\pi}}$$

$$\begin{Bmatrix} u_1 \\ u_2 \\ u_3 \end{Bmatrix}^{hc} = \frac{\alpha(1-2\nu)}{16\pi k_m^T (1-\nu)} \frac{\gamma(\lambda_l \ A_T - B_T)}{G} \begin{Bmatrix} r_{,1} \\ r_{,2} \\ r_{,3} \end{Bmatrix}$$

$$\begin{bmatrix} \sigma_{11} & \sigma_{12} & \sigma_{13} \\ Sym & \sigma_{22} & \sigma_{23} \\ Sym & Sym & \sigma_{33} \end{bmatrix}^{hc} = \frac{\gamma\alpha(1-2\nu)}{8\pi k_m^T (1-\nu)} \frac{1}{R} \begin{bmatrix} S_{11} & S_{12} & S_{13} \\ Sym & S_{22} & S_{23} \\ Sym & Sym & S_{33} \end{bmatrix}$$

$$S_{11} = \lambda_l \left(C_T - \left(r_{,1}\right)^2 \times D_T \right) - E_T + \left(r_{,1}\right)^2 \times F_T, \qquad S_{12} = -\lambda_l \times r_{,1} \times r_{,2} \times D_T + r_{,1} \times r_{,2} \times F_T$$

$$S_{13} = -\lambda_l \times r_{,1} \times r_{,3} \times D_T + r_{,1} \times r_{,3} \times F_T, \qquad S_{22} = \lambda_l \left(C_T - \left(r_{,2}\right)^2 \times D_T \right) - E_T + \left(r_{,2}\right)^2 \times F_T$$

$$S_{23} = -\lambda_l \times r_{,2} \times r_{,3} \times D_T + r_{,2} \times r_{,3} \times F_T, \qquad S_{33} = \lambda_l \left(C_T - \left(r_{,3}\right)^2 \times D_T \right) - E_T + \left(r_{,3}\right)^2 \times F_T$$

$$A_T = 1 - \frac{1}{\xi_T \sqrt{\pi}} e^{-\xi_T^2} + \left(\frac{1}{2\xi_T^2} - 1 \right) erf\left(\xi_T\right), \qquad B_T = \frac{1}{\xi_T \sqrt{\pi}} e^{-\xi_T^2} - \frac{erf\left(\xi_T\right)}{2\xi_T^2}$$

$$C_T = \left(\frac{1}{2\xi_T^2} + 1 \right) erf\left(\xi_T\right) - 1 - \frac{1}{\xi_T \sqrt{\pi}} e^{-\xi_T^2}, \qquad D_T = 1 - \frac{3}{\xi_T \sqrt{\pi}} e^{-\xi_T^2} + \left(\frac{3}{2\xi_T^2} - 1 \right) erf\left(\xi_T\right)$$

$$E_T = -\frac{erf\left(\xi_T\right)}{2\xi_T^2} + \left(2\xi_T - \frac{1}{\xi_T} \right) \frac{e^{-\xi_T^2}}{\sqrt{\pi}}, \qquad F_T = -\frac{3erf\left(\xi_T\right)}{2\xi_T^2} - \left(2\xi_T - \frac{3}{\xi_T} \right) \frac{e^{-\xi_T^2}}{\sqrt{\pi}}$$

For $\omega^2 = 1.0$.

In the stated relations, super script “hc” means continuous heat source.

A.5. Continuous point force

Following equations are response of thermoporoelastic partial differential equation to unit continuous point force. To present fundamental solution for point force we always assume that the surface that force is applied on it has a normal in local “3” direction, as shown in Figure A. 2.

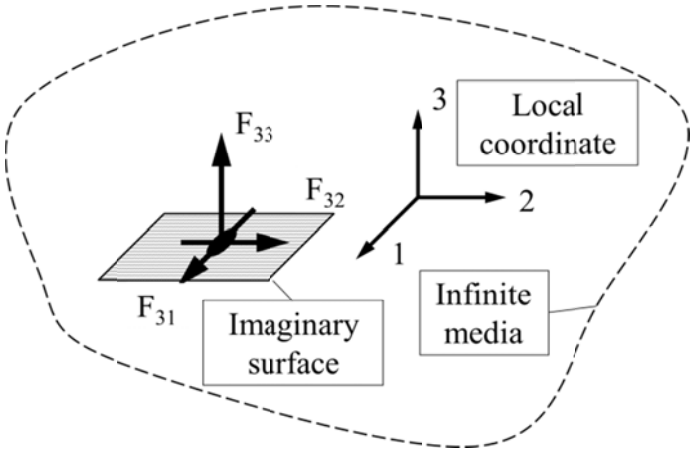

Figure A. 2. Point force on imaginary surface

Pore pressure, displacement and stresses due to point force are:

$$\{P\}^{Fc} = \frac{1}{4\pi\alpha(1-2\nu)}\frac{\nu_u-\nu}{1-\nu_u}\frac{A_p \times PP}{R^2}$$

$$\begin{Bmatrix} u_1 \\ u_2 \\ u_3 \end{Bmatrix}^{Fc} = \frac{1}{16\pi G(1-\nu)}\frac{1}{R}\begin{Bmatrix} U_1 \\ U_2 \\ U_3 \end{Bmatrix}$$

$$\begin{bmatrix} \sigma_{11} & \sigma_{12} & \sigma_{13} \\ Sym & \sigma_{22} & \sigma_{23} \\ Sym & Sym & \sigma_{33} \end{bmatrix}^{Fc} = \frac{1}{8\pi(1-\nu)}\frac{1}{R^2}\begin{bmatrix} S_{11} & S_{12} & S_{13} \\ Sym & S_{22} & S_{23} \\ Sym & Sym & S_{33} \end{bmatrix}$$

In these relations, super script “Fc” means continuous point force. In previous relations, $PP, U_1, U_2, U_3, S_{11}, S_{12}, S_{13}, S_{22}, S_{23}, S_{33}$, depends on direction of point force. To define these parameters for each force direction, we need following definition:

$$A_p = erf\left(\xi_p\right) - \frac{2\xi_p}{\sqrt{\pi}} e^{-\xi_p^2}, \qquad B_p = \left(1 - \frac{1}{2\xi_p^2}\right) erf\left(\xi_p\right) + \frac{1}{\xi_p\sqrt{\pi}} e^{-\xi_p^2}$$

$$C_p = \frac{3}{\xi_p\sqrt{\pi}} e^{-\xi_p^2} + \left(1 - \frac{3}{2\xi_p^2}\right) erf\left(\xi_p\right), \qquad D_p = \left(\frac{3}{2\xi_p^2} + 1\right) erf\left(\xi_p\right) - \left(\frac{3}{\xi_p^2} + 4\right) \frac{\xi_p}{\sqrt{\pi}} e^{-\xi_p^2}$$

$$E_p = \left(1 - \frac{3}{2\xi_p^2}\right) erf\left(\xi_p\right) + \frac{3}{\xi_p\sqrt{\pi}} e^{-\xi_p^2}, \qquad F_p = \left(1 - \frac{5}{2\xi_p^2}\right) erf\left(\xi_p\right) + \left(\frac{5}{\xi_p^2} + \frac{4}{3}\right) \frac{\xi_p}{\sqrt{\pi}} e^{-\xi_p^2}$$

For "F_{33}" or "F_3", corresponding parameters are:

$$PP = r_{,3}$$

$$U_1 = r_{,1} \times r_{,3} - \frac{\nu_u - \nu}{1 - \nu_u}\left(-r_{,1} \times r_{,3}\right) C_p$$

$$U_2 = r_{,2} \times r_{,3} - \frac{\nu_u - \nu}{1 - \nu_u}\left(-r_{,2} \times r_{,3}\right) C_p$$

$$U_3 = 3 - 4\nu + \left(r_{,3}\right)^2 - \frac{\nu_u - \nu}{1 - \nu_u}\left[B_p - \left(r_{,3}\right)^2 C_p\right]$$

$$S_{11} = \left(1 - 2\nu\right) r_{,3} - 3\left[\left(r_{,1}\right)^2 \times r_{,3}\right] - \frac{\nu_u - \nu}{1 - \nu_u}\left[D_p \times r_{,3} + 3F_p\left[\left(r_{,1}\right)^2 \times r_{,3}\right]\right],$$

$$S_{12} = -3\left[r_{,1} \times r_{,2} \times r_{,3}\right] - \frac{\nu_u - \nu}{1 - \nu_u}\left[3F_p\left[r_{,1} \times r_{,2} \times r_{,3}\right]\right],$$

$$S_{13} = -\left(1 - 2\nu\right) r_{,1} - 3\left[r_{,1} \times \left(r_{,3}\right)^2\right] - \frac{\nu_u - \nu}{1 - \nu_u}\left[-E_p \times r_{,1} + 3F_p\left[r_{,1} \times \left(r_{,3}\right)^2\right]\right],$$

$$S_{22} = \left(1 - 2\nu\right) r_{,3} - 3\left[\left(r_{,2}\right)^2 \times r_{,3}\right] - \frac{\nu_u - \nu}{1 - \nu_u}\left[D_p \times r_{,3} + 3F_p\left[\left(r_{,2}\right)^2 \times r_{,3}\right]\right],$$

$$S_{23} = -\left(1 - 2\nu\right) r_{,2} - 3\left[r_{,2} \times \left(r_{,3}\right)^2\right] - \frac{\nu_u - \nu}{1 - \nu_u}\left[-E_p \times r_{,2} + 3F_p\left[r_{,2} \times \left(r_{,3}\right)^2\right]\right],$$

$$S_{33} = -\left(1 - 2\nu\right) r_{,3} - 3\left[\left(r_{,3}\right)^3\right] - \frac{\nu_u - \nu}{1 - \nu_u}\left[D_p \times r_{,3} - 2E_p \times r_{,3} + 3F_p\left[\left(r_{,3}\right)^3\right]\right]$$

For "F_{31}" or "F_1", corresponding parameters are:

$$PP = r_{,1}$$

$$U_1 = 3 - 4\nu + \left(r_{,1}\right)^2 - \frac{\nu_u - \nu}{1-\nu_u}\left[B_p - \left(r_{,1}\right)^2 C_p\right]$$

$$U_2 = r_{,1} \times r_{,2} - \frac{\nu_u - \nu}{1-\nu_u}\left(-r_{,1} \times r_{,2}\right) C_p$$

$$U_3 = r_{,1} \times r_{,3} - \frac{\nu_u - \nu}{1-\nu_u}\left(-r_{,1} \times r_{,3}\right) C_p$$

$$S_{11} = -\left(1-2\nu\right) r_{,1} - 3\left[\left(r_{,1}\right)^3\right] - \frac{\nu_u - \nu}{1-\nu_u}\left[D_p \times r_{,1} - 2E_p \times r_{,1} + 3F_p\left[\left(r_{,1}\right)^3\right]\right],$$

$$S_{12} = -\left(1-2\nu\right) r_{,2} - 3\left[\left(r_{,1}\right)^2 \times r_{,2}\right] - \frac{\nu_u - \nu}{1-\nu_u}\left[-E_p \times r_{,2} + 3F_p\left[\left(r_{,1}\right)^2 \times r_{,2}\right]\right],$$

$$S_{13} = -\left(1-2\nu\right) r_{,3} - 3\left[\left(r_{,1}\right)^2 \times r_{,3}\right] - \frac{\nu_u - \nu}{1-\nu_u}\left[-E_p \times r_{,2} + 3F_p\left[\left(r_{,1}\right)^2 \times r_{,3}\right]\right],$$

$$S_{22} = \left(1-2\nu\right) r_{,1} - 3\left[r_{,1} \times \left(r_{,2}\right)^2\right] - \frac{\nu_u - \nu}{1-\nu_u}\left[D_p \times r_{,1} + 3F_p\left[r_{,1} \times \left(r_{,2}\right)^2\right]\right],$$

$$S_{23} = -3\left[r_{,1} \times r_{,2} \times r_{,3}\right] - \frac{\nu_u - \nu}{1-\nu_u}\left[3F_p\left[r_{,1} \times r_{,2} \times r_{,3}\right]\right],$$

$$S_{33} = \left(1-2\nu\right) r_{,1} - 3\left[r_{,1} \times \left(r_{,3}\right)^2\right] - \frac{\nu_u - \nu}{1-\nu_u}\left[D_p \times r_{,1} + 3F_p\left[r_{,1} \times \left(r_{,3}\right)^2\right]\right]$$

For "F_{21}" or "F_2", corresponding parameters are:

$$PP = r_{,2}$$

$$U_1 = r_{,1} \times r_{,2} - \frac{\nu_u - \nu}{1-\nu_u}\left(-r_{,1} \times r_{,2}\right) C_p$$

$$U_2 = 3 - 4\nu + \left(r_{,2}\right)^2 - \frac{\nu_u - \nu}{1-\nu_u}\left[B_p - \left(r_{,2}\right)^2 C_p\right]$$

$$U_3 = r_{,2} \times r_{,3} - \frac{\nu_u - \nu}{1-\nu_u}\left(-r_{,2} \times r_{,3}\right) C_p$$

$$S_{11} = \left(1-2\nu\right) r_{,2} - 3\left[\left(r_{,1}\right)^2 \times r_{,2}\right] - \frac{\nu_u - \nu}{1-\nu_u}\left[D_p \times r_{,2} + 3F_p\left[\left(r_{,1}\right)^2 \times r_{,2}\right]\right],$$

$$S_{12} = -\left(1-2\nu\right) r_{,1} - 3\left[r_{,1} \times \left(r_{,2}\right)^2\right] - \frac{\nu_u - \nu}{1-\nu_u}\left[-E_p \times r_{,1} + 3F_p\left[r_{,1} \times \left(r_{,2}\right)^2\right]\right],$$

$$S_{13} = -3\left[r_{,1} \times r_{,2} \times r_{,3}\right] - \frac{\nu_u - \nu}{1-\nu_u}\left[3F_p\left[r_{,1} \times r_{,2} \times r_{,3}\right]\right],$$

$$S_{22} = -(1-2\nu) r_{,2} - 3\left[\left(r_{,2}\right)^3\right] - \frac{\nu_u - \nu}{1-\nu_u}\left[D_p \times r_{,2} - 2E_p \times r_{,2} + 3F_p\left[\left(r_{,2}\right)^3\right]\right],$$

$$S_{23} = -(1-2\nu) r_{,3} - 3\left[\left(r_{,2}\right)^2 \times r_{,3}\right] - \frac{\nu_u - \nu}{1-\nu_u}\left[-E_p \times r_{,3} + 3F_p\left[\left(r_{,2}\right)^2 \times r_{,3}\right]\right],$$

$$S_{33} = (1-2\nu) r_{,2} - 3\left[r_{,2} \times \left(r_{,3}\right)^2\right] - \frac{\nu_u - \nu}{1-\nu_u}\left[D_p \times r_{,2} + 3F_p\left[r_{,2} \times \left(r_{,3}\right)^2\right]\right]$$

A.6. Continuous point displacement discontinuity

Positive sign convention for displacement discontinuities (DD_{33}, DD_{31}, and DD_{32}) is shown in Figure A. 3. Solution of thermoporoelastic field equation to displacement discontinuities is presented below.

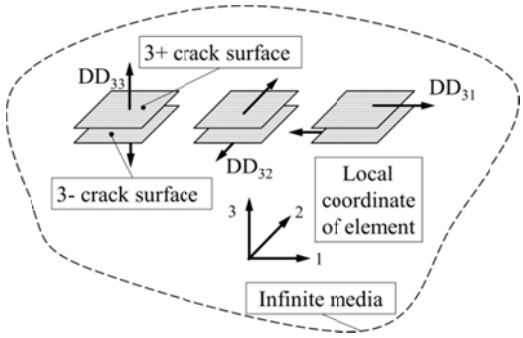

Figure A. 3. Positive displacement discontinuities on crack element

$$\{P\}^{dc} = \frac{G}{2\pi\alpha(1-2\nu)} \times \frac{\nu_u - \nu}{1-\nu_u} \times \frac{PP}{R^3}$$

$$\begin{Bmatrix} u_1 \\ u_2 \\ u_3 \end{Bmatrix}^{dc} = \frac{1}{8\pi(1-\nu)} \frac{1}{R^2} \begin{Bmatrix} U_1 \\ U_2 \\ U_3 \end{Bmatrix}$$

$$\begin{bmatrix} \sigma_{11} & \sigma_{12} & \sigma_{13} \\ Sym & \sigma_{22} & \sigma_{23} \\ Sym & Sym & \sigma_{33} \end{bmatrix}^{dc} = \frac{G}{4\pi(1-\nu)} \times \frac{1}{R^3} \begin{bmatrix} S_{11} & S_{12} & S_{13} \\ Sym & S_{22} & S_{23} \\ Sym & Sym & S_{33} \end{bmatrix}$$

In these relations, super script "dc" means continuous displacement discontinuity. In previous relations, $PP, U_1, U_2, U_3, S_{11}, S_{12}, S_{13}, S_{22}, S_{23}, S_{33}$, depends on direction of displacement discontinuity. To define these parameters for each direction, we need following definition:

$$A_p = \left(2+4\xi_p^2\right)\frac{\xi_p}{\sqrt{\pi}}e^{-\xi_p^2} - erf(\xi_p),$$

$$B_p = 3erf(\xi_p) - \left(6+4\xi_p^2\right)\frac{\xi_p}{\sqrt{\pi}}e^{-\xi_p^2},$$

$$C_p = \left(\frac{3}{2\xi_p^2}+1\right)erf\left(\xi_p\right) - \left(\frac{3}{\xi_p^2}+4\right)\frac{\xi_p}{\sqrt{\pi}}e^{-\xi_p^2},$$

$$D_p = \left(1-\frac{3}{2\xi_p^2}\right)erf\left(\xi_p\right) + \frac{3}{\xi_p\sqrt{\pi}}e^{-\xi_p^2},$$

$$E_p = \left(1-\frac{5}{2\xi_p^2}\right)erf\left(\xi_p\right) + \left(\frac{5}{\xi_p^2}+\frac{4}{3}\right)\frac{\xi_p}{\sqrt{\pi}}e^{-\xi_p^2},$$

$$F_p = \left(3+\frac{3}{2\xi_p^2}\right)erf(\xi_p) - \left(8+\frac{3}{\xi_p^2}+8\xi_p^2\right)\frac{\xi_p}{\sqrt{\pi}}e^{-\xi_p^2},$$

$$G_p = \left(1-\frac{3}{2\xi_p^2}\right)erf(\xi_p) + \frac{3}{\xi_p\sqrt{\pi}}e^{-\xi_p^2},$$

$$H_p = -\left(1+\frac{5}{2\xi_p^2}\right)erf(\xi_p) + \left(\frac{16}{3}+\frac{5}{\xi_p^2}+\frac{8\xi_p^2}{3}\right)\frac{\xi_p}{\sqrt{\pi}}e^{-\xi_p^2},$$

$$I_p = \left(1-\frac{5}{2\xi_p^2}\right)erf(\xi_p) + \left(\frac{4}{3}+\frac{5}{\xi_p^2}\right)\frac{\xi_p}{\sqrt{\pi}}e^{-\xi_p^2},$$

$$J_p = \left(1-\frac{7}{2\xi_p^2}\right)erf(\xi_p) + \left(\frac{8}{3}+\frac{7}{\xi_p^2}+\frac{8\xi_p^2}{15}\right)\frac{\xi_p}{\sqrt{\pi}}e^{-\xi_p^2}$$

For "DD_{33}" corresponding parameters are:

$$PP = A_p + \left(r_{,3}\right)^2 B_p$$

$$U_1 = -\left(1-2\nu\right) r_{,1} + 3\left(r_{,1} \times \left(r_{,3}\right)^2\right) + \frac{\nu_u - \nu}{1-\nu_u}\left[C_p \times r_{,1} + 3E_p\left(r_{,1} \times \left(r_{,3}\right)^2\right)\right],$$

$$U_2 = -\left(1-2\nu\right) r_{,2} + 3\left(r_{,2} \times \left(r_{,3}\right)^2\right) + \frac{\nu_u - \nu}{1-\nu_u}\left[C_p \times r_{,2} + 3E_p\left(r_{,2} \times \left(r_{,3}\right)^2\right)\right],$$

$$U_3 = \left(1-2\nu\right) r_{,3} + 3\left(r_{,3}\right)^3 + \frac{\nu_u - \nu}{1-\nu_u}\left[C_p \times r_{,3} - 2D_p \times r_3 + 3E_p\left(r_{,3}\right)^3\right],$$

$$S_{11} = -\left(1-4\nu\right) - 15\left(r_{,1} \times r_{,3}\right)^2 + 3\left(1-2\nu\right)\left(\left(r_{,1}\right)^2 + \left(r_{,3}\right)^2\right) + \frac{\nu_u - \nu}{1-\nu_u}\begin{bmatrix} F_p + 3H_p\left(\left(r_{,1}\right)^2 + \left(r_{,3}\right)^2\right) \\ -15J_p\left(r_{,1} \times r_{,3}\right)^2 \end{bmatrix},$$

$$S_{12} = -15\left(r_{,1} \times r_{,2} \times \left(r_{,3}\right)^2\right) + 3\left(1-2\nu\right)\left(r_{,1} \times r_{,2}\right) + \frac{\nu_u - \nu}{1-\nu_u}\left[3H_p\left(r_{,1} \times r_{,2}\right) - 15J_p\left(r_{,1} \times r_{,2} \times \left(r_{,3}\right)^2\right)\right],$$

$$S_{13} = -15\left(r_{,1} \times \left(r_{,3}\right)^3\right) + 3\left(r_{,1} \times r_{,3}\right) + \frac{\nu_u - \nu}{1-\nu_u}\left[\left(3H_p + 6I_p\right)\left(r_{,1} \times r_{,3}\right) - 15J_p\left(r_{,1} \times \left(r_{,3}\right)^3\right)\right],$$

$$S_{22} = -\left(1-4\nu\right) - 15\left(r_{,2} \times r_{,3}\right)^2 + 3\left(1-2\nu\right)\left(\left(r_{,2}\right)^2 + \left(r_{,3}\right)^2\right) + \frac{\nu_u - \nu}{1-\nu_u}\begin{bmatrix} F_p + 3H_p\left(\left(r_{,2}\right)^2 + \left(r_{,3}\right)^2\right) \\ -15J_p\left(r_{,2} \times r_{,3}\right)^2 \end{bmatrix},$$

$$S_{23} = -15\left(r_{,2} \times \left(r_{,3}\right)^3\right) + 3\left(r_{,2} \times r_{,3}\right) + \frac{\nu_u - \nu}{1-\nu_u}\left[\left(3H_p + 6I_p\right)\left(r_{,2} \times r_{,3}\right) - 15J_p\left(r_{,2} \times \left(r_{,3}\right)^3\right)\right],$$

$$S_{33} = 1 - 15\left(r_{,3}\right)^4 + 6\left(r_{,3}\right)^2 + \frac{\nu_u - \nu}{1-\nu_u}\left[F_p - 2G_p + 6H_p\left(r_{,3}\right)^2 + 12I_p\left(r_{,3}\right)^2 - 15J_p\left(r_{,3}\right)^4\right]$$

For "DD_{31}" corresponding parameters are:

$$PP = \left(r_{,1} \times r_{,3}\right) B_p$$

$$U_1 = \left(1-2\nu\right) r_{,3} + 3\left(\left(r_{,1}\right)^2 \times r_{,3}\right) + \frac{\nu_u - \nu}{1-\nu_u}\left[-D_p \times r_{,3} + 3E_p\left(\left(r_{,1}\right)^2 \times r_{,3}\right)\right],$$

$$U_2 = 3\left(r_{,1} \times r_{,2} \times r_{,3}\right) + \frac{\nu_u - \nu}{1-\nu_u}\left[3E_p\left(r_{,1} \times r_{,2} \times r_{,3}\right)\right],$$

$$U_3 = \left(1-2\nu\right) r_{,1} + 3\left(r_{,1} \times \left(r_{,3}\right)^2\right) + \frac{\nu_u - \nu}{1-\nu_u}\left[-D_p \times r_{,1} + 3E_p\left(r_{,1} \times \left(r_{,3}\right)^2\right)\right]$$

$$S_{11} = -15\left(\left(r_{,1}\right)^3 \times r_{,3}\right) + 3\left(r_{,1} \times r_{,3}\right) + \frac{\nu_u - \nu}{1-\nu_u}\left[3H_p\left(r_{,1} \times r_{,3}\right) + 2I_p\left(r_{,1} \times r_{,3}\right) - 15J_p\left(\left(r_{,1}\right)^3 \times r_{,3}\right)\right],$$

$$S_{12} = -15\left(\left(r_{,1}\right)^2 \times r_{,2} \times r_{,3}\right) + 3\nu\left(r_{,2} \times r_{,3}\right) + \frac{\nu_u - \nu}{1-\nu_u}\left[3I_p\left(r_{,2} \times r_{,3}\right) - 15J_p\left(\left(r_{,1}\right)^2 \times r_{,2} \times r_{,3}\right)\right],$$

$$S_{13} = 1-2\nu-15\left(r_{,1} \times r_{,3}\right)^2 + 3\nu\left(\left(r_{,1}\right)^2 + \left(r_{,3}\right)^2\right) + \frac{\nu_u - \nu}{1-\nu_u}\begin{bmatrix} -G_p + 3I_p\left(\left(r_{,1}\right)^2 + \left(r_{,3}\right)^2\right) - \\ 15J_p\left(r_{,1} \times r_{,3}\right)^2 \end{bmatrix},$$

$$S_{22} = -15\left(r_{,1} \times \left(r_{,2}\right)^2 \times r_{,3}\right) + 3\left(1-2\nu\right)\left(r_{,1} \times r_{,3}\right) + \frac{\nu_u - \nu}{1-\nu_u}\left[3H_p\left(r_{,1} \times r_{,3}\right) - 15J_p\left(r_{,1} \times \left(r_{,2}\right)^2 \times r_{,3}\right)\right],$$

$$S_{23} = -15\left(r_{,1} \times r_{,2} \times \left(r_{,3}\right)^2\right) + 3\nu\left(r_{,1} \times r_{,2}\right) + \frac{\nu_u - \nu}{1-\nu_u}\left[3I_p\left(r_{,1} \times r_{,2}\right) - 15J_p\left(r_{,1} \times r_{,2} \times \left(r_{,3}\right)^2\right)\right],$$

$$S_{33} = -15\left(r_{,1} \times \left(r_{,3}\right)^3\right) + 3\left(r_{,1} \times r_{,3}\right) + \frac{\nu_u - \nu}{1-\nu_u}\left[3H_p\left(r_{,1} \times r_{,3}\right) + 6I_p\left(r_{,1} \times r_{,3}\right) - 15J_p\left(r_{,1} \times \left(r_{,3}\right)^3\right)\right]$$

For "DD_{32}" corresponding parameters are:

$$PP = \left(r_{,2} \times r_{,3}\right) B_p$$

$$U_1 = 3\left(r_{,1} \times r_{,2} \times r_{,3}\right) + \frac{\nu_u - \nu}{1-\nu_u}\left[3E_p\left(r_{,1} \times r_{,2} \times r_{,3}\right)\right],$$

$$U_2 = \left(1-2\nu\right) r_{,3} + 3\left(\left(r_{,2}\right)^2 \times r_{,3}\right) + \frac{\nu_u - \nu}{1-\nu_u}\left[-D_p \times r_{,3} + 3E_p\left(\left(r_{,2}\right)^2 \times r_{,3}\right)\right],$$

$$U_3 = \left(1-2\nu\right) r_{,2} + 3\left(r_{,2} \times \left(r_{,3}\right)^2\right) + \frac{\nu_u - \nu}{1-\nu_u}\left[-D_p \times r_{,2} + 3E_p\left(r_{,2} \times \left(r_{,3}\right)^2\right)\right]$$

$$S_{11} = -15\left(\left(r_{,1}\right)^2 \times r_{,2} \times r_{,3}\right) + 3\left(1-2\nu\right)\left(r_{,2} \times r_{,3}\right) + \frac{\nu_u - \nu}{1-\nu_u}\left[3H_p\left(r_{,2} \times r_{,3}\right) - 15J_p\left(\left(r_{,1}\right)^2 \times r_{,2} \times r_{,3}\right)\right],$$

$$S_{12} = -15\left(r_{,1} \times \left(r_{,2}\right)^2 \times r_{,3}\right) + 3\nu\left(r_{,1} \times r_{,3}\right) + \frac{\nu_u - \nu}{1-\nu_u}\left[3I_p\left(r_{,1} \times r_{,3}\right) - 15J_p\left(r_{,1} \times \left(r_{,2}\right)^2 \times r_{,3}\right)\right],$$

$$S_{13} = -15\left(r_{,1} \times r_{,2} \times \left(r_{,3}\right)^2\right) + 3\nu\left(r_{,1} \times r_{,2}\right) + \frac{\nu_u - \nu}{1-\nu_u}\left[3I_p\left(r_{,1} \times r_{,2}\right) - 15J_p\left(r_{,1} \times r_{,2} \times \left(r_{,3}\right)^2\right)\right],$$

$$S_{22} = -15\left(\left(r_{,2}\right)^3 \times r_{,3}\right) + 3\left(r_{,2} \times r_{,3}\right) + \frac{\nu_u - \nu}{1-\nu_u}\left[3H_p\left(r_{,2} \times r_{,3}\right) + 6I_p\left(r_{,2} \times r_{,3}\right) - 15J_p\left(\left(r_{,2}\right)^3 \times r_{,3}\right)\right],$$

$$S_{23} = 1-2\nu-15\left(r_{,2} \times r_{,3}\right)^2 + 3\nu\left(\left(r_{,2}\right)^2 + \left(r_{,3}\right)^2\right) + \frac{\nu_u - \nu}{1-\nu_u}\begin{bmatrix} -G_p + 3I_p\left(\left(r_{,2}\right)^2 + \left(r_{,3}\right)^2\right) - \\ 15J_p\left(r_{,2} \times r_{,3}\right)^2 \end{bmatrix},$$

$$S_{33} = -15\left(r_{,2} \times \left(r_{,3}\right)^3\right) + 3\left(r_{,2} \times r_{,3}\right) + \frac{\nu_u - \nu}{1-\nu_u}\left[3H_p\left(r_{,2} \times r_{,3}\right) + 6I_p\left(r_{,2} \times r_{,3}\right) - 15J_p\left(r_{,2} \times \left(r_{,3}\right)^3\right)\right]$$

APPENDIX B

SINGULAR SOLUTIONS CHARACTERISTICS

In this appendix, effects of continuous point disturbances (1 lit/sec fluid source, 1166 Watt heat sink, 1 mm normal displacement discontinuity, 1 mm shear displacement discontinuity, 1 MPa normal traction discontinuity, and 1 MPa shear traction discontinuity) are studied in thermoporoelastic media. Moreover, to study effects of direct and indirect coupling between hydraulic and thermal processes, presence of heat sink in thermo-poroelastic media is studied. Difference between direct (Thermoporoelastic) and indirect (Thermo-poroelastic) coupling between thermal and hydraulic processes is shown in Figure B. 1.

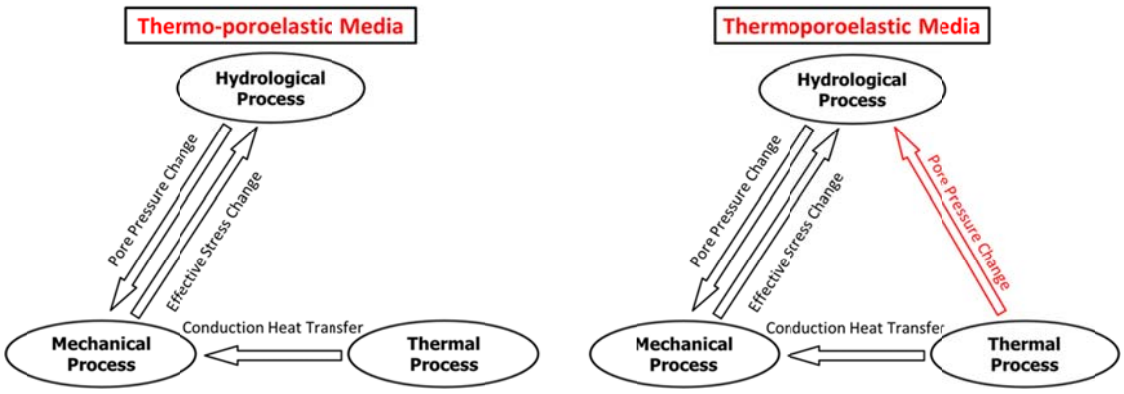

Figure B. 1. Direct versus indirect coupling between thermal and hydraulic processes

Table B. 1 presents media properties that are necessary to investigate effects of different disturbances.

Thermoporoelastic or thermo-poroelastic media is considered at zero initial condition. Each disturbance is located in the origin of global Cartesian coordinate in the

media. Effects are studied at three cross sections (20m × 20m), as shown in Figure B. 2. A unit radius concentric circle in each cross section is contrived for location reference. Since in singular solutions, results are not accurate very near to the location of disturbance, the unit circles are considered and there is not any data inside of them.

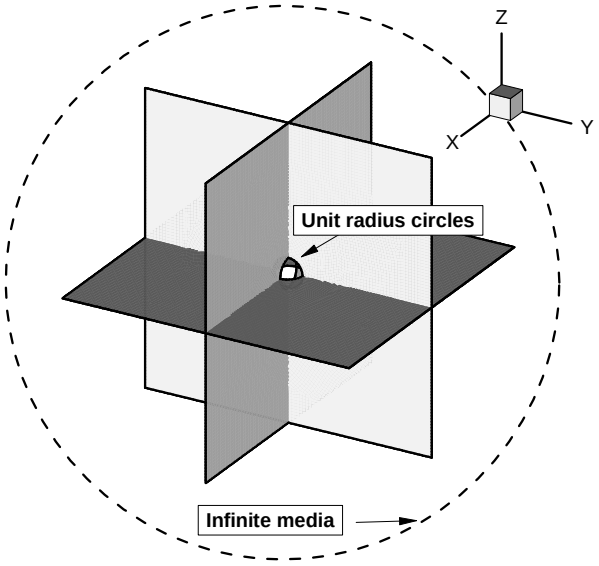

Figure B. 2. Three cross sections to investigate each singularity effects

Table B. 1. Media properties for simulating disturbance effects

Shear modulus	(Pa)	8.30×10^{9}
Drained Poisson's ratio	(-)	0.25
Undrained Poisson's ratio	(-)	0.47
Biot coefficient	(-)	0.96
Base permeability	(m^2)	1.0×10^{-17}
Porosity	(-)	0.01
Fluid density	(Kg/m^3)	1000.0
Fluid viscosity	($N.s/m^2$)	0.0003
Rock density	(Kg/m^3)	2650.0
Rock thermal conductivity	(W/m/K)	2.90
Specific heat capacity of rock	(J/kg/K)	800.0
Linear thermal expansion of rock	(1/K)	8.00×10^{-6}
Linear thermal expansion of fluid	(1/K)	1.00×10^{-4}

Disturbance effects are studied at two different time scales, after 20 minutes (all left side figures in following plots) and after 100 days (all right side figures in following plots). As it can be seen, the circle in the middle of cross sections is focused on all figures to see near effect better.

B.1. Isothermal continuous point fluid source effect

In Figure B. 4 to Figure B. 13 effect of 0.001 m^3/sec isothermal fluid sources on the origin of thermoporoelastic media (as shown in Figure B. 3) is presented. Same as thesis sign convention, compression is negative and tension is positive in all figures. Effects of the isothermal fluid source can be considered as special effects of fluid injection into reservoir.

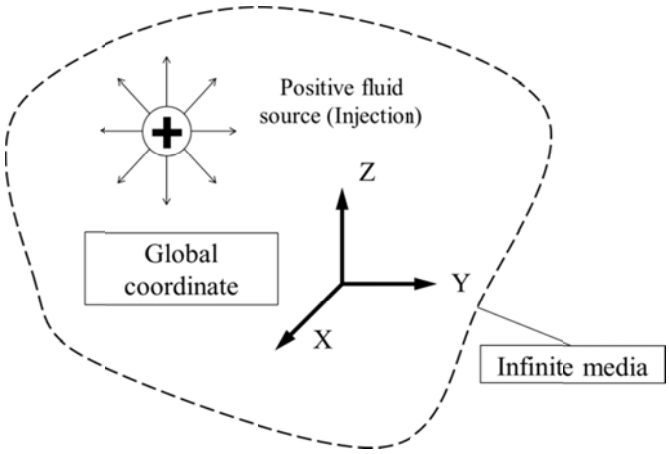

Figure B. 3 Point fluid source in the origin of porous media

Induced displacements field from point fluid source are shown in Figure B. 4 to Figure B. 6. All displacement components are inverse symmetric around the origin of global coordinates and have maximum value of 0.25 mm after 20 minutes. When time proceeds, magnitude of each displacement component is increased.

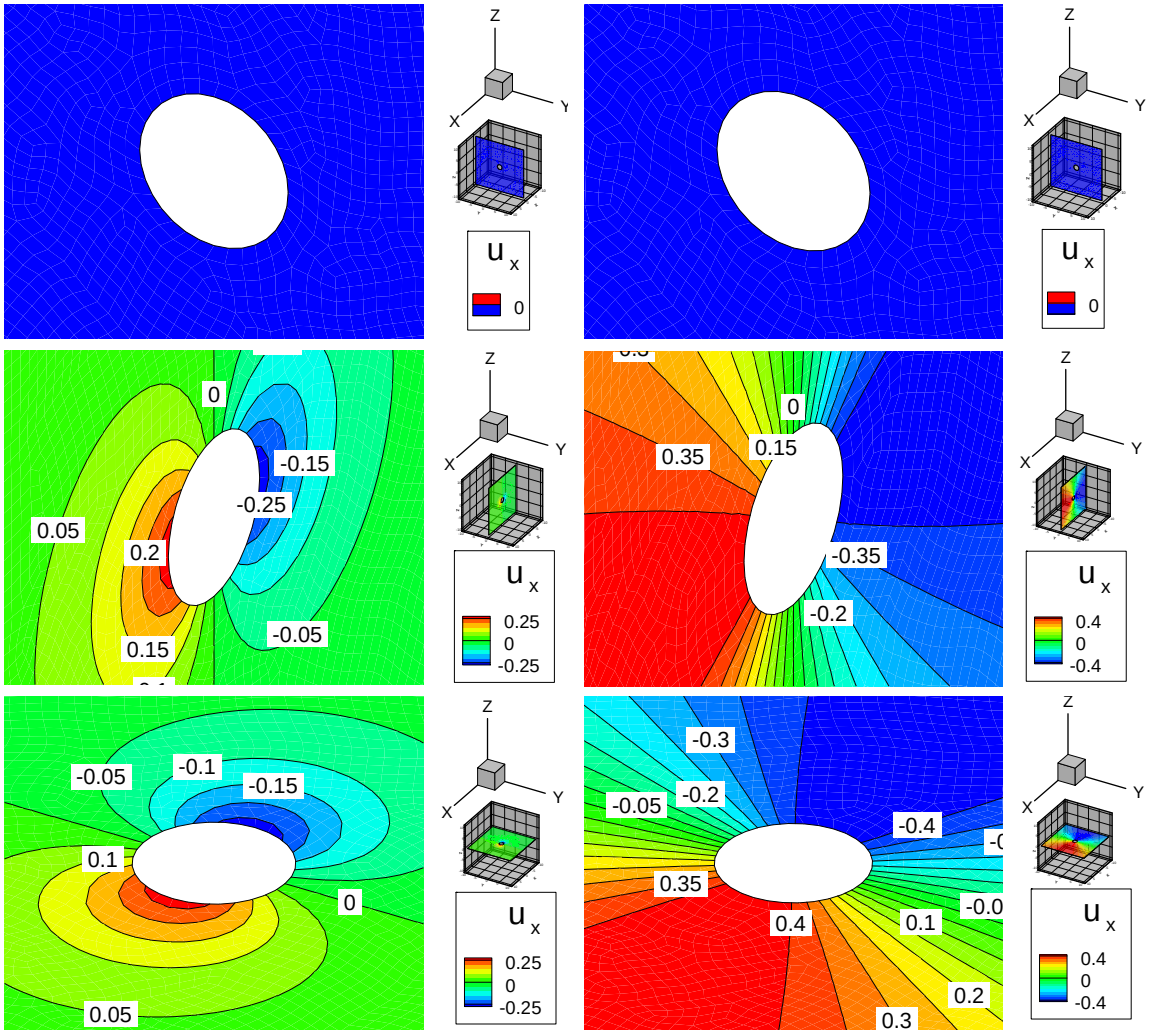

Figure B. 4. Induced X displacement (mm) distribution due to 0.001 m^3/sec fluid source at origin, after 20 minutes (left side figures), and after 100 days (right side figures)

Affected area due to fluid injection is extended to larger size after long time. Obviously amplified displacement in larger area after relatively long time (100 days) is due to diffusion process. Generally after long time, media changed its behavior from undrained to drain and shows more displacements. As expected due to symmetry of fluid injection, there is analogous effect on all displacement components.

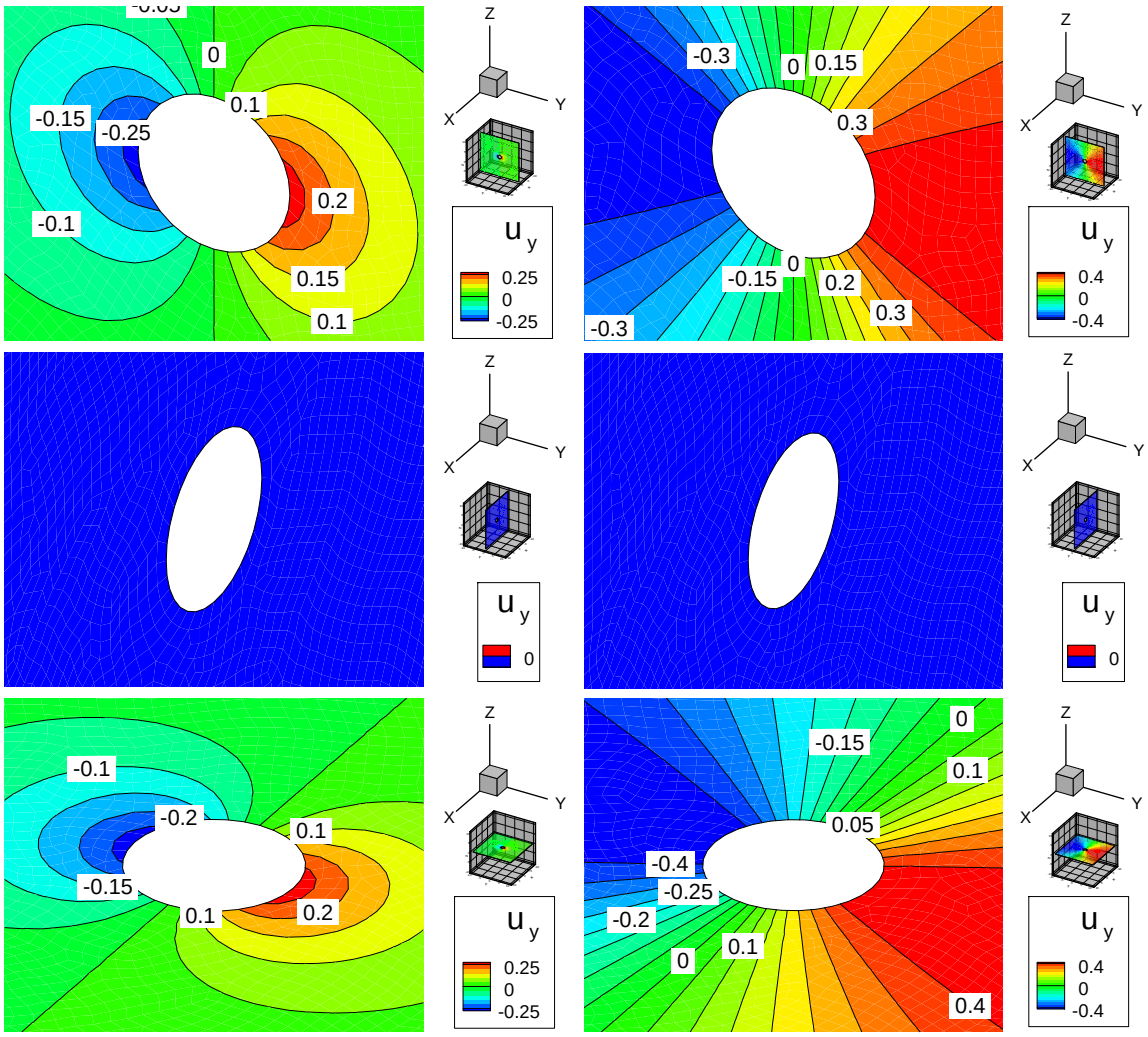

Figure B. 5. Induced Y displacement (mm) distribution due to 0.001 m^3/sec fluid source at origin, after 20 minutes (left side figures), and after 100 days (right side figures)

Induced displacement makes the stress field which is shown in Figure B. 7 to Figure B. 12. As one can see in Figure B. 7, Figure B. 10 and Figure B. 12, major components of stresses are always compressive, identical to each other and their value is increased by time due to diffusion process.

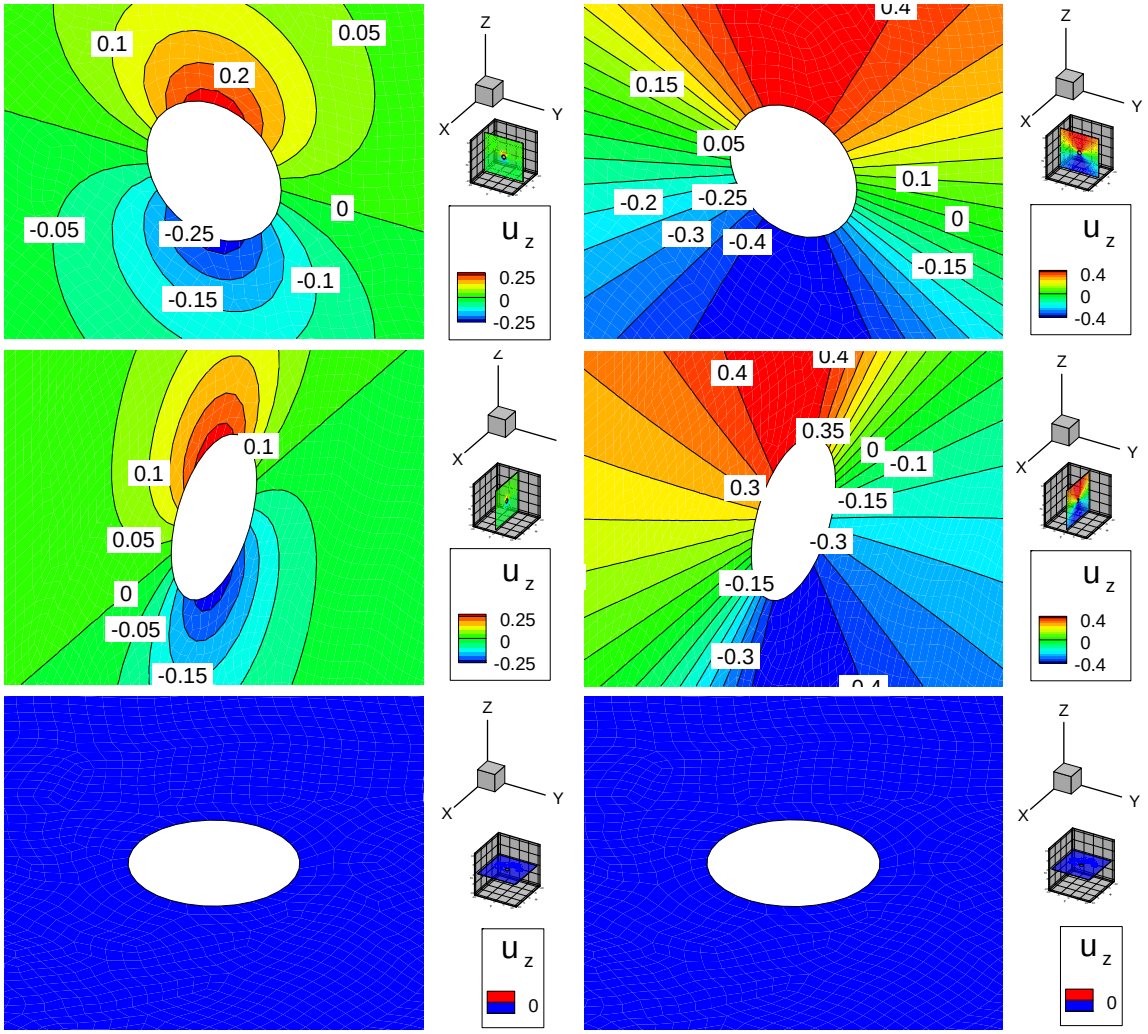

Figure B. 6. Induced Z displacement (mm) distribution due to 0.001 m^3/sec fluid source at origin, after 20 minutes (left figures), and after 100 days (right figures)

After 20 minutes maximum absolute value of compressive stress in major components of stress tensor, is about 9(MPa) and then it increases to 14 (MPa) after 100 days. This is again due to diffusion process and the fact that in this specific formation, diffusion rate is faster than injection rate and displacement increased in long time.

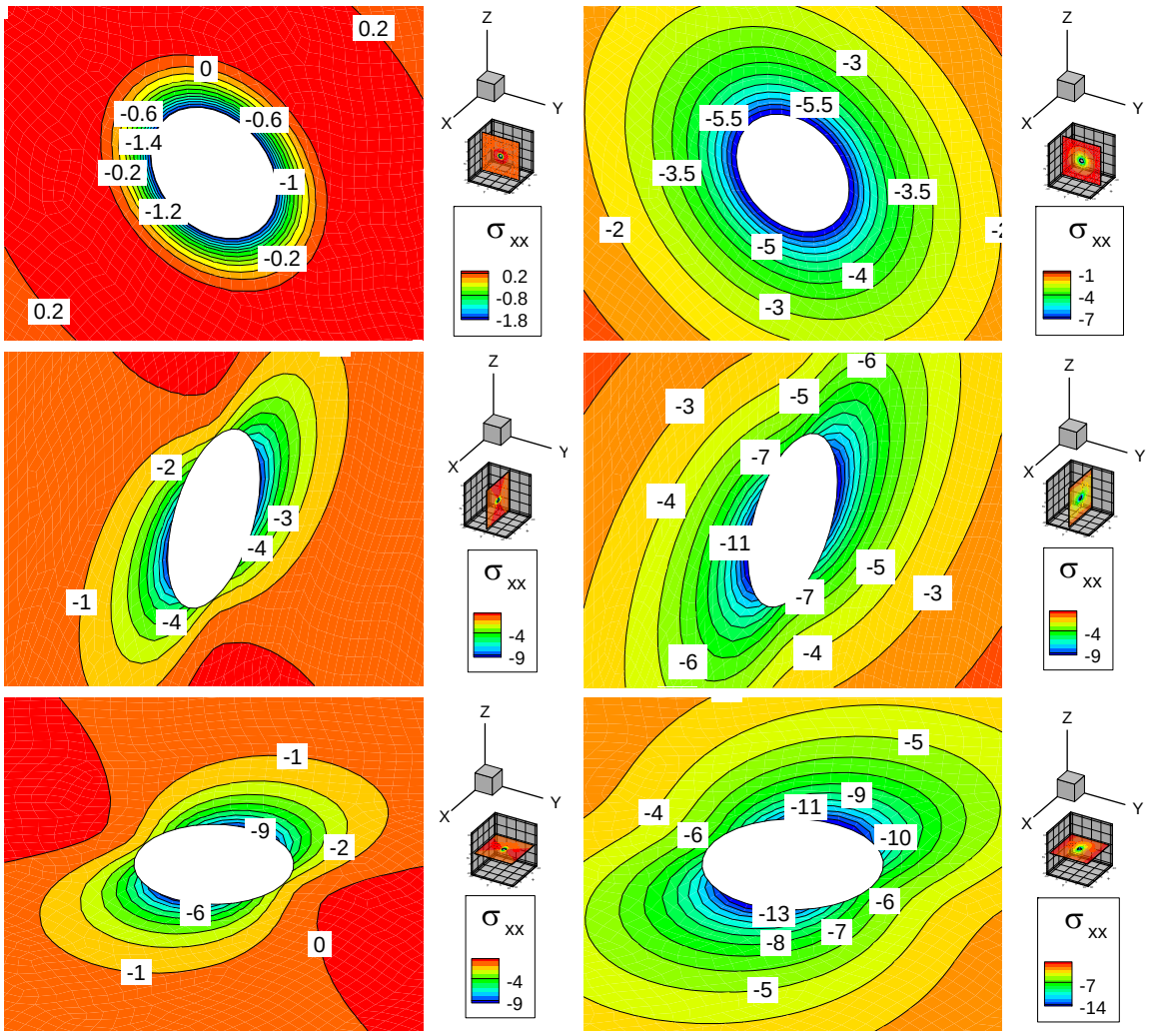

Figure B. 7 Induced total normal XX stress (MPa) distribution due to 0.001 m^3/sec fluid source at origin, after 20 minutes (left side figures), and after 100 days (right side figures)

Injection procedure induces some shear stresses (Up to 3.5 MPa, in Figure B. 8, Figure B. 9, and Figure B. 11) in media. Induced shear stresses might destabilize natural fractures in shear mode and produce micro seismicity. The interesting fact is that by increasing time the amount of shear stresses does not change and remain constant. However, when someone considers distribution of induced normal stresses, shear

stresses and pore pressure (Figure B. 13) all together, it will be clear that by increasing time, effect of injection procedure will be destabilizing natural fractures.

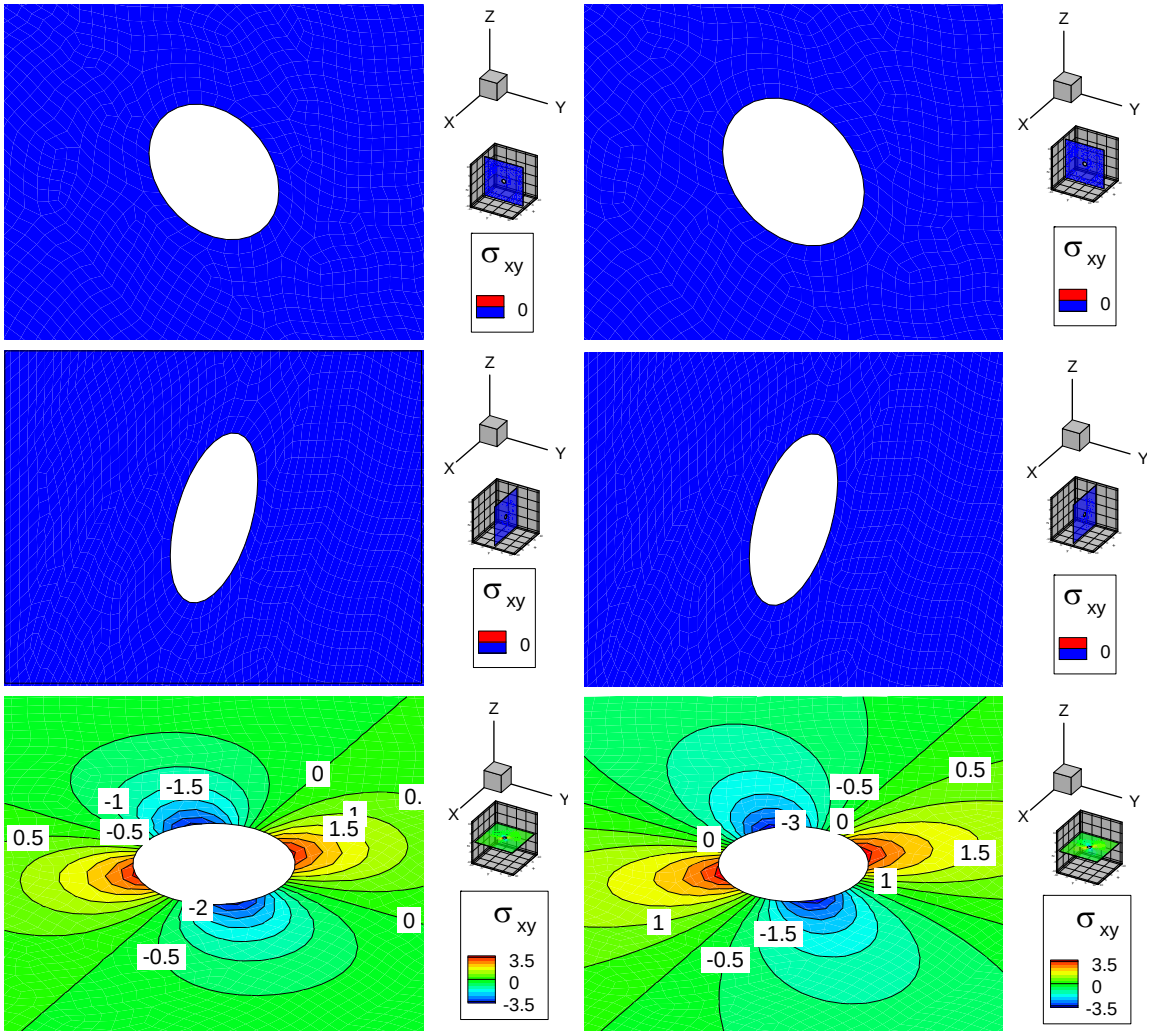

Figure B. 8 Induced shear XY stress (MPa) distribution due to 0.001 m^3/sec fluid source at origin, after 20 minutes (left side figures), and after 100 days (right side figures)

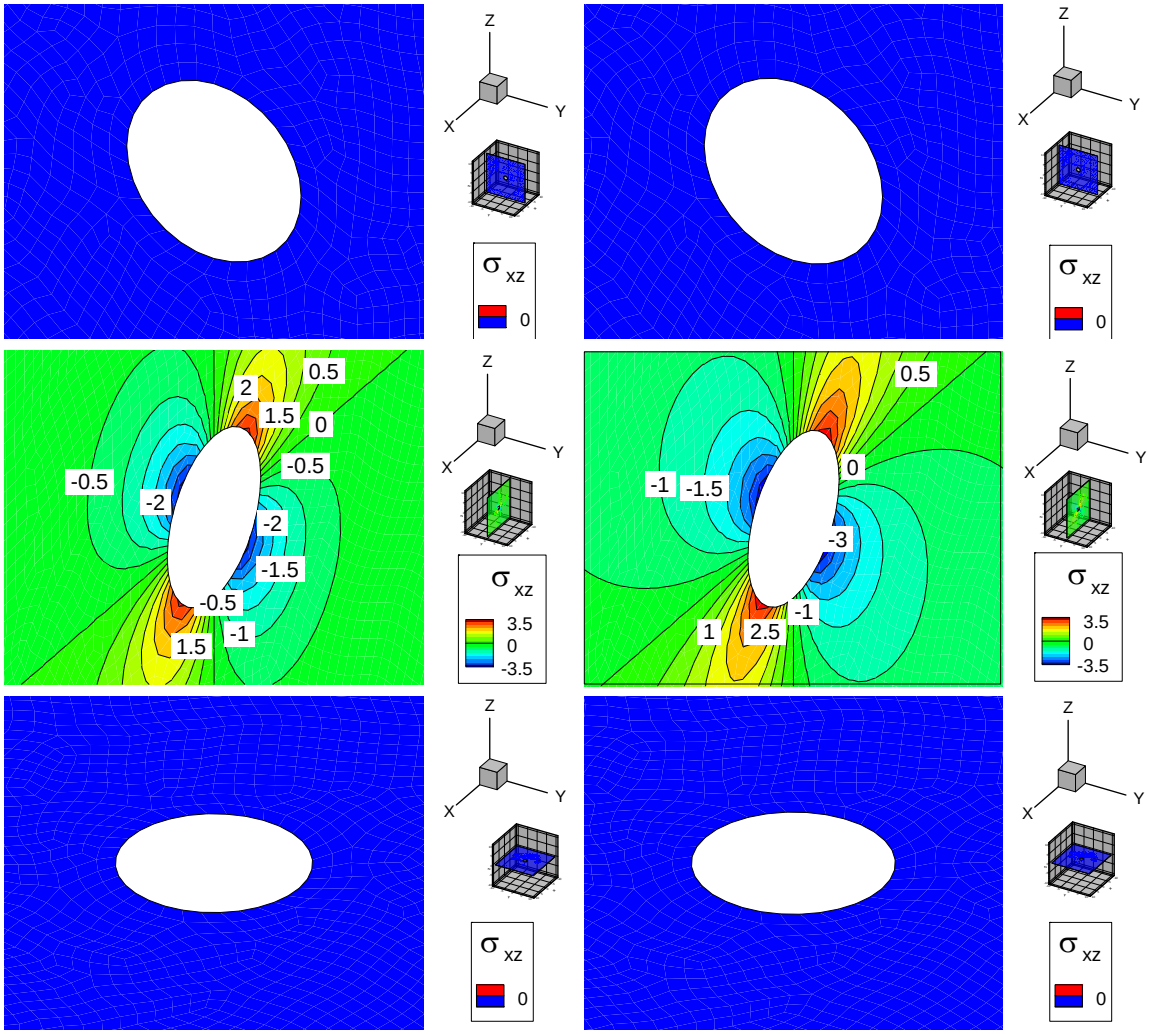

Figure B. 9 Induced shear XZ stress (MPa) distribution due to 0.001 m^3/sec fluid source at origin, after 20 minutes (left side figures), and after 100 days (right side figures)

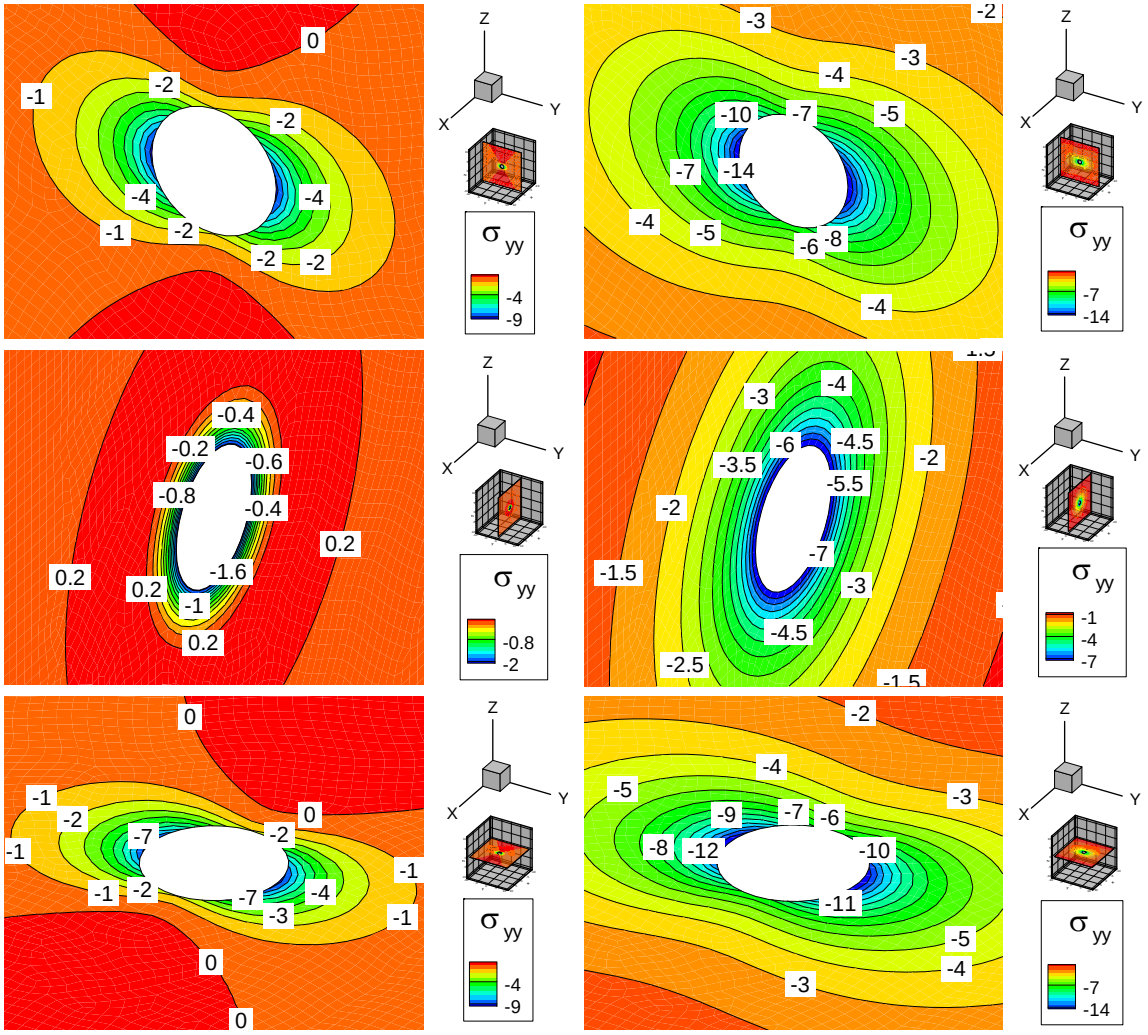

Figure B. 10 Induced total normal YY stress (MPa) distribution due to 0.001 m^3/sec fluid source at origin, after 20 minutes (left side figures), and after 100 days (right side figures)

It should be mentioned that adding total normal stresses with induced pore pressure define the effective stress regime, which is the most important parameter in defining the status of natural fractures. It is also valuable to mention that because of isothermal injection procedure the pore pressure and stress change does not induce any temperature to media.

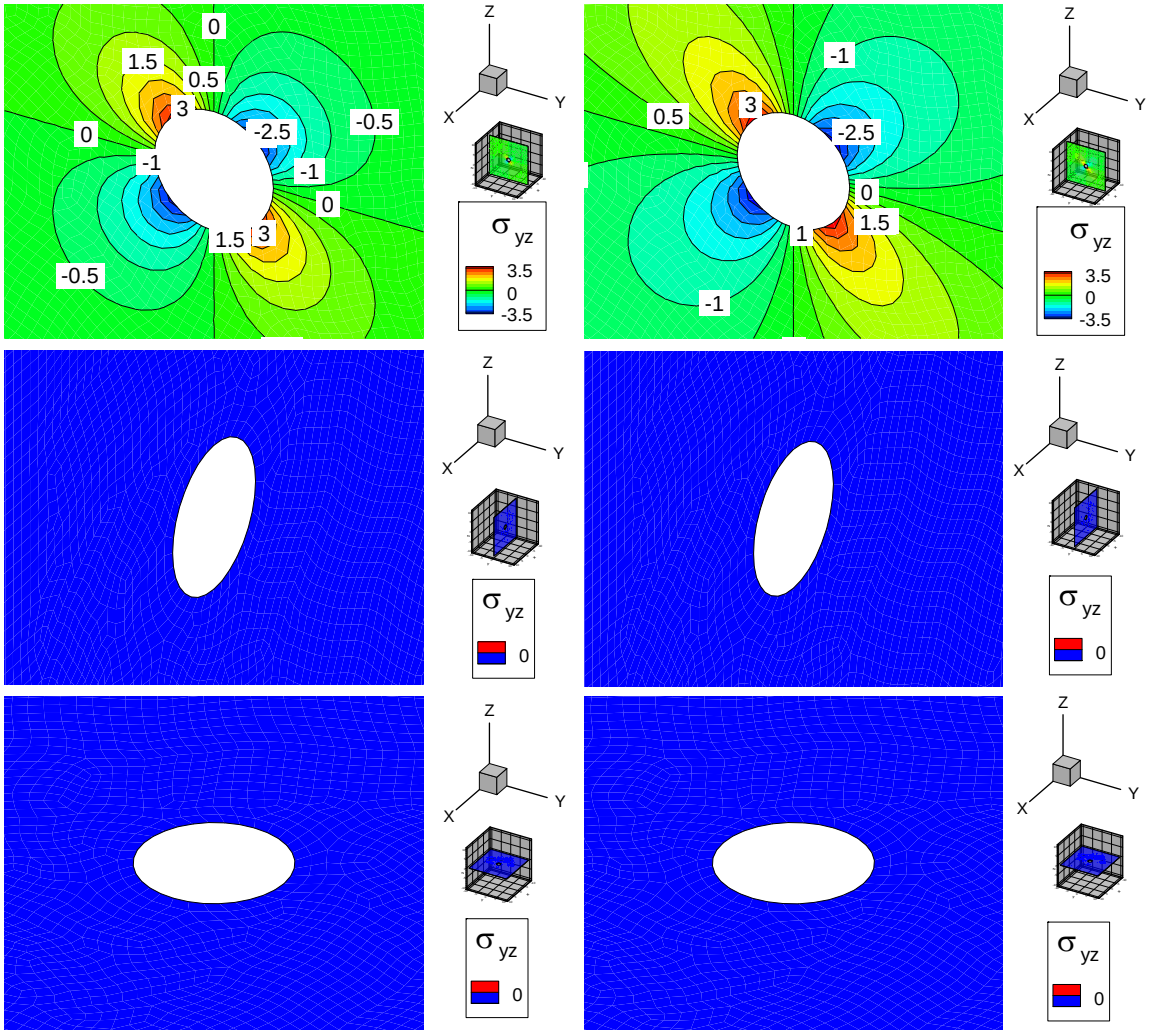

Figure B. 11 Induced shear YZ stress (MPa) distribution due to 0.001 m^3/sec fluid source at origin, after 20 minutes (left side figures), and after 100 days (right side figures)

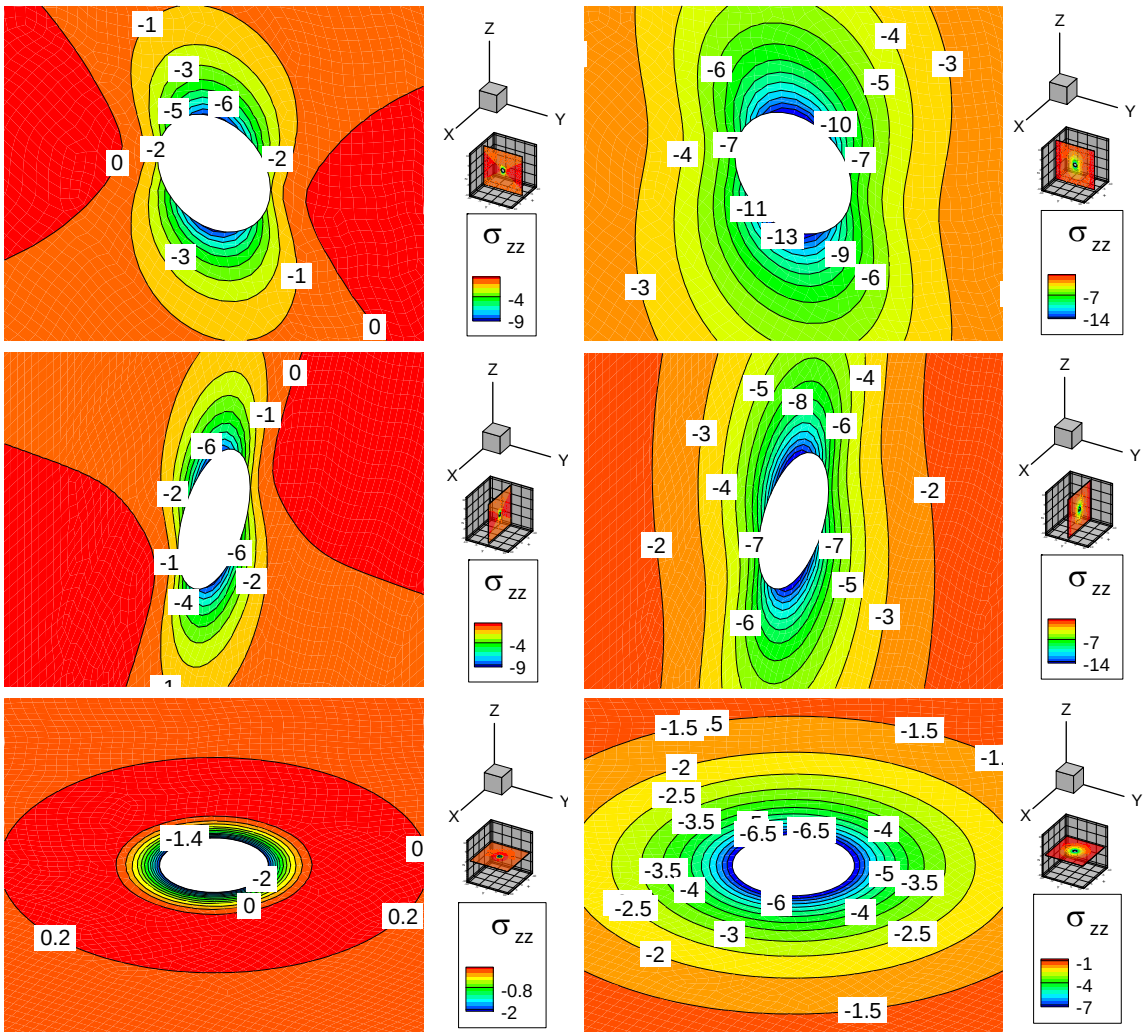

Figure B. 12 Induced total normal ZZ stress (MPa) distribution due to 0.001 m^3/sec fluid source at origin, after 20 minutes (left side figures), and after 100 days (right side figures)

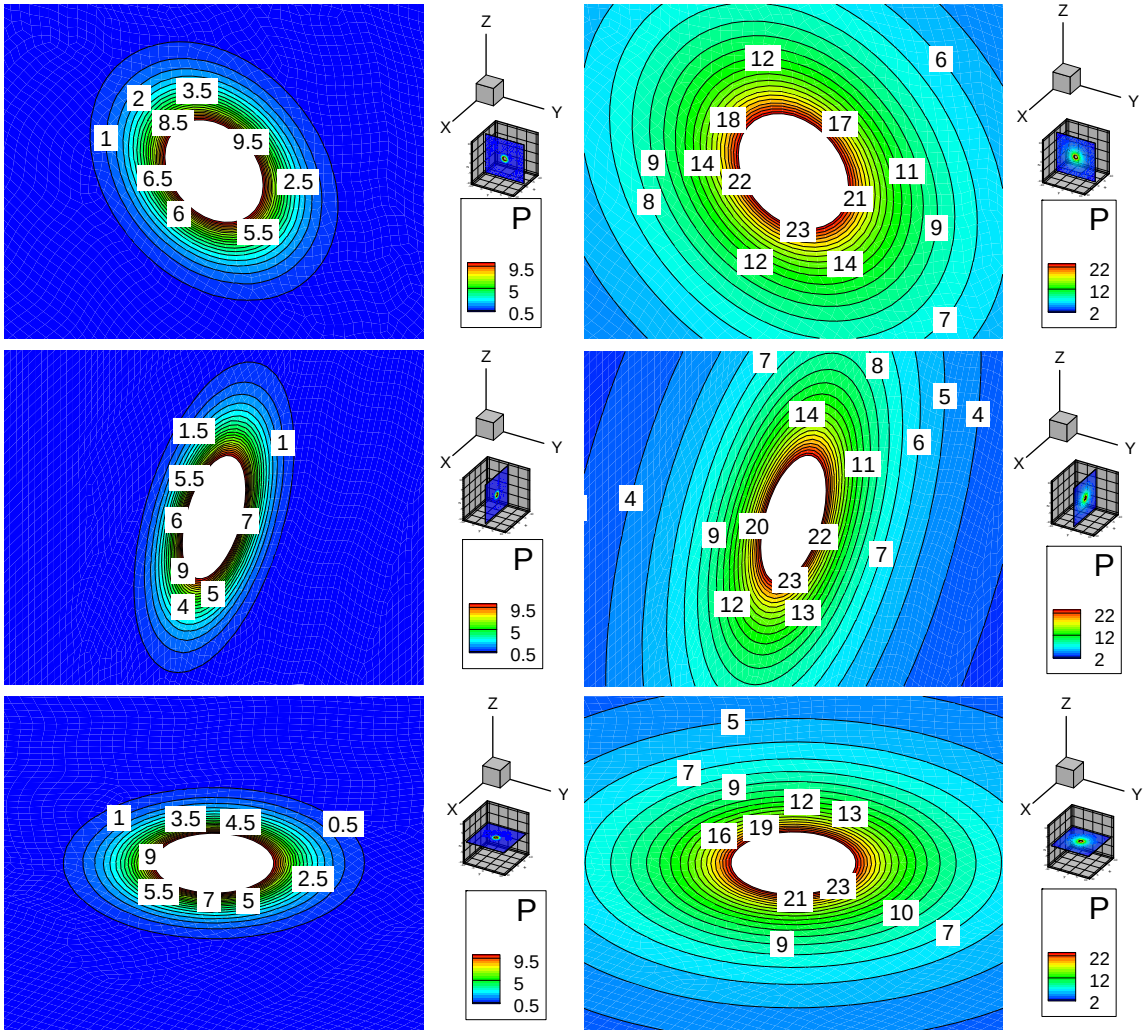

Figure B. 13 Induced pore pressure (MPa) distribution due to 0.001 m^3/sec fluid source at origin, after 20 minutes (left side figures), and after 100 days (right side figures)

Figure B. 13 shows pore pressure distribution due to injection process. It shows that when time proceeds maximum induced pore pressure increased from 9.5 (MPa) to 22 (MPa). This is because of the fact that injection rate continues during 100 days and clearly more fluid enters to media and as a consequence induced pore pressure increased.

B.2. Continuous point heat sink effect in thermoelastic media

In Figure B. 15 to Figure B. 24 effect of 1166 Joule/sec (Watt) point heat sink on the origin of thermo-poroelastic media (as shown in Figure B. 14) is presented. Induced amount of heat can increase temperature of 1 m^3 water by 1 Kelvin after an hour. Cooling effects might be considered as effects of enhanced geothermal reservoir with unit square meter contact surface.

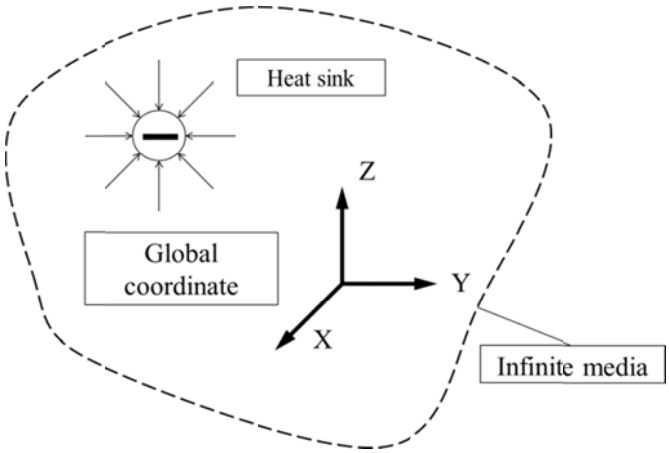

Figure B. 14 Point heat sink in the origin of thermoelastic media

Displacement fields due to the stated heat sink are presented in Figure B. 15 to Figure B. 17. As one can see in these figures, displacements fields are completely symmetric around the origin of Cartesian coordinate system, as like as induced displacement field due to fluid source. By comparing Figure B. 15 to Figure B. 17 with corresponding ones for fluid source, it will be obvious that thermal effect is very slow and its effect comes after long time (100 days).

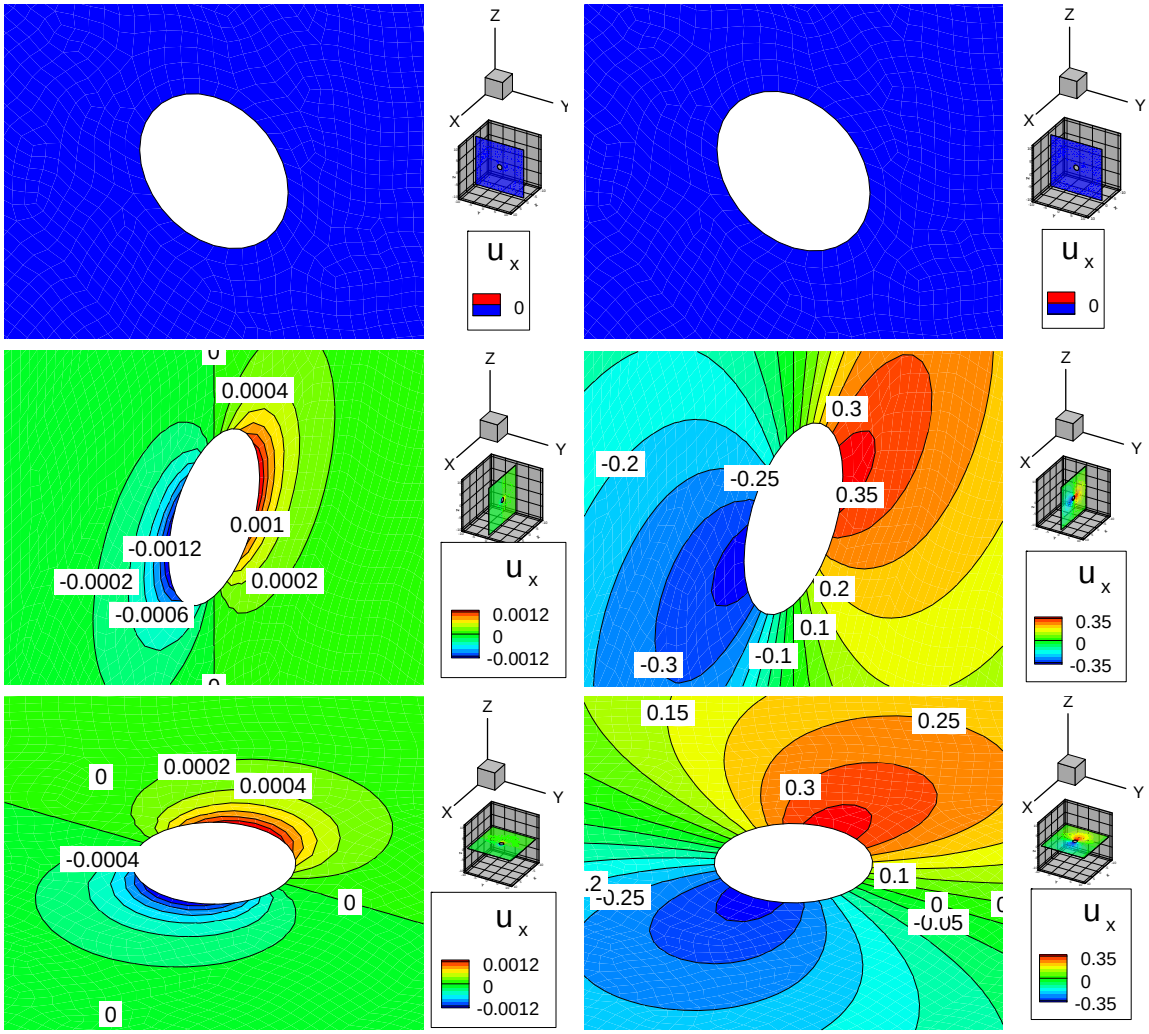

Figure B. 15 Induced X displacement (mm) distribution due to 1166 Watt heat sink at origin of thermo-poroelastic media, after 20 minutes (left side figures), and after 100 days (right side figures)

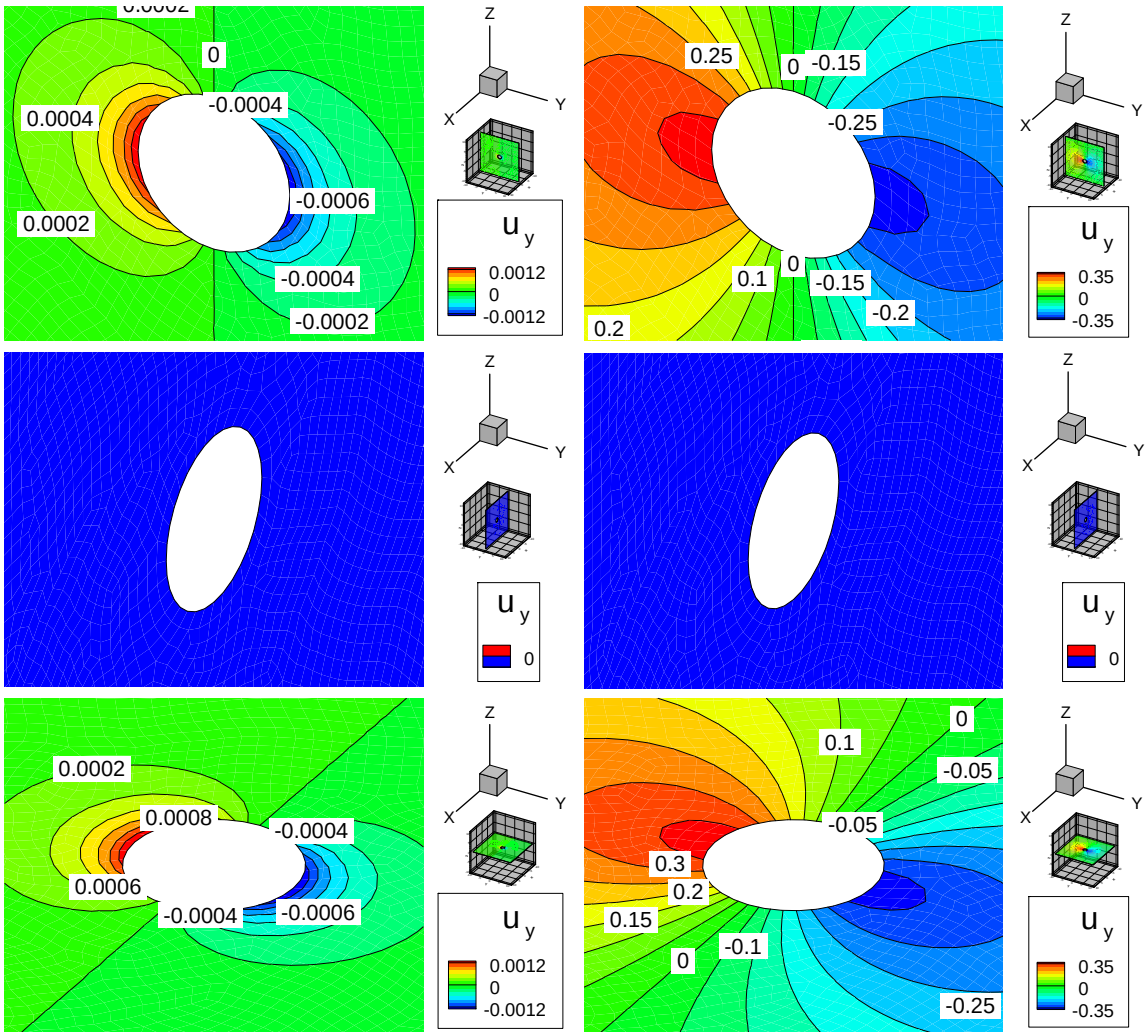

Figure B. 16 Induced Y displacement (mm) distribution due to 1166 Watt heat sink at origin of thermo-poroelastic media, after 20 minutes (left side figures), and after 100 days (right side figures)

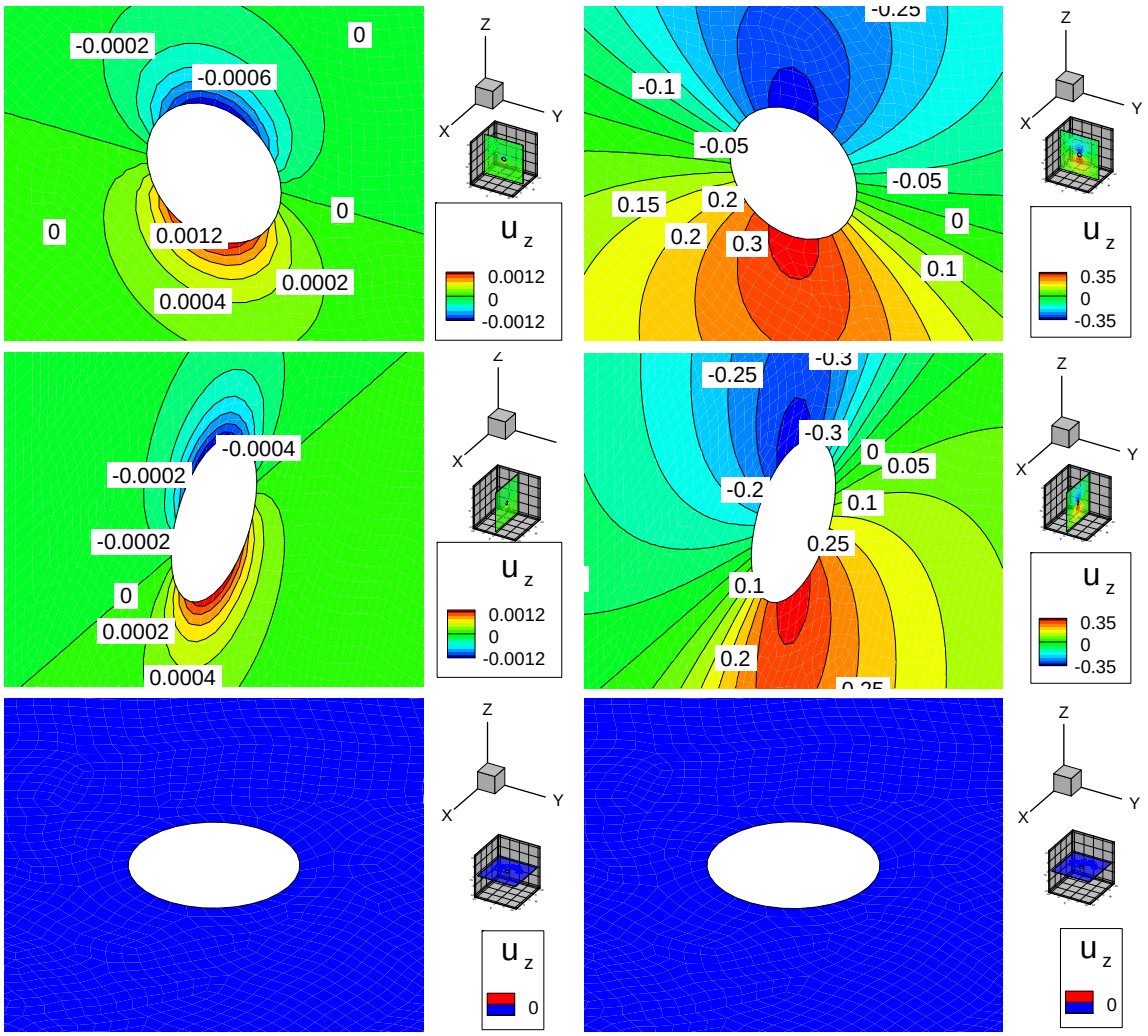

Figure B. 17 Induced Z displacement (mm) distribution due to 1166 Watt heat sink at origin of thermo-poroelastic media, after 20 minutes (left side figures), and after 100 days (right side figures)

Induced displacements fields apply some stresses to media, which is presented in Figure B. 18 to Figure B. 23. Same as displacement fields, all stress components are small at early time and they can be ignored for early time (e.g. 20 minutes) analysis. But when time goes by, e.g. after 100 days, there are considerable amount of induced tensile (10 MPa) and shear stresses (3 MPa) that might apply some sort of instabilities to natural

fractures or weakening plans. In other words, thermally induced stresses might apply instability to reservoir after long time, but not in early time. Induced temperature is shown in Figure B. 24, and proves that thermal stresses come into play after long time.

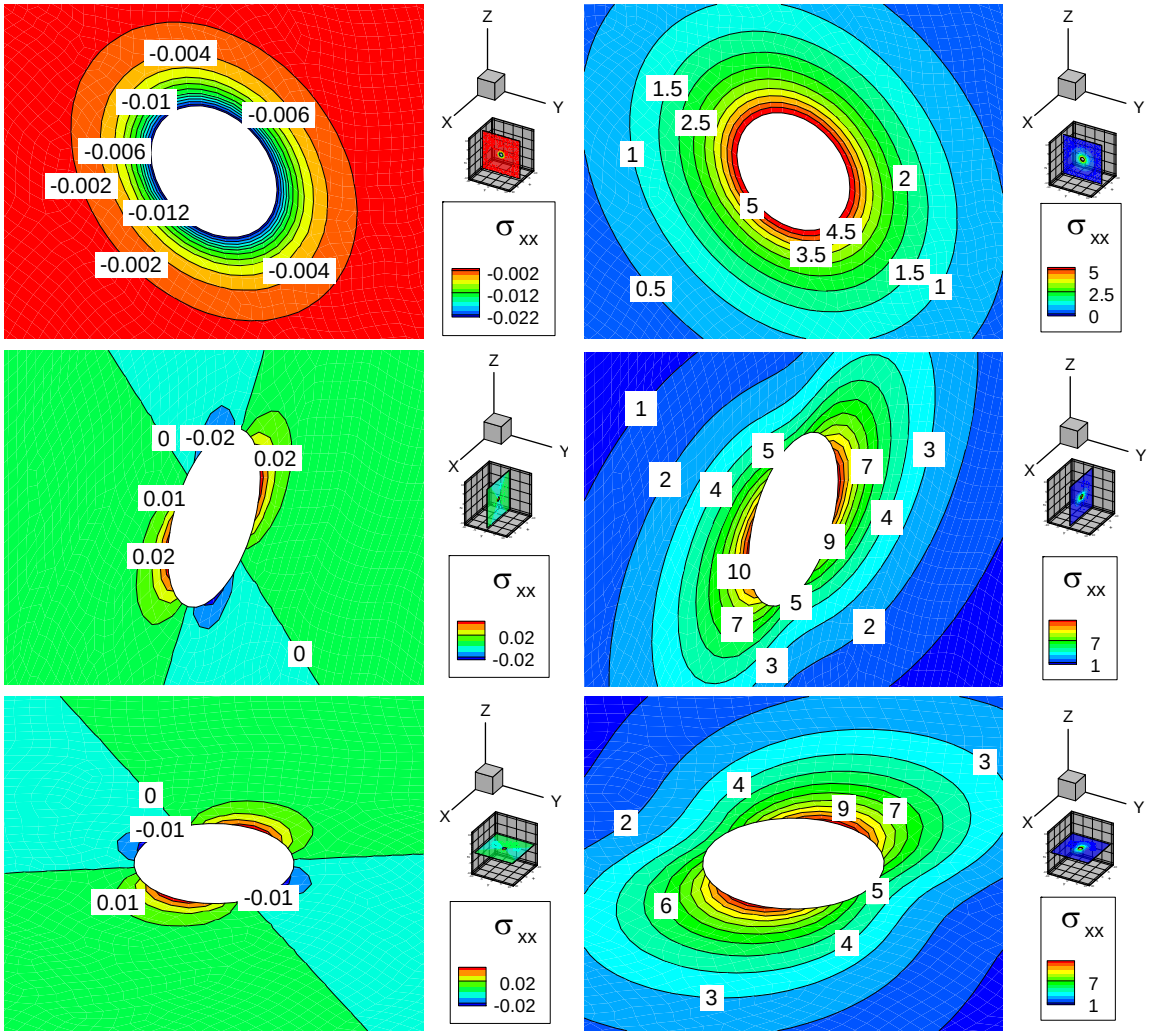

Figure B. 18 Induced total normal XX stress (MPa) distribution due to 1166 Watt heat sink at origin of thermo-poroelastic media, after 20 minutes (left side figures), and after 100 days (right side figures)

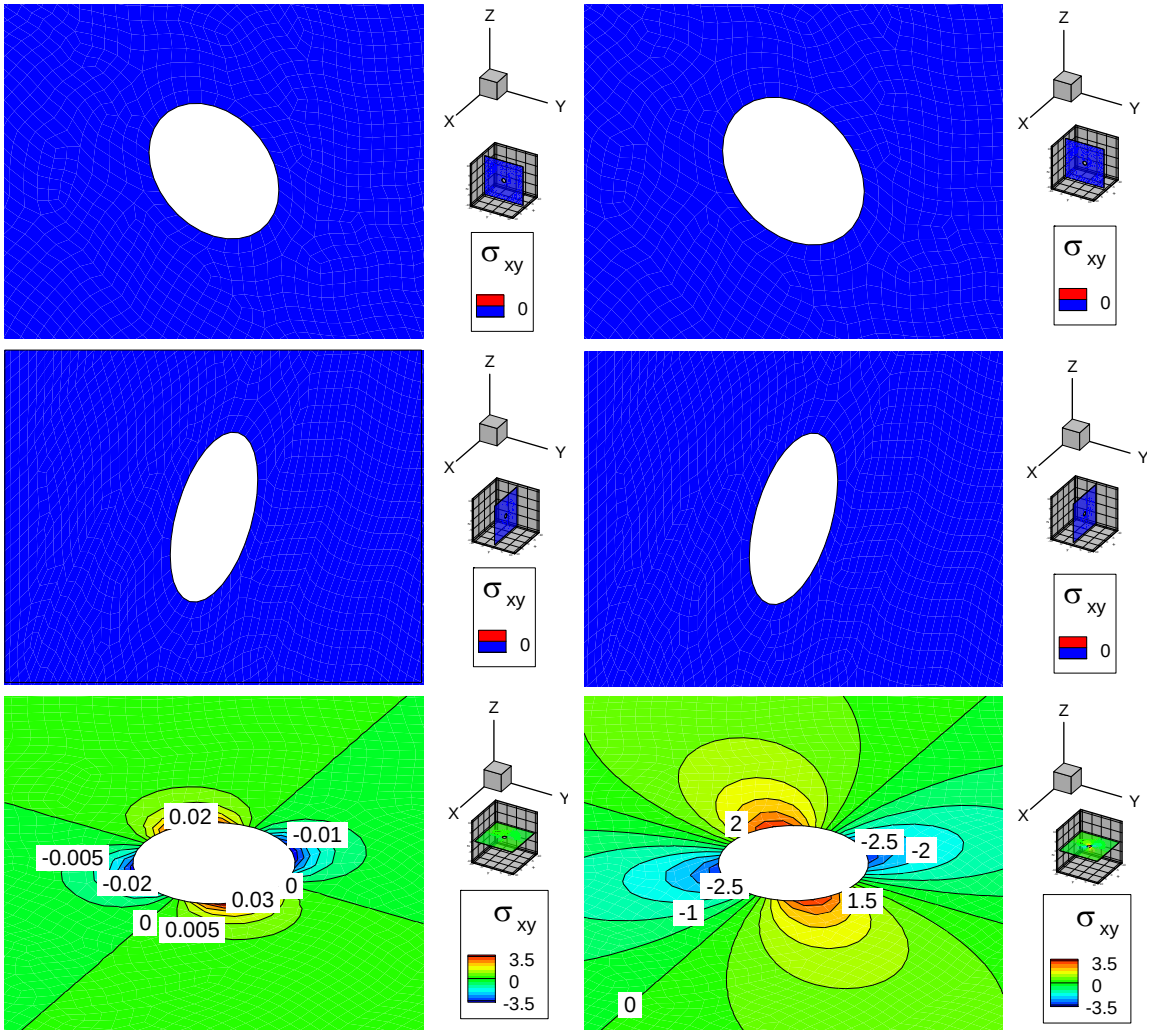

Figure B. 19 Induced shear XY stress (MPa) distribution due to 1166 Watt heat sink at origin of thermo-poroelastic media, after 20 minutes (left side figures), and after 100 days (right side figures)

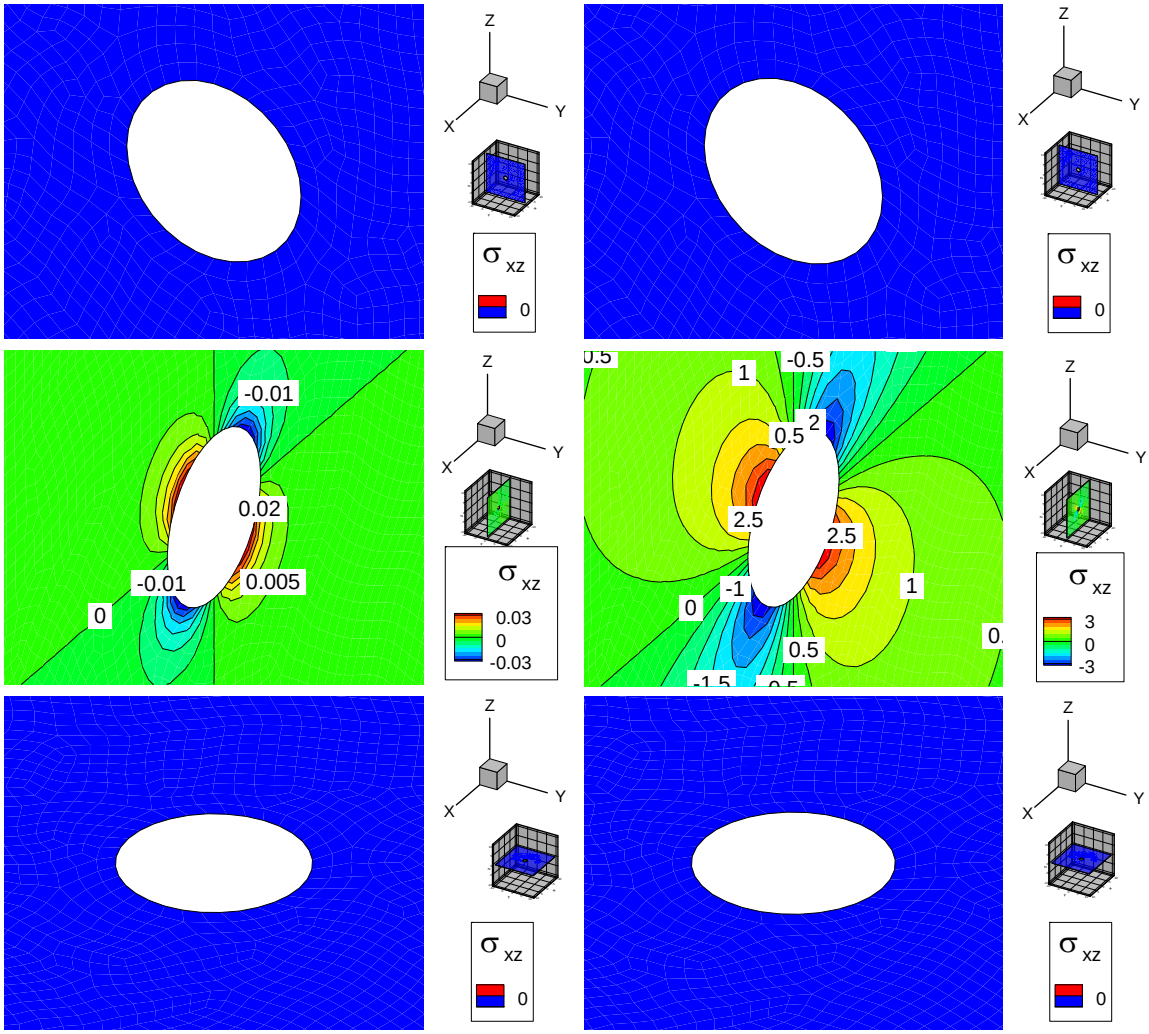

Figure B. 20 Induced shear XZ stress (MPa) distribution due to 1166 Watt heat sink at origin of thermo-poroelastic media, after 20 minutes (left side figures), and after 100 days (right side figures)

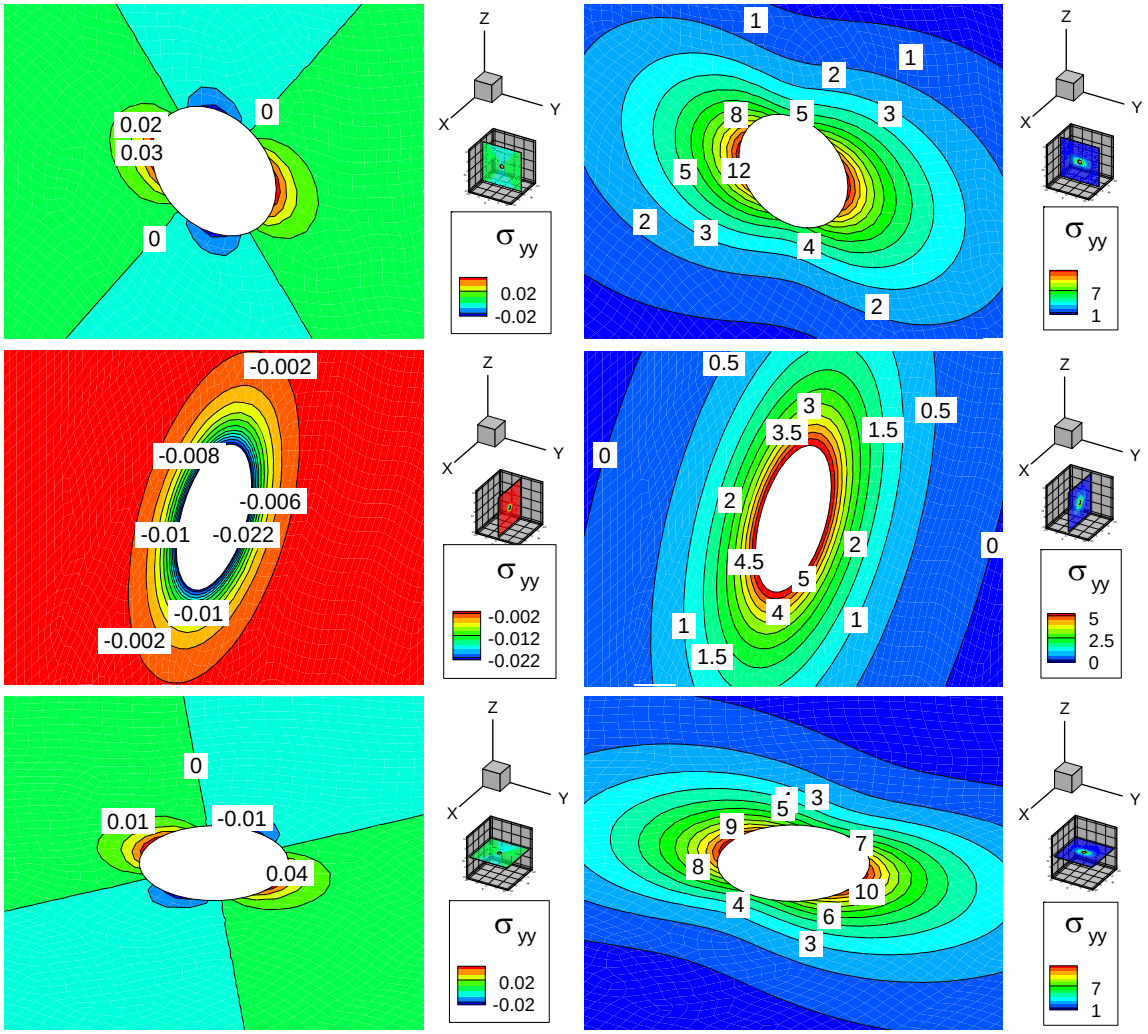

Figure B. 21 Induced total normal YY stress (MPa) distribution due to 1166 Watt heat sink at origin of thermo-poroelastic media, after 20 minutes (left side figures), and after 100 days (right side figures)

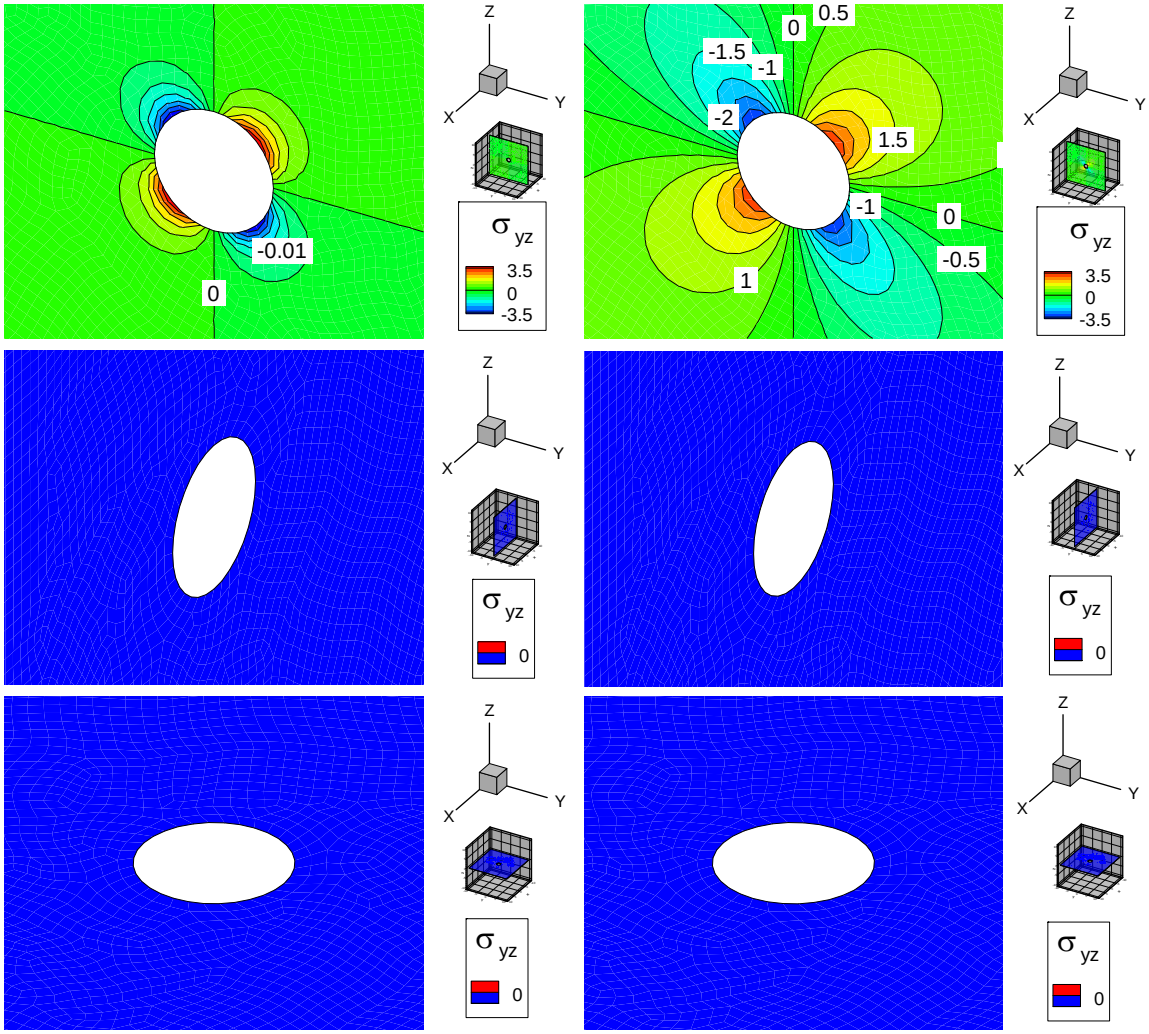

Figure B. 22 Induced shear YZ stress (MPa) distribution due to 1166 Watt heat at origin of thermo-poroelastic media, after 20 minutes (left side figures), and after 100 days (right side figures)

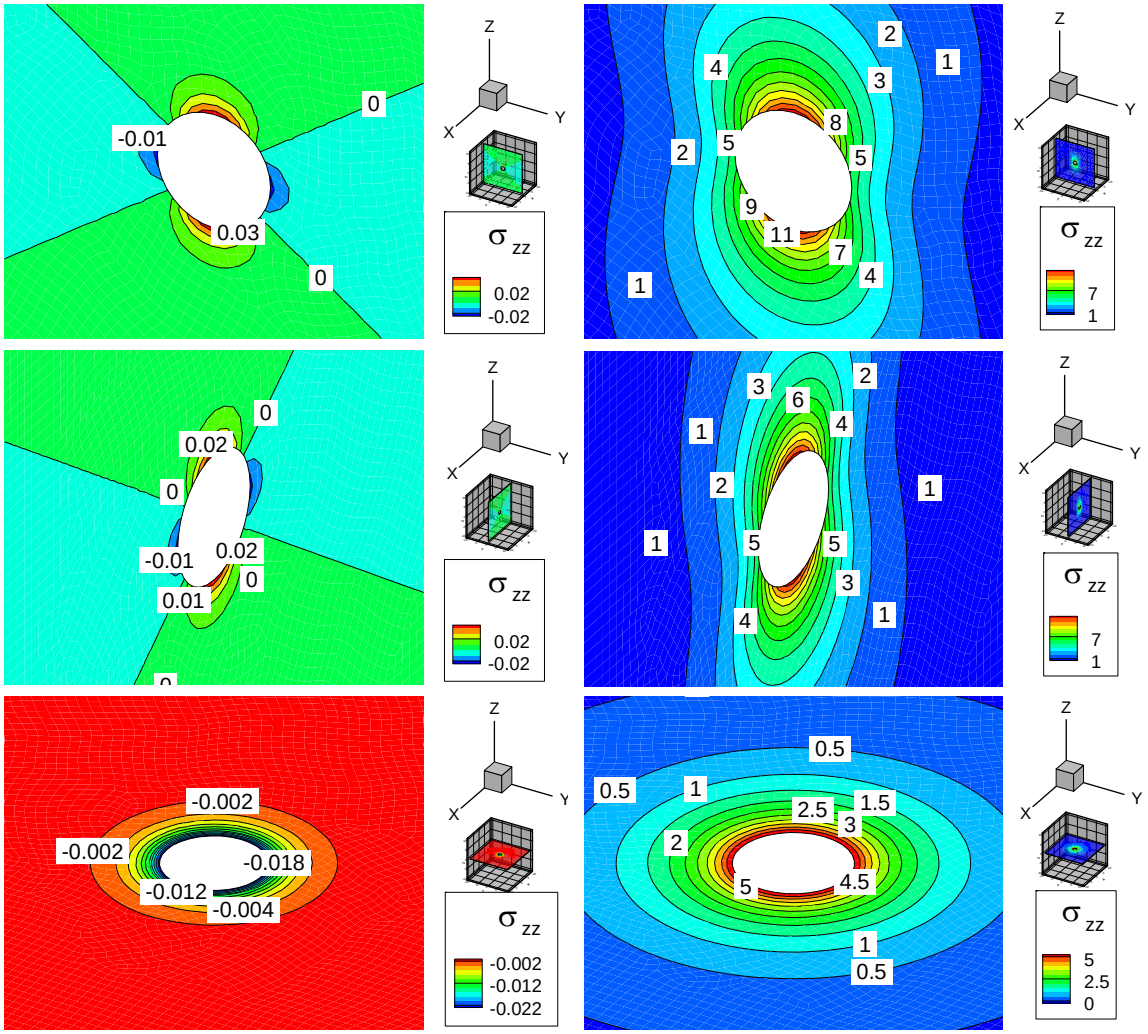

Figure B. 23 Induced total normal ZZ stress (MPa) distribution due to 1166 Watt heat sink at origin of thermo-poroelastic media, after 20 minutes (left side figures), and after 100 days (right side figures)

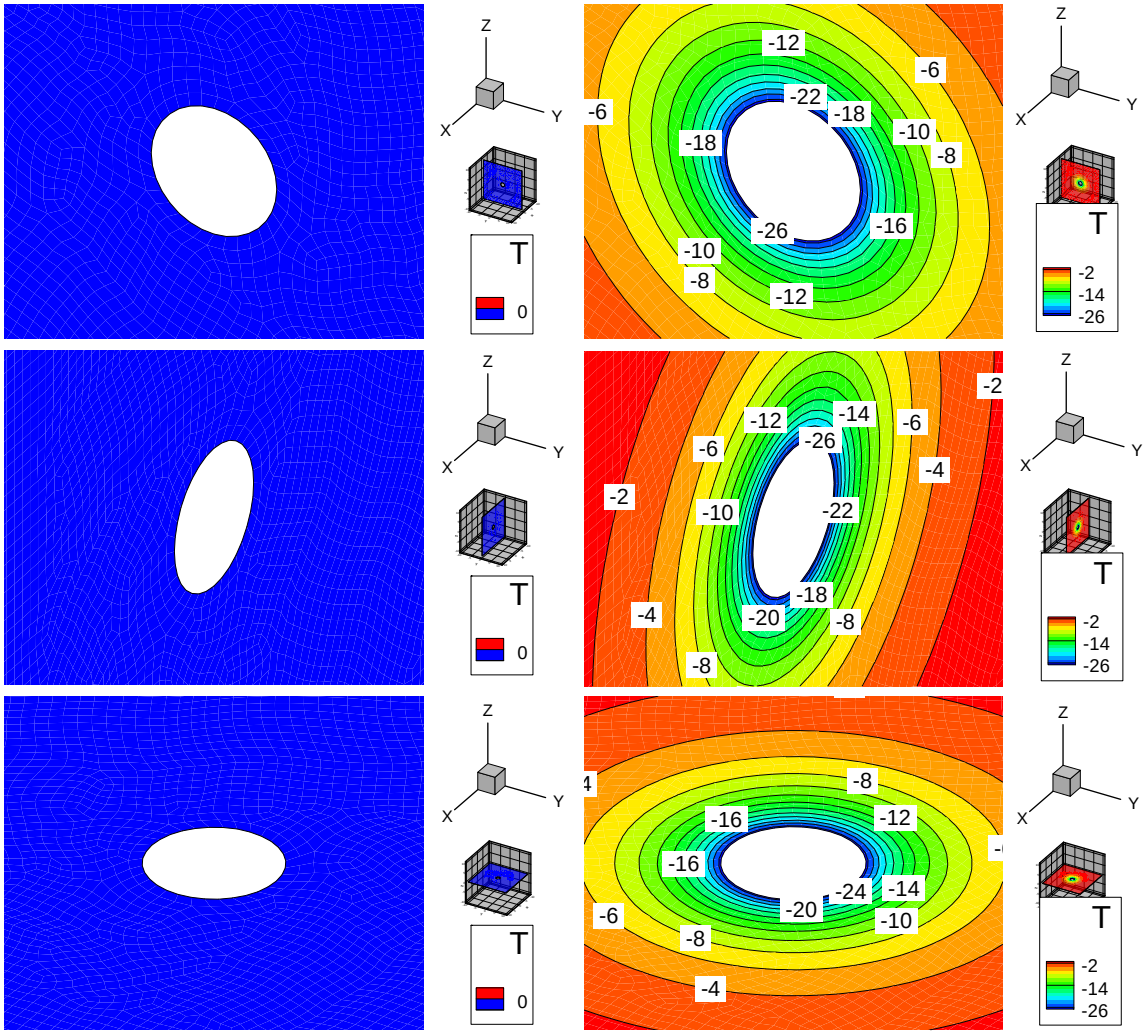

Figure B. 24 Induced temperature (K) distribution due to 1166 Watt heat sink at origin of thermo-poroelastic media, after 20 minutes (left side figures), and after 100 days (right side figures)

Induced temperature due to point heat sink in thermo-poroelastic media is shown in Figure B. 24. As it is expected, induced temperature has spherical symmetry and it value changes faster near heat sink than far from heat sink. The special trend in temperature change near and far from heat sink can be seen also on induced stresses and displacements field.

B.3. Continuous point heat sink effect in thermoporoelastic media

In Figure B. 25 to Figure B. 35 effects of 1166 Joule/sec (Watt) point heat sink on the origin of thermoporoelastic media is presented. The difference between this section and previous one is the physics of media. In previous section, temperature field does not induce pore pressure directly, but in current section, temperature field induced pore pressure directly.

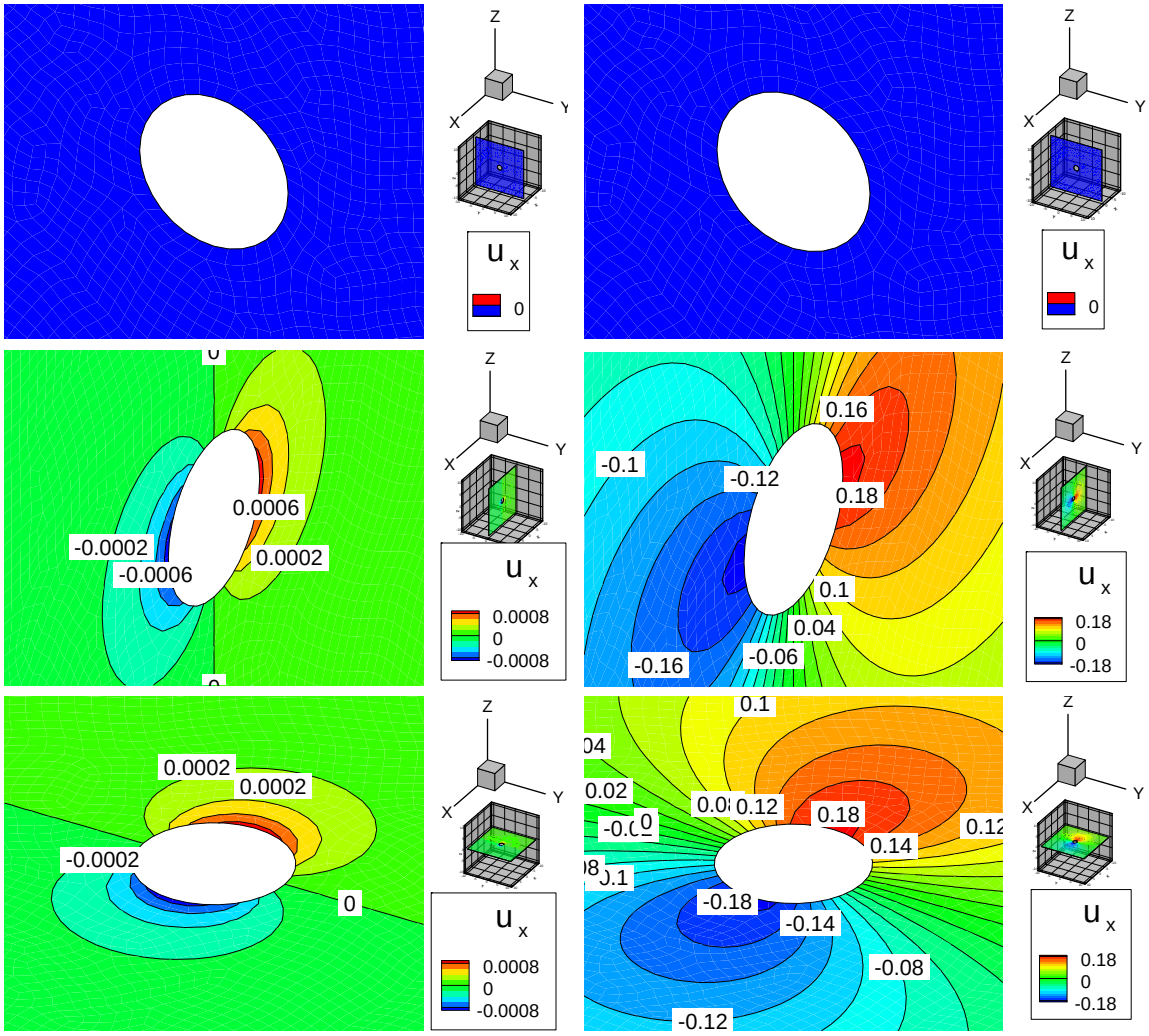

Figure B. 25 Induced X displacement (mm) distribution due to 1166 Watt heat sink at origin of thermoporoelastic media, after 20 minutes (left side figures), and after 100 days (right side figures)

Same as thermo-poroelastic section heat sink is located at the origin of Cartesian coordinates.

Induced displacement fields due to the heat sink are presented in Figure B. 25 to Figure B. 27. Same as thermo-poroelastic figures, displacements fields have spherical symmetry around the origin of coordinate system.

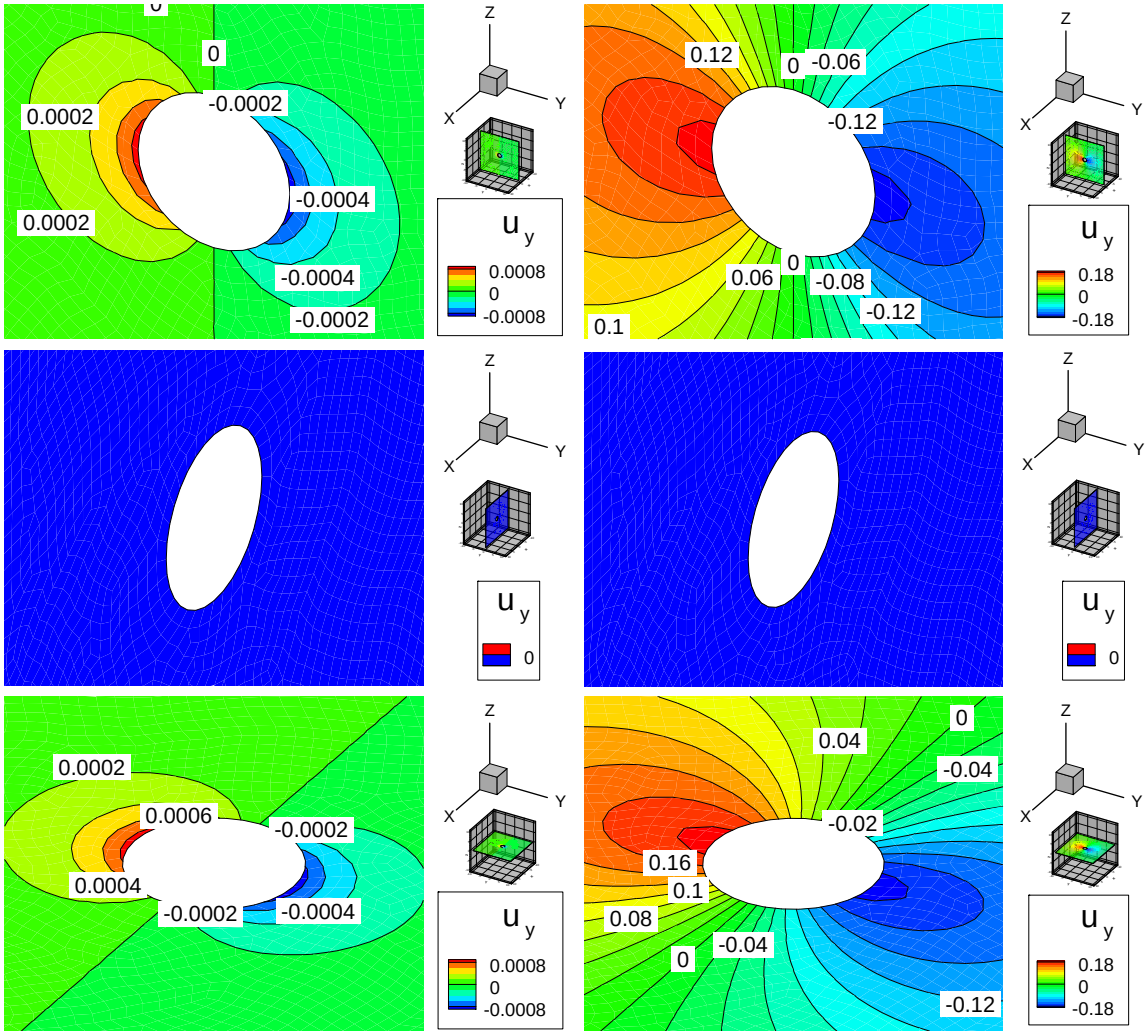

Figure B. 26 Induced Y displacement (mm) distribution due to 1166 Watt heat sink at origin of thermoporoelastic media, after 20 minutes (left side figures), and after 100 days (right side figures)

As it can be seen from comparison of Figure B. 25 to Figure B. 27 with those ones for thermo-poroelastic media, value of displacement fields at long time is same for both media. However induced displacements in thermoporoelastic media after short time have larger magnitude than induced displacements in thermo-poroelastic media. It is due to negative induced pore pressure (Figure B. 34) that increases effective stress initially and then due to pore pressure diffusion effective stress goes back to its original value.

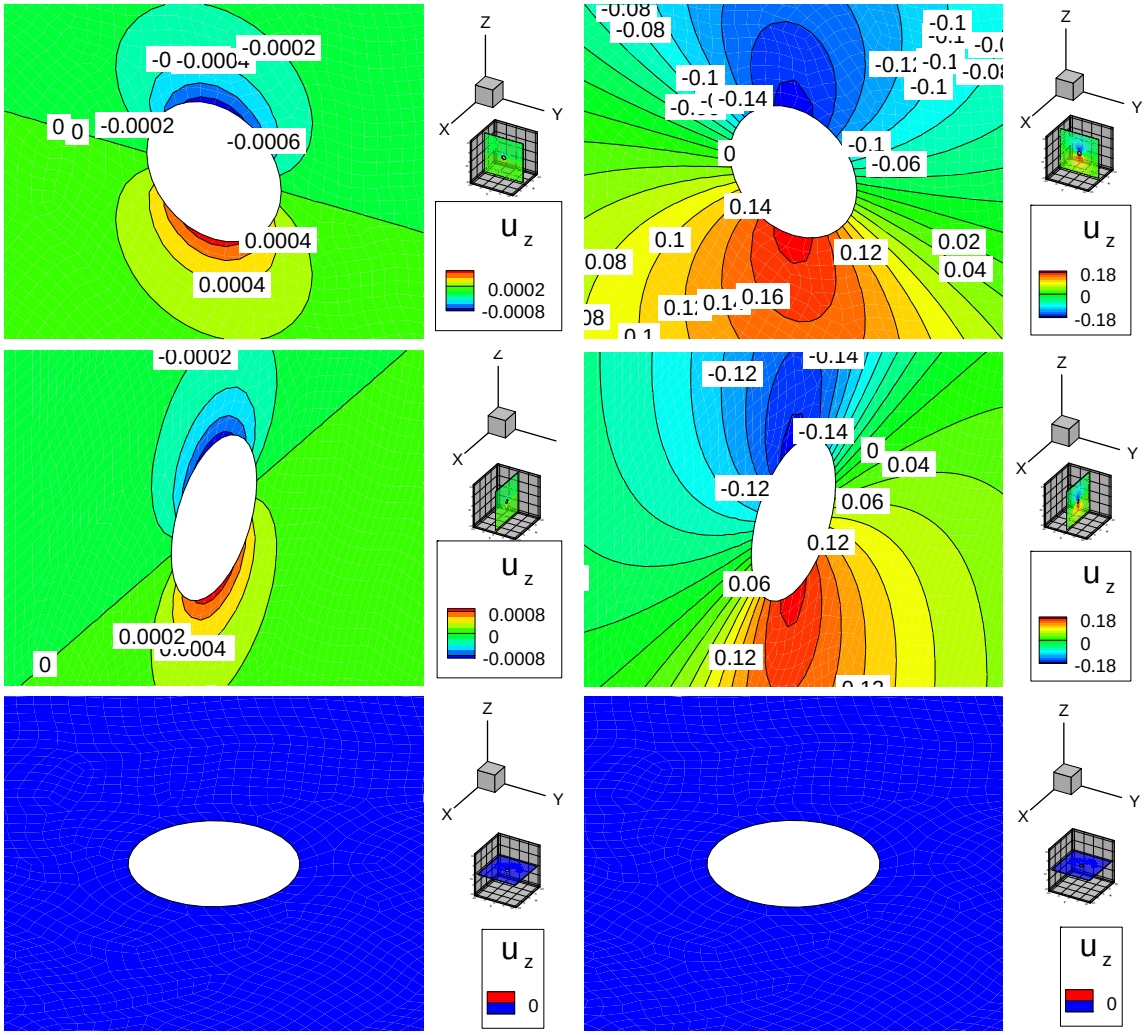

Figure B. 27 Induced Z displacement (mm) distribution due to 1166 Watt heat sink at origin of thermoporoelastic media, after 20 minutes (left side figures), and after 100 days (right side figures)

Like as thermo-poroelastic section, thermal effects in thermoporoelastic media are very slow and its effect comes into play after long time (100 days).

Induced stresses are presented in Figure B. 28 to Figure B. 33. Same as displacement fields, all induced stresses are same as thermo-poroelasticity in long time.

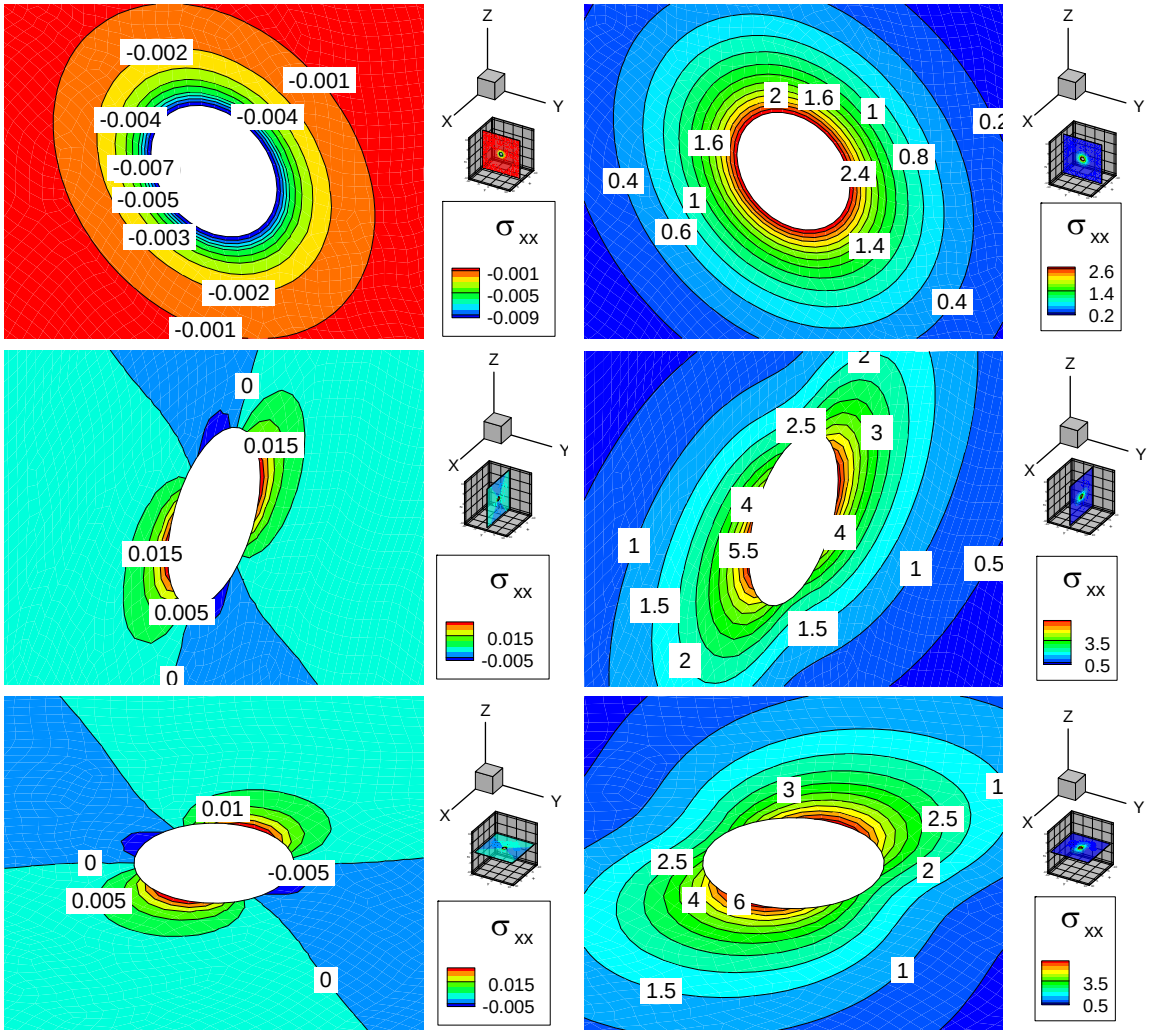

Figure B. 28 Induced total normal XX stress (MPa) distribution due to 1166 Watt heat sink at origin of thermoporoelastic, after 20 minutes (left side figures), and after 100 days (right side figures)

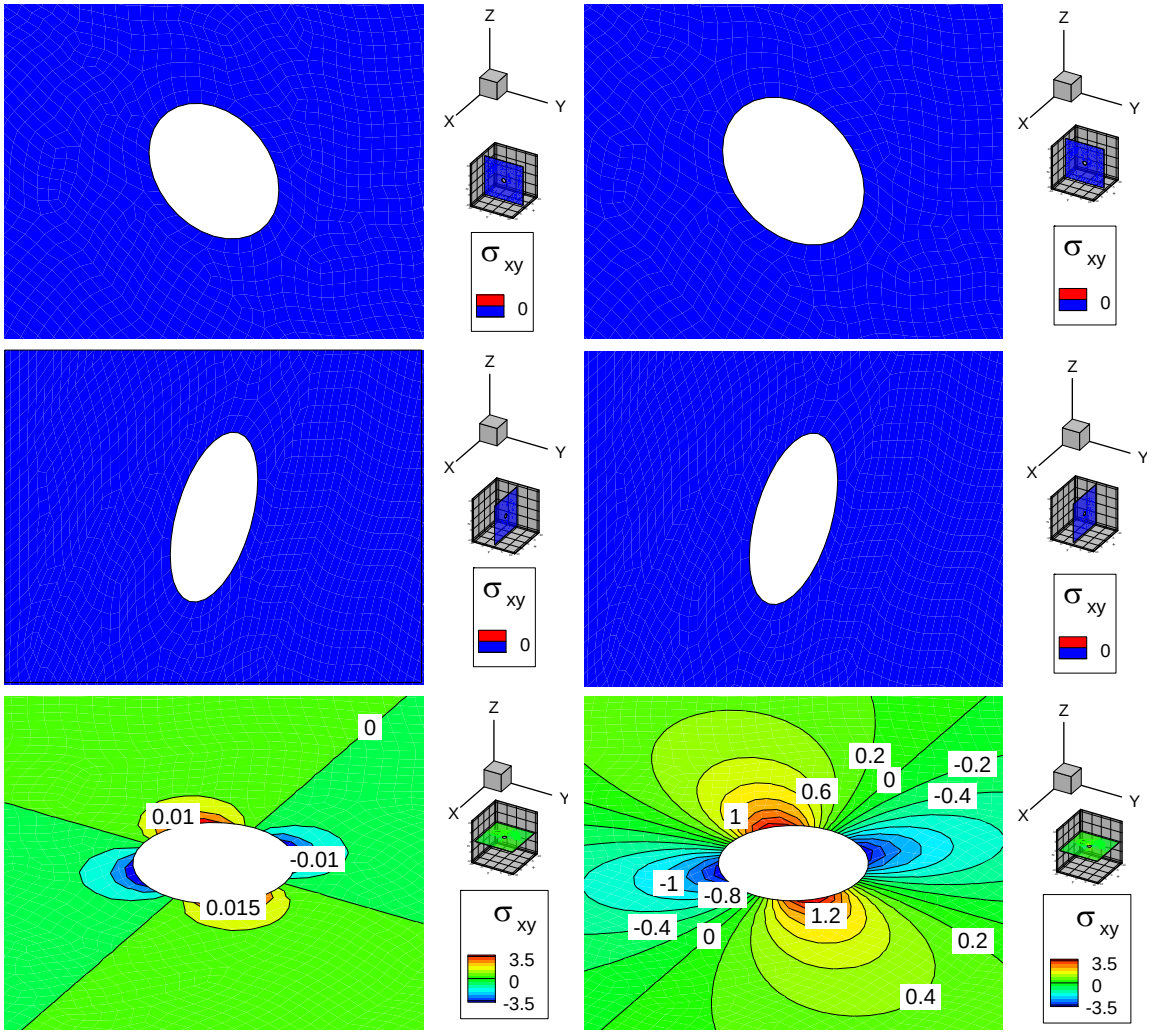

Figure B. 29 Induced shear XY stress (MPa) distribution due to 1166 Watt heat sink at origin of thermoporoelastic media, after 20 minutes (left side figures), and after 100 days (right side figures)

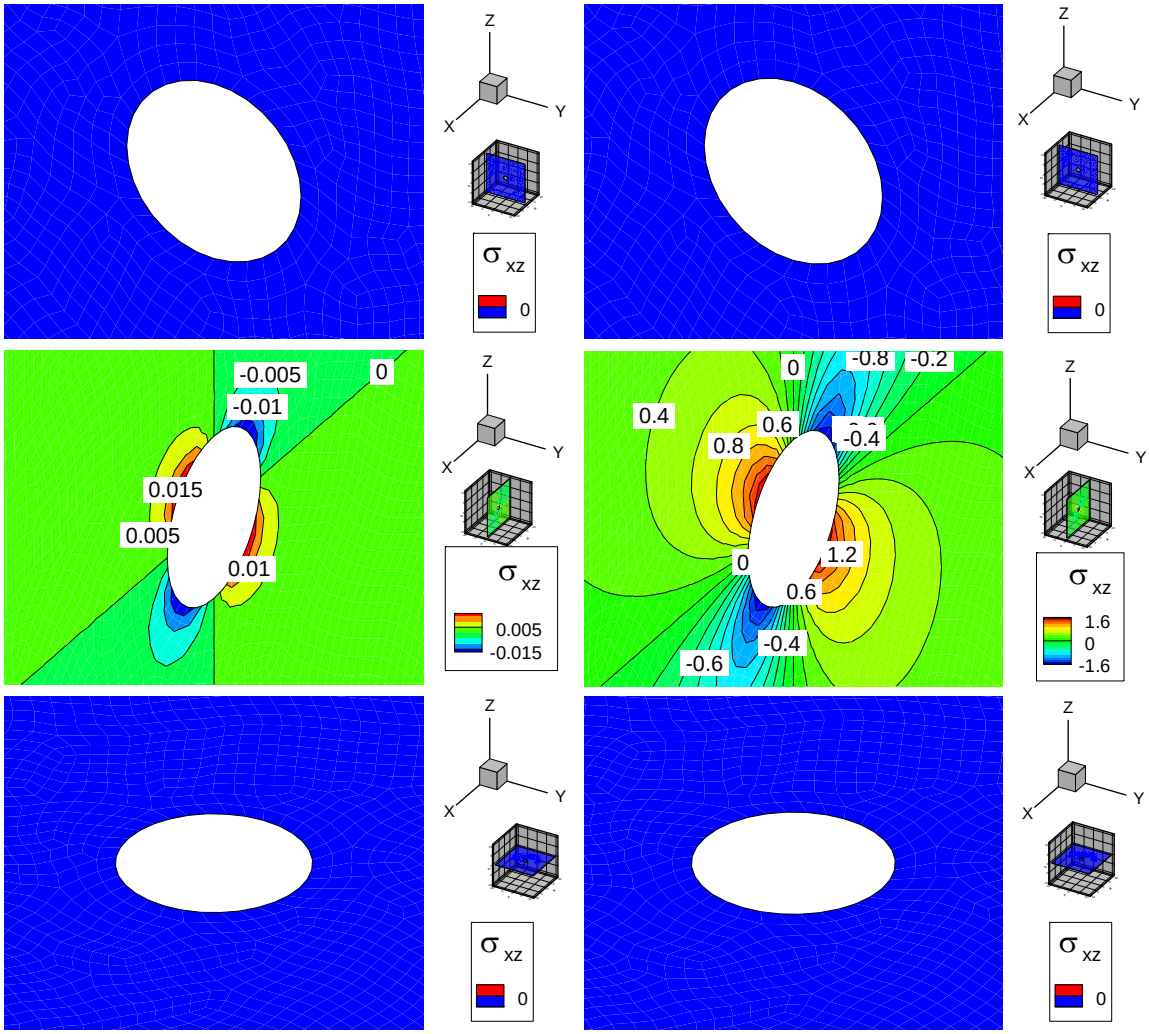

Figure B. 30 Induced shear XZ stress (MPa) distribution due to 1166 Watt heat sink at origin of thermoporoelastic media, after 20 minutes (left side figures), and after 100 days (right side figures)

Similar to thermo-poroelastic case, induced stresses are small at early time and they can be ignored for early time analysis. However, when time goes on (e.g. after 100 days), there are considerable amount of induced tensile (5 MPa) and shear stresses (1.6 MPa) that might apply instabilities to natural fractures or weakening plan as same as thermo-poroelastic model.

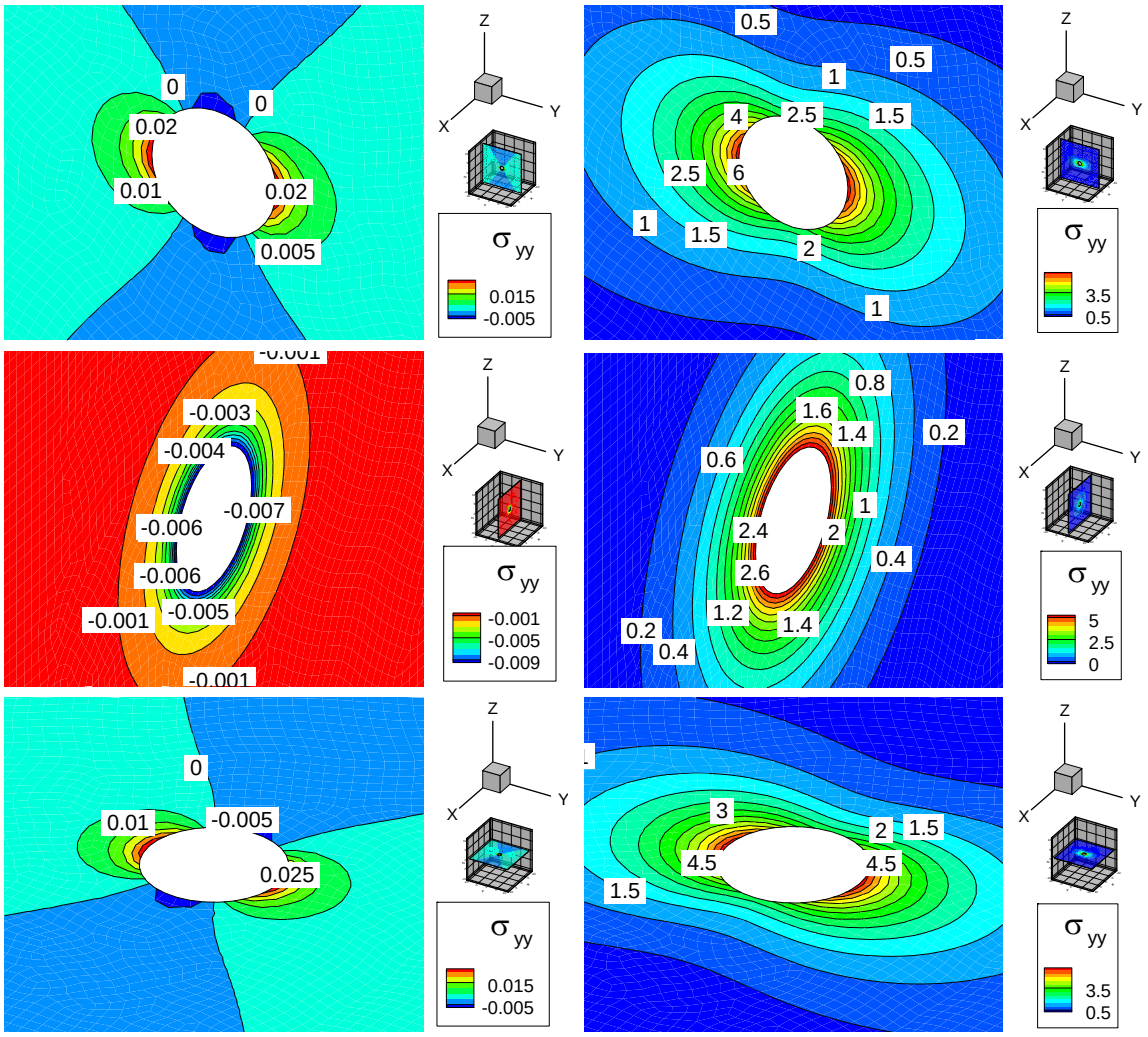

Figure B. 31 Induced total normal YY stress (MPa) distribution due to 1166 Watt heat sink at origin of thermoporoelastic, after 20 minutes (left side figures), and after 100 days (right side figures)

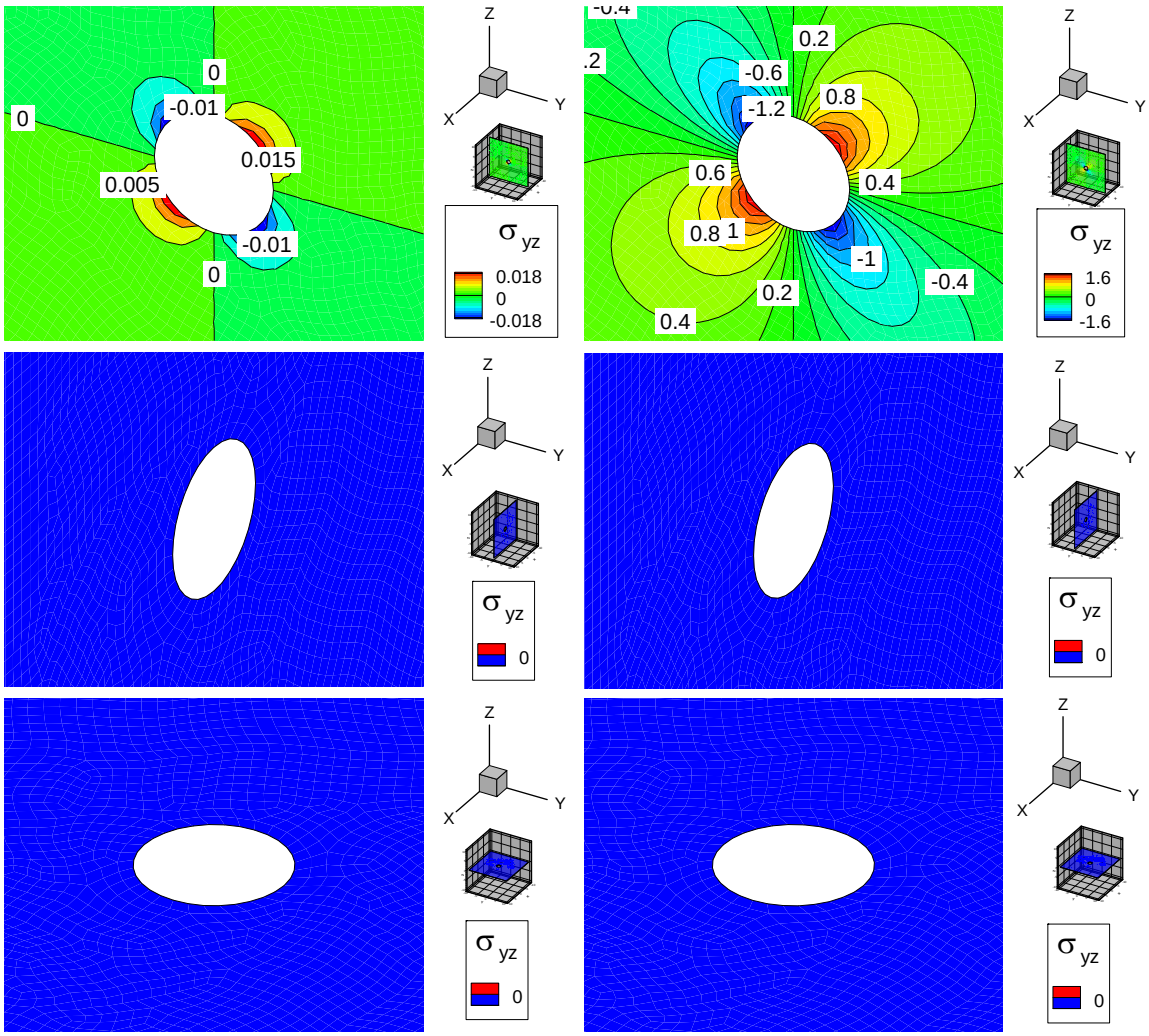

Figure B. 32 Induced shear YZ stress (MPa) distribution due to 1166 Watt heat at origin of thermoporoelastic media, after 20 minutes (left side figures), and after 100 days (right side figures)

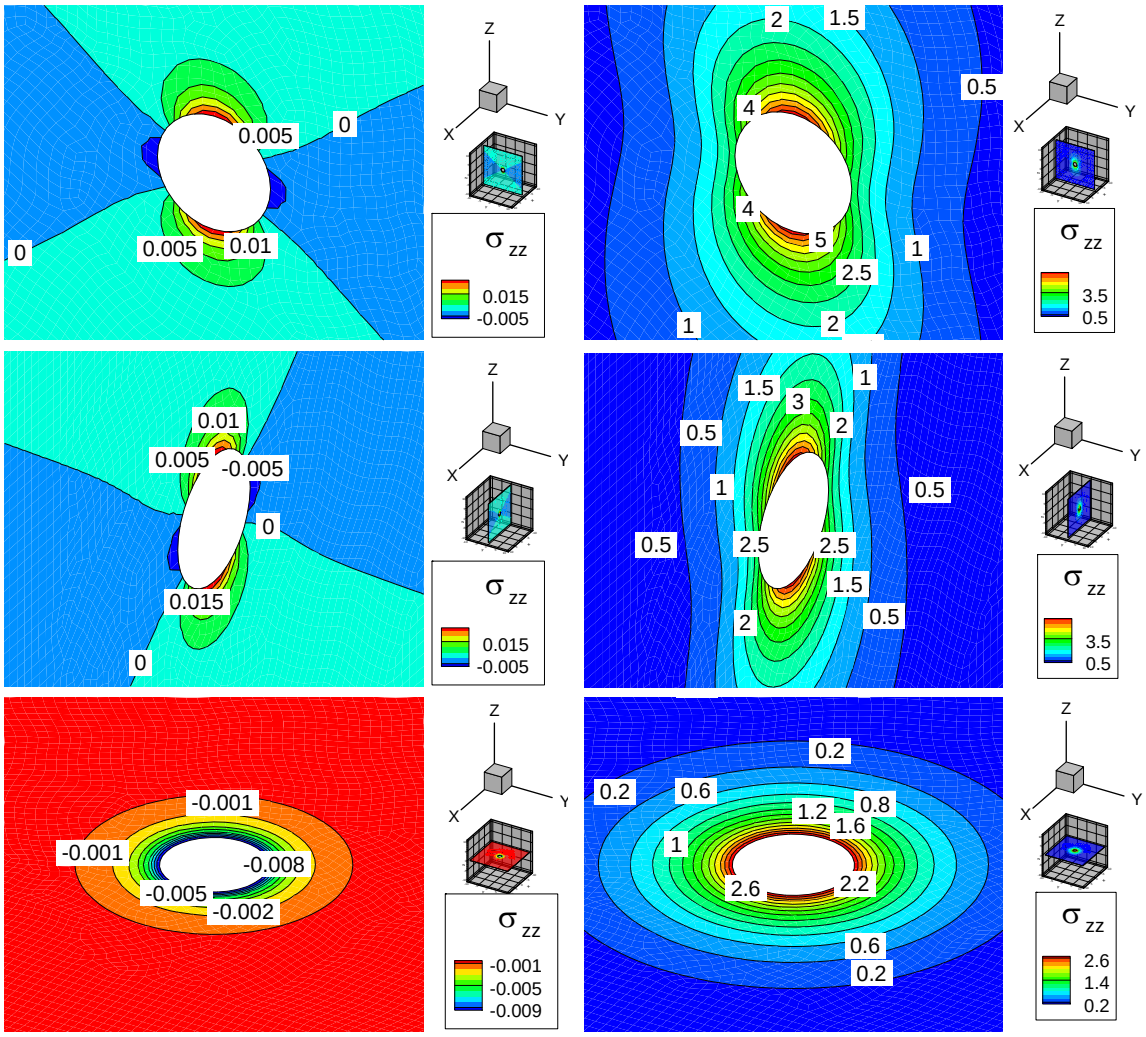

Figure B. 33 Induced total normal ZZ stress (MPa) distribution due to 1166 Watt heat sink at origin of thermoporoelastic media, after 20 minutes (left side figures), and after 100 days (right side figures)

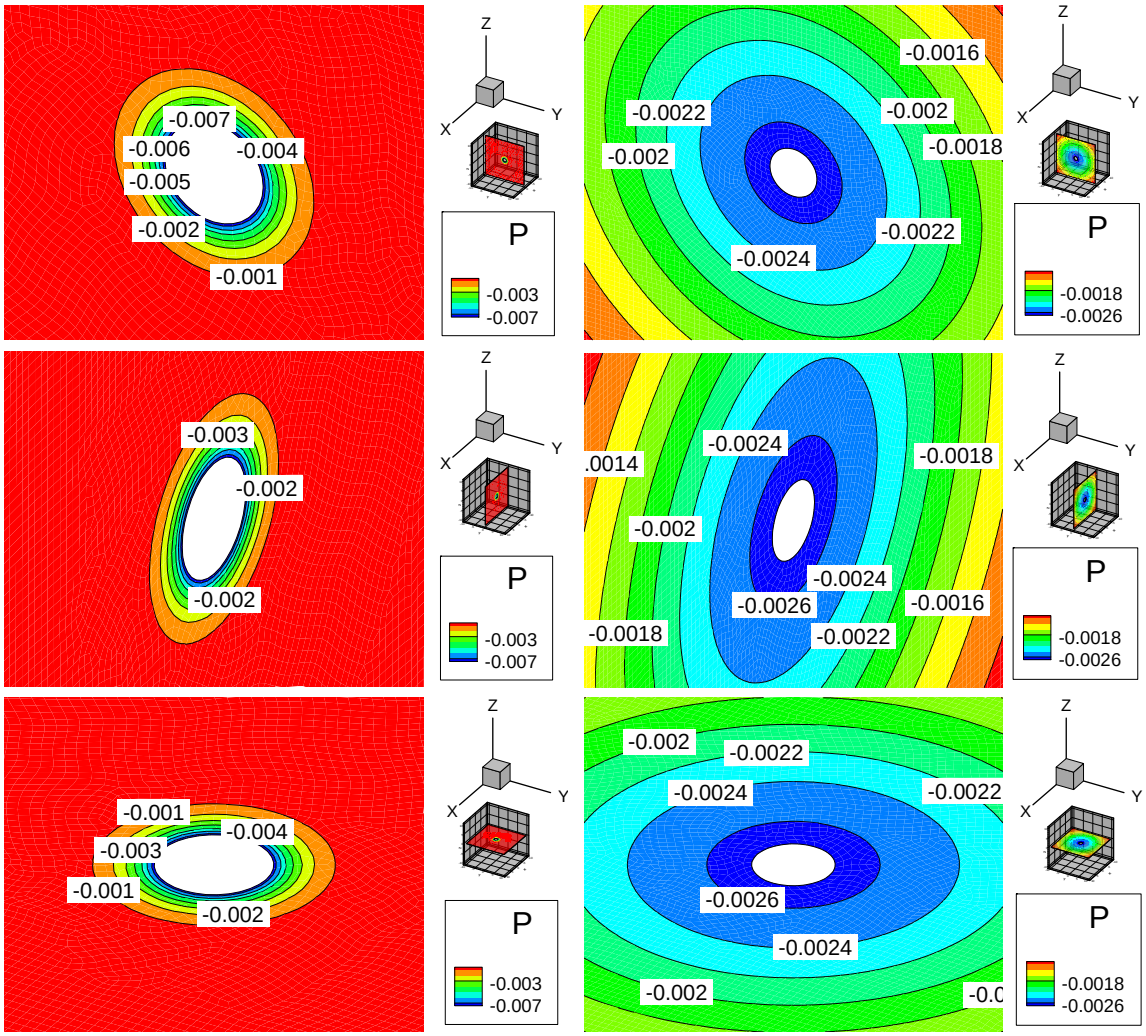

Figure B. 34 Induced pore pressure (MPa) distribution due to 1166 Watt heat sink at origin of thermoporoelastic media, after 20 minutes (left side figures), and after 100 days (right side figures)

Figure B. 34, presents induced pore pressure due to heat sink. As it can be seen, from the beginning of heat sink application to media pore pressure around sink changed and decreased. After long time, affected area increased, however amount of induced pore pressure decreased. This is because of the fact that after some time proceeds,

temperature distribution around heat sinks moves toward constant value around heat sink and then negative induced pore pressure diffuse and its magnitude decrease.

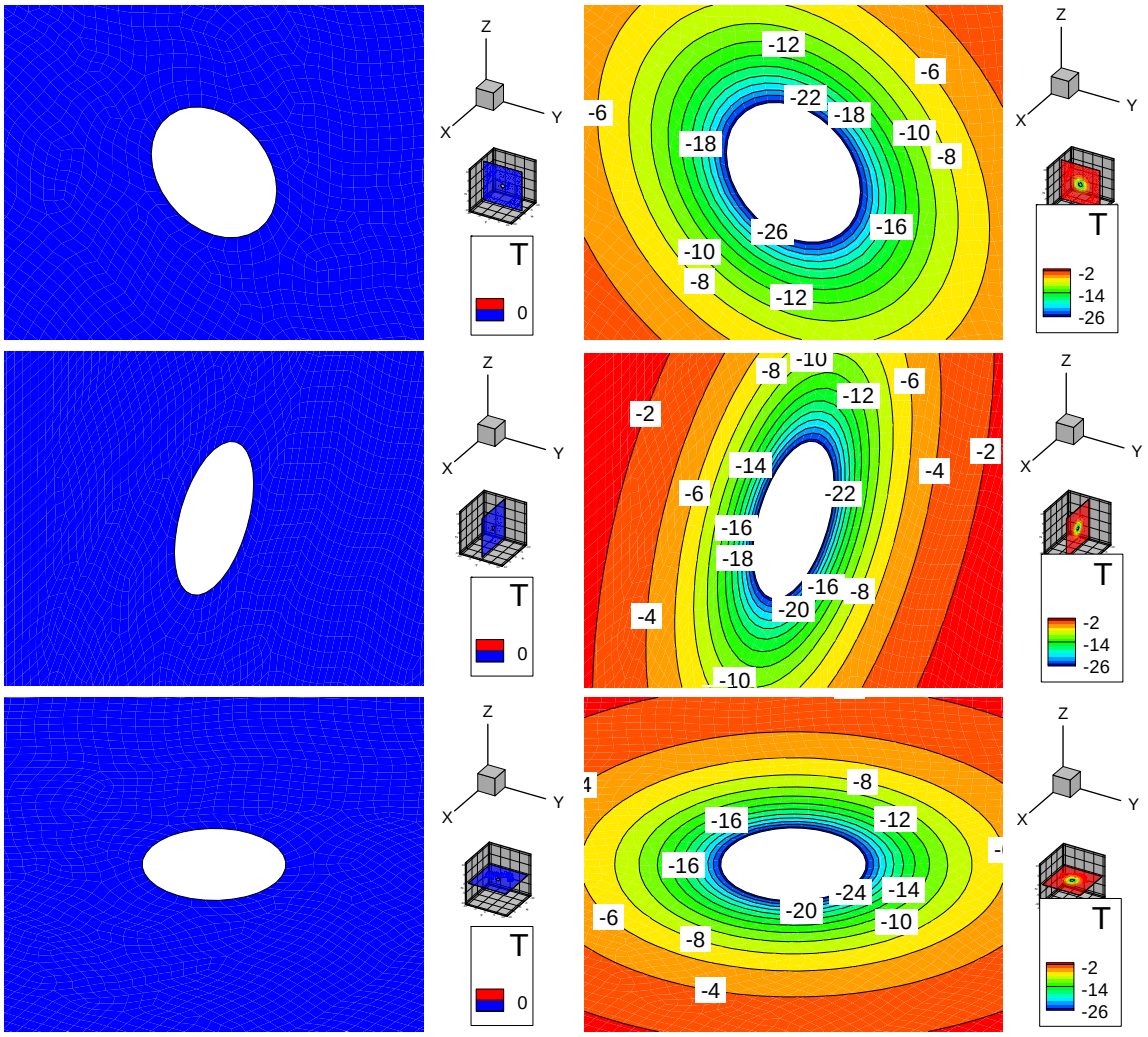

Figure B. 35 Induced temperature (K) distribution due to 1166 Watt heat sink at origin of thermoporoelastic media, after 20 minutes (left side figures), and after 100 days (right side figures)

Figure B. 35 shows temperature distribution in thermoporoelastic media due to heat sink. As it can be seen by comparing this figure with Figure B. 24, temperature distribution is completely same in both thermoporoelastic and thermo-poroelastic media.

B.4. Continuous point normal displacement discontinuity effect

In Figure B. 37 to Figure B. 46 effects of 1 mm point normal displacement discontinuity (in Z direction) on the origin of thermoporoelastic media (as shown in Figure B. 36) is presented. Same as previous sections, compression is negative and tension is positive. Physically, one might imagine normal displacement discontinuity effects as effects of crack which opposing surfaces have been displaced normally relative to one another.

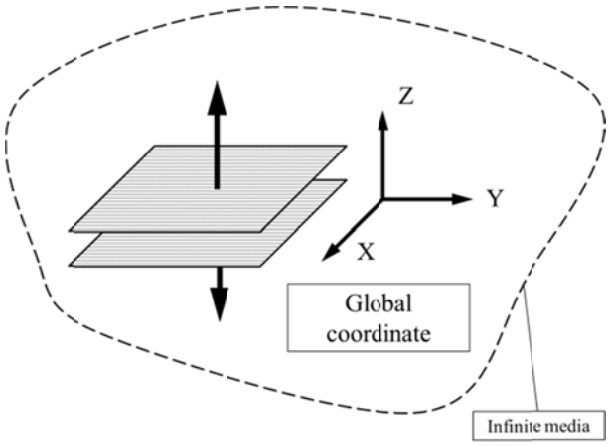

Figure B. 36 Point normal Z displacement discontinuity in the origin of thermoporoelastic media

It is clear from induced displacement fields that when time goes by, maximum X and Y induced displacements increase by very small amount; however extents of the displacement fields enlarges after long time. This is because of diffusion process that extended the effects to larger area after long time.

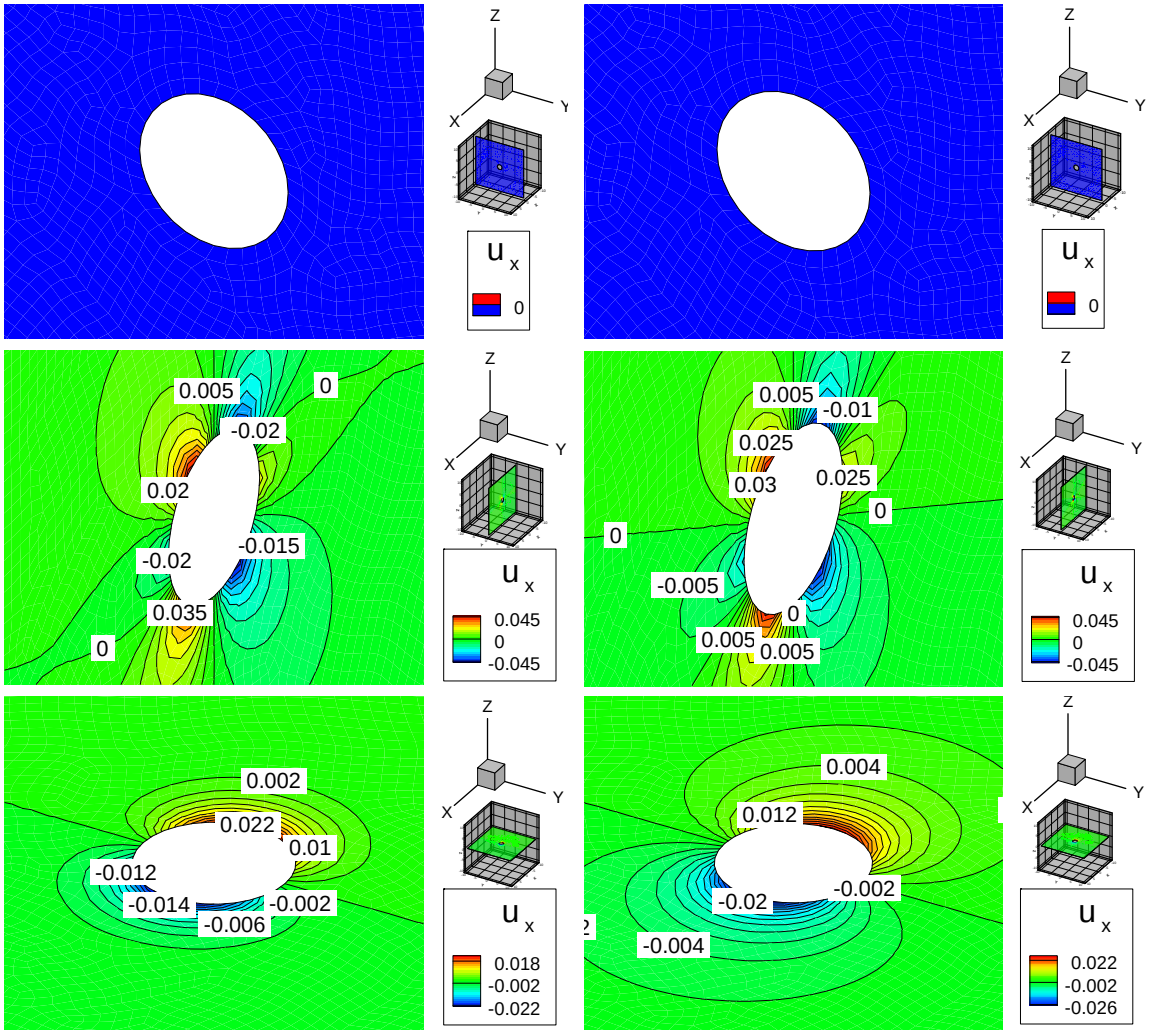

Figure B. 37 Induced X displacement (mm) distribution due to 1 mm normal displacement discontinuity (At Z direction) at origin, after 20 minutes (left side figures), and after 100 days (right side figures)

Induced displacement in Z direction (see Figure B. 39) does not show sensible changes when time proceeds. This is due to the fact that normal DD is applied in Z direction and induced displacement affected the media from beginning and diffusion process does not have sensible effect on Z displacement. As it is expected XY surface is

symmetry plane and Z displacement increased near origin of coordinate which is the location of 1 mm Z direction displacement discontinuity.

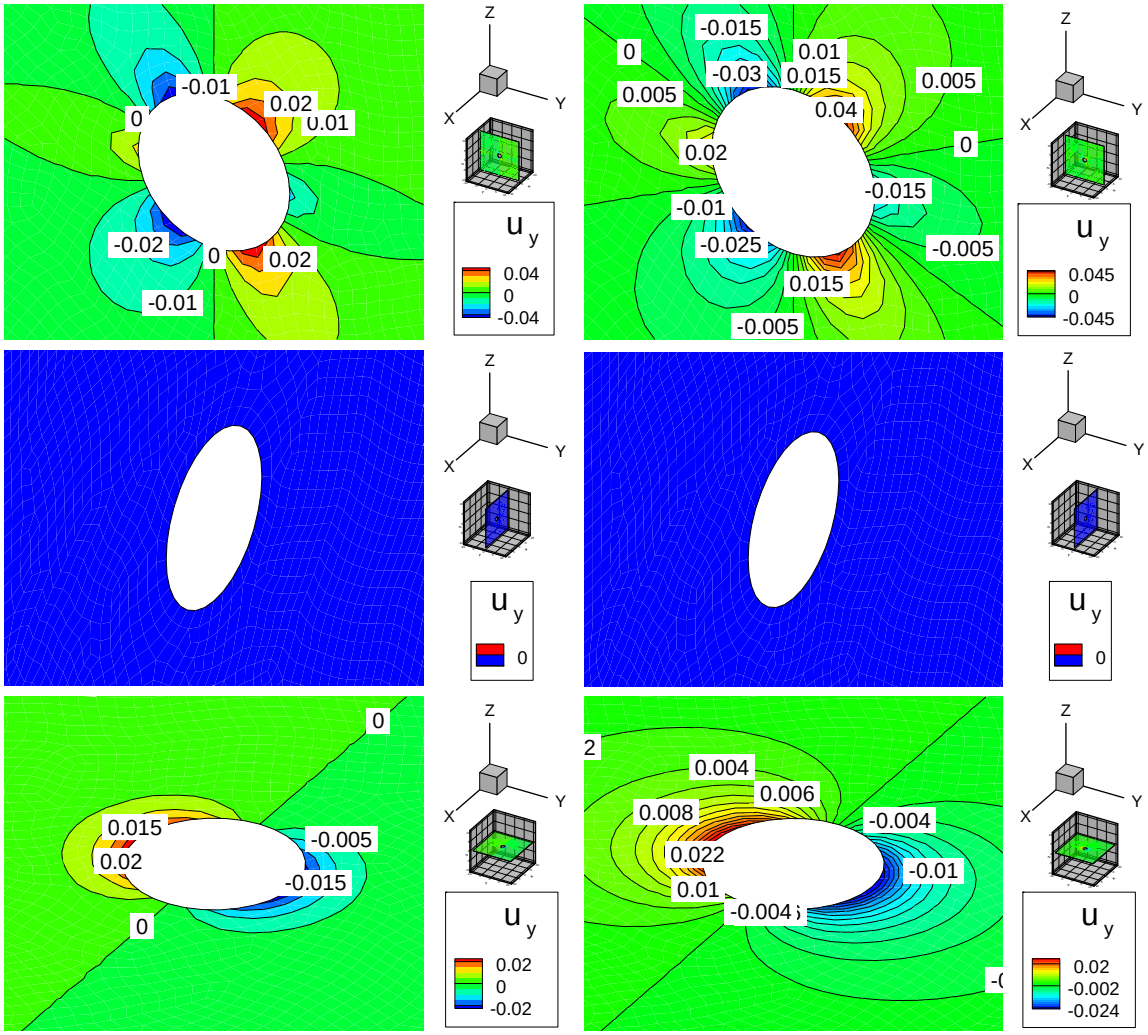

Figure B. 38 Induced Y displacement (mm) distribution due to 1 mm normal displacement discontinuity (At Z direction) at origin, after 20 minutes (left side figures), and after 100 days (right side figures)

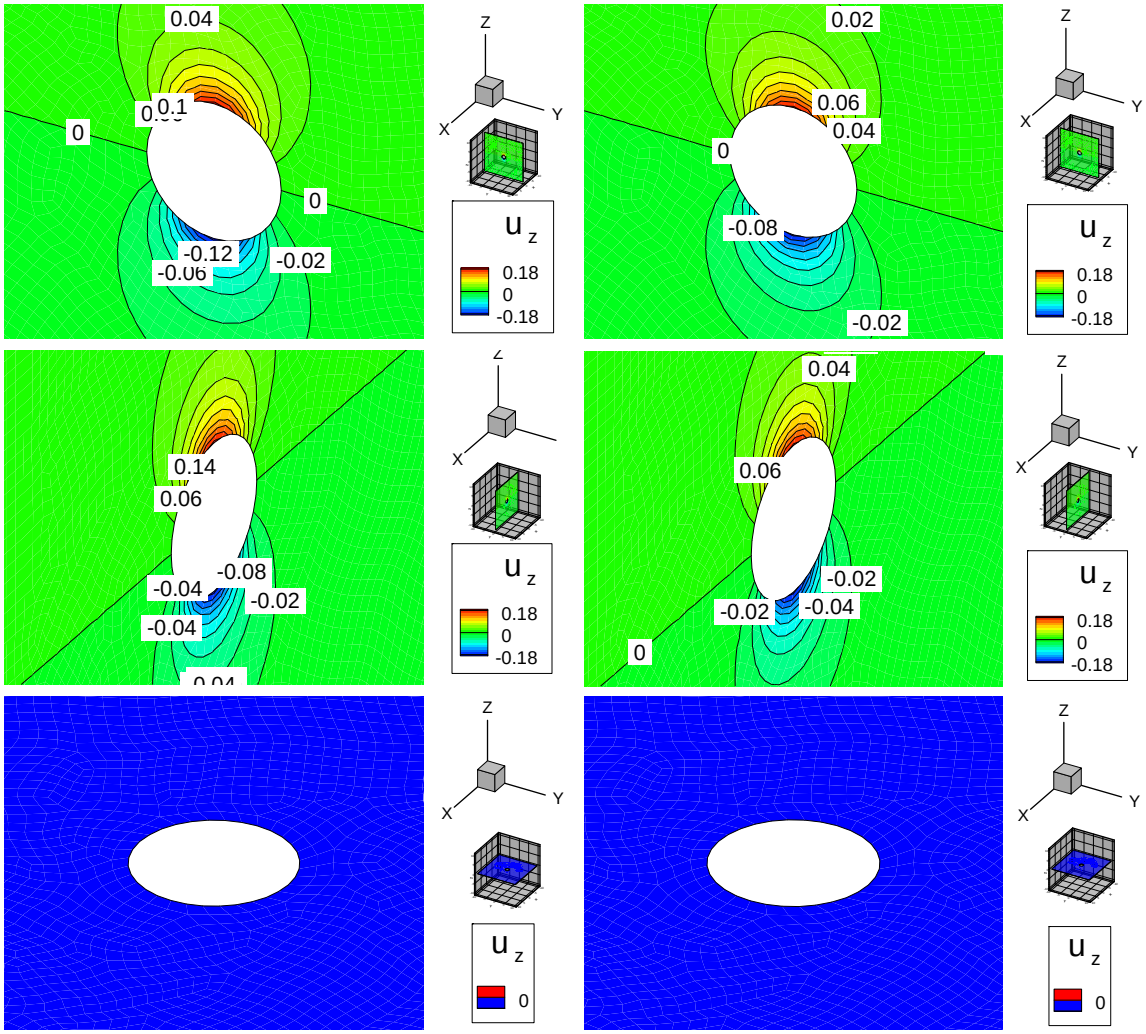

Figure B. 39 Induced Z displacement (mm) distribution due to 1 mm normal displacement discontinuity (At Z direction) at origin, after 20 minutes (left side figures), and after 100 days (right side figures)

Total stress components are shown in Figure B. 40 to Figure B. 45. Figure B. 40 and Figure B. 43 shows XX and YY stress components. As one can see when time precedes these stress components will be more tensile. This is due to diffusion process that relaxes media after disseminating pressure and increases tensile stress in these directions.

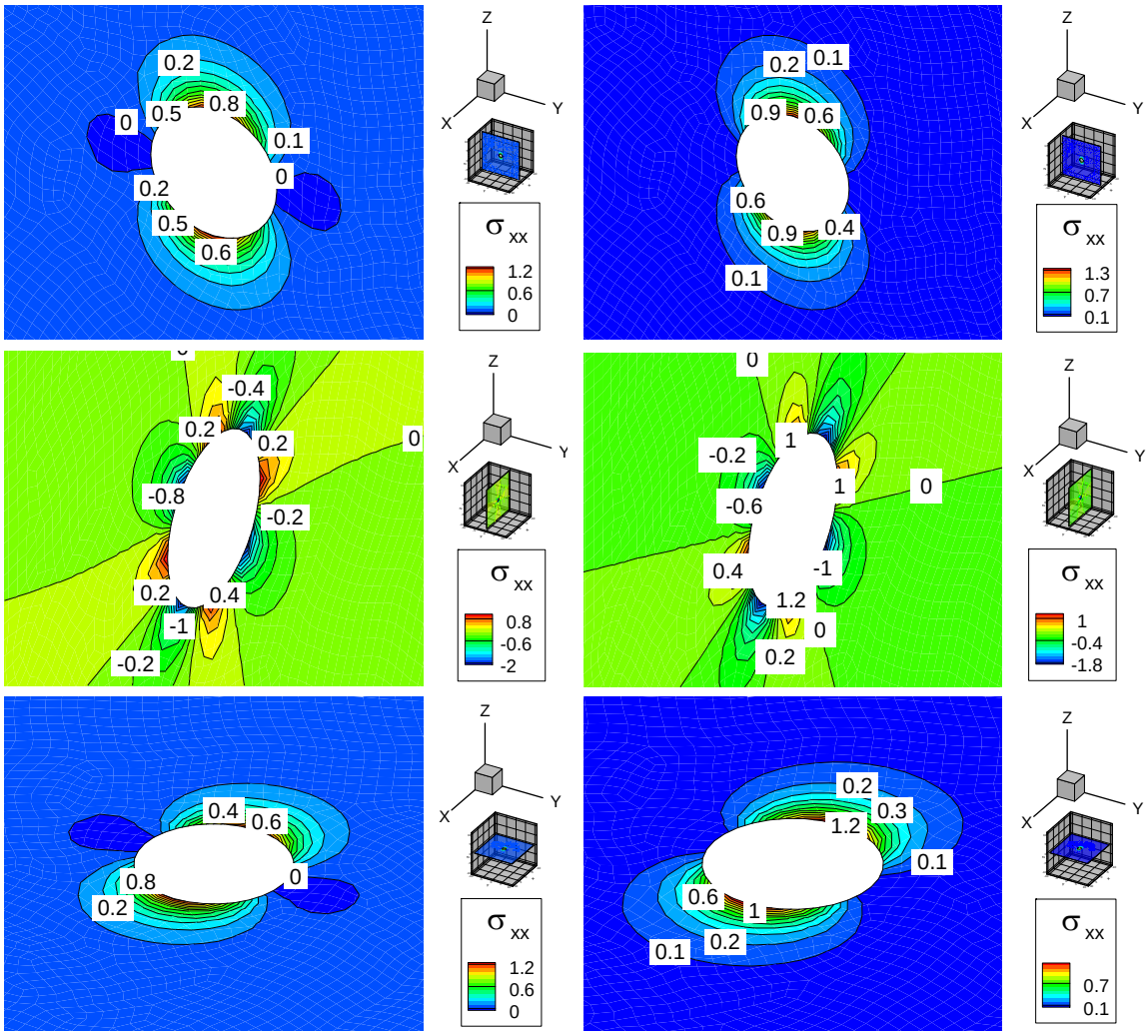

Figure B. 40 Induced total normal XX stress (MPa) distribution due to 1 mm normal displacement discontinuity (At Z direction) at origin, after 20 minutes (left side figures), and after 100 days (right side figures)

Shear stress components are shown in Figure B. 41, Figure B. 42, and Figure B. 44. As it can be seen from these figures magnitude and extent of shear does not change during time and remain constant. This is because of the fact diffusion process does not

have any effect on shear stress components, and it only changes major stress components slightly and more importantly changes the pore pressure distribution.

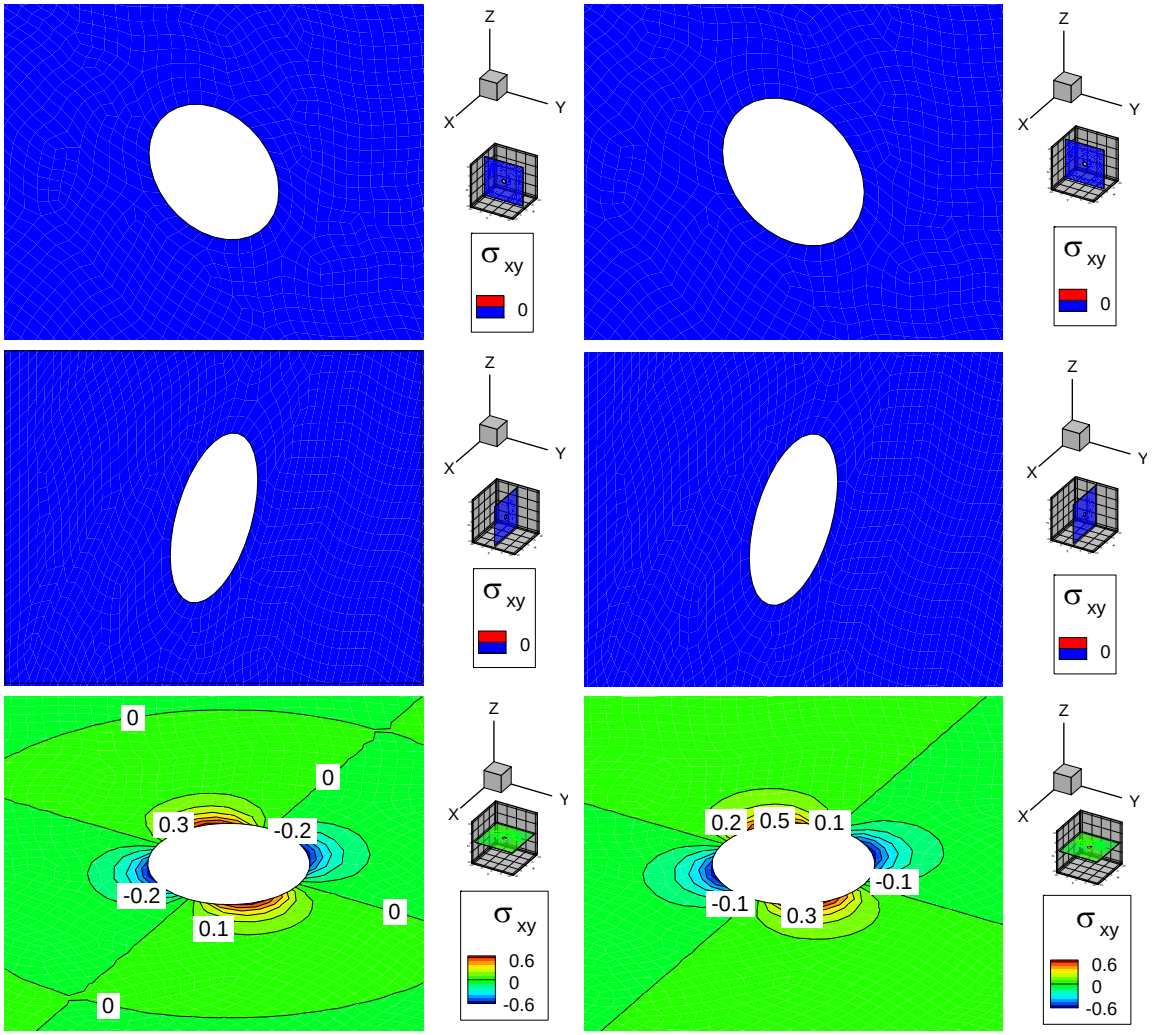

Figure B. 41 Induced shear XY stress (MPa) distribution due to 1 mm normal displacement discontinuity (At Z direction) at origin, after 20 minutes (left side figures), and after 100 days (right side figures)

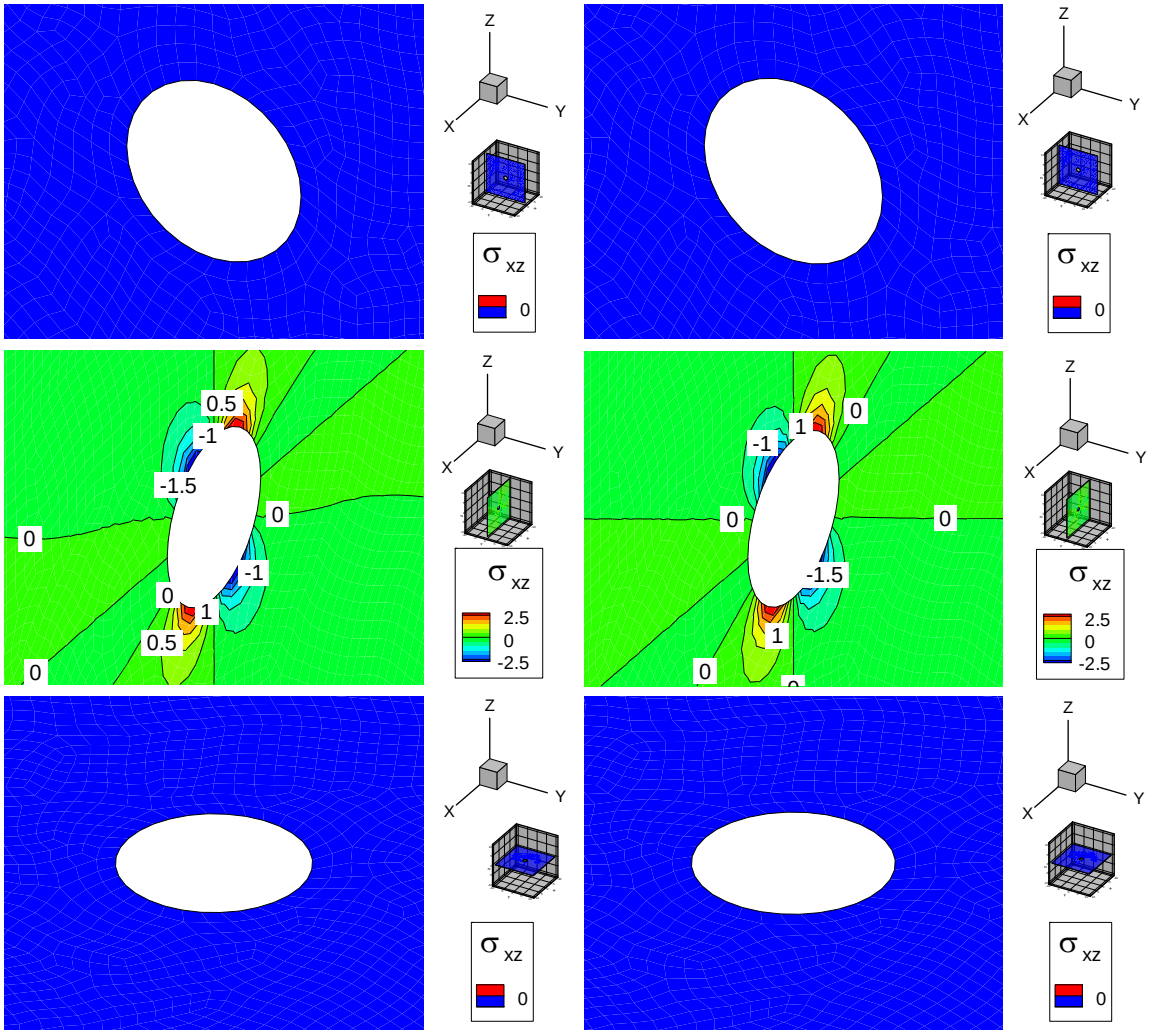

Figure B. 42 Induced shear XZ stress (MPa) distribution due to 1 mm normal displacement discontinuity (At Z direction) at origin, after 20 minutes (left side figures), and after 100 days (right side figures)

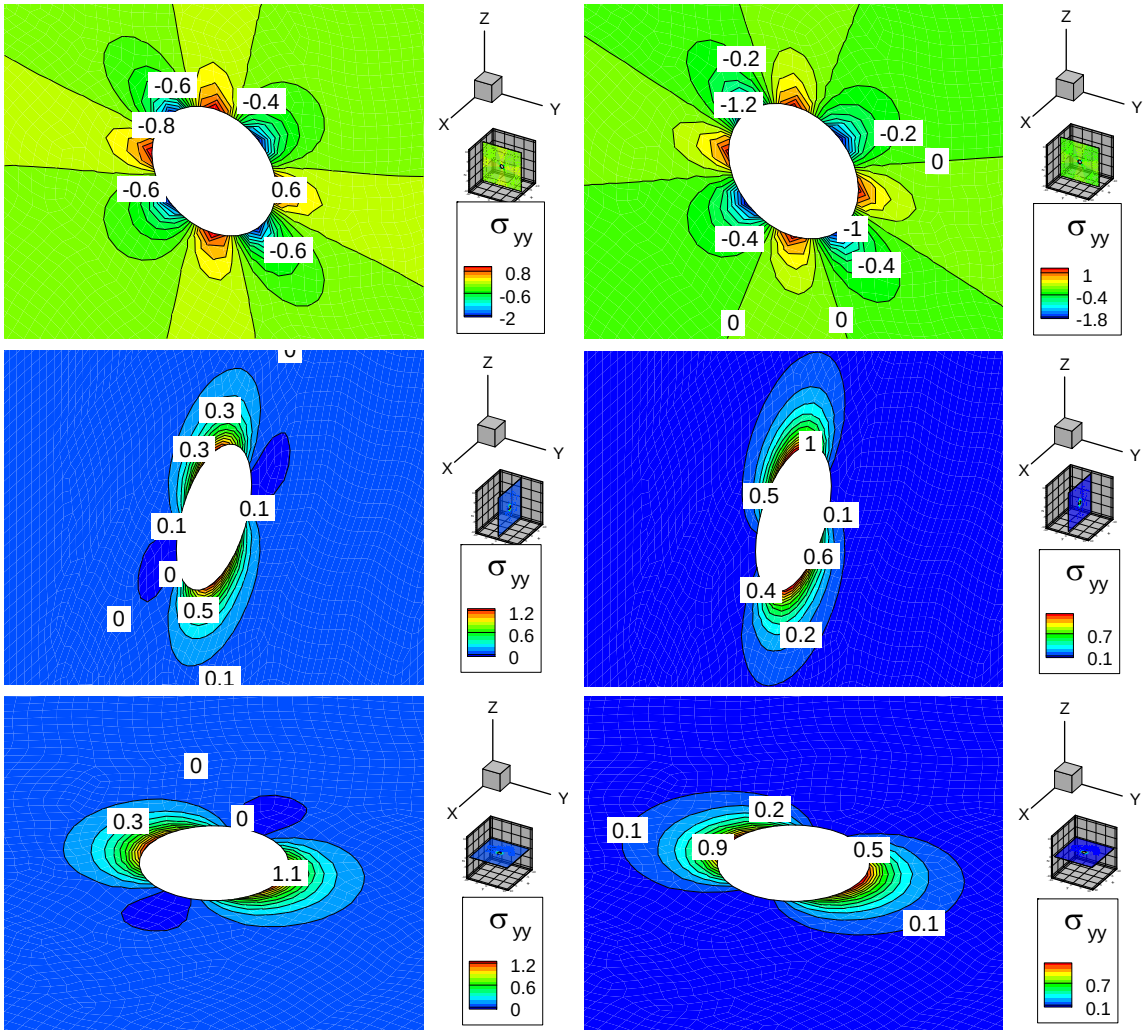

Figure B. 43 Induced total normal YY stress (MPa) distribution due to 1 mm normal displacement discontinuity (At Z direction) at origin, after 20 minutes (left side figures), and after 100 days (right side figures)

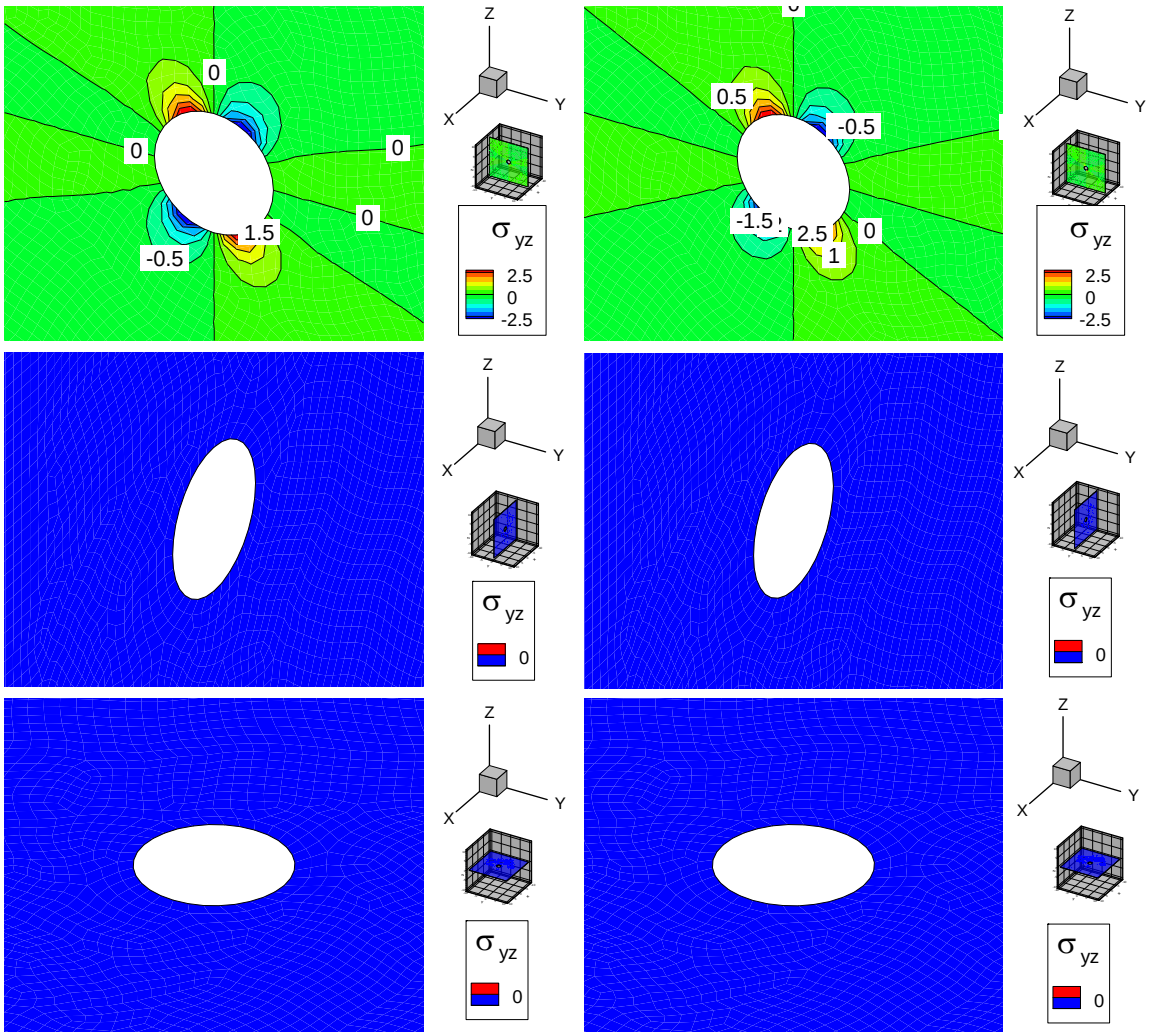

Figure B. 44 Induced shear YZ stress (MPa) distribution due to 1 mm normal displacement discontinuity (At Z direction) at origin, after 20 minutes (left side figures), and after 100 days (right side figures)

Induced ZZ stress (stress component in the direction of applied DD) is shown in Figure B. 45. It shows that magnitude and extent of ZZ stress does not change when time proceeds. It is consistent with induced Z displacement field that does not change during time. The figure shows that total stress component during diffusion process does not experience sensible change.

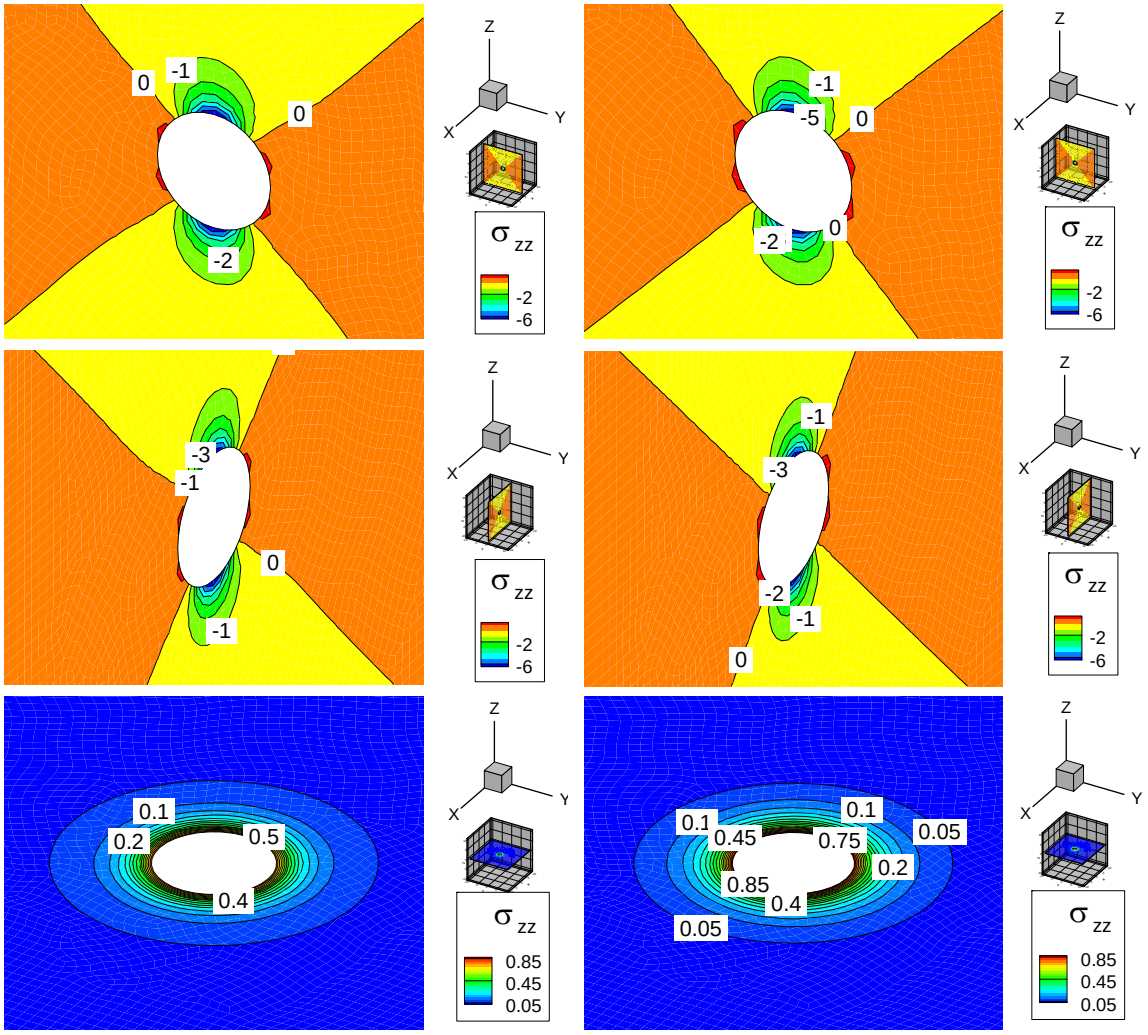

Figure B. 45 Induced total normal ZZ stress (MPa) distribution due to 1 mm normal displacement discontinuity (At Z direction) at origin, after 20 minutes (left side figures), and after 100 days (right side figures)

Interesting observation is induced pore pressure distribution (Figure B. 46), which could be said that completely removed after 100 days. This shows that normal DD effect is very important for early time and should be considered in geomechanics behavior of reservoir from early time. So, at the start of reservoir behavior due to induced normal displacement discontinuity, induced pore pressure has maximum value

and as a consequence effective stress has minimum value and the system can experienced instabilities.

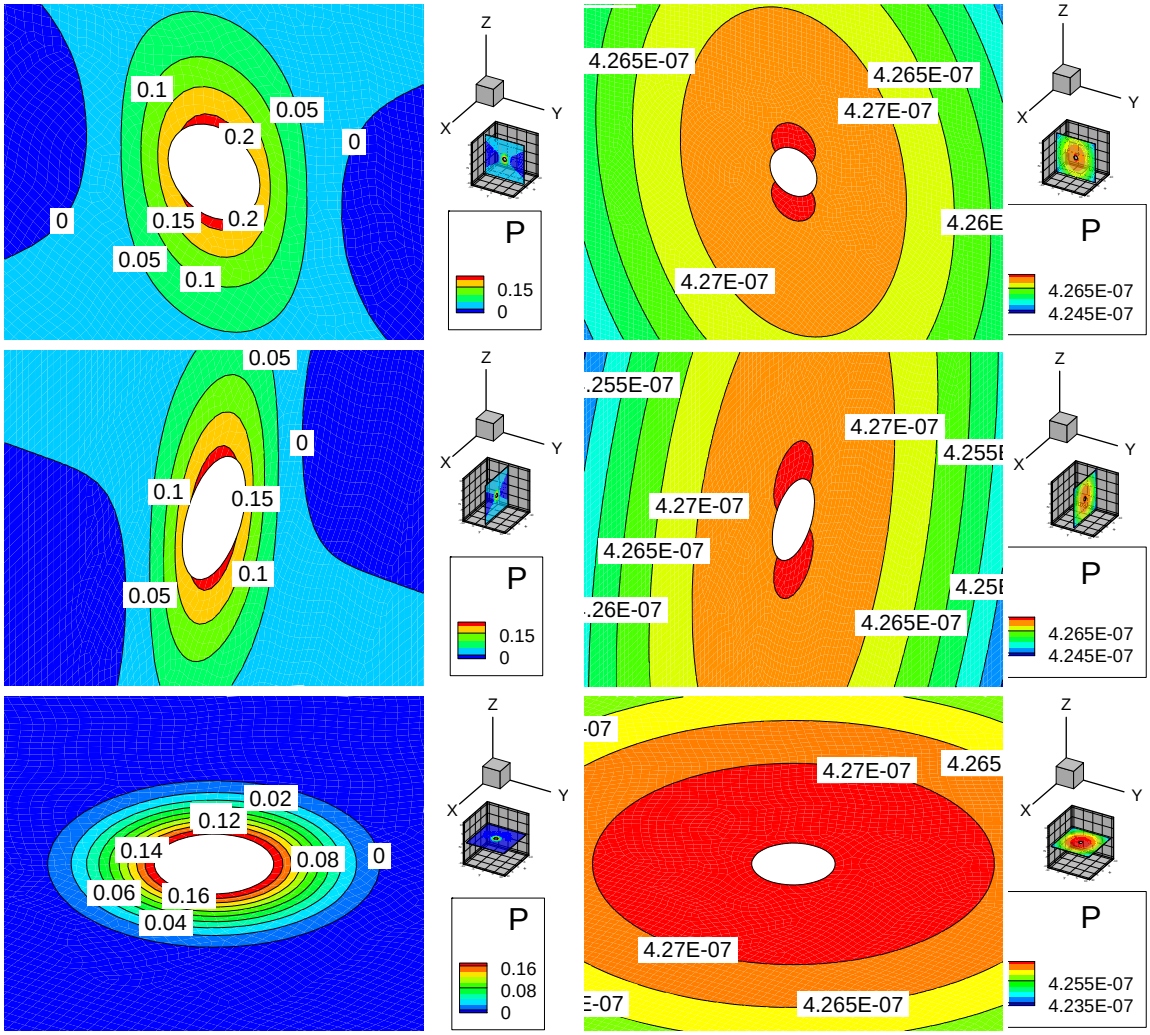

Figure B. 46 Induced pore pressure (MPa) distribution due to 1 mm normal displacement discontinuity (At Z direction) at origin, after 20 minutes (left side figures), and after 100 days (right side figures)

B.5. Continuous point shear displacement discontinuity effect

In Figure B. 48 to Figure B. 57 effects of 1 mm point shear displacement discontinuity (in X direction, as shown in Figure B. 47) on the origin of media are presented. The following effects might be considered as effects of unit shear slip on unit area natural fractures.

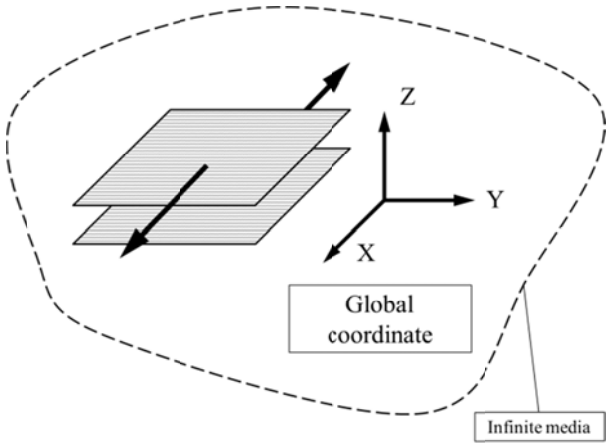

Figure B. 47 Point shear X DD in the origin of poroelastic media

It should be noted that shear X displacement discontinuity is constant during time.

Induced displacement fields are shown in Figure B. 48, Figure B. 49, and Figure B. 50. It can be seen from these figures that maximum magnitude of X and Z displacement do not change during two time scales. However displacement extent will increase when time proceeds. This is because of diffusion process that disseminates induced pore pressure and cause displacement field to extent into larger area. On the other hand pore pressure diffusion effect is not comparable with initial induced displacement (X and Z), so magnitude of maximum displacement does not changed.

Moreover, it can be observed that induced Y displacement is zero in all three major cross sections, and it is believed that if some points near to the disturbance location exist, induced Y displacement would be visible.

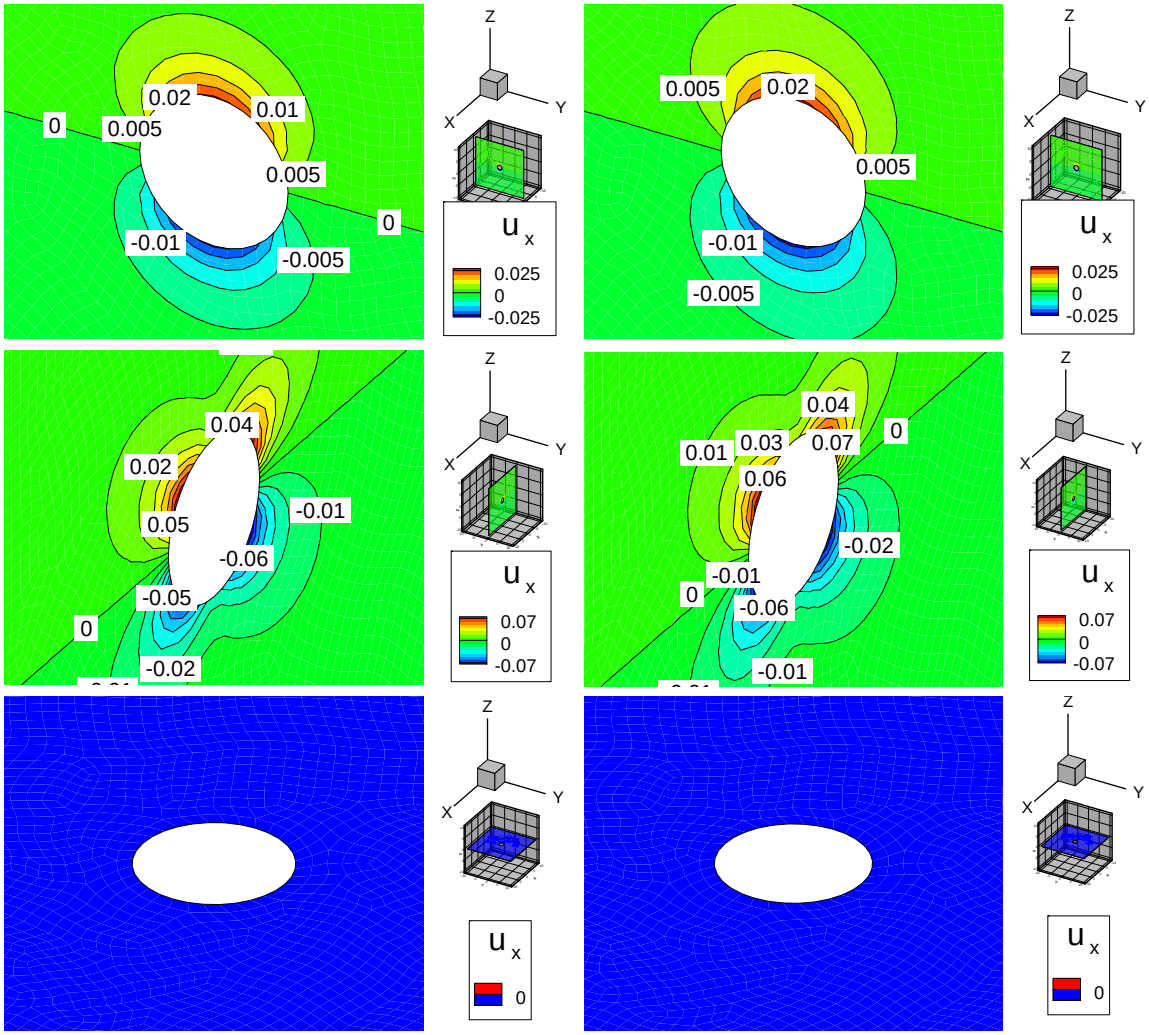

Figure B. 48 Induced X displacement (mm) distribution due to 1 mm shear displacement discontinuity (At X direction) at origin, after 20 minutes (left side figures), and after 100 days (right side figures)

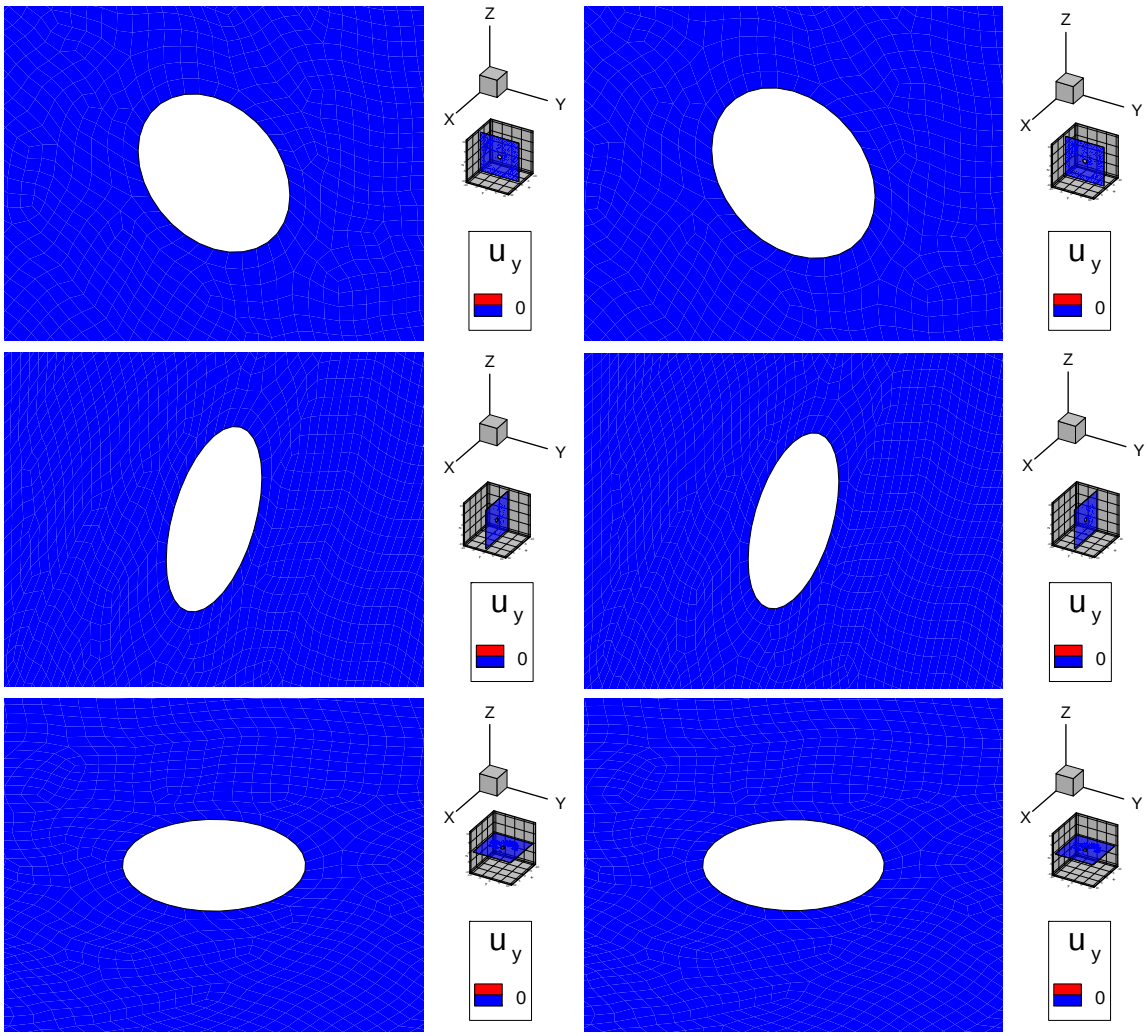

Figure B. 49 Induced Y displacement (mm) distribution due to 1 mm shear displacement discontinuity (At X direction) at origin, after 20 minutes (left side figures), and after 100 days (right side figures)

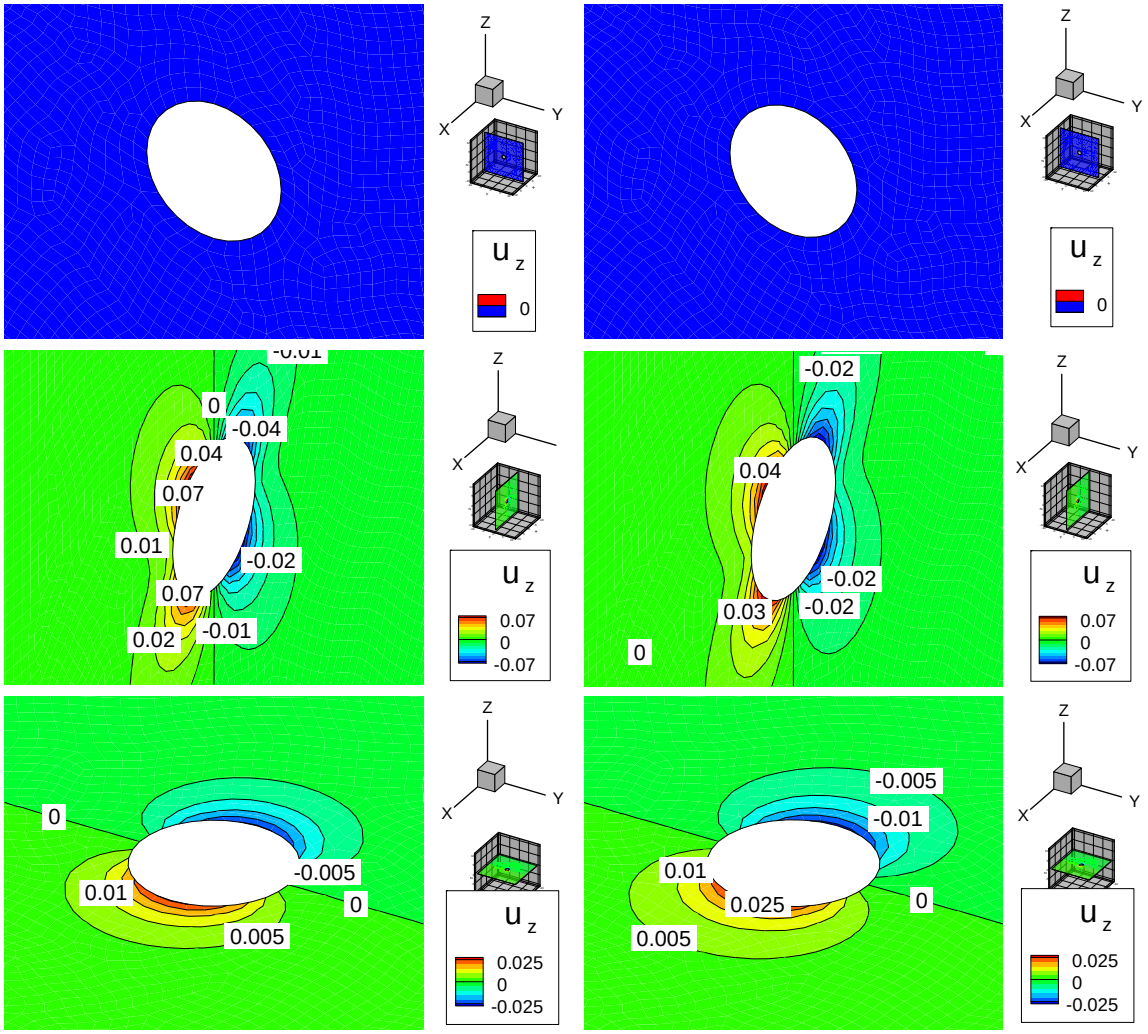

Figure B. 50 Induced Z displacement (mm) distribution due to 1 mm shear displacement discontinuity (At X direction) at origin, after 20 minutes (left side figures), and after 100 days (right side figures)

Induced XX stress is shown in Figure B. 51. It can be seen that 1 mm shear slip cause tensile and compression stress up to 2.5 MPa. This amount of stress might be enough to destabilize existing weakening features like natural fractures.

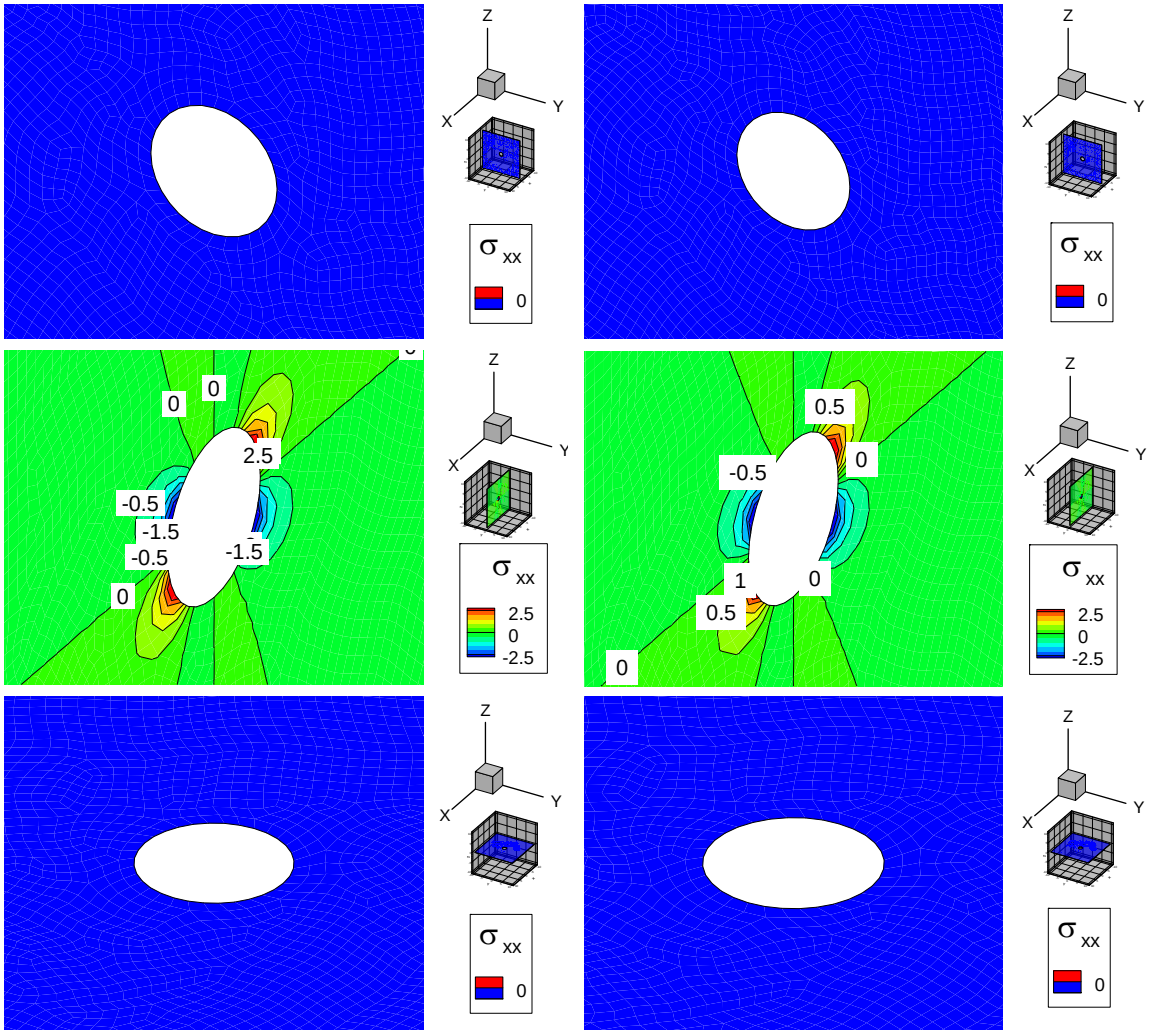

Figure B. 51 Induced total normal XX stress (MPa) distribution due to 1 mm shear displacement discontinuity (At X direction) at origin, after 20 minutes (left side figures), and after 100 days (right side figures)

Induced shear stresses are shown in Figure B. 52, Figure B. 53, and Figure B. 55. It can be seen from these figures and previous ones that magnitude of induced shear and normal stresses on different location is considerable and proves the claim that if we ignored the effect of shear slip on fractures, it would deviates results from physics based case.

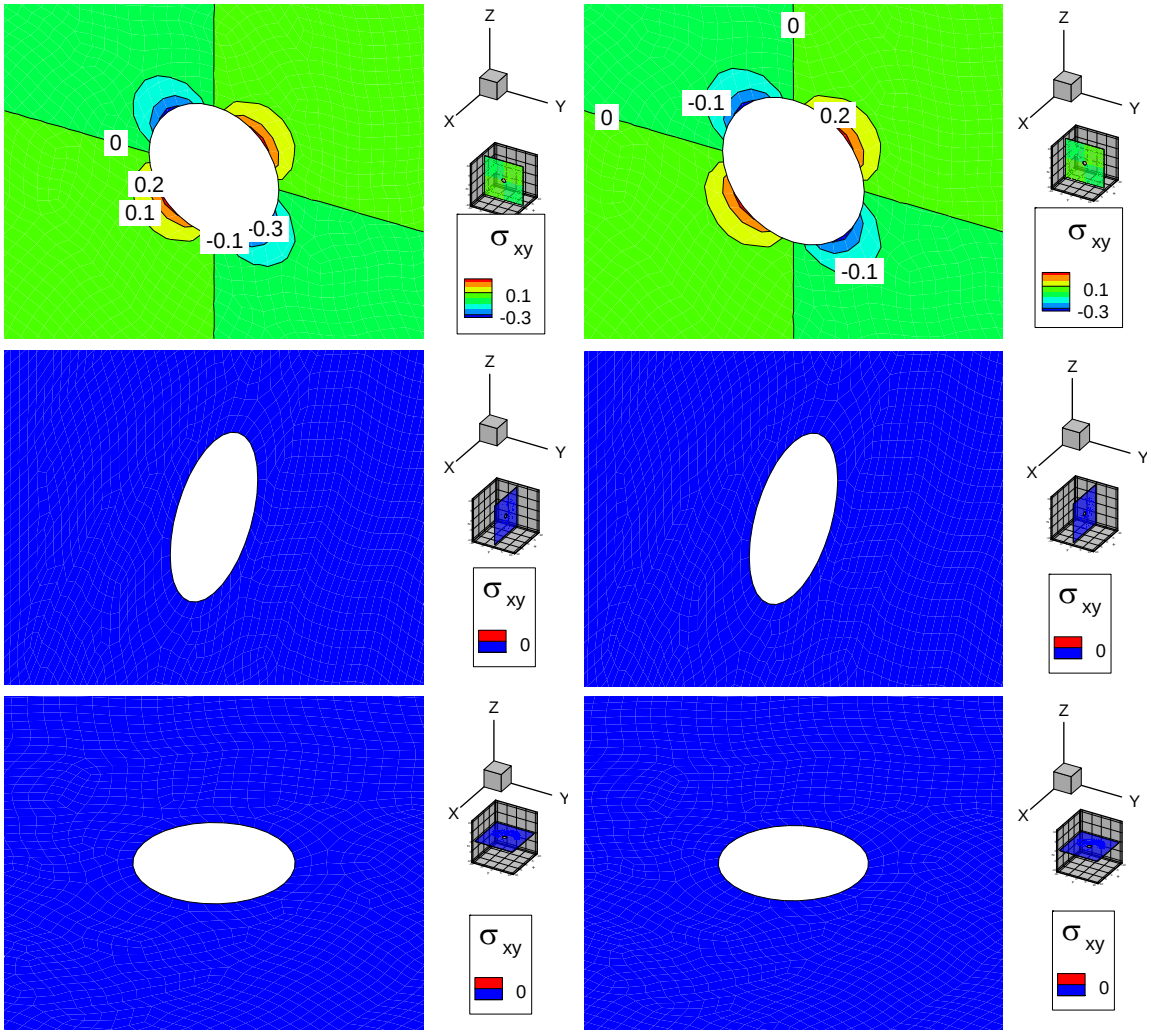

Figure B. 52 Induced shear XY stress (MPa) distribution due to 1 mm shear displacement discontinuity (At X direction) at origin, after 20 minutes (left side figures), and after 100 days (right side figures)

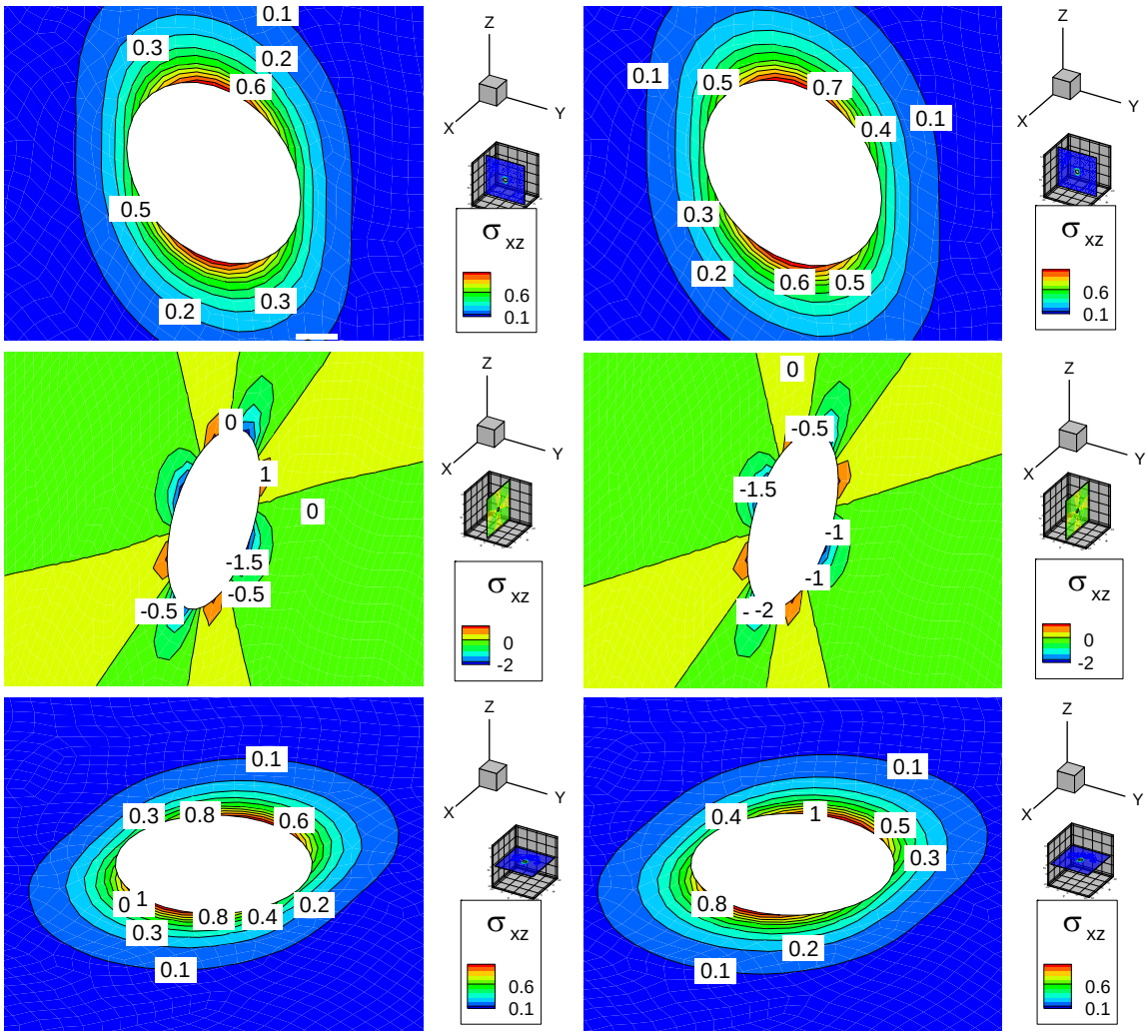

Figure B. 53 Induced shear XZ stress (MPa) distribution due to 1 mm shear displacement discontinuity (At X direction) at origin, after 20 minutes (left side figures), and after 100 days (right side figures)

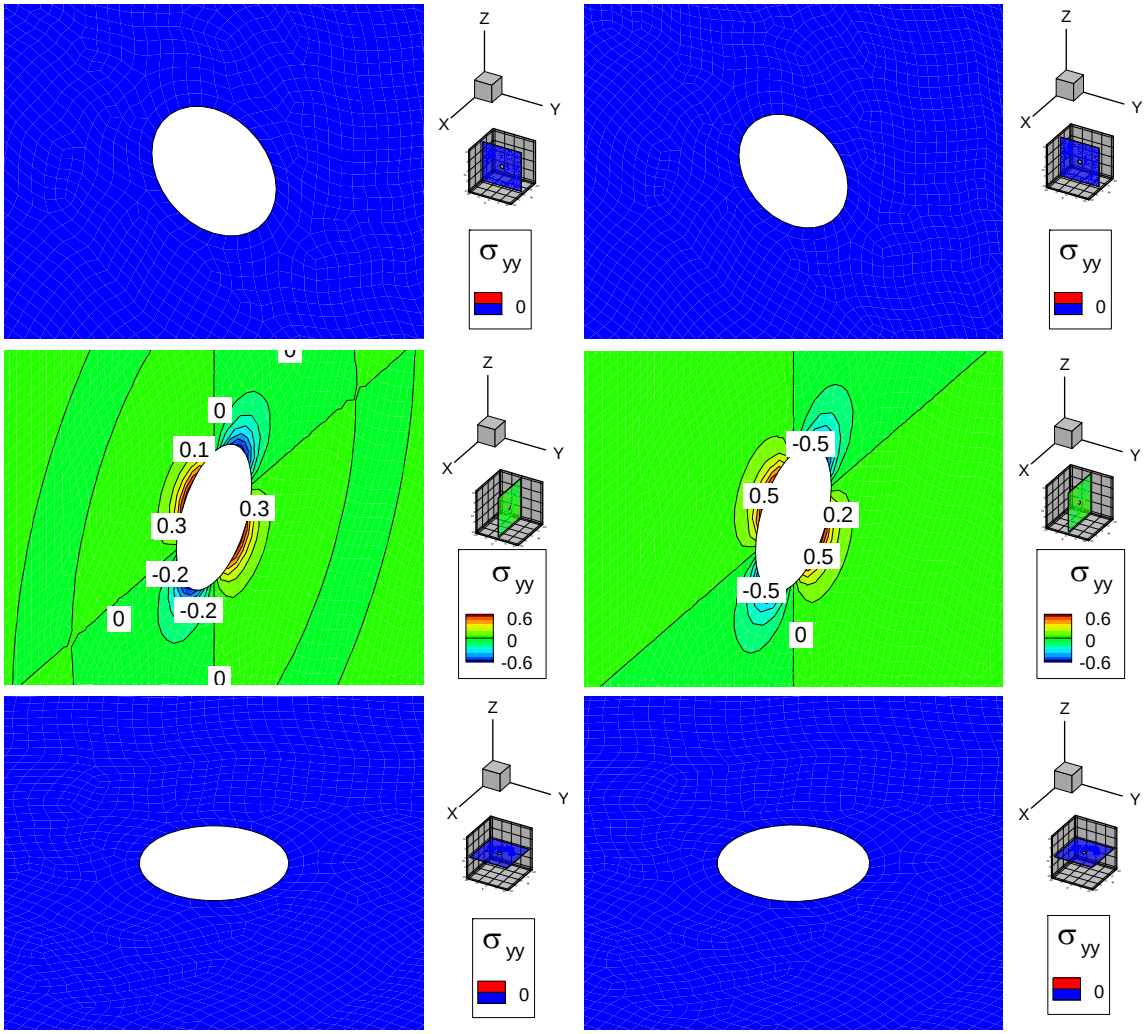

Figure B. 54 Induced total normal YY stress (MPa) distribution due to 1 mm shear displacement discontinuity (At X direction) at origin, after 20 minutes (left side figures), and after 100 days (right side figures)

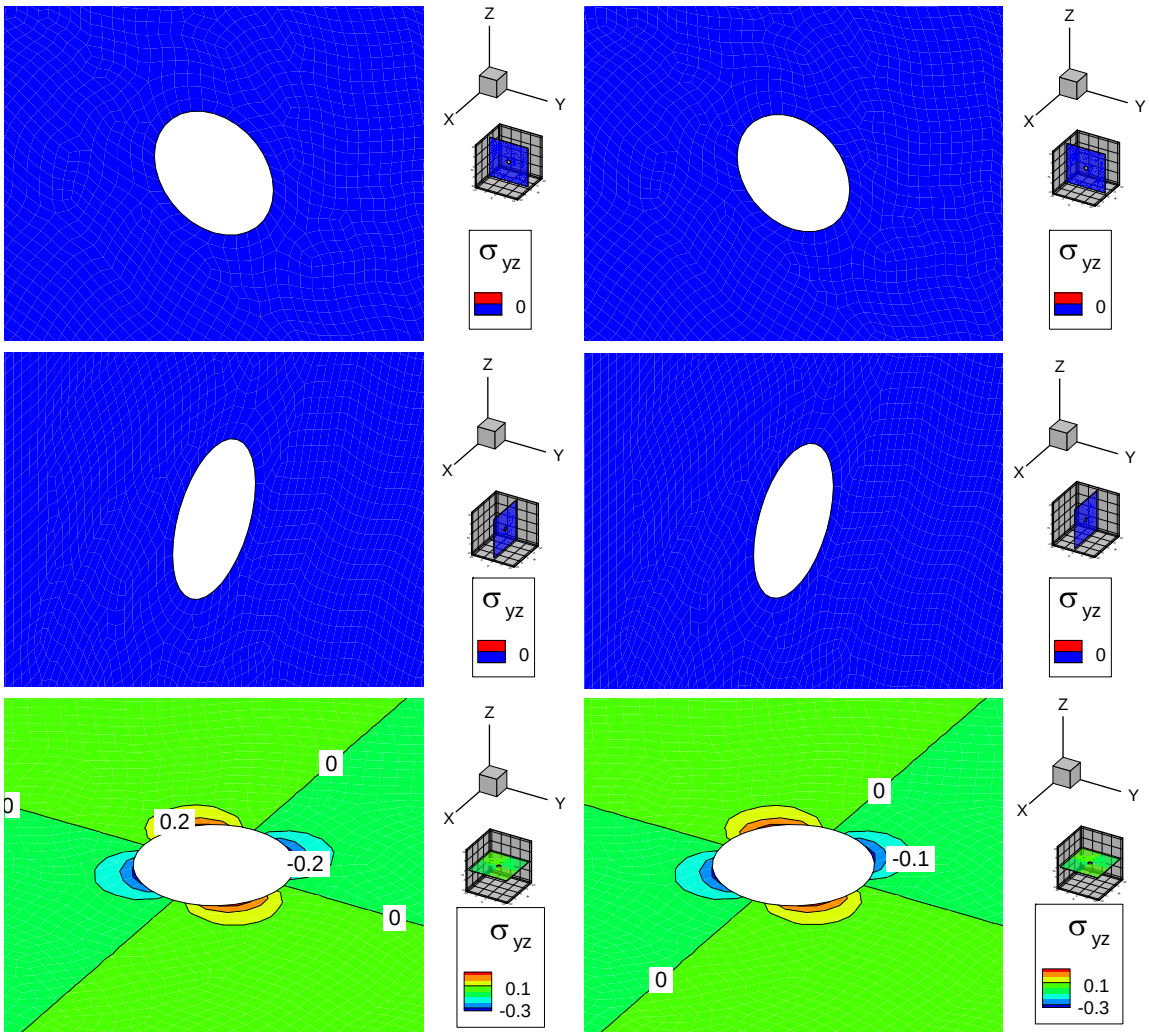

Figure B. 55 Induced shear YZ stress (MPa) distribution due to 1 mm shear displacement discontinuity (At X direction) at origin, after 20 minutes (left side figures), and after 100 days (right side figures)

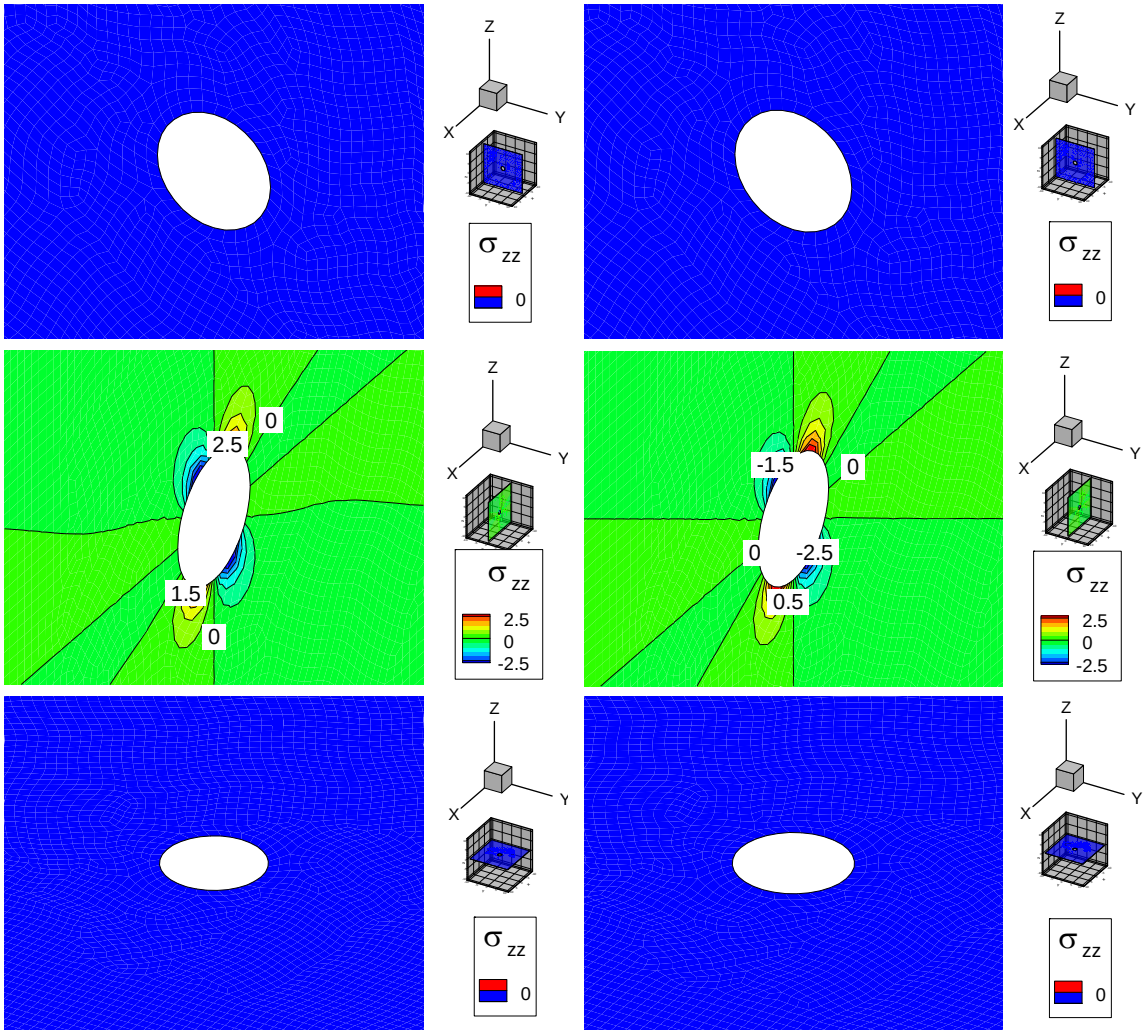

Figure B. 56 Induced total normal ZZ stress (MPa) distribution due to 1 mm shear displacement discontinuity (At X direction) at origin, after 20 minutes (left side figures), and after 100 days (right side figures)

Induced pore pressure is shown in Figure B. 57. It is clear that positive induced pore pressure is located in front of point DD (positive pressure in positive or negative X and Z) and negative induced pore pressure is located behind of point DD. Induced pore pressure has maximum value in early time and then decays by time. However, induced

pore pressure value is small in all time and it can be said that shear DD does not have considerable effect on pore pressure distribution.

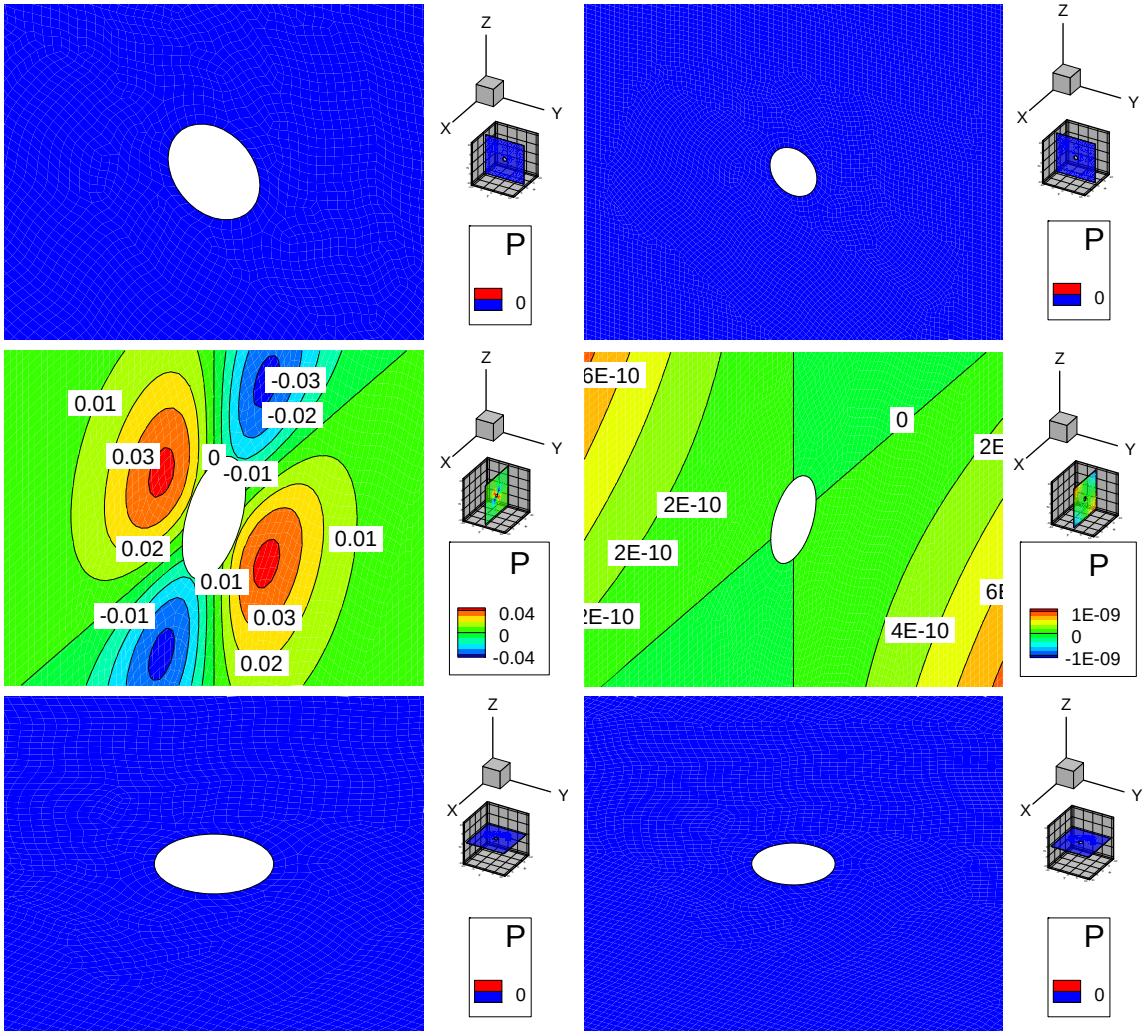

Figure B. 57 Induced pore pressure (MPa) distribution due to 1 mm shear displacement discontinuity (At X direction) at origin, after 20 minutes (left side figures), and after 100 days (right side figures)

B.6. Continuous point normal force effect

In Figure B. 59 to Figure B. 68 effects of 1 MPa point normal traction discontinuity (in Z direction) is shown. Normal traction discontinuity is applied on unit surface which is located in the origin of thermoporoelastic media (as shown in Figure B. 58). Presented effects in this section might be considered as effects of part of wellbore surface with unit area, across which 1 MPa normal stress will be released (due to drilling process).

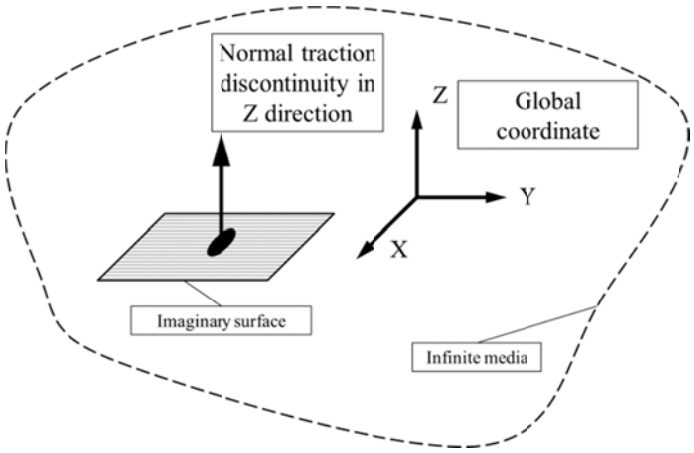

Figure B. 58 Point normal Z traction discontinuity in the origin of poroelastic media

Induced displacement field is shown in Figure B. 59, Figure B. 60, and Figure B. 61. As it can be seen induced displacement is small and its magnitude is constant during time. These figures show that the effects of normal traction discontinuity in media are constant during analysis of reservoir problem and they should be considered for short or long time analysis.

It should be noted here that, the presented effects in this appendix are for unit area and specially for this section for unit normal traction discontinuity. To find out

about effects of larger traction discontinuity area or larger traction discontinuity magnitude, presented effects should multiplied by surface area and discontinuity magnitude.

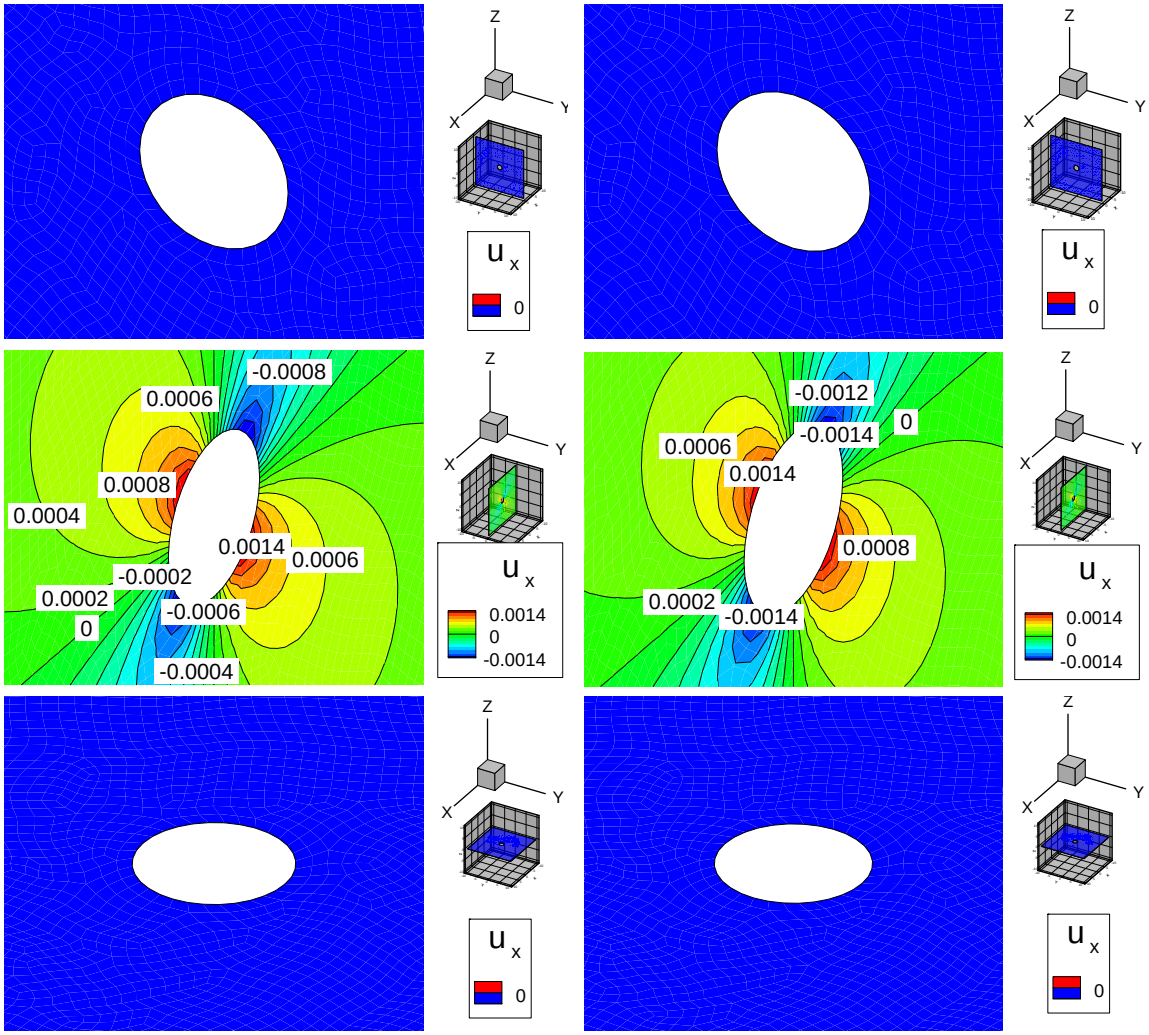

Figure B. 59 Induced X displacement (mm) distribution due to 1 MPa normal traction discontinuity (At Z direction) at origin, after 20 minutes (left side figures), and after 100 days (right side figures)

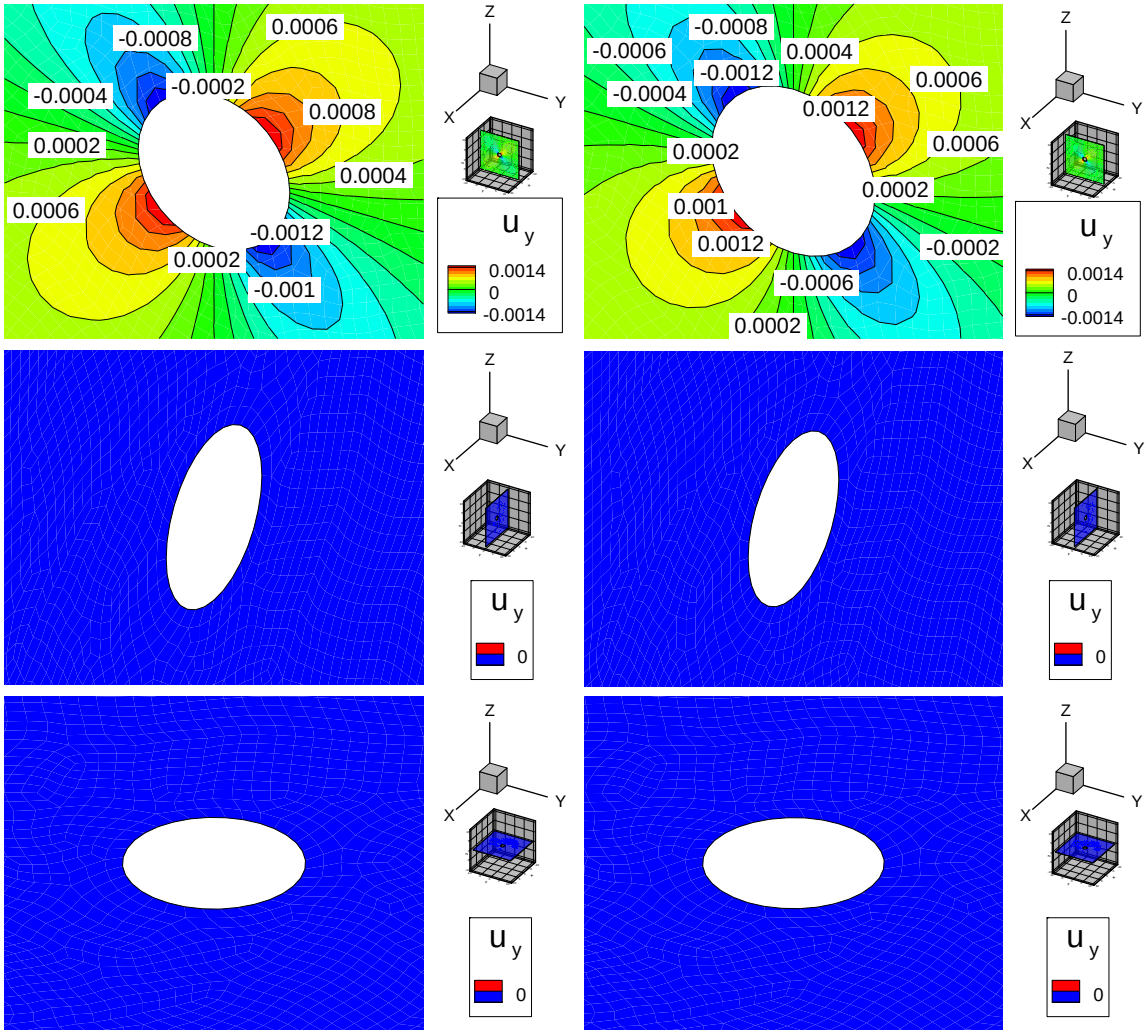

Figure B. 60 Induced Y displacement (mm) distribution due to 1 MPa normal traction discontinuity (At Z direction) at origin, after 20 minutes (left side figures), and after 100 days (right side figures)

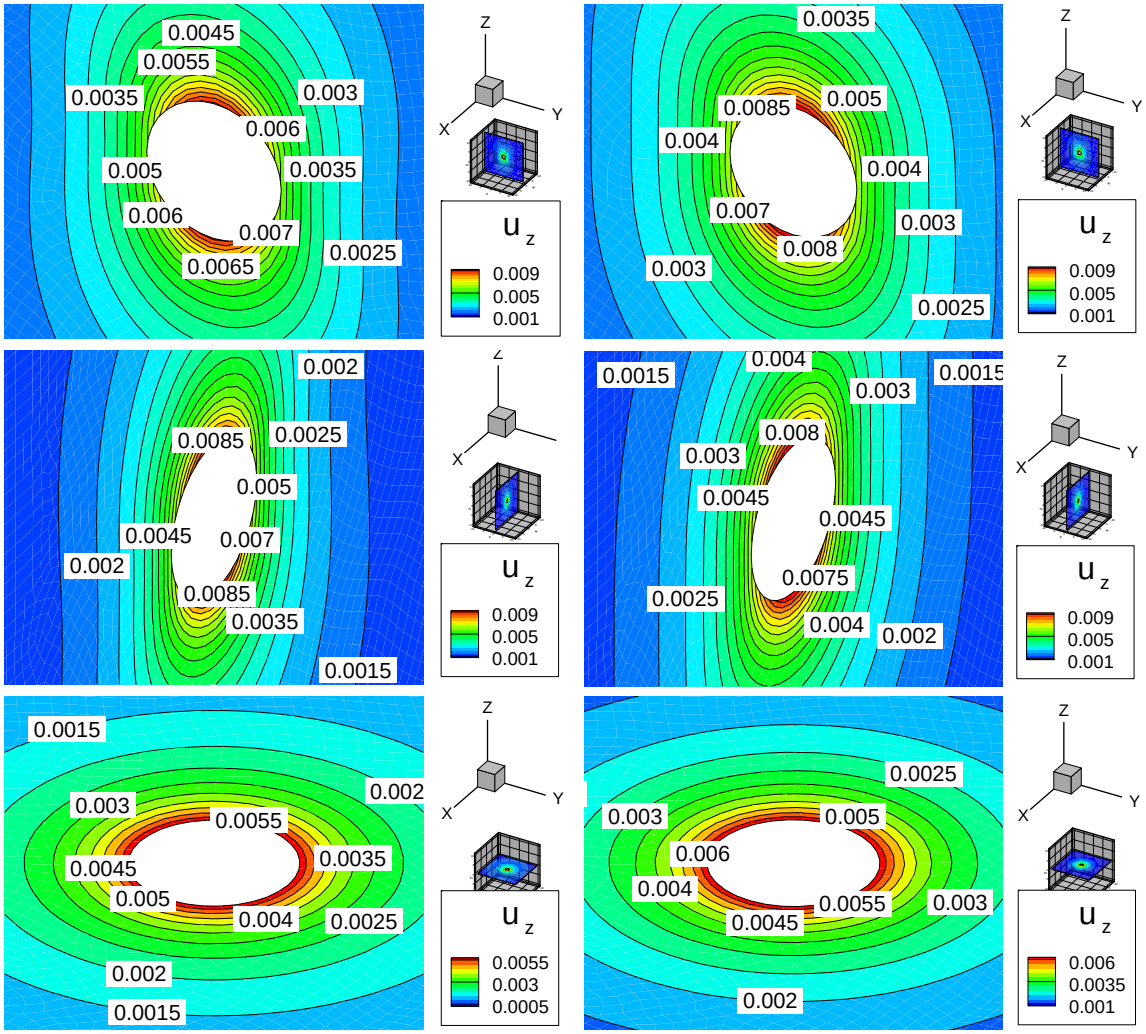

Figure B. 61 Induced Z displacement (mm) distribution due to 1 MPa normal traction discontinuity (At Z direction) at origin, after 20 minutes (left side figures), and after 100 days (right side figures)

Induced stress fields due to 1 MPa traction discontinuity is shown in Figure B. 62 to Figure B. 67. It is obvious from the figures that magnitude of induced stress changes by small amount (presented effects magnified by area of discontinuity and discontinuity magnitude) and it might apply some instability near disturbance location.

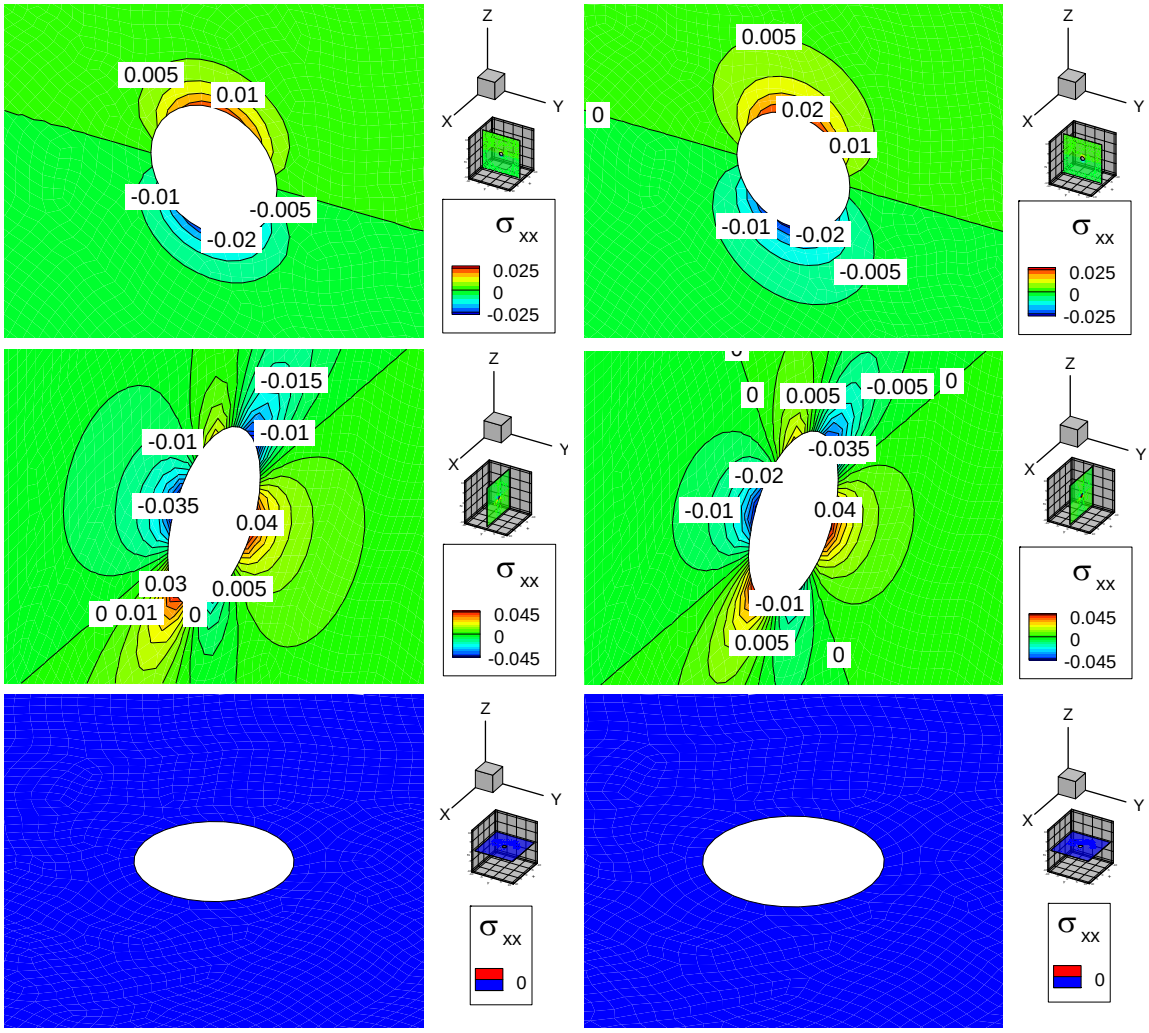

Figure B. 62 Induced total normal XX stress (MPa) distribution due to 1 MPa normal traction discontinuity (At Z direction) at origin, after 20 minutes (left side figures), and after 100 days (right side figures)

XX and YY components of induced stresses are shown in Figure B. 62 and Figure B. 65, respectively. It is obvious from the figures that XX and YY stresses change from tensile to compression and their magnitude does not change when time proceeds. Figures show that diffusion process does not have considerable effect on induced stress field.

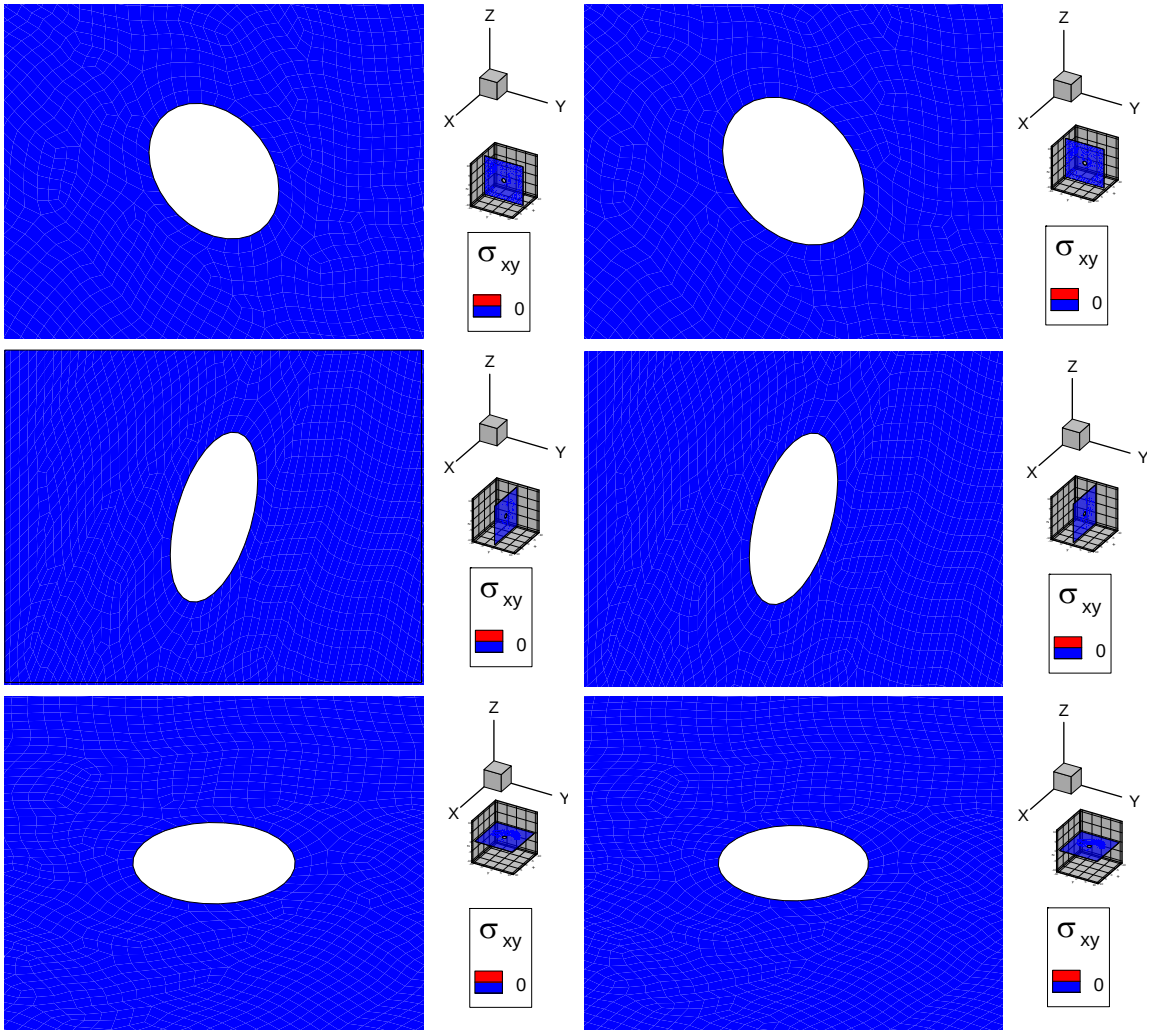

Figure B. 63 Induced shear XY stress (MPa) distribution due to 1 MPa normal traction discontinuity (At Z direction) at origin, after 20 minutes (left side figures), and after 100 days (right side figures)

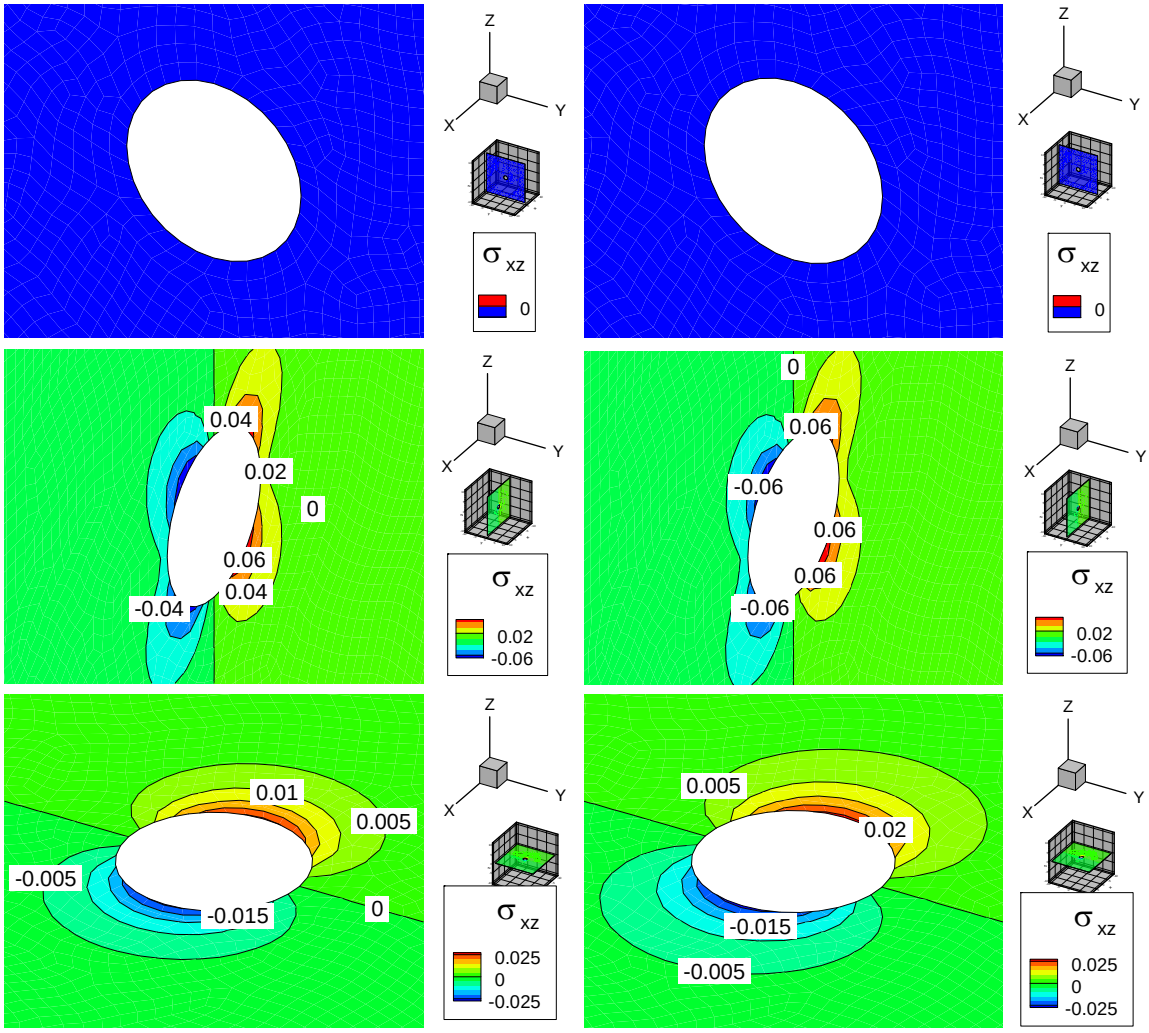

Figure B. 64 Induced shear XZ stress (MPa) distribution due to 1 MPa normal traction discontinuity (At Z direction) at origin, after 20 minutes (left side figures), and after 100 days (right side figures)

Shear stresses are shown in Figure B. 63, Figure B. 64, and Figure B. 66. As well as other stress components, induced shear stress has small magnitude. However if it is magnified by discontinuity area or discontinuity magnitude, it would be considerable and changes status of weakening planes in the reservoir.

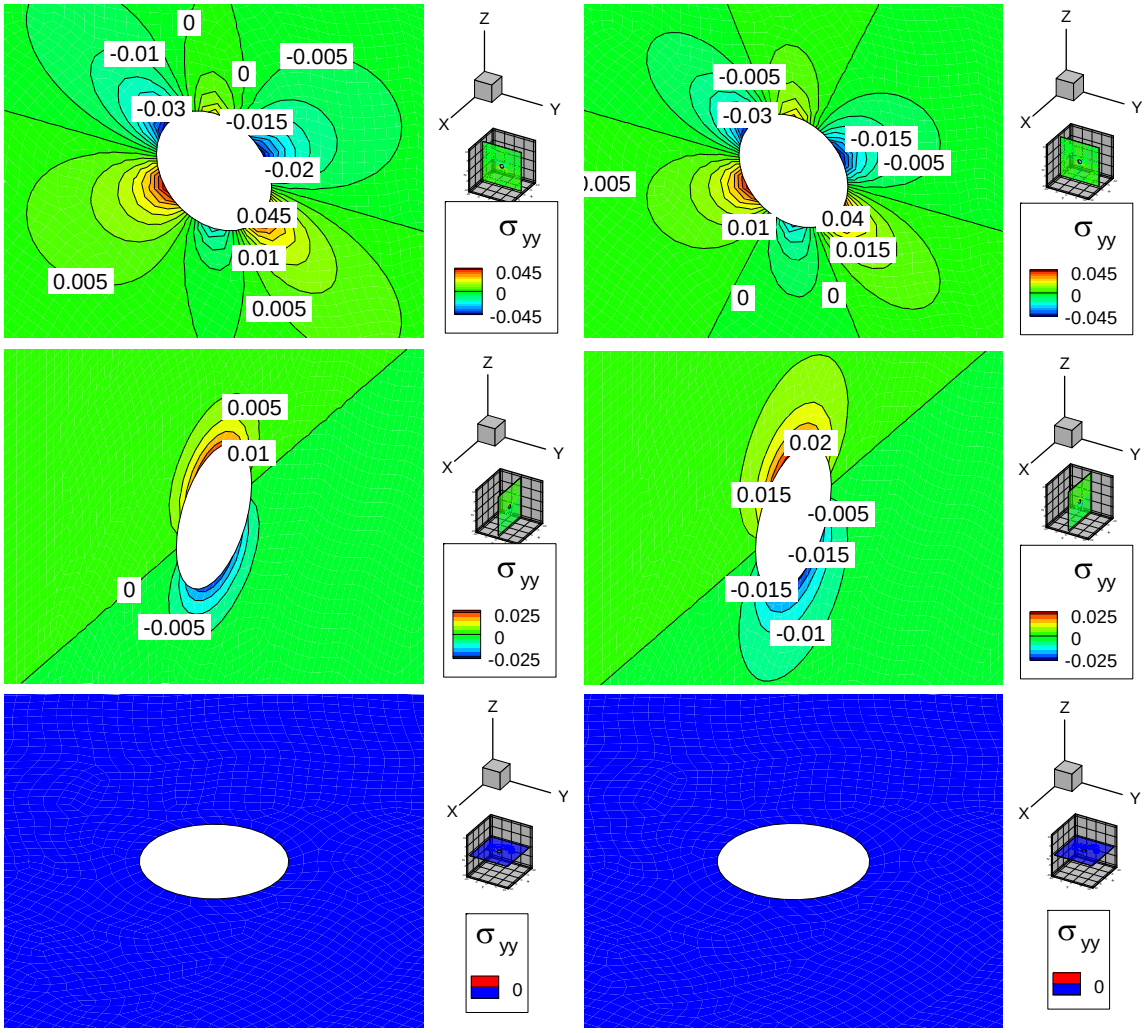

Figure B. 65 Induced total normal YY stress (MPa) distribution due to 1 MPa normal traction discontinuity (At Z direction) at origin, after 20 minutes (left side figures), and after 100 days (right side figures)

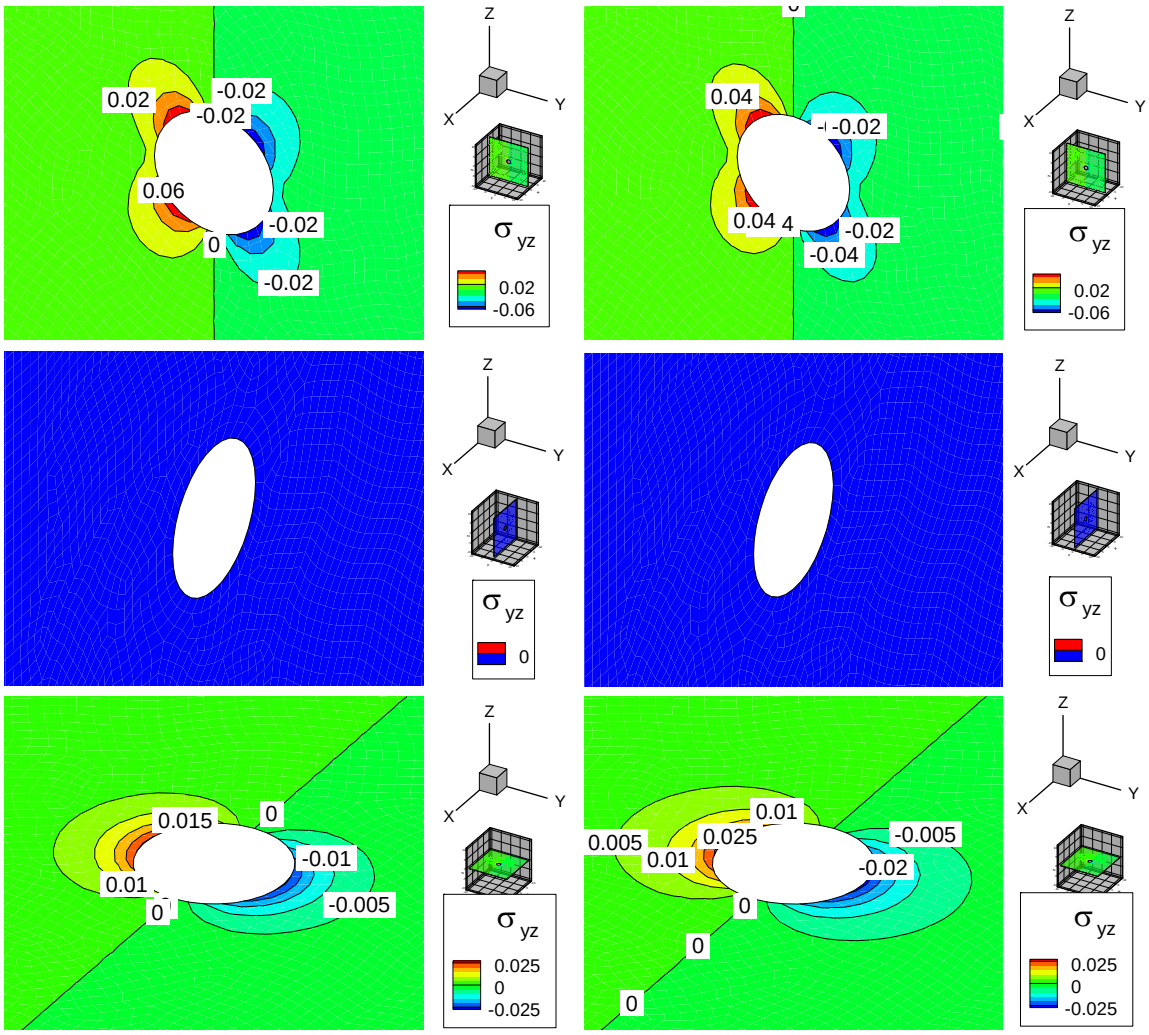

Figure B. 66 Induced shear YZ stress (MPa) distribution due to 1 MPa normal traction discontinuity (At Z direction) at origin, after 20 minutes (left side figures), and after 100 days (right side figures)

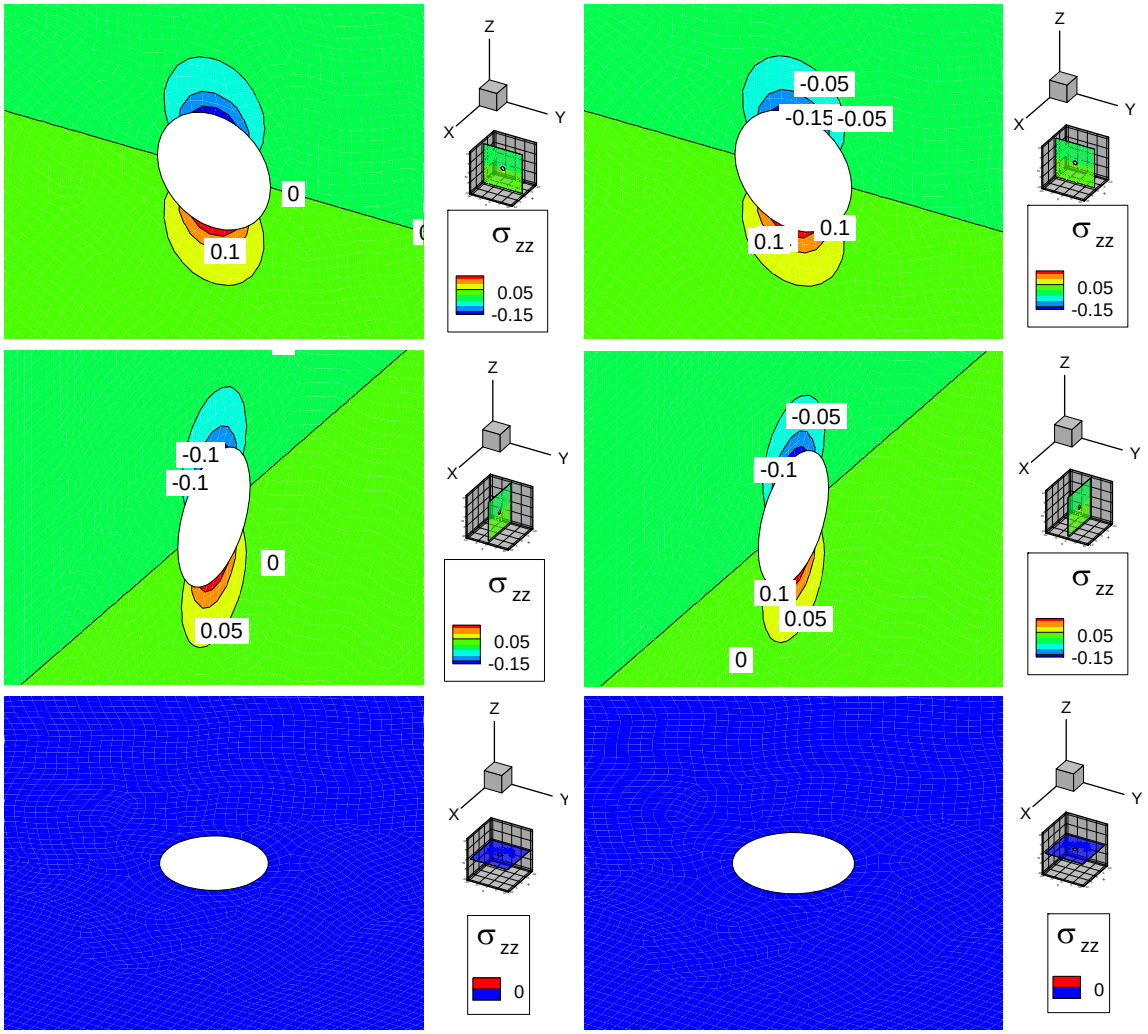

Figure B. 67 Induced total normal ZZ stress (MPa) distribution due to 1 MPa normal traction discontinuity (At Z direction) at origin, after 20 minutes (left side figures), and after 100 days (right side figures)

Comparison of ZZ component of induced stress with other components shows that normal traction discontinuity has maximum effect in its direction (in this case in Z direction) and induces maximum amount of stress in the stated direction.

Induced pore pressure (Figure B. 68) is less than 0.01 MPa initially and disseminates when time proceeds.

As it is expected positive pore pressure is always located in front of applied traction discontinuity and negative is located behind of it.

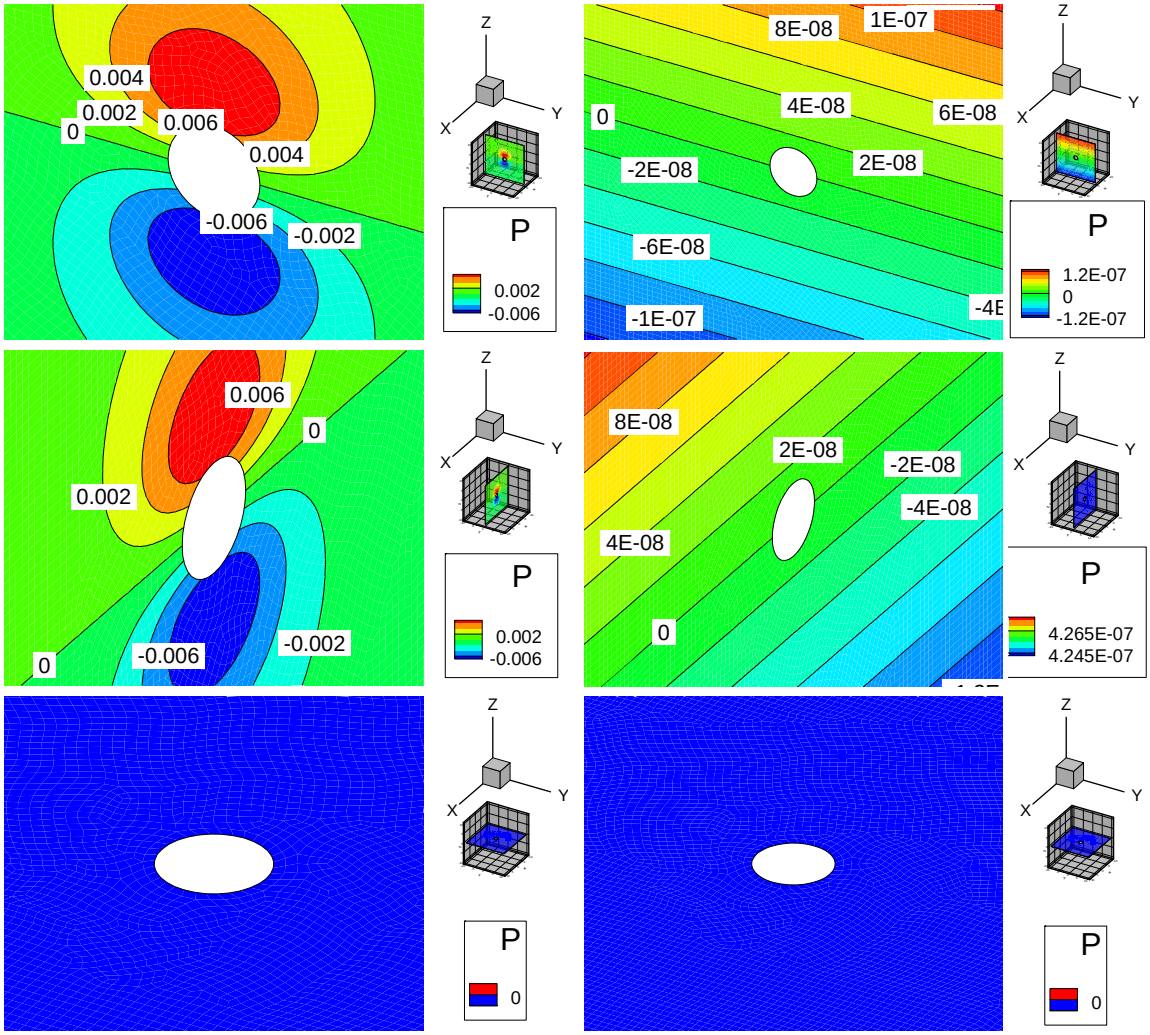

Figure B. 68 Induced pore pressure (MPa) distribution due to 1 MPa normal traction discontinuity (At Z direction) at origin, after 20 minutes (left side figures), and after 100 days (right side figures)

B.7. Continuous point shear force effect

In Figure B. 70 to Figure B. 79 effects of 1 MPa point shear traction discontinuity (in X direction, as shown in Figure B. 69) is presented. Traction discontinuity is applied on a surface with unit area on the origin of thermoporoelastic media. These effects might be considered as same as effects of surface with unit area, across which 1 MPa shear stress discontinuity exist (like as wellbore surface across which shear stress releases).

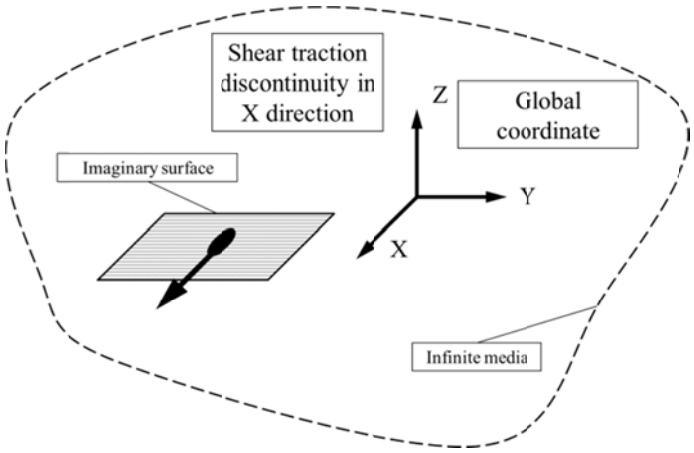

Figure B. 69 Point shear X traction discontinuity in the origin of poroelastic media

Induced displacement fields are shown in Figure B. 70 to Figure B. 72. Induced displacement field is very small and almost constant during time and does not change considerably by increasing time. These might magnified by discontinuity magnitude and also surface area.

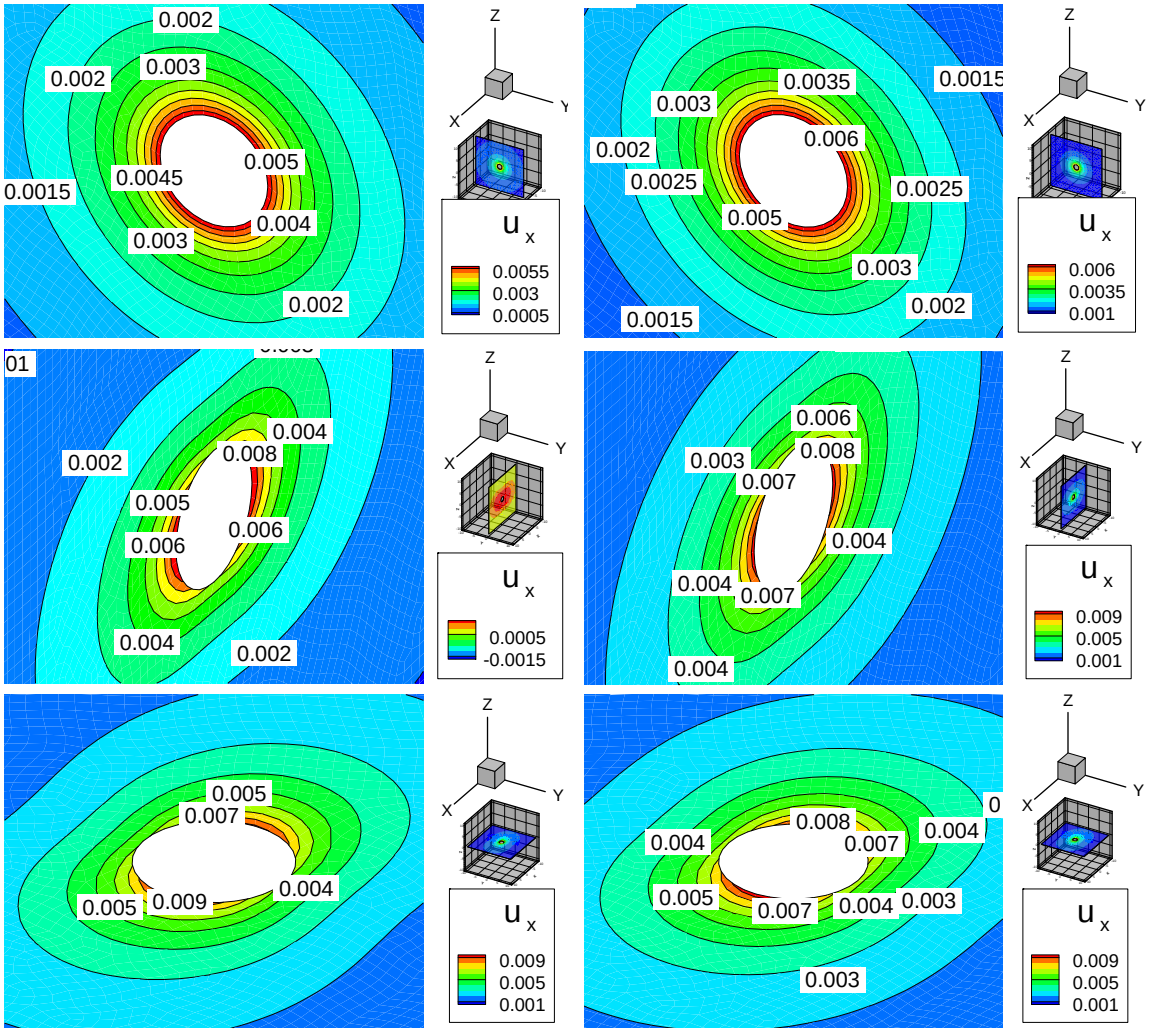

Figure B. 70 Induced X displacement (mm) distribution due to 1 MPa shear traction discontinuity (At X direction) at origin, after 20 minutes (left side figures), and after 100 days (right side figures)

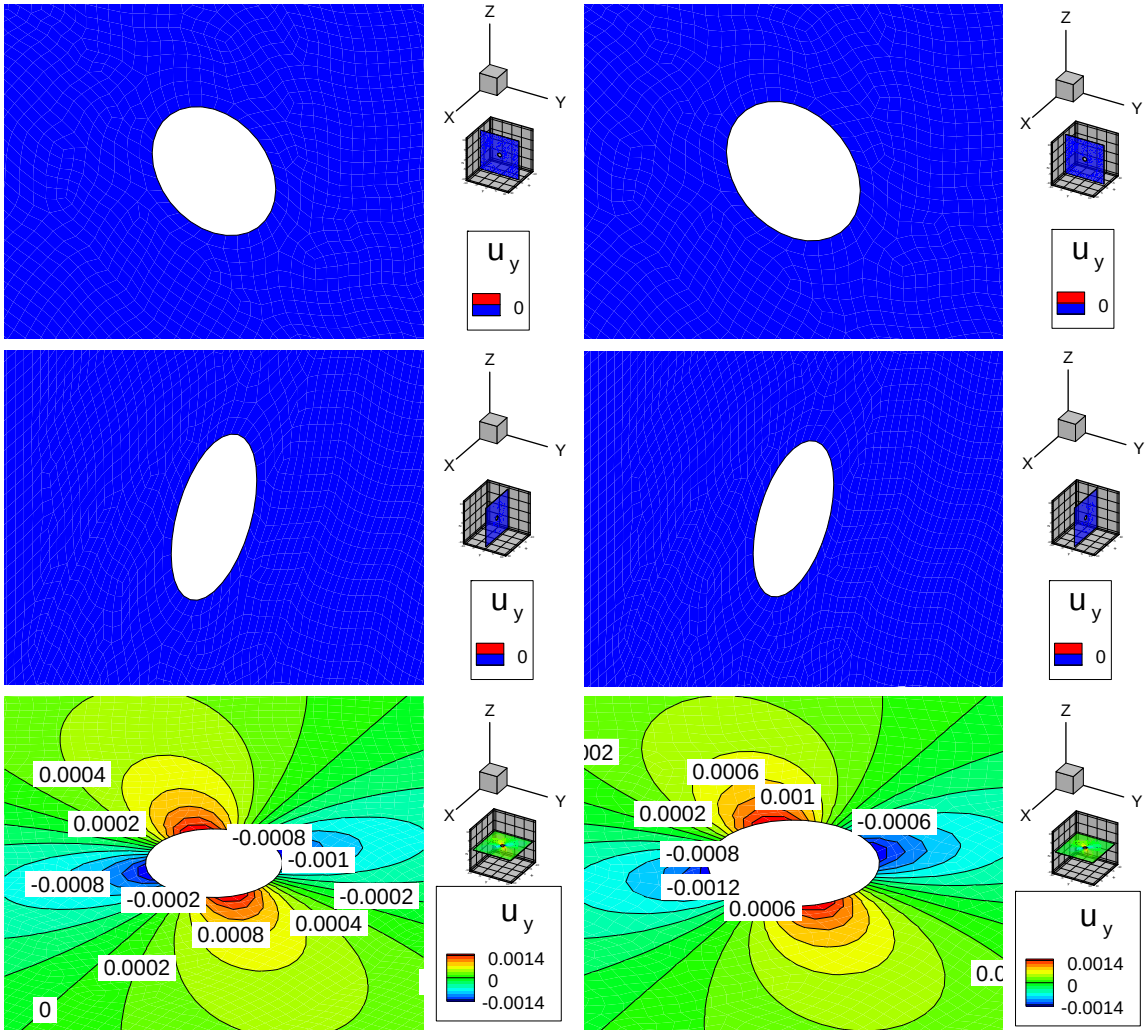

Figure B. 71 Induced Y displacement (mm) distribution due to 1 MPa shear traction discontinuity (At X direction) at origin, after 20 minutes (left side figures), and after 100 days (right side figures)

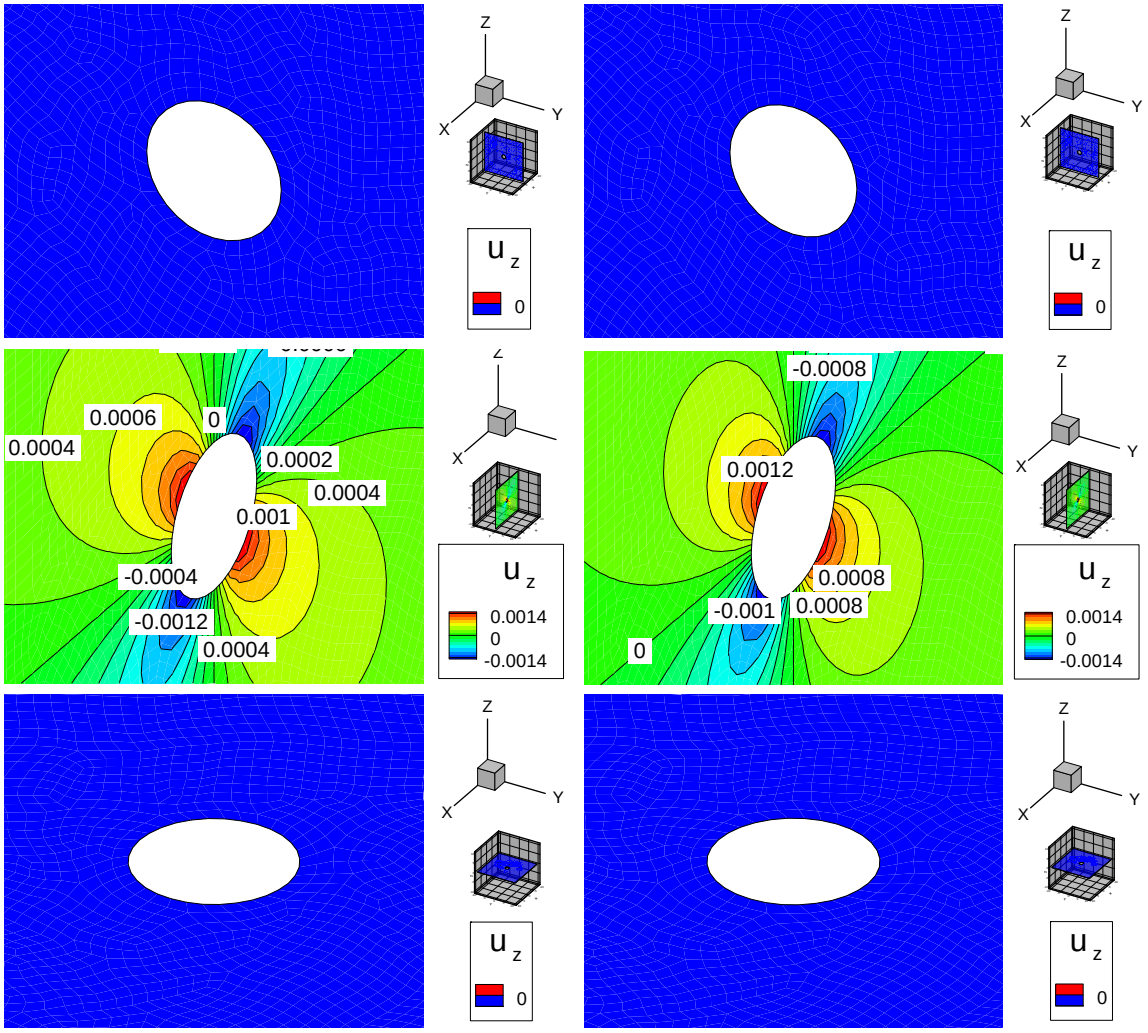

Figure B. 72 Induced Z displacement (mm) distribution due to 1 MPa shear traction discontinuity (At X direction) at origin, after 20 minutes (left side figures), and after 100 days (right side figures)

Induced stress field is shown through Figure B. 73 to Figure B. 78. As can be seen from the figures, magnitude of induced stress does not change by time. However extent of induced stress is growing and affects bigger area. This is due to diffusion process.

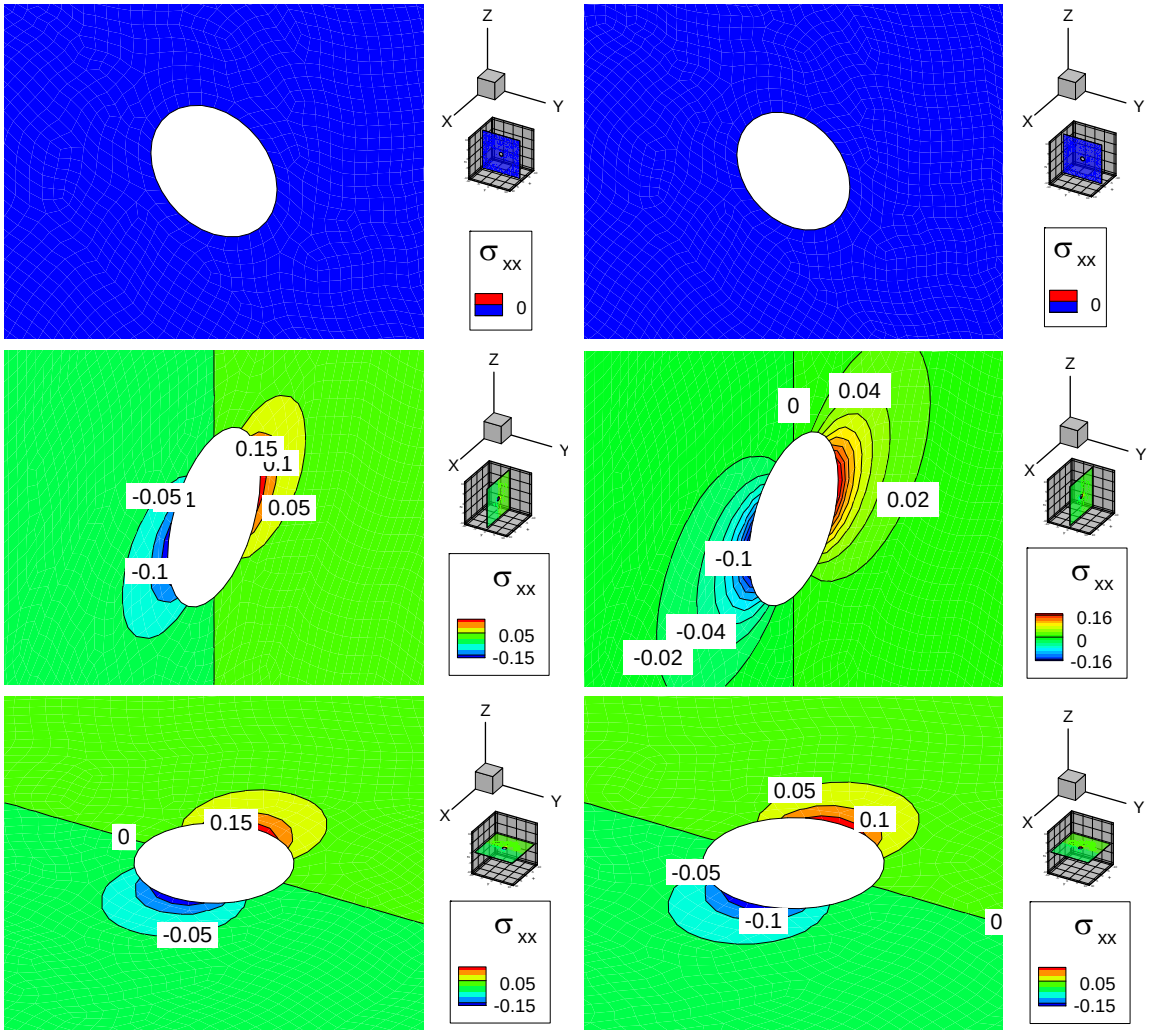

Figure B. 73 Induced total normal XX stress (MPa) distribution due to 1 MPa shear traction discontinuity (At X direction) at origin, after 20 minutes (left side figures), and after 100 days (right side figures)

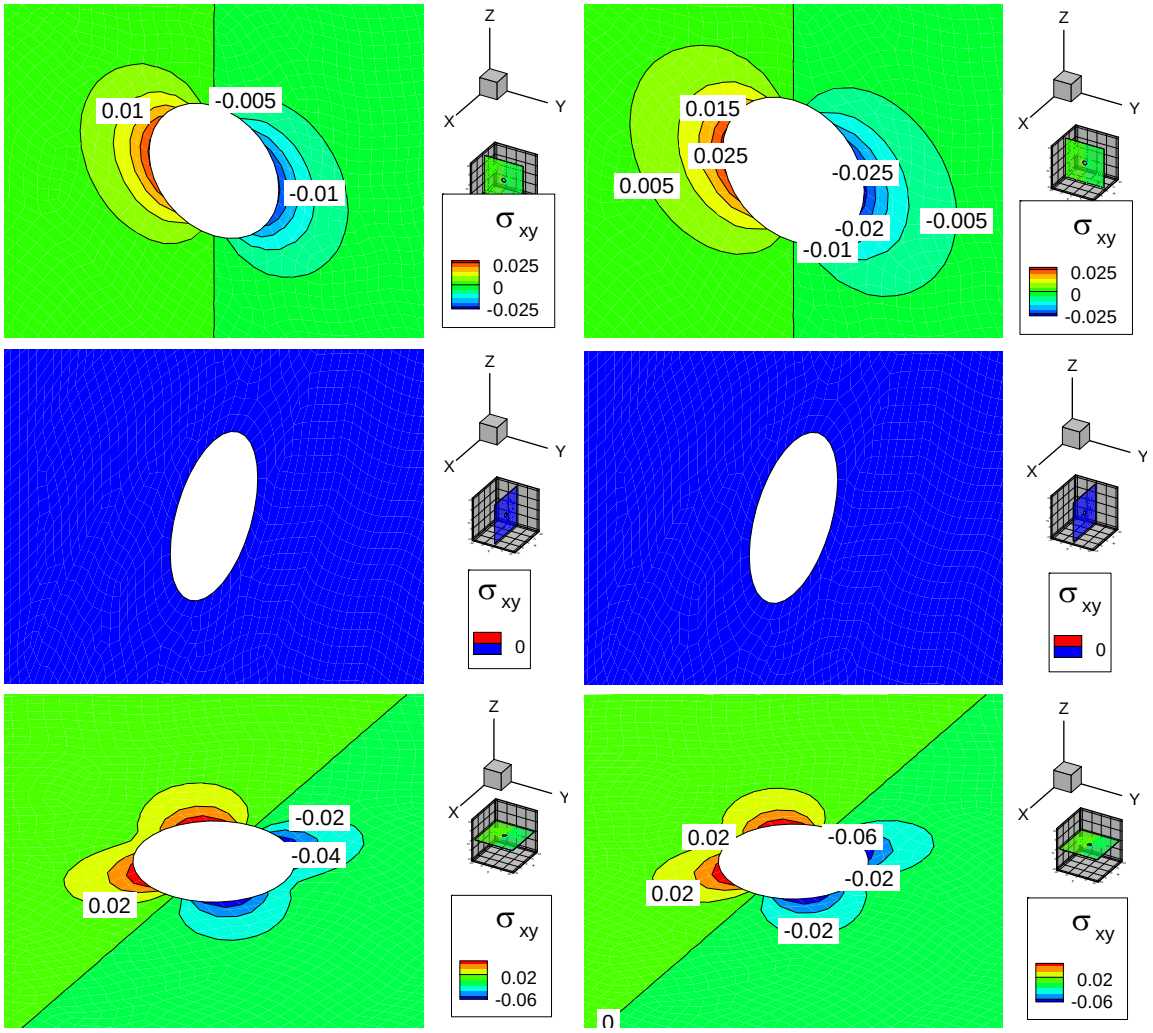

Figure B. 74 Induced shear XY stress (MPa) distribution due to 1 MPa shear displacement discontinuity (At X direction) at origin, after 20 minutes (left side figures), and after 100 days (right side figures)

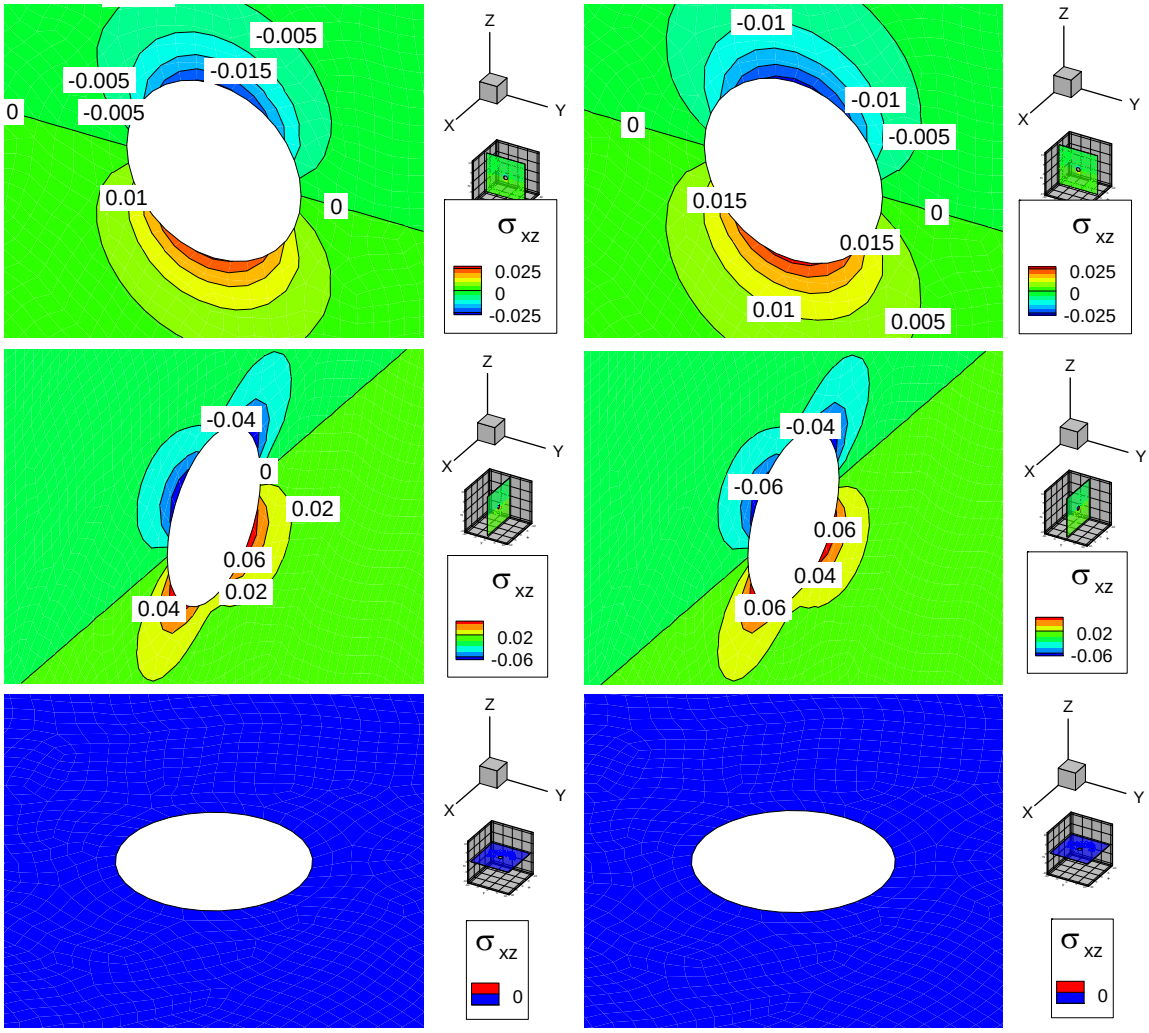

Figure B. 75 Induced shear XZ stress (MPa) distribution due to 1 MPa shear traction discontinuity (At X direction) at origin, after 20 minutes (left side figures), and after 100 days (right side figures)

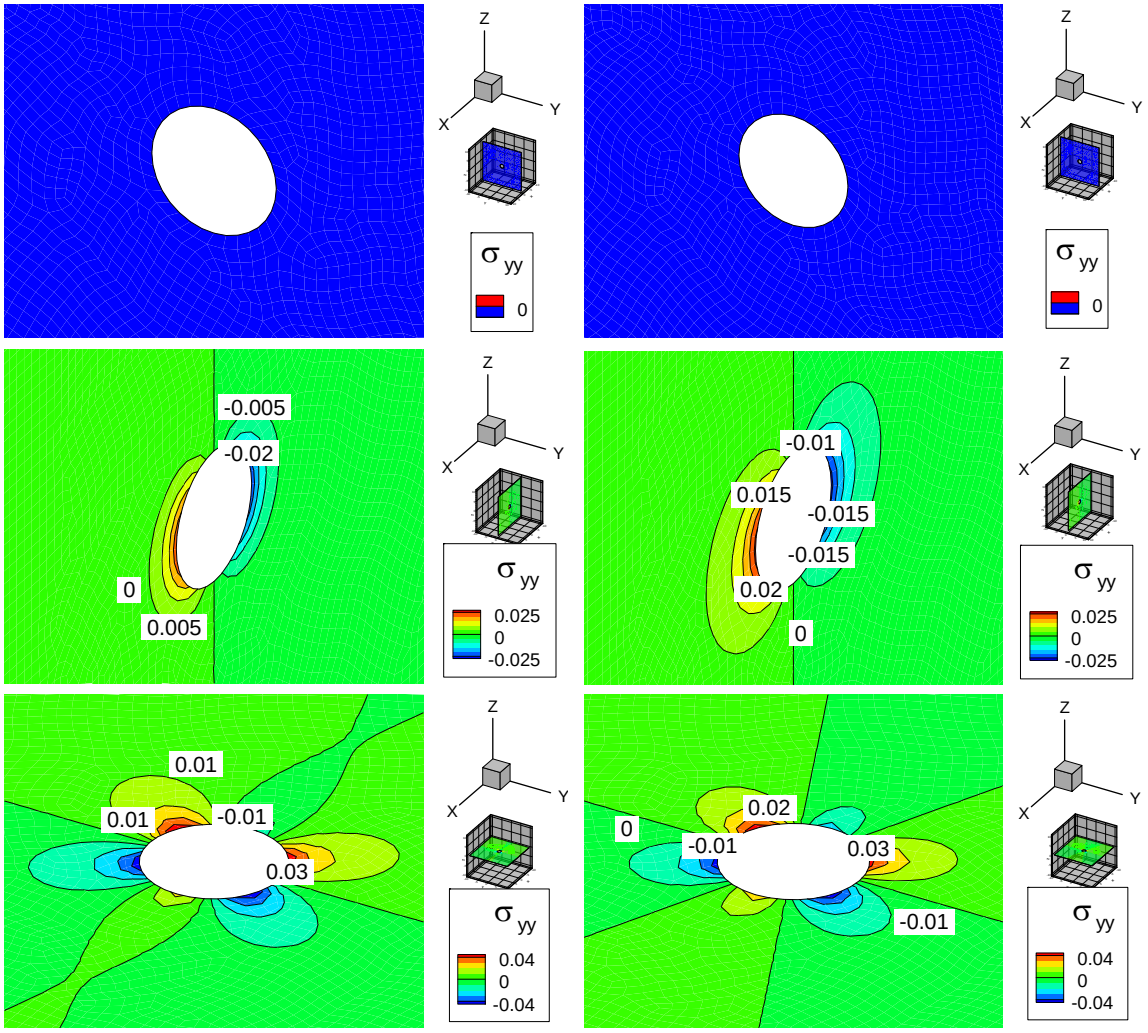

Figure B. 76 Induced total normal YY stress (MPa) distribution due to 1 MPa shear traction discontinuity (At X direction) at origin, after 20 minutes (left side figures), and after 100 days (right side figures)

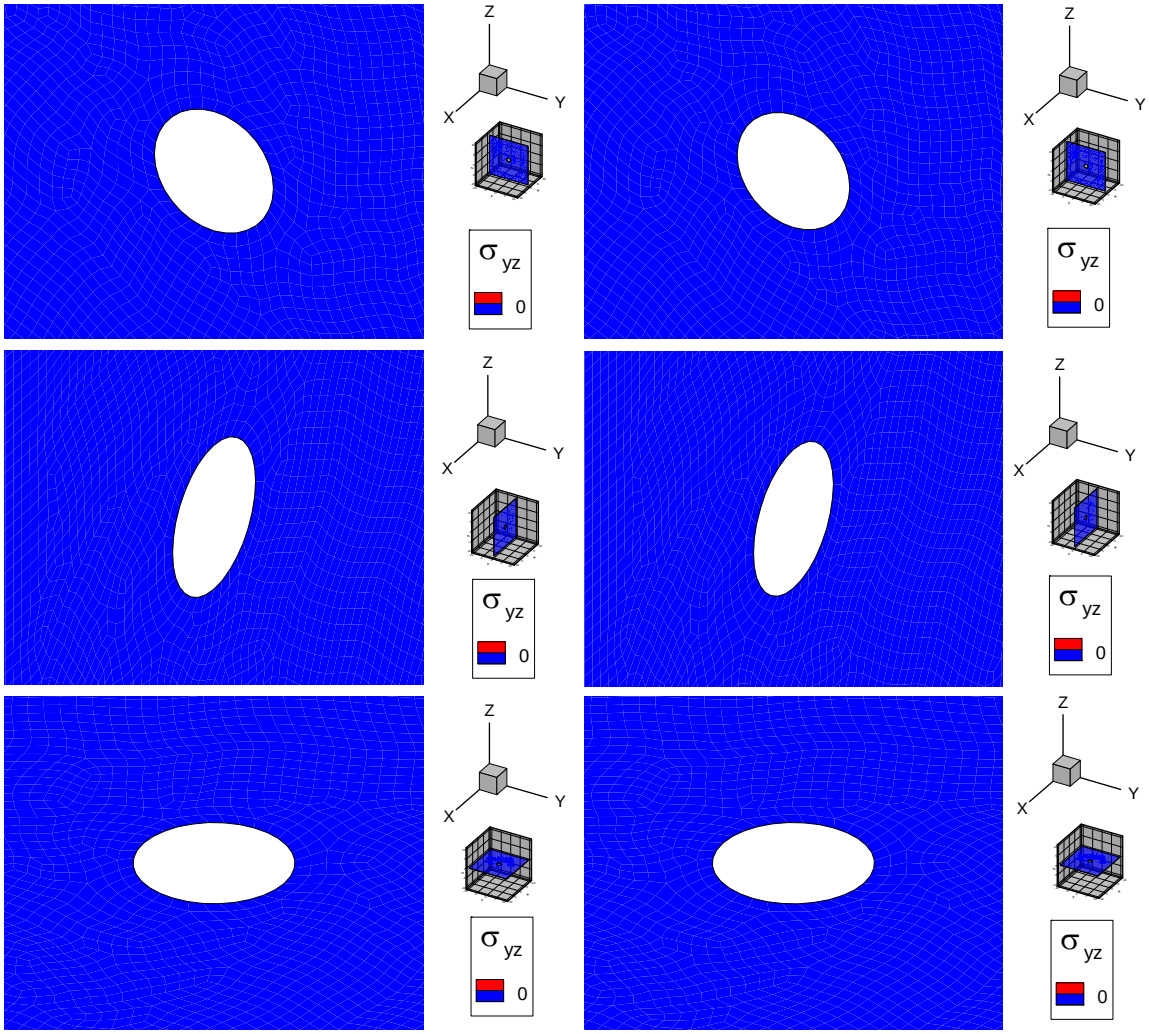

Figure B. 77 Induced shear YZ stress (MPa) distribution due to 1 MPa shear traction discontinuity (At X direction) at origin, after 20 minutes (left side figures), and after 100 days (right side figures)

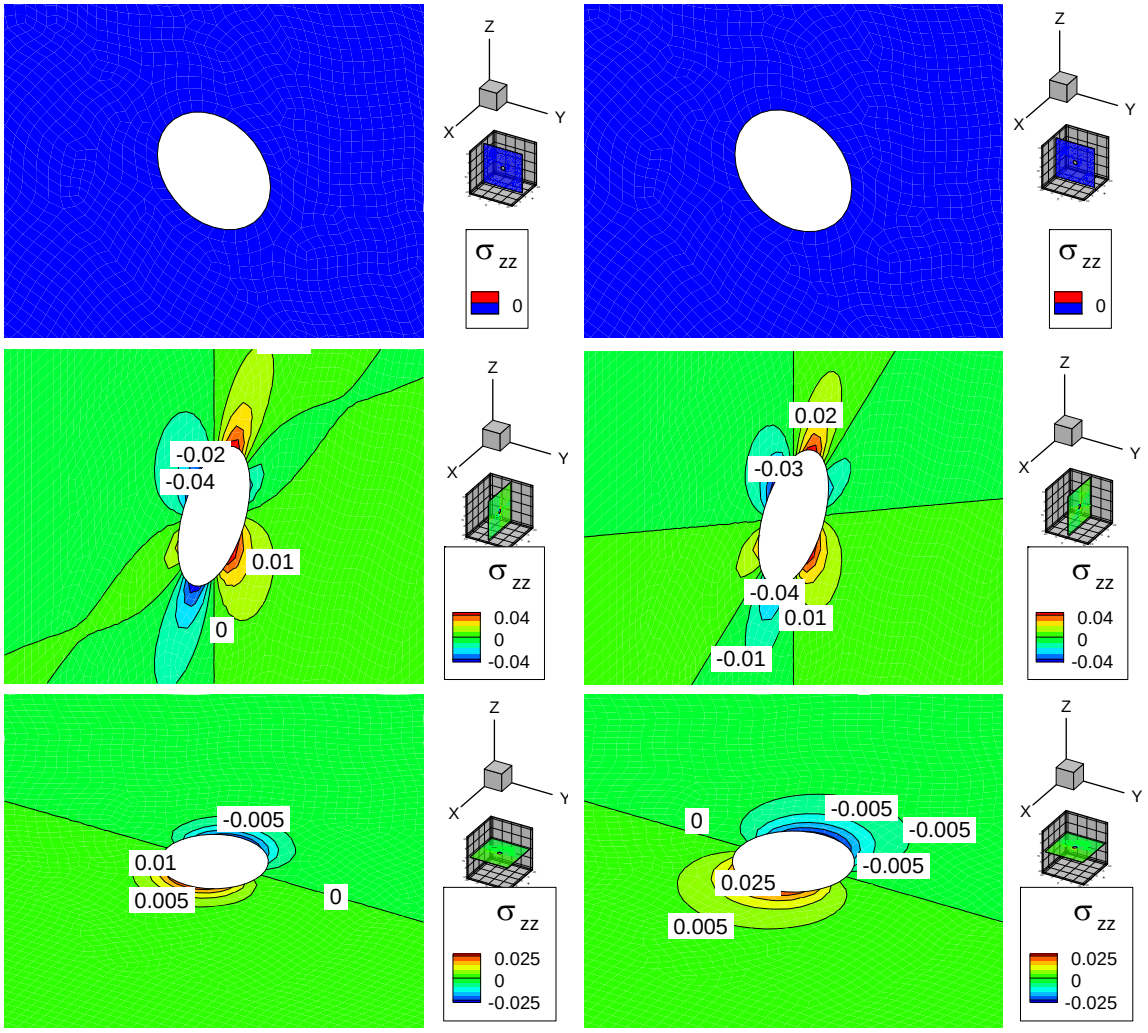

Figure B. 78 Induced total normal ZZ stress (MPa) distribution due to 1 MPa shear traction discontinuity (At X direction) at origin, after 20 minutes (left side figures), and after 100 days (right side figures)

Induced pore pressure is shown in Figure B. 79. Magnitude of induced pore pressure is not considerable and as a consequence pressure diffusion does not have much effect on displacement effect. As like as normal traction discontinuity effect, induced stresses are negligible for 1 MPa discontinuity and one can say that maximum induced

stress is in the applied force direction, which in this case is in X direction. Furthermore, induced pore pressure is very small and completely removed after 100 days.

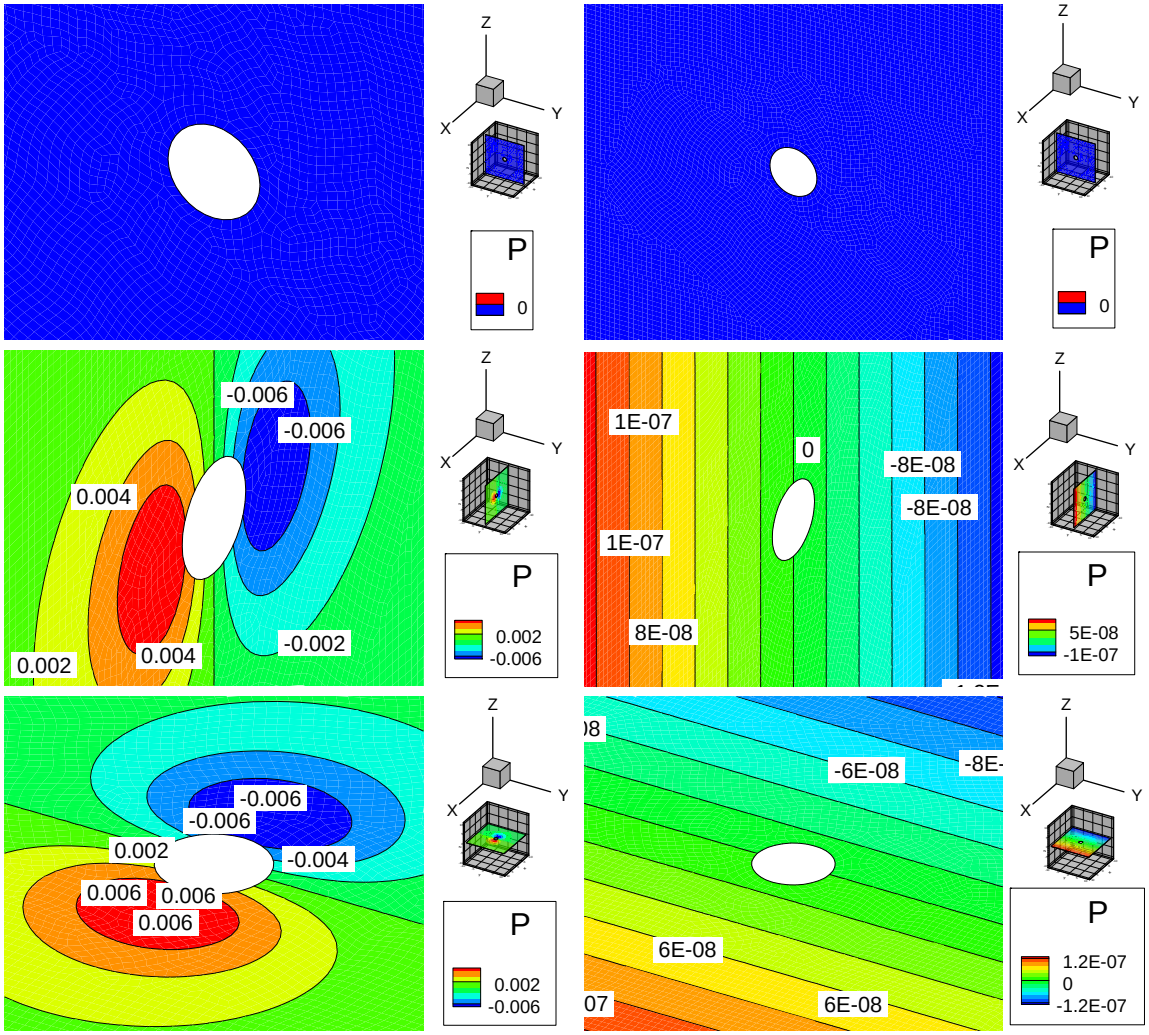

Figure B. 79 Induced pore pressure (MPa) distribution due to 1 MPa shear traction discontinuity (At X direction) at origin, after 20 minutes (left side figures), and after 100 days (right side figures)

APPENDIX C

COORDINATES TRANSFORMATION

Cartesian coordinate transformation is needed to calculate stress components in local coordinates of receiving points (receiver point that sense effects). In the transformation, origin of Cartesian coordinates fixed at global origin of model and axis rotate to be aligned to specific coordinates. There are three major Cartesian coordinates during stress calculation, global, influencing, and influenced element coordinates (see Figure C. 1).

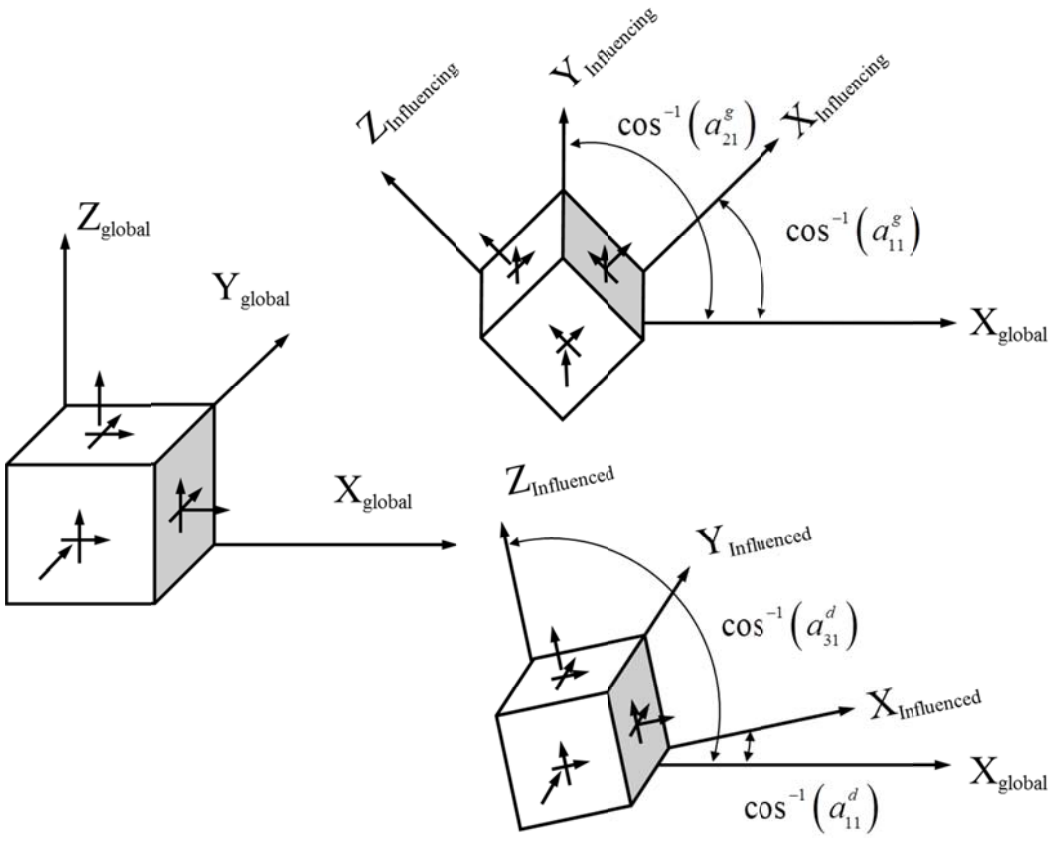

Figure C. 1. Major Cartesian coordinates

Stress components σ_{ij} in global Cartesian coordinates are transformed into new Cartesian coordinates, influenced (σ_{ij}^{d}) or influencing (σ_{ij}^{g}) coordinates, according to the tensor transformation rule:

$$\sigma_{ij}^{new} = a_{im}\, a_{jn}\, \sigma_{mn}$$

where a_{ij} is shown in Figure C. 1. Expanding indicial notations and simplifying terms using the symmetry of the stress tensor, gives the following relations:

$$\sigma_{11}^{new} = a_{11}^2\,\sigma_{11} + a_{12}^2\,\sigma_{22} + a_{13}^2\,\sigma_{33} + 2\,a_{11}\,a_{12}\,\sigma_{12} + 2\,a_{11}\,a_{13}\,\sigma_{13} + 2\,a_{12}\,a_{13}\,\sigma_{23}$$

$$\sigma_{22}^{new} = a_{21}^2\,\sigma_{11} + a_{22}^2\,\sigma_{22} + a_{23}^2\,\sigma_{33} + 2\,a_{21}\,a_{22}\,\sigma_{12} + 2\,a_{21}\,a_{23}\,\sigma_{13} + 2\,a_{22}\,a_{23}\,\sigma_{23}$$

$$\sigma_{33}^{new} = a_{31}^2\,\sigma_{11} + a_{32}^2\,\sigma_{22} + a_{33}^2\,\sigma_{33} + 2\,a_{31}\,a_{32}\,\sigma_{12} + 2\,a_{31}\,a_{33}\,\sigma_{13} + 2\,a_{32}\,a_{33}\,\sigma_{23}$$

$$\sigma_{12}^{new} = a_{11}\,a_{21}\,\sigma_{11} + a_{12}\,a_{22}\,\sigma_{22} + a_{13}\,a_{23}\,\sigma_{33} + \left(a_{11}\,a_{22} + a_{12}\,a_{21}\right)\sigma_{12} +$$
$$\left(a_{12}\,a_{23} + a_{13}\,a_{22}\right)\sigma_{23} + \left(a_{11}\,a_{23} + a_{13}\,a_{21}\right)\sigma_{13}$$

$$\sigma_{23}^{new} = a_{21}\,a_{31}\,\sigma_{11} + a_{22}\,a_{32}\,\sigma_{22} + a_{23}\,a_{33}\,\sigma_{33} + \left(a_{21}\,a_{32} + a_{22}\,a_{31}\right)\sigma_{12} +$$
$$\left(a_{22}\,a_{33} + a_{23}\,a_{32}\right)\sigma_{23} + \left(a_{21}\,a_{33} + a_{23}\,a_{31}\right)\sigma_{13}$$

$$\sigma_{13}^{new} = a_{11}\,a_{31}\,\sigma_{11} + a_{12}\,a_{32}\,\sigma_{22} + a_{13}\,a_{33}\,\sigma_{33} + \left(a_{11}\,a_{32} + a_{12}\,a_{31}\right)\sigma_{12} +$$
$$\left(a_{12}\,a_{33} + a_{13}\,a_{32}\right)\sigma_{23} + \left(a_{11}\,a_{33} + a_{13}\,a_{31}\right)\sigma_{13}$$

Note that in numerical procedure to calculate stress components, it is essential to convert stress tensor from local coordinate of influencing element to local coordinate of influenced element.

APPENDIX D

SPECIAL ALGORITHM FOR SINGULAR INTEGRALS

It can be observed from fundamental solution forms (Appendix A) that when it is tried to calculate effects of an elements on itself, the integrand reaches an infinite value at influencing point ($R \to 0.0$). Usually, the singular integral is defined by removing a small circle including the influencing point, and then taking the limit as the circle radius disappears. However in this appendix, proposed numerical method by [93, 94] for strong and hyper singular integral evaluation is reviewed. Strong or hyper singular integral occurs during numerical integration of generated stress fundamental solution due to fictitious stress or displacement discontinuity, respectively.

Generally during integration of thermoporoelastic fundamental solutions over an element, three types of singularities occur; weak, strong and hyper singularity. Weak singularity has a form of $\int_{\Gamma} (1/R)\, d\Gamma$, where Γ is a region that includes the condition that $R \to 0.0$. Weak singularity will be solved with increasing number of gauss points near singular point [86, 87]. The fundamental solution for induced pore pressure due to continuous point source has following form:

$$\{p\}^{sc} = \frac{1}{4\pi\ \kappa R} erfc\left(\xi_p\right)$$

If R goes to zero, consequently ξ_p goes to zero and complementary error function will have a unit value. Therefore, induced pore pressure will have following form near singular point:

$$\{p\}^{sc} = \frac{1}{4\pi\ \kappa R}$$

As it can be seen, kernel has $1/R$ singularity. Weak singularity can be eliminated by mapping from Cartesian coordinates to polar coordinates or can be captured by increasing number of gauss points [86, 87].

Strong singularity can have any form of $\int_{\Gamma}\left(1/R^2\right)d\Gamma$, $\int_{\Gamma}\left(r_i/R^2\right)d\Gamma$ $\int_{\Gamma}\left(\left(r_i\right)^2/R^2\right)d\Gamma$, $\int_{\Gamma}\left(\left(r_i\times r_j\right)/R^2\right)d\Gamma$, $\int_{\Gamma}\left(\left(\left(r_i\right)^2\times r_j\right)/R^2\right)d\Gamma$ where i and j can have value of 1 or 2. As like as weak singularity, strong singularity needs special treatment to evaluate. Strong singularity occurs when one tries to find an influence of an element on displacement or stress distribution of itself. So, influencing element and influenced element local coordinate system would be same and at influencing point R goes to zero.

As an example of strong singularity, one can look at Fundamental solution for first component of stress tensor (σ_{11}) due to unit fictitious force in "1" direction (F1). It has following format:

$$\left(\sigma_{11}\right)^{Fc} = \frac{1}{8\pi\left(1-\nu\right)}\frac{1}{R^2}\left\{-\left(1-2\nu\right)r_1 - 3\left[\left(r_1\right)^3\right] - \frac{\nu_u-\nu}{1-\nu_u}\left[D_p\times r_1 - 2E_p\times r_1 + 3F_p\left[\left(r_1\right)^3\right]\right]\right\}$$

Like as weak singularity case, it could show that when R goes to zero, subsequently ξ_p goes to zero and error function can be approximated by its Tailor expansion:

$$erf\left(\xi\right) = \frac{2\xi}{\sqrt{\pi}}\left(1-\frac{\xi^2}{3}+\frac{\xi^4}{10}-\frac{\xi^6}{42}+\frac{\xi^8}{216}-\frac{\xi^{10}}{1320}+\frac{\xi^{12}}{9360}-\ldots\right)$$

If Taylor expansion of error function is considered in side of D_p, E_p, F_p definitions, it would be seen that all of these time dependent functions in case of self-influence calculation, disappear and go to zero. Hence near singular point, σ_{11} due to fictitious force in "1" direction can be rewritten in following format:

$$\left(\sigma_{11}\right)^{Fc} = \frac{1}{8\pi\left(1-\nu\right)}\frac{1}{R^2}\left\{-\left(1-2\nu\right)r_1 - 3\left[\left(r_1\right)^3\right]\right\}$$

As it can be seen from preceding relation, stress has combination of strong singularity modes and should be treated specially to accurately calculate its value.

Strong singularity can be considered as a special case of hyper singularity. In following section, a numerical algorithm to evaluate any probable hyper singular integral is described. During method description, some changes that is essential to apply to the method to estimate strong singular integral is pointed out.

Hyper singular integrals might have following forms during numerical integration: $\int_\Gamma \left(1/R^3\right)d\Gamma$, $\int_\Gamma \left(r_i \times r_j/R^3\right)d\Gamma$, $\int_\Gamma \left(\left(r_i\right)^2/R^3\right)d\Gamma$ where i and j can be 1 or 2. To evaluate an integral in the Γ region which includes singular point, special procedure was proposed by [86, 87]. The method is based on Taylor expansion of all terms inside of integral near singular point.

In general, each integral consist of singular kernel and Jacobian determinant. To describe the method, initially different terms in the kernel were expanded around singular point and then Jacobian determinant is expanded. Then the expansions are combined to have series expansions of all terms inside of integral.

Let's assume that $\mathbf{x}=(x_1,x_2,x_3)$ is an influenced point global coordinates in an element and $\mathbf{y}=(y_1,y_2,y_3)$ is an influencing point global coordinates in same element. Corresponding local coordinates of points within mapped element are $\boldsymbol{\xi}=(\xi_1,\xi_2,0)$ and $\boldsymbol{\eta}=(\eta_1,\eta_2,0)$ (note that element are planar and third component of coordinates is zero). By employing a Taylor expansion of $(\mathbf{x}-\mathbf{y})$ around singular point, following relation will be obtained:

$$x_i-y_i=\left[\left.\frac{\partial x_i}{\partial\xi_1}\right|_{\boldsymbol{\xi}=\boldsymbol{\eta}}(\xi_1-\eta_1)+\left.\frac{\partial x_i}{\partial\xi_2}\right|_{\boldsymbol{\xi}=\boldsymbol{\eta}}(\xi_2-\eta_2)\right]+$$
$$\left[\left.\frac{\partial^2 x_i}{\partial\xi_1^2}\right|_{\boldsymbol{\xi}=\boldsymbol{\eta}}\frac{(\xi_1-\eta_1)^2}{2}+\left.\frac{\partial^2 x_i}{\partial\xi_1\times\partial\xi_2}\right|_{\boldsymbol{\xi}=\boldsymbol{\eta}}(\xi_1-\eta_1)(\xi_2-\eta_2)+\left.\frac{\partial^2 x_i}{\partial\xi_2^2}\right|_{\boldsymbol{\xi}=\boldsymbol{\eta}}\frac{(\xi_2-\eta_2)^2}{2}\right]+\ldots$$

Second bracket in the preceding relation is needed only for hyper singular integral evaluation. For strong singular integral evaluation, Taylor expansion until first bracket is sufficient.

For strong or hyper singularity evaluation, quadrilateral element is mapped into a unit square with 8 nodes. Location of node 5 to 8 is in the middle of each side of an element (see Figure D. 1). Singularity happens at the origin of mapped element ($\boldsymbol{\eta}=(0,0)$) and it is necessary to have more gauss point near the point. So mapped element is divided by four triangles as showed in Figure D. 2 and the integral is evaluated at each triangle and then the sum of each triangle share will be the total value of integral.

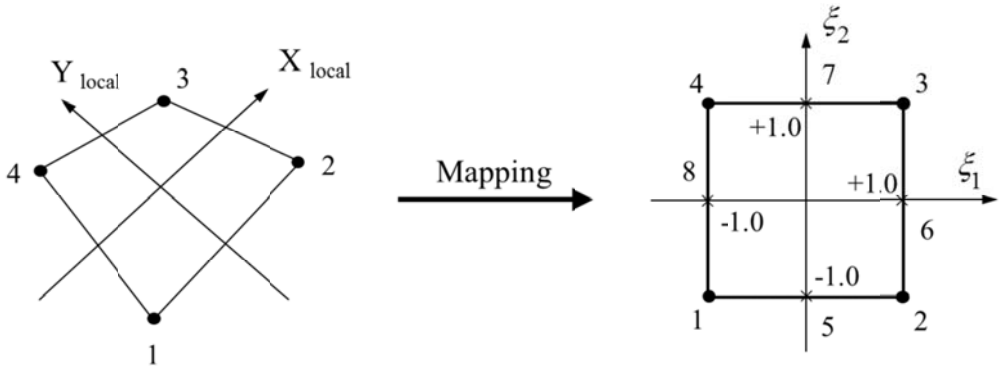

Figure D. 1 Special mapping for singularity evaluation

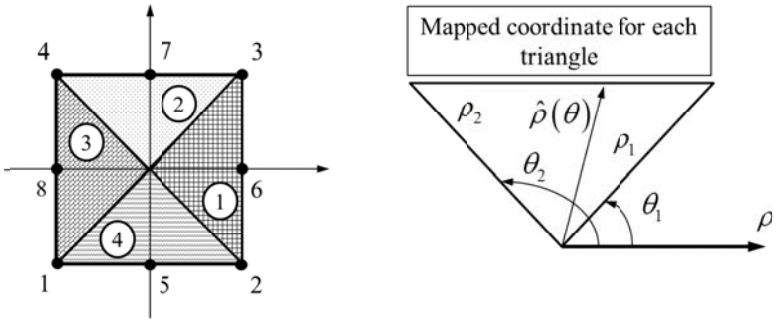

Figure D. 2. Mapped element divided by four triangles

If the introduced polar coordinates in Figure D. 2 applied to former relation, it can be rewritten as:

$$x_i - y_i = \left[\left.\frac{\partial x_i}{\partial \xi_1}\right|_{\xi=\eta} \cos\theta + \left.\frac{\partial x_i}{\partial \xi_2}\right|_{\xi=\eta} \sin\theta \right] +$$

$$\left[\left.\frac{\partial^2 x_i}{\partial \xi_1^2}\right|_{\xi=\eta} \frac{\cos^2\theta}{2} + \left.\frac{\partial^2 x_i}{\partial \xi_1 \times \partial \xi_2}\right|_{\xi=\eta} \cos\theta\sin\theta + \left.\frac{\partial^2 x_i}{\partial \xi_2^2}\right|_{\xi=\eta} \frac{\sin^2\theta}{2} \right] + O\left(\rho^3\right)$$

Or, more concisely:

$$x_i - y_i = \rho \times A_i(\theta) + \rho^2 \times B_i(\theta) + O\left(\rho^3\right)$$

where i can be 1,2 or 3, and $A(\theta)$ and $B(\theta)$ are simple trigonometric functions of θ as:

$$A(\theta)=\left\{\sum_{k=1}^{3}\left[A_i(\theta)\right]\right\}^{0.5},\quad B(\theta)=\left\{\sum_{k=1}^{3}\left[B_i(\theta)\right]\right\}^{0.5}$$

$$A_i=\left[\left.\frac{\partial x_i}{\partial\xi_1}\right|_{\xi=0,\eta=0}\cos\theta+\left.\frac{\partial x_i}{\partial\xi_2}\right|_{\xi=0,\eta=0}\sin\theta\right],$$

$$B_i=\left[\left.\frac{\partial^2 x_i}{\partial\xi_1^2}\right|_{\xi=0,\eta=0}\frac{\cos^2\theta}{2}+\frac{\partial^2 x_i}{\partial\xi_1\times\partial\xi_2}\cos\theta\sin\theta+\left.\frac{\partial^2 x_i}{\partial\xi_2^2}\right|_{\xi=0,\eta=0}\frac{\sin^2\theta}{2}\right]$$

In addition to Taylor expansion of $(\mathbf{x}-\mathbf{y})$ term, it is necessary to expand $1/R$ and $1/R^3$. Therefore, based on former relations and introduced polar coordinates, following relations can be derived:

$$\frac{1}{R}=\frac{1}{\rho A}\left[1-\frac{A_kB_k}{A^2}\rho+O(\rho^2)\right]$$

$$\frac{1}{R^3}=\frac{1}{\rho^3A^3}-\frac{3A_kB_k}{\rho^2A^5}+O\left(\frac{1}{\rho}\right)$$

By considering former relation of (x_i-y_i) and $1/R$, it can be derived that:

$$r_{,i}=\frac{x_i-y_i}{R}=\frac{A_i}{A}+\rho\left(\frac{B_i}{A}-A_i\frac{A_kB_k}{A^3}\right)+O(\rho^2)$$

In side of expanded relations, Taylor expansion of Jacobian determinant is necessary. By using introduced polar coordinates, Jacobian determinant can be expanded as:

$$J(\boldsymbol{\xi})=J(\boldsymbol{\eta})+\rho\left[\left.\frac{\partial J}{\partial\xi_1}\right|_{\boldsymbol{\xi}=\boldsymbol{\eta}}\cos\theta+\left.\frac{\partial J}{\partial\xi_2}\right|_{\boldsymbol{\xi}=\boldsymbol{\eta}}\sin\theta\right]+O(\rho^2)=J_0+\rho J_1+O(\rho^2)$$

where;

$$J = |\mathbf{J}| = \frac{\partial x}{\partial \xi_1}\frac{\partial y}{\partial \xi_2} - \frac{\partial y}{\partial \xi_1}\frac{\partial x}{\partial \xi_2}$$

$$\frac{\partial J}{\partial \xi_1} = \frac{\partial^2 x}{\partial \xi_1^2}\frac{\partial y}{\partial \xi_2} + \frac{\partial x}{\partial \xi_1}\frac{\partial^2 y}{\partial \xi_1 \times \partial \xi_2} - \frac{\partial^2 y}{\partial \xi_1^2}\frac{\partial x}{\partial \xi_2} - \frac{\partial y}{\partial \xi_1}\frac{\partial^2 x}{\partial \xi_1 \times \partial \xi_2}$$

$$\frac{\partial J}{\partial \xi_2} = \frac{\partial^2 x}{\partial \xi_1 \times \partial \xi_2}\frac{\partial y}{\partial \xi_2} + \frac{\partial x}{\partial \xi_1}\frac{\partial^2 y}{\partial \xi_2^2} - \frac{\partial^2 y}{\partial \xi_1 \times \partial \xi_2}\frac{\partial x}{\partial \xi_2} - \frac{\partial y}{\partial \xi_1}\frac{\partial^2 x}{\partial \xi_2^2}$$

To be able to evaluate $\partial J/\partial \xi_1$ and $\partial J/\partial \xi_2$, it is necessary to calculate second order derivative of x and y, and consequently second order shape functions. The main reason that four points added to a mapped element is to have second order shape functions (see Figure D. 2). To evaluate Taylor expansion of Jacobian determinant, following matrices are defined:

$$\mathbf{Der} = \begin{bmatrix} \frac{\partial N_1}{\partial \xi_1} & \frac{\partial N_2}{\partial \xi_1} & \frac{\partial N_3}{\partial \xi_1} & \frac{\partial N_4}{\partial \xi_1} & \frac{\partial N_5}{\partial \xi_1} & \frac{\partial N_6}{\partial \xi_1} & \frac{\partial N_7}{\partial \xi_1} & \frac{\partial N_8}{\partial \xi_1} \\ \frac{\partial N_1}{\partial \xi_2} & \frac{\partial N_2}{\partial \xi_2} & \frac{\partial N_3}{\partial \xi_2} & \frac{\partial N_4}{\partial \xi_2} & \frac{\partial N_5}{\partial \xi_2} & \frac{\partial N_6}{\partial \xi_2} & \frac{\partial N_7}{\partial \xi_2} & \frac{\partial N_8}{\partial \xi_2} \end{bmatrix}$$

$$\mathbf{Coord} = \begin{bmatrix} x_1 & x_2 & x_3 & x_4 & x_5 & x_6 & x_7 & x_8 \\ y_1 & y_2 & y_3 & y_4 & y_5 & y_6 & y_7 & y_8 \end{bmatrix}$$

$$\mathbf{Der\text{-}2nd} = \begin{bmatrix} \frac{\partial^2 N_1}{\partial \xi_1^2} & \frac{\partial^2 N_2}{\partial \xi_1^2} & \cdots & \frac{\partial^2 N_7}{\partial \xi_1^2} & \frac{\partial^2 N_8}{\partial \xi_1^2} \\ \frac{\partial^2 N_1}{\partial \xi_1 \times \partial \xi_2} & \frac{\partial^2 N_2}{\partial \xi_1 \times \partial \xi_2} & \cdots & \frac{\partial^2 N_7}{\partial \xi_1 \times \partial \xi_2} & \frac{\partial^2 N_8}{\partial \xi_1 \times \partial \xi_2} \\ \frac{\partial^2 N_1}{\partial \xi_2^2} & \frac{\partial^2 N_2}{\partial \xi_2^2} & \cdots & \frac{\partial^2 N_7}{\partial \xi_2^2} & \frac{\partial^2 N_8}{\partial \xi_2^2} \end{bmatrix}$$

where N_1 to N_8 are as follows:

$$N_1 = 0.25(1-\xi_1)(1-\xi_2)(-\xi_1-\xi_2-1)$$
$$N_2 = 0.25(1+\xi_1)(1-\xi_2)(\xi_1-\xi_2-1)$$
$$N_3 = 0.25(1+\xi_1)(1+\xi_2)(\xi_1+\xi_2-1)$$
$$N_4 = 0.25(1-\xi_1)(1+\xi_2)(-\xi_1+\xi_2-1)$$
$$N_5 = 0.50(1-\xi_1^2)(1-\xi_2)$$
$$N_6 = 0.50(1+\xi_1)(1-\xi_2^2)$$
$$N_7 = 0.50(1-\xi_1^2)(1+\xi_2)$$
$$N_8 = 0.50(1-\xi_1)(1-\xi_2^2)$$

Based on preceding relations, Jacobian and second derivative of geometric variables can be defined as follows:

$$\mathbf{J} = \begin{bmatrix} \dfrac{\partial x}{\partial \xi_1} & \dfrac{\partial y}{\partial \xi_1} \\ \dfrac{\partial x}{\partial \xi_2} & \dfrac{\partial y}{\partial \xi_2} \end{bmatrix} = (\mathbf{Der})(\mathbf{Coord})^T$$

$$\begin{bmatrix} \dfrac{\partial^2 x}{\partial \xi_1^2} & \dfrac{\partial^2 y}{\partial \xi_1^2} \\ \dfrac{\partial^2 x}{\partial \xi_1 \times \partial \xi_2} & \dfrac{\partial^2 y}{\partial \xi_1 \times \partial \xi_2} \\ \dfrac{\partial^2 x}{\partial \xi_2^2} & \dfrac{\partial^2 y}{\partial \xi_2^2} \end{bmatrix} = (\mathbf{Der\text{ - }2nd})(\mathbf{Coord})^T$$

Currently, $J, \partial J/\partial \xi_1$ and $\partial J/\partial \xi_2$ can be defined and then J_0 and J_1 would be evaluated. Now, with referring to $1/R^3$, $r_{,i}$ and $|\mathbf{J}|$ Taylor expansions, any combination of hyper singular integral kernel, can be expressed as a series expansion with respect to ρ in the following form:

$$F(\rho,\theta) = \frac{F_{-2}(\theta)}{\rho^2} + \frac{F_{-1}(\theta)}{\rho} + O(1)$$

Then the final form of integral can be written as follows:

$$I=\sum_{tn=1}^{4}\left\{\int_{(\theta_1)^{tn}}^{(\theta_2)^{tn}}\int_{0}^{\hat{\rho}(\theta)}F(\rho,\theta)\,d\rho\,d\theta\right\}=$$

$$\left\{\begin{array}{l}\displaystyle\int_{(\theta_1)^{tn}}^{(\theta_2)^{tn}}\int_{0}^{\hat{\rho}(\theta)}\left\{F(\rho,\theta)-\left[\frac{F_{-2}(\theta)}{\rho^2}-\frac{F_{-1}(\theta)}{\rho}\right]\right\}d\rho\,d\theta+\\ \displaystyle\int_{(\theta_1)^{tn}}^{(\theta_2)^{tn}}\left\{F_{-1}(\theta)\ln\left|\frac{\hat{\rho}(\theta)}{\beta(\theta)}\right|-F_{-2}(\theta)\left[\frac{\gamma(\theta)}{\beta^2(\theta)}+\frac{1}{\hat{\rho}(\theta)}\right]\right\}d\theta\end{array}\right\}$$

where $\beta(\theta)=1/A(\theta)$, $\gamma(\theta)=-A_kB_k/A^4$. All integrations involved in preceding equation are regular and can be evaluated directly by standard numerical methods. In presented formulation subscript "tn" is number of triangles that is shown in Figure D. 2 and $\theta_1,\theta_2,\hat{\rho}(\theta)$ are geometric parameters that are shown in Figure D. 2. With the help of distinctive procedure that is summarized here and completely presented in [86, 87], a hyper singular integral with following form is expanded and evaluated as an example:

$$I=\sum_{tn=1}^{4}\left\{\int_{(\theta_1)^{tn}}^{(\theta_2)^{tn}}\int_{0}^{\hat{\rho}(\theta)}\frac{r_{,1}}{R^3}|\mathbf{J}|\,\rho\,d\rho\,d\theta\right\}$$

By employing preceding Taylor expansion relations of $r_{,1}$, $1/R^3$, $|\mathbf{J}|$, the following formulas are established:

$$r_{,i}=d_{i0}(\theta)+\rho\,d_{i1}(\theta)+O(\rho^2)$$

$$d_{i0}(\theta)=\frac{A_i}{A},\ d_{i1}(\theta)=\frac{B_i}{A}-A_i\frac{A_kB_k}{A^3}$$

$$\frac{1}{R^3}=\frac{S_{-3}(\theta)}{\rho^3}+\frac{S_{-2}(\theta)}{\rho^2}+O\left(\frac{1}{\rho}\right)$$
$$S_{-3}(\theta)=\frac{1}{A^3},\ S_{-2}(\theta)=-\frac{3A_kB_k}{A^5}$$

$$J=|\mathbf{J}|$$
$$J=J_0+\rho J_1(\theta)+O(\rho^2)$$
$$J_0=J(0.0,0.0)$$
$$J_1(\theta)=\frac{\partial J}{\partial \xi_1}\cos\theta+\frac{\partial J}{\partial \xi_2}\sin\theta$$

Now, by substituting these relations into integration core, the outcome will be:

$$F(\rho,\theta)=\frac{r_{,x}}{R^3}J\times\rho$$
$$=\rho\left[\frac{S_{-3}(\theta)}{\rho^3}+\frac{S_{-2}(\theta)}{\rho^2}+O\left(\frac{1}{\rho}\right)\right]\left\{\left[d_{i0}(\theta)+\rho d_{i1}(\theta)+O(\rho^2)\right]\times\left[J_0+\rho J_1(\theta)+O(\rho^2)\right]\right\}$$
$$=\left[\frac{S_{-3}(\theta)}{\rho^2}+\frac{S_{-2}(\theta)}{\rho}+O(1)\right]\left\{d_{i0}(\theta)J_0+\rho\left(d_{i0}(\theta)J_1(\theta)+d_{i1}(\theta)J_0\right)+O(\rho^2)\right\}$$
$$=\frac{S_{-3}(\theta)\times d_{i0}(\theta)J_0}{\rho^2}+\frac{S_{-2}(\theta)\times d_{i0}(\theta)J_0+S_{-3}(\theta)\times\left(d_{i0}(\theta)J_1(\theta)+d_{i1}(\theta)J_0\right)}{\rho}+O(1)$$

$$F_{-2}(\theta)=S_{-3}(\theta)\times d_{i0}(\theta)J_0$$
$$F_{-1}(\theta)=S_{-2}(\theta)\times d_{i0}(\theta)J_0+S_{-3}(\theta)\times\left(d_{i0}(\theta)J_1(\theta)+d_{i1}(\theta)J_0\right)$$

By using the presented formulation the hyper singular integral can be treated as a usual Gauss integral and it can be evaluated numerically. Strong singularity evaluation is same as above, except the degree of singularity which is one degree less and as a consequence each term inside of integration core will be expanded one degree fewer than above.